Molecular Ions

Geometric and Electronic Structures

NATO Advanced Science Institutes Series

A series of edited volumes comprising multifaceted studies of contemporary scientific issues by some of the best scientific minds in the world, assembled in cooperation with NATO Scientific Affairs Division.

This series is published by an international board of publishers in conjunction with NATO Scientific Affairs Division

A Life Sciences **B Physics**	Plenum Publishing Corporation New York and London
C Mathematical and Physical Sciences	D. Reidel Publishing Company Dordrecht, Boston, and London
D Behavioral and Social Sciences **E Applied Sciences**	Martinus Nijhoff Publishers The Hague, Boston, and London
F Computer and Systems Sciences **G Ecological Sciences**	Springer Verlag Heidelberg, Berlin, and New York

Recent Volumes in Series B: Physics

Volume 87 —Relativistic Effects in Atoms, Molecules, and Solids
edited by G. L. Malli

Volume 88 —Collective Excitations in Solids
edited by Baldassare Di Bartolo

Volume 89a—Electrical Breakdown and Discharges in Gases: Fundamental Processes and Breakdown
edited by Erich E. Kunhardt and Lawrence H. Luesen

Volume 89b—Electrical Breakdown and Discharges in Gases: Macroscopic Processes and Discharges
edited by Erich E. Kunhardt and Lawrence H. Luessen

Volume 90 —Molecular Ions: Geometric and Electronic Structures
edited by Joseph Berkowitz and Karl Ontjes-Groeneveld

Volume 91 —Integrated Optics: Physics and Applications
edited by S. Martellucci and A. N. Chester

Volume 92 —The Physics of Superionic Conductors and Electrode Materials
edited by John W. Perram

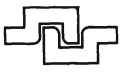

Molecular Ions

Geometric and Electronic Structures

Edited by

Joseph Berkowitz

Argonne National Laboratory
Argonne, Illinois, U.S.A.

and

Karl-Ontjes Groeneveld

Johann Wolfgang Goethe-Universität
Frankfurt am Main, Federal Republic of Germany

Plenum Press
New York and London
Published in cooperation with NATO Scientific Affairs Division

Proceedings of a NATO Advanced Study Institute on Molecular Ions:
Geometric and Electronic Structures,
held September 30–October 10, 1980,
on the Isle of Kos, Greece

Library of Congress Cataloging in Publication Data

NATO Advanced Study Institute on Molecular Ions: Geometric and Electronic Structures (1980: Isle of Kos, Greece)
Molecular ions.

(NATO advanced science institutes series. Series B, Physics; v. 90)
"Published in cooperation with NATO Scientific Affairs Division."
"Proceedings of a NATO Advanced Study Institute on Molecular Ions: Geometric and Electronic Structures, held September 30–October 10, 1980, on the Isle of Kos, Greece"—Verso of t.p.
Bibliography: p.
Includes index.
1. Ions—Congresses. 2. Molecular structure—Congresses. I. Berkowitz, Joseph, 1930– . II. Groeneveld, Karl-Ontjes, 1935– . III. Title. IV. Series.
QD561.N37 1980 541.3'72 83-2446

ISBN-13: 978-1-4613-3666-2 e-ISBN-13: 978-1-4613-3664-8

DOI: 10.1007/978-1-4613-3664-8

Softcover reprint of the hardcover 1st edition 1983

A Division of Plenum Publishing Corporation
233 Spring Street, New York, N.Y. 10013

PREFACE

The present volume contains contributions presented at the NATO Advanced Study Institute on Molecular Ions held on the island of Kos, Greece, from September 30 to October 10, 1980. The meeting was attended by some 60 participants from 15 different countries. It was the first meeting devoted exclusively to the topic of molecular ions. Its vitality derived from bringing together experts and students from a wide variety of disciplines, whose studies bear upon the structure of molecular ions. The aim of the meeting was to assemble these scientists, representing many countries in Europe and North America, to discuss the advances and capabilities of the various experimental and theoretical approaches and to point out unsolved problems and directions for future research. The format, involving lecturers and students, served as a tutorial.

Molecular ions play an important role in very diverse fields of nature such as reactions in the ionosphere, the processes of formation of molecules in dense interstellar clouds, and the magnetohydrodynamics of plasmas used for energy generation.

Our understanding of the properties of molecular ions, their electronic and geometric structures, has been developing from a variety of sources, as far removed as tickling ions with radiofrequency radiation and smashing them apart at relativistic energies. Various laser techniques are described, and the queen of structural determination, spectroscopy, is well represented. On the instrumental side, older techniques have been perfected and new methods have evolved. Various levels of sophistication of quantum-mechanical calculations are presented, and the impetus toward convergence between theory and experiment can be seen.

The prospects seem very good for many more molecular ion structures to be determined in the next couple of years than the handful of triatomics and even fewer polyatomics now known.

The complete volume represents frontier knowledge about the field of molecular ions, their geometric and electronic structures.

Unfortunately the book was delayed in the publishing process for reasons outside the editors' control. Etymologically, the Latin word "moles" means "burden, load, heaviness"; "molecule" corresponds to "little burden" -- quite an inappropriate term for the effort invested in overcoming the above-mentioned delay, for which the editors apologize.

Joseph Berkowitz

Argonne, IL

Karl-Ontjes E. Groeneveld

Frankfurt/Main

ACKNOWLEDGMENTS

The editors wish to acknowledge the generous support of NATO Scientific Affairs Division, Brussels, administered by Mario di Lullo. Support by the Office of Naval Research of the U.S. Department of the Navy through the help of F. E. Saalfeld and the National Science Foundation, Washington, D.C., U.S.A., is gratefully acknowledged. Most helpful support by the Badische Anilin and Soda Fabrik/Ludwigshafen through Klaus Bethge is recognized. The institutional support provided by the Physics Department of Argonne National Laboratory and by the University of Frankfurt/Main was essential for the ASI. Many individuals contributed to the successful organization of the ASI; the editors recognize especially the efforts of institutional secretaries and the members of the organizing committee and Dr. J. Theodorakopoulos, H.J. Frischkorn, and Peter Koschar.

CONTENTS

I. INTRODUCTORY PRESENTATION

II. MICROWAVE AND LASER SPECTROSCOPY OF MOLECULAR IONS

III. SPECTROSCOPIES OF MOLECULAR IONS (IR, Visible, UV, and Photoelectron)

Contributed Papers

Contributed Papers

V. STRUCTURAL AND RELATED STUDIES USING MeV MOLECULAR IONS

VI. OTHER STUDIES OF MOLECULAR ION PROPERTIES

Contributed Papers

SPECTROSCOPY OF MOLECULAR IONS - A HISTORICAL SURVEY

Alan Carrington

Department of Chemistry
University of Southampton
Hampshire, England

INTRODUCTION

The spectroscopy of gaseous molecular ions has always presented exciting challenges and some of the contemporary work in this field is of the very highest quality and originality. The would-be historian attempting to locate the foundations of the subject, however, will find it a confusing task -- but he will encounter some gems of prose and foresight in the process. Dr. Arthur Schuster working in Clerk Maxwell's laboratory in Cambridge was one of the first to observe the green-yellow glow produced by an electric discharge in oxygen [1] and comments (1878): "The many unexplained phenomena attending the passage of electricity through gases will probably for some time to come occupy the attention of experimental physicists. It is desirable that the subject should be approached from as many different sides as possible. One of our most powerful instruments of research is the spectroscope ...". One doubts that Schuster could foresee the many types of "spectroscope" which would be developed during the succeeding 100 years, but his statement could be made with as much validity today. Even earlier, in 1877, Schuster writes [2]: "As the science of spectroscopy advances we shall be able to determine the physical conditions which exist on the surface of the sun with as great a degree of certainty and a much smaller degree of discomfort than if we were placed there ourselves". Most contemporary editors would greet that sentence with a red pen, more's the pity, but would not deny that spectroscopy and astronomy have often overlapped to the mutual benefit of their development.

The emission spectrum of the O_2^+ ion was certainly one of the first such spectra to be observed, although it was not recognized

as such by Schuster. By 1924 Johnson [3], in a careful study, had concluded that the emission was not due to ozone but to an oxygen-type molecule. The situation was muddied somewhat by Stark who attributed the spectrum to "... a monoatomic oxygen molecule" but in 1927 Ellsworth and Hopfield [4] made an essentially correct analysis of the vibrational structure and described the emission spectrum as the second-negative system of the O_2^+ ion. Unfortunately the emission in question, which we would now describe as being due to the $A^2\Pi_u \rightarrow X^2\Pi_g$ transition, is also now known as the first-negative system!

During the late 1920's a number of electronic emission spectra of diatomic molecular ions were observed, identified and analyzed correctly. They included HCl^+, BeH^+, and N_2^+ [5,6]. The traditional methods of electronic spectroscopy have continued to be productive, and have provided most of the definitive information which is available about molecular ion structure. Much of this article will be concerned with recent and novel approaches to the solutions of old problems but those who work with lasers, ion beams, quadrupole traps, computers, etc. (including the author) might be reminded of the beauty, depth, and precision of the information provided by the classic methods of electronic spectroscopy, particularly the spectrographic method. It is to this subject which we turn first.

ELECTRONIC SPECTROSCOPY

The electronic spectroscopy of molecular ions has been reviewed by Herzberg [7]. Emission spectra are usually excited by an appropriate discharge in a low pressure gas; this method often produces electronically-excited neutral molecules and radicals in addition to ions, so that the problems of disentangling overlapping spectra are often acute. Among many examples the reader might enjoy the beautiful emission spectrum of CN^+ obtained by Lutz [8]. Absorption spectra are usually obtained through a modification of the flash photolysis technique, in which the ions are produced by an electrical pulse and the absorption spectrum photographed after a short time interval. Excellent examples are the absorption spectrum of C_2^- obtained by Herzberg and Lagerqvist [9] and the emission spectrum of $HeNe^+$ observed recently by Dabrowski and Herzberg [10]. Laboratory studies have confirmed that molecular ions are often present in astronomical sources. For example, the absorption spectrum of CH^+ is observed in interstellar regions, the spectrum of H_2O^+ has been observed in the tail of the comet Kohoutek [11], whilst the CO^+ and CO_2^+ ions are now known to be present in the upper atmosphere of Mars [12]. All of these ions have been studied in the laboratory by spectrographic techniques, and more recently electron impact or laser-induced fluorescence techniques have been applied to the study of

more complex ions (see, for example, Miller [13], Leach [14], and Maier [15] and further references given by these authors).

PHOTOIONIZATION AND PHOTODISSOCIATION METHODS

Alternative approaches to the determination of electronic state energies in ions have involved processes such as photoionization or photodissociation, combined with momentum analysis of electrons, atomic or molecular fragments. The most widely developed of these methods is the technique known as photoelectron spectroscopy in which a neutral gas is ionized by monochromatic radiation from an appropriate source and the kinetic energy of the ionized electron determined. Through the use of high energy radiation sources it is possible to produce the conjugate positive ion in electronic states of increasing energy and in many cases this technique has so far been the sole source of information (see, for example, [16]). The disadvantage of photoelectron spectroscopy is its relatively low resolution which is two to three orders of magnitude lower than that obtained by Doppler-limited spectrographic methods. A variant of photoelectron spectroscopy which yields much higher resolution consists of employing a tunable radiation source and detecting the photoelectrons produced with threshold energies of 2 to 3mV. The present lack of suitable radiation sources, particularly of shorter wavelength, means that this technique has been of limited application so far, but a nice example is to be found in the work of Peatman on the H_2^+ ion [17].

Photodissociation methods employ either cyclotron resonance methods for ion detection or ion beams. Irradiation of a beam of HD^+ ions, for example, with an argon ion laser beam leads to photodissociation; the H^+ or D^+ ions produced may then be momentum analyzed and the results used to determine vibrational energies of the parent ion. Again, the technique is of low resolution compared with conventional spectroscopic methods (see, for example, Van Asselt, Maas and Los [18]) except in certain special cases involving predissociation which we describe later.

RADIOFREQUENCY SPECTRUM OF H_2^+

Only one ion, the H_2^+ ion, has been successfully studied by radiofrequency spectroscopy. The ideas and techniques employed have, however, been developed by others and the work therefore occupies an important position in the development of the subject. The principles were first outlined by Dehmelt and Jefferts [19]; the H_2^+ ions are formed by electron impact on H_2 and are contained in a quadrupole radiofrequency trap for periods of several seconds. They are irradiated with polarized white light in the presence of a magnetic field. Photodissociation occurs and at the end of a

prescribed time interval of irradiation, the number of H_2^+ ions remaining is counted. Now the measured photodissociation rate depends, among other things, on the spatial orientation of the H_2^+ ions so that different magnetic sublevels photodissociate at different rates. Consequently, as photodissociation proceeds the remaining H_2^+ ions develop a degree of preferred spatial alignment. Application of a radiofrequency field with the appropriate crossed polarization tends to destroy the spatial alignment when the radiofrequency is resonant with an appropriate spectroscopic transition. Since a partially aligned sample photodissociates more slowly than an unaligned one, the photodissociation rate is increased by the presence of a resonant radiofrequency field. Hence radiofrequency transitions can be detected by sweeping either the frequency or the applied magnetic field and monitoring the photodissociation rate. Richardson, Dehmelt and Jefferts [20] detected magnetic resonance hyperfine transitions and subsequent papers by Jefferts [21] describe the observation of swept frequency hyperfine transitions. Very high resolution was obtained, with linewidths down to 1kHz or less.

While the original experiment has not been applied to other ions, the idea of using the dependence of photodissociation rate on internal state distribution has been used in other techniques which employ ion beams.

ROTATIONAL SPECTROSCOPY

Detection of molecular ions by microwave spectroscopy has proved to be extremely difficult and the first successful studies were actually reported by radioastronomers. An interstellar line at 89190MHz was correctly attributed to HCO^+ and subsequently interstellar lines for N_2H^+ were detected and identified [22,23]. The same transitions in these two ions were then studied in the laboratory by Woods and his colleagues [24]. In a series of outstanding papers they described the development of a microwave spectrometer which could be used to study transient molecular species (ions and free radicals) present in a discharge plasma. Most microwave spectroscopists had believed that such experiments were not feasible, noise and non-resonant microwave absorption being unacceptably severe. A careful analysis by Woods [25] showed these views to be over-pessimistic, and Woods and Dixon [26] described a spectrometer which was used to detect microwave spectra of the HCO^+, N_2H^+, and CO^+ [27,24,28] ions. The spectrometer employed a free space cell with a sustained dc glow discharge, and high sensitivity was achieved either by Zeeman modulation or source modulation. It should be noted that for the three ions studied the frequency search problem was removed because of the data already available, and it will be interesting to see if laboratory detection of ions whose spectra are unknown will be

achieved.

An alternative approach to the rotational spectroscopy of molecular ions is through magnetic resonance techniques and the method known as laser magnetic resonance is particularly sensitive. The radiation source is a far-infrared molecular laser and radicals or ions which are paramagnetic can be tuned into resonance with the laser by means of an external magnetic field. Saykally and Evenson [29] have recently succeeded in observing rotational transitions in the HBr^+ ion using this method. They obtained excellent signal-to-noise ratios and resolution sufficient for the observation of bromine hyperfine structure. This technique is likely to prove successful in other cases in the near future.

ION BEAM STUDIES

The attractions of an ion beam as a medium for spectroscopy are readily evident; many positive ions can be extracted from electron impact sources, mass analysis using magnetic or electrostatic selection enables separation and identification of the ions, and the ion beam intensity is easily determined. The technology of mass spectrometry is highly developed, and is commercially available. The only real disadvantage is that even for intense molecular ion beams, the ion density is too low for absorption spectroscopy and only in certain special cases is electronic emission spectroscopy feasible. Consequently, much effort has been devoted to the development of indirect techniques for the detection of spectroscopic transitions [30]. The underlying principle of these techniques is that changes in internal state distribution produced by absorption of radiation should lead to changes in flux, of either the parent ion which absorbs the radiation, or of a secondary ion. We now describe four different applications of this principle, all taken from the recent literature.

Electron Photodetachment

One of the earliest examples of a successful spectroscopic experiment using an ion beam was described by Lineberger and Patterson [31]. They formed a beam of C_2^- ions and observed that irradiation with near-ultraviolet or visible light from a laser source led to photodetachment of an electron with the production of neutral C_2 molecules which could be detected directly. Single step photodetachment is of interest in itself but provides only limited spectroscopic information. However, Lineberger and Patterson found that by scanning the laser wavelength electronic excitation of the C_2^- could be induced, the excited C_2^- ions then absorbing a second photon to produce the detected C_2 particles:

$$C_2^- \left(^2\Sigma_g^+\right) \xrightarrow{h\nu} C_2^- \left(^2\Sigma_u^+\right) \rightarrow C_2 + e^-$$

A well-resolved electronic spectrum of C_2^- was obtained, with good signal-to-noise ratio.

Predissociation

A number of authors have described studies of the O_2^+ ion which depend upon predissociation [32]. Electron impact ionization of O_2 leads to substantial population of the metastable $^4\Pi_u$ state. Radiation in the wavelength wave 4000-5000Å excites transitions to the $^4\Sigma_g^-$ state, which undergoes predissociation with the production of O^+ ions which can be separated from O_2^+ and detected. Some workers have used a swept-frequency dye laser as the radiation source, while others have used a fixed-frequency argon ion laser beam aligned to be colinear with the ion beam. Variation of the ion beam potential enables the ion velocity and hence Doppler shift to be swept, so that spectra can be obtained. The technique is very sensitive because each photon absorbed leads to the production of one O^+ ion; ions can be detected with virtually 100% efficiency. The resolution is also high because of a subtle effect known as kinematic compression or velocity bunching which occurs for fast ion beams, and which greatly reduces the Doppler width.

Charge Exchange

Undoubtedly the most important technique for observing spectra of ion beams is that developed by Wing and his collaborators which utilizes charge exchange reactions between the ions and neutral molecules. In a classic experiment Wing, Ruff, Lamb, and Spezeski [33] showed that vibration-rotation transitions in the HD^+ ion could be detected by measuring the attenuation of beam intensity produced by charge-exchange with H_2 and observing the change in beam intensity which occurred when vibration-rotation transitions were pumped with a CO infrared laser. They used the Doppler tuning method and observed rotational components of the $1 \leftarrow 0$, $2 \leftarrow 1$, and $3 \leftarrow 2$ vibrational bands, with linewidths down to a few MHz. Subsequently, Wing and his coworkers have used the same technique to observe vibration-rotation transitions in HeH^+ [34] and D_3^+ [35].

Carrington, Milverton, Sarre [36] have shown that charge-exchange can also be used to detect electronic absorption spectra of molecular ions in beams. They studied the CO^+ ion and, using ^{13}C enriched carbon monoxide, were able to demonstrate the very

high resolution attainable by resolving ^{13}C nuclear hyperfine structure.

Photodissociation

Carrington, Roberts, and Buttenshaw [37] have recently described an alternative method of obtaining vibration-rotation spectra of the HD^+ ion which is complementary to the charge-exchange technique of Wing. Electron impact ionization of HD produces an HD^+ ion beam in which all the vibrational levels (v = 0 to 21) up to the dissociation limit are populated. Consequently, a CO_2 infrared laser beam ($h\nu \sim 1000 cm^{-1}$) can induce transitions from the highest vibrational levels of the ground electronic state to the repulsive excited state; photoproduct H^+ and D^+ are produced and can be detected. The photodissociation arises from absorption of one photon, but if the laser frequency is tuned into resonance with a vibration-rotation transition, an increase in the H^+ and D^+ photoproduct yield is observed, arising from absorption of two photons. Carrington, Roberts, and Buttenshaw again used the Doppler tuning method for spectroscopic scanning and observed the first five R-branch components of the $v = 18 \leftarrow 16$ band with very high sensitivity. The main interest in this technique is not so much that it applies to molecular ions, but rather that it opens a route to the study of molecules near to dissociation by high-resolution spectroscopy. Undoubtedly there are many other ions which can be approached by this technique.

VIBRATION-ROTATION SPECTROSCOPY

Finally we turn to studies of the vibration-rotation spectra of ions by techniques which are somewhat more conventional in that they do involve the detection of the infrared radiation. There the conventionality ceases; one example is the observation of the vibration-rotation spectra of NO^+ in hot air resulting from a high altitude nuclear explosion! The other major example is the recent and beautiful work of Oka [38] who has detected the infrared absorption spectrum of the H_3^+ ion. Oka uses a tunable infrared laser source ($4400-2400 cm^{-1}$) in which radiation from an argon ion laser and a tunable dye laser are mixed in a lithium niobate crystal. The infrared radiation makes multiple passes through a dc discharge cell containing H_2 at 1 torr pressure and direct absorption lines are detected. Fifteen vibration-rotation lines have been observed so far and the measured frequencies are in excellent agreement with *ab initio* calculations of Carney and Porter [39] made several years earlier. The calculations were, in fact, of great value in simplifying the spectroscopic search problem. This work of Oka, and the simultaneous independent detection of vibration-transitions in D_3^+ by Shy, Farley, and Wing [35] using the ion beam charge-

exchange technique open new possibilities for the study of molecular ions. The new techniques have come of age, and together with the classical methods of electronic spectroscopy can be expected to solve major problems in the coming years.

ACKNOWLEDGMENT

I am grateful to the Royal Society for the award of a Research Professorship and to the Science Research Council for support of my research into molecular ion spectroscopy.

REFERENCES

1. A. Schuster, Proc. Roy. Soc. A27, 383 (1878).
2. A. Schuster, Nature, 17, 148 (1877).
3. R. C. Johnson, Proc. Roy. Soc. A105, 683 (1924).
4. V. M. Ellsworth and J. J. Hopfield, Phys. Rev. 29, 79 (1927).
5. B. A. Brice and F. A. Jenkins, Nature 123, 944 (1929).
6. E. Bengtsson, Nature 123, 529 (1929).
7. G. Herzberg, Quart. Rev. 25, 201 (1971).
8. B. L. Lutz, Astrophys. J. 163, 131 (1971).
9. G. Herzberg and A. Lagerqvist, Canad. J. Phys. 46, 2363 (1968).
10. I. Dabrowski and G. Herzberg, J. Mol. Spectr. 73, 183 (1978).
11. P. A. Wehinger, S. Wyckoff, G. H. Herbig, G. Herzberg, and H. Lew, Astrophys. J. 190, L43 (1974).
12. C. A. Barth, C. W. Hord, J. B. Pearce, K. K. Kelly, G. P. Anderson, and A. I. Stewart, J. Geophys. Res., April, 2215 (1971).
13. V. E. Bondybey and T. A. Miller, J. Chem. Phys. 70, 138 (1979).
14. C. Cossart-Magos, D. Cossart, and S. Leach, Mol. Phys. 37, 793 (1979).
15. J. P. Maier, O. Marthaler, M. Mohraz, and R. H. Shiley, Chem. Phys. 47, 307 (1980).
16. J. W. Rabalais, L. Karlsson, L. O. Werme, T. Bergmark, and K. Siegbahn, J. Chem. Phys. 58, 3370 (1973).
17. W. B. Peatman, J. Chem. Phys. 64, 4093 (1976).
18. N. P. F. B. Van Asselt, J. G. Maas, and J. Los, Chem. Phys. 11, 253 (1975).
19. H. G. Dehmelt and K. B. Jefferts, Phys. Rev. 125, 1318 (1962).
20. C. B. Richardson, K. B. Jefferts, and H. G. Dehmelt, Phys. Rev. 165, 80 (1968).
21. K. B. Jefferts, Phys. Rev. Lett. 23, 1476 (1969); Phys. Rev. Lett. 20, 39 (1968).
22. S. Green, J. A. Montgomery, Jr., and P. Thaddeus, Astrophys. J. 193, L89 (1974).

23. P. Thaddeus and B. E. Turner, Astrophys. J. 201, L25 (1975).
24. R. J. Saykally, T. A. Dixon, T. G. Anderson, P. G. Szanto, and R. C. Woods, Astrophys. J. 205, L101 (1976).
25. R. C. Woods, Rev. Sci. Instrum. 44, 282 (1973).
26. R. C. Woods and T. A. Dixon, Rev. Sci. Instrum. 45, 1122 (1974).
27. R. C. Woods, T. A. Dixon, R. J. Saykally, and P. G. Szanto, Phys. Rev. Lett. 35, 1269 (1975).
28. T. A. Dixon and R. C. Woods, Phys. Rev. Lett. 34, 61 (1975).
29. R. J. Saykally and K. M. Evenson, Phys. Rev. Lett. 43, 515 (1979).
30. A. Carrington, Proc. Roy. Soc. A367, 433 (1979).
31. W. C. Lineberger and T. A. Patterson, Chem. Phys. Lett. 13, 40 (1972).
32. A. Carrington, P. G. Roberts, and P. J. Sarre, Mol. Phys. 35 1523 (1978); J. T. Moseley, M. Tadjeddine, J. Durup, J.-B. Ozenne, C. Pernot, and A. Tabché-Fouhaillé, Phys. Rev. Lett. 37, 891 (1976).
33. W. H. Wing, G. A. Ruff, W. E. Lamb, Jr., and J. J. Spezeski, Phys. Rev. Lett. 36, 1488 (1976).
34. D. E. Tollirer, G. A. Kyrala, and W. H. Wing, Phys. Rev. Lett. 43, 1719 (1979).
35. J. T. Shy, J. W. Farley, and W. H. Wing, Phys. Rev. Lett., to be published (1980).
36. A. Carrington, D. R. J. Milverton, and P. J. Sarre, Mol. Phys. 35, 1505 (1978).
37. A. Carrington, J. A. Buttenshaw, and P. G. Roberts, Mol. Phys. 38, 1711 (1979).
38. T. Oka, Phys. Rev. Lett., to be published (1980).
39. G. D. Carney and R. N. Porter, J. Chem. Phys. 65, 3547 (1976).

MICROWAVE STUDIES OF MOLECULAR IONS

R. Claude Woods

Department of Chemistry
University of Wisconsin
Madison, Wisconsin 53706

For stable neutral molecules in the gas phase microwave spectroscopy has for about three decades provided the most reliable and precise information available on molecular structure and internal properties, e.g., dipole moments, hyperfine interaction constants, or barriers to internal rotation or inversion. Rotational transitions, which are sensitive to the molecule's moments of inertia and thus its structure, are observed directly and with very high resolution, so that their frequencies can be measured with great accuracy. The experimental frequencies are so exact, in fact, that the accuracy of the microwave structure obtained is always limited by the theoretical problems associated with the vibration-rotation interaction (non-rigidity) in the molecule rather than experimental errors. The most satisfactory type of structure is the equilibrium (r_e) type, which accounts completely for vibration-rotation coupling by using the equilibrium rotational constants,

$$B_e = B_{v_1,v_2,\ldots} + \sum_i \alpha_i \left(v_i + \frac{1}{2}\right) \propto 1/I_e$$

Experimentally this requires that spectra in excited vibrational states corresponding to all the normal modes of the molecule be obtained and analyzed, a requirement so demanding that r_e structures (accurate typically to .00001Å, or about 1 nuclear diameter) have only been found for diatomics and some triatomics. The next best type of structure is the substitution type r_s, which requires only ground vibrational state data, but requires it for many isotopic forms, namely a standard form plus a form singly substituted at each atom (N + 1 species for a N-atomic molecule). These r_s structures (accurate to about ±.001Å) have been obtained for a

great many molecules with up to about eight or ten atoms. In recent years a great deal of effort in a number of groups has gone into extending these studies to transient molecular species, a regime in which the intrinsically modest sensitivity of microwave spectroscopy quickly becomes the limiting factor. Nevertheless, some considerable success has come from these efforts, and in particular in our laboratory some successful microwave studies of molecular ions have now been carried out [1-3]. We have obtained spectra of CO^+, HCO^+, and HN_2^+, as well as several neutral transient species, and for the two triatomic ions we have found complete r_s structures, the most accurate molecular structures available for any free polyatomic ions. The major emphasis of our research now is the extention of this technique to a number of other molecular ions. In our experiments the ions are produced in a large DC glow discharge tube, through which microwave radiation is passed in a free space mode. We have three such tubes: (a) 15cm diameter by 4m long, (b) 45cm by 5m, and (c) a newly completed 10cm by 3m version. Discharge pressures are typically 5-200mTorr, voltages, 1000-2000V, and currents are typically a few hundred milliamps except in the newest model, where water-cooled electrodes and a larger power supply permit currents up to 1.2 amps. Each tube can be operated either near room temperature, or with liquid nitrogen cooling to near 77°K. The details of construction of tube (a) above, which has been used for all ion studies to date, have previously been published [4]. The newer tube (c) is part of the completely new and independent system that is designed to maximize the future prospects of detecting ions; its decreased diameter and increased maximum current yield plasma densities about one order of magnitude higher than the older system [tube (a)]. These total electron densities are measured by microwave interferometry, and up to $10^{11}/cm^3$ has been achieved for Ar in the new system. The older tube is equipped with magnets and other facilities for doing Zeeman modulation on paramagnetic species, e.g., CO^+, but in fact all studies of ions to now have employed some form of source modulation, even those on CO^+. The microwave source frequency and the collection of absorption spectral data are controlled by a minicomputer [5] and spectral data in digital forms are stored on magnetic tape for further processing, e.g., least squares lineshape analysis. The exact nature of the source modulation and the computer control scheme and the associated software have been dramatically modified for the better in the past year, as will be described below. The new system is also equipped with a quadrupole mass spectrometer and a high resolution UV-visible emission spectrometer that will permit us to measure and optimize the concentrations of particular ions or transient species before beginning to search for their normally weak microwave spectra.

The first ion that we detected several years ago was CO^+, whose $N = 0 \rightarrow 1$ rotational frequency near 118GHz could be predicted

from available optical data to within 300MHz. The transitions were located after weeks of searching and eventually the two members of the spin doublet [J = (1/2) → (3/2) and (1/2) → (1/2)] were measured to ±.05MHz. The spectrum was best in a 10-1 helium to carbon monoxide discharge at liquid nitrogen temperature. More recently we have measured the corresponding lines in the $C^{18}O^+$ and $^{13}CO^+$ varieties. In the latter case, ^{13}C magnetic hyperfine constants were obtained, and they were found to agree well with the values obtained by Carrington and coworkers using the ion beam-laser beam technique [6]. CO^+ has not yet been detected by radioastronomy, notwithstanding the fact that the precise frequency is now known, presumably due to the fast reaction with hydrogen $H_2 + CO^+ \rightarrow HCO^+ + H$. The ion HCO^+, on the other hand, was seen first (1970) by radioastronomy [7], as an unidentified species (X-ogen) that was subsequently (1970) suggested by Klemperer to be HCO^+ [8]. Our later (1975) observation of the very same X-ogen transition in a laboratory hydrogen-carbon monoxide discharge totally confirmed the Klemperer assignment. We have now measured the 0 → 1 transitions in six isotopic forms (HCO^+, DCO^+, $H^{13}CO^+$, $D^{13}CO^+$, $HC^{18}O^+$, and $DC^{18}O^+$), which are more than enough for a complete substitution (r_s) structure. We obtain r_{HC} = 1.093Å and r_{CO} = 1.107Å. Our results for $H^{13}CO^+$ confirmed the assignment of the corresponding radioastronomical transition [9] and our frequencies for DCO^+ and $HC^{18}O^+$ led to subsequent detection of these important species in the interstellar medium [10,11]. The isoelectric species HN_2^+ was also first detected by radioastronomy [12], and in this case identification was possible on the basis of the quadrupole hyperfine pattern in the astrophysical spectra [13]. Again we could see the same transition (near 93GHz) in a laboratory discharge (nitrogen-hydrogen mixture) and we later extended the observations to a total of six isotopic forms. The r_s structure thus obtained is r_{NH} = 1.032Å and r_{NN} = 1.095Å. Our frequency for the DN_2^+ species [14] soon made it possible for radioastronomers to detect it in the interstellar medium [15], and as in the case of HCO^+ the ratio DN_2^+/HN_2^+ was far greater than the cosmic deuterium abundance would suggest, due to a chemical fractionation process. The structural studies of HCO^+ and HN_2^+ were all done with liquid nitrogen cooling of the discharge tube.

All these studies were done with a scheme of "double square wave" frequency modulation of the source. The waveform applied to the frequency controlling electrode is an audio pulse signal with a voltage sequence (0, +v, 0, -V, 0, +v, ..., etc.) and the resultant absorption lineshape for an unsplit line after demodulation in a lock-in amplifier is a series of three peaks in a -1, +2, -1 intensity sequence. The great disadvantage of this scheme (and almost all other source modulation techniques) is that phase locking of the source to a stable reference oscillator is impossible. In the past year we have switched over to a new "tone burst" modulation scheme invented by Pickett [16]. The modulation

waveform applied in this case is an R. F. sine wave (e.g., 1MHz) turned on and off at some audio frequency (e.g., 50kHz) and the demodulated lineshape is almost the same as for the double square wave method. Now, however, it is possible to phase lock the source, using a digital phase detector also developed by Pickett [17], and thus to program the frequency digitally to great precision with the computer. The spectral purity, resolution, measurement accuracy, sensitivity and degree to which the spectrometer can be automated are all significantly enhanced by this new technique. In addition, the specifics of this scheme make possible a very useful baseline suppression algorithm for the computer processing of the spectra. A completely new software system implementing all this has now been completed for the older spectrometer. The microwave spectrometer for the new discharge tube [tube (c) above] will also incorporate these innovations and several others, including a liquid helium cooled InSb detector which should both improve the sensitivity and extend this upper frequency limit for spectroscopy. The components for the new system are almost all in hand now, and it should be operational soon.

In addition to information on molecular structure and electronic structure (through quantities like hyperfine coupling constants), microwave spectroscopy is capable of providing significant dynamical information on ions in the plasma environment. Relative intensities can in principle provide rotational and vibrational temperatures of ions. Linewidths at high pressure can yield cross-sections for collisions with other molecules, and thus help in understanding intermolecular forces, while linewidths in the lowest pressure region are controlled by the Doppler effect and can yield translational temperatures for ions. Since the ions undergo unidirectional drift in the electric field of the DC discharge, there is also a Doppler shift or change in apparent center frequency and this can in principle yield ion mobilities. Detailed knowledge of these dynamical quantities is highly useful in predicting intensities of microwave absorption lines and thus in planning experiments on new ions. For this reason we have been carrying out a series of very detailed studies of the HCO^+ transition at 89GHz. We have looked for vibrational satellite lines for both HCO^+ and CO^+ without success, indicating a rather low vibrational temperature for these ions. On the other hand, most neutral molecules, especially transient ones, have very prominent vibrational satellite spectra indicating high vibrational temperatures. It is these vibrational excited state transitions that must be observed if an r_e structure is ever to be obtained for HCO^+. We have more successfully been studying the pressure broadening linewidth of HCO^+. The initial measurements were for the broadening of HCO^+ by H_2 at liquid nitrogen temperature and used the older double square wave modulation. These preliminary experiments yielded $\Delta\nu \cong 29$MHz/Torr and have already been published [18]. We

are now using the new modulation and computer control scheme and have been able to obtain HCO^+ spectra at room temperature and with large amounts of noble gases added. We already have results for the $\Delta\nu$ parameter for HCO^+-H_2 at 300° (~15MHz/Torr) and HCO^+-Ar at 300° (~15MHz/Torr) and hope to extend this to a 77° and 300° value for H_2, He, Ne, or Ar as the collision partner. The $\Delta\nu$'s appear to be two to three times greater than those for comparable neutral molecules. The new instrumental scheme permits reliable low pressure linewidths to be measured and so far these Doppler widths appear to indicate an ion kinetic temperature of about 1200°K for the "room temperature" discharge. Previous measurements of the neutral molecule O_2 in oxygen discharges indicate translational temperatures near 300°K in similar current conditions and also rotational temperatures near 350°K, i.e., only very modest excitation. No rotational temperature data is yet available for ions. Finally, we are attempting to obtain reliable Doppler shift data. This requires center frequency measurements accurate to 1 part in 10^8, and this in turn pushes to their limits the entire instrumental system and least squares lineshape analysis. The main goal here is to obtain very accurate rest frequency measurements so that astrophysical Doppler profiles can be reliably converted into velocity distributions.

One of the greatest difficulties in microwave spectroscopy of transient species has been the blind search problem. One normally doesn't know either the frequency at which the spectra will occur or the proper conditions for optimizing the production of the species. This can lead to frustrating and unproductive searches when spectra are weak. The quadrupole mass spectrometer that is incorporated into our new system is designed to eliminate just this blind search problem. Ions (or neutral molecules) escaping through a pinhole in the wall of the discharge tube are mass analyzed and detected with high sensitivity. One can tune the mass spectrometer to a given mass peak and find for that ion the optimum production conditions: current, pressure, flow rate, temperature, gas mixture, etc. Combining the relative ion intensity data from the mass spectrometer with the total ion density from microwave interferometry one can even obtain approximately an absolute ion concentration. Inserting this into the theoretical formula for absorption intensity one can say with some reliability whether or not a microwave experiment on a new ion is feasible. The most difficult aspect of sampling ions in a DC discharge is the voltage tracking required between the plasma potential and the ion optics and mass filter. We have been developing an electronic feedback system for this purpose. The mass spectrometer is now operational and is also interfaced to and controlled by a minicomputer. The final component of our new system is a high resolution 1.5 meter UV-visible spectrometer. This can act as a monitor of metastable concentrations, just as the mass spectrometer does for ions. For ions the high resolution optical spectra appear to

offer an avenue for determination of rotational temperatures, which are particularly hard to obtain otherwise. With the combination of increased ion production, increased microwave spectrometer sensitivity, and diagnostic tools like mass spectrometry we hope to be able to obtain microwave spectra of a number of new ions, including perhaps some negative ones.

REFERENCES

1. T. A. Dixon and R. C. Woods, Phys. Rev. Lett. 34, 61 (1975).
2. R. C. Woods, T. A. Dixon, R. J. Saykally, and P. G. Szanto, Phys. Rev. Lett. 35, 1269 (1975).
3. R. J. Saykally, T. A. Dixon, T. G. Anderson, P. G. Szanto, and R. C. Woods, Ap. J. Lett. 205, 101 (1976).
4. R. C. Woods, Rev. Sci. Instrum. 44, 282 (1973).
5. R. C. Woods and T. A. Dixon, Rev. Sci. Instrum. 45, 1122 (1974).
6. A. Carrington, D. R. J. Milverton, and P. J. Sarre, Mol. Phys. 35, 1505 (1978).
7. D. Buhl and L. E. Snyder, Nature 228, 267 (1970).
8. W. Klemperer, Nature 227, 1230 (1970).
9. L. E. Snyder, J. M. Hollis, B. L. Ulich, F. T. Lovas, and D. Buhl, Bull. Am. Astron. Soc. 7, 497 (1975).
10. J. M. Hollis, L. E. Snyder, F. J. Lovas, and D. Buhl, Ap. J. Lett. 209, 83 (1976).
11. W. D. Langer, R. W. Wilson, P. S. Henry, and M. Guelin, Ap. J. Lett. 225, 139 (1978).
12. B. E. Turner, Ap. J. Lett. 193, 83 (1974).
13. S. Green, J. A. Montgomery, and P. Thaddeus, Ap. J. Lett. 193, 89 (1974).
14. T. G. Anderson, T. A. Dixon, N. D. Piltch, R. J. Saykally, P. G. Szanto, and R. C. Woods, Ap. J. Lett. 216, 85 (1977).
15. L. E. Snyder, J. M. Hollis, D. Buhl, and W. D. Watson, Ap. J. Lett. 218, 61 (1977).
16. H. M. Pickett and T. L. Boyd, Chem. Phys. Lett. 58, 446 (1978).
17. H. M. Pickett, Rev. Sci. Instrum. 48, 706 (1977).
18. T. G. Anderson, C. S. Gudeman, T. A. Dixon, and R. C. Woods, J. Chem. Phys. 72, 1332 (1980).

FAST-BEAM LASER SPECTROSCOPY OF MOLECULAR IONS

William H. Wing

Physics Department and Optical Sciences Center
University of Arizona
Tucson, Arizona 85721

INTRODUCTION

Historically, studies of stable atoms and molecules containing one and two electrons were crucial to the development of the quantum theory of matter. For example, attempting to explain from first principles the simple spectrum of the one-electron hydrogen atom led N. Bohr to discover quantization of angular momentum. The puzzle of the missing triplet ground state in the two-electron helium atom was solved by W. Pauli's postulation of the famous and far-reaching Exclusion Principle. The theory of the covalent chemical bond was developed by W. Heitler and F. London for the two-electron hydrogen molecule. The discovery by W. E. Lamb and R. C. Retherford that the $2^2S_{1/2}$ level of the hydrogen atom was displaced from the $2^2P_{1/2}$ level, contrary to the prediction of the theory of P. A. M. Dirac, spurred the development of modern quantum electrodynamics. The list of such advances can be extended greatly.

Such theoretical developments were based on the need to understand experimental results, principally those obtained by high resolution spectroscopy. The spectroscopy of the atomic species just mentioned, as well as that of the hydrogen molecule, was well advanced before the middle of this century, using the techniques then available. However, there is a group of bound systems which resisted application of the classical techniques. These are the molecular ions, which class includes most of the possible one- and two-electron bound molecules (Table I). They have succumbed to high-resolution spectroscopic investigation (10^{-6} to 10^{-7} absolute accuracy) only very recently: in fact, within the past five years. Most of the work has been accomplished

Table I. Stable One- and Two-Electron Systems

Electrons	Nuclei	Examples
1	1	H, He^+, Li^{++}, ... atoms
1	2	H_2^+, HeH^{++} molecular ions
2	1	H^-, He, Li^+, ... atoms
2	2	H_2 molecule, HeH^+ molecular ion
2	3	H_3^+ molecular ion

using a new type of spectroscopic instrument, the Doppler-tuned laser beam-ion beam spectrometer, whose development was begun at Yale University in 1971 and completed at the University of Arizona in 1976. Other workers also have made use of this technique, and some of their results have been reported in this conference.

In this talk I will discuss the three molecular ions (HD^+, $^4HeH^+$, and D_3^+) that we have studied [1-6] at the University of Arizona, describe the operating principles of the University of Arizona instrument, mention briefly some of the advantages and limitations of this technique, and suggest some future research directions.

The hydrogen molecular ion is the simplest molecule, containing only three bodies. Therefore it is the natural testing ground for high-precision molecular theory calculations. As is well known from elementary texts on quantum mechanics, the three-body problem can be solved analytically with the assumption that two of the bodies (the nuclei) are massive and have negligible kinetic energies compared to the third. With the nuclei fixed in space, the electron's Schrödinger equation can be separated into three ordinary differential equations, which can then be solved by function series or continued-fraction methods. The electron probability distribution in the H_2^+ ground state was first obtained in this way by Burrau [7]. One then treats the electron's energy eigenvalue as part of the effective central potential in which the nuclei vibrate and rotate, and solves for the nuclear eigenfunctions and eigenenergies numerically. This is the so-called "clamped-nuclei," or lowest Born-Oppenheimer, approximation. More accurate treatments lead to the adiabatic approximation and to nonadiabatic, or nonrelativistically exact, calculations, usually done variationally. When "full reality" is considered, one must include corrections due to special relativity, quantum electrodynamics, finite nuclear size, hyperfine structure, etc. --

Table II(a). HD^+ Energies

Quantity	Energy (MHz)
Dissociation energy	660,000,000
Lowest vibrational spacing	57,000,000
Lowest rotational spacing	1,300,000
Largest hyperfine splitting	1,000

Table II(b). Post-Born-Oppenheimer Theoretical Corrections to Lowest Vibrational Spacing in HD^+

Correction	Shift (MHz)
Adiabatic	-15,000
Nonadiabatic	- 4,500
Relativistic	+ 1,000
Radiative	- 150

1 cm^{-1} = 30,000 MHz.

in short, all the effects that arise in high-accuracy treatments of the hydrogen atom. Table II summarizes typical sizes of some of these for the HD^+ isotope.

Although most of these effects are very small, ultimately they must be included to bring theory and experiment into accord. This process will provide a stringent test of both experimental techniques and theoretical calculations in a system other than the familiar hydrogen atom. While it is not now clear what the accuracy limits are for either theory or experiment, it is clear that they have not been reached in either direction. Ultimately, of course, the possibility of agreement will be restricted by our knowledge of the fundamental constants. By a slight alteration of emphasis, new constant values can then be obtained.

The only electronic state of the hydrogen molecular ion that is strongly bound and readily accessible (and the only one that has been observed) is the ground state, $1s\sigma^2\Sigma_g^+$. Thus it is logical to study the vibration-rotational spectrum of this level. We chose to study the isotope HD^+ because of its moderately large electric-dipole transition moment, which results from displacement of its charge and mass centers.

The HeH^+ molecular ion is of interest because it is composed of the two most abundant elements in the universe, and therefore

is likely to be present in certain regions of the interstellar medium, and of stellar atmospheres. Theoretically, the first quantum-mechanical calculation of HeH^+ structure was that of Glockler and Fuller [8] in 1933. The most accurate calculation of ground-state rotation-vibrational energy levels has been made by Bishop and Cheung [9]. As with H_2^+, only the ground electronic state ($X^1\Sigma^+$) has a deep and well-shaped potential well, although some of the excited electronic states also exhibit minima. Because the electrons tend to collect around the He^{++} nucleus, the molecule possesses a large static electric-dipole moment, and interacts strongly with radiation.

The H_3^+ ion is the simplest polyatomic molecule, and is therefore the object of much interest on the part of theoretical chemists since it is the first system that is complex enough to provide a realistic test of calculational techniques applicable to complicated molecules. It is triangular in shape. The most accurate published calculation of H_3^+ and D_3^+ rotation-vibrational spectra, including the effects of strong vibration-rotation interaction, is that of Carney and Porter [10]. The homonuclear variants of this molecule (H_3^+ and D_3^+) have two distinct vibrational modes: a breathing mode, which is optically inactive, and a doubly-degenerate optically-active mode (ν_2 mode).

EXPERIMENTAL DETAILS

I will describe the apparatus as it was used in the experiment on HD^+ [1,4]. The HD^+ molecules are processed in three stages, as sketched in Figure 1. The apparatus is diagrammed in Figure 2. The equipment is an optical-frequency analogue of a molecular beam electric resonance spectrometer, but each part is, of course, quite different. In an electron gun, HD^+ ions are formed from HD and quickly extracted and accelerated before gas-phase reactions can occur. Vibrational populations are proportional to Franck-Condon factors for HD ionization, while rotational populations are determined by the Boltzmann distribution at the source gas temperature of about 300°K. Relatively little angular momentum (hence little heat) is added during the ionization process. Next the ion beam is illuminated by a nearly-colinear CO laser beam. The ion beam velocity is adjusted to bring a CO laser line frequency into resonance with a nearby HD^+ transition frequency via the Doppler effect. An extra benefit of the fast-beam method is that the velocity spread in the moving beam is reduced by a factor of 20 to 50 from that in the ion source. This is a readily obtainable result of the acceleration kinematics. Thus quite a narrow resonance is seen. This "bonus" became apparent in 1971 during the initial design phases of the experiment and was mentioned in progress reports of that date [11].

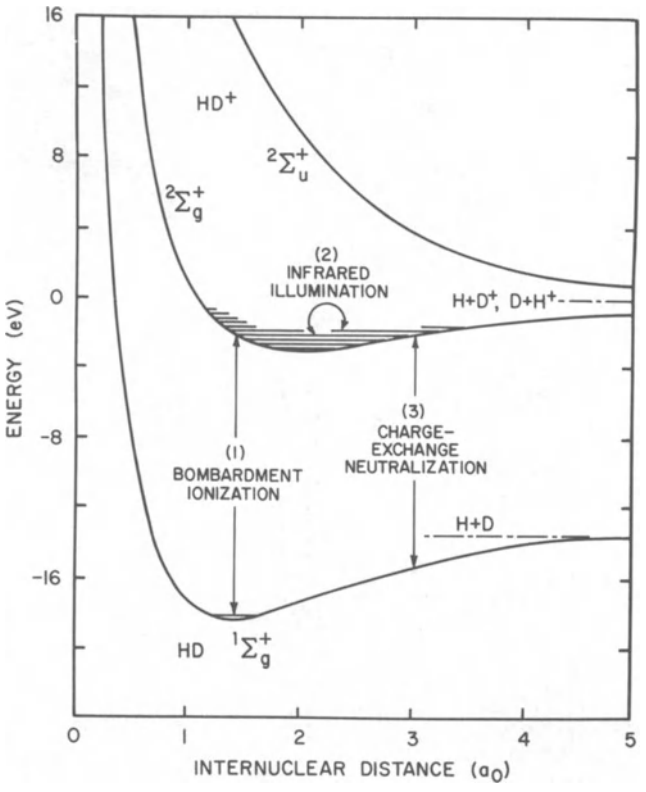

Fig. 1. Transition scheme for HD^+ laser resonance experiment.

If the populations of the resonating states are unequal, as is generally the case, a net transfer will occur, allowing the possibility of detection. Then the HD^+ frequency is calculated from the CO frequency (typically 1600 to 1900 cm^{-1}) and the relativistic Doppler shift.

Because of extremely low population densities in the ion beam, it seemed impractical to look directly for optical absorption or emission at resonance. Instead we pass the irradiated ion beam into a gas target chamber where a fraction of the ions is neutralized by charge exchange. If ions in the two resonating states have unequal charge-exchange cross sections, it is easy to show that when the laser beam is turned on the charged-particle fraction of the beam will change slightly in intensity.

In our case, the beam current is typically 3×10^{-7}A and the resonance signal typically 3×10^{-6} of that. A 1-kHz laser beam chopper and a lock-in amplifier permit detection of signals of this size, if attention is paid to minimizing the ion beam noise.

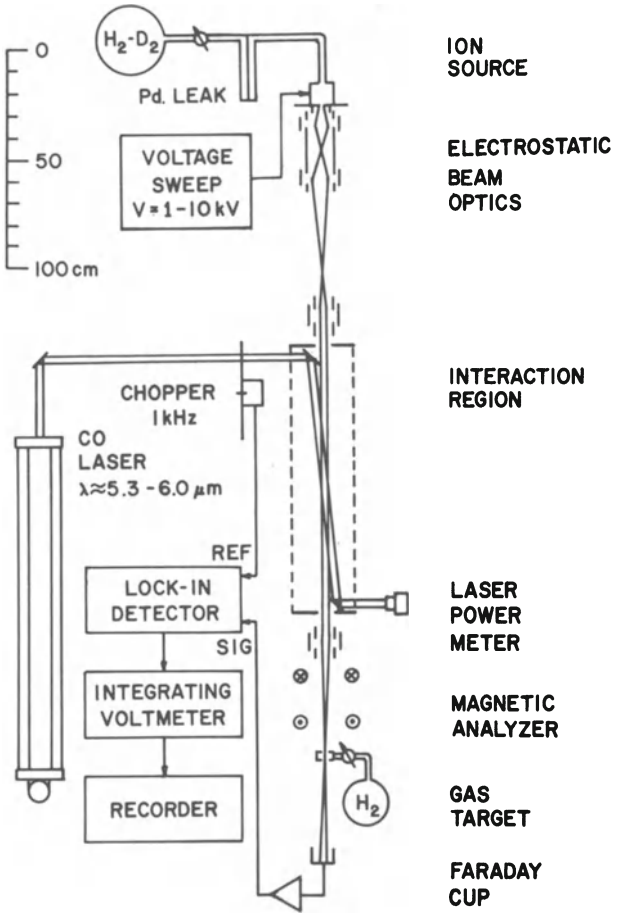

Fig. 2. Laser beam-ion beam resonance apparatus.

We have succeeded in keeping it near the shot-noise level. The choice of target gas is not critical; signals have been seen using N_2, Ar, and H_2 targets.

Small variations of detail were necessary for study of the $^4HeH^+$ [2,5] and D_3^+ ions [3,6]. Both are made via ion-molecule reactions in the ion source, rather than by direct ionization of a neutral molecular gas. Therefore population distributions among vibration-rotational states are considerably different than for HD^+; roughly speaking, somewhat smaller vibrational excitation and considerably greater rotational excitation occurs. To enhance the formation rates, we raised the source gas pressure and modified the source so as to increase ion residence time [12]. Nonetheless, ion beam currents were smaller; in fact, less than 10^{-8}A for $^4HeH^+$.

Very little is known about the collision process in the detector (step 3 of Figure 2); most likely it is charge-exchange neutralization followed by dissociation of the unstable neutral. Finally, the initial uncertainty in theoretical spectral line positions was much greater for these cases than for HD^+, and signals were expected (and found) to be weaker. Several hundred hours of scanning were required to find the first resonance in each case. To reduce the tedium of searching, we attached to the spectrometer an inexpensive microcomputer, which controls the voltage sweep and acquires data.

RESULTS

The detailed spectroscopic data for HD^+, $^4HeH^+$, and D_3^+ can be seen in the cited publications [1-3]. Additional material can be found in the Ph.D. theses of J. J. Spezeski [4], D. E. Tolliver [5], and J.-T. Shy [6], and still more is in preparation for publication. Here I will briefly summarize and comment on the main results.

In HD^+ several vibration-rotational transitions have been studied in detail and measured to ±0.4 ppm accuracy (±0.007 cm^{-1}), and several additional ones have been seen. The frequencies of those involving the lowest vibrational and rotational levels (0,1 and 0,1,2 respectively) agree within ±0.001 to ±0.002 cm^{-1} (out of typically 1700 cm^{-1}) with the 1977 calculations of Bishop and Cheung [13] and the recent ones of Wolniewicz and Poll [14]. This level of verification of the theory ($\pm 1 \times 10^{-6}$) is only moderately lower than the accuracy of the proton/electron mass ratio ($\pm 4 \times 10^{-7}$), which enters as the square-root in the vibrational frequencies of a molecule. In fact, considered as a fundamental-constant determination, the HD^+ experiment and theory together corroborate the 1973 adjusted value [15] of m_p/m_e and reject the erroneous 1969 value [16], both at the 2-s.d. level. An accuracy improvement in the theory by a factor of 5, and in the experiment by a factor of 2, is all that is required to yield a fully competitive value of m_p/m_e. For the experiment, this requires mainly comparatively straightforward improvements in laser calibration accuracy.

Experiment [2] and theory [9] for HeH^+ differ by 0.14 to 0.25 cm^{-1} (out of typically 1800 cm^{-1}). The disagreement is greater than in the HD^+ case because the $^4HeH^+$ theory is less complete. The Bishop-Cheung calculation neglects nonadiabatic, relativistic, and quantum-electrodynamic effects, which together contribute shifts of about 0.2 cm^{-1} to HD^+ transition frequencies. Therefore, given these omissions, the agreement is satisfactory.

In the case of D_3^+, the difference between theory [3] and experiment [10] is only 0.003 to 0.03 cm^{-1} for the transitions that have been assigned. However, the apparently remarkable theoretical accuracy must be examined carefully. In contrast to the diatomic cases, the theory for D_3^+ is not really a first-principles theory. Carney and Porter [9] made a careful clamped-nuclei theory (at, therefore, a lower accuracy level than was the case for HD^+ and HeH^+). They then brought theory and experiment into agreement by adjusting the rotationless vibrational frequency by +8.9 cm^{-1} and the equilibrium internuclear spacing by -0.8%. By this device they were able to obtain good agreement for four transitions using two adjustable parameters. The importance of their work lies in the fact that it shows the basic correctness of the theory of the very substantial rotation-vibration interaction in this molecule, and indicates where the post-Born-Oppenheimer refinements of the principles will have their main effects.

A qualitatively similar situation holds for the very fine direct absorption measurements of Oka on H_3^+ [17]. In both his case and ours, the experimental errors are so small (± 0.005 and ± 0.0007 cm^{-1}, respectively) that the experimental data can be regarded as sharp.

STRENGTHS, LIMITATIONS, POSSIBLE IMPROVEMENTS, AND FUTURE DIRECTIONS

To summarize, then: The principal advantages of this unorthodox form of spectroscopy are

- --Suitability for highly reactive ions (and, in principle, neutrals formed by high-speed charge exchange);
- --Doppler-effect tuning, permitting use of fixed-frequency lasers, with fractional tuning at present $\gtrsim 10^{-3}$;
- --Requirement of only small samples: $I \gtrsim 10^{-9}$A;
- --Non-optical detection with 100% efficiency;
- --High resolution.

While its limitations are

- --Involvement of complex and exotic apparatus, not commercially available;
- --Weak signals;
- --Resolution so high that exploration for unknown spectra is not easy.

These limitations would be ameliorated, and the method's utility enhanced, by higher signal-to-noise ratio. The best place to look for stronger signals seems to be in the detection method. The charge-exchange method and other non-optical detection methods actually work better for electronic than for vibrational transitions, because of the greater dissimilarity of collisional properties of the initial and final states in the electronic case. One

possibility for improvement, which we are exploring, is to decelerate the ions entering region 3 into the kinetic energy range where ion-molecule reactions dominate, since these have collision cross sections that are very vibrational-state dependent, and also may depend significantly on rotational state.

Finally, I will list some future directions for this research, recognizing that these may change rapidly as new ideas appear.

It is clear that there are many interesting and important molecular ions whose spectra are unexplored at present. We are beginning to work on H_2D^+, which is of special astrophysical interest. One could also mention $^3He^4He^+$, CH^+, and many similar examples. The limitations, as the molecules grow progressively more complex, are the increasing experimenters' time required and decreasing signal strength.

A second project, as I mentioned earlier, is to remeasure the proton/electron mass ratio via HD^+ spectroscopy.

A third and related area is spectroscopy of H atom Rydberg states, with the aim of remeasuring the Rydberg constant.

A fourth avenue of research is the study of ion-molecule reactions and high-speed collisions in known vibration-rotational states, by examining resonance intensities. Very little work of this sort has been done before. We have already seen, for example, a splitting of a $^4HeH^+$ spectral line in the 4-3 or 3-2 vibrational band, which results from two production mechanisms in the ion source having different released kinetic energies. Lower bands show no such phenomenon. It appears that with this observation we are on the verge of opening an exciting new topic in the field of molecular reaction dynamics.

ACKNOWLEDGEMENT

Over the years, this work has been supported by grants and contracts from the U. S. Air Force Office of Scientific Research, the Research Corporation, the U. S. National Bureau of Standards, the U. S. National Science Foundation, and the Petroleum Research Fund of the American Chemical Society, for all of which I am most grateful.

REFERENCES

1. W. H. Wing, G. A. Ruff, W. E. Lamb, Jr., and J. J. Spezeski, Phys. Rev. Lett. 36, 1488 (1976).

2. D. E. Tolliver, G. A. Kyrala, and W. H. Wing, Phys. Rev. Lett. 43, 1719 (1979).
3. J. -T. Shy, J. W. Farley, W. E. Lamb, Jr., and W. H. Wing, Phys. Rev. Lett. 45, 535 (1980).
4. J. J. Spezeski, Ph.D. Thesis, Yale University, 1977 (Available from University Microfilsm, Ann Arbor, Michigan, U.S.A.).
5. D. E. Tolliver, Ph.D. Thesis, University of Arizona, 1980 (Available from University Microfilms, Ann Arbor, Michigan, U.S.A.).
6. J. -T. Shy, Ph.D. Thesis, University of Arizona (in preparation).
7. Ø. Burrau, Det. Kgl. Danske Vid. Selskab 7, 1 (1927).
8. G. Glockler and D. L. Fuller, J. Chem. Phys. 1, 886 (1933).
9. D. M. Bishop and L. M. Cheung, J. Mol. Spectrosc. 75, 462 (1979).
10. G. D. Carney and R. N. Porter, Phys. Rev. Lett. 45, 537 (1980).
11. W. H. Wing, in: Report AFOSR-70-1132-TR (AD70887), V. W. Hughes, W. R. Bennett, Jr., and W. E. Lamb., Jr., available from National Technical Information Service, Springfield, Virginia 22151 (1972).
12. G. A. Kyrala, D. E. Tolliver, and W. H. Wing, Int. J. Mass Spectrom. Ion Phys. 33, 367 (1980).
13. D. M. Bishop and L. M. Cheung, Phys. Rev. A 16, 640 (1977).
14. L. Wolniewicz and J. D. Poll, to be published.
15. E. R. Cohen and B. N. Taylor, J. Phys. Chem. Ref. Data 2, 663 (1973).
16. B. N. Taylor, W. H. Parker, and D. N. Langenberg, Rev. Mod. Phys. 41, 375 (1969).
17. T. Oka, Phys. Rev. Lett. 45, 531 (1980).
18. J. -T. Shy, John W. Farley, and William H. Wing, Phys. Rev. A 24, 1146 (1981).
19. J. -T. Shy, R. DeSerio, J. W. Farley, and W. H. Wing, in preparation.

Note added in proof: Recently the instrument described in this paper has yielded the spectra of H_2D^+ [18] and HD_2^+ [19].

VIBRATION-ROTATION SPECTROSCOPY OF THE HD^+ ION

Alan Carrington

Department of Chemistry
University of Southampton
Hampshire, England

INTRODUCTION

An approach to the spectroscopy of molecular ions which has obvious appeal is to use the well-established technique of mass spectrometry for producing an appropriate mass-selected ion beam, and to allow the ion beam to interact with electromagnetic radiation. One soon concludes, however, that the direct detection of the absorption of radiation will be difficult, and probably impossible. The reason is that even an intense molecular ion beam (e.g., 10^{12} ions/sec) has a very low ion density. Consequently, the successful approaches to date have involved indirect detection of absorption spectra; the basic principle is that one attempts to detect the changes in internal state of the ion, brought about by the absorption of radiation, through changes in either the parent ion beam intensity or secondary ion intensities [1]. In the case of the HD^+ ion two successful approaches have been described, one involving charge-exchange reaction with H_2, the other involving photodissociation. These experiments are described in detail in the third and fourth sections of this review.

ELECTRON IMPACT IONIZATION OF HD

Beams of HD^+ ions are produced by electron bombardment of HD gas and extraction by acceleration to potentials of several kilovolts. HD^+ in its $^2\Sigma$ ground state has a dissociation energy of $21{,}500 cm^{-1}$ and supports vibrational levels up to and including $v = 21$. Electron impact ionization produces HD^+ ions in which all the vibrational levels are populated to some extent. Even the highest bound vibrational level, $v = 21$, has a calculated population

factor of ~0.0001. The relative rotational level populations will, however, be close to those of neutral HD at the source temperature.

The first excited electronic state of HD^+ is repulsive and at large internuclear separation the ground and excited states correlate with the same dissociation limits, $H^+ + D$ and $H + D^+$, with the atoms in their ground states. These two dissociation limits are separated by $29cm^{-1}$.

Excitation of HD^+ with an appropriate radiation source which induces transitions from the bound to the repulsive state leads to photodissociation; the H^+ or D^+ photofragments can be readily detected with a suitable magnetic (or electrostatic) analyzer and electron multiplier detector. Numerous investigations of the photodissociation produced by visible lasers have been reported; however, because of the population of the highest vibrational levels in the beam, even an infrared laser can produce photofragmentation. We have observed strong photodissociation produced by a CO_2 laser operating at $930cm^{-1}$. This photodissociation is the necessary basis of our spectroscopic studies described in the fourth section.

CHARGE-EXCHANGE DETECTION OF VIBRATION-ROTATION TRANSITIONS

The most significant spectroscopic study of an ion beam has been that described by Wing et al [2] who detected vibration-rotation transitions in HD^+ by using the charge-exchange reaction with H_2:

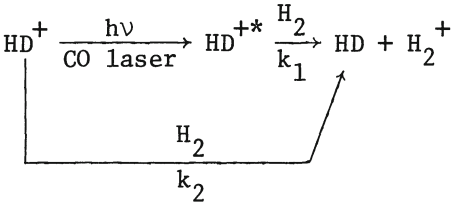

Vibration-rotation transitions in the HD^+ ions are excited with a carbon monoxide infrared laser, combined with Doppler tuning of the ion beam. H_2 gas is introduced and attenuates the intensity of the HD^+ beam because of charge-exchange reactions with both the parent (k_2) and laser-excited (k_1) ions. The intensity of the HD^+ beam is monitored and is found to change on laser excitation because k_1 and k_2 are not equal. Wing et al obtained signal-to-noise ratios of the order 10:1 and detected rotational components of the $v'' = 1 \rightarrow 0$, $2 \rightarrow 1$ and $3 \rightarrow 2$ bands.

TWO-PHOTON DISSOCIATION SPECTROSCOPY

As we have already discussed in the second section, photodissociation of an HD^+ beam can be induced by a CO_2 infrared laser beam because of significant population of the vibrational levels close to the dissociation limit. This photodissociation is readily observed using a tandem mass spectrometer system in which the photofragment H^+ or D^+ ions can be separated from the parent HD^+ ions. Single-photon dissociation is of considerable interest, but it does not provide precise spectroscopic information. However, Carrington, Buttenshaw, and Roberts [3] have developed a two-photon technique in which the first photon is used to drive a vibration-rotation transition, while the second photon induces dissociation. Using a CO_2 laser and Doppler tuning of the ion beam they have observed the first five members of the R-branch of the $18 \leftarrow 16$ vibrational band. Signal-to-noise ratios of 100:1 are readily obtained and the observed linewidths are ~50MHz.

Theoretical calculations of the vibration-rotation levels of HD^+ have been reported by Hunter, Yau and Pritchard [4] and most recently by Wolniewicz and Poll [5]. The latter calculations are in agreement with the measurements of Wing et al to within 0.003 cm^{-1}, and with the measurements of Carrington et al on the high vibrational levels to within $0.01cm^{-1}$ or better.

DEVELOPMENTS IN THE TWO-PHOTON DISSOCIATION TECHNIQUE

We are at present planning a new ion beam system which is to be built by Vacuum Generators and is based on that company's ZAB mass spectrometer system. With increased sensitivity a number of novel studies of the HD^+ ion are possible and in this section we indicate how greater sensitivity is to be obtained. The main features of the new machine which are important to our work are as follows:

(a) The parent ion beam intensity is likely to be ten times greater than that at present available; moreover, the maximum source potential will be 10kV compared with 5kV at present, yielding a factor of $\sqrt{2}$ increase in Doppler tuning range.
(b) The ion beam is mass analyzed with a 60°12" radius magnetic sector and the photofragment ions separated with an electrostatic sector. The ions form a focus between the two sectors, at which point interaction with the laser radiation will occur. Interaction between ions and photons is likely to be some fifty times more efficient than in our present machine, in which the ion beam is not focused.
(c) The collection efficiency of the electrostatic sector is likely to be 5-10 times higher than in our present machine.

In summary, we hope for an increase in signal-to-noise ratio of two orders of magnitude.

We also intend to improve the technique by using two lasers instead of one. The optimum sensitivity depends upon producing the maximum photodissociation yield; consequently, high laser power is required. However, relatively low power is required to drive the resonant vibration-rotation transition and indeed it is likely that our present spectral lines are power broadened. The new ion beam machine will therefore be linked with two lasers; one of these will operate as a CO_2 laser of high power to maximize the photodissociation, while the other will be used as a CO_2 or CO laser to drive the resonant transitions.

DEVELOPMENTS IN THE VIBRATION-ROTATION SPECTROSCOPY OF HD^+

With improvements to the apparatus we hope it will be possible to observe satellite components which yield values of the ^1H and ^2H nuclear hyperfine constants. Each vibration-rotation level in HD^+ has a complex structure due to hyperfine and spin-rotation coupling. However, because the spin-rotation interaction is extremely small (~10MHz) the electric dipole intensity is almost entirely confined to transitions which do not yield hyperfine couplings; any splittings in the lines observed so far would arise only from differences in the hyperfine couplings for the two vibrational levels involved. Transitions which yield the hyperfine couplings are three to four orders of magnitude lower in intensity, but they may be observable with the increased sensitivity expected for the new apparatus.

Our major goal is to observe transitions which involve the highest vibrational levels, $v = 20$ and $v = 21$. The $v = 21$, $N = 1$ level is calculated to lie only $0.7cm^{-1}$ below the lower dissociation limit ($H^+ + D$). Consequently, we anticipate that the non-adiabatic effects will be very large and that, in this level, the HD^+ ion will exhibit unsymmetrical charge distribution, with the positive charge displaced towards the proton. Measurements of the proton and deuterium hyperfine constants would therefore be of particular interest.

We think it might also be possible to observe directly the quasibound levels above the dissociation limit, and we might also be able to probe lower lying vibrational levels through multiphoton transitions induced by a pulsed laser. The most attractive general feature, however, is the potential ability to study by high resolution spectroscopy levels close to the dissociation limit.

APPLICATIONS TO OTHER MOLECULAR IONS

In principle the two-photon dissociation technique described in this paper can be applied to other more complex ions if the high-lying vibrational levels are appreciably populated. In fact, we have found that photodissociation of ions with a CO_2 laser is a quite general feature. We have observed [6] such dissociations in the following cases:

HD^+, $^3He^4He^+$, NH_3^+, NH_2^+, NH^+, CH_5^+, CH_4^+, CH_3^+, CH_2^+, CH^+, H_3O^+, H_2O^+, OH^+

In every case above (except He_2^+) photodissociation involves removal of a hydrogen atom and production of the fragment ion with mass reduced by one unit. The extent of photodissociation varies from $1:10^3$ in the cases of NH_3^+ and CH_4^+ to $1:10^4$ for HD^+ and $1:10^6$ for CH^+, measurements being made with 10W CW laser power at $\sim 930 cm^{-1}$. In a number of cases we have confirmed the fragmentation yield to be linear in laser power; we do not, therefore, believe that multiphoton dissociation is involved. Ions which do not appear to photodissociate include N_2O^+ and H_3^+. We see no reason why we should not be able to detect resonant transitions in the ions listed above, thus opening a route to the study of polyatomic molecules close to their dissociation limits.

ACKNOWLEDGMENT

I am grateful to the Royal Society for the award of a Research Professorship and to the Science Research Council for support of my research into molecular ion spectroscopy.

REFERENCES

1. A. Carrington, Proc. Roy. Soc. A367, 433 (1979).
2. W. H. Wing, G. A. Ruff, W. E. Lamb, Jr., and J. J. Spezeski, Phys. Rev. Lett. 36, 1488 (1976).
3. A. Carrington, J. A. Buttenshaw, and P. G. Roberts, Mol. Phys. 38, 1711 (1979).
4. G. Hunter, A. W. Yau, and H. O. Pritchard, Atomic Data and Nuclear Data Tables, 14, 11 (1974).
5. L. Wolniewicz and D. Poll, to be published.
6. A. Carrington and J. A. Buttenshaw, unpublished work.

STRUCTURES OF MOLECULAR IONS FROM LASER MAGNETIC RESONANCE SPECTROSCOPY

Richard J. Saykally and Karen G. Lubic

Department of Chemistry
The University of California
Berkeley, California

and

Kenneth M. Evenson

National Bureau of Standards
Boulder, Colorado 80302

INTRODUCTION

The status of molecular ion spectroscopy was elegantly reviewed by Dr. G. H. Herzberg in his Faraday Lecture to the Chemical Society [1] in September of 1971. As of that time thirty-three diatomic ions and six polyatomic ions had been studied by spectroscopic methods. All of these had been observed by absorption or emission in the visible region of the spectrum, except for H_2^+; it had become the first molecular ion to be detected by a high resolution (better than the optical Doppler width) technique in 1968 through the work of K. B. Jefferts [2].

The last decade has witnessed dramatic advances in the spectroscopy of molecular ions. The HCO^+ [3] and HNN^+ [4] ions have been established as important and ubiquitous constituents of interstellar clouds by the powerful new radio astronomy techniques that have been used to detect them. Microwave spectroscopy has been successful in detection of rotational spectra and the determination of precise structures for CO^+ [5], HCO^+ [6], and HNN^+ [7]. Ion beam spectroscopy has produced vibrational spectra of HD^+ [8], HeH^+ [9], and D_3^+ [10] and high resolution electronic spectra of CO^+ [11], H_2O^+ [12], O_2^+ [13,14], and HD^+ [15]. Far infrared laser magnetic resonance spectroscopy has been used to detect pure rotational spectra of HBr^+ [16]. Most recently, vibrational

absorption spectra of H_3^+ have been detected with a tunable infrared difference frequency laser system [17]. In addition, optical spectra have been observed for a number of molecular ions stored in radiofrequency traps by laser induced fluorescence [18].

As of this date spectra of over 60 different molecular ions have been detected. Nine of these ions have been studied with high resolution methods. In this paper we will discuss the use of one of these promising new techniques -- far-infrared laser magnetic resonance -- to obtain detailed information on the geometrical and electronic structures of molecular ions. We begin by reviewing the general principles of LMR and describing the experimental design.

THE LASER MAGNETIC RESONANCE EXPERIMENT

LMR [19] is very closely related to the technique of gas-phase electron paramagnetic resonance developed by Radford and by Carrington and his collaborators over a decade ago. In both experiments the paramagnetic energy levels of an atom or molecule contained in a resonant cavity are tuned by a dc magnetic field until their energy difference matches that of a fixed frequency source. The final product of the spectrometers is then an absorption spectrum as a function of magnetic flux density. The principal distinction between the two experiments is that EPR transitions are usually between different magnetic sublevels (M_J) of a particular angular momentum state (J), whereas the LMR transitions occur between different rotational states. The laser magnetic resonance experiment therefore has the prerequisite that a given transition frequency must lie very close (within 1% on the average) to a far-infrared lasing transition. It was this requirement that severely constrained the applicability of LMR during the first decade of its inception, since only a few laser lines were then available from the H_2O and HCN gas lasers that were used as sources. The optically-pumped far-infrared laser has now dramatically expanded the scope of LMR, providing a discretely tunable source covering most of the far-infrared (50-1000 μm).

LMR derives its power from the really remarkable combination of sensitivity and resolution it can produce. Using the OH radical for comparison, it has been found that EPR can detect a density of about 2×10^{10} cm^{-3}, while microwave spectroscopy is at least an order of magnitude less sensitive. Resonance fluorescence methods (with a water vapor discharge source) can detect near 3×10^9 cm^{-3}. With laser magnetic resonance we can detect an OH density of 5×10^5 cm^{-3}. The only technique presently more sensitive is laser induced fluorescence, with a proven detection limit of 1×10^6 cm^{-3} in ambient air, but certainly much less with optimum conditions. This method, however, is limited in resolution by the optical

Doppler width ($\sim$1 GHz on the average), while LMR produces a collision-broadening linewidth of about 10 MHz at normal operating pressures (1 torr), and an easily accessible Doppler width of about 1 MHz. Sub-Doppler resolution can often be effected by using saturation dip techniques because the sample is located inside the optical cavity of the laser. Therefore, LMR can give us essentially the resolution of a microwave spectroscopy experiment with up to a million times the sensitivity!

A schematic diagram of the optically pumped LMR spectrometer built at the National Bureau of Standards in Boulder, Colorado is given in Figure 1. A gas (e.g., CH_3OH) having a strong vibrational absorption line that coincides with a CO_2 laser frequency is pumped nearly transversely by a CW, grating and piezoelectrically tuned CO_2 laser operating on a single mode with powers of up to 50 watts. The far-infrared lasing action is induced between rotational states of the upper vibrational level and oscillates inside the cavity defined by one fixed mirror and another mounted on a micrometer drive. The cavity mode spacing ($c/2\ell$ = 150 MHz) is much larger than the gain profile (5 MHz), so the laser length can be adjusted to select a single longitudinal mode, while higher order transverse modes are extinguished with an iris diaphragm. A piece of 13μm thick polypropylene stretched on a mount at the Brewster angle separates the transversely-pumped gain cell from the sample region of the cavity. This polarizes the laser radiation, and the polarization can then be rotated to select either σ or π orientation relative to the magnetic field. The sample region of the cavity is located between the pole faces of a 15" electromagnet, operating with 15 cm pole tips and a 7.2 cm airgap. Maximum fields of 20 kG can be obtained with this configuration.

The total power oscillating inside the cavity is monitored by coupling a small fraction of it out of a polyethylene window with a 4 mm diameter copper mirror machine at 45° which is mounted on a small rod. This coupling mirror can be inserted into the laser mode pattern to optimize the output coupling for each laser line. A liquid helium cooled gallium-doped germanium bolometer which has a NEP of about 6×10^{-12} WHz$^{-1/2}$ is used to detect the coupled radiation. An ac magnetic field of up to 50 G is produced by a set of Helmholtz coils operating at 1kHz, and lock-in detection is used to process the signals. The LMR spectrometer operates within an order of magnitude of the quantum noise limit set by the laser, about 1.4×10^{-12} watts. The minimum detectable one-way intracavity loss has been shown to be about 2×10^{-10}; this is roughly 1000 times less than could be achieved with a single pass through an external cell. After normalizing with the effective path length inside the cavity (about 75 cm, determined by the flame extent and the finesse of the cavity) we find that the direct interaction between the absorbing intracavity sample and the laser gain medium produces an enhancement in the sensitivity of about a

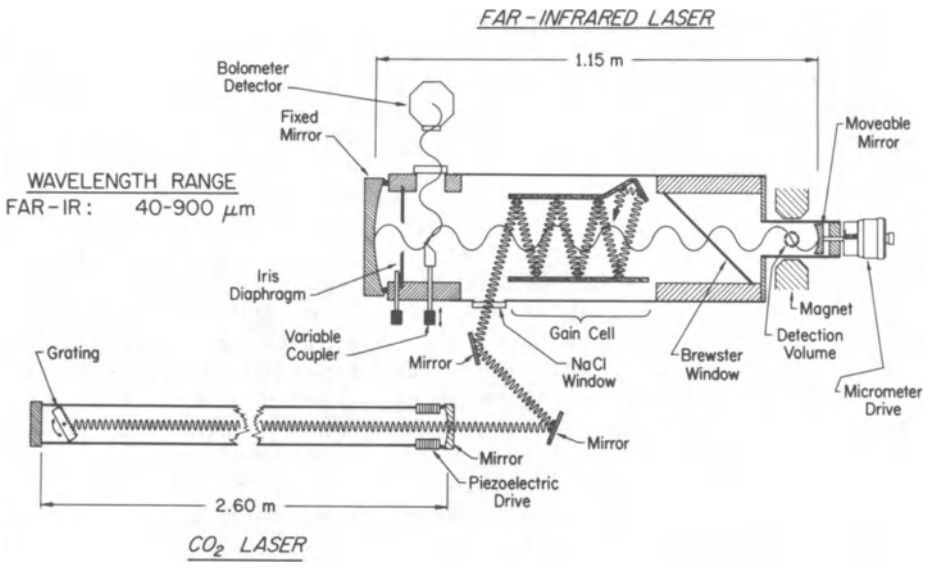

Fig. 1. Schematic diagram of an optically pumped far infrared LMR spectrometer.

factor of 20.

All of the free radicals observed until 1978 were generated in low pressure (1 Torr) flames burning inside the laser cavity. The methane fluorine atom reaction has been a particularly affluent souce of radicals. Evenson and his co-workers have now observed CH, CH_2, CCH, CH_2F, CF, CF_2, and C atoms in this one flame alone [19]. By modifying the laser design to accommodate an intracavity positive column discharge and incorporating a solenoid magnet to provide the field, we were able to detect the LMR spectra of metastable states of CO and O_2, the O atom, and the HBr^+ molecular ion. These experiments will be discussed in the next section.

LASER MAGNETIC RESONANCE DETECTION OF A MOLECULAR ION

The discharge LMR spectrometer consists of a 7.6 cm diameter by 38 cm long quartz far-infrared gain cell pumped transversely by a 2.3 meter CO_2 laser with a 30 watt single line output. The pumping geometry and output coupling is otherwise identical to that in Figure 1. The gain cell is separated from the 5 cm diameter by 58 cm long sample region by a 13 μm beamsplitter. Instead of being located inside the pole faces of a 15" transverse magnet, the sample region is centered inside the bore of a 5 cm diameter by 33 cam long solenoid magnet cooled by liquid nitrogen. The magnet can produce fields of 6 kG with a homogeneity of 0.1% over a

15 cm length. An ac modulation field was provided by a solenoidal coil wound to be concentric with the liquid nitrogen-cooled magnet. Since the solenoid produces an axial magnetic field, only σ-type transitions can be observed with this system. A dc glow discharge is maintained between a water-cooled copper cathode located in a sidearm outside of the optical cavity and a cylindrical copper anode located about 3 cm from the beamsplitter. Magnetic field measurements are made by placing a calibrated shunt resistor (0.01 Ω) in series with the magnet, keeping it at a constant temperature in a thermostated oil bath, and measuring the voltage drop across it with a digital voltmeter. The relationship between voltage and magnetic field in the sample region is calibrated with a NMR gaussmeter, and was determined to be linear over the entire range of fields available. With this system, flux densities can easily be measured with a precision of about 0.5 G.

The vacuum for the sample region is provided by a 750 l/min mechanical pump. Generally the discharge is operated at about 1 Torr total pressure with a fairly slow flow rate (~100 l/min). Pressures in both the sample region and gain cell are monitored with capacitance manometers.

The plasma is generally run at relatively low currents (<50 mA). The plasma density at zero magnetic field is in the range 10^8-10^{10} cm^{-3}. With an axial magnetic field one can expect the plasma density to increase markedly because the ambipolar diffusion of the electrons and ions to the walls is inhibited. We have, in fact, observed this effect in some of our spectra. In discharges of this nature, one generally observes a high electron temperature (20,000°K) while the translational and rotational degrees of freedom of molecules in the plasma are nearly thermalized at the wall temperature. Because vibrational relaxation is so much slower, vibrational temperatures can often exceed several thousand degrees.

The electric field in the positive column plasma filling the laser cavity is a few volts/cm. As a consequence, the positive ions will experience a net drift velocity of a few hundred meters per second toward the cathode in addition to their predominant radial motion. In the microwave studies of ions at the University of Wisconsin [5-7], this drift velocity was measured by virtue of the resulting Doppler shift of about 100 kilohertz in the microwave absorption frequency. In the LMR experiment the plasma is sampled by a standing wave rather than a traveling wave; therefore the slow drift velocity will manifest itself as a broadening of the absorption lines rather than a frequency shift.

The presence of the plasma causes a definite shift in the resonant frequency of the cavity, as expected from its higher refractive index. In principle, this shift could provide a direct

measurement of the plasma density. The plasma also introduces high frequency noise into the lock-in-detection system. One of the major experimental problems is simply to minimize this plasma noise, which is done empirically by varying pressure, current, and gas composition.

The first experiments performed with this glow discharge apparatus consisted of detecting spectra of OH and O_2 in the plasma. The J = 1 → 2 fine structure transition in atomic oxygen was then found at 63. 1 μm, using $^{13}CH_3OH$ as the lasing medium. The measured fine structure splitting was determined to be 158.3098(7) cm^{-1} using precise g-factors from earlier EPR studies. The O atoms were produced in a discharge through a 1% mixture of O_2 in He. The signal intensity was found to be proportional to the current over the range 0-100mA and was roughly independent of the total pressure. The transition is shown in Figure 2 [20].

The J = 8 → 9 rotational transition of the $a^1\Delta_g$ state of O_2 was found next, using the 392 μm laser line of CH_3OH in a discharge through pure O_2. This spectrum is particularly interesting because it demonstrated the capability of this spectrometer to produce sub-Doppler saturation dip spectra, as exhibited in Figure 3. It was analyzed along with several others observed for the $a^1\Delta_g$ state in the conventional LMR apparatus, using the afterglow of a 2450 MHz discharge as the source of metastables. The results of this work

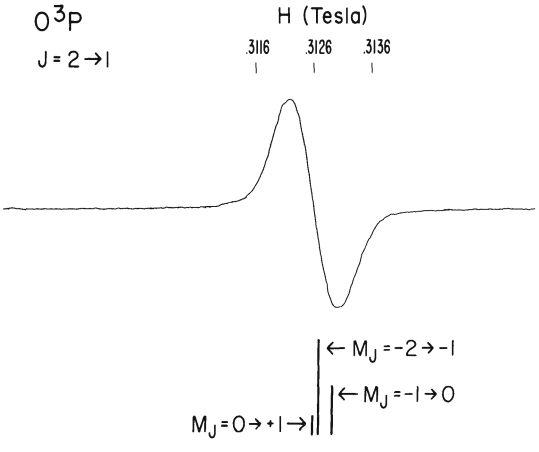

Fig. 2. The J = 2 → 1 transitions of O (2^3P). The line shape for these transitions, observed in a 40 mA glow discharge through a mixture of ∿2% O_2 in helium at 133 Pa total pressure with the 63.1 μm laser line of $^{13}CH_3OH$ pumped by the 10.3 μm P(12) line of a CO_2 laser, is shown along with the calculated positions and intensities of the individual m-components.

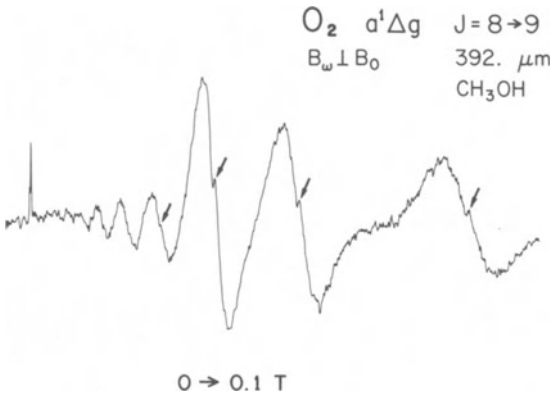

Fig. 3. Laser magnetic resonance spectrum of the J = 8 → 9 transition of $a^1\Delta_g$ O_2 observed with the 392.1 μm line of CH_3OH. Saturation dips are marked with arrows.

will be published shortly [21].

Another interesting result was the detection of pure rotational spectra of the metastable $a^3\Pi$ state of CO [22]. This state is quite short-lived, with a radiative lifetime of about 7.5 msec. These results are being analyzed along with earlier molecular beam and microwave data [23] in an attempt to obtain a more reliable set of molecular parameters for this state.

Of course, all of these experiments were done as "tune-ups" for the ultimate experiment -- a search for the spectrum of a molecular ion! A consideration of the possible candidates for this initial experiment revealed HCl^+ as being the best suited. It had been carefully studied by optical spectroscopy [24] and its rotational transitions could be predicted accurately. Its discharge kinetics had been the subject of flowing afterglow experiments [25] and it could be expected to be an abundant ion in a discharge through a dilute mixture of HCl in He. And it had a reasonably close coincidence between a low-J rotational transition and a known laser line. However, a series of intense searches for the spectrum of HCl^+ failed, for reasons which are not yet totally clear. We decided to try the experiment on the analogous HBr^+ ion.

The search was based on predictions of rotational transition frequencies from the optical work of Barrow and Caunt [26]. An energy level diagram of the $^2\Pi$ ground state calculated from their results is given in Figure 4. A discharge through a few percent of HBr in helium at about 1 torr was used to generate the ion. After considerable effort, a spectrum which could quite definitively be attributed to HBr^+ was observed. This was the J = 3/2 → 5/2

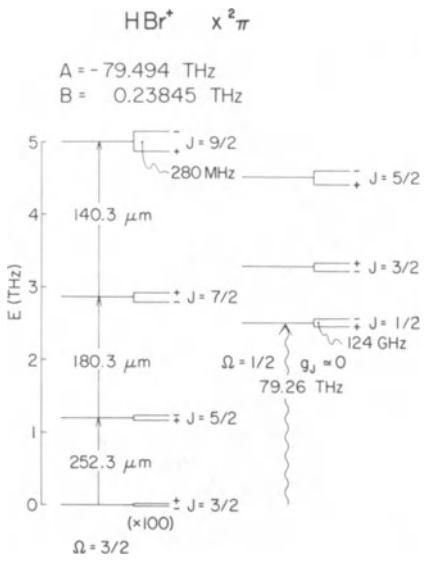

Fig. 4. Energy level diagram for the $^2\Pi$ ground state of HBr^+. The small lambda doubling in the $\Omega = 3/2$ state (Case A notation) is multiplied by 100; that in the diamagnetic $\Omega = 1/2$ state is to scale. The molecular parameters used to calculate the energies are taken from Ref. 26.

transition in the $\Omega = 3/2$ ground state, shown in Figure 5.

The maximum signal-to-noise ratio was obtained with a current of 15 mA and 1 torr of a 1% mixture of HBr in helium. An increase in the HBr content beyond a few percent caused the lines to disappear. Similarly, the addition of small amounts of air, O_2, H_2, or H_2O to the discharge resulted in large decreases in the signal. When HBr was replaced by DBr the spectra could not be obtained.

The strongest evidence that the spectrum was due to HBr^+ is provided by spectroscopic considerations. The transition was found very near the resonant field predicted from optical data. Because there are two equally abundant bromine isotopes (masses 79 and 81) each having a nuclear spin of 3/2, one expects to observe two sets of quartets for every M_J transition, with each line split by the lambda doubling. This is exactly the pattern that was found. Because we could only reach fields of 5 kG at this time, only the fastest tuning Zeeman component could be observed ($J = -3/2 \rightarrow -1/2$). By shifting the laser frequency ($d\nu$) and observing the shift in magnetic field (dH) we determined the sign of the tuning rate $dH/d\nu$, which told us that the laser frequency was above the zero field transition frequency, as predicted.

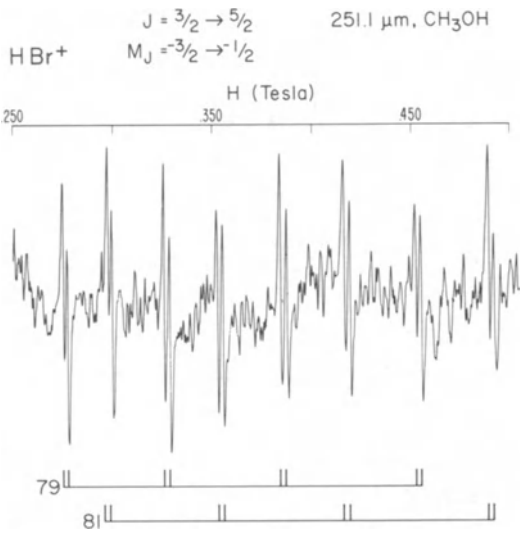

Fig. 5. The laser magnetic resonance spectrum of the J = 3/2 → 5/2 transition of HBr^+ observed at 251.1 μm (CH_3OH). This spectrum was recorded on a single scan with a 0.1 sec time constant in a glow discharge through 1% HBr in helium at a pressure of 133 Pa (1 torr). The positions of the eight doublets represent the hyperfine splitting in the M_J = -3/2 → -1/2 Zeeman transition. The doublet splitting is due to the lambda doubling.

With this degree of assurance as to the identity of the carrier, we searched for and easily found the J = 5/2 → 7/2 transition with the 180.7 μm line of CD_3OH, as shown in Figure 6. Again, the spectral features were much as predicted. The chemistry tests were repeated as before with the same results. Then the J = 3/2 → 5/2 transition was detected with a different laser line, the 253.7 μm line of CH_3OH. The J = 3/2 → 5/2 transition of DBr^+, predicted by scaling the hydrogen isotope constants for reduced mass was then found. Finally, the J = 5/2 → 7/2 transition of HBr^+ in the v = 1 state was detected just where it was predicted to be. Several other strong laser lines were used to check for spurious transitions, with negative results.

In subsequent experiments, the maximum field of the magnet was extended out to 6.2 kG. The spectra were then taken over the entire range of fields, and the next M_J components of all of the transitions were found. Magnetic flux densities were measured for the three v = 0 HBr^+ spectra with accuracies of ±1 kG, using the digital voltmeter scheme described earlier. Attempts were made to detect an increase in the linewidth by operating the discharge

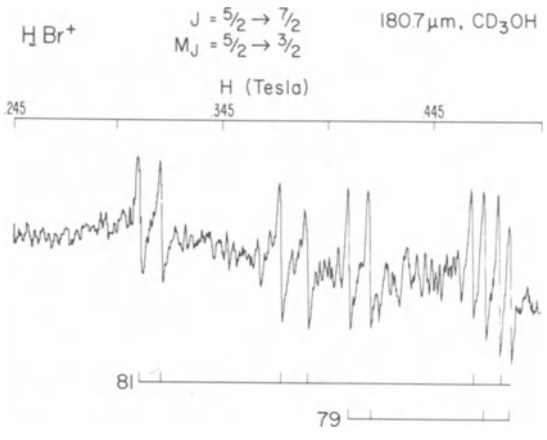

Fig. 6. The $J = 5/2 \rightarrow 7/2$ transition of HBr^+ observed at 180.7 μm (CD_3OH) under the same conditions used in Figure 2. Only the first eight hyperfine lines of the $M_J = 5/2 \rightarrow 3/2$ Zeeman component could be reached with available magnetic fields.

in an abnormal glow mode with a higher voltage drop but these experiments predictably failed. As can be seen in Figure 5, the intensity of the otherwise equally intense hyperfine components shows a small but definite increase as the field is increased.

ASSIGNMENT AND ANALYSIS OF THE SPECTRUM

As with all spectroscopic techniques, there is good news and bad news about laser magnetic resonance. The good news is the tremendous sensitivity and high resolution that can be obtained, and the fact that about 90% of the features of a LMR spectrum for a "nice" molecule (one that does not exhibit Paschen-Bach effects) can be predicted, explained, and understood in terms of very simple first-order expressions. The bad news pertains to the remaining 10% that cannot. It becomes very laborious, time-consuming, and expensive to correctly account for it. LMR produces data that are among the most difficult molecular spectra to analyze accurately. In this section we will discuss the problem of assignment and analysis of the LMR spectrum of HBr^+.

The Zeeman energy of a paramagnetic atom or molecule can be expressed to first-order as

$$E = E_0 + \mu_0 \, Hg_J \, M_J \qquad (1)$$

where E_0 is the zero-field energy, μ_0 is the Bohr magneton, H is

the magnetic flux density, g_J is an effective g-factor for the angular momentum state J, and M_J is the space projection of J. For a $\Delta M_J = 0$ transition between states E' (upper) and E" (lower) we obtain

$$\nu_L = \nu_0 + \mu_0 H(g' - g'') M_J'' \tag{2}$$

where $\nu_0 = E_0' - E_0''$ and $\nu_L = E' - E''$ is the frequency difference which must match the laser frequency at resonance. For $\Delta M_J = \pm 1$ transitions we get

$$\nu_L = \nu_0 + \mu_0 H(g' - g'') M_J'' \pm \mu_0 Hg' \tag{3}$$

The magnetic tuning rates of these transition frequencies are

$$\frac{\partial \nu_L}{\partial H} = \nu_0(g' - g'') M_J'' \qquad \Delta M_J = 0$$

$$= \mu_0(g' - g'') M_J'' \pm \mu_0 g' \qquad \Delta M_J = \pm 1 \tag{4}$$

Solving (2) and (3) for the resonant magnetic fields we obtain

$$H = \frac{\nu_L - \nu_0}{\mu_0(g' - g'') M_J''} \qquad \Delta M_J = 0$$

$$H = \frac{\nu_L - \nu_0}{\mu_0(g' - g'') M_J'' \pm \mu_0 g'} \qquad \Delta M_J = \pm 1 \tag{5}$$

If we plot the reciprocal of the resonant fields versus M_J'', we obtain a straight line in each case with a slope of

$$\frac{\partial(1/H)}{\partial M_J''} = \frac{\mu_0(g' - g'')}{\nu_L - \nu_0}$$

For a $\Delta M_J = 0$ transition the intercept is zero, but for a $\Delta M_J = \pm 1$ transition it has the value

$$\frac{\mu_0 g'}{\nu_L - \nu_0}$$

These plots are very useful in initially assigning a LMR spectrum.

Another very useful tool for the assignment of a spectrum is

the "laser pulling" experiment. The reciprocal of the tuning rate given by (4) determines which direction the resonant field will shift if the laser frequency is shifted to the red or blue. If the sign of the term g' - g" is known (as it usually is), this will tell us the sign of M_J" and thus whether the laser frequency is above or below the zero-field transition frequency.

Specializing to the present case of a $^2\Pi$ molecule described by Hund's Case A, we note that the effective g-factor for a given J state is given by the vector model as

$$g_J = \frac{(\Lambda + 2.002\Sigma)\ \Omega}{J(J+1)} \tag{6}$$

Therefore g' - g" will always be negative for pure rotational transitions between the $\Omega = 3/2$ levels. This tells us that the fastest tuning Zeeman transition will be that with the largest negative M_J value if $\nu_L > \nu_0$ or the largest positive M_J if $\nu_L < \nu_0$. For a $\Delta M_J = \pm 1$ transition, we see from (5) that the fastest tuning transition will also be that with $\Delta M_J = +1$ if $\nu_L > \nu_0$ or $\Delta M_J = -1$ if $\nu_L < \nu_0$. In both of these last cases, the opposite branch ($\Delta M_J = -1$ if $\nu_L > \nu_0$ or $\Delta M_J = +1$ if $\nu_L < \nu_0$) will occur at higher fields. The relative intensities for all of these transitions are easily obtained from standard matrix elements of the direction cosine operator. With equations (1) through (6) and the direction cosine results the main features of the LMR spectrum can be predicted very easily.

Hyperfine interactions in LMR spectra are usually described at all but the lowest fields (<1 kG) by a decoupled representation, i.e., with nuclear spin independently quantized in the space-fixed axis system defined by the magnetic field. Therefore the effect of a nuclear spin I will be to split each Zeeman transition into 2I + 1 equally intense components. In a Case A molecule, the magnetic hyperfine energy can be expressed as simply

$$E_{MHf} = a_J\ M_I\ M_J \tag{7}$$

where a_J is an effective hyperfine constant for the state labeled by J. Because of the $\Delta M_I = 0$ selection rule the effect of the magnetic hyperfine interaction is to split each Zeeman component of a transition into 2I + 1 equally spaced lines. This can be expressed in frequency space as

$$\begin{aligned} \Delta\nu_{hf} &= M_I\ M_J"(a_J' - a_J") && \Delta M_J = 0 \\ &= M_I[(a_J' - a_J")\ M_J" \pm a'] && \Delta M_J = \pm 1 \end{aligned} \tag{8}$$

To transform these expressions into magnetic field space, we multiply by the term $(\partial H/d\nu)$. Note that we desire the shift in the field corresponding to a shift in the zero-field frequency ν_0 (not ν_L) caused by the hyperfine interactions. This derivative has the opposite sign of that of field with respect to ν_L. The result is

$$\Delta H_{hf} = \frac{M_I(a_J' - a_J'')(-1)}{\mu_0(g' - g'')} \qquad \Delta M_J = 0$$

$$= \frac{M_I[(a_J' - a_J'')\, M_J'' \pm a_J](-1)}{\mu_0(g' - g'')\, M_J'' \pm \mu_0\, g'} \qquad \Delta M_J = +1 \qquad (9)$$

The form of the magnetic hyperfine coupling constant a_J can be obtained easily from the theory of gas phase electron resonance spectroscopy, so nicely worked out by Carrington and co-workers [27] a decade ago. For terms diagonal in all quantum numbers, the magnetic hyperfine constant for a Case A $^2\Pi$ state can be expressed as

$$a_J = \frac{\Omega h}{J(J + 1)} \qquad (10)$$

where $h = a + \Sigma(b + c)$, and a, b, and c are the Frosch and Foley hyperfine interaction constants, defined as reduced matrix elements over the unpaired electron density. From (9) we see that the shift in magnetic field due to the magnetic hyperfine interaction in a $\Delta M_J = 0$ spectrum is independent of M_J, and thus the hyperfine splitting is also independent of M_J in this case. For a $\Delta M_J = \pm 1$ spectrum that is not generally the case. Also, we note that for a positive h, $(a_J' - a_J'')$ is negative for $\Delta J = +1$ transitions with no change in Ω (pure rotational transitions). Since $(g_J' - g_J'')$ is also negative for these cases, the sign of the shift in the resonant field position caused by the magnetic hyperfine effect depends only on the sign of M_I for $\Delta M_J = 0$. For $\Delta M_J = \pm 1$ this is not generally true, and we must consider each specific case. However, it is usually true that for the fastest tuning transitions, the sign of M_J'' and the $\pm$ in (9) are correlated such that for a positive h the $+M_I$ component always appears at lowest field in both $\Delta M_J = 0$ and $\Delta M_J = +1$ transitions, at least in the situations we are considering. In summary, the appearance of magnetic hyperfine structure in the pure rotational LMR spectrum of a $^2\Pi_{3/2}$ molecule will be that of $(2I + 1)$ equally spaced, equally intense lines, with the $+M_I$ transitions appearing first in the low-field M_J components.

The presence of a nuclear electric quadrupole moment will destroy the equal spacing of hyperfine lines. The first-order

quadrupole energy in a decoupled basis can be expressed as

$$E_Q = Q_J[3M_J^2 - J(J+1)][3M_I^2 - I(I+1)] \qquad (11)$$

where

$$Q_J = \frac{eqQ}{4} \frac{[3\Omega^2 - J(J+1)]}{\{(2J-1)\,J(J+1)(2J+1)[3I - I(I+1)]\}}$$

Although this expression does not simplify as nicely as that for the magnetic hyperfine, we can still draw some useful generalizations from it. Because of the squared dependence on M_I the quadrupole interaction will cause the otherwise equally-spaced hyperfine levels to "bunch up"; that is, the spacing will either increase or decrease from lower to higher energies. The essentially $1/J^4$ dependence of Q_J causes the lower J state of the transition to dominate this effect in the transition. From (7) we noted that the order of the M_I states is opposite in Zeeman levels with opposite sign of M_J. This fact, together with the squared dependence on M_J in (11) means that the "bunching" of levels will occur in the same direction (from low to high energy or vice versa) in a $+M_J$ state as that in a $-M_J$ state. Therefore, whether the laser is above or below the zero field transition frequency will reverse the appearance of the hyperfine pattern. This is very similar to EPR patterns, which are reversed with a sign change in M_J. The pattern will depend only on the sign and magnitude of Q_J. We can deduce that for positive Q_J the hyperfine lines will converge to low fields when $\nu_L > \nu_0$, and if Q_J is negative or if $\nu_L < \nu_0$ they converge to high fields, for $|M_J| = J$.

Next we will consider the lambda doubling. At this stage we only want to determine how to assign the parity correctly. The lowest energy Krönig symmetry will generally be that which is the same as the lowest $^2\Sigma$ state, which will dominate the lambda doubling perturbation, e.g., if the lowest $^2\Sigma$ state has + Krönig symmetry, then + symmetry levels of the $^2\Pi$ state will be lower than - levels. We must then multiply the Krönig symmetry by the rotational phase factor $(-1)^{J-S}$ to get total parity. Therefore, for the usual case of a $^2\Sigma^+$ perturber, we have + parity the lowest for J = 1/2, - the lowest for J = 3/2, + the lowest for J = 5/2, and so on. In the $\Omega = 3/2$ state, lambda doubling increases with J. Therefore the upper state of a transition will determine the relative parity of the lambda-doubling components. Very simply, in a J = 3/2 → 5/2 transition under the above conditions, the - → + parity component occurs at lower energy than the + → - (parity must change in electric dipole transitions, of course). Therefore if the laser is at a lower frequency than the zero field rotational frequency, the - → + transition will appear at the lower

magnetic field, and vice-versa.

Finally, we shall discuss the very simple case of having different isotopic masses for a given molecule. Different masses will, of course, produce different rotational constants and hence different rotational energies. For light molecules (CH, OH, etc.) the isotope shift in the energies is large, such that different isotopes don't generally appear in the same spectrum, except through coincidence. For heavier molecules, the isotope shift may be small enough so that several species can be observed simultaneously. Then if the laser is above the zero-field transition frequency, the lighter isotopes appear at lowest fields; if ν_L is below ν_0, then the heavier isotopes appear first.

With only these simple ideas, an LMR spectrum can usually be assigned. The next step was to carry out a nonlinear least squares fit of the transition using a far more exact Hamiltonian. Again, most of the theory required to analyze LMR spectra was worked out earlier by Carrington, Levy, and Miller [28]. J. M. Brown [29] has since developed a more precise Zeeman Hamiltonian, and we have adopted his approach for $^2\Pi$ molecules. The detailed effective Hamiltonian used is given in almost complete form by Brown et al in [29], and we will not reproduce it here. The quadrupole interaction was not included in that work, however, and we have used the expressions from [28], to obtain its matrix elements in a decoupled Case A representation. The form of the effective $^2\Pi$ Hamiltonian used is

$$H_{eff} = H_{so} + H_{rot} + H_{cd} + H_{sr} + H_{LD} + H_{cdLD} + H_{hfs} + H_{cdhfs} + H_z \qquad (12)$$

where H_{so} represents spin-orbit coupling, H_{rot} and H_{cd} represent the rotational kinetic energy and centrifugal distortion, H_{sr} is the electron spin-rotation interaction, H_{LD} and H_{cdLD} represent the lambda doubling interaction and its centrifugal distortion corrections, H_{hfs} and H_{cdhfs} are the hyperfine interactions and distortion corrections, and H_z is the Zeeman interaction.

A computer program was written to set up the matrix elements of (12) including terms off-diagonal by ± 1 unit in J. For HBr^+ the matrices are 24 x 24 for each M_J value. Each M_J matrix is diagonalized and sorted at the appropriate resonant field position, differences are taken and the frequencies for each transition are then computed; the parameters are then iteratively adjusted until these transition frequencies converge to within some tolerance of the laser frequency. The size and structure of the data set dictates which of the parameters can be determined by this method.

INTERPRETATION OF MOLECULAR PARAMETERS IN TERMS OF ELECTRONIC STRUCTURE

Once a LMR spectrum has been detected, measured, and assigned, and the parameters extracted from a suitable analysis (such as a nonlinear regression method), the parameters are interpreted in terms of various integrals over the electronic distribution of the molecule. This subject has been developed to a high degree of sophistication for the purpose of analyzing microwave and electron paramagnetic resonance spectra [27,28,30]. We will review some of the salient aspects very briefly, but we do not present a detailed set of results for HBr^+ because our analysis is still in a very preliminary stage.

From a pure rotational LMR spectrum we can directly obtain the rotational constants, centrifugal distortion constants, hyperfine constants, lambda doubling constants, electron spin-rotation constants, quadrupole coupling parameters. In addition, measurement of cross-spin transitions ($\Delta\Omega \neq 0$) will directly measure the spin-orbit parameter and the spin-spin parameter for states with $S \geq 1$. If the data are precise enough, higher-order corrections to the g-factors that occur in the Zeeman Hamiltonian can be determined.

Once these parameters are determined, details of the electronic structure are revealed from their definitions as integrals over the electronic distributions. The rotational constants are the reciprocals of the moments of inertia averaged over the vibrational motion in the state they are measured for. The quantities of fundamental interest are not these effective rotational constants, but rather the equilibrium values, from which one can deduce the equilibrium structure of the molecule. This is possible only when rotational transitions have been measured in at least one excited level of every vibrational mode, which is usually not possible. One is thus generally forced to use the effective moments of inertia as an approximation to the equilibrium values. While the structure problem seems totally trivial for a diatomic molecule, the measurement of four isotopes of HBr^+ allows a rather precise determination of the bond distance through the use of Kraitchman's equations [31]. For a linear molecule this reduces to

$$|Z| = [\mu^{-1}(I_x' - I_x)]^{1/2} \tag{13}$$

where Z is the center-of-mass coordinate for the isotopically substituted atom, and I' and I are moments of inertia of the substituted and original molecules. Because we have measured two isotopes of both bromine and hydrogen, subtraction of the coordinates obtained from (13) will yield a precise approximation for

the equilibrium bond distance, in which the effect of the vibrational averaging has been largely eliminated. In general, LMR has the same capability as microwave spectroscopy for obtaining these precise substitution geometries for small molecules.

The magnetic hyperfine parameter h used in (10) is defined as

$$h = a + \Sigma(b + c) \tag{14}$$

The Frosch and Foley hyperfine constants a, b, and c are in turn defined as follows [30].

$$a = 2g_I \mu_N \mu_0 \left\langle \frac{1}{r^3} \right\rangle \text{ nuclear spin-electron orbit}$$

$$b + \frac{c}{3} = \frac{16\pi}{3} g_I \mu_N \mu_0 \Psi^2(0) \text{ Fermi contact}$$

$$c = 3g_i \mu_N \mu_0 \left\langle \frac{3\cos^2\theta - 1}{r^3} \right\rangle \text{ nuclear spin-electron spin} \tag{15}$$

In addition there is the parity-dependent spin-spin parameter

$$d = 3g_I \mu_N \mu_0 \left\langle \frac{\sin^2\theta}{r^3} \right\rangle$$

In these expressions r is the distance between the nucleus and the electrons and the average is over the unpaired electron density. If one can determine all of these integrals, then a detailed view of the unpaired electron distribution can be obtained. For example, the value of $\Psi^2(0)$ is non-negligible only for electrons in s orbitals, while a will be appreciable only for orbitals with non-zero orbital angular momentum, and c will similarly vanish for a spherical (s) orbital. By comparing values of $\langle 1/r^3 \rangle$, $\Psi^2(0)$,

$$\left\langle \frac{3\cos^2\theta - 1}{r^3} \right\rangle \text{ and } \left\langle \frac{\sin^2\theta}{r^3} \right\rangle$$

obtained from spectroscopic measurements of a, b, c, and d with values obtained for the free atoms, one can deduce the degree of atomic orbital (s, p, ...) character for a given open-shell molecular orbital system, and from this draw qualitative conclusions regarding the nature of the chemical bonding (double bond character, etc.) in the molecule.

The quadrupole coupling constant eqQ, provides similar but complementary information on the electronic structure. In this

constant, e is the nuclear charge and Q is the nuclear quadrupole moment, while $q = \langle \partial^2 V/\partial Z^2 \rangle$ is the field gradient at the nucleus, which can be expressed as

$$q = e\left\langle \frac{3\cos^2\theta - 1}{r^3} \right\rangle \tag{16}$$

The average in this expression is to be taken over the entire electron distribution, not just over the unpaired electron density. Evaluation of q can provide considerable insight as to the degree of ionic character of a bond, the amount of mixing of s and p atomic orbitals in a given molecular orbital, and also about the amount of multiple bond character.

We have shown that far-infrared laser magnetic resonance spectroscopy is a powerful new method for studying molecular ion structures. While our results for HBr^+ are most encouraging with respect to prospects for expanding the study to other charged species we should remind ourselves that these were a series of very difficult experiments. There are other promising candidates for LMR studies, including diatomics, like HCl^+, HF^+, HI^+, OH^+, NH^+, O_2^+, SH^+, PH^+, and polyatomics like H_2O^+, H_2S^+, NNO^+, and OCS^+; however, we should not expect any of these to be much easier to observe than HBr^+. Spectra, and the resulting determination of geometrical and electronic structures of other ions are very likely to proceed from LMR studies in the future, but each is guaranteed to contribute a certain amount of gray hair to the experimenters who do them.

ACKNOWLEDGMENT

The experimental part of this work was done at the National Bureau of Standards in Boulder, Colorado. R. J. S. thanks the National Research Council for a post-doctoral fellowship during that time (1977-79). The analysis of the HBr^+ spectra is being carried out at the University of California, Berkeley, by K. G. Lubic, who thanks the University for a Regents Fellowship (1980) and R. J. Saykally. R. J. S. and K. G. L. gratefully acknowledge support from the National Science Foundation grant CHE80-07042.

REFERENCES

1. G. H. Herzberg, Spectra and structures of molecular ions, in Quarterly Reviews (The Chemical Society, London, 1971), p. 201.
2. K. B. Jefferts, Phys. Rev. Lett. 20, 39 (1968); 23, 1476 (1969).

3. D. Buhl and L. E. Snyder, Nature 228, 267 (1970).
4. B. E. Turner, App. J. 193, L83 (1974).
5. T. A. Dixon and R. C. Woods, Phys. Rev. Lett. 34, 61 (1975).
6. R. C. Woods, T. A. Dixon, R. J. Saykally, and P. G. Szanto, Phys. Rev. Lett. 35, 1269 (1975).
7. R. J. Saykally, T. A. Dixon, T. G. Anderson, P. G. Szanto, and R. C. Woods, App. J. 205, L101 (1976).
8. W. H. Wing, G. A. Ruff, W. E. Lamb, and J. J. Spezeski, Phys. Rev. Lett. 36, 1488 (1976).
9. D. E. Tolliver, G. A. Kyrala, W. H. Wing, Phys. Rev. Lett. 43, 1719 (1979).
10. J. T. Shy, J. W. Farley, W. E. Lamb, Jr., and W. H. Wing, Phys. Rev. Lett. 45, 535 (1980).
11. A. Carrington, P. L. Milverton, and P. G. Sarre, Mol. Phys. 35, 1505 (1978).
12. A. Carrington, P. L. Milverton, P. G. Roberts, and P. J. Sarre, J. Chem. Phys. 68, 5659 (1978).
13. A. Carrington, P. G. Roberts, and P. J. Sarre, Mol. Phys. 35, 1523 (1978).
14. M. Tadjeddine, R. Abouaf, P. C. Cosby, B. A. Huber, and J. T. Moseley, J. Chem. Phys. 69, 710 (1978); J. T. Moseley, P. C. Cosby, J. B. Ozenne, and J. Durup, J. Chem. Phys. 70, 1474 (1979).
15. A. Carrington, private communication (1980).
16. R. J. Saykally and K. M. Evenson, Phys. Rev. Lett. 43, 515 (1979).
17. T. Oka, Phys. Rev. Lett. 45, 531 (1980).
18. F. Grieman, Ph.D. Thesis, University of California, Berkeley, CA and F. J. Grieman, B. H. Mahan, A. O'Keefe, and J. S. Winn, to be published.
19. K. M. Evenson, R. J. Saykally, D. A. Jennings, R. F. Curl, Jr., and J. M. Brown, Far infrared laser magnetic resonance, in: "Chemical and Biochemical Applications of Lasers", Vol. V, C. B. Moore, ed., Academic Press, New York (1980).
20. R. J. Saykally and K. M. Evenson, J. Chem. Phys. 71, 1564 (1979).
21. A. Scalabrin, R. J. Saykally, K. M. Evenson, H. E. Radford, and M. Mizushima, J. Mol. Spectrom. (to be published).
22. R. J. Saykally and K. M. Evenson, J. Chem. Phys. (to be published).
23. R. J. Saykally, Ph.D. Thesis, University of Wisconsin, Madison, WI (1977).
24. K. L. Saenger, R. N. Zare, and C. W. Mathews, J. Mol. Spectrom. 61, 216 (1976).
25. F. C. Fehsenfeld and E. E. Fergeson, J. Chem. Phys. 60, 5132 (1974).
26. R. F. Barrow and A. D. Caunt, Proc. Phys. Soc. A66, 617 (1953).
27. A. Carrington, "Microwave Spectroscopy of Free Radicals," Academic Press, New York (1974).

28. A. Carrington, D. H. Levy, and T. A. Miller, Adv. Chem. Phys. 18, 149 (1970).
29. J. M. Brown, M. Kaise, C. M. L. Kerr, and D. J. Milton. Mol. Phys. 36, 553 (1978).
30. C. H. Townes and A. L. Schawlow, "Microwave Spectroscopy," Dover, Inc., New York (1975).
31. J. Kraitchman, Am. J. Phys. 21, 17 (1953).

LASER INDUCED FLUORESCENCE OF TRAPPED MOLECULAR IONS

John S. Winn

Department of Chemistry, University of California,
and Materials & Molecular Research Division
Lawrence Berkeley Laboratory, Berkeley, California 94720

INTRODUCTION

Laser induced fluorescence (LIF) spectra (laser excitation spectra) are conceptually among the most simple spectra to obtain. One need only confine a gaseous sample in a suitable container, direct a laser along one axis of the container, and monitor the sample's fluorescence at a right angle to the laser beam. As the laser wavelength is changed, the changes in fluorescence intensity map the absorption spectrum of the sample. (More precisely, only absorption to states which have a significant radiative decay component are monitored.) For ion spectroscopy, one could benefit in many ways by such an experiment. Most optical ion spectra have been observed by emission techniques, and, aside from the problems of spectral analysis, discharge emission methods often produce the spectra of many species, some of which may be unknown or uncertain. Implicit in the description of LIF given above is certainty as to the chemical identity of the carrier of the spectrum.

This article describes a method by which the simplifying aspects of LIF can be extended to molecular ions (albeit with a considerable increase in experimental complexity over that necessary for stable neutral molecules). Briefly, we use a quadrupole ion trap to store and spatially confine ions. The trap is mass-selective, affording species identification over a large mass range. The laser is pulsed, allowing time-resolved studies of various types. This experiment has been developed over several years in collaboration with Professor Bruce Mahan, Dr. Fred Grieman, and Mr. Tony O'Keefe. The article is divided into two main sections. The first describes the apparatus in some detail, and the second gives selected results demonstrating the types of

measurements which are made possible. Further details of the apparatus can be found elsewhere [1].

EXPERIMENTAL METHOD

Ion Trap

The experimental apparatus is based on the ability to confine a sufficient number of molecular ions in an electric field of suitable geometry. There are many types of trap designs discussed in the literature [2]. Before discussing the design we have chosen, a few comments are in order on the desirability of using a trap over other ion sources.

One alternative technique, exemplified by the work of Carrington [3], is to use an ion beam source. A beam has the advantages of spatial localization and velocity control, and high resolution spectra can result from various methods which reduce the Doppler width of the beam-laser interaction. A decided disadvantage is the relatively low number density of ions in a focussed, mass selected ion beam. For example, a typical mass 40 ion beam with a cross-sectional area of 0.04 cm^2, a laboratory energy of 100 eV, and an ion current of 1 nA has an ion density of 7×10^4 cm^{-3}. Of these 7×10^4 ions, a crossed ion-laser beam interaction geometry would irradiate only $\sim$3000 ions per cm of irradiated ion beam length, assuming a 2 x 2 mm ion beam cross-section. By the time one multiplies this figure by a typical population distribution for what are generally rather hot ions, the number of ions in any given quantum state has fallen below detectability by LIF.

One can use discharge flow methods, as demonstrated by Miller and coworkers [4]. The ion density is considerably greater and the ions can be equilibrated to the temperature of the carrier gas. This temperature can be made significantly lower than ambient. One potential drawback is the lack of ionized species isolation and identification which a mass spectrometer allows. The identification of the carrier of a spectrum is not automatic in a discharge flow where perhaps many types of ions or radicals are present.

The ion trap therefore offers the following experimental conditions. The ion density can be made sufficiently large ($\gtrsim 10^6$ cm^{-3}) for a reasonable detection probability. The trapped ion mass can be varied, allowing unambiguous chemical identification. The trap can be operated at sufficiently low pressures so that ions can be confined in a collision-free environment for long times (long compared to fluorescence decay times and, generally,

for times which are limited by the ion-neutral collision rate). From the very nature of collision-free trapping, one gains the added benefit that the ion state distribution reflects the nascent distribution resulting from the chosen ionization method. For favorable systems, one can trap ions for times on the order of many collision periods. One can in this way study inelastic collision processes and perhaps follow the course of reactive ion-molecule collisions. On the negative side, the rather high velocity and chaotic motion characteristic of trapped ions limits the spectral resolution. Progress has been made toward reducing the velocity spread of trapped ions; the rather spectacular results [5] obtained by laser cooling of atomic ions is one potentially useful method.

The ion trap we use is cylindrical in geometry. Design criteria for such traps have appeared in the literature [6]. The cylindrical design was chosen over a more conventional hyperbolic design [2] primarily to allow the various apertures needed for light entrance and exit to be cut into the trap without seriously disturbing the electric fields. A cut-away assembly drawing, showing more than the trap itself, is shown in Figure 1. The trap itself consists of two end, or cap, electrodes which are electrically grounded (2 and 5 in Figure 1) and a cylindrical center electrode (denoted 3 in Figure 1). Two dimensions determine the trap geometry: the cap-to-cap spacing, $2z_1$, and the radius of the cylindrical center electrode, r_1. By changing the removeable cap electrode cones (horizontally shaded portions of 2 and 5 in Figure 1), we can alter the z_1 to r_1 ratio. In our design, r_1 = 1.43 cm, and cap electrode cones are available to permit $z_1 = r_1$ or $2z_1^2 = r_1^2$. The latter geometry closely approximates the ideal hyperbolic case [6].

Trapping is achieved by applying a potential of the form $U + V \cos \omega t$ to the center electrode. U is a constant potential; V is the amplitude of an r.f. potential of frequency ω. By changing the ratio U/V one changes the range of masses which can be trapped. By changing the magnitudes of U and V while maintaining a constant ratio, one changes the center of this range of masses. Thus one can trap all ions, ions of only one mass, or ions of neighboring masses. In our design, the maximum mass we can trap is $\sim$100 amu and the maximum useable resolution is $m/\Delta m \sim 40$.

The other components of the trap region shown in Figure 1 are described briefly below. Ionization is attained by electron bombardment from the electron gun (13). The gun uses a thoriated W filament and is tightly enclosed to reduce scattered filament light. The electron current ($\sim$50 μA maximum) is monitored by a small Faraday cup (4). Laser light passes through the trap in a direction perpendicular to the plane of Figure 1. How this is

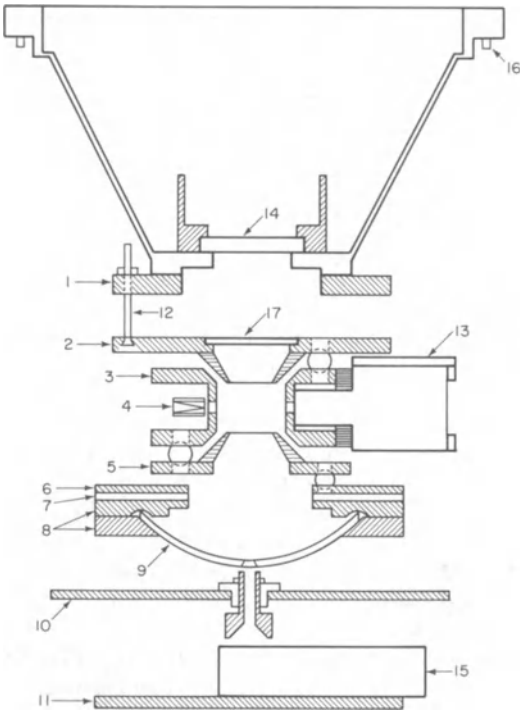

Fig. 1. Cross-sectional drawing of the ion trap assembly. Numbered items are identified in the text.

done is described in greater detail below. Fluorescence passes through the planar end electrodes, which are wire mesh. If emitted downwards, the light is reflected back up by the metallic spherical mirror (9). Upward fluorescence is gathered by a Fresnel lens (17), directed through a quartz window (14) through the vacuum and onto the photocathode of the detection photomultiplier (not shown in Figure 1).

To determine the ion density, a magnetic strip electron multiplier (15) is located beneath the trap. A magnetic shield (10) isolates this device from the trap region. By applying appropriate voltages to the trap, mirror, and associated plates (6, 8, and a Cu insert in 10), ions are pulsed out of the trap and detected. It is vital that ions are pulsed out of the trap at the same point in the r.f. cycle of the trap in order to obtain reproduceable measures of the ion density.

Ancillary pieces shown in Figure 1 include the multiplier mount (11), a Teflon insulator (7), one of the height adjustment assemblies (1 and 12) and the locating pin (16) which precisely repositions the trap assembly into the vacuum chamber. Note also

that ceramic balls are used to position, insulate, and space the trap electrodes.

An assembly diagram of the remainder of the trap chamber is shown in Figure 2. The laser beam entry and exit arms are shown in relation to the trap itself. Extensive light baffles are used to reduce scattered light, as are (occasionally) bandpass filters before the photomultiplier.

Optical System

The laser is a Molectron nitrogen laser pumped dye laser. Due to Doppler motion, the laser bandwidth need be no less than $\sim 0.6\ cm^{-1}$. The laser pulse is 5 to 10 nsec in duration with an energy of 50 and 500 μJ/pulse. Laser power on a shot-to-shot basis is monitored with a photodiode. The laser repetition rate is usually kept at its maximum of 40 Hz. Laser wavelength is monitored optogalvanically [7]. A hollow cathode discharge in Ne is mounted past the exit window. Impedance changes in the discharge due to laser excitation of excited Ne atoms are monitored as the laser wavelength is changed. The numerous Ne* transitions throughout the visible region of the spectrum provide calibration markers.

Fluorescence is collected by the lens and mirror system mentioned above. They have a geometric collection efficiency of 10%. The detector is a cooled photomultiplier tube operated in a photon-counting mode.

Experimental Timing

Since the laser is pulsed and the ions are stored for, at most, some small fraction of a second, the entire experiment is continuously cycled under computer control. A typical cycle follows. The electron gun is fired for about 2 msec. Mass selection and fluorescence decay (from electron bombardment) is allowed to occur for about 0.1 to 1.0 msec. The laser is fired and its power recorded. After a second delay of up to several μsec (but more typically tens of nsec), the gain of the photomultiplier tube is switched from a low to a useable, high value, and fluorescence counts are accumulated. Ions are then pulsed from the trap and their density recorded. The optogalvanic signal is measured, and one cycle is ended. This cycle is repeated at a given wavelength for a predetermined number of laser shots. The wavelength is then advanced a preset amount, and a new set of cycles is initiated. The relevant signal is the raw fluorescence normalized to laser power and ion density recorded as a function of the laser frequency. Spectra are stored on disks for later manipulation and display by the computer.

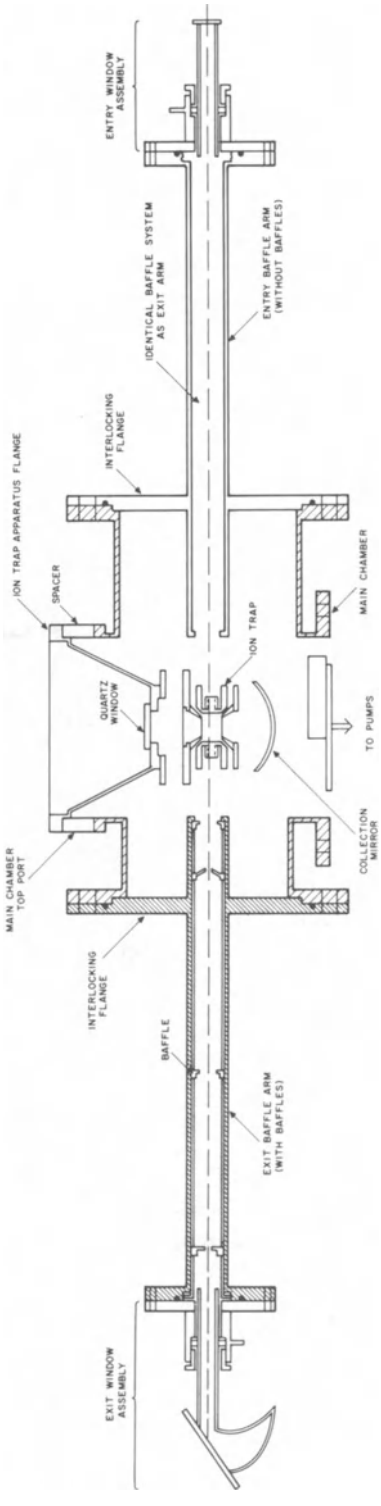

Fig. 2. Assembly drawing of the vacuum chamber with the trap assembly in place. The photomultiplier detector mounts onto the ion trap apparatus flange and views the trap through the quartz window.

Ten nsec, the laser pulse duration time, is generally a brief period in the radiative lifetime of an electronically excited molecule. We can thus measure radiative decay by changing the experimental setup slightly. We keep the laser fixed at one wavelength in coincidence with a previously assigned feature in the spectrum. Then the fluorescence is monitored after each laser shot by a fast multichannel scaler (minimum channel width = 10 nsec). Data are accumulated for hundreds to many thousands of laser shots. Background radiation is subtracted from this signal by detuning the laser and repeating the measurement. A normal single exponential fluorescence decay curve results.

Other Experimental Remarks

We typically fill the vacuum chamber to a pressure $\sim 10^{-5}$ torr with the necessary parent neutral ion. Primary ions are easily produced. Fragment ions, however, are subject to large, and generally unknown, repulsive kicks when they are formed. The laboratory kinetic energy gained by these kicks depend on fragment masses and details of the dissociation dynamics. One possible result is an inability to stabilize high velocity fragments by the trap fields themselves. We have successfully found the CH^+ fragment from both CH_4 and C_2H_2 ionization, as discussed below, but we have not yet explored the possible difficulties of trapping fragment ions in general.

Trapped ions zip around the trap with high velocity. As a result, the addition of a buffer gas is likely to heat ions rather than collisionally cool them. Whether this is an advantage or a disadvantage depends on one's point of view. Likewise, the initial state distribution of the ions depends on the molecule and the energy distribution of the ionizing electrons. Electrons are injected into the trap, and they undergo energy changes which are difficult to control. As a result, more detailed studies of the ionization process itself could be done with, for instance, a photoionization source, but only at a considerable loss in ion density.

EXPERIMENTAL RESULTS

Diatomic LIF Spectra

Given the limitations in spectral resolution of our experiment, the relatively sparse level structure of light diatomic ions becomes the most advantageous to explore. Our spectra of the fragment ions CH^+ and CD^+ will be described briefly here as examples of the types of spectra one can expect. Further details of these spectra can be found elsewhere [8].

Table I. Molecular Constants for CH^+ and CD^+. Energies are in cm^{-1} units.

	$CH^+(0,0)$ band $\nu_{00} = 23596.81(01)$*		
	$X\ ^1\Pi^+$		$A\ ^1\Pi$
B_0	13.9303(40)	B_0^{RP}	11.4532(37)
D_0	$1.373(11) \times 10^{-3}$	B_0^Q	11.4169(41)
		D_0^{RP}	$2.050(9) \times 10^{-3}$
		D_0^Q	$2.049(11) \times 10^{-3}$
		q_0	0.038
	$CD^+(0,0)$ band $\nu_{00} = 23747.71(1)$		
B_0	7.627(20)	B_0^{RP}	6.285(20)
D_0	$1.06(15) \times 10^{-3}$	B_0^Q	6.280(21)
H_0	$1.55(35) \times 10^{-6}$	D_0^{RP}	$1.08(14) \times 10^{-3}$
		D_0^Q	$1.16(16) \times 10^{-3}$
		H_0^{RP}	$1.12(29) \times 10^{-6}$
		H_0^Q	$1.41(37) \times 10^{-6}$
		q_0	0.016

The best known and most important band system of CH^+ is the $A\ ^1\Pi \leftarrow X\ ^1\Sigma^+$ system. This system has been characterized in emission [9] and is of importance to the astrophysical problem of CH^+ formation via radiative association [10]. We have produced CH^+ and CD^+ from CH_4, C_2H_2, and the perdeuterated compounds. The (0,0) and (2,1) bands have been measured, and an example [the $CH^+(0,0)$ band] is shown in Figure 3. The spectrum is easily assigned, but

Table I (Cont'd)

$CD^+(2,1)$ band $\nu_{21} = 24095.08(1)$			
B_1	7.416(46)	B_2^{RP}	5.492(44)
D_1	$1.25(56) \times 10^{-3}$	B_2^{Q}	5.479(49)
H_1	$4.5(2.0) \times 10^{-6}$	D_2^{RP}	$8.8(4.8) \times 10^{-4}$
		D_2^{Q}	$7.1(6.2) \times 10^{-4}$
		H_2^{RP}	$2.5(1.5) \times 10^{-6}$
		H_2^{Q}	$1.2(2.2) \times 10^{-6}$
		q_2	0.014

*Numbers in parentheses represent a one standard deviation uncertainty in the last digits of each constant.

the rotational distribution indicated significantly hotter ions than are seen in emission. Emission spectra followed the R branch out to the R(7) line; we have seen lines out to R(21). While we gain in quantity of information, we are, as Figure 3 indicated, limited in resolution to a few tenths of a wavenumber. In this case, the gain in quantity was the more desirable outcome. We found that the new lines at high J could not be fit by the existing molecular constants. We therefore refit our CH^+ and CD^+ lines to a new set of constants which are given in Table I.

We have also observed known bands in N_2^+ and CO^+. While we do not add new spectroscopic information to that already known for these molecules, our data on them are of interest for other reasons, as discussed below.

Polyatomic LIF Spectra

We have observed spectra for two polyatomic ions in detail, $BrCN^+$ and 1,3,5-trifluorobenzene cation. Spectra have also been

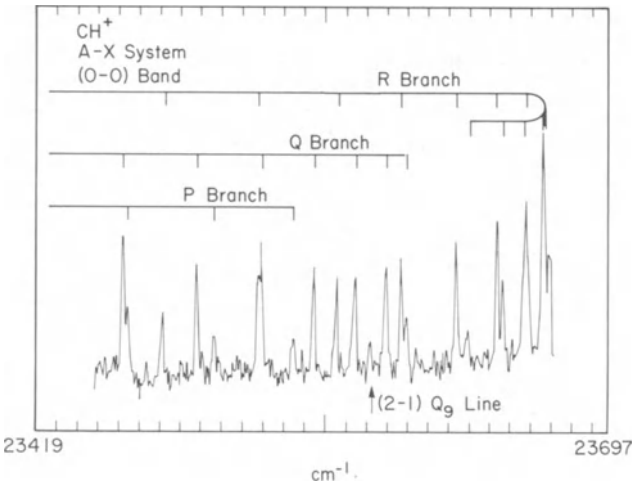

Fig. 3. LIF spectrum of the (0,0) band of the CH^+ A-X system. Features from the (2,1) band (such as Q_9) appear weakly in this spectral region.

found for H_2S^+ and $ClCN^+$, but these have not been examined in great detail.

For $BrCN^+$, the B $^2\Pi \leftarrow$ X $^2\Pi$ system extending from 20,000 to 24,500 cm^{-1} was investigated [11]. The ions were found to be internally hot, and rotational resolution was impossible. However, a vibrational progression, assigned to the ν_1 mode (primarily C-Br stretch) of the B state was observed. The frequency was found to be 441 ± 18 cm^{-1}. This is an average band spacing and does not properly account for anharmonicities, nor are observed irregularities in the band-to-band spacings fully explained. Each band is split by the spin-orbit interactions of each state. We find a difference in the spin-orbit constants to be A" - A' = 224 ± 43 cm^{-1}.

$BrCN^+$ is not the ideal ion to study by this method. Not only are the ions hot and the levels closely spaced, but overlapped sequence bands and Fermi interaction (between ν_2" = 290 cm^{-1} and ν_1' = 441 cm^{-1} or ν_1" = 509 cm^{-1}) cause nonsystematic spacings and intensity irregularities.

To test our trap near the limit of its mass range, we investigated the B A_2" $\leftarrow$ X E" band system of the 1,3,5-trifluorobenzene cation, which has a mass of 132 amu. We were able to trap the ion, but with a mass resolution of only 15. This value is purely the

result of the particular power supply we used to operate the trap. Thus, we may have co-trapped fragment ions along with the desired parent, but our spectra [1] agreed well with those obtained by others [4,12]. In general, the many bands we observed were in good agreement with those of previous assignments, but we lacked the resolution (due to the ion temperature) needed to provide the more detailed interpretations of Miller and Bondybey, who worked with colder gaseous ions and with matrix isolated ions.

Radiative Lifetimes

We have tested the ability of our apparatus to record radiative lifetimes over a considerable range of values. The strong N_2^+ first negative system, $B\ ^2\Sigma_u^+ \rightarrow X\ ^2\Sigma_g^+$, is characterized by a 60 nsec radiative lifetime, which we measure without difficulty. This value is not constant throughout the spectra, however. Perturbations by the longer-lived $A\ ^2\Pi_u$ state are known [13], and perturbations by an unknown $^4\Sigma_u^+$ state have been suspected [14]. Our N_2^+ spectra extend to high rotational quantum number, N, and we plan a systematic search for lifetime perturbations throughout the spectra [15].

At the long end of the radiative lifetime scale, we have observed and verified the 3.25 μsec lifetime of the CO^+ $A\ ^2\Pi \rightarrow X\ ^2\Sigma^+$ (v' = 2) band. The lifetime of CH^+ is known to be intermediate to these extremes. Other measurements have relied on fast electron pulse excitation to initiate the experiment. As Erman [16] has shown, these measurements can be systematically low due to the rapid spatial dissipation of ions from the viewing region due to ion-ion repulsive forces. His result, 630 nsec, was the largest reported experimental value, yet it is below the theoretical range (660 - 800 nsec) predicted by the *ab initio* calculations of Yoshimine, Green, and Thaddeus [17]. Our method does not suffer from such a systematic error. Therefore, we measured the lifetime of CH^+ ($A\ ^1\Pi$) in order to compare to the electron excitation value and the *ab initio* value. Our result [8] was 815 ± 25 nsec, in good agreement with the upper range of the theoretical value and clearly at odds with the electron excitation value.

Ion State Distributions

The collision-free nature of the trap affords us the opportunity to probe the nascent internal state distribution of ionized molecules and fragments. Of course, we use the term "nascent" to mean the distribution in the ground or optically metastable states which result after radiative cascade from the truly nascent excited states which may be formed. Emission spectra, when recorded under single collision conditions, yield

these excited state distributions. In a more practical vein, however, the ground or metastable state distributions we observe are of considerable importance to experiments which use ions after fast decay processes have occurred, but before thermalizing collisions (or infrared fluorescence) have otherwise altered the energy distribution. Inelastic and reactive scattering experiments with ion beams are clear examples of such a situation.

Ionization of CO is one case we have begun to study. The comet-tail system, $A\ ^2\Pi - X\ ^2\Sigma^+$, mentioned above in regards to lifetime measurements, is a useful band system to use in probing the X state internal energy distribution. We produce CO^+ by bombardment with electrons of roughly 150 eV energy. Cross-sections for excitation to levels in the A state have been measured [18], and high vibrational levels of the A state are known to be populated with significant probability. Moreover, the A → X Franck-Condon factors are known, and they indicate that the X state will become vibrationally hot as a result of A → X decay. The X state is not expected to be formed in high vibrational levels as a result of primary ionization from room temperature CO.

Figure 4 verifies this prediction. Portions of the (7,7) and (4,5) LIF bands are shown. Population in X (v" = 7 or 5) is essentially all due to cascade from the A state. We are currently measuring other band intensities, from which we expect to obtain a very complete picture of the ionization of CO.

A second example involves the fragment ions CH^+ and CD^+. As noted above, we find [8] these ions to be rather hot; we estimate a rotational temperature near 3000 K and a vibrational temperature near 5500 K. Somewhat more remarkable is the observation that these temperatures are obtained whether we use CH_4 or C_2H_2 as the parent gas.

E. Collisional Energy Transfer and Product State Analysis

The translational motion of trapped ions is well above the ambient temperature of the parent gas. A temperature of ~4000 K is typical [8,19]. If we produce N_2^+, for instance, we find [1] a rotational distribution in the ground state characterized by a temperature of 300 ± 25 K. This result is obtained following a 1 msec ionization period on pure N_2 at a pressure of ~5 x 10^{-6} torr. (Recall that under these conditions, the ion-neutral collision rate is ~1 $msec^{-1}$.) We can easily follow the consequences of a few collisions by raising the N_2 pressure, by waiting for longer times before we fire the laser, and/or by adding a non-trapped, chemically inert buffer gas at a higher concentration. For example, a spectrum of N_2^+ produced by a 1 msec ionization of a mixture of Kr (3 x 10^{-4} torr) and N_2 (5 x 10^{-5} torr) shows considerable collision

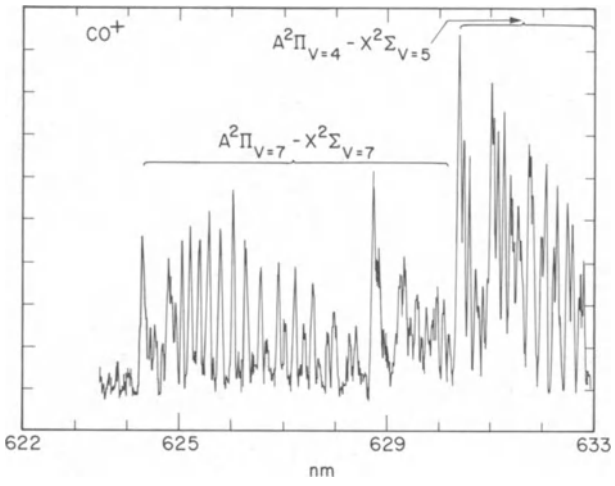

Fig. 4. LIF spectrum of the (7,7) and (4,5) bands of the CO^+ A-X system.

induced rotational heating. The rotational temperature rises to 585 ± 15 K. (An increase in vibrational temperature is also apparent from the spectrum, but the effect is more difficult to make quantitative.)

This experiment shows two important facts. First, ions can be confined for times long enough that the consequences of several collisions can be probed, and secondly, these consequences can be measured. For reactive collisions, we envision, but have not yet attempted, an experiment of the following type. A mixture of a heavy gas (such as N_2) and a light gas (such as H_2) with the light gas in excess is admitted to the trap. The mass resolution is adjusted to yield trapping of the heavy primary ion and the only slightly heavier product ion which would result from a reactive collision (such as N_2H^+). Many exothermic ion-molecule reactions are known to proceed at virtually every collision. We have constrained the reaction dynamics by a choice of masses which insures that the product will not receive a large translational impulse on reaction. We therefore co-trap the primary reactant ion and the ion-molecule reaction product which we investigate by LIF. As the alert reader has no doubt noticed, the principle drawback of this scheme is the general lack of spectroscopic data on most product ions which are otherwise suitable for such an experiment.

SUMMARY

This article has given an overview of the experimental opportunities afforded by studying the laser induced fluorescence spectra of molecular ions confined in a mass selective ion trap.

The advantages include species identification, collision control ranging from none to several collisions, timed measurements leading to radiative lifetimes, delayed excitation leading to the study of collisional alteration of the nascent ion state distribution, and the spectroscopic advantages LIF spectra give to complement emission spectra. The primary disadvantages are the large Doppler widths of spectral lines and, as always, an ion density that borders on the low end of usefulness.

ACKNOWLEDGMENT

This research was supported by the U. S. Department of Energy, Office of Basic Energy Sciences, Division of Chemical Sciences under Contract No. W-7405-Eng-48. The radiative lifetime of CH^+ and the spectrum of CO^+ shown in Figure 4 were obtained using a Nd:YAG pumped dye laser supplied by the San Francisco Laser Center, supported by a grant to the University of California and Stanford University from the National Science Foundation under grant CHE79-16250.

REFERENCES

1. F. J. Grieman, "Laser induced fluorescence of trapped molecular ions," Lawrence Berkeley Laboratory Report LBL-10021 (1979) (Ph.D. Thesis).
2. P. H. Dawson and N. R. Whetton, Adv. Elec. and Electron Phys. 27, 59 (1969); H. G. Dehmelt, Adv. At. Mol. Phys. 3, 53 (1967).
3. A. Carrington, D. R. J. Milverton, P. G. Roberts, and P. J. Sarre, J. Chem. Phys. 68, 5659 (1979).
4. T. A. Miller, V. E. Bondybey, and J. H. English, J. Chem. Phys. 70, 2919 (1979).
5. D. J. Wineland, J. C. Berquist, W. M. Itano, and R. E. Drullinger, Opt. Lett. 5, 245 (1980).
6. M. Benalin and C. Audoin, Int. J. Mass Spec. Ion Phys. 11, 421 (1973); R. F. Bonner, J. E. Fulford, and R. E. March, Int. J. Mass Spec. Ion Phys. 24, 255 (1977).
7. D. S. King and P. K. Schenck, Laser Focus, p. 60 (March 1978).
8. F. J. Grieman, B. H. Mahan, and A. O'Keefe, J. Chem. Phys. 72, 4246 (1980); F. J. Grieman, B. H. Mahan, A. O'Keefe, and J. S. Winn (to appear in Discussions of the Faraday Soc. 71, 1981).
9. A. E. Douglas and G. Herzberg, Can. J. Res. 20, 71 (1942); A. E. Douglas and J. R. Morton, Ap. J. 131, 1 (1960).
10. A. Dalgarno, in: "Atomic Processes and Applications," P. G. Burke and B. L. Moiseiwitsch, ed., North Holland, Amsterdam (1976), p. 110.
11. F. J. Grieman, B. H. Mahan, and A. O'Keefe, J. Chem. Phys. (in press).
12. V. E. Bondybey, T. A. Miller, and J. H. English, J. Chem.

Phys. 71, 1088 (1979) and reference therein.
13. R. A. Gottscho, R. W. Field, K. A. Dick, and W. Benesch, J. Mol. Spectrosc. 74, 435 (1979).
14. J. Dufay and O. Nedelec, C. R. Acad. Sci. Ser. B 285, 173 (1977).
15. A. O'Keefe and J. S. Winn (unpublished results).
16. P. Erman, Ap. J. 213, 289 (1977).
17. M. Yoshimine, S. Greene, and P. Thaddeus, Ap. J. 183, 899 (1973).
18. R. F. Holland and W. G. Maier, II, J. Chem. Phys. 56, 5229 (1972); J. F. M. Aarts and F. J. DeHeer, Physica 49, 425 (1970); J. M. Ajello, J. Chem. Phys. 55, 3158 (1971).
19. R. D. Knight and M. H. Prior, J. App. Phys. 50, 3044 (1979).

DETERMINATION OF MOLECULAR ION STRUCTURES BY PHOTOELECTRON SPECTROSCOPY

G. L. Goodman and J. Berkowitz

Argonne National Laboratory

Argonne, Illinois 60439 U.S.A.*

I. INTRODUCTION

Let us differentiate at the outset between photoelectron spectroscopy (PES) and photoionization mass spectrometry (PIMS). In PES, a fixed wavelength of light (most commonly the He I resonance line at 584A ≡ 21.2 eV) crosses a molecular target, causing some ionization. The kinetic energies of electrons thus liberated are measured by an electron energy analyzer. From the energy conservation condition

$$h\nu = (I.P.)_n + (K.E.)_n,$$

where $(K.E.)_n$ are the measured electron kinetic energies, one can deduce the various ionization potentials of the molecule $(I.P.)_n$ up to a maximum I.P. of $h\nu$. The $(I.P.)_n$ correspond to states of the molecular ion. The assignment of these states to appropriate symmetry classifications is often aided by some level of molecular orbital calculation. The most direct approach, and one most commonly used in the past, is to compute the orbital energies of the neutral molecule, and to identify the $(I.P.)_n$ as the negative of the orbital energies, often referred to as invoking Koopmans' theorem. The ordering of the $(I.P.)_n$ according to symmetry is usually, but not invariably, given correctly by this method. A cursory examination of the molecular orbitals involved can usually tell us if an electron has been removed from a bonding, antibonding or non-bonding orbital, resulting in an ionic state that is less/more weakly bound than the corresponding neutral molecule. More sophisticated calculations taking into effect relaxation of the molecule ion include ΔSCF and Green's function techniques.

*Work performed under the auspices of the Division of Basic Energy Sciences of the U.S. Department of Energy.

In the valence region, single electron excitations are most prevalent. The difference in I.P. between two states gives us an accurate determination of the transition frequency, and hence provides a valuable aid in the analysis of the optical spectra of these ions. Often one can observe resolved vibrational frequencies of the ions in their various states. Hence, PES is a valuable tool in elucidating the electronic structure of molecular ions. It has the further advantage that photoelectron spectra of a vast array of molecules have by now been measured (see, for example, Refs. [1] and [2]), providing our largest source of information about molecular ions. PES can also provide information about the geometric structure of molecular ions. This will be the main topic of the ensuing lectures.

PIMS is a measurement of the relative ionization yield of ions of a particular mass, using a tunable, variable wavelength light source as the ionizer. The onset of ionization at the lowest photon energy usually corresponds to the first ionization potential. PIMS is not as generally useful as PES for the determination of molecular ion structures. However, there are a few cases where it can prove helpful. In PIMS of simple molecules, one can often observe sharp resonant structure. This is a consequence of excitation to Rydberg levels converging to a higher ionization potential than the first. Interaction of the quasi-discrete Rydberg state with the ionization continuum results in ionization, and hence the resonant peak structure.

The Rydberg state, which can be viewed as a molecular ion with a distant Rydberg electron, will rapidly approach the properties of the molecular ion (vibration frequencies, geometry) as the principal quantum number of the Rydberg electron increases. If one could make a rotational analysis of the autoionization structure, one would have a means of determining the geometrical structure of the Rydberg state, and thus approximate the structure of the molecular ion. However, the autoionization process is usually too rapid, smearing out the rotational fine structure. Occasionally, one can perform such an analysis of Rydberg levels below the first ionization threshold. In such cases the Rydberg levels are detected by photoabsorption.

If vibrational levels are resolved as autoionization resonances, and if the autoionization process (and competing processes) are not sensitive to the vibrational state, then Franck-Condon analysis of the vibrational intensity distribution can provide geometric information about the Rydberg state, and by inference, the molecular ion. This can be hazardous, because of the assumptions mentioned.

The decomposition of molecular ions, as studied by PIMS, can sometimes yield information about the structure of fragment ions. This approach is often aided by isotopic substitution. We provide one example below.

The isotopic forms CH_3OD and CD_3OH of methanol were studied by PIMS [3a]. The first fragment observed as the photon energy increased could be interpreted as CH_3OH^+ or CH_2OH^+. The isotopic study revealed that it was predominantly the latter, providing indirect evidence that CH_2OH^+ is more stable than CH_3O^+. A higher energy fragment could be described as COH^+ or HCO^+. Again, the isotopic study concluded that the latter was far more probable, and hence presumably the more stable form. Ab initio calculations have drawn the same conclusion. However, an intermediate energy fragment having the mass corresponding to CH_2O^+ (formaldehyde ion) was actually found to have the structure $CHOH^+$ near its energy threshold from CH_3OH^+. We shall show later that ionization of CH_2O does result in a CH_2O^+ structure. Our best evidence to date from ab initio calculations (see note added in proof, Ref. [3a], and Ref. [3b]) is that $CHOH^+$ and CH_2O^+ have very nearly the same stability (i.e., heat of formation) and hence the structure initially formed may be strongly influenced by kinetic or stereochemical factors.

Finally, we should mention that transition states of ions (short-lived intermediates representing a transition path between parent and fragment ions) are often inferred from rates of unimolecular decay and theories adapted to this process. This is a specialized field, and not directly related to the present topic, which concerns the structure of stable molecular ions.

II. THE DIATOMIC FRANCK-CONDON ANALYSIS

A. General Theory and Background

Spectroscopic determination of molecular structure is predicated on achieving sufficient optical resolution to observe rotational fine structure. A rotational analysis then enables one to deduce moments of inertia, and thereupon a molecular geometry. When data of this quality are available, accurate molecular geometries can be calculated. Since the number density of molecular ion sources is usually not very large, the corresponding emission spectra are usually tenuous and one cannot often afford the luxury of acquiring a high resolution spectrum.

Photoelectron spectroscopy, combined with the Franck-Condon principle, offers an alternative method of obtaining information about the geometrical structure of molecular ions. A consequence of this principle is that the relative intensities of the vibrational components of an electronic band depend upon the change of geometrical structure in the ionization process. Since the structure of the neutral ground state is usually known, and the photoelectron spectrum contains information about the change in structure upon ionization, one can in principle calculate the structure of the molecular ion in each of its observable ionic states. Actually, one needs to know the frequencies and normal modes of both neutral and

ionic states, so that the fitting variable is the geometrical change along one or another normal mode. In vibrationally resolved spectra, this information is available. Even here, however, there may be some ambiguity. The calculated best fit may provide, e.g., a change of internuclear distance Δr, with undetermined sign. Some additional information, or chemical intuition must be invoked in such cases.

A major advantage of the photoelectron spectral approach to molecular ion structure is that a very large class of molecular ions becomes accessible to study. All species for which vibrationally resolved photoelectron spectra have been obtained are candidates for analysis. This represents a wealth of relatively untapped information. Even when vibrationally resolved spectra are not available, a moment analysis of unresolved spectra [4] can provide structural information. Species which are excluded from such an analysis are stable ions which do not have correspondingly stable neutral counterparts, such as H_3^+, H_3O^+, and HeH^+. However, species excluded by other techniques because they don't have transition dipole moments are accessible here.

The simplest class of molecules to which the Franck-Condon approach can be applied are diatomics with vibrationally resolved photoelectron spectra not involving hot bands, i.e., the progenitor neutral molecule is only in the $v'' = 0$ state. Several molecules fitting this criterion have been studied, including HF [5], CS [6], SO [7], PN [8], NS [9]. In these cases, Morse curves have been used to describe neutral and ionic states, thereby including anharmonic effects. The internuclear distances of the ionic states calculated by this method are usually accurate to ≤ 0.01 Å, as can be judged by comparing with optically derived information in test cases. For HF^+ and CS^+, the ground state internuclear distances initially obtained by the Franck-Condon method were 1.002 Å and 1.500 Å, respectively; those subsequently deduced from optical spectra were 1.0011 Å and 1.495 Å. Unfortunately, it is difficult to provide many new examples applicable to this simple analysis. The common volatile diatomic molecules, such as O_2, CO, NO, N_2, have well-known ionic structures. Diatomic molecules generated by electric discharge or high temperature techniques may have hot bands or may not have vibrationally resolved photoelectron spectra. Even volatile diatomics can sometimes introduce minor difficulties. In the usual formulation of the Franck-Condon calculation, the wave functions of initial and final state are expressed in the adiabatic approximation

$$\Psi = \psi_e (x, X) \phi (X),$$

where $\psi_e (x, X)$ is the electronic wavefunction,

$\phi(X)$ is the vibrational wavefunction and

x, X are the electronic and nuclear coordinates, respectively.

The intensity of the transition is proportional to the square of the electric dipole transition moment M, i.e.,

$$M = \int\int \psi_e' \phi' M(x, X) \psi_e'' \phi'' dx dX.$$

Integrating over the electronic coordinates first, and designating that integral by R_e, we can write

$$M = \int R_e(X) \phi' \phi'' dX.$$

However, in the case of $H_2(^1\Sigma_g^+) \rightarrow H_2^+(^2\Sigma_g^+)$ it has been shown [10, 11] that R_e varies significantly over the experimental range, and hence the experimental relative intensities depart from the values deduced with the Franck-Condon factors, i.e., the square of the overlap integrals of the vibrational wavefunctions.

In the sections that follow, we shall extend this approach to

a) Diatomic spectra containing hot bands, i.e., cases where the neutral progenitor has a Boltzmann distribution;

b) Diatomic spectra containing hot bands and unresolved vibrational structure;

c) Certain cases of polyatomic species.

In so doing, we shall bring a large class of experimental data within the scope of Franck-Condon analysis.

For the section that follows, it will be convenient to employ a formalism developed by Cederbaum and Domcke [4], which we shall briefly sketch. These authors use a Green's function approach to compute ionization energies to a higher order of approximation than given by Koopmans' theorem. Of relevance here is their extension of this formalism to include vibrational effects. An important advantage of this approach is that only data for the initial electronic state (i.e., the ground state of the molecule) are required. The Franck-Condon factors are expressed in terms of certain coupling constants, which they say can be easily calculated in the single-particle approximation, but can be modified to include many-body effects. They further state that "because of its simplicity, the method is applicable to fairly large polyatomic molecules, yielding reasonably accurate results with moderate computational expense."

They expand the most general vibrational Hamiltonian for an arbitrary electronic state in terms of the normal coordinates of the ground electronic state. This Hamiltonian splits into 4 terms:

$$H = H_E + H_N + H_{EN}^{(1)} + H_{EN}^{(2)},$$

where

H_E = the electronic Hamiltonian at the equilibrium position of the ground state. In the Green's function formalism, this term of the Hamiltonian is the basis of their earlier work, calculating vertical ionization energies to higher order.

H_N = the dependence of the ground state on nuclear coordinates (vibrations), including anharmonic effects.

$H_{EN}^{(1)}$ = the dependence of the difference of electronic energy between ionic and ground electronic state on nuclear coordinates, within the single-particle approximation.

$H_{EN}^{(2)}$ = same as $H_{EN}^{(1)}$, but for 2-particle correlation energy.

They then simplify the Hamiltonian in several ways.

1. Adiabatic approximation - they discuss going beyond this approximation for cases of Jahn-Teller splitting, but only qualitatively.

2. Harmonic approximation - neglect of anharmonicity, ΔT_N and ΔV_o in their H_N.

3. Single-particle approximation - neglecting electron-electron interaction integrals.

For diatomic molecules, Domcke and Cederbaum [12] show that anharmonic effects and their linear coupling constant κ enter together in such a way as to partially cancel the quadratic coupling constant γ, which enables the harmonic approximation to remain fairly good for a large number of cases.

With these approximations, they develop an equation for the transition probability (simplified for $v_1, v_2, \ldots = 0$ for the ground electronic state) in which the overlap of the wave functions of two displaced M-dimensional harmonic oscillators with different frequencies is expressed as a finite linear combination of the overlaps of the corresponding non-displaced oscillators. In this expression, factors enter which are overlaps between excited state functions evaluated at the excited state equilibrium position and excited state functions evaluated at the ground state equilibrium position.

In the one-dimensional case (diatomic molecule) the vibrational intensities reduce to a Poisson distribution,

$$\frac{a^n}{n!} e^{-a}$$

when $\omega_i = \omega_s$.

(ω_i = frequency of ion, ω_s = frequency of neutral).

where

$$\alpha = \left(\frac{\kappa_s{}^i}{\omega_s}\right)^2$$

$$\kappa_s{}^i = \text{linear coupling constant} = \frac{1}{\sqrt{2}}\left(\frac{\partial \varepsilon_j}{\partial Q_s}\right)_0$$

ε_i is the ionization energy of state i

Q_s is a normal coordinate.

In the polyatomic case, when the quadratic coupling constants vanish (i.e., $\omega_i = \omega_s$), the transition probability becomes

$$P_i(\omega) = |\tau_{ei}|^2 \sum_{n_1 \ldots n_m = 0}^{\infty} \left[\prod_{s=1}^{M} \frac{\alpha_s^{n_s}}{n_s!} e^{-\alpha_s} \right] \times \delta(\omega - \varepsilon_i(0) + \Delta_i + \Sigma n_s \omega_s)$$

where

$$\Delta_i = -\Sigma_s \alpha_s \omega_s$$

and $|\tau_{ei}|^2$ is the electronic cross section for ionization.

They then make the important point that a totally resolved photoelectron spectrum, in which the individual vibrational intensities can be measured and related to Franck-Condon factors, is not absolutely necessary. Even a poorly resolved or unresolved spectrum can be analyzed by its moments, which depend upon the coupling constants $\kappa_s{}^i$, $\gamma_{ss}{}^i$, and on ω_s.

In such an analysis, we can take

M_0 = normalization of spectrum, e.g., sum of vibrational intensities = 1 or (in unresolved spectra), area = 1.

$M_1 = \Sigma I_n v_n = 0$, or appropriate integration in unresolved case, where I_n, v_n = intensity and energy of vibrational level n.

$$M_2 = \Sigma I_n v_n{}^2$$

M_2 is the critical quantity to be determined. With their assumption of $\gamma = 0$, or $\omega_i = \omega_s$, $M_2 = \alpha\omega_s{}^2$.

Therefore, a determination of M_2 and knowledge of ω_s enables us to compute α, which can be related to an internuclear distance in the ion.

Cederbaum and Domcke conclude that a low-resolution spectrum is well-characterized by its first few moments, and that the center of gravity and the width of the vibrational spectrum can be determined without knowing anything about the details of the vibrational motion in the ionic state.

We have found that the approximation $\omega_i = \omega_s$, or $\gamma = 0$, leads to a poor description of the width of the experimental spectrum, although the intensity distribution is not too bad. From Eqs. 5.44b and 5.56 in Cederbaum and Domcke's paper [4], and taking $M_1 = 0$ in our normalization, we obtain

$$\Delta = \frac{\omega_i - \omega_s}{2} - (M_2 - 2\gamma^2)\frac{\omega_s}{\omega_i^2}$$

for the diatomic case. The approximation $\omega_i = \omega_s$, $\gamma = 0$ reduces this expression to

$$-\Delta \cdot \omega_i = M_2$$

It is this expression which we have tested, and for which the width was not well reproduced. We have improved upon this approximation by noting that

$$2\gamma^2 = (\omega_i^2 - \omega_s^2)^2/8\omega_s^2 \text{ and } M_2 = \kappa^2 + 2\gamma^2,$$

from which we can obtain κ if we know ω_s, ω_i, and M_2. Note that since $\kappa = \pm\sqrt{M_2 - 2\gamma^2}$, there is an ambiguity in the sign of κ. The internuclear distance of the ion, within their harmonic approximation is then computed from

$$R_{ion} - R_o = \Delta R = \frac{\hbar}{\omega_i^2}\sqrt{\frac{2\omega_s}{\mu}} \cdot \kappa,$$

where μ is the reduced mass. The ambiguity in the sign of κ results in a corresponding ambiguity in the sign of ΔR, which must be resolved by other considerations. We can also arrive at κ by least squares matching of the calculated intensity distribution and the experimental one.

If the ionic state is described by a Morse potential, instead of their harmonic potential, then one can show that

$$\Delta R = \ell n\ Y/\beta_i$$

Table 1

Ground State Molecular Ion	R_1(expt)[a]	R_1 (from best harmonic approx.)	R_1 (Morse potential)	References	
				PES Energies	PES Intensities
O_2^+	1.1227Å	1.1428	1.1110	O. Edquist, E. Lindholm, L.E. Selin & L. Åsbrink, Phys. Scripta 1, 25 (1970).	J.L. Gardner & J.A.R. Samson, J. Electr. Spectr. 13, 7 (1978).
NO^+	1.06322	1.0876	1.0601	O. Edquist, L. Åsbrink & J. E. Lindholm, Z. Naturf. 26A, 1407 (1971).	Ref. 1, p. 54
H_2^+	1.052	1.3073	1.0432	James Peek, Pvt. Comm.	Ref. 10
	(1.0569 theory)	1.3588	1.0595	" " " "	J. L. Gardner & J.A.R. Samson, J. Electr. Spectr. 8, 123 (1976)
N_2^+	1.11642	1.1153	1.1141	Used vibr. const. of N_2^+ from Ref. 16.	J. L. Gardner & J.A.R. Samson, J. Electr. Spectr. 13, 7 (1978) using 584Å intensities.
CO^+	1.11514	1.1132	1.1122	Used vibr. const. of CO^+ from Ref. 16	Gardner & Samson (immed. above) supplemented for v' = 2 from Ref. 1, p. 50 - all at 584Å.
HF^+	1.0011	1.0057	0.9871	Used vibr. const. of HF^+ from Ref. 16	Ref. 5.
F_2^+	1.322	1.3374	1.2994	Used vibr. const. of F_2^+ from ref. 16.	Est'd. from spectrum of Ref. 14

[a] From K. P. Huber and G. Herzberg, Ref. 16.

with

$$\beta_i = \left(\frac{\omega}{2D_i}\right)^{1/2} \frac{\omega_i}{\hbar} \quad \text{and} \quad Y = [1 + \sqrt{1 - 4x}]/2$$

where

$$x = \frac{\kappa}{\omega_i}\left(\frac{\omega_s}{D_i}\right)^{1/2},$$

and D_i is the dissociation energy of the ionic state.

We have tested these formulae by calculating the second moment M_2 of vibrationally resolved photoelectron spectra for the simple molecules O_2, NO, H_2, CO, HF, and F_2 in their first photoelectron bands, corresponding to the ionic ground states of these molecules. From these second moments we have calculated internuclear distances with both the harmonic potential and the Morse potential, and compared both with optically determined internuclear distances. The results are summarized in Table 1. These various cases include examples involving removal of bonding, antibonding and non-bonding electrons. It appears as if the Morse potential yields comparable or more accurate internuclear distances than the harmonic potential, except for the case of F_2. For the case of H_2, the Morse potential is far superior. Overall, the Morse potential yielded values for the internuclear distances within 0.01 Å except for HF^+ (0.014 Å) and F_2^+ (0.023 Å).

B. Test of Franck-Condon Intensities in Vibrationally Resolved Photoelectron Spectra, Incorporating Boltzmann Terms

We have found three molecular sytems convenient for the testing of theory at this level: Br_2, I_2, and S_2. In order to derive molecular parameters for ionic states when hot bands are present we shall find it more convenient (and also more transparent to the reader) to calculate the vibrational intensity profile that best matches the experiment, instead of the second moment approach. The latter requires a priori knowledge of the difference in frequency between neutral and ionic state, whereas the fitting procedure yields the ionic frequency directly.

1. Development of the Fitting Procedure

In their early paper [13], Cederbaum and Domcke present a generalized formula for the intensities of individual vibrational bands starting from a vibrationally excited electronic ground state. In our current terminology, this may be written

$$P_i(\omega) = |\tau_{ei}|^2 \sum_{n_1 \ldots n_m = 0}^{\infty} |< m_1 \ldots m_M|U|n_1 \ldots n_m >|^2$$

$$\times\ \delta(\omega - \varepsilon_i(0) + \Delta_i - \sum_{s=1}^{M} m_s\omega_s + \sum_{i=1}^{M} n_i\omega_i)$$

The matrix element in this expression incorporates Franck-Condon factors connecting initial and final states that may have different frequencies. The additional term $\Sigma m_s\omega_s$ allows for an energy offset due to hot bands.

The integral term $\sum_{n_1 \ldots n_m = 0}^{\infty} |< m_1 \ldots m_m|U|n_1 \ldots n_m >|^2$ reduces, in the diatomic case and when the overlaps between non-displaced harmonic oscillators are delta functions ($\omega_i = \omega_s$) to

$$|< m|U|n >|^2 = \frac{\alpha^{m+n}}{n!m!} e^{-\alpha}\left[\sum_{\ell=0}^{[m,n]} \frac{(-\alpha)^{-\ell}\ m!\ n!}{\ell!(m-\ell)!\ (n-\ell)!}\right]^2$$

where [m,n] denotes the lesser of the two.

This expression implies that the quadratic coupling constant $\gamma = 0$, and corresponds to Cederbaum and Domcke's "best" harmonic approximation. It also corresponds to the observations of other authors that the vibrational intensity distribution is much more sensitive to the offset in internuclear distance than it is to a change in frequency. Some calculations have been performed in which the full overlap expressions were evaluated allowing upper state frequency to differ from lower state frequency, and the results were usually not perceptibly different from those obtained using the above expression (see Appendix 1).

However, the energy scale is sensitive to the frequency of the ion, and this has been included by allowing ω_i to differ from ω_s in the δ term. In fact, we have found that the appearance of the spectrum is sensitive to anharmonic terms, and have included them in the δ expression.

In order to compare the calculated vibrational intensity distribution with the experimental one, the above expression must be weighted with a Boltzmann factor and summed over the initial states. In addition, each vibrational line must be given a width characteristic of the instrumental resolution and inherent line width. For the latter, we have used a Gaussian function whose half-width was either set by the resolution given by the respective authors or deduced from the experimental spectrum. From the best fit, we deduce

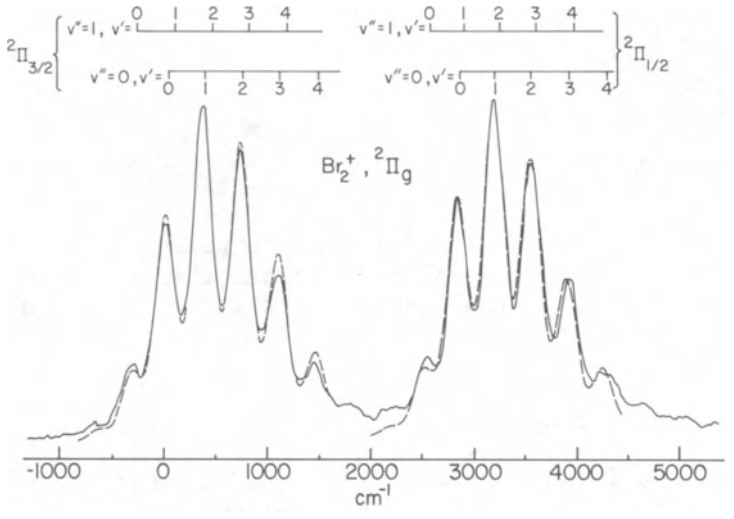

Fig. 1. Comparison of experimental and calculated photoelectron spectra for $Br_2(X^1\Sigma^+) \rightarrow Br_2^+(^2\Pi_{3/2,g}$, and $^2\Pi_{1/2,g})$. Expt. from Ref. 14, solid line; calculated spectrum, dotted line.

a value of a. This can be converted into an expression for κ, the linear coupling constant, by combining Eqs. (23), (25), and (45) given by Cederbaum and Domcke [13] and becomes

$$\kappa = \pm[\omega_1^3 \, a/\omega_s]^{1/2}$$

This value of κ can then be introduced into either the harmonic or Morse potential formulae previously given to deduce ΔR.

2. Br_2

Cornford et al. [14] have published a photoelectron spectrum of Br_2, and conveniently display an enlarged version of the incompletely resolved vibrational structure in the spin-orbit parnters (the $^2\Pi_{3/2,g}$ and $^2\Pi_{1/2,g}$ states of the ion). We reproduce this spectrum in Fig. 1.

The authors state that the experiment was performed at room temperature, which we have taken as 298°K. The stated resolution, 0.03 eV, was used for the Gaussian. The best fits to each of the states are drawn as dotted lines in Fig. 1. The assignment of the vibrational quantum numbers of the ionic states given by Cornford et al. is confirmed. The energy scale used in the calculations fits that given in the experimental spectrum. For the $^2\Pi_{3/2,g}$ state, the residual discrepancy occurs in the higher vibrational components, which are given with somewhat higher intensity by the calculation.

For the $^2\Pi_{1/2,g}$ state the hot bands are somewhat weaker in the calculations. In both cases, the overall fits are very good.

The parameters for best fit are as follows:

	$^2\Pi_{3/2,g}$	$^2\Pi_{1/2,g}$
ω_i	371 cm^{-1}	360 cm^{-1}
a	1.6	1.45
$\omega_i x_i$	1.86 cm^{-1}	1.8 cm^{-1}

We note here that Cornford, et al., reported the same frequency for both states (360 cm^{-1}), whereas Huberman [15] gives a value from optical spectra of 376 cm^{-1}. Neither 360 cm^{-1} nor 376 cm^{-1} gives as good a fit for $^2\Pi_{3/2,g}$ as our selected value. By contrast, ω_i = 360 cm^{-1} provides a much better fit for $^2\Pi_{1/2,g}$ than either 371 or 376 cm^{-1}.

The internuclear distances* derived from the a values are as follows:

	$^2\Pi_{3/2,g}$	$^2\Pi_{1/2,g}$
Harmonic potential	2.196 Å	2.199 Å
Morse potential	2.166	2.172

As in the case of F_2^+ which we had explored earlier, the Morse potential gives a larger ΔR for Br_2^+. In that case, the result from optical spectroscopy was between the Morse and harmonic results, but closer to the harmonic value. Cornford et al., using a simpler Franck-Condon analysis, arrived at $R \cong 2.186$ Å for both states. Our average values are 2.181 ± 0.015 Å for $^2\Pi_{3/2,g}$ and 2.186 ± 0.013 Å for $^2\Pi_{1/2,g}$.

*Values of $R_{neutral}$, μ, and D_i are taken from Huber and Herzberg [16].

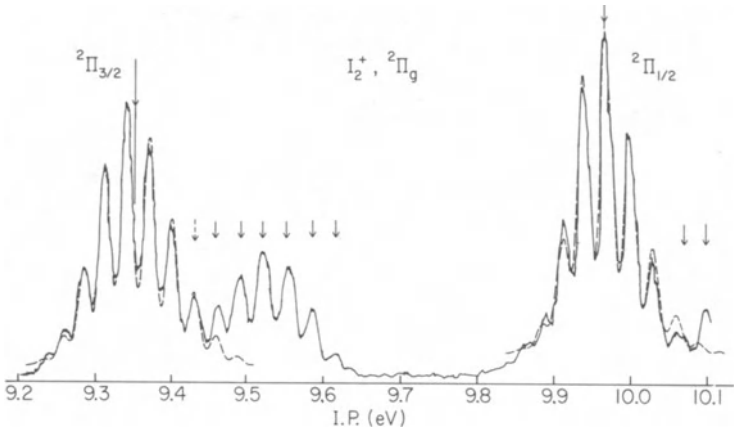

Fig. 2. Comparison of experimental and calculated photoelectron spectra for $I_2(X^1\Sigma^+) \rightarrow I_2^+(^2\Pi_{3/2,g}$ and $^2\Pi_{1/2,g})$. Expt. from Ref. 17, solid line; calculated spectrum, dotted line.

3. I_2

In this case, the hot bands present a more serious problem, and initially led to a misassignment of the adiabatic ionization potential. Higginson et al. [17] have performed photoelectron spectroscopic temperature variation experiments, using two different electron energy analyzers.

The results of the first such experiment, performed at 32°C, is shown in Fig. 2. Both the $^2\Pi_{3/2,g}$ and $^2\Pi_{1/2,g}$ states are displayed. In addition, "impurity" lines due to the presence of 744 Å radiation as well as the dominant 736 Å radiation are indicated by vertical arrows.

Our best fit (shown as dotted lines in Fig. 2) was obtained by choosing a resolution width of 0.018 eV. Our energy scale is the same as that given in their figure. The calculated hot band intensities are somewhat weaker in the $^2\Pi_{1/2,g}$ than the experimental intensities, but not as notably so in the $^2\Pi_{3/2,g}$ case. A slightly higher temperature than given by the authors could improve the agreement, which is nonetheless very good. The satisfactory agreement confirms the assignments of Higginson et al., and their conclusion that the Rydberg series limit for the adiabatic ionization potential obtained by Venkateswarlu [18] is in error, as is the value obtained by temperature dependent photoionization mass spectrometry [19].

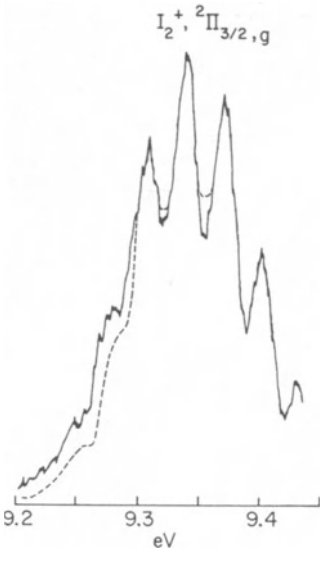

Fig. 3. Experimental photoelectron spectrum for $I_2(X^1\Sigma^+) \rightarrow I_2^+({}^2\Pi_{3/2,g})$ at -10°C (dotted line) and +30°C (solid line) from Ref. 17.

The parameters for best fit are as follows:

	$^2\Pi_{3/2,g}$	$^2\Pi_{1/2,g}$
ω_i	242 cm^{-1}	242 cm^{-1}
a	1.4	1.0
$\omega_i x_i$	(1.21 cm^{-1})	(1.21 cm^{-1})

Higginson et al. inferred ω_i = 240 cm^{-1} for $^2\Pi_{3/2,g}$ and 220 cm^{-1} for $^2\Pi_{1/2,g}$, whereas we are unable to see a significant difference in ω_i between these states.

The internuclear distances* derived from the a values are as follows:

*Values of $R_{neutral}$, μ, and D_i are taken from Huber and Herzberg [16].

	$^2\Pi_{3/2,g}$	$^2\Pi_{1/2,g}$
Harmonic potential	2.588 Å	2.600 Å
Morse potential	2.567	2.586

As with the Br_2^+ case, the Morse potential yields a larger ΔR. Our average values are 2.578 ± 0.010 Å for $^2\Pi_{3/2,g}$ and 2.593 ± 0.007 Å for $^2\Pi_{1/2,g}$.

Higginson et al. also provide spectra of the $^2\Pi_{3/2,g}$ state taken on another analyzer, with poorer resolution, but at two temperatures (-10°C and +30°C). We reproduce these spectra in Fig. 3. This time we were unable to reproduce their spectrum with the energy scale on their figure, unless we changed the ω_i deduced from the higher resolution spectrum. We changed the energy scale by 5% in order to make the peak positions correspond. The Gaussian width function was increased to 0.022 eV to correspond to the resolution of the second instrument, and the prescribed temperatures were used in the calculations. The results are displayed in Fig. 4 as solid lines for +30°C spectrum and dotted lines for the -10°C spectrum, to correspond to their convention. A reduction in the hot band region is observed in the calculated spectrum, but we also note a reduction in the higher energy bands not observed in the experimental spectrum. The -10°C experiment also shows signs of diminished resolution, and indicates the difficulty of performing successive experiments at different temperatures with identical resolution. The previous conclusion regarding the location of the adiabatic ionization potential is confirmed.

The two I_2^+ states are convenient cases to distinguish two slightly different uses of the term "vertical ionization potential" seen in the literature. The empirical approach selects the largest peak in a resolved spectrum, or the peak in an unresolved spectrum. If viewed as a vertical transition from R_e of the lower electronic state to that same internuclear distance for the upper state potential energy curve, this intersection can occur at a particular vibrational level or between levels. If it occurs at or very near a particular vibrational level, the empirical and theoretical vertical ionization potentials will coincide, as noted by the arrow in Fig. 2, $^2\Pi_{1/2,g}$.

If the intersection occurs between upper state vibrational levels, the theoretical vertical ionization potential occurs in a valley, as indicated by the arrow in Fig. 2, $^2\Pi_{3/2,g}$.

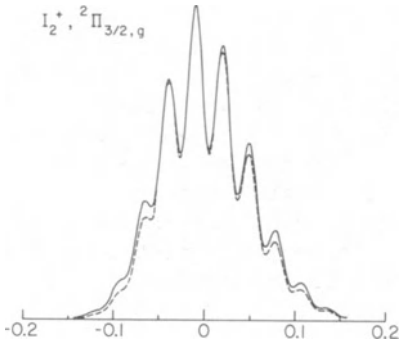

Fig. 4. Calculated photoelectron spectrum for $I_2(X^1\Sigma^+) \rightarrow I_2^+(^2\Pi_{3/2,g})$ at -10°C (dotted line) and +30°C (solid line).

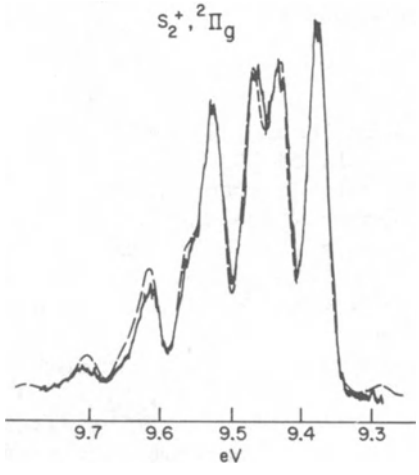

Fig. 5. Comparison of experimental and calculated photoelectron spectra for $S_2(X^2\Sigma_g^-) \rightarrow S_2^+(^2\Pi_{1/2,g}$ and $^2\Pi_{3/2})$. Expt. from Ref. 20, solid line; calcualted spectrum, dotted line.

4. S_2^+

Although S_2 must usually be generated at relatively high temperature, Dyke et al. [20] succeeded in cooling the heated vapor by transporting it in helium carrier gas. Their photoelectron spectrum of the ionic ground state, $^2\Pi_g$, is reproduced as solid lines in Fig. 5. This spectrum reveals not only resolved (incompletely) vibrational structure, but spin-orbit splitting of the $^2\Pi_g$ state as

well. Our best fit to this spectrum required a variation of the spin-orbit separation, the spin-orbit ratio, vibrational frequency of the ionic state(s) and a corresponding anharmonicity. Their stated energy resolution for argon was 0.020-0.025 eV; to fit the vibrational bands of S_2^+, we required a half-width of 0.033 eV for the Gaussian function. The energy scale was that given in their figure. The calculated spectrum that best fit their data is shown as dotted lines in Fig. 5 at a temperature of 300°K. The best fit is quite satisfactory, reproducing peak energy positions, peak heights and valleys with barely perceptible deviations. Even the shoulders are well-reproduced.

The parameters for best fit are as follows:

Spin-orbit separation	427 cm^{-1}
Spin-orbit ratio of intensities	1.41
ω_i (same for both s/o components)	751.7 cm^{-1}
$\omega_i x_i$ (same for both s/o components)	8.3 cm^{-1}
α (same for both s/o components)	0.87

The spin-orbit separation deduced from our best fit differs from that given by Dyke et al. (470 ± 25 cm^{-1}) but is quite close to the value predicted by Leach [21], 433 cm^{-1}. The spin-orbit ratio is within the range calculated by Lee et al. [22]. The value of ω_i deduced is significantly lower than that given by Dyke et al. (These authors at one point state that ω_i is 70 cm^{-1} larger than that in neutral S_2 (taken as 720 cm^{-1}) and in a later table present a value of 770 cm^{-1}). It is also lower than the values for lower members of Rydberg series found by Mahajan et al. [23] which range from 746 to 827 cm^{-1}. We have recently become aware of a preprint by Tsuji et al. [23a] on the A → X emission spectrum of S_2^+. These authors deduce ω_i = 807 ± 3 cm^{-1}, $\omega_i x_i$ = 3.5 ± 0.3 cm^{-1} and a spin-orbit separation of 455 ± 6 cm^{-1}. The discrepancy between our deduced values for ω_i and S-O separation and those of Tsuji et al. can be attributed to the energy scale of the published photoelectron spectrum. Our values for both these quantities are ca. 7% lower than those of Tsuji et al. Prof. Jonathan [23b] has indicated that the spectrum published by Dyke et al. did not necessarily have the best energy calibration of the several spectra which they obtained for S_2. The larger discrepancy in the anharmonicity constant may be related to a non-linearity in the energy scale of the published spectrum. The value of α deduced (which is insensitive to the energy scale) corresponds to an internuclear distance of 1.819 Å (harmonic potential) and 1.801 Å (Morse potential), or an average value of 1.810 ± 0.009 Å. Dyke et al., using a stick diagram Franck-Condon fit, have deduced 1.82_5 Å.

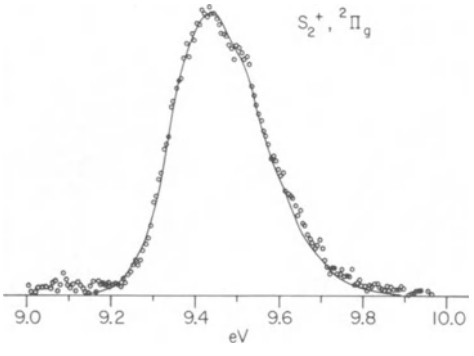

Fig. 6. Comparison of experimental and calculated photoelectron spectra for vibrationally unresolved $S_2(X^3\Sigma_g^-) \rightarrow S_2^+(^2\Pi_g)$. Expt. from Ref. 24, circles; calculated spectrum, solid line.

C. Test of Franck-Condon Intensities in Vibrationally Unresolved Spectra, Incorporating Boltzmann Terms

1. S_2^+

Berkowitz [24] has reported a photoelectron spectrum of S_2 in which the vapor was generated by the thermal decomposition process

$$HgS(s) \rightarrow Hg(g) + \frac{1}{2} S_2(g).$$

The temperature characterizing this process was ∿670°K, which generates a broader Boltzmann distribution than in the experiment of Dyke et al. The Gaussian width for this experiment was 0.086_6 eV, rather accurately given by the half-width of the nearly atomic Hg photoelectron line. All the molecular parameters used to optimize the fit to the spectrum of Dyke et al. were retained in the subsequent calculation. A background with a slight slope was subtracted from the experimental data.

The experimental spectrum for the ground state of S_2^+ is reproduced as circles in Fig. 6; the calculated spectrum based on the aforementioned parameters, is shown as a solid line in Fig. 6. The agreement between calculated and experimental spectra is seen to be quite good. The quality of the comparison begins to be noticeably poorer with changes of ±0.06 in the a value.

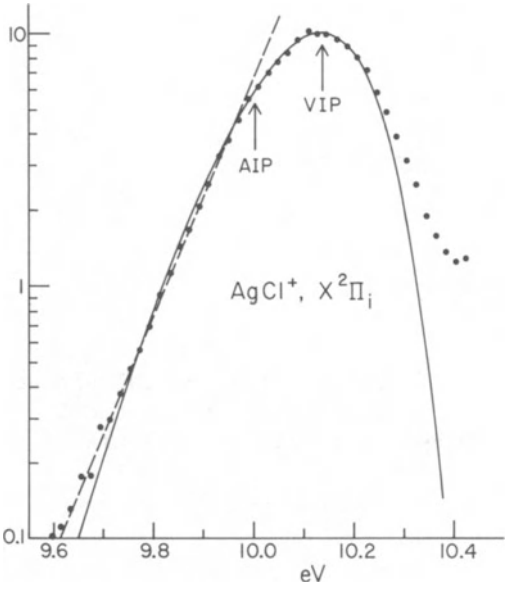

Fig. 7. Comparison of experimental and calculated photoelectron spectra for vibrationally unresolved $AgCl(X^1\Sigma) \rightarrow AgCl^+(^2\Pi)$. Expt. from Ref.25, dots; calculated spectrum, solid lines.

We should remark here that it becomes quite important to know the temperature of the molecular beam and the working resolution of the experimental apparatus rather accurately when attempting to fit unresolved spectra incorporating Boltzmann terms.

2. $AgCl^+$

Berkowitz, Batson, and Goodman [25] have recently reported the photoelectron spectra of AgCl, AgBr, and AgI. We focus here on the first band of $AgCl^+$, which is almost completely resolved from the second band. The Gaussian width characterizing the experimental apparatus was measured concurrently on an argon calibration line, and found to be 0.07 eV. The temperature of the oven was measured to be $\sim$1275°K. The vibrational frequency and anharmonicity of neutral ground state AgCl were taken from Huber and Herzberg [16]. This state of $AgCl^+$ is a $^2\Pi$ state formed by ionization from a chlorine-like orbital. It is spin-orbit split - the splitting was estimated to be 0.05 eV, and the spin-orbit ratio taken as unity. The parameters varied for best fit were a, ω_i, and the corresponding anharmonicity, x_{ei}. The experimental spectrum covers two decades in relative intensity, and is shown on semilogarithmic coordinates as dotes in Fig. 7. Two independent sets of experimental data were compared, and found to be virtually identical. The calculated spec-

trum that best fit the experimental points is shown as a solid line in Fig. 7. The extended overlap was found to be necessary here because of the rather large differences between ω_s and ω_i, together with a substantial value for a. The fit is quite satisfactory, except for the wings, which are affected in the experimental spectrum on one side by a background subtraction and on the other by the nearby second band. The parameters for best fit are

$$a = 2.3$$

$$\omega_i = 294 \text{ cm}^{-1}$$

$$\omega_i x_{ei} = 0.88 \text{ cm}^{-1}.$$

The quality of the match between experimental and calculated curves was found to be sensitive to ±0.1 in a and ±2% in ω_i.

In this case, the harmonic potential calculation leads to ΔR = 0.14 Å, the Morse potential to ΔR = +0.10 Å. The internuclear distance of the $X^2\Pi$ state of $AgCl^+$ is thus calculated to be 2.40 ± 0.02 Å.

We have drawn a dotted line through the experimental threshold region. The departure of the experimental curve from linearity is one estimate of the adiabatic ionization potential. In the detailed analysis presented here, the adiabatic ionization potential is computed to be 10.00_3 eV, whereas the departure from linearity occurs at ∿9.95 eV, which gives some estimate of the error that might be incurred by employing the simple scheme.

III. THE POLYATOMIC FRANCK-CONDON ANALYSIS

A. General Theory

The vibrations of a polyatomic molecule may be described in terms of a set of normal coordinates Q_k^n. Under the assumption of a harmonic force field, the total vibrational wavefunction ϕ_n for (say) the neutral ground state can be written as the product of 3N-6 Hermite orthogonal functions (3N-5 for linear molecules)

$$\phi_n(Q_1^n, Q_2^n, Q_3^n \cdots Q_{3N-6}^n) = \phi_{n_1}(Q_1^n)\ \phi_{n_2}(Q_2^n) \cdots$$

$$\phi_{n(N-6)}(Q_{3N-6}^n), \tag{1}$$

where N is the number of atoms in the molecule.

A similar expression can be written for the ionic state ϕ_i, where the normal coordinates Q_k^i are in general different. Within the same Franck-Condon approximation employed for diatomic molecules

a transition between neutral and ionic states involving excitation of some vibrational modes may be written

$$M(v_j^n, v_j^i) = M(v_1^n, \ldots, v_{3N-6}^n, v_1^i, \ldots, v_{3N-6}^i) =$$

$$R_e \prod_{k=1}^{3N-6} \int \phi_{nk}(Q_k^n)\phi_{ik}(Q_k^i)dQ_k^n, \tag{2}$$

where we have treated the electronic transition moment as a constant (R_e) over a narrow energy range. To evaluate this integral it is necessary to determine the appropriate linear transformation between Q_k^n and Q_k^i. For diatomic molecules, only a displacement of the origin occurs. The simplest corresponding relationship in the polyatomic case is

$$Q_k^i = Q_k^n + D_k \tag{3}$$

This is essentially the transformation employed by Coon et al. [26], in their treatment of the polyatomic Franck-Condon problem. It assumes no change in symmetry between lower and upper states, and in addition, that the normal coordinates are the same linear combination of symmetry coordinates (see below).

A more general transformation, given initially by Duschinsky [27], is

$$Q_k^i = \sum_j J_{kj} Q_j^n + D_k \tag{4}$$

Using the simpler transformation of Eq. (3), the integral of Eq. (2) becomes

$$M(v_j^n, v_j^i) = R_e \int \phi_{i1}(Q_1^n + D_1)\phi_{n1}(Q_1^n)\phi_{i2}(Q_2^n + D_2)\phi_{n2}(Q_2^n) \ldots$$

$$dQ_1^n dQ_2^n \ldots dQ_{3N-6}^n \tag{5}$$

This is a product of one-dimensional Franck-Condon overlap integrals. The vibrational intensity distribution for a particular normal mode is independent of the other normal modes. The magnitude of the displacement in a particular normal mode, D_k, can be evaluated from its vibrational intensity distribution in the photoelectron spectrum. The ambiguity in the sign of D_k exists here, as in the diatomic case.

When changes in bond lengths and angles occur simultaneously, the magnitude and direction of some or all of the normal coordinates may differ in the ionic and neutral state. The Duschinsky transformation (Eq. (4)) should then be used. Sharp and Rosenstock [28] have shown that the displacements can then be evaluated by the expressions

$$\underset{\sim}{J} = (\underset{\sim}{L}^{i})^{-1}\underset{\sim}{L}^{n} \tag{6}$$

and

$$\underset{\sim}{D} = (\underset{\sim}{L}^{i})^{-1}\ \underset{\sim}{\Delta R} \tag{7}$$

where

$$\vec{S}^{i} = \underset{\sim}{L}^{i}\underset{\sim}{Q}^{i} \tag{8}$$

and

$$\vec{S}^{n} = \underset{\sim}{L}^{n}\underset{\sim}{Q}^{n} \tag{9}$$

The $\vec{S}^{i}$ and $\vec{S}^{n}$ are symmetry coordinates for the ionic and neutral states, respectively, and the $\underset{\sim}{L}$ matrices relate normal to symmetry coordinates in each case (see Appendix 2). $\underset{\sim}{\Delta R}$ is the vector connecting the origins of the two states.

Obviously, this more accurate transformation requires a knowledge of the force field and normal coordinates of the ionic state as well as the neutral ground state. In most cases, the information for the ionic state is not known. It must be assumed, and the calculation performed iteratively. This calculation scheme, as well as other more recent methods for calculating the multidimensional Franck-Condon integral, are outlined in Appendix 1. Within the limitations of Eqs. (3) and (5), a fit to the vibrational intensity distributions determines the magnitude of the displacements D_k along the normal coordinates Q_k^i. To determine the actual change in geometry, it is necessary to relate the change in symmetry coordinates S_k^i to the change in normal coordinates Q_k^i by the $\underset{\sim}{L}^{i}$ matrix, the latter being obtained from a normal coordinate analysis. The change in internal coordinates may then be evaluated from the change in symmetry coordinates.

We have already noted that the vibrational intensity distribution is determined by the magnitude of the normal coordinate displacement D_k. This is true for totally symmetric vibrations. For non-totally symmetric vibrations D_k must equal zero, since a finite value would imply a change of symmetry. Hence, non-totally symmetric vibrations can be seen only weakly, and then only in even quantum increments ($\Delta v = 2,4$, etc.) except for cases of electronic coupling (such as Jahn-Teller degeneracies) where selected non-totally symmetric modes are involved in the coupling between electronic states. In general, more totally symmetric vibrational progressions appear in molecules of lower symmetry, but they are all needed to characterize the change in geometry. The ambiguity in sign for each normal coordinate can rapidly lead to a large number

Table 2. Vibrational Progressions Observed in the Photoelectron Spectra of the Symmetric Linear Molecules CO_2, CS_2, CSe_2, and the Asymmetric Linear Molecules OCS, OCSe, and SCSe (from Ref. 29)

Ionic state	Vibrational level $n_1\ n_2\ n_3$	Franck–Condon factors					
		CO_2^+		CS_2^+		CSe_2^+	
		Exptl	Calc	Exptl	Calc	Exptl	Calc
$X^2\Pi_g$	000	0.80	0.81	1.0	1.0	1.0	1.0
	100	0.15	0.16				
	200	~0.02	0.01				
	002	~0.03	0.02				
$A^2\Pi_u$	000	0.08	0.06	0.10	0.07	0.01	0.002
	100	0.20	0.19	0.20	0.20	0.03	0.013
	200	0.23	0.27	0.24	0.27	0.06	0.043
	300	0.21	0.24	0.19	0.23	0.09	0.092
	400	0.13	0.15	0.13	0.14	0.13	0.143
	500	0.08	0.07	0.09	0.06	0.15	0.173
	600	0.04	0.02	0.05	0.02	0.14	0.171
	700	0.03	0.01	0.02	0.01	0.13	0.142
	800	0.01	0.001			0.10	0.100
	900					0.07	0.061
	1000					0.05	0.033
	1100					0.03	0.015
	1200					0.02	0.006
	1300					0.01	0.002
$B^2\Sigma_u^+$	000	0.89	0.90	0.87	0.89	0.71	0.73
	100	0.10	0.10	0.10	0.10	0.24	0.25
	200	~0.01	<0.01	~0.02	<0.01	~0.05	0.02
$C^2\Sigma_g^+$	000	0.88	0.91	0.87	0.85	1.0	1.0
	100	0.06	0.06	0.11	0.11		
	002	0.06	0.03	~0.02	0.04		

Ionic state		OCS^+		$OCSe^+$		$SCSe^+$	
		Exptl	Calc	Exptl	Calc	Exptl	Calc
$X^2\Pi$	000	0.45	0.41	a		0.78	0.76
	001	0.27	0.27			0.09	0.09
	002	~0.09	0.07				0.004
	003		<0.01				
	100	0.13	0.12			0.13	0.13
	101	0.07	0.08				0.02
	102		0.02				
	200		0.02				
	201		0.01				
$A^2\Pi$	000	0.05	0.048	0.03[b]	0	0.01	0.01
	001	0.08	0.105	0.04	0.004	0.05	0.05
	002	0.10	0.110	0.05	0.02	0.13	0.11
	003	0.07	0.074	0.07	0.04	0.17	0.18
	004	0.04	0.036	0.10	0.08	0.19	0.20
	005	Overlap with 200	0.013	0.10	0.12	0.16	0.18
	006		0.004	0.11	0.15	0.13	0.13
	007			0.11	0.16	0.08	0.08
	008			0.11	0.14	0.06	0.04
	009			0.10	0.11	0.03	0.02
	0010			0.08	0.08		
	0011			0.07	0.05		
	0012			0.05	0.03		
	0013				0.015		
	100	0.05	0.047				
	101	0.10	0.102				

Table 2 (Continued)

Ionic state	Vibrational level $n_1\ n_2\ n_3$	Franck–Condon factors					
		OCS^+		$OCSe^+$		$SCSe^+$	
		Exptl	Calc	Exptl	Calc	Exptl	Calc
	102	0.10	0.107				
	103	0.09	0.072				
	104	0.05	0.035				
	105	0.02	0.013				
	106	~0.01	0.004				
	005 + 200	(0.06)	0.022				
	201	0.06	0.048				
	202	0.07	0.050				
	203	0.05	0.034				
	204		0.016				
	300	Overlap with $B^2\Sigma^+$ state	0.002				
	301		0.014				
	302		0.015				
	303		0.010				
	304		0.005				
$B^2\Sigma^+$	000	1.0		0.96	0.96	0.83	0.83
	001			~0.04	0.04	0.14	0.14
	002					~0.03	0.03
$C^2\Sigma^+$	000	0.48	0.43	0.44	0.42	0.70	0.67
	001	0.16	0.15	0.12	0.12	0.17	0.17
	002		0.03		0.02		0.01
	100	0.24	0.22	0.25	0.25	0.13	0.12
	101	~0.03	0.07	0.10	0.07		0.03
	102		0.02		0.01		
	200	0.07	0.05	0.09	0.08		
	201	0	0.02		0.02		
	300	~0.02	0.01		0.02		

[a]FCF was not measured because of severe overlap. [b]A single vibrational progression in ν_3 was assumed.

of possibilities. The matching of isotopically substituted spectra can help to resolve some of this ambiguity.

B. Applications

1. Linear to Linear Transitions in Triatomic Molecules

This is the simplest polyatomic Franck-Condon problem. In the conventional notation, ν_1 = symmetric stretching mode, ν_2 = bending mode, ν_3 = asymmetric stretching mode. For symmetric linear triatomics, ν_1 is the only totally symmetric mode; ν_2 and ν_3 can only be observed in double quantum transitions. For asymmetric linear triatomics, ν_3 and well as ν_1 are totally symmetric modes. Frost, Lee, and McDowell [29] present data for the symmetric molecules CO_2, CS_2, and CSe_2, as well as the asymmetric molecules OCS, OCSe, and SCSe. As anticipated, the symmetric molecules display progressions only in ν_1 in the 4 states observed in photoelectron spectra ($\tilde{X}^2\Pi_g$, $\tilde{A}^2\Pi_u$, $\tilde{B}^2\Sigma_u^+$, $C^2\tilde{\Sigma}_g^+$), although some indication of double quantum transitions in ν_3 is found (see Table 2). The asymmetric molecules display progressions in both ν_1 and ν_3.

Table 3. Bond Lengths Derived by Franck-Condon Analysis for the Ions CO_2^+, CS_2^+, CSe_2^+, OCS^+, $OCSe^+$, $SCSe^+$, and N_2O^+ in Various States (from Ref. 29)

Molecule XCY	Electronic state	$d_1 \times 10^{20}$ $g^{1/2}$-cm	$d_3 \times 10^{20}$ $g^{1/2}$-cm	Δr(C–X) (Å)	Δr(C–Y) (Å)	r(C–X)[a] (Å)	r(C–Y)[a] (Å)
OCO	$X^1\Sigma_g^+$					1.162[b]	1.162[b]
OCO^+	$X^2\Pi_g$	0.124	0.124	0.017	0.017	1.179(1.177)	1.179(1.177)
	$A^2\Pi_u$	0.503	0.503	0.069	0.069	1.231(1.228)	1.231(1.228)
	$B^2\Sigma_u^+$	0.095	0.095	0.013	0.013	1.175(1.180)	1.175(1.180)
	$C^2\Sigma_g^+$	0.073	0.073	0.010	0.010	1.172	1.172
SCS	$X^1\Sigma_g^+$					1.555[b]	1.555[b]
SCS^+	$X^2\Pi_g$	0	0	0	0	1.555(1.554)	1.555(1.554)
	$A^2\Pi_u$	0.702	0.702	0.068	0.068	1.623	1.623
	$B^2\Sigma_u^+$	0.144	0.144	0.014	0.014	1.569(1.564)	1.569(1.564)
	$C^2\Sigma_g^+$	0.144	0.144	0.014	0.014	1.569	1.569
SeCSe	$X^1\Sigma_g^+$					1.711[c]	1.711[c]
$SeCSe^+$	$X^2\Pi_g$	0	0	0	0	1.711	1.711
	$A^2\Pi_u$	1.425	1.425	0.088	0.088	1.799	1.799
	$B^2\Sigma_u^+$	0.324	0.324	0.020	0.020	1.731	1.731
	$C^2\Sigma_g^+$	0	0	0	0	1.711	1.711
OCS	$X^1\Sigma^+$					1.160[b]	1.560[b]
OCS^+	$X^2\Pi$	0.126	0.281	−0.024	0.074	1.136	1.634
	$A^2\Pi$	0.230	0.534	0.092	0.046	1.252	1.606
	$B^2\Sigma^+$	0	0	0	0	1.160	1.560
	$C^2\Sigma^+$	0.166	0.211	−0.039	0.069	1.121	1.629
OCSe	$X^1\Sigma^+$					1.159[c]	1.709[c]
$OCSe^+$	$X^2\Pi$						
	$A^2\Pi$[d]	0	1.170	0.031	0.181	1.190	1.890
	$B^2\Sigma^+$	0.048	0	−0.014	0.009	1.145	1.718
	$C^2\Sigma^+$	0.181	0.219	−0.048	0.067	1.111	1.776
SCSe	$X^1\Sigma^+$					1.557[c]	1.709[c]
$SCSe^+$	$X^2\Pi$	0.115	0.161	−0.020	0.041	1.537	1.750
	$A^2\Pi$	0	1.054	0.063	0.104	1.620	1.813
	$B^2\Sigma^+$	0	0.119	−0.007	−0.012	1.550	1.738
	$C^2\Sigma^+$	0.122	0.234	−0.017	0.050	1.540	1.759
NNO	$X^1\Sigma^+$					1.128[b]	1.184[b]
NNO^+	$X^2\Pi$	0.046	0.078	0.022	0.007	1.150(1.555)	1.191(1.185)
	$A^2\Sigma^+$	0.063	0.131	0.011	−0.041	1.139(1.140)	1.143(1.141)

[a] Values in parentheses are experimental bond lengths from G. Herzberg, "Electronic Spectra of Polyatomic Molecules" (Van Nostrand-Reinhold, New York (1966)

[b] From Herzberg, see a.

[c] From Ref. 30

[d] A single vibrational progression in ν_3 was assumed.

Table 4. Alternative Values of Bond Length Changes between Neutral Ground State and Various Ionic States of XCN (X = Cl, Br, I) Derived by Franck-Condon Analysis (from Ref. 33)

Molecule	State of ion	$\Delta r_3 = \Delta r$(CHal)/Å	$\Delta r_1 = \Delta r$(CN)/Å
ClCN	$\tilde{X}\,^2\Pi_{3/2}$ and $\tilde{X}\,^2\Pi_{1/2}$	1. $0{\cdot}012 \pm 0{\cdot}014$	$-0{\cdot}078 \pm 0{\cdot}012$
		2. $-0{\cdot}012 \pm 0{\cdot}014$	$0{\cdot}078 \pm 0{\cdot}012$
		3. $0{\cdot}076 \pm 0{\cdot}014$	$-0{\cdot}048 \pm 0{\cdot}012$
		4. $-0{\cdot}076 \pm 0{\cdot}014$	$0{\cdot}048 \pm 0{\cdot}012$
BrCN	$\tilde{X}\,^2\Pi_{3/2}$ and $\tilde{X}\,^2\Pi_{1/2}$	1. $0{\cdot}012 \pm 0{\cdot}015$	$0{\cdot}037 \pm 0{\cdot}011$
		2. $-0{\cdot}012 \pm 0{\cdot}015$	$-0{\cdot}037 \pm 0{\cdot}011$
		3. $0{\cdot}070 \pm 0{\cdot}015$	$-0{\cdot}059 \pm 0{\cdot}011$
		4. $-0{\cdot}070 \pm 0{\cdot}015$	$0{\cdot}059 \pm 0{\cdot}011$
ICN	$\tilde{X}\,^2\Pi_{3/2}$	1. $0{\cdot}028 \pm 0{\cdot}016$	$0{\cdot}023 \pm 0{\cdot}010$
		2. $-0{\cdot}028 \pm 0{\cdot}016$	$-0{\cdot}023 \pm 0{\cdot}010$
		3. $0{\cdot}048 \pm 0{\cdot}016$	$-0{\cdot}013 \pm 0{\cdot}010$
		4. $-0{\cdot}048 \pm 0{\cdot}016$	$0{\cdot}013 \pm 0{\cdot}010$
ICN	$\tilde{X}\,^2\Pi_{1/2}$	1. $0{\cdot}028 \pm 0{\cdot}016$	$0{\cdot}034 \pm 0{\cdot}010$
		2. $-0{\cdot}028 \pm 0{\cdot}016$	$-0{\cdot}034 \pm 0{\cdot}010$
		3. $0{\cdot}060 \pm 0{\cdot}016$	$-0{\cdot}021 \pm 0{\cdot}010$
		4. $-0{\cdot}060 \pm 0{\cdot}016$	$0{\cdot}021 \pm 0{\cdot}010$
ClCN	$\tilde{I}\,^2\Sigma^+$	1. $0{\cdot}04 \pm 0{\cdot}02$	$-0{\cdot}01 \pm 0{\cdot}02$
		2. $-0{\cdot}04 \pm 0{\cdot}02$	$0{\cdot}01 \pm 0{\cdot}02$
BrCN	$\tilde{I}\,^2\Sigma^+$	1. $0{\cdot}04 \pm 0{\cdot}02$	$-0{\cdot}01 \pm 0{\cdot}02$
		2. $-0{\cdot}04 \pm 0{\cdot}02$	$0{\cdot}01 \pm 0{\cdot}02$
ClCN	$\tilde{2}\,^2\Pi$	1. $-0{\cdot}20 \pm 0{\cdot}04$	$-0{\cdot}02 \pm 0{\cdot}08$
		2. $0{\cdot}20 \pm 0{\cdot}04$	$0{\cdot}02 \pm 0{\cdot}08$

For the symmetric molecules, Eqs. (3) and (5) are directly applicable without further qualification, since only a single normal coordinate is involved, and there is no change in symmetry. The displacement coordinate D_k is readily obtained from a Franck-Condon fit. With the aid of $\underset{\sim}{F}$ and $\underset{\sim}{G}$ matrices available from Wentink [30] the transformation matrix $\underset{\sim}{L}$ can be calculated, and from Eqs. (8) or (9), the change in internal coordinate. The ambiguity in sign can be rationalized in this case by identifying an increase in stretching frequency with a decrease in bond length, and conversely.

For the asymmetric triatomics, Frost et al. have apparently treated ν_1 and ν_3 independently (i.e., without mixing), according to the approximation of Coon et al. [26], as given in Eqs. (3) and (5). Their results for the aforementioned set of molecules, as well as N_2O, are given in Table 3. Franck-Condon analyses of N_2O have also been reported by Rosenstock [31] and Hollas and Sutherley [32]. Where independent spectroscopic evidence is available (see values in parentheses in Table 3) the results are quite accurate ($\Delta r \leqslant 0.006$ Å). In most of the cases covered, the Franck-Condon analysis is the best information we have on the geometrical structure of these ions.

Table 5. Selected Values of Bond Length Changes (in Å) between Neutral Ground State and Various Ionic States of XCN (X = Cl, Br, I) (from Ref. 33)

	Ground state of molecule		$\tilde{X}$ states of positive ion		$\tilde{1}$ state of positive ion		$\tilde{2}$ state of positive ion	
	r(CHal)	r(CN)	Δr(CHal)	Δr(CN)	Δr(CHal)	Δr(CN)	Δr(CHal)	Δr(CN)
ClCN	1·631	1·159	$-0·076 \pm 0·014$	$0·048 \pm 0·012$	$\pm(0·04 \pm 0·02)$	$\mp(0·01 \pm 0·02)$	$0·20 \pm 0·04$	$0·02 \pm 0·08$
BrCN	1·789	1·158	$-0·070 \pm 0·015$	$0·059 \pm 0·011$	$\pm(0·04 \pm 0·02)$	$\mp(0·01 \pm 0·02)$	—	—
ICN	1·994	1·159	$-0·048 \pm 0·016$†	$0·013 \pm 0·010$†	—	—	—	—
			$-0·060 \pm 0·016$‡	$0·021 \pm 0·010$‡				

† $\tilde{X}\,^2\Pi_{3/2}$ state.
‡ $\tilde{X}\,^2\Pi_{1/2}$ state.

Hollas and Sutherley [33] have examined the ground states of $ClCN^+$, $BrCN^+$, and ICN^+, as well as selected excited states. Here again, ν_1 and ν_3 modes are excited in the photoelectron spectra. Their analysis differs somewhat from that of Frost et al. [29], since they use an $\underset{\sim}{L}$ matrix appropriate to the ionic state. The force constants for the ionic state are obtained from the vibrational separations in the photoelectron spectrum. Their resulting geometry changes, including all possible solutions due to ambiguity in sign, are given in Table 4. Basing their selection largely on the Badger's rule-like criterion relating frequency changes to corresponding ones in internuclear distance, they present a final set of solutions reproduced in Table 5.

Hollas and Sutherley [34] subsequently examined the first photoelectron band in HCN and DCN. Here, the primary progression is ν_3, the C ≡ N stretching vibration, with virtually no evidence for ν_1. An analysis similar to their earlier XCN work, but involving some uncertainty in the $\underset{\sim}{L}$ matrix for the ion due to lack of information concerning ν_1 (ion) leads them to conclude that Δr (C-N) = ±0.06 ± 0.012 Å and Δr (C-H) = ±0.02 ± 0.05 Å for the transition to the $\tilde{X}^2\Pi$ state, the increases in bond lengths being considered more probable. Neutral HCN has r(C-N) = 1.156 Å and r(C-H) = 1.064 Å. However, their analysis must be treated with caution, since subsequent data with higher resolution [34b] reveal intermixing of $^2\Sigma$ vibrational components with the $^2\Pi$ components they have used. A more extensive treatment of this photoelectron spectrum has been given by Köppel et al. [34c].

2. Transitions from Bent Triatomic Molecules, Specifically H_2O and Its Isotopes

For H_2O in its C_{2v} symmetry, there are 2 totally symmetric normal modes - the symmetric stretch ν_1 and the bending vibration ν_2. The 584 Å photoelectron spectrum of H_2O is reproduced in Fig. 8. The first band (which has received most attention in Franck-Condon

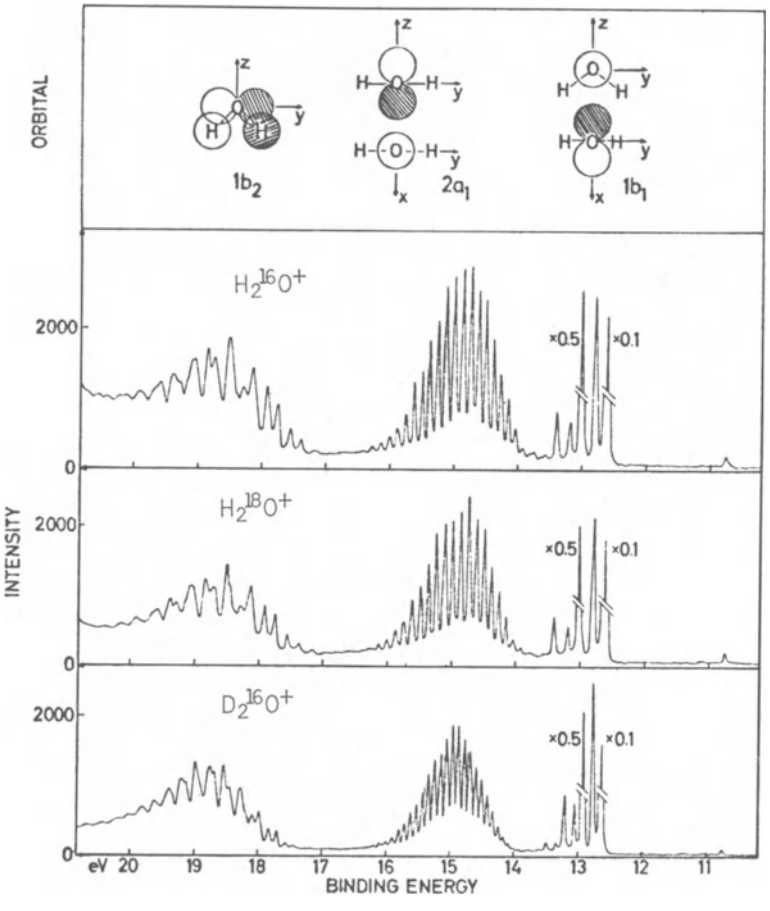

Fig. 8. The He I photoelectron spectrum of H_2O (from L. Karlsson, L. Mattsson, R. Jadrny, R. G. Albridge, S. Pinchas, T. Bergmark, and K. Siegbahn, J. Chem. Phys., 62, 4745 (1975)).

analyses) displays progressions in ν_1 and ν_2. It represents a bent-to-bent transition. The second band is an extended progression in ν_2, with no other frequency excited. It has generally been interpreted as a transition to a linear state of H_2O^+, designated $\tilde{A}\ ^2A_1$. Brundle and Turner [35] describe this state as probably slightly non-linear, but less than the corresponding state in NH_2. Potts and Price [36] argue that if it were significantly non-linear, there would be a barrier between the equivalent bent forms. If vibrational levels existed below and above the barrier in the potential, one should be able to observe a halving in the vibrational frequency intervals upon surmounting the barrier. Since even the lowest vibrational peaks display about the same intervals, the barrier must be insignificant. Dixon et al. [37] concur with the linear geometry,

Table 6. Geometric Structure of H_2O^+ ($\tilde{X}\ ^2B_1$) Deduced by Various Workers and Methods

	Botter & Rosenstock,[a] 1968 / Brundle & Turner,[b] 1968	Botter & Rosenstock,[c] 1969	Potts & Price,[d] 1972	Dixon, et al,[e] 1976	Botter & Carlier,[f] 1977	Lew & Heiber,[g] 1973	Jungen, et al,[h] 1980
r(O-H)	1.00Å	0.995±0.005Å	1.016Å	1.03Å	1.001±0.001Å	0.999Å	1.010Å
∢(H-O-H)	110°	<109°	110.2°	109.4°	110.2±0.2°	110.5°	108.8°
Comments	Botter-Rosenstock calculations, best fit to Brundle-Turner data, harmonic potential	Anharmonicity added to potential	Data fitted with "single Franck-Condon factor."	Franck-Condon fit to data using method of Coon, et al.	Best mutual fit to data on 3 isotopic forms, H_2O, D_2O and HDO.	Rotational analysis of optical spectrum of ionic transition	More elaborate analysis of the optical transition

a. R. Botter and H.M. Rosenstock, Adv. Mass Spectrometry 4, 579 (1968).

b. Ref. 35.

c. R. Botter and H.M. Rosenstock, J. Res. NBS 73A, 313 (1969).

d. Ref. 36.

e. Ref. 37.

f. R. Botter and J. Carlier, J. Electr. Spectr. 12, 55 (1977).

g. Ref. 39.

h. Ref. 38.

but add that the bending potential is very anharmonic. Jungen et al. [38] have recently made a detailed study of the optical transition $\tilde{A} \rightarrow \tilde{X}$ in H_2O^+ (which is beyond the scope of the present work) and conclude that the $\tilde{A}$ state is linear and has r(O-H) = 0.997 Å.

The third band in the photoelectron spectrum is complex and includes some broadening due to predissociation. Various interpretations have been offered [35-37] but probably none are yet definitive.

As mentioned earlier, the first band has been a favorite testing ground for Franck-Condon analyses. These are summarized in Table 6, together with dates and methods used. It is noteworthy that the rotationally resolved optical spectrum [39] became available in 1973 but the earliest result from Franck-Condon analysis [35] provided almost identically the same result.

3. Linear Tetratomic Molecules

a) C_2H_2

In their early paper, Sharp and Rosenstock [28] used their formalism to fit a rather primitive vibrational intensity distribution obtained from step-like structure in the photoionization of C_2H_2 and C_2D_2 near threshold. In acetylene there are two totally symmetric vibrations, conventionally designated ν_1 (primarily C-H stretch) and ν_2 (primarily C-C stretch). They were able to infer a progression in ν_2, with a spacing of ca. 1850 cm^{-1}, rather similar to subsequent data obtained from photoelectron spectroscopy. No progression in ν_1 could be identified, and hence its frequency had to be estimated. The experimental relative vibrational intensities in $C_2H_2^+$ and $C_2D_2^+$ were not consistent with their analysis but the experiment was subsequently repeated [40] and the anomaly disappeared. They deduced an increase in the C-C distance from 1.20 Å in neutral acetylene to 1.250 ± 0.005 Å in the ground state of $C_2H_2^+$ with no significant change in the C-H distance, 1.06 Å.

Hollas and Sutherley [41] used their photoelectron spectral data and the method of Coon et al. [26] to determine geometrical parameters. Here, too, a progression was observable only in ν_2, and since these authors use an L matrix characteristic of the ion, ν_1 had to be estimated. Despite the different methods used, their result is virtually indistinguishable from that of Sharp and Rosenstock: r(C-C) = 1.25_5 ± 0.01 Å and r(C-H) = 1.06 ± 0.01 Å.

At about the same time, Heilbronner et al. [42] also performed an analysis of the first band in the photoelectron spectrum of C_2H_2 reported by Baker and Turner [43]. Their level of approximation corresponds to Eqs. (3) and (5) in our development. They used an L matrix corresponding to the neutral ground state. They deduced r(C-C) = +0.042 Å and r(C-H) = +0.013 Å, again in good agreement

Table 7. Geometries of the Neutral Monohaloacetylenes[a], in Å

	r(CH)	r(CC)	r(CX)
HCCF	1.058	1.200	1.275
HCCCl	1.058	1.211	1.632
HCCBr	1.058	1.200	1.800
HCCI	1.058	1.200	2.000

[a]From G. R. Hunt and M. K. Wilson, J. Chem. Phys. 34, 1301 (1961).

Changes in internuclear distances for the monohaloacetylenes upon ionization.

X	process (1)	ΔR_{CH}/Å	ΔR_{CC}/Å	ΔR_{CX}/Å
F	$(\tilde{X}) \leftarrow (X)$	0.021	0.053	-0.062
Cl	$(\tilde{X}) \leftarrow (X)$	0.010	0.026	-0.067
	$(\tilde{A}) \leftarrow (X)$	0.006	0.029	0.129
Br	$(\tilde{A}) \leftarrow (X)$	0.006	0.028	0.154
I	$(\tilde{X}) \leftarrow (X)$	0.009	0.025	-0.078
	$(A) \leftarrow (X)$	0.004	0.017	0.150
H	(X) (X)	0.013	0.041	0.013

with Sharp and Rosenstock's initial calculation, but revealing the level of discrepancy between different methods and sources of photoelectron data in a rather simple case.

In subsequent cases where the Franck-Condon analysis is less certain we shall have occasion to compare these calculated ionic structures with ab initio calculations primarily performed by Prof. Pople's group. As a point of reference we note here that Lathan et al. [94] compute r(CC) = 1.247 Å and r(CH) = 1.102 Å for $C_2H_2^+$, in fairly good agreement with the Franck-Condon results and showing the same increase in bond length.

b) Haloacetylenes (HCCX, X = F, Cl, Br, I)

Heilbronner et al. [42] have extended their study to the monohaloacetylenes. The first two bands in the photoelectron spectrum have been analyzed, corresponding to the formation of the spin-orbit

split ionic states $\tilde{X}\ ^2\Pi_{3/2}$ and $\tilde{A}\ ^2\Pi_{1/2}$. For the $\tilde{X}$ of C_2HBr there exists an accidental degeneracy between the spin-orbit splitting and twice the vibrational spacing, which prevents measurement of reliable intensity ratios. In principle, three totally symmetric vibrations exist for these molecules. In each of the cases which could be studied, progressions in ν_2 and ν_3 were observed for the $\tilde{X}$ state, but only ν_3 progressions could be identified in transitions to the $\tilde{A}$ state. (The approximate identifications are ν_1 = C-H stretch, ν_2 = C-C stretch and ν_3 = C-X stretch.)

The resulting internal coordinate changes from their analysis are reproduced in Table 7. For completeness, we also present the geometries of the corresponding neutral molecules, enabling one to compute the geometries of the ions.

c) C_2N_2

Cyanogen, having the same symmetry as acetylene, also has the two totally symmetric vibrations ν_1 and ν_2. Hollas and Sutherley [34] have made a Franck-Condon analysis of the first two bands in the photoelectron spectrum. Unlike C_2H_2, it is ν_1 (the C-N stretch) which forms a progression, with no detectable evidence of ν_2 excitation. As in their previous work, they calculate internal coordinate changes from

$$\underset{\sim}{R} = \underset{\sim}{L}\ \underset{\sim}{Q}$$

where the $\underset{\sim}{L}$ matrix is constructed from the ion's force field. The ionic ν_2 frequency is estimated, and within reasonable bounds, it is found that the final result is insensitive to this choice. For the transition to the $\tilde{X}^2\Pi_g$ state of $C_2N_2^+$ they deduce a most likely Δr(C-N = +0.043 ± 0.008 Å and Δr(C-C = -0.042 ± 0.010 Å, with a possible but less likely choice involving the negative of these quantities. Their deductions for the first excited $^2\Sigma_g^+$ state are Δr(C-N) = ±0.018 ± 0.010 Å and Δr(C-C) = ±0.014 ± 0.005 Å, with both solutions equally likely. The dimensions of neutral C_2N_2 are given as r(C-N) = 1.154 Å, r(C-C) = 1.389 Å.

It is noteworthy in this molecule that both the C-N and C-C bond lengths have comparable displacements in both states, although only one frequency (nominally the C-N stretch) is active. This is a consequence of the off-diagonal element in the $\underset{\sim}{L}$ matrix being of similar magnitude to the diagonal elements.

Cederbaum et al. [45] have also studied cyanogen with the Green's function method, and provide a table of their linear coupling constants κ_s for each of the bands in the photoelectron spectrum. Using their formula [13]

$$\underset{\sim}{S_i} - \underset{\sim}{S_n} = -\sqrt{2}\ \underset{\sim}{L}\ \underset{\sim}{\omega}^{-1/2}(\underset{\sim}{\omega} + 4\underset{\sim}{\gamma})^{-1}\kappa \qquad (10)$$

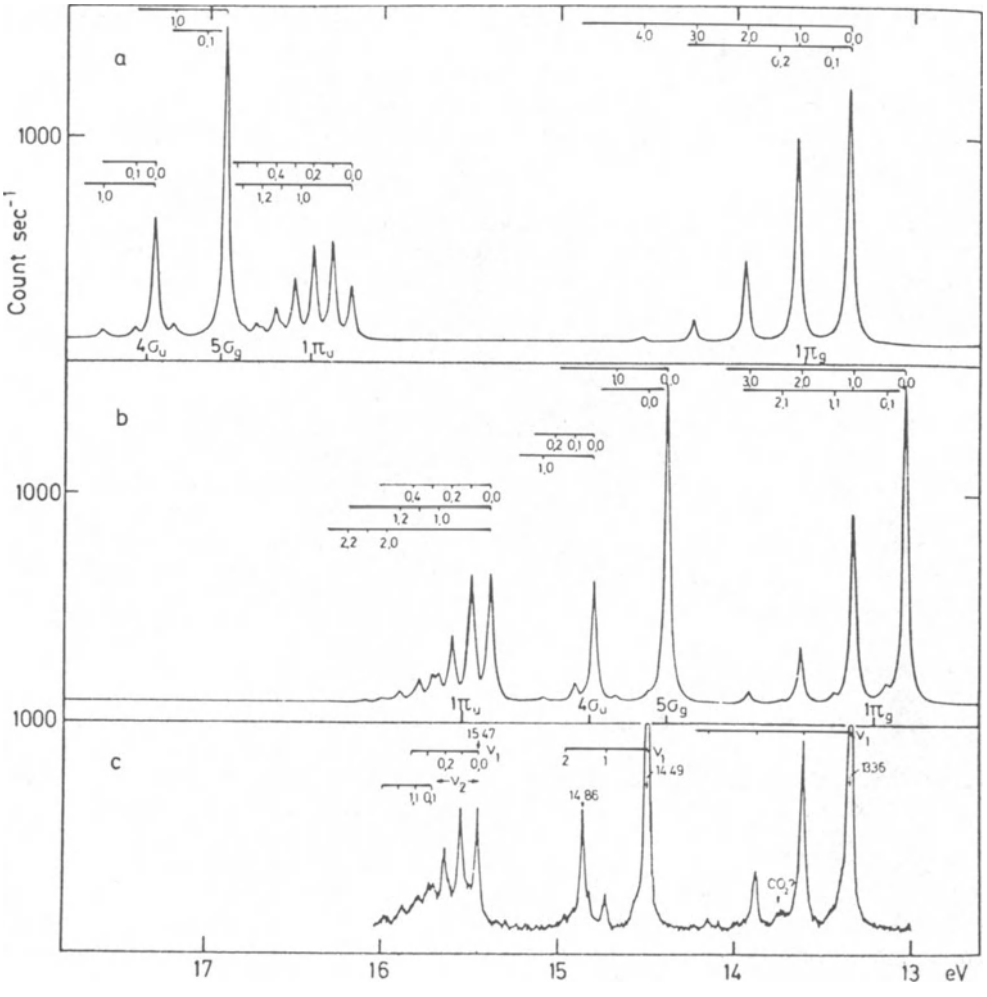

Fig. 9. A comparison of the calculated and experimental photoelectron spectrum of cyanogen. (a) The spectrum calculated on the Hartree-Fock level. (b) The spectrum calculated including correlation and reorganization effects. The vibrational lines have been taken to be of Lorentzian type with a half-width of 0.036 eV which corresponds to the resolution of the spectrometer used in the experiment. The calculated "centre of gravity" of each band is indicated in the figure. (c) The experimental spectrum (from Ref. 45).

together with our computed L̃ matrix for neutral ground state C_2N_2, and making their usual assumption that the second order coupling constant $\gamma = 0$, we obtain $\Delta(CN) = +0.033$ Å and $\Delta(CC) = -0.045$ Å for the ionic ground state, $\tilde{X}^2\Pi_g$, which are close in magnitude to those of Hollas and Sutherley, and correspond to their preferred choice of sign.

For the first excited $^2\Sigma_g^+$ state we obtain $\Delta(CN) = -0.007$ Å and $\Delta(CC) = -0.000_5$ Å from the κ's of Cederbaum et al. However, a comparison of their calculated spectrum with the experimental one (see Fig. 9) reveals that they have underestimated both κ's for this transition. An estimate of more appropriate κ's from the photoelectron spectrum yields $\Delta(CN) \cong -0.016$ Å and $\Delta(CC) = +0.006$ Å, which is close to one of the alternatives deduced by Hollas and Sutherley. For the $^2\Sigma_u^+$ transition there is very little geometry change, and the uncertainty in κ does not warrant a detailed calculation. For the $^2\Pi_u$ transition, we compute $\Delta(CN) = +0.032$ Å and $\Delta(CC) = +0.037$ Å.

4. Tetratomic C_{3v}, Specifically NH_3

The best resolved PES of NH_3 is given by Rabalais et al. [46] (Fig. 10). For the ionic ground state, $^2A_1$, the most prominent feature is a long progression in the out-of-plane bending vibration ν_2', with negative anharmonicity and spacings ranging from ≈111 meV to ≈140 meV. The bending frequency for the pyramidal ground state [47] is 120 meV. Rabalais et al. [46] also observe a similar, though very weak, progression shifted by ≈340 meV towards higher binding energy, which they attribute to simultaneous excitation of one quantum of ν_1' (symmetric stretch) and n quanta of ν_2'. The ground state frequency for the symmetric stretch [47], $\nu_2'' = 418$ meV. The maximum of the main progression is at n = 6 or 7.

Botter and Rosenstock [48, 49], assuming a planar structure for NH_3^+, $^2A_1$, calculated the vibrational intensity distribution using the method of Sharp and Rosenstock [28]. They found a maximum in the bending progression at v' = 4 if the N-H distance remained unchanged. Furthermore, they argued that there should be an appreciable excitation of combination bands involving the N-H stretching mode if the N-H distance remained unchanged. Since the data available to them did not reveal such combination bands, they were forced to assume an appreciable decrease in the N-H bond length (0.06-0.07 Å) in order to produce a progression consisting purely of ν_2'. They noted that Walsh and Warsop [50] had made such a prediction. From studies of NH_3 Rydberg levels, they concluded that the n = 3 level would have an appreciable increase in bond length compared with the ground state, but higher series members would have successively smaller N-H distances, converging to an ionic structure with N-H distance smaller than the neutral ground state. This conclusion was based on observed shifts in zero point energy of the n = 4 state and n = 3 state between NH_3 and ND_3, and a larger sepa-

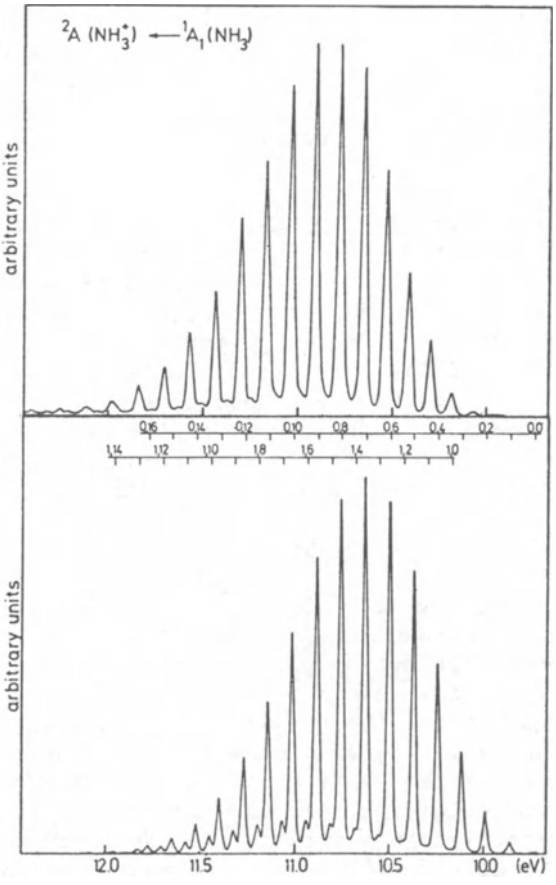

Fig. 10. The first band in the photoelectron spectrum of NH_3 as recorded by Rabalais et al. [46] (upper part) and the calculated spectrum (lower part). The calculation is an absolute one, including the calculation of the position of the band on the energy scale. The assignment of the lines to the bending and the stretching vibration is indicated on top of the calculated spectrum (from Ref. 56).

ration of the band heads of the n = 4 transition than the n = 3 transition.

Douglas [51] performed a rotational analysis of the $\nu_2 = 1$ band in the A state of ND_3, deduced that it was planar and had an N-D bond length of 1.08 Å. (The neutral ground state [52] has an N-H bond length of 1.0124 Å and H-N-H angle of 106.67°.)

Earlier, Douglas and Hollas [53] had examined a more highly excited electronic state of NH_3 (the 1600 Å system) and deduced a

planar structure with N-H bond length of 1.027 Å or 1.040 Å. Hence, this limited information would appear to parallel the conclusions of Walsh and Warsop [50]. However, these states are not successive members of a Rydberg series; the excitation is n = 3, ℓ = 0 or 1.

Harshbarger [54] and Durmaz et al. [55] used fairly sophisticated potential functions for ground and excited states of NH_3, and performed Franck-Condon calculations. They obtained maxima at v' = 4, whereas the experimental spectrum displayed a maximum at v' = 6 for $\tilde{A}$ state excitation. Various ad hoc assumptions (accidental coincidence of 3 × ν_2' with ν_1', variation of electronic transition moment with vibrational state excited) were invoked by these authors, and were not very satisfactory.

This was the state of affairs when Domcke et al. [56] performed their Green's function calculation on NH_3, and determined the vibrational coupling constants. Their mocked-up spectrum, based upon the derivative of the potential surface of the $^2A_1$ ionic state with respect to ground state normal coordinates matched the experimental spectrum rather well, reproducing the maximum intensity of ν_2' at v = 6 (see Fig. 10). Their calculation revealed an excitation of the ν_1' mode which was distinctly more prominent than in the experimental spectrum. They reported first order coupling constants for both the symmetric stretching coordinate $S_1(Q)$ and the bending coordinate $S_2(Q_2)$, and the corresponding derivatives, which we reproduce below.

	$(\partial E/\partial S)_o$ eV/bohr	κ eV
$S_1(Q_1)$	-0.761	-0.114
$S_2(Q_2)$	-1.308	-0.349

Using the relationship between internal coordinate changes and the coupling constant κ given by Cederbaum and Domcke [13] (our Eq. (10)), a computed L matrix, γ = 0 and ω for the ground state, we calculate a reduction in N-H bond length of 0.011 Å and a totally unrealistic increase in H-N-H bond angle of 43°, which overshoots the planar structure by ∿30°.

If we assume a planar structure for the $^2A_1$ ionic state and treat the symmetric stretch and out-of-plane bending potential as being harmonic, and uncoupled, we can differentiate and find the minimum of energy.

We can derive an alternative expression for the displacements. Let us expand the potential of the ionic state in a Taylor series, first about the neutral ground state's equilibrium position, and then about the ionic state's equilibrium position. Thus

$$V_i = V_o + (Q-Q_o)\left.\frac{\partial V}{\partial Q}\right|_{Q=Q_o} + 0\ (Q-Q_o)^2 \tag{11}$$

$$V_i = V_o' + \frac{1}{2}(Q-Q_i)^2\left.\frac{\partial^2 V}{\partial Q^2}\right|_{Q=Q_i} = V_o' + \frac{1}{2}(Q-Q_o-\Delta Q)^2\left.\frac{\partial^2 V}{\partial Q^2}\right|_{Q=Q_i} =$$

$$V_o' + \frac{1}{2}(Q-Q_o)^2\left.\frac{\partial^2 V}{\partial Q^2}\right|_{Q=Q_i} - \Delta Q(Q-Q_o)\left.\frac{\partial^2 V}{\partial Q^2}\right|_{Q=Q_i} +$$

$$\frac{\Delta Q^2}{2}\left.\frac{\partial^2 V}{\partial Q^2}\right|_{Q=Q_i} \tag{12}$$

Identifying coefficients of $(Q-Q_o)$ in (11) and (12) we obtain

$$\left.\frac{\partial V}{\partial Q}\right|_{Q=Q_o} = -\Delta Q\left.\frac{\partial^2 V}{\partial Q^2}\right|_{Q=Q_i}$$

Therefore,

$$\Delta Q = Q_i - Q_o = -\left.\frac{\partial V}{\partial Q}\right|_{Q=Q_o} \Big/ \left.\frac{\partial^2 V}{\partial Q^2}\right|_{Q=Q_i},$$

where Q_i is the ionic state equilibrium position for a vibrational symmetry coordinate, and Q_o is the neutral ground state equilibrium position for the same coordinate. In the table above, Domcke et al. [56] present values of

$$\left.\frac{\partial E}{\partial S}\right|_{S=S_o}$$

for the symmetric stretch and bending coordinates. The term

$$\left.\frac{\partial^2 V}{\partial Q^2}\right|_{Q=Q_i}$$

is the force constant for a particular vibrational motion in the ionic state. From energy level spacings given by Rabalais et al. [46], we deduce k_1 (symmetric stretching force constant) of 4.435 mdynes/Å. Substituting the first derivatives from Domcke et al. [56], and our calculated force constants, we obtain

$\Delta R(N-H) = +0.052$ Å and Δ(H-N-H angle) = 49°.

Table 8. Alternative Coordinate Displacements upon Ionization of $H_2CO \rightarrow \tilde{X}$ (H_2CO^+), Measured Along the Symmetry Coordinates in Å and Degrees [59]

	H_2CO			
	+++	++-	-+-	+--
ΔS_1	0.021	0.032	-0.018	+0.029
ΔS_2	0.021	0.011	+0.014	-0.024
ΔS_3	-2.43°	+5.84°	+6.65°	+1.62°
	D_2CO			
ΔS_1	0.030	0.044	-0.015	+0.029
ΔS_2	0.009	0.004	+0.019	-0.023
ΔS_3	-5.15°	+4.91°	+6.79°	+3.27°

In both calculations, the change in angle calculated far exceeds that to produce planarity. It is probably due to an inadequate representation of the ionic potential with respect to the bending coordinate, neglecting important anharmonic terms. However, the symmetric stretching mode, which is of a different symmetry species in D_{3h} symmetry and therefore is clearly separable from the bending mode is more accurately described. We therefore believe that the first derivative with respect to the stretching mode given by Domcke et al. [56] leads to an increase in N-H bond length in the ionic state. The expression for ΔR given by Cederbaum and Domcke [13] using the $\underset{\sim}{L}$ matrix formulation is very sensitive to small off-diagonal elements, and may be responsible for the weak apparent reduction in N-H bond length.

Some support for our tentative conclusion of an increase in N-H bond length in this transition is provided by the ab initio calculations of Lathan et al. [57]. These authors find 1.003 Å for r(NH) in NH_3, and r(NH) = 1.056 Å for the planar ground state of NH_3^+, using their STO-3G basis set, and a similar increase in r(NH) using their larger 4-31G basis set. With a still larger basis set that approaches the Hartree Fock limit, Hariharan and Pople [58] still find an increase in r(NH), but it is now only 0.008 Å.

Table 9. Alternative Coordinate Displacements upon Ionization of $H_2CO \rightarrow \tilde{X}(H_2CO^+)$ Measured Along the Symmetry Coordinates in Å and Degrees (using parameters of Domcke and Cederbaum [12])

	H_2CO			
	+++	++-	-+-	+--
ΔS_1	+0.0228	+0.0374	-0.0193	+0.0339
ΔS_2	+0.0317	+0.0154	+0.0186	-0.0350
ΔS_3	-3.10°	+8.78°	+9.64°	+2.24°
	D_2CO			
ΔS_1	+0.0452	+0.0571	-0.0209	+0.0329
ΔS_2	+0.0169	+0.0122	+0.0305	-0.0352
ΔS_3	-4.37°	+4.96°	+7.34°	+2.00°

5. Tetratomic C_{2v} Molecules

a) CH_2O (Formaladehyde)

The determination of the geometric structure of CH_2O^+ in its electronic ground state from a study of the photoelectron spectrum of CH_2O offers to provide us with a benchmark comparison of the method of Domcke and Cederbaum with one relying entirely on parameters derived from the photoelecton spectrum. The 584 Å photoelectron spectra of H_2CO, D_2CO (and also HDCO) have been published by Turner et al. [1]. Moule [59] has examined the vibrational structure of the first electronic band in the PES, and finds evidence for excitation of ν_1(C-H stretch), ν_2(C-O stretch), and ν_3(H-C-H angle deformation). Using the symmetry coordinates

$$S_1 = \frac{1}{\sqrt{2}} (\Delta r_1 + Ar_2)$$

$$S_2 = \Delta R$$

$$S_3 = \sqrt{\frac{3}{2}}\, r_0 \phi$$

and the force constants of Shimanouchi and Suzuki [60], he deduces the normal coordinates Q_1, Q_2, and Q_3 in terms of the symmetry coordinates. From the relative intensities of overtones of Q_1, Q_2, and Q_3 appearing in the photoelectron spectrum, he determines the most probable displacement along each of the normal coordinates. Each of these displacements is indeterminate in sign. Hence, 2^3 or 8 possible displacements can match the photoelectron spectrum. He then requires that the structure of D_2CO^+ match that of H_2CO^+. This reduces his choice to two groups of displacements and their negative counterparts. His final selection is made by comparison with two semi-empirical calculations (CNDO/2 and MINDO 3) of the presumed change of structure between H_2CO and H_2CO^+. We have attempted to repeat Moule's calculation, and we believe that there is an error in sign in his $\underset{\sim}{L}$ matrix which affects his final choice. With his $\underset{\sim}{L}$ matrix, we cannot reproduce the observed frequencies, but with a change of sign of one coordinate, we can. Our revised tabulation of his symmetry coordinate displacements with respect to normal coordinate displacements is given in Table 8.

By comparing corresponding displacements in H_2CO and D_2CO, we can rule out the alternatives in columns 1 and 2. We reserve a decision between columns 3 and 4 until further considerations.

Domcke and Cederbaum [12] calculate the derivative of the ionic state potential surface with respect to ground state normal coordinates, in the Franck-Condon region. They do not report these derivatives directly, but use them to determine coupling constants κ and coupling parameters a_i. With these coupling parameters they calculate a mocked-up photoelectron spectrum for both H_2CO and D_2CO, to be compared with experiment. If the comparison is deemed adequate, they content themselves with a proper interpretation of the photoelectron spectrum. We have used their a_i's to compute corresponding κ_i's (which introduces an ambiguity in sign) and then employed their formula relating a change in symmetry coordinate to a κ value, i.e.,

$$\Delta S_k = -\sqrt{2}\,\hbar\,\underset{\sim}{L}\,\underset{\sim}{\kappa}/\underset{\sim}{\omega}^{3/2}$$

This enables us to construct a new table of changes in symmetry coordinates upon ionization of H_2CO^+ and D_2CO^+, which we reproduce in Table 9 above.

Here again, comparing corresponding displacements in H_2CO and D_2CO, columns 1 and 2 can be eliminated. In this case, column 4 appears to provide a distinctly better match than column 3.

It is now of some interest to compare with an improved displacement analysis performed by Moule, in which he computes an $\underset{\sim}{L}$ matrix for the ionic state based upon a normal coordinate treatment of this state. His revised displacements are given in Table 10.

Table 10. Alternative Coordinate Displacements for $H_2CO \rightarrow \tilde{X}(H_2CO^+)$ Using an L Matrix Appropriate for the Ionic State (after Moule [59], but with revised sign)

	H_2CO			
	+++	++-	-+-	+--
ΔS_1	+0.019	+0.028	-0.022	+0.031
ΔS_2	+0.016	+0.018	+0.021	-0.019
ΔS_3	-4.17°	+5.07°	+5.78°	+3.46°
	D_2CO			
ΔS_1	+0.029	+0.040	-0.020	+0.031
ΔS_2	+0.008	+0.009	+0.021	-0.019
ΔS_3	-5.39°	+5.15°	+6.68°	+3.86°

Table 11. Final Selection of Geometry for $\tilde{X}(H_2CO^+)$ as Deduced from Franck-Condon Analyses. The Geometry of Neutral H_2CO is Shown for Comparison

	$\tilde{X}(H_2CO)$[a]	$\tilde{X}(H_2CO^+)_{Moule}$[b]	$\tilde{X}(H_2CO^+)_{Domcke}$[c]
r(C-H)	1.101Å	1.123Å	1.125Å
r(C-O)	1.203Å	1.184Å	1.168Å
H-C-H angle	116°31'	119°30'	118°13'

[a] "Equilibrium" geometry from K. Tagaki and T. Oka, J. Phys. Soc. Japan 18, 1174(1963). This does not agree with column 1 of Table 2 in Moule's paper.[59]

[b] Based on Moule's L matrix for the ionized state, with a sign change.

[c] Based on Domcke and Cederbaum's[12] coupling parameters α_i.

Table 12. Changes of Geometry on Ionization of CF_2S and CCl_2S (from Ref. 62)

structure	CS bond/Å (±.02)	CX bond/Å (±2)	XCX angle/deg (±2)
thiocarbonyl fluoride			
(1) sulphur lone pair, 10.69 eV			
1	+0.09	-0.03	+8
2	+0.10	-0.03	+2.5
3	+0.08	-0.06	+2
4	+0.06	-0.06	+7.5
(2) C = S π orbital, 11.72 eV			
1	+0.12	-0.03	+11
2	+0.13	-0.04	+3.5
3	+0.07	-0.09	+10
4	+0.09	-0.09	+2
(3) σ-bonding orbital 15.06 eV			
1	+0.05	-0.06	+10
2	+0.08	-0.10	+1
3	+0.10	-0.01	+11
4	+0.13	-0.04	+1
(5) fluorine lone pair, 17.85 eV			
1	+0.04	+0.05	+6
thiocarbonyl chloride			
(1) C = S π orbital, 10.86 eV			
1	+0.14	-0.07	

Moule's revised displacements for columns 3 and 4 are now very similar to those deduced from Domcke and Cederbaum's coupling parameters. Both now lean toward column 4 as the preferred alternative, although the results from Moule are more equivocal. Our choice between these alternatives will be influenced by chemical considerations. Özkan et al. [61] have performed near Hartree-Fock calculations on $\tilde{X}(H_2CO)$ and $\tilde{X}(H_2CO^+)$, and have shown that the nominally nonbonding orbital involved in this ionization actually has appreciable electron density at the H atom positions, as well as O atom. Removal of an electron from this orbital should increase the C-H distance and widen the H-C-H angle. The alternative in column 4 matches this requirement. A detailed comparison of the experimental photoelectron spectrum with the calculated one of Domcke and Cederbaum [12] indicates that their coupling parameter a_2 has been overestimated for D_2CO. The corresponding C-H and C-O bond length changes

have therefore probably been overestimated. On the other hand, Moule has chosen to give full weight to ν_1 in a vibrational component of the H_2CO spectrum which has contributions from (0,1,1) and (0,0,2). This, too, has the effect of overestimating the change in C-H distance. With the above caveats, our final structure for $\tilde{X}(H_2CO^+)$ from the two analyses is given in Table 11.

Comparison of these results with the molecular orbital calculations of Lathan et al. [44] shows agreement in two respects: the opening of the H-C-H angle upon ionization, and a small increase in the CH bond length. However, the latter calculations display a significant increase in the C-O bond length. An increase in all 3 coordinates is not compatible with either Moule's or Domcke and Cederbaum's Franck-Condon analysis. The calculations of Özkan et al. [61] yield a rather flat potential along the C-O coordinate, which probably makes the equilibrium C-O position very sensitive to fine details in the ab initio calculation.

b) CF_2S and CCl_2S

Mines et al. [62] have reported the photoelectron spectra of thiocarbonyl fluoride and thiocarbonyl chloride. Using the method of Coon et al. [26], they have calculated displacements for 4 bands in CF_2S and the second band in CCl_2S. In the first 3 bands of CF_2S, 3 totally symmetric modes are excited. The ambiguity in sign leads to $2^3 = 8$ alternatives, which they are only able to reduce to 4. Their results are summarized in Table 12. The geometry of neutral CF_2S has been obtained by Careless, et al. [63]. The dimensions are r(CF) = 1.315 ± 0.010 Å, r(CS) = 1.589 ± 0.010 Å and F-C-F angle 107.1° ± 1.0°.

6. C_{2h} Tetratomic - trans-HNNH (Diazene)

The photoelectron spectra of trans-HNNH and trans-DNND have been reported by Frost et al. [64]. A calculated spectrum, using the Green's function method and derived coupling constants, has been performed by von Niessen et al. [65]. These latter authors present renormalized derivatives of the ionized states with respect to symmetry coordinates, and also tables of their coupling parameters a for both N_2H_2 and N_2D_2. They mention an unsatisfactory state of affairs for the force constants of the neutral species. We have been unable to reproduce an $\underset{\sim}{L}$ matrix which connects their tabulated derivatives $\left(\frac{\partial \varepsilon_i}{\partial S_\ell}\right)$ and their a_k's. If we employ their tabulated $\left(\frac{\partial \varepsilon_i}{\partial S_\ell}\right)$ and the relationship $\Delta\underset{\sim}{S} = \underset{\sim}{F}^{-1}\underset{\sim}{D}$, where $\Delta\underset{\sim}{S}$ is the vector change of symmetry coordinate, $\underset{\sim}{F}^{-1}$ is the inverse force constant matrix for the neutral molecule [66] and $\underset{\sim}{D}$ is the column vector corresponding to $\left(\frac{\partial \varepsilon_i}{\partial S_\ell}\right)$ for the ionic ground state, we compute Δ(NH) = +0.025 Å,

Δ(NN) = -0.083 Å and Δ(H-N-N angle) = +13.8°. When combined with the parameters of the neutral ground state [67] [r(NH) = 1.028 ± 0.005 Å, r(NN) = 1.252 ± 0.002 Å, H-N-N angle = 106°51' ± 28'] we obtain for the ground state of $N_2H_2^+$ the following geometry: r(NH) = 1.053 Å, r(NN) = 1.169 Å, and H-N-N angle = 120°39'. This result compares very favorably with an ab initio calculation for the $N_2H_2^+$ (C_{2h}) ground state performed by Lathan et al. [44] who obtain r(NH) = 1.079 Å, r(NN) = 1.213 Å, and H-N-N angle = 123.1°. In our calculation of displacements, we have taken the negative of the derivatives given in Table 5 of the paper by von Niessen et al. [65], which appears to arise as a result of the change in definition of the sign of the energy. This result is consistent with the observations from the photoelectron spectrum, where the bending frequency ν_2 is seen to diminish from its value in the neutral molecule by at least 400 cm^{-1}, while ν_3 (predominantly N-N stretch) is observed to increase by $\sim$300 cm^{-1}

7. Hexatomics - C_2H_4 (Ethylene)

Carlier and Botter [68] have obtained the photoelectron spectrum of C_2H_4 and 6 deuterated molecules - C_2D_4, C_2D_3H, C_2H_3D, cis-$C_2H_2D_2$, trans-$C_2H_2D_2$, and gem-$C_2H_2D_2$. In the first electronic band they can identify progressions in ν_2 (symmetric C-C stretch), ν_3 (symmetric H-C-H bend) and ν_4 (torsion), the latter a non-totally symmetric mode presumably appearing only in double quanta if the molecular ion remains planar.

To our knowledge, their work is the most elaborate Franck-Condon analysis yet attempted. They have employed the more precise Duschinsky transformation (Eq. (4)) using Eq. (6) to obtain the $\underset{\sim}{J}$ matrix and Eq. (7) to calculate the displacement in coordinate space. They reduce ambiguities by requiring agreement in displacement among the isotopic species. They conclude that the C-C bond has increased from 1.339 Å in neutral ethylene to 1.41 Å in the ion, the H-C-H angle remains essentially unchanged at 117°50' and each of the CH_2 moieties has twisted out of the plane by 8-9°. The change from planar geometry accounts for the strong excitation of the torsional mode ν_4 in the spectrum. In the point group of the ion, ν_4 is a totally symmetric mode.

Köppel et al. [69] have used their Green's function calculation to determine vibronic coupling constants for the 3 totally symmetric modes ν_1, ν_2, and ν_3. In addition, they find that ν_4 can appear because it has the proper symmetry (A_u) to couple the two lowest ionic states; which are separated in energy by $\sim$2 eV. The large number of coupling constants and the inability to separate the totally symmetric and torsional motions here requires them to resort to some approximations in the simulation of a photoelectron spectrum. From their best fit of coupling constants, they calculate a geometry for $C_2H_4^+$ (ground state) very close to that deduced by

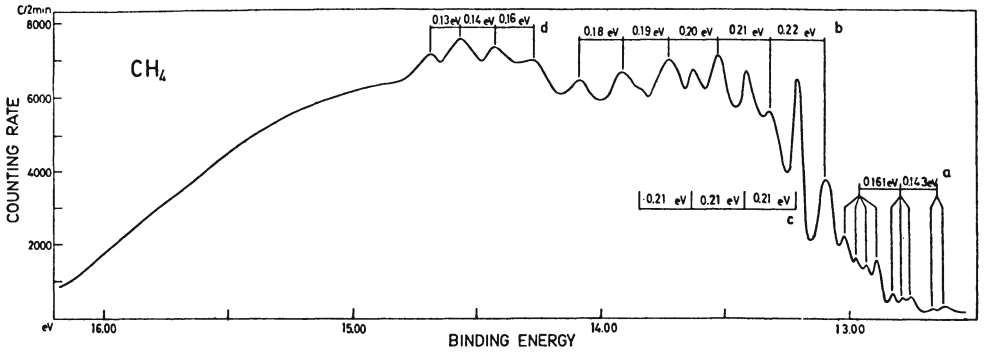

Fig. 11. He I photoelectron spectrum of CH_4 (from Ref. 78).

Carlier, r(CC) = 1.405 A, H-C-H angle unchanged, and the total twist angle between the planes defined by the CH_2 moieties equalling 25°.

It should be remarked that the twisted structure of $C_2H_4^+$ was recognized a long time ago. Mulliken [70] apparently first drew this conclusion from a study of the torsional vibrational progression in a Rydberg progression of ethylene, together with early LCAO-MO calculations on the effects of hyperconjugation in the ground state of $C_2H_4^+$ [71]. A number of subsequent authors [72-75] have provided more detailed descriptions of Rydberg state geometries. The consensus of this later work is that the barrier to planarity is $\leqslant$0.1 eV, whereas the barrier to a perpendicular orientation of the CH_2 planes is more than an order of magnitude larger.

However, Lathan et al. [76, 44] conclude on the basis of their STO-3G basis function calculations that $C_2H_4^+$ is planar. The calculation of such a low barrier presents a severe test for ab initio calculations. A more extended basis set was used by Rodwell et al. [77], with and without configuration interaction, and still arrived at a planar equilibrium geometry for $C_2H_4^+$. However, the bond lengths and H-C-H angles were kept constant in this exploration of the twisting potential curve.

8. CH_4^+ and First Excited NH_3^+ - The Influence of Jahn-Teller Effects Upon the Photoelectron Spectrum

It would be most desirable to deduce the structure of CH_4^+ in its ground state, since it is expected to be a significant interstellar species. The photoelectron spectrum [78] (see Fig. 11) is very broad, and it is difficult to identify more than one vibrational progression. It is known that this state is degenerate, and Jahn-Teller split. Dixon [79] has performed ab initio calculations on CH_4^+, and then computed the distortions induced by vibronic coupling. In this way, he has succeeded in qualitatively rationalizing the

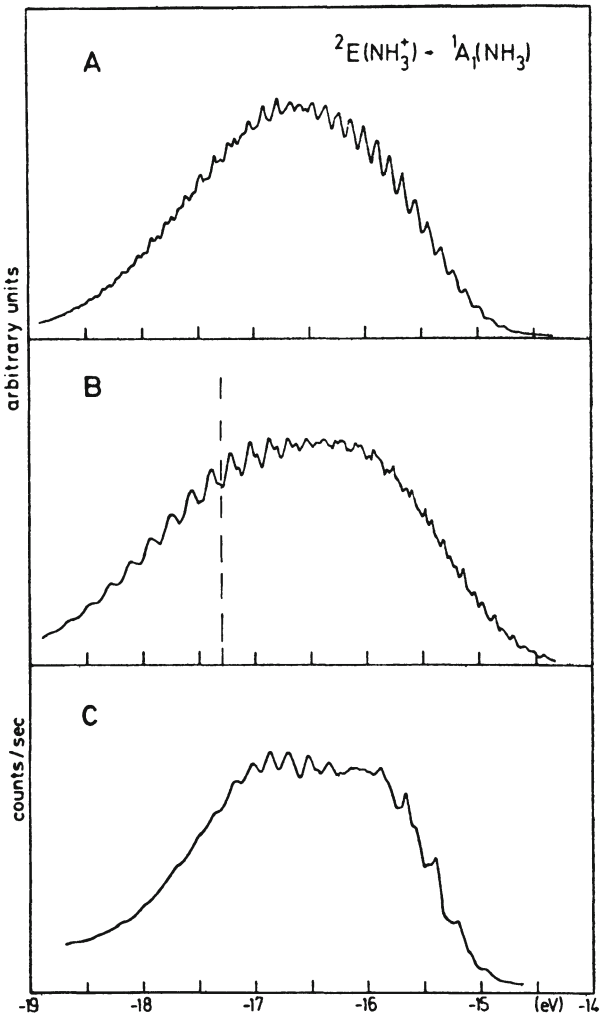

Fig. 12. The E-band of ammonia as determined by many-body theory (parts A, B) and experiment [46] (part C). Parts A and B differ only in the individual vibrational spacings (from Ref. 82).

spectrum. He concludes that distortions occur to C_{3v} and D_{2d} symmetry, the latter being the more stable by about 0.2 eV. However, any attempt to infer geometrical parameters from the photoelectron spectrum by the methods discussed in this review appears to be overly ambitious at this time. We note parenthetically that Arents and Allen [80], Lathan et al. [57, 76], and Meyer [81] have performed ab initio calculations on CH_4^+. These differ in basis sets used, and Meyer's calculation includes configuration interaction. Arents and Allen and Lathan et al. both conclude that D_{2d} is the most

stable structure of CH_4^+ in its ground state, with C_{3v} about 0.15 eV higher in energy. This would seem to fit nicely with Dixon's analysis. However, Meyer's calculation is more extensive, and produces the lowest total energy even in the single configuration Hartree-Fock limit, and therefore must be considered the most accurate calculation to date. He finds C_{2v} to be the most stable structure, more stable than D_{2d} by 0.15 eV. (This distortion was not considered explicitly by Dixon or Arents and Allen. Lathan et al. found C_{2v} to be intermediate in stability between D_{2d} and C_{3v}.) Hence, Meyer's result casts doubt upon Dixon's interpretation of the photoelectron spectrum of methane.

Köppel et al. [82] have attempted a study on an analogous Jahn-Teller split state - the first excited state of NH_3^+ - using their Green's function method and incorporating the Jahn-Teller coupling. A comparison of their calculated spectrum and the experimental one is presented in Fig. 12. The features in the experimental spectrum are not very prominent, but insofar as they exist they are not well reproduced in the calculated spectrum, although the width of the band is approximately correct. Since the qualitative features are not clearly reproduced the computation of a geometric structure for this state from the coupling parameters given by Köppel et al. is not warranted at this time.

IV. Conclusions, and Prognosis for Future Research

A. Franck-Condon analyses of vibrationally resolved photoelectron spectra of diatomic molecules can be used to determine the internuclear distances of the correspondng molecular ions usually to 0.01 Å or better.

High temperature photoelectron spectra of diatomic molecules can be analyzed, even when vibrationally unresolved. In such cases, it is important that the instrumental resolution and temperature be carefully measured.

B. The direct determination of geometry for polyatomic ions by Franck-Condon analysis becomes very difficult in practice if the number of totally symmetric modes appearing as progressions in the photoelectron spectrum is ≥ 4, which implies a selection among $\geq 2^4$ possibilities due to sign ambiguity. This basic fact circumscribes the domain of applicability of the direct approach.

The Cederbaum-Domcke procedure can conceivably be used for larger systems, since one obtains the sign, as well as magnitude of the coupling constants which are proportional to displacements in symmetry coordinates. To our knowledge, there is currently only one group using the many-body form of this method. However, Barrow et al. [83] have recently shown that a relatively simple X_α calculation

can be used to determine these coupling constants, which may permit extension of this scheme to larger groups.

C. We are unaware of any general solution to the problem of determining an accurate change of geometry in a linear $\leftrightarrow$ bent transition (where a vibrational degree of freedom is lost or acquired), although there have been two recent studies of this question in specific cases (HCN, Ref. 34c and H_2O, Ref. 38).

APPENDIX 1

Summary of Approximation Schemes and References for Calculation of Franck-Condon Factors

A. Diatomic Molecules

1. If harmonic oscillators and their corresponding functions (Hermite polynomials with Gaussian function) are used for upper and lower states, with no change in vibrational frequency, then the intensity distribution is a Poisson distribution. A modified Poisson distribution results if the lower state is itself a Boltzmann distribution. A particularly simple form for the ratio of intensities of successive members is given in the paper of Coon et al. [26].

2. If the final state is permitted to have a different frequency, solution of the Franck-Condon integral leads to a recursion formula explicitly given by Cederbaum and Domcke [13].

3. If Morse potentials are used for upper and lower states, characterized by individual r_e, ω_e, and $\omega_e x_e$, rigorous use requires a numerical integration.

In approximate use, a Morse potential is a means of introducing anharmonicity, which influences the interpretation of a and κ values, in the Cederbaum and Domcke notation [4].

B. Polyatomic Molecules

1. Calculations usually are not performed beyond the harmonic oscillator approximation.

2. In general, one tries to factor the Franck-Condon integral as a product of one-dimensional integrals. More elaborate treatments have been presented [28, 84].

3. If only one totally symmetric normal coordinate is excited, the Franck-Condon calculation reduces to that of a one-dimensional

oscillator. However, for a polyatomic molecule the normal coordinate excited corresponds to a linear combination of symmetry coordinates, whereas for a diatomic molecule it is a unique displacement coordinate.

4. In general, the excitation of a single normal coordinate in the spectrum corresponds not just to a displacement in the normal coordinate, but to a rotation as well, if one wants to describe the final normal coordinate position in terms of the ground state normal coordinate. If we assume the same symmetry coordinates are appropriate for ionic and neutral states, then

$$\underset{\sim}{S} = \underset{\sim}{L}^{n}\,\underset{\sim}{Q}^{n}$$

$$\underset{\sim}{S} = \underset{\sim}{L}^{i}\,\underset{\sim}{Q}^{i} \text{ and } \underset{\sim}{Q}^{i} = (\underset{\sim}{L}^{i})^{-1}\underset{\sim}{L}^{n}\underset{\sim}{Q}^{n}$$

This is the relationship between final normal coordinates and initial normal coordinates, and is the basis for the Duschinsky transformation [27]. If in addition we allow for a displacement ($\underset{\sim}{d}^{in}$) in one normal coordinate, we arrive at

$$\underset{\sim}{Q}^{i} = \underset{\sim}{d}^{in} + (\underset{\sim}{L}^{i})^{-1}\underset{\sim}{L}^{n}\underset{\sim}{Q}^{n}$$

Coon et al. [26] determine the displacement $\underset{\sim}{d}^{in}$ separately for each normal coordinate which appears as a progression in the ionic state. This displacement in normal coordinate is related to a displacement in symmetry coordinates ($\underset{\sim}{D}^{in}$) by the expression

$$\underset{\sim}{D}^{in} = \underset{\sim}{L}^{i}\,\underset{\sim}{d}^{in},$$

The method of calculating the $\underset{\sim}{L}$ matrix is briefly described in Appendix 2.

5. To calculate $\underset{\sim}{L}^{i}$, one must know or assume $\underset{\sim}{G}^{i}$ and $\underset{\sim}{F}^{i}$. The corresponding $\underset{\sim}{G}^{n}$ and $\underset{\sim}{F}^{n}$ are usually known. $\underset{\sim}{F}^{i}$ is usually assumed to be diagonal, with some elements corresponding to observed frequency intervals in a progression in the ionic state, and others (not observed) chosen identical or similar to ground state elements. $\underset{\sim}{G}^{i}$ can be taken to be identical to $\underset{\sim}{G}^{n}$ for an initial calculation, which results in $\underset{\sim}{L}^{i}$ and hence, a new geometry. The new geometry defines a revised $\underset{\sim}{G}^{i}$.

6. Doktorov et al. [84] show that the product of one-dimensional oscillators is appropriate when the mixing between normal coordinates in going from neutral to ionic state is small. In addition, however, they describe a method of deriving from experimental intensities the mixing parameters, and thereby the Duschinsky transformation. Knowledge of $\underset{\sim}{G}^{i}$ and $\underset{\sim}{F}^{i}$ is not required in their method, but only $\underset{\sim}{G}^{n}$ and $\underset{\sim}{F}^{n}$. This, together with relative intensities in the vibrational progressions and measured ionic state frequencies suffices to determine the ionic geometry.

7. Sharp and Rosenstock [28] assume at the outset the $\underset{\sim}{G}^i$, $\underset{\sim}{F}^i$, and hence $\underset{\sim}{L}^i$, as well as the $\underset{\sim}{d}^{in}$ in the Duschinsky transformation. They then calculate a set of vibrational intensities and compare with experiment. A revised set of assumptions is then employed, and the process continued until the best agreement with experiment is found.

8. Faulkner and Richardson [85] transform both the initial normal coordinates (Q^n) and the final normal coordinates (Q^i) into an intermediate set of coordinates which enables them to factor the multidimensional Franck-Condon integral into a product of one-dimensional harmonic oscillator integrals. In this new coordinate system the normal coordinates are scaled and the origins are shifted. Application of their method requires prior knowledge or assumptions about geometry and force fields of initial and final state, similar to Sharp and Rosenstock's method, and therefore requires iteration. The calculation of the Franck-Condon integrals is asserted to be simpler and more rapid than the methods of Sharp and Rosenstock (multidimensional generator function method) or of Doktorov et al. (dynamical group representations of the molecular vibrational Hamiltonian).

The initial formulation of Faulkner and Richardson required that one of the vibrational wave functions in the Franck-Condon integral have zero quanta in all of the vibrational coordinates. This restriction has been removed in a subsequent extension of this method by Kulander [86].

9. Cederbaum and Domcke [4] require an ab initio calculation to determine linear coupling constants which are proportional to changes in symmetry coordinates. This method, while requiring an ab initio calculation, does not explicitly require calculation of Franck-Condon factors, except for generating a mocked-up spectrum to compare with experiment. In such cases, these Franck-Condon factors can be approximated by a Poisson distribution of one-dimensional oscillators.

APPENDIX 2

How to Calculate an $\underset{\sim}{L}$ Matrix

The $\underset{\sim}{G}$ (inverse mass) and $\underset{\sim}{F}$ (force constant) matrices are calculated by standard methods [87]. Their product, when diagonalized, gives the eigenvalues related to the normal vibrational frequencies, i.e.,

$$|\underset{\sim}{GF} - \lambda_n \underset{\sim}{E}| = 0, \text{ where } \lambda_n = 4\pi^2 \nu_n^2$$

For each eigenvalue λ_n there corresponds a vector v_n which can be determined from the secular equation. The set of column vectors v_n for all λ_n can be described by a matrix $\underset{\sim}{V}$, which, apart from normalization, is equal to the desired matrix $\underset{\sim}{L}$, i.e.,

$$\underset{\sim}{L} = \underset{\sim}{V}\underset{\sim}{N},$$

where $\underset{\sim}{N}$ is a diagonal matrix. The normalization for $\underset{\sim}{L}$ is chosen so that

$$\underset{\sim}{L}\underset{\sim}{L}^{+} = \underset{\sim}{G}.$$

Thus,

$$(\underset{\sim}{V}\underset{\sim}{N})\ (\underset{\sim}{V}\underset{\sim}{N})^{+} = \underset{\sim}{G}$$

$$\underset{\sim}{N}\underset{\sim}{N}^{+} = \underset{\sim}{V}^{-1}\underset{\sim}{G}(\underset{\sim}{V}^{+})^{-1}$$

or, since $\underset{\sim}{N}$ is a diagonal matrix,

$$\underset{\sim}{N} = [\underset{\sim}{V}^{-1}\underset{\sim}{G}(\underset{\sim}{V}^{+})^{-1}]^{1/2}.$$

References

1. D. W. Turner, C. Baker, A. D. Baker, and C. R. Brundle, "Molecular Photoelectron Spectroscopy," Wiley-Interscience, London (1970).
2. K. Siegbahn, D. A. Allison, and J. H. Allison, in: "Handbook of Spectroscopy," J. E. Robinson, ed., Vol. 1, pp. 258-749. CRC Press, Cleveland, Ohio (1974).
3a. J. Berkowitz, J. Chem. Phys., 69, 3044 (1978).
3b. Y. Osamura, J. D. Goddard, H. F. Schaefer III, and K. S. Kim, J. Chem. Phys., 74, 617 (1981).
4. L. S. Cederbaum and W. Domcke, in: Adv. Chem. Phys. Vol. XXXVI, pp. 205-344 (esp. p. 286). I. Prigogine and S. A. Rice, eds., J. Wiley and Sons, New York (1977).
5. J. Berkowitz, Chem. Phys. Lett., 11, 21 (1971).
6. N. Jonathan, A. Morris, M. Okuda, K. J. Ross, and D. J. Smith, J. C. S. Faraday Disc. Chem. Soc., 54, 48 (1972).
7. J. M. Dyke, L. Golob, N. Jonathan, A. Morris, M. Okuda, and D. J. Smith, J. C. S. Faraday II, 70, 1818 (1974).
8. D. K. Bulgin, J. M. Dyke, and A. Morris, J. C. S. Faraday II, 73, 983 (1977).
9. J. M. Dyke, A. Morris, and I. R. Trickle, J. C. S. Faraday II, 73, 147 (1977).
10. J. Berkowitz and R. Spohr, J. Electr. Spectr., 2, 143 (1973).
11. Y. Itikawa, J. Electr. Spectr., 2, 125 (1973).
12. W. Domcke and L. S. Cederbaum, J. Chem. Phys., 64, 612 (1976).
13. L. S. Cederbaum and W. Domcke, J. Chem. Phys., 64, 603 (1976).
14. A. B. Cornford, D. C. Frost, C. A. McDowell, J. L. Ragle, and I. A. Stenhouse, J. Chem. Phys., 54, 2651 (1971).
15. F. P. Huberman, J. Mol. Spectry., 20, 29 (1966).
16. K. P. Huber and G. Herzberg, "Molecular Spectra and Molecular Structure IV. Constants of Diatomic Molecules," Van Nostrand Reinhold Co., New York (1979).

17. B. R. Higginson, D. R. Lloyd, and P. J. Roberts, Chem. Phys. Lett., 19, 480 (1973).
18. P. Venkateswarlu, Can. J. Phys., 48, 1055 (1970).
19. V. H. Dibeler, J. A. Walker, K. E. McCulloh, and H. M. Rosenstock, Int. J. Mass Spectry. Ion Phys., 7, 209 (1971).
20. J. M. Dyke, L. Golob, N. Jonathan, and A. Morris, J. C. S. Faraday II, 71, 1026 (1975).
21. S. Leach, Acta Physica Polonica, 34, 705 (1968).
22. S.-T. Lee, S. Süzer, and D. A. Shirley, Chem. Phys. Lett., 41, 25 (1976).
23. C. G. Mahajan, G. Lakshminarayana, and N. A. Narasimham, Indian J. Pure Appl. Phys., 14, 488 (1976).
23a. M. Tsuji, I. Murakami, and Y. Nishimura, Chem. Phys. Lett., 75, 536 (1980).
23b. N. Jonathan, private communication.
24. J. Berkowitz, J. Chem. Phys., 62, 4074 (1975).
25. J. Berkowitz, C. H. Batson, and G. L. Goodman, J. Chem. Phys., 72, 5829 (1980).
26. J. B. Coon, R. E. de Wames, and C. M. Loyd, J. Mol. Spec., 8, 285 (1962).
27. F. Duschinsky, Acta Physicochim. URSS, 7, 551 (1937).
28. T. E. Sharp and H. M. Rosenstock, J. Chem. Phys., 41, 3453 (1964).
29. D. C. Frost, S. T. Lee, and C. A. McDowell, J. Chem. Phys., 59, 5484 (1973).
30. T. Wentink, J. Chem. Phys., 30, 109 (1959).
31. H. M. Rosenstock, Int. J. Mass Spectry. Ion Phys., 7, 33 (1971).
32. J. M. Hollas and T. A. Sutherley, Chem. Phys. Lett., 21, 167 (1973).
33. J. M. Hollas and T. A. Sutherley, Mol. Phys., 22, 213 (1971).
34a. J. M. Hollas and T. A. Sutherley, Mol. Phys., 24, 1123 (1972).
34b. C. Fridh and L. Åsbrink, J. Electr. Spectr., 7, 119 (1975).
34c. H. Köppel, L. S. Cederbaum, W. Domcke, and W. von Niessen, Chem. Phys., 37, 303 (1979).
35. C. R. Brundle and D. W. Turner, Proc. Roy. Soc., A307, 27 (1968).
36. A. W. Potts and W. C. Price, Proc. Roy. Soc., A326, 181 (1972).
37. R. N. Dixon, G. Duxbury, J. W. Rabalais, and L. Åsbrink, Mol. Phys., 31, 423 (1976).
38. Ch. Jungen, K.-E. J. Hallin, and A. J. Merer, Mol. Phys., 40, 25 (1980).
39. H. Lew and I. Heiber, J. Chem. Phys., 58, 1246 (1973).
40. R. Botter, V. H. Dibeler, J. A. Walker, and H. M. Rosenstock, J. Chem. Phys., 44, 1271 (1966).
41. J. M. Hollas and T. A. Sutherley, Mol. Phys., 21, 183 (1971).
42. E. Heilbronner, K. A. Muszkat, and J. Schäublin, Helvetica Chimica Acta, 54, 58 (1971).
43. C. Baker and D. W. Turner, Proc. Roy. Soc., A308, 19 (1968).
44. W. A. Lathan, L. A. Curtiss, W. J. Hehre, J. B. Lisle, and J. A. Pople, Progress in Phys. Org. Chem., Vol. 11, A. Streitweiser,

Jr., and R. W. Taft, eds., J. Wiley and Sons, New York (1974), p. 175.
45. L. S. Cederbaum, W. Domcke, and W. von Niessen, Chem. Phys., 10, 459 (1975).
46. J. W. Rabalais, L. Karlsson, L. O. Werme, T. Bergmark, and K. Siegbahn, J. Chem. Phys., 58, 3370 (1973).
47. J. L. Duncan and I. M. Mills, Spectrochim. Acta, 20, 523 (1964).
48. R. Botter and H. M. Rosenstock, "Adv. Mass Spectry," Vol. 4, 579 (1968).
49. H. M. Rosenstock and R. Botter, "Recent Dev. in Mass Spectry," K. Ogata and T. Hayakawa, eds., U. of Tokyo Press (1970), p. 797.
50. A. D. Walsh and P. A. Warsop, Trans. Far. Soc., 57, 345 (1961).
51. A. E. Douglas, Disc. Far. Soc., 35, 158 (1963).
52. Y. Morino, K. Kuchitsa, and S. Yamamoto, Spectrochim. Acta, 24A, 335 (1968).
53. A. E. Douglas and J. M. Hollas, Can. J. Phys., 39, 479 (1961).
54. W. R. Harshbarger, J. Chem. Phys., 53, 903 (1970).
55. S. Durmaz, J. N. Murrell, J. M. Taylor, and R. Suffolk, Mol. Phys., 19, 533 (1970).
56. W. Domcke, L. S. Cederbaum, H. Köppel, and W. von Niessen, Mol. Phys., 34, 1759 (1977).
57. W. A. Lathan, W. J. Hehre, L. A. Curtiss, and J. A. Pople, J. Am. Chem. Soc., 93, 6377 (1971).
58. R. C. Hariharan and J. A. Pople, Mol. Phys., 27, 209 (1974).
59. D. C. Moule, in: "Vibrational Spectra and Structure," Vol. 6, J. R. Durig, ed., Elsevier Sci. Publ. Co., Amsterdam (1977), p. 228.
60. T. Shimanouchi and I. Suzuki, J. Chem. Phys., 42, 296 (1965).
61. I. Özkan, S. Y. Chu, and L. Goodman, J. Chem. Phys., 63, 2195 (1975).
62. G. W. Mines, R. K. Thomas, and H. Thompson, Proc. Roy. Soc., A333, 171 (1973).
63. A. J. Careless, H. W. Kroto, and B. M. Landsberg, Chem. Phys., 1, 371 (1973).
64. D. C. Frost, S. T. Lee, C. A. McDowell, and N. P. C. Westwood, J. Chem. Phys., 64, 4719 (1976).
65. W. von Niessen, W. Domcke, L. S. Cederbaum, and W. P. Kraemer, J. Chem. Phys., 67, 44 (1977).
66. J. W. Nibler and V. E. Bondybey, J. Chem. Phys., 60, 1307 (1974).
67. M. Carlotti, J. W. C. Johns, and A. Trombetti, Can. J. Phys., 52, 340 (1974).
68. J. Carlier and R. Botter, J. Electr. Spectr., 17, 91 (1979); see also Ph.D. Thesis of J. Carlier, Univ. Pierre and Marie Curie, Paris (1979).
69. H. Köppel, W. Domcke, L. S. Cederbaum, and W. von Niessen, J. Chem. Phys., 69, 4252 (1978).
70. R. S. Mulliken, Tetrahedron, 5, 523 (1959).

71. R. S. Mulliken and C. C. J. Roothaan, Chem. Revs., 41, 219 (1947).
72. A. J. Lorquet and J. C. Lorquet, J. Chem. Phys., 49, 4955 (1968).
73. A. J. Merer and L. Schoonveld, Can. J. Phys., 47, 1731 (1969).
74. S. D. Peyerimhoff and R. J. Buenker, Theoret. Chim. Acta, 27, 243 (1972).
75. P. D. Foo and K. K. Innes, J. Chem. Phys., 60, 4582 (1974).
76. W. A. Lathan, W. J. Hehre, and J. A. Pople, J. Am. Chem. Soc., 93, 808 (1971).
77. W. R. Rodwell, M. F. Guest, D. T. Clark, and D. Shuttleworth, Chem. Phys. Letter., 45, 50 (1977).
78. J. W. Rabalais, T. Bergmark, L. O. Werme, L. Karlsson, and K. Siegbahn, Phys. Scripta, 3, 13 (1971).
79. R. N. Dixon, Mol. Phys., 20, 113 (1971).
80. J. Arents and L. C. Allen, J. Chem. Phys., 53, 73 (1970).
81. W. Meyer, J. Chem. Phys., 58, 1017 (1973).
82. H. Köppel, L. S. Cederbaum, W. Domcke, and W. von Niessen, Mol. Phys., 35, 1283 (1978).
83. W. L. Barrow, H. Sambe, and R. H. Felton, Chem. Phys. Lett., 68, 170 (1979).
84. E. V. Doktorov, I. A. Malkin, and V. I. Man'ko, J. Mol. Spect., 56, 1 (1975); 64, 302 (1977).
85. T. R. Faulkner and F. S. Richardson, J. Chem. Phys., 70, 1201 (1979).
86. K. C. Kulander, J. Chem. Phys., 71, 2736 (1979).
87. E. B. Wilson, J. C. Decius, P. C. Cross, "Molecular Vibrations," McGraw-Hill, New York, (1955).

GAS-PHASE STRUCTURE STUDIES ON OPEN-SHELL ORGANIC CATIONS BY MEANS OF THEIR RADIATIVE DECAY

John P. Maier, Oskar Marthaler,
Liubomir Misev, and Fritz Thommen

Physikalisch-Chemisches Institut
der Universität Basel
Klingelbergstrasse 80
CH-4056 Basel/Switzerland

1. Introduction

One of the traditional ways of obtaining data on the electronic and geometric structure of gaseous species is by emission spectroscopy [1]. Historically, the study of the rotational details of the band systems in the emission spectra of many diatomic, and some triatomic, cations provided fundamental knowledge of their structures [2]. These aspects are discussed and illustrated by Herzberg in a review article on the Spectra and Structure of Molecular Ions [3] as well as in further publications [4, 5].

The focus of attention of this review-type contribution are the studies of the structure of open-shell polyatomic organic cations, relying on their radiative channel of relaxation, which have been, and are being, carried out in Basel [6]. The three different techniques employed for these investigations will be outlined by reference to the experimental arrangements and to selected examples, illustrating the structural details obtainable for such cations.

The foundation of these studies is the detection of the emission spectra of polyatomic cations. This was consequently the first objective of our studies as at the onset the emission spectra of only six triatomic cations (and of their isotopes), CO_2^+, CS_2^+, COS^+, N_2O^+, H_2S^+, H_2O^+, as well as that of diacetylene cation were known [3, 5]. It should be emphasized that these high resolution spectra yielded the first detailed information on the electronic and geometric structure of polyatomic cations. The development of

the photoelectron spectroscopic technique provided a general means to obtain the energetic data of the accessible doublet states ($^2\tilde{X}$, $^2\tilde{A}$, $^2\tilde{B}$ ...) of open-shell cations [7]. This information we used extensively in the search for the radiative decay of organic cations, and as a result the emission spectra of around hundred such species have been obtained [6]. The structural information forthcoming from these spectra have been the vibrational frequencies, mainly of the totally symmetric modes, for the cations in their ground states ($^2\tilde{X}$) as well as the possibility to infer the symmetries of the emitting states ($^2\tilde{B}$, $^2\tilde{A}$) in conjunction with the photoelectron spectroscopic studies. Rotational details have, more recently, also become accessible.

The emission spectral studies were prerequisite for the application of the two further techniques to gain a detailed insight into the structure, and decay behavior of organic cations. In order to obtain vibrational data for the excited electronic state ($^2\tilde{A}$, $^2\tilde{B}$) of the cations, laser induced fluorescence technique is used. In addition this provides another way to attain high resolution electronic spectra. The technique was first introduced to molecular cations in the gaseous phase to N_2^+ [8], and subsequently applied to CO_2^+ [9] as well as to a few of the organic cations, of fluorinated [10] and chlorinated [11] benzenes and of 2,4-hexadiyne [12], which we found earlier to decay radiatively.

The third approach to investigate the structure of cations relies on the detection of coincidences between energy selected photoelectrons and undispersed emitted photons. This technique was first demonstrated in connection with cascade-free lifetime measurements of di- and triatomic cations in selected vibrational levels [13]. We have applied this method, in addition, to the determination of fluorescence quantum yields of organic cations, in the case of the smaller species in specific vibrational levels, and in the larger for chosen internal energies. The results of such measurements often complement the emission and laser excitation spectral data and can be of help in their interpretation.

These three approaches will now be described individually. The examples chosen are meant to exemplify how these techniques are used in a complementary way to obtain spectroscopic information on the structure of open-shell cations.

2. Emission Spectroscopy

2.1. Apparative

The apparatus constructed for the measurements of emission spectra of organic cations is schematically represented in Fig. 1 [14,15]. It was designed with several considerations in mind. A controlled means of producing the cations was felt desirable in

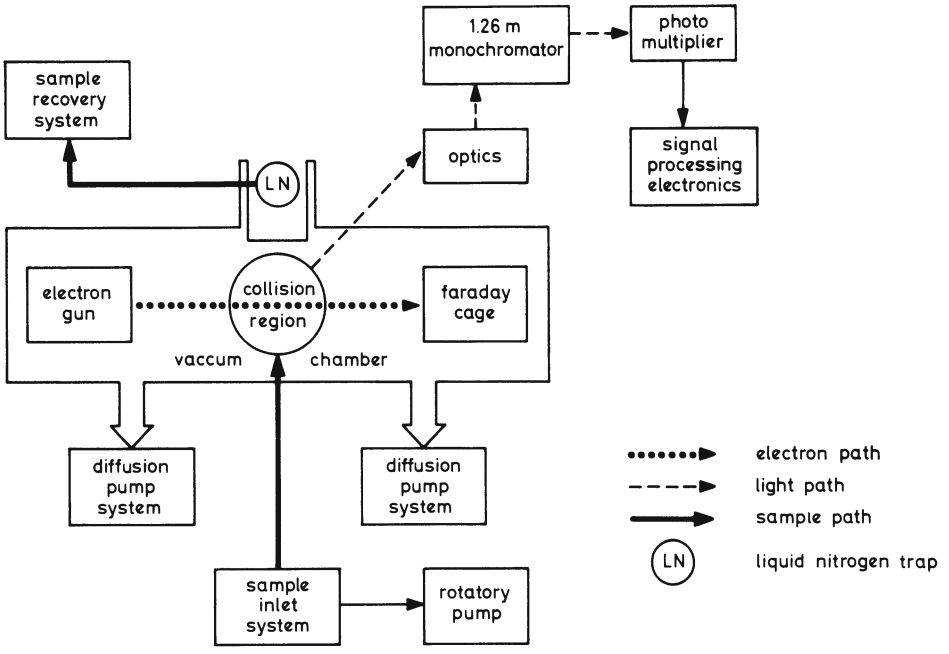

Fig. 1. Schematic representation of the apparatus used for emission spectroscopy.

"clean" surroundings. In spite of the non-specificity of the electron impact excitation, it was chosen for intensity reasons as well as the relative ease of energy variation and gating of the beam as compared to photon sources. The electron energy (E_i) is usually kept around 20-40 eV to attenuate fragment emissions. Thus all the accessible states of the cation are produced:

$$M \xrightarrow{e(E_i)} M^{\oplus}(\tilde{X}); M^{\oplus}(\tilde{A}) \cdots M^{\oplus}(\tilde{J};\ \text{I.E.} \leqslant E_i)$$

$$M^{\oplus}(\tilde{J}) \rightsquigarrow h\nu + M^{\oplus}(\tilde{X})$$

and any resultant emission is wavelength dispersed.

The sample is introduced as an effusive beam into the collision region, where it is excited by the perpendicular running electron beam, and is removed efficiently by the liquid nitrogen trap. The position of the sample beam is externally adjusted by a X-Y-Z translator for optimal signal intensity and the relatively small collision region is optically matched to a monochromator. The 1.26 m monochromator indicated in Fig. 1 has now replaced the 0.5 m one

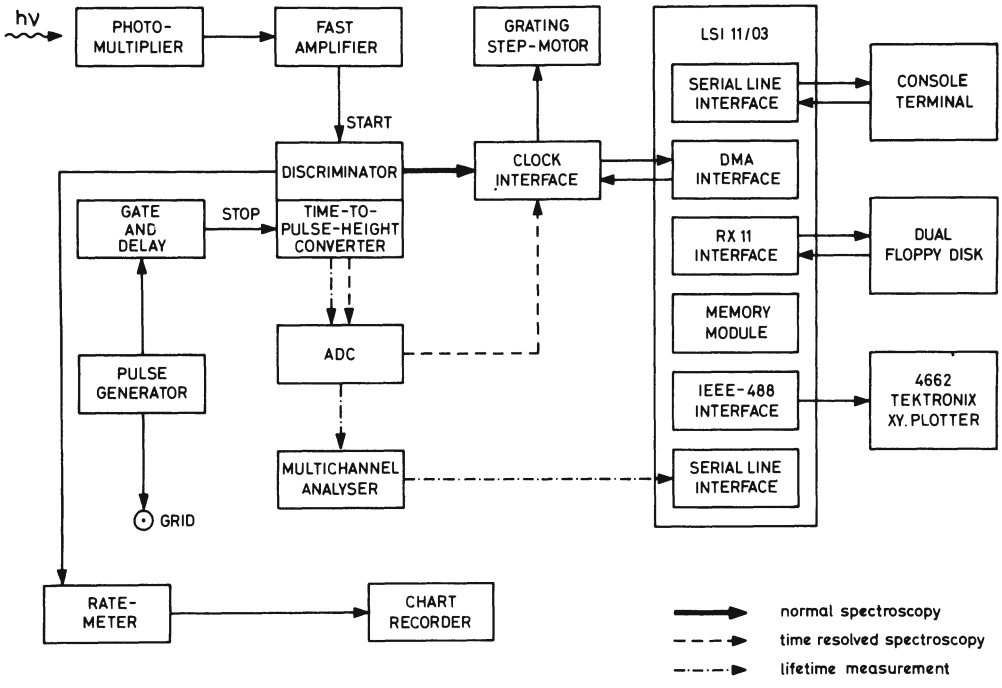

Fig. 2. Block diagram of the signal and on-line data processing arrangement for emission spectroscopy.

used in all the earlier measurements. A cooled, red-sensitive, high quantum efficiency GaAs photomultiplier detects the photons. Typical excitation conditions are 1-5 mA electron current at 20-40 eV impact energies. In the lifetime or time-resolved measurements, the electron beam is gated at around 500 kHz with a fall-time of ≈6 ns. Since a lot of the samples used are rather reactive, they are usually introduced into the apparatus from glass-vessels held at the lowest temperatures necessary to produce sufficient vapor pressure. At the end of the measurements the sample deposited on the cooled-trap is recovered.

Figure 2 shows the block-diagram of the signal processing, single-photon counting and on-line data acquisition arrangement. The different routes for the three types of measurements — normal, time-resolved and lifetime — are indicated. The diagram is self-explanatory and the data are thus digitally recorded by means of the LSI 11/03 microcomputer.

Table 1. Polyatomic Cations for Which Emission Spectra have Been Detected and Their Measured Lifetimes (τ) in the Excited Electronic State (zeroth vibrational level). The Assumed Symmetry is Given

Cation	Transition	τ(ns)	Ref.
$Cl-C\equiv N^+$	$C_{\infty v}$ $\tilde{B}^2\Pi \rightarrow \tilde{X}^2\Pi$	205±20	[16]
		⩾4400	
$Br-C\equiv N^+$		270±30	[16]
		⩾3000	
$I-C\equiv N^+$	$\tilde{A}^2\Sigma^+ \rightarrow \tilde{X}^2\Pi$	300±30	[16]
		⩾1200	
$Cl-C\equiv C-H^+$	$C_{\infty v}$ $\tilde{A}^2\Pi \rightarrow \tilde{X}^2\Pi$	17 ± 3^S	[17]
$Br-C\equiv C-H^+$		12 ± 3^S	[17]
$I-C\equiv C-H^+$		15 ± 3^S	[17]
$Cl-C\equiv C-Cl^+$	$D_{\infty h}$ $\tilde{A}^2\Pi_g \rightarrow \tilde{X}^2\Pi_u$	13 ± 2^S	[18]
$Br-C\equiv C-Br^+$		28 ± 3^S	[18]
$I-C\equiv C-I^+$		51 ± 5^S	[18]
$H\{C\equiv C\}_2H^+$		71±3	[19]
$D\{C\equiv C\}_2D^+$		78±4	[19]
$Cl\{C\equiv C\}_2H^+$	$C_{\infty v}$ $\tilde{A}^2\Pi \rightarrow \tilde{X}^2\Pi$	41±2	[20]
$Br\{C\equiv C\}_2H^+$		27±3	[20]
$F\{C\equiv C\}_2F^+$	$D_{\infty h}$ $\tilde{A}^2\Pi_u \rightarrow \tilde{X}^2\Pi_g$	28±3	[21]
$Cl\{C\equiv C\}_2Cl^+$		21 ± 3^S	[22]
$Br\{C\equiv C\}_2Br^+$		12±2	[22]
$I\{C\equiv C\}_2I^+$		⩽6	[22]
$N\equiv C-C\equiv C-C\equiv N^+$	$D_{\infty h}$ $\tilde{A}^2\Sigma_g^+ \rightarrow \tilde{X}^2\Pi_u$	13±2	[23]

Table 1 (continued)

Cation		Transition	τ(ns)	Ref.
$CH_3-C\equiv C-C\equiv N^+$	C_{3v}	$\tilde{A}^2A_1 \rightarrow \tilde{X}^2E$	215±22	[24]
c-1,2-difluoroethylene$^+$	C_{2v}	$\tilde{A}^2A_1 \rightarrow \tilde{X}^2B_1$	320±30	[25]
$H\{C\equiv C\}_2-CN^+$	$C_{\infty v}$	$\tilde{A}^2\Pi \rightarrow \tilde{X}^2\Pi$	15±2	[26]
$CH_3-C\equiv C-Cl^+$	C_{3v}	$\tilde{A}^2E \rightarrow \tilde{X}^2E$	19±3[s]	[20]
$CH_3-C\equiv C-Br^+$			13±3[s]	[20]
$H\{C\equiv C\}_3H^+$	$D_{\infty h}$	$\tilde{A}^2\Pi_g \rightarrow \tilde{X}^2\Pi_u$	17±2	[19]
$N\equiv C\{C\equiv C\}_2C\equiv N^+$	$D_{\infty h}$	$\tilde{A}^2\Pi_u \rightarrow \tilde{X}^2\Pi_g$	⩽6	[27]
$CH_3\{C\equiv C\}_2H^+$	C_{3v}	$\tilde{A}^2E \rightarrow \tilde{X}^2E$	48±3	[28]
$CH_3\{C\equiv C\}_2D^+$			46±3	[28]
$CD_3\{C\equiv C\}_2H^+$			51±3	[28]
$CD_3\{C\equiv C\}_2D^+$			53±3	[28]
$CH_3\{C\equiv C\}_2Cl^+$			22±2	[20]
$CH_3\{C\equiv C\}_2Br^+$			10±2	[20]
$CF_3\{C\equiv C\}_2F^+$			30±3	[21]
$H\{C\equiv C\}_4H^+$	$D_{\infty h}$	$\tilde{A}^2\Pi_u \rightarrow \tilde{X}^2\Pi_g$	⩽6	[19]
$CH_3\{C\equiv C\}_2C\equiv N^+$	C_{3v}	$\tilde{A}^2E \rightarrow \tilde{X}^2E$	8±2	[26]
$CH_3\{C\equiv C\}_2CH_3^+$	D_{3d}	$\tilde{A}^2E_u \rightarrow \tilde{X}^2E_g$	24±2	[29]
$CH_3\{C\equiv C\}_2CD_3^+$			28±3	[28]
$CD_3\{C\equiv C\}_2CD_3^+$			32±3	[28]
$CF_3\{C\equiv C\}_2CF_3^+$			46±2	[21]

$C_2H_5\{C\equiv C\}_2H^+$	C_s	$\tilde{A}^2A'' \rightarrow \tilde{X}^2A''$	⩽6	[29]
B-trifluoroborazine$^+$	D_{3h}	$\tilde{A}^2A_2'' \rightarrow \tilde{X}^2E''$	⩽6	[30]
1,3-difluorobenzene$^+$			⩽6	[31]
1,2,3-trifluorobenzene$^+$			48±4	[24]
1,3,5-trifluorobenzene$^+$			58±2	[31]
1,2,4-trifluorobenzene$^+$			10±2	[31]
1,2,3,4-tetrafluorobenzene$^+$		$\tilde{B}(\pi^{-1}) \rightarrow \tilde{A}(\pi^{-1}), \tilde{X}(\pi^{-1})$	50±2	[31]
1,2,3,5-tetrafluorobenzene$^+$			50±2	[31]
1,2,4,5-tetrafluorobenzene$^+$			30±2	[31]
Pentafluorobenzene$^+$			47±2	[31]
Hexafluorobenzene$^+$			48±2	[31]
1,3-dichlorobenzene$^+$			⩽6	[32]
1,4-dichlorobenzene$^+$		$\tilde{B}(\pi^{-1}) \rightarrow \tilde{A}(\pi^{-1}), \tilde{X}(\pi^{-1})$	⩽6	[32]
1,3,5-trichlorobenzene$^+$			22±2	[32]
1-chloro-3,5-difluorobenzene$^+$			⩽6	[33]
1-chloro-2,3,6-trifluorobenzene$^+$			21±3	[33]
1-chloro-2,4,5-trifluorobenzene$^+$			⩽6	[33]
1-chloro-2,3,4,5-tetrafluorobenzene$^+$			27±2	[33]
1-chloro-2,3,5,6-tetrafluorobenzene$^+$			52±2	[33]
1-chloro-pentafluorobenzene$^+$			43±3	[33]
1,3-dichloro-2-fluorobenzene$^+$			14±3	[33]
1,3-dichloro-4-fluorobenzene$^+$		$\tilde{B}(\pi^{-1}) \rightarrow \tilde{A}(\pi^{-1}), \tilde{X}(\pi^{-1})$	8±2	[33]
1,3-dichloro-5-fluorobenzene$^+$			8±2	[33]

Table 1 (continued)

Cation	Transition	τ(ns)	Ref.
1,3-dichloro-2,4-difluorobenzene$^+$	$\tilde{B}(\pi^{-1}) \rightarrow \tilde{A}(\pi^{-1}), \tilde{X}(\pi^{-1})$	29±3	[33]
1,3-dichloro-2,5-difluorobenzene$^+$		38±2	[33]
1,3-dichloro-2,4,6-trifluorobenzene$^+$		38±3	[33]
1,4-dichloro-2-fluorobenzene$^+$		⩽6	[33]
1,4-dichloro-2,5-difluorobenzene$^+$		⩽6	[33]
1,3,5-trichloro-2-fluorobenzene$^+$		22±2	[33]
1,3,5-trichloro-2,4,6-trifluorobenzene$^+$		34±2	[33]
1,2,4,5-tetrachloro-3-fluorobenzene$^+$		-	[33]
1,3-dibromotetrafluorobenzene$^+$		⩽6	[34]
1,4-dibromotetrafluorobenzene$^+$		⩽6	[34]
1,3,5-tribromotrifluorobenzene$^+$		⩽6	[34]
2,5-difluorophenol$^+$	C_s $\tilde{B}(\pi^{-1}) \rightarrow \tilde{X}(\pi^{-1})$	13±3	[35]
3,5-difluorophenol$^+$		36±4	[35]
2,3,4-trifluorophenol$^+$		26±3	[35]
2,4,5-trifluorophenol$^+$		⩽6	[35]
2,3,5,6-tetrafluorophenol$^+$		41±4	[35]
Pentafluorophenol$^+$		31±3	[35]
Pentafluoroaniline$^+$	C_s $\tilde{B}(\pi^{-1}) \rightarrow \tilde{A}(\pi^{-1}), \tilde{X}(\pi^{-1})$	⩽6	[36]
Pentafluorobenzaldehyde$^+$		⩽6	[36]
Pentafluorobenzonitrile$^+$		⩽6	[36]
Pentafluoronitrosobenzene$^+$		⩽6	[36]

t-1,3,5-hexatriene$^+$	C_{2h}	$\tilde{A}^2B_g \rightarrow \tilde{X}^2A_u$	17±2	[37]
c-1,3,5-hexatriene$^+$	C_{2v}	$\tilde{A}^2A_2 \rightarrow \tilde{X}^2B_1$	⩽6	[37]
$C_2H_5\{C\equiv C\}_2C\equiv N^+$	C_s	$\tilde{A}^2A'' \rightarrow \tilde{X}^2A''$	⩽6	[26]
2,5-dichlorotoluene$^+$	C_s	$\tilde{B}(\pi^{-1}) \rightarrow \tilde{A}(\pi^{-1}), \tilde{X}(\pi^{-1})$	⩽6	[36]
3,5-dichlorotoluene$^+$			10±2	[36]
Pentafluorobenzoic acid$^+$			⩽6	[36]
Pentafluoromethoxybenzene$^+$			⩽6	[36]
Pentafluorotoluene$^+$			43±2	[36]
Perfluorotoluene$^+$			45±2	[36]
2,3,5,6-tetrafluorotoluene$^+$			43±2	[36]
all t-1,3,5-heptatriene$^+$	C_s	$\tilde{A}^2A'' \rightarrow \tilde{X}^2A''$	9±2	[38]
all t-1,3,5,7-octatetraene$^+$	C_{2h}	$\tilde{A}^2A_u \rightarrow \tilde{X}^2B_g$	⩽6	[39]
3,5-octadiyne$^+$	C_s	$\tilde{A}^2A'' \rightarrow \tilde{X}^2A''$	7±2	[28]
2,5-dichloro-p-xylene$^+$	C_s	$\tilde{B}(\pi^{-1}) \rightarrow \tilde{A}(\pi^{-1}), \tilde{X}(\pi^{-1})$	⩽6	[36]
Perfluoro-p-xylene$^+$			11±3	[36]
2,4,6-trifluoromesitylene$^+$	C_{3v}	$\tilde{B}^2A_1 \rightarrow \tilde{X}^2E$	37±2	[36]
t-Bu$\{C\equiv C\}_3$t-Bu$^+$	"$D_{\infty h}$"	$\tilde{A}^2\Pi_g \rightarrow \tilde{X}^2\Pi_u$	-	[40]

[s] These lifetimes are of the short component when a non-exponential decay curve is observed.

2.2. Some Examples

Using the apparatus outlined above, the emission spectra of around hundred polyatomic organic cations have been found. In all the cases the band systems lie between 250 nm and 900 nm and have been identified, by comparison with the corresponding photoelectron spectra, as the $^2\tilde{A} \rightarrow {}^2\tilde{X}$, or $^2\tilde{B} \rightarrow {}^2\tilde{A}$, $^2\tilde{X}$, electronic transitions of the respective cation. Since these observations were crucial for the more detailed studies to be described, all the open-shell cations whose radiative decay has been established are listed in Table 1. The references given are to the individual studies reporting the emission spectra, their analyses concerning vibrational and electronic structure, as well as their lifetimes and decay behavior. These comprise of a wide range of species; from triatomic to 32-atomic cations.

These emission spectra have, by and large, been recorded with optical resolution around 0.2 nm, except when very low emission intensities, or time-resolved measurements, precluded this. In Fig. 3 are shown two such spectra of a small and large cation; of dicyanoacetylene [23] (which had to be recorded in a time-resolved mode to suppress the overlapping bands due to the cyano radical) and of 1,3,5-trichlorobenzene [32].

The primary structural information on these cations forthcoming from such data are vibrational frequencies and the means to infer the symmetry of the excited electronic state with the help of ancillary knowledge, such as that from the photoelectron spectroscopic studies. Thus, in the example of dicyanoacetylene cation, the photoelectron spectra and ab initio many body Green's function calculations [41] show that the $^2\tilde{A}$ state symmetry is either $^2\Sigma_g^+$ or $^2\Sigma_u^+$ (in the $D_{\infty h}$ point group). The observation of the emission spectra allows one to conclude that the symmetry could be $^2\Sigma_g^+$. Similarly, for 1,3,5-trichlorobenzene cation the combination of the data shows that the symmetry of the $\tilde{B}$ state can only be $^2A_2''$ (under D_{3h} symmetry classification) [32]. Many further examples may be found not only among the cations listed in Table 1, but also for those cations whose emission spectra could not be detected. These include the fluoro-, chloro-, and chlorofluorobenzene cations for which a consistent pattern has been established [31-36]. The symmetry of the $\tilde{B}$ states is found to correspond to the ionization of electrons either from the π system (π^{-1}) or from the σ one (σ^{-1}) depending whether the radiative relaxation is observed, or not, respectively. In the case of benzene cation itself, the lack of radiative decay from the $\tilde{A}$ state, as well as evidence from other experiments, is consistent with the $^2E_{2g}$ symmetry assignment [31]. Other cases have been tabulated and discussed in an earlier review [6].

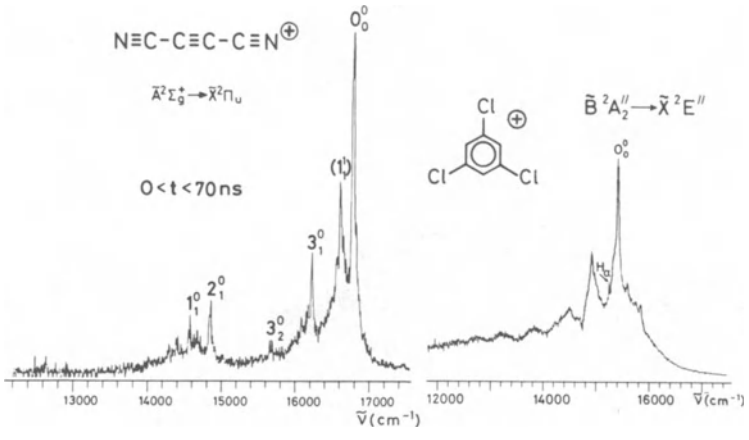

Fig. 3. Emission spectra of the cations of dicyanoacetylene (time resolved in the indicated interval) and of 1,3,5-trichlorobenzene. The optical resolutions used were 0.4 nm and 0.16 nm respectively.

The vibrational frequencies which can be inferred from the analyses of the band systems (cf. Fig. 3) are mainly of the totally symmetric fundamentals for the cationic ground states. For the excited state usually only the lowest frequency ones are obtained from the weak bands discernible to the higher energy side of the 0_0^0 bands. The number of the frequencies which can be deduced varies according to the size and symmetry of the species. In the smaller cations, most of the totally symmetric fundamentals are excited, e.g., all the three for dicyanoacetylene (Fig. 3). In somewhat larger cations, such as of 1,3-pentadiyne [28], which is discussed in Section 3.2, the frequencies of five of the seven totally symmetric fundamentals are obtained and can be compared to the ground molecular state values (see Table 3 later). As a general guideline it has been found that these frequencies do not differ by more than about 10% from each other.

In the case of the largest cations vibrational frequencies are still obtainable even though the complexity of the emission spectra increases (cf. Fig. 3). The problem is however the assignment of these to specific modes because of the large choice possible, except when the symmetry is high as with 1,3,5-trichlorobenzene cation, and often even the molecular values have not been assigned. In fact, in some of the studies of the smaller cations, the emission spectra have provided the first set of frequency values as the molecular data are not known [21]. On the other hand in higher resolution emission studies of the fluorinated benzenes, a vibrational analysis proved possible in spite of the fact that the band systems are con-

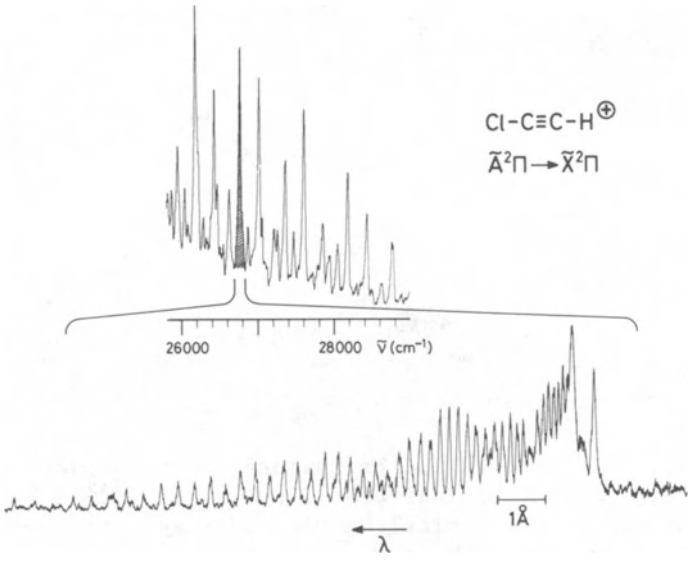

Fig. 4. High resolution recording (0.006 nm) of one vibronic band of the $\tilde{A}^2\Pi \rightarrow \tilde{X}^2\Pi$ emission band system (at top recorded with 0.16 nm) of chloroacetylene cation.

gested [42]. In addition the emission spectra of the hexafluoro-, 1,3,5-trifluoro-, and 1,3,5-trichlorobenzene cations have provided a unique means to study the Jahn-Teller effects in the cationic ground states and consequently to infer the resultant structure deformations [43, 44].

It has now also become possible to record the emission spectra of cations with optical resolutions down to 0.004 nm using the apparatus described. The aim of these studies is to obtain more accurate vibrational frequencies and for the smaller species the rotational structure. In Fig. 4 is shown an example of such data for chloroacetylene cation. The upper spectra is a portion of the $\tilde{A}^2\Pi \rightarrow \tilde{X}^2\Pi$ band system recorded with 0.16 nm resolution. The high resolution recording (0.006 nm) of one of the vibronic bands shown below reveals the rotational details. As yet, among polyatomic cations comprised of more than three atoms, only the emission spectrum of diacetylene cation $\tilde{A}^2\Pi_u \rightarrow \tilde{X}^2\Pi_g$, has been rotationally analyzed [45].

As a final example of the structure studies of organic open-shell cations, trans- and cis-1,3,5-hexatriene cations are chosen because these illustrate a further aspect. These two species belong to about a dozen organic cations which have been found to relax from their excited electronic states ($^2\tilde{A}$) by radiative and frag-

Table 2. Open-Shell Organic Cations (M^+) for Which the Radiative (quantum yield $>10^{-5}$) and Fragmentation Decay Channels are Both Detected. Not All the Fragmentation Channels Accessible, or All the Isotopic Derivatives Studied are Listed

Fragment Ions	M^+	Emission	References
C_2HF^+	c-$CHF{=}CHF^+$	$\tilde{A}^2A_1 \rightarrow \tilde{X}^2B_1$	[25]
$C_3H_3^+$	$CH_3{-}C{\equiv}C{-}Cl^+$		[20]
	$CH_3{-}C{\equiv}C{-}Br^+$		[20]
$C_5H_3^+$	$CH_3(C{\equiv}C)_2Cl^+$	$\tilde{A}^2E \rightarrow \tilde{X}^2E$	[20]
	$CH_3(C{\equiv}C)_3Br^+$		[20]
	$CH_3(C{\equiv}C)_2H^+$		[28]
$C_6H_5^+$, $C_6H_4^+$	$CH_3(C{\equiv}C)_2CH_3^+$	$\tilde{A}^2E_u \rightarrow \tilde{X}^2E_g$	[29]
$C_4H_4^+$	$C_2H_5(C{\equiv}C)_2H^+$	$\tilde{A}^2A'' \rightarrow \tilde{X}^2A''$	[29]
$C_6H_7^+$	t-1,3,5-hexatriene$^+$	$\tilde{A}^2B_g \rightarrow \tilde{X}^2A_u$	[37]
	c-1,3,5-hexatriene$^+$	$\tilde{A}^2A_2 \rightarrow \tilde{X}^2B_1$	[37]
$C_7H_{10}^+$, $C_7H_9^+$	all t-1,3,5-heptatriene$^+$	$\tilde{A}^2A'' \rightarrow \tilde{X}^2A''$	[38]
$C_6H_7^+$, $C_6H_6^+$			
$C_8H_9^+$, $C_7H_7^+$	all t-1,3,5,7-octatetraene$^+$	$\tilde{A}^2A_u \rightarrow \tilde{X}^2B_g$	[39]
$C_7H_7^+$	$C_2H_5(C{\equiv}C)_2C_2H_5^+$	$\tilde{A}^2A'' \rightarrow \tilde{X}^2A''$	[28]

mentation pathways [6]. The reason of interest here is, that not only the emitted photons, but also the resultant parent and fragment ions can be used as a probe of their structures. In Table 2 are summarized the cations for which such a behavior has been established. The accessibility of the fragmentation pathways was first established using photon or electron fragment ion appearance potentials when the emission spectra of the indicated electronic transitions (Table 2) were found. As a result, some of these cations were subsequently studied by the photoelectron-photoion coincidence technique [46], as was the case with the hexatriene cations [38].

In the diagram of Fig. 5, the information inferred on the structure and decay of the trans- and cis-1,3,5-hexatriene cations is presented. The emission spectra of the two isomer cations are distinct showing that, within the measured lifetimes, these species retain their structures, and furthermore that isomerization from the zeroth vibrational level of the $\tilde{A}$ state of one isomer to the other in the $\tilde{A}$ state does not take place. The radiative decay is, however, a minor pathway as the emission quantum yields were estimated from the lifetimes [37] and from the integrated extinction

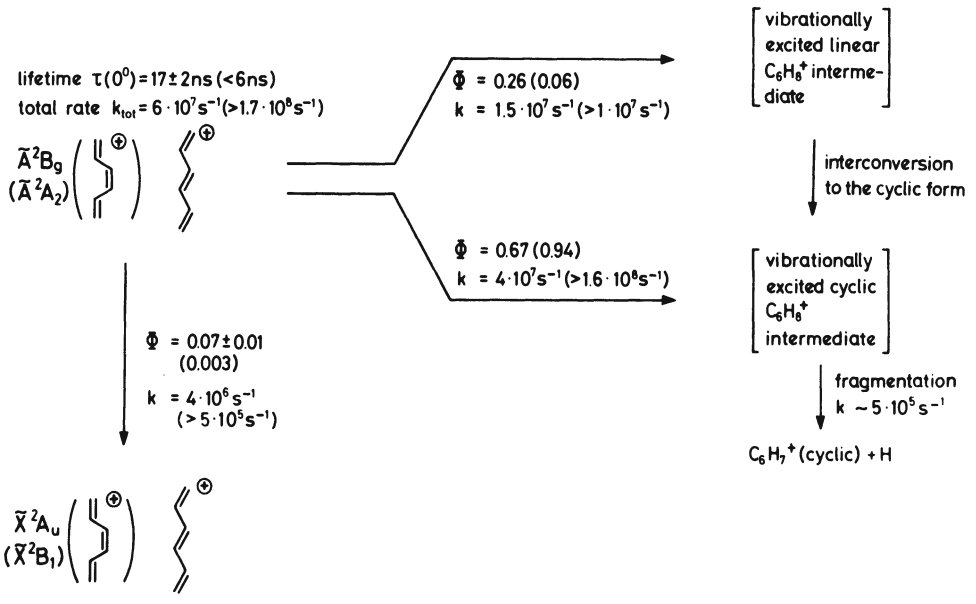

Fig. 5. Summary of the structure and relaxation decay of trans- (and cis-) 1,3,5-hexatriene cations produced in the $\tilde{A}$ 0° state.

coefficients of the matrix absorption spectra [47] to be only about 7% and 0.3% for the trans- and cis- species respectively [38]. The photoelectron-photoion coincidence measurements yielded the branching ratios of the $C_6H_8^+$, and $C_6H_7^+$ ions detected on initial formation of the $\tilde{A}$ 0° states. The latter measurements identify the mass of the detected ions but the geometric and electronic structures of the ions are not characterized. Nevertheless, by pooling these and the emission data, as well as ancillary information available from the matrix absorption spectra and other fragmentation studies, reasonable conclusions on the structures could be reached (Fig. 5). Apart from the radiative decay in which the identity of the two isomer cations is retained, one of the non-radiative decay channels leads first to a linear $C_6H_8^+$ ion which is only slowly transformed to a cyclic cation. The latter precursor, which is also formed by a more direct pathway, can then lose a hydrogen atom to yield the only energetically accessible (from the $\tilde{A}$ 0° state of the hexatriene cations) fragment ion, cyclic $C_6H_7^+$. Further examples of combining the radiative and fragmentation data are discussed in Section 4.2.

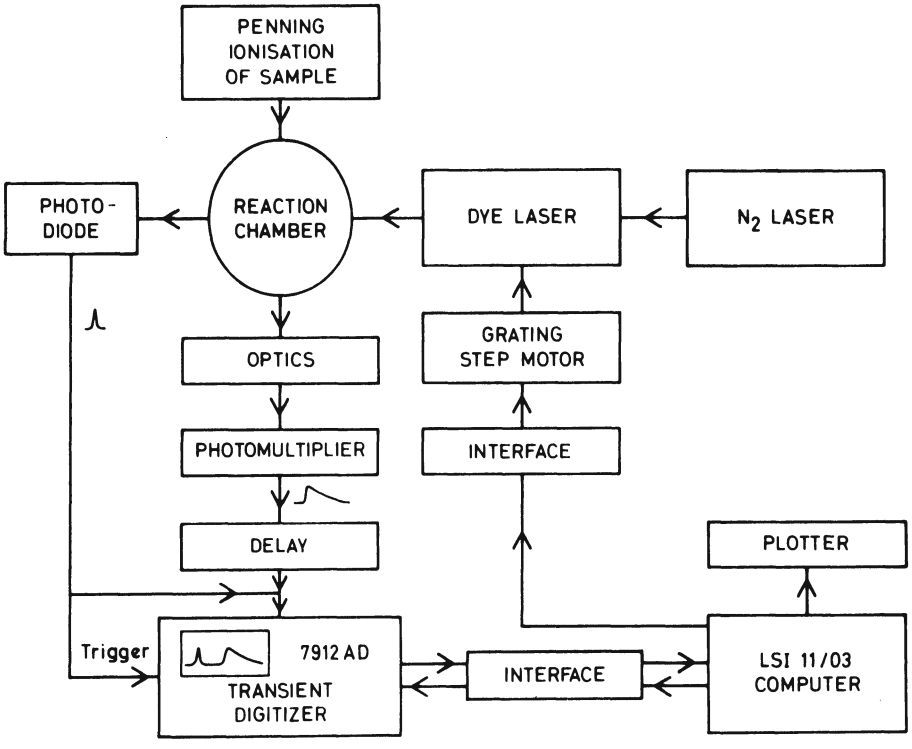

Fig. 6. Block diagram of the apparatus used to obtain laser induced excitation spectra.

3. Laser Induced Fluorescence

3.1. Apparative

The essential lay-out of the apparatus used for the recording of the laser induced excitation spectra of cations is given in Fig. 6. The principle of the technique [8] is the following:

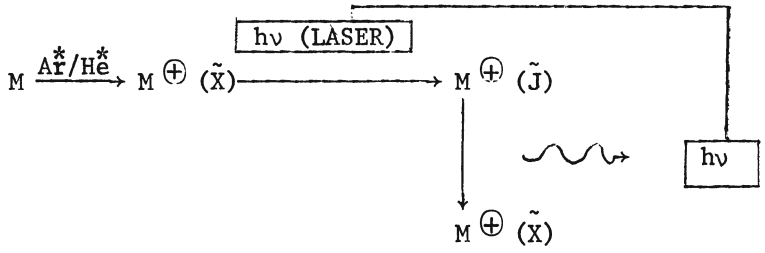

The cations are produced in their ground states by Penning ionization of the parent species using argon or helium metastables. The excitation spectra are obtained by pumping the $\tilde{J} \leftarrow \tilde{X}$ electronic

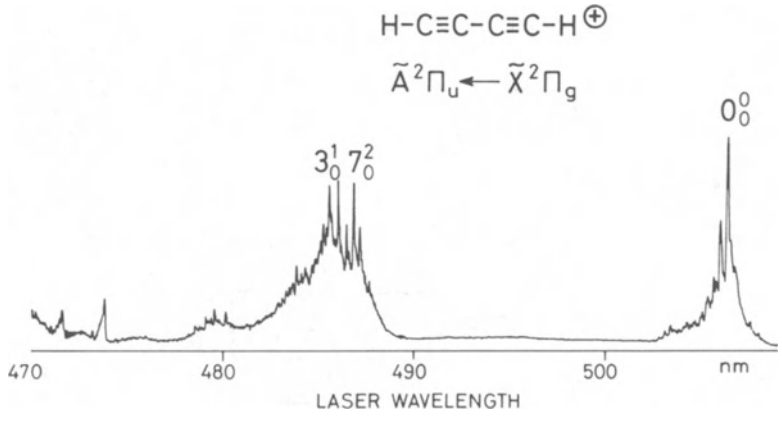

Fig. 7. A portion of the $\tilde{A}^2\Pi_u \leftrightarrow \tilde{X}^2\Pi_g$ laser excitation spectrum of diacetylene cation recorded with 0.02 nm bandwidth.

transition of the cation with a tunable dye laser while monitoring the undispersed fluorescence. The excited state $\tilde{J}$ has therefore to decay radiatively (cf. Table 1).

The apparative details [48] are similar to those described [49]. In the examples of excitation spectra to be shown, the laser bandwidth was 0.02 nm and the energy per pulse of the order of 0.1 mJ. The dye laser is pumped by a nitrogen laser at a repetition frequency around 30 Hz and the overall time resolution is ≈3 ns. Both signal from the photomultiplier and of a photodiode sampling the laser intensity are stored and repetitively accumulated (typically 32 times per wavelength setting) by a programmable digitizer. The digital data are then transferred to a microcomputer which evaluates the value corrected for laser intensity variation and then advances the laser wavelength. In order to cover the wavelength range of the excitation spectra, usually two or three dye solutions are necessary. These are joined up by recording bands common to the successive segments and normalizing their intensities. The samples are again introduced from vessels held at the lowest ambient temperature possible.

3.2. Some Examples

These examples are chosen from our own studies, where the aim has been, so far, to obtain the vibrational frequency data for the cations in the excited electronic state. As has been noted in the introduction, extensive investigations of the halogenated benzene cations in particular have been carried out using this technique [10, 11].

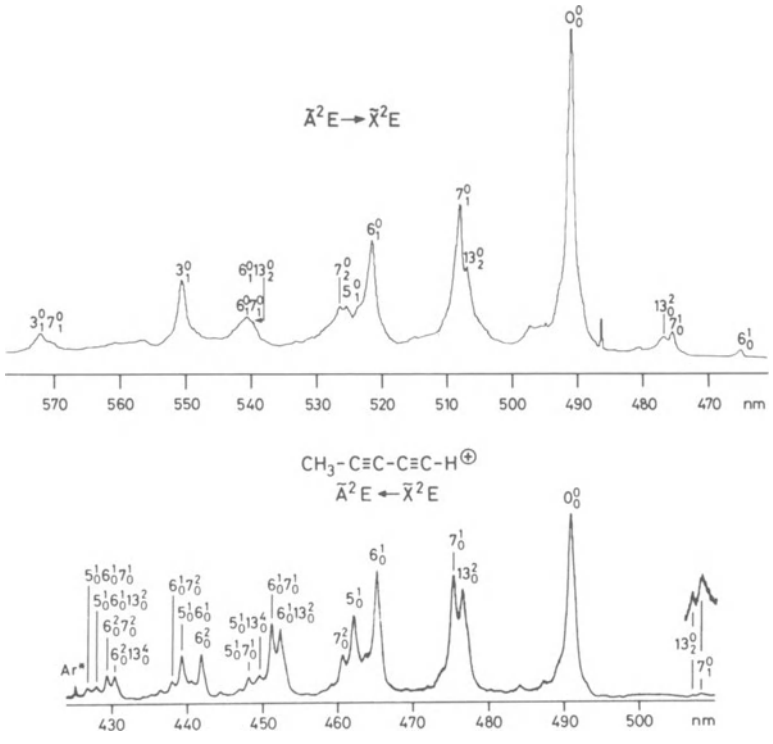

Fig. 8. Emission (upper) and laser excitation (lower) spectra of the $\tilde{A}^2E \leftrightarrow \tilde{X}^2E$ transition of 1,3-pentadiyne cation, recorded with 0.16 nm and 0.02 nm bandwidths, respectively.

Figure 7 shows a portion of the laser excited excitation spectrum of the $\tilde{A}^2\Pi_u \leftrightarrow \tilde{X}^2\Pi_g$ transition of diacetylene cation, which was the first large organic cation observed in emission [45]. The full spectrum shows the excitation of two of the three totally symmetric fundamentals as well as the double excitation of a degenerate bending mode (ν_7) which has a totally symmetric component and gains the intensity by Fermi interaction with the energetically close lying ν_3 fundamental. The structure of most of the bands is due to sequence transitions. The excitation spectrum of 1,3-pentadiyne cation, $\tilde{A}^2E \leftrightarrow \tilde{X}^2E$, is shown as the bottom part of Fig. 8 [48] and at the top is reproduced the emission spectrum [28]. The assignment of the respective bands in the spectra to the vibrational fundamentals is indicated (under C_{3v} symmetry classification). It can be seen that there is quite a similarity between the two spectra in their vibrational structure. The inferred vibrational frequencies are collected in Table 3 for the $\tilde{X}^2E$ and $\tilde{A}^2E$ cationic states, where the molecular ground state, X^1A_1, values are also given [50].

Table 3. Vibrational Frequencies (±10 cm^{-1}) of the Totally Symmetric Fundamentals, A_1, of 1,3-Pentadiyne Cation (under C_{3v} classification) in the Ground, $\tilde{X}^2E$, and First Excited, $\tilde{A}^2E$, Electronic States Obtained from the Emission [28] and Laser Excitation Spectra [48], Respectively. The Ground Molecular State, X^1A_1, Values and the Approximate Description of the Modes are Taken from Ref. [50].

Fundamental		X^1A_1	$\tilde{X}^2E$	$\tilde{A}^2E$
ν_1	ν (C≡C-H)	3316		
ν_2	$\nu_s(CH_3)$	2919		
ν_3	ν (C≡C_C)	2257	2205	2135
ν_4	ν (C≡C_H)	2072		2000
ν_5	δ (CH_3)	1375	1340	1270
ν_6	ν_a(C-C)	1152	1190	1130
ν_7	ν_s(C-C)	686	685	665
ν_{13}	δ (C-C≡C)	320	320	305

In the case of large open-shell cations, vibrational frequencies can still be deduced from the spectra. This is illustrated by the excitation spectrum of 3,5-difluorophenol cation, $\tilde{B}^2A'' \leftrightarrow \tilde{X}^2A''$ where the frequencies are listed above the bands (Fig. 9) [51]. The complementary emission spectrum [35] and the inferred frequencies are shown in the upper half of the figure. For such cations of low symmetry, the attribution of the frequencies to specific fundamentals is not possible in view of the number of totally symmetric modes alone (23 in the example shown). Nevertheless, the above discussed examples emphasize the complementary nature of the laser excitation and emission spectra in providing the vibrational structure data for open-shell cations.

4. Photoelectron-Photon Coincidence Spectroscopy

4.1. Apparative

The essence of the technique is to detect coincidences between ejected electrons and emitted photons following ionization with a monochromatic photon source [13]. The latter is usually either

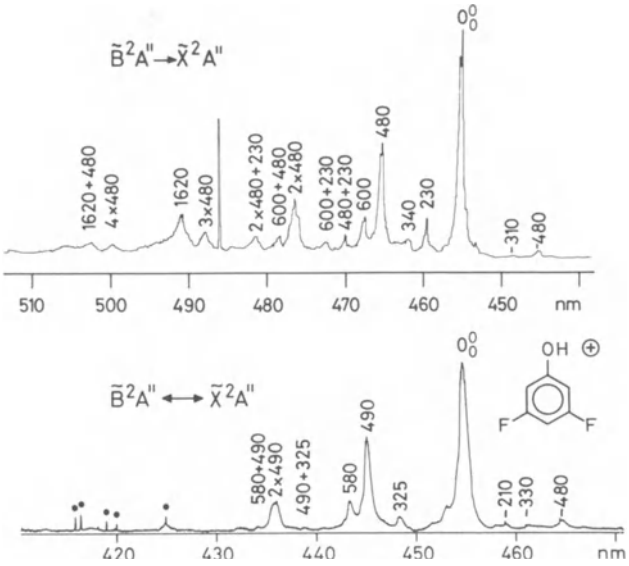

Fig. 9. Emission (upper) and laser excitation (lower) spectra of the $\tilde{B}^2A'' \leftrightarrow \tilde{X}^2A''$ transition of 3,5-difluorophenol cation, recorded with 0.12 nm and 0.02 nm bandwidths respectively.

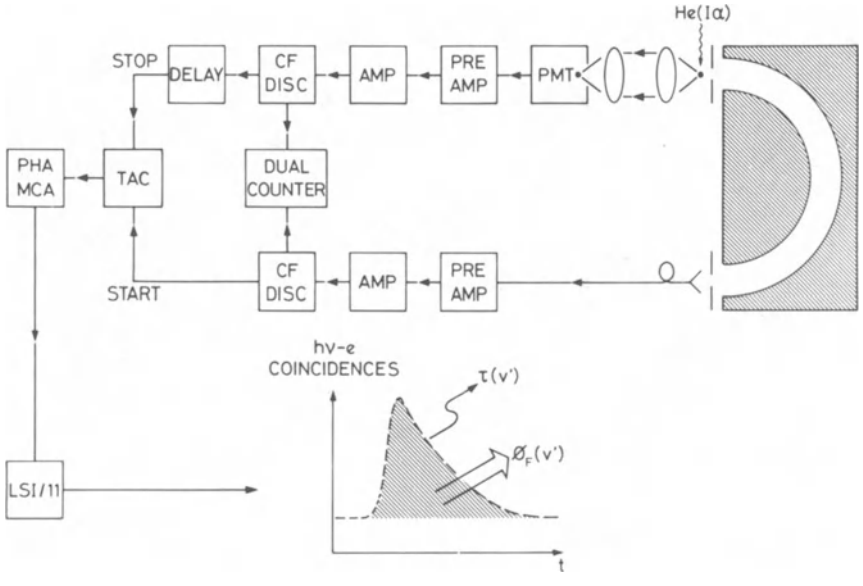

Fig. 10. Block diagram of the photoelectron-photon coincidence apparatus.

the He(Iα) or the Ne(I) resonance line but a continuum source has also been used [52]. As the electrons are energy selected, ($e_{K.E}$) the internal energy of the cations produced in the $J_{v'}$ state is defined:

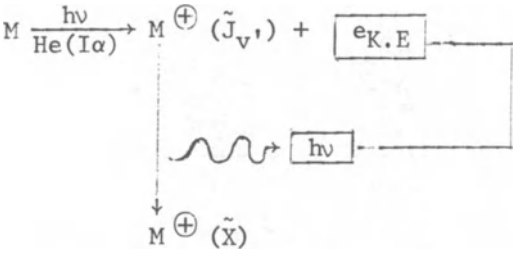

The detection of the true coincidences between the electrons and the undispersed photons shows that either the cation in the state $\tilde{J}_{v'}$ decays radiatively, or that a fragment or isomer cation formed by a non-radiative decay of the $\tilde{J}_{v'}$ state does. The decay coincidence curve yields the cascade-free lifetime of the emitting species and, furthermore, by appropriate calibration of the apparatus the fluorescence quantum yields, $\phi_F(v')$, of the state $\tilde{J}_{v'}$ defined by the kinetic energy and spread of the electrons, can be determined. With the latter aspects in forefront, the apparatus depicted schematically in Fig. 10 was designed and constructed [53].

The electrons are energy dispersed by a 180° hemispherical analyzer (55 mm mean radius) operating with a resolving power $E/\Delta E \approx 80$. The photons are collected from a well-defined ionization region by a f/1 lens system. The event pulses generated by the channeltron and photomultiplier are electronically handled as indicated in the diagram of Fig. 10. The time intervals between the electron and the photon events are registered by a multichannel analyzer operating in the pulse-height analysis mode. The data are then transferred to a microcomputer for evaluation. In order to obtain the fluorescence quantum yields, the rate of detection of true electrons, N_e, and rate of detection of true coincidences, N_T, have to be determined, i.e., $N_e = N_i f_e g(v')$ and $N_T = N_i f_e f_{h\nu} g(v') \phi_F(v')$ from which follows $N_T/N_e = f_{h\nu}\phi_F(v')$. In these relationships N_i is the ionization rate, $g(v')$ is the branching ratio for formation of the cation in the state $\tilde{J}_{v'}$ at the photoionization wavelength used and f_e and $f_{h\nu}$ are the overall collection efficiencies for electrons and photons respectively. The absolute value of $f_{h\nu}$ as function of wavelength has therefore to be known. The complications due to the wavelength dependence are largely circumvented by choosing a photomultiplier (RCA C31034A) with a uniform quantum efficiency over a large wavelength range. As the range of most emission band systems of organic cations is less than 100 nm [6], the few percent $f_{h\nu}$ variation can be tolerated and the individual band intensities of the emission system do not have to be convoluted with the $f_{h\nu}(\lambda)$

function. The absolute calibration is achieved with cations for which unity fluorescence quantum yields are known or have been established. These include $N_2^+\tilde{B}^2\Sigma_u^+ v' = 0$, $N_2O^+(\tilde{A}^2\Sigma^+\ 0^0)$ and $CO_2^+ \cdot (\tilde{A}^2\Pi_u\ 0^0)$. In practice both f_e (5-10 eV) $f_{h\nu}$ ($300 < \lambda < 700$ nm) are of the order of $2 \cdot 10^{-3}$. In order to keep down the rate of false coincidences, $N_f = N_e' \cdot N_{h\nu} \cdot \Delta t$ where $N_e' = N_e + N_{e,sc}$, and $N_{h\nu}$ is the detection rate of photons ($N_{h\nu} = N_i \cdot f_{h\nu} \cdot \sum_{v'} g(v') \cdot \phi_F(v') + N_{h\nu,\,sc}$) and Δt is the selected time interval, the scattered electrons ($N_{e,sc}$) and photons ($N_{h\nu,sc}$) have to be minimized. Finally, the design chosen is a compromise in the energy and time resolution dictated by the electron channel [53]. It should also be pointed out that the data accumulation times are time demanding; typically half-a-day per measurement in order to attain the 5% accuracy for the $\phi_F(v')$ and $\tau(v')$ values.

4.2. Some Examples

The importance of these measurements is several-fold and they form an integral part of the structure studies of open-shell polyatomic cations. The fluorescence quantum yields reveal the fraction of cations retaining their structure and together with lifetime measurements allow the oscillator strengths of the electronic transitions to be estimated. The technique is a means to show directly that also higher vibrationally excited levels decay radiatively, and to locate (under coincidence conditions) the wavelength region of the emitted photons with cut-off filters. This information can then be used in the spectroscopic investigations of these cations with the emission and laser excitation methods described. On the dynamic side, the $\phi_F(v')$ and $\tau(v')$ data enable one to obtain the radiative and non-radiative rate constants as function of the internal energy.

The first example is that of CO_2^+ cation in selected vibrational levels of the $\tilde{A}^2\Pi_u$ and $\tilde{B}^2\Sigma_u^+$ states [53]. Figure 11 shows the He(Iα) photoelectron spectrum, recorded under the coincidence conditions indicating the levels studied. A typical coincidence curve is reproduced in the inset. The $\phi_F(v')$ and $\tau(v')$ values obtained are summarized in Table 4. For the $\tilde{A}^2\Pi_u$ state levels 0^0 and 1^n n = 1-4, $\phi_F = 1$ within the 5% uncertainty and the lifetimes are constant. In the case of $\tilde{B}^2\Sigma_u^+$ state, however, new spectroscopic and structural aspects emerge. The observation of coincidences for the 1^1 and 1^2 levels proves that these levels emit, as transitions from these levels have not as yet been identified in the $\tilde{B}^2\Sigma_u^+ \rightarrow \tilde{X}^2\Pi_g$ emission spectrum [54]. The implication is that the intensity is concentrated in their sequence transitions. For the 0^0 level it was reported earlier, using the threshold photoelectron-photon coincidence approach, that about a third of the emission intensity lies at wavelengths $330 \leqslant \lambda \leqslant 450$ nm and two thirds

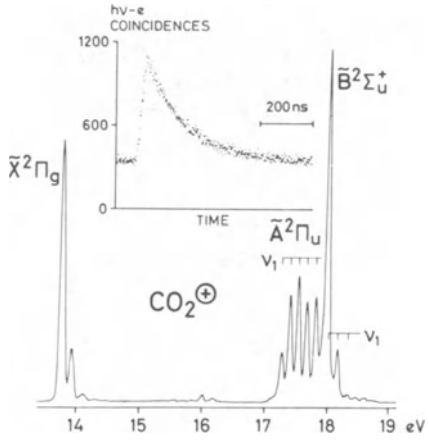

Fig. 11. He(Iα) photoelectron spectrum showing the vibrational levels of the $\tilde{A}^2\Pi_u$ and $\tilde{B}^2\Sigma_u^+$ states of CO_2^+ for which the photoelectron-photon coincidence measurements were carried out (cf. Table 4). The inset is a coincidence curve for the $\tilde{B}^2\Sigma_u^+$ 0^0 state; N_e - 500 Hz; $N_{h\nu}$ — 8 kHz; N_e - 1.62 Hz, accumulated in 12 hours.

Table 4. Summary of the Fluorescence Quantum Yield and Lifetime Measurements by the Photoelectron-Photon Coincidence Technique of State Selected CO_2^+ [53]

State	Level	$\phi_F(v')$	τ (ns)
$\tilde{A}^2\Pi_u$	0^0	1.00±0.05	124±6
	1^1	0.98±0.05	122±6
	1^2	0.98±0.05	124±6
	1^3	1.00±0.05	124±6
	1^4	0.99±0.05	124±6
$\tilde{B}^2\Sigma_u^+$	0^0	1.00±0.05	140±7
		(0.36±0.04)[a]	
	1^1	0.78±0.04	118±6
		(0.23±0.04)[a]	
	1^2	0.59±0.09	120±18

[a] measured for λ >330 nm

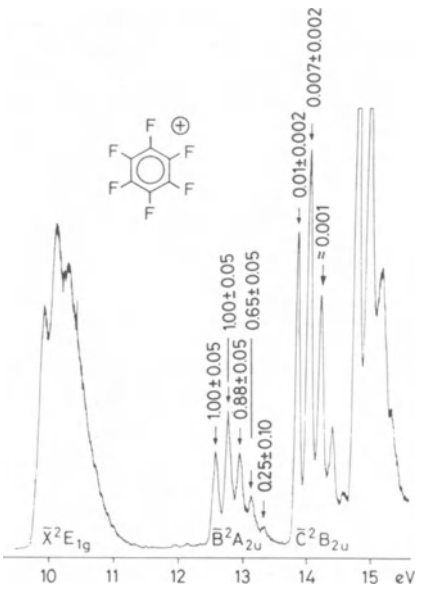

Fig. 12. He(Iα) photoelectron spectrum of hexafluorobenzene indicating the measured fluorescence quantum yields for the selected levels of the $\tilde{B}$ and $\tilde{C}$ cationic states.

at $200 \leqslant \lambda \leqslant 330$ nm [52]. These two regions are associated with the $\tilde{A}^2\Pi_u \rightarrow \tilde{X}^2\Pi_g$ and $\tilde{B}^2\Sigma_u^+ \rightarrow \tilde{X}^2\Pi_g$ transitions of CO_2^+. The same situation prevails also for the 1^1 vibrational level (Table 4). Thus these results show clearly that these levels of the $\tilde{B}^2\Sigma_u^+$ state are coupled with the $\tilde{A}^2\Pi_u$ state. This phenomenon has been discussed in detail [55] in view of the data obtained from a related technique, that based on the detection of coincidences between mass selected ions and emitted photons [56]. In the latter technique [57], although the carriers causing the emission are mass identified, their internal energy is not.

The photoelectron-photon coincidence measurements on hexafluorobenzene cation show that photons are emitted not only from all the vibrational levels of the $\tilde{B}^2A_{2u}$ state populated in the photoionization process, but also on preparation of the cation in the $\tilde{C}^2B_{2u}$ state (Fig. 12) [58, 59]. Consideration of these data, including their wavelength dependence, as well as the emission spectrum [31] $\tilde{B}^2A_{2u} \rightarrow \tilde{X}^2E_{1g}$, leads one to conclude that the $\tilde{C} \rightsquigarrow \tilde{B}$ internal conversion takes place followed by a radiative transition between highly vibrationally excited levels of the $\tilde{B}$ and $\tilde{X}$ states. This results in the emission to be shifted to longer wavelengths, i.e., $400 < \lambda < 650$ nm. Thus an additional means to probe the structure of this cation via the $\tilde{C}^2B_{2u}$ state becomes apparent from these results.

The final cation to be discussed is that of cis-1,2-difluoroethylene, which is one of the species which decay not only radiatively but also by fragmentation (Table 2). The summary in Fig. 13 refers to this cation generated in the zeroth level of the $\tilde{A}^2A_1$ state, but corresponding schemes can be evaluated from the data on the excited vibrational levels. The necessary information to construct the shown scheme comes from the photoelectron-photon [60] and photoelectron-photoion coincidence [61] measurements as well as from emission spectroscopy [25]. The latter yielded the $\tilde{A}^2A_1$ 0^0 lifetime as well as the vibrational frequencies of four of the five totally symmetric fundamentals in the $\tilde{X}^2B_1$ state. The radiative and non-radiative rates for the depletion of the zeroth level of the $\tilde{A}$ state can be evaluated from the measured fluorescence quantum yield. However, the $C_2H_2F_2^+$ branching ratio determined is by a factor 3 to 4 larger than the $\phi_F(0^0)$ value (Fig. 13). The implication of this is that around two thirds of the $C_2H_2F_2^+$ ions detected after a flight-time of ≈35 μs in the photoelectron-photoion coincidence measurements [61] are probably in the ground state, $\tilde{X}^2B_1$, in highly excited vibrational levels or they are excited isomeric cations. The fragmentation rate can also be evaluated and, as is known from mass-spectroscopic studies [61], it is slow (Fig. 13). It is therefore seen that the non-radiative decay competing with the radiative one (for the 0^0 level) is two orders of magnitude faster than the fragmentation rate, and that the vibrationally excited $C_2H_2F_2^+$ cation has adequate time to rearrange to a suitable structure before the elimination of HF.

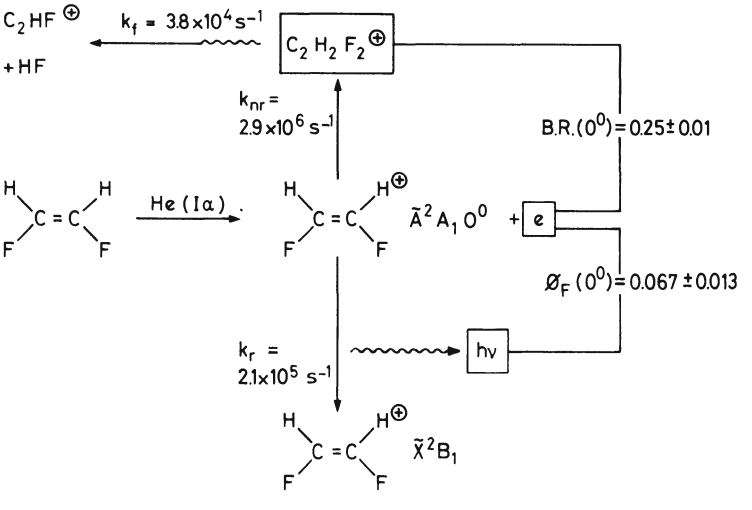

Fig. 13. Summary of the structure and decay of cis-1,2-difluoroethylene cation prepared in the $\tilde{A}^2A_1$ 0^0 state.

The examples given throughout this article were meant to show how the complementary application of the different spectroscopic techniques, and of the respective data, yield a detailed insight into the decay and structure of open-shell organic cations. To conclude, the following paragraph summarizes the present scope and resolution limits (energy and time) of the three techniques hitherto described.

Technique	Information on Cations	Resolution
Emission spectroscopy	Ground state vibrational frequencies; rotational structure, lifetimes of lowest levels of excited states	$\geqslant$0.004 nm 6 ns
Laser-induced fluorescence	Excited state vibrational frequencies; rotational structure; lifetimes (at threshold) of excited state levels	0.02 or 0.002 nm 5 ns
Photoelectron-photon coincidence	Fluorescence quantum yields and cascade-free lifetimes of excited state levels	$E/\Delta E \approx 80$ 15 ns (for 10 eV electrons)

Acknowledgements

The research investigations described in this article have been financed throughout the years by the Schweizerischer Nationalfonds zur Förderung der wissenschaftlichen Forschung (Project No. 2.212.0-79, E 33). Ciba-Geigy SA, Sandoz SA and F. Hoffmann- La Roche & Cie SA, Basel are also thanked for financial support.

References

1. G. Herzberg, "Molecular Spectra and Molecular Structure," Vol. I, van Nostrand, New York (1950); Vol. III, van Nostrand, New York (1966).
2. G. Herzberg, "The Spectra and Structure of Simple Free Radicals," Cornell University Press (1971).
3. G. Herzberg, Quart. Rev. Chem. Soc., 25, 201 (1971).
4. G. Herzberg, Science, 177, 123 (1972).
5. S. Leach, in: "The Spectroscopy of the Excited State," NATO Advanced Study Institute, Plenum Press (1976).
6. See J. P. Maier, in: "Kinetics of Ion-Molecular Reactions," P. Ausloos, ed., Plenum Press, New York (1979); J. P. Maier, Chimia, 34, 219 (1980) for previous reviews of this field.

7. D. W. Turner, C. Baker, A. D. Baker, and C. R. Brundle, "Molecular Photoelectron Spectroscopy," Wiley-Interscience, London (1970), and references therein.
8. P. C. Engelking and A. L. Smith, Chem. Phys. Letters, 36, 22 (1975).
9. V. E. Bondybey and T. A. Miller, J. Chem. Phys., 67, 1790 (1977).
10. V. E. Bondybey and T. A. Miller, J. Chem. Phys., 70, 138 (1979).
11. T. A. Miller, V. E. Bondybey, and J. H. English, J. Chem. Phys., 70, 2919 (1979).
12. T. E. Miller, V. E. Bondybey, and B. R. Zegarski, J. Chem. Phys., 70, 4982 (1979).
13. M. Bloch and D. W. Turner, Chem. Phys. Letters, 30, 344 (1975).
14. M. Allan, PhD Thesis, University of Basel (1976).
15. O. Marthaler, PhD Thesis, University of Basel (1980).
16. M. Allan and J. P. Maier, Chem. Phys. Letters, 41, 231 (1976).
17. M. Allan, E. Kloster-Jensen, and J. P. Maier, J. C. S. Faraday II, 73, 1406 (1977).
18. M. Allan, E. Kloster-Jensen, and J. P. Maier, J. C. S. Faraday II, 73, 1417 (1977).
19. M. Allan, E. Kloster-Jensen, and J. P. Maier, Chem. Phys., 7, 11 (1976).
20. J. P. Maier, O. Marthaler, and E. Kloster-Jensen, J. Electron Spect., 18, 251 (1980).
21. M. Allan, J. P. Maier, O. Marthaler, and J.-P. Stadelmann, J. Chem. Phys., 70, 5271 (1979).
22. M. Allan, E. Kloster-Jensen, J. P. Maier, and O. Marthaler, J. Electron Spectr., 14, 359 (1978).
23. J. P. Maier, O. Marthaler, and F. Thommen, Chem. Phys. Letters, 60, 193 (1979).
24. J. P. Maier, O. Marthaler, and F. Thommen, to be published.
25. J. P. Maier, O. Marthaler, and G. Bieri, Chem. Phys., 44, 131 (1979).
26. G. Bieri, E. Kloster-Jensen, S. Kvisle, J. P. Maier, and O. Marthaler, J. C. S. Faraday II, 76, 676 (1980).
27. E. Kloster-Jensen, J. P. Maier, O. Marthaler, and M. Mohraz, J. Chem. Phys., 71, 3125 (1979).
28. J. P. Maier, O. Marthaler, and E. Kloster-Jensen, J. Chem. Phys., 72, 701 (1979).
29. M. Allan, J. P. Maier, O. Marthaler, and E. Kloster-Jensen, Chem. Phys., 29, 331 (1978).
30. T. B. Jones, J. P. Maier, and O. Marthaler, Inorg. Chem., 18, 2140 (1979).
31. M. Allan and J. P. Maier, Chem. Phys. Letters, 34, 442 (1975); M. Allan, J. P. Maier, and O. Marthaler, Chem. Phys., 26, 131 (1977).
32. J. P. Maier and O. Marthaler, Chem. Phys., 32, 419 (1978).
33. J. P. Maier, O. Marthaler, M. Mohraz, and R. H. Shiley, Chem. Phys., 47, 295 (1980).

34. J. P. Maier, O. Marthaler, M. Mohraz, and R. H. Shiley, Chem. Phys., 47, 307 (1980).
35. J. P. Maier, O. Marthaler, M. Mohraz, and R. H. Shiley, J. Electron Spectr., 19, 11 (1980).
36. J. P. Maier, O. Marthaler, and M. Mohraz, J. Chim. Phys., 77, 661 (1980).
37. M. Allan and J. P. Maier, Chem. Phys. Letters, 43, 94 (1976).
38. M. Allan, J. Dannacher, and J. P. Maier, J. Chem. Phys., 73, 3114(1980).
39. T. B. Jones and J. P. Maier, Int. J. Mass Spectrom. Ion Phys., 31, 287 (1979).
40. Unpublished results from this laboratory.
41. G. Bieri, E. Heilbronner, V. Hornung, E. Kloster-Jensen, J. P. Maier, F. Thommen, and W. von Niessen, Chem. Phys., 36, 1 (1979).
42. C. Cossart-Magos, D. Cossart, and S. Leach, Mol. Phys., 37, 793 (1979).
43. C. Cossart-Magos, D. Cossart, and S. Leach, Chem. Phys., 41, 363, 345 (1979); C. Cossart-Magos and S. Leach, Chem. Phys., 48, 329, 349 (1980).
44. V. E. Bondybey, T. A. Miller, and J. H. English, J. Chem. Phys., 71, 1088 (1979); T. Sears, T. A. Miller, and V. E. Bondybey, J. Chem. Phys., 72, 6070 (1980).
45. J. H. Callomon, Canad. J. Phys., 34, 1046 (1956).
46. See for example, J. Dannacher, E. Heilbronner, J.-P. Stadelmann, and J. Vogt, Helv. Chim. Acta, 62, 2186 (1979).
47. T. Shida, T. Kato, and Y. Nosaka, J. Phys. Chem., 81, 1095 (1977).
48. J. P. Maier and L. Misev, Chem. Phys., 51, 311 (1980).
49. J. M. Cook, T. A. Miller, and V. E. Bondybey, J. Chem. Phys., 69, 2563 (1978).
50. J. Lamotte, J.-C. Lavelley, and R. Romanet, J. Chim. Phys., 70, 1077 (1973).
51. J. P. Maier and L. Misev, Helv. Chim. Acta, 63, 1920 (1980).
52. E. W. Schlag, R. Frey, B. Gotchev, W. B. Peatman, and H. Pollak, Chem. Phys. Letters, 51, 406 (1977).
53. J. P. Maier and F. Thommen, Chem. Phys., 51, 319 (1980).
54. D. Gauyacq, M. Horani, S. Leach, and J. Rostas, Can. J. Phys., 53, 2040 (1975).
55. S. Leach, P. S. Stannard, and W. M. Gelbart, Mol. Phys., 36, 1119 (1978).
56. S. Leach, M. Devoret, and J. H. D. Eland, Chem. Phys., 33, 113 (1978).
57. J. H. D. Eland, M. Devoret, and S. Leach, Chem. Phys. Letters, 43, 97 (1976).
58. D. L. Ames, M. Bloch, H. Q. Porter, and D. W. Turner, in: "Molecular Spectroscopy," Institute of Petroleum, London (1976), p. 399.

59. J. P. Maier and F. Thommen, Chem. Phys., 57, 319 (1981).
60. J. P. Maier and F. Thommen, J. C. S. Faraday II, 77, 845 (1981).
61. J.-P. Stadelmann and J. Vogt, Int. J. Mass Spectrom. Ion Phys., 35, 83 (1980).

INFRARED ABSORPTION SPECTRA OF MOLECULAR IONS IN SOLID ARGON

Lester Andrews

Chemistry Department
University of Virginia
McCormick Road
Charlottesville, VA 22901

Introduction

Molecular ions are of considerable chemical and physical interest for comparing the spectroscopic and bonding properties of neutral molecules with their positive and negative molecular ions. The study of molecular ions in the gas phase by photoelectron, photoionization mass and ion cyclotron resonance spectroscoies can be complemented by infrared and optical absorption spectra of the molecular ion trapped in a solid inert gas host. Further ion studies with tunable infrared lasers will be greatly aided by the vibrational data obtained for molecular ions in noble gas solids. The ion-matrix interaction is of fundamental and practical interest as matrix spectra of ions are related to the gas phase.

Charged species in matrices form two general classes described in the literature as "isolated" and "chemically bound" with respect to the counterion. The first ionic species characterized in matrices, $Li^+O_2^-$, is of the latter type where the lithium cation and the superoxide anion are Coulombically bound together [1, 2], and charge-transfer occurs because this electrostatic attraction more than makes up for the difference between the ionization energy of lithium and the electron affinity of oxygen. The next molecular ions identified in matrices, $B_2H_6^-$ and C_2^-, are of the "isolated" type where the cation is separated by an undetermined number of matrix atoms from the anion [3, 4]. These ionic systems have been characterized as "Coulomb ion pair" which exist because of essentially zero overlap between the wavefunctions for the electron on the recipient molecule and the cation that provided the electron [5]. Clearly, the formation of ions of the "isolated" type re-

quires that the ionization energy of a precursor atom or molecule in the matrix host be supplied by an external souce which produces a cation and an electron. The electron may be trapped by another molecule or fragment elsewhere in the matrix, forming a negative ion.

These early studies of $Li^+O_2^-$, $B_2H_6^-$, and C_2^- employed different methods of production, chemical reaction, photoionization of sodium in the sample or photoionization of the C_2H_2 precursor with and without added cesium, respectively. Different matrix spectroscopic techniques, infrared absorption, electron spin resonance, and optical absorption were used for detection in these studies. Experimental methods for the production and investigation of molecular ions in noble gas matrices will be described in the next section.

Experimental Methods

The most direct method for producing ions in matrices is to react alkali metal atoms with an electron acceptor molecule during condensation with excess argon at cryogenic temperatures. This method, developed by Andrews and Pimentel in a study of the lithium atom-nitric oxide reaction [6], necessarily gives a chemically bound ion pair due to the Coulombic attraction between anion and cation that is required to sustain charge transfer. In the case of $M^+O_2^-$ species, vibrational spectra clearly demonstrate an M^+ effect on the O_2^- stretching mode and the bound nature of the ion pair [7].

The first technique used to prepare isolated ions involved mercury arc photoionization of sodium atoms in the sample to provide electrons for capture by molecules elsewhere in the matrix [3]. This method, which has been discussed by Kasai [8], produces "Coulomb ion pairs" with Na^+ separated from the anion by several or more layers of argon atoms such that the anion is not affected by the alkali cation.

Another important technique for preparing isolated ions employed vacuum-ultraviolet photoionization of a precursor molecule with a LiF-filtered hydrogen or argon resonance lamp. In the C_2H_2 experiments of Milligan and Jacox, hydrogen-resonance photolysis produced C_2 at 238.2 nm and new absorptions at 520.6 and 472.5 nm. The latter absorptions were enhanced in subsequent studies with cesium atoms added to the sample, which supported their identification as C_2^- [4]. Brus and Bondybey later explained that the C_2^- anion was produced as a "Coulomb ion pair" with $C_2H_2^+$ by direct photoionization of C_2H_2, with a red shift in the ionization energy owing to solvation of the charged products in the matrix [9] followed by electron capture by the C_2 photolysis product [5].

Radiolysis, a well-known method for producing free radicals, has also been used to generate ions for infrared matrix-isolation study. Proton currents of 20-40 μA were extracted from a radiofrequency

discharge through hydrogen, accelerated to 2 keV, and directed at a condensing matrix sample containing a reagent molecule [10]. The first studies on CCl_4 produced CCl_3^+ at 1037 cm^{-1}, which was stable to photolysis, and photosensitive absorptions at 927, 502, and 374 cm^{-1}, which were attributed to CCl_4^+ and Cl_3^+, in addition to a very large yield of CCl_3 radical at 898 cm^{-1} [10, 11].

Recently, argon discharge tubes have become a major method for producing charged species in matrices. Argon is excited by a microwave discharge while passing through a quartz tube with a 1-mm orifice directed at the sample. Jacox has proposed that the charged products are formed upon collision with excited metastable argon atoms from the discharge tube [12] whereas Wight, et al., have attributed the formation of charged species to photoionization by argon resonance radiation emanating from the open discharge tube owing to the absence of charged products when the 1-mm orifice was placed in the side of the discharge tube [13]. Support for this proposal is found in studies by Smardzewski using a capillary array in the discharge tube to deactivate metastable argon atoms which reduced the charged product yield by the transmission of the array [14]. Further evidence to support radiation as the method of energy transfer from the discharge to the sample comes from studies where a LiF filter placed in front of the discharge tube reduced the product yield to 15 ± 5%, which is appropriate for the transmission of LiF at 11.6-11.8 eV [11]. However, the yield of some charged species was reduced still lower by the LiF filter; this points to a participation by excited argon atoms or higher energy radiation not transmitted by LiF in the reaction mechanism [15]. Further studies in this laboratory employed 3-mm and 10-mm orifice discharge tubes; the yield of charged species increased on going from the 1-mm to the 3-mm orifice tube and the 10-mm open tube produced the highest yield of photolytically stable charged species and a lower yield of photosensitive charged species [15]. The 10-mm open discharge tube operates at lower argon pressure which provides enhanced emission from Ar^+ and higher argon excited states; this tube functions as a windowless resonance lamp with the major output at 11.6-11.8 eV and substantial radiation between 13 and 15 eV [16]. The windowless discharge lamp and sample configuration used in this laboratory is shown in Fig. 1. Reagent molecules are subjected to the intense vacuum ultraviolet radiation from the open discharge tube during condensation with excess argon at 15 K, which traps molecule ions for spectroscopic study.

Another chemical method for producing new charged species, developed by Ault and Andrews, involves the reaction of salt vapor with a suitable precursor molecule during condensation with excess argon at 15 K. Matrix reactions with NaCl and Cl_2 produced $Na^+Cl_3^-$; CsCl and HCl gave $Cs^+HCl_2^-$ [17-19]. This technique is particularly useful for the synthesis of less stable polyhalides like $Cs^+F_3^-$ and $Cs^+BrF_2^-$ for spectroscopic study [20, 21].

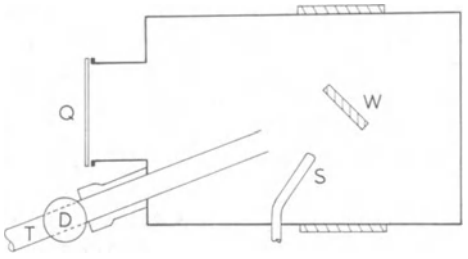

Fig. 1. Vacuum vessel base cross section for matrix photoionization experiments showing position of 15 K cold window-W, gas deposition line-S, open discharge tube-T, microwave discharge cavity-D, and quartz photolysis window-Q.

An electrical discharge technique for producing and trapping charged species in solid argon has been very recently developed by Kelsall and Andrews [22]. Potentials in the +30 to +2000 volts d.c. range were applied to a stainless steel electrode positioned in the center of the cold window and a discharge was maintained in the condensing matrix gas. This method was particularly effective for the production and trapping of CF_3^+.

Spectroscopic measurements on matrix-isolated species have typically involved conventional spectroscopic methods with special sampling techniques developed to obtain the measurement with a particular spectroscopy. Thus, infrared and optical absorption experiments require salt and sapphire or quartz optics for transmission of the examining radiation. Laser-Raman or laser-induced fluorescence experiments use a tilted metal wedge for sample collection; the laser beam is directed vertically at the sample surface and scattered or emitted light is focussed into a monochromator and detection system for analysis [23, 24].

We now turn to the spectroscopy and characterization of a number of interesting molecular ions in noble gas matrices using these techniques. This discussion is not intended to be complete as other recent reviews on the subject have appeared [24-26].

Alkali Metal Superoxides - $M^+O_2^-$

The five alkali superoxide molecules were characterized by sharp weak intraionic $(O \leftrightarrow O)^-$ stretching modes and strong symmetric and antisymmetric interionic $M^+ \leftrightarrow O_2^-$ stretching modes in their infrared spectra; the vibrational assignments were verified by isotopic substitution [2, 7, 27]. The isosceles triangular structure for $Li^+O_2^-$ was dictated by the scrambled oxygen isotopic spectrum, which demonstrated equivalent oxygen atoms, and the $Li^+O_2^-$ ion-pair characterization was first suggested from agreement

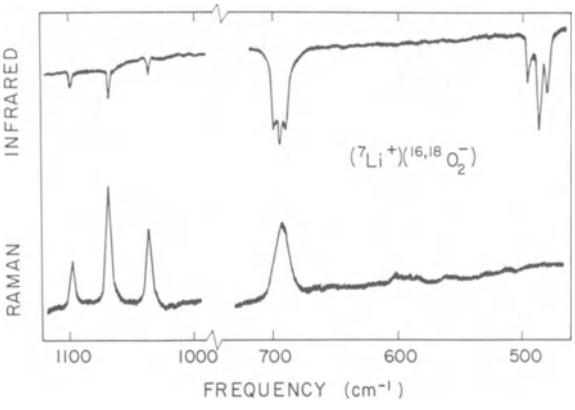

Fig. 2. Infrared and Raman spectra of lithium superoxide, $Li^{+}O_2^{-}$ using lithium-7 and 30% $^{18}O_2$, 50% $^{16}O^{18}O$, 20% $^{16}O_2$ at concentrations of $Ar/O_2 = 100$. Raman spectrum recorded using 200 mW of 4880 Å excitation and long wavelength pass dielectric filter in 1000 cm^{-1} region.

between its $(O \leftrightarrow O)$ stretching mode and the Raman value for O_2^{-} from crystals [1, 2]. The ionic model for $Li^{+}O_2^{-}$ was confirmed by the matrix-Raman spectrum of $Li^{+}O_2^{-}$, which gave a very strong intraionic $(O \leftrightarrow O)^{-}$ stretching mode signal within 0.5 cm^{-1} of the weak infrared absorption with identical isotopic data [24, 28]. Infrared and Raman spectra of the mixed oxygen isotopic $Li^{+}O_2^{-}$ species are compared in Fig. 2. Further support for an $M^{+}O_2^{-}$ ionic model of polarizable ion pairs was derived from the M^{+} effect on the O_2^{-} vibrational frequency, ν_1, which ranged from 1094 cm^{-1} for $Na^{+}O_2^{-}$ to 1114 cm^{-1} for $Cs^{+}O_2^{-}$ as is listed in Table 1. A similar trend was found for the $M^{+}NO^{-}$ molecules [29]. Note the larger dependence of the interionic ν_2 and ν_3 modes on M^{+}. Complementary ESR studies have verified the ionic nature of these $M^{+}O_2^{-}$ molecules [30, 31]. The magnitude of the sodium hyperfine splitting in $Na^{+}O_2^{-}$ demonstrated the bound ion-pair nature of the species and that the Na^{+} ion is located equidistant from the two oxygen atoms.

Optical absorption studies on $M^{+}O_2^{-}$ matrix systems exhibited an absorption near 250 nm, in excellent agreement with the spectrum of O_2^{-} doped into alkali halide crystals [32]. Finally, the LiO_2 molecule has been the subject of a number of theoretical calculations [33] which have verified the charge-transfer model and isosceles triangular geometry for LiO_2 deduced from the infrared matrix spectrum.

Table 1. Fundamental Frequencies (cm^{-1}) Assigned to the ν_1 Intraionic and ν_2 and ν_3 Interionic Modes of the C_{2v} Alkali Metal Superoxide Molecules in Solid Argon at 15 K

Molecule	ν_1	ν_2	ν_3
$^6LiO_2$	1097.4	743.8	507.3
$^7LiO_2$	1096.9	698.8	492.4
NaO_2	1094	390.7	332.8
KO_2	1108	307.5	---
RbO_2	1111.3	255.0	282.5
CsO_2	1115.6	236.5	268.6

$M^+O_3^-$ and O_3^-

Following the alkali metal-oxygen matrix reactions, an extensive study of alkali metal-ozone reactions was performed in this laboratory [34, 35]. The infrared spectra were characterized by very intense bands near 800 cm^{-1} depending upon the alkali atom, and weaker bands near 600 cm^{-1} for the heavier alkali metal reagents. The very strong 800 cm^{-1} bands were assigned to ν_3 and the weak 600 cm^{-1} absorptions were attributed to ν_2 of O_3^- in the $M^+O_3^-$ species, produced by the charge-transfer alkali metal-ozone reaction. The small variation in ν_3 ozonide modes as a function of M^+ demonstrates that the cation is adjacent to the ozonide ion as required by the energetics of the charge-transfer reaction. Similar ESR studies done on the sodium-ozone reaction product observed a quartet subsplitting due to sodium hyperfine structure which verifies the ionic nature of the $Na^+O_3^-$ species [36]. Furthermore, a comparison of the calculated and experimental anisotropic part of the sodium hyperfine splitting tensor determines the location of the Na^+ ion to be above the O_3^- plane and equidistant from the two terminal oxygen atoms; the latter conclusion was also reached from the infrared spectrum of scrambled oxygen isotopic $Na^{+16,18}O_3^-$ species [34].

The infrared ν_3 absorption and a visible electronic band system for the ozonide ion were reported by Jacox and Milligan using the photoreaction of N_2O, O_2 and alkali atoms [37]. These workers proposed a mechanism involving the photoproduction and reaction of

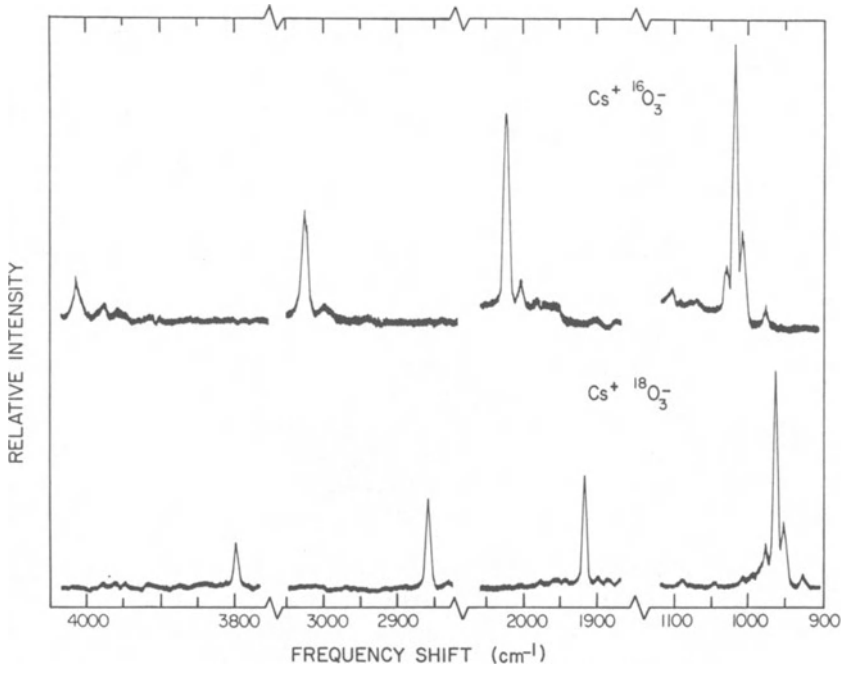

Fig. 3. Resonance Raman spectra of the ozonide ion in $Cs^{+16}O_3^-$ and $Cs^{+18}O_3^-$. All spectra: 20 cm^{-1} min^{-1} scanning speed, 250 μ slitwidth, 1 sec risetime, 65 mW of 4880 Å excitation. Top spectrum: $Ar/^{16}O_3$ = 100, 0.3 × 10^{-9} range. Bottom spectrum: $Ar/^{18}O_3$ = 100, 99.3% oxygen-18, 1 × 10^{-9} range. (Andrews and Spiker, Ref. 35.)

O^- with O_2 to give O_3^-. Andrews and Tevault have argued against this mechanism in favor of O atom reaction with $M^+O_2^-$ to give $M^+O_3^-$ since the bound ion-pair $M^+O_3^-$ species and not "isolated" O_3^- was in fact formed in the photolysis experiments [38]. The intimate involvement of alkali metal atoms is often overlooked in interpreting alkali metal matrix-reaction systems.

The "isolated" O_3^- ion has been produced by proton radiolysis and argon resonance photoionization of argon-oxygen samples [39, 13]. It is interesting to note that the ν_3 fundamental of O_3^- without an adjacent cation, 804.3 cm^{-1}, is in agreement with values for the $Na^+O_3^-$, $Ca^+O_3^-$, $Sr^+O_3^-$, and Ba^+O_3 species but this mode for ion pairs with Li, K, Rb, Cs, and Mg varies from 787 to 844 cm^{-1} [34, 40, 41]. It has been suggested that the Na^+ cation, in the out-of-plane position determined from the ESR study, may not perturb the O_3^- vibrations whereas coplanar $M^+O_3^-$ arrangements may lead to slight metal ion perturbations of the O_3^- vibrations [39].

The Raman studies on $M^+O_3^-$ are of interest in part because of resonance enhancement of the scattering intensity. A detailed study of the vibronic absorption spectrum of $M^+O_3^-$ species in noble gas matrices produced a strong vibronic absorption with 12 components and an origin at 18180 ± 50 cm^{-1}, and ω_1' values of 878 ± 8 cm^{-1} for $Na^{+16}O_3^-$ and 834 ± 8 cm^{-1} for $Na^{+18}O_3^-$ [42]. Accordingly, argon and krypton ion laser lines are ideal for a resonance Raman study of the $M^+O_3^-$ species in solid argon where the low temperature matrix retards decomposition of photosensitive molecules and quenches fluorescence so that the resonance Raman spectrum can be observed.

Blue excitation of $Cs^+O_3^-$ at 488.0 nm yielded a regular progression of fundamental and overtone bands at 1018, 2028, 3024, and 4014 cm^{-1} with decreasing intensities. The $Cs^{+18}O_3^-$ species produced a progression out to $5\nu_1$; bands were observed at 962, 1915, 2859, 3795, and 4724 cm^{-1} [35]. Isotopic ozonide spectra are shown in Fig. 3. The regularly decreasing intensity pattern for an overtone progression is characteristic of the resonance Raman effect.

The use of different exciting lines for a $Na^+O_3^-$ sample produced a profile similar to the absorption spectrum [35]. The 647.1 nm line gave a weak 1011 cm^{-1} fundamental and excitation at 568.2 nm produced a strong fundamental at 1011 cm^{-1} and a weak overtone at 2013 cm^{-1} . The 530.9 nm line produced an intense fundamental, first overtone and a weak second overtone at 3001 cm^{-1}. Excitation at 514.5 nm yielded intense fundamental, intense first and second overtones and a weak third overtone at 3977 cm^{-1}; the 488.0 nm line produced a similar spectrum. The 457.9 nm line gave the intense fundamental and two moderately intense overtones. This increase in overtone intensity relative to fundamental intensity as the exciting wavelength enters the electronic absorption is characteristic of resonance Raman spectra.

$M^+X_2^-$ Species

The alkali dihalide species are of interest as transient intermediates in the alkali metal atom-halogen molecule reaction and for comparison to V centers in irradiated alkali halide crystals. Alkali metal reactions with F_2 produced a strong Raman band between 452 and 475 cm^{-1} depending on the alkali metal counterion, as listed in Table 2, and a strong ultraviolet absorption at 310 nm. The Raman bands were assigned to the intraionic $(F \leftrightarrow F)^-$ mode and the alkali metal dependence was attributed to interaction with the interionic $M^+ \leftrightarrow F_2^-$ mode; the 310 nm absorption was assigned to the $\sigma \leftrightarrow \sigma^*$ transition for F_2^- in the $M^+F_2^-$ species [43, 44].

Matrix reactions of chlorine and alkali metal atoms gave extraordinarily intense Raman signals in the 225-264 cm^{-1} shifted region, again depending on the counterion, which are assigned to the intraionic $(Cl \leftrightarrow Cl)^-$ stretching mode. The alkali metal dependence

Table 2. Fundamental Frequencies (cm^{-1}) Assigned to the ν_1 Intraionic $(X \leftrightarrow X)^-$ Mode of the $M^+X_2^-$ Species Observed in Matrix Raman Spectra

	F_2^-	Cl_2^-	Br_2^-	I_2^-
Li^+	452	256	149	115
Na^+	475	225	115	114
K^+	464	264	160	113
Rb^+	462	260	159	116
Cs^+	459	259	157	115

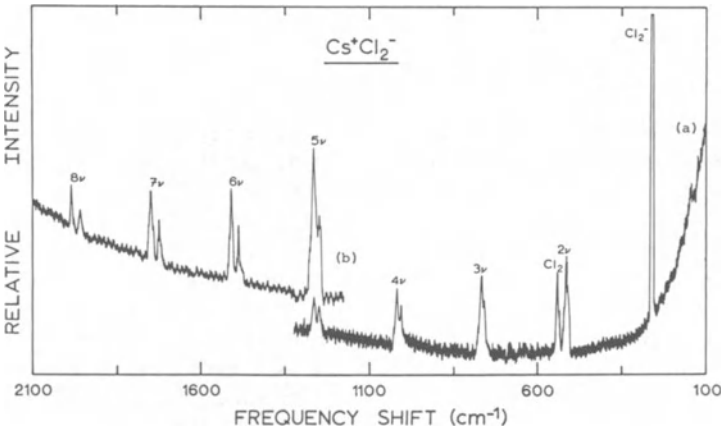

Fig. 4. Resonance Raman spectrum of argon matrix-isolated $Cs^+Cl_2^-$ at 16 K. Note resolution of $^{35}Cl_2^-$ and $^{35}Cl^{37}Cl^-$ splittings in overtones. Parameters: 75 mW of 4579 Å excitation, 20 cm^{-1}/min scan speec, (a) 0.3×10^{-9} A range, 3 sec rise time; (b) 0.1×10^{-9} A range, 10 sec rise time. (Howard and Andrews, Ref. 45.)

is due to interaction with the interionic $M^+ \leftrightarrow Cl_2^-$ stretching mode which is predicted to be higher in the $Na^+Cl_2^-$ case, forcing the $(Cl \leftrightarrow Cl)^-$ mode down to 225 cm^{-1}, and in the $K^+Cl_2^-$ species, the interionic mode is predicted near 200 cm^{-1}, forcing the $(Cl \leftrightarrow Cl)^-$ vibration up to 264 cm^{-1}.

Owing to the orange color of these matrix samples, resonance enhancement of the intensity was suspected and intense overtone

series were observed with argon laser excitation [45]. In the $Cs^+Cl_2^-$ case, 457.9 excitation produced an extremely strong 259 cm^{-1} fundamental and seven overtones with regularly decreasing intensities and increasing resolution of chlorine isotopic splittings out the progression, which is illustrated in Fig. 4. A very strong optical absorption at 350 nm is responsible for the resonance Raman intensity enhancement for the $M^+Cl_2^-$ species [44]. This near-ultraviolet absorption for the dichloride ion in the $M^+Cl_2^-$ species is in excellent agreement with the 350 nm maximum in the photodissociation cross-section of the gaseous Cl_2^- ion [46]. The matrix-isolated $M^+Cl_2^-$ species is stabilized sufficiently by the ion-pair arrangement in the matrix to enable resonance Raman spectra of Cl_2^- to be obtained without shifting the electronic spectrum of the Cl_2^- anion.

Resonance Raman and optical spectra have been observed for the $M^+Br_2^-$, $M^+I_2^-$, and $M^+I_3^-$ species [47-50]. Red laser excitation produced resonance Raman spectra for I_2^- in the $M^+I_2^-$ ion pair. Spectra for I_3^- in the $M^+I_3^-$ species compare very favorably with solution spectra [51].

Bihalide Ions - HX_2^- and $M^+HX_2^-$

Perhaps the most interesting controversy in matrix-isolation spectroscopy over the last decade has involved the bichloride species. Noble and Pimentel first reported strong new absorptions at 696 and 956 cm^{-1} after passing $Ar/HCl/Cl_2$ mixtures through a coaxial microwave discharge tube and onto a 14 K surface. Chlorine isotopic splittings on the 956 cm^{-1} band required two equivalent chlorine atoms and the H/D frequency ratio for the strong absorption, 696/464 = 1.50, indicated a centrosymmetric species which was identified as ClHCl radical [52]. Milligan and Jacox observed the same two absorptions following hydrogen resonance photolysis of Ar/HCl samples and mercury arc photolysis of Ar/HCl/Cs mixtures and suggested that these two absorptions might instead be contributed by the $(ClHCl)^-$ anion [53]. Similar studies on HBr systems were interpreted as BrHBr radial or anion [54, 55]. The formation of bihalide anions was suggested to involve dissociative electron capture of HX into H and X^- with bihalide anion stabilization resulting from subsequent reaction of X^- with HX [55].

The absorptions attributed to $ClHCl^-$ by Milligan and Jacox were independent of the nature of the electron donor which characterize these anions as "isolated" from their counterion in the matrix. In the alkali metal experiments with HCl and HBr, weak bands appeared before photolysis which were produced in great yield by the matrix reaction of the hydrogen halide with alkali halide molecules and identified by Ault and Andrews as the bound ion-pair $M^+HCl_2^-$ and $M^+HBr_2^-$ species [17, 18, 56]. The near agreement between the infrared absorptions for the $M^+HCl_2^-$ species and the 696 cm^{-1} absorption, which are compared in Table 3, provides strong support for the isolated HCl_2^- anion identification.

Table 3. Antisymmetric Hydrogen and Deuterium Stretching Fundamentals (cm^{-1}) for Isolated Bihalide Ions and $M^+HX_2^-$ Ion Pairs in Solid Argon

Ion	H	D
HF_2^-	1377	965[a]
$Na^+HF_2^-$	1284	935[b]
$K^+HF_2^-$	1314	958[b]
$Cs^+HF_2^-$	1364	969[b]
HCl_2^-	696	464[c]
$Na^+HCl_2^-$	658	436[d]
$K^+HCl_2^-$	737	498[d]
$Rb^+HCl_2^-$	729	512[d]
$Cs^+HCl_2^-$	723	507[d]
HBr_2^-	728	498[e]
$Na^+HBr_2^-$	670	478[f]
$K^+HBr_2^-$	726	509[f]
$Rb^+HBr_2^-$	729	507[f]
$Cs^+HBr_2^-$	727	504[f]
HI_2^-	682	470[g]
$Na^+HI_2^-$	603[h]	
$K^+HI_2^-$	670[h]	
$Rb^+HI_2^-$	674[h]	
$Cs^+HI_2^-$	673	468[h]

[a]Ref. 59. [b]Ref. 58. [c]Ref. 55.

[d]Ref. 18. [e]Ref. 55. [f]Ref. 56.

[g]P.N. Noble, J. Chem. Phys. 56, 2088 (1972).

[h]C.M. Ellison and B.S. Ault, J. Phys. Chem. 83, 832 (1979).

A series of microwave discharge experiments performed in this laboratory showed that hydrogen atoms and chlorine codeposited without vacuum ultraviolet light produced HCl without any of the 696 cm^{-1} absorption. However, when the coaxial discharge was exposed to the matrix with the same reagents, the 696 cm^{-1} band was an intense component of the product spectrum. It was suggested that ionizing radiation from the coaxial discharge was required to produce the 696 cm^{-1} band which supported its charged identification [13].

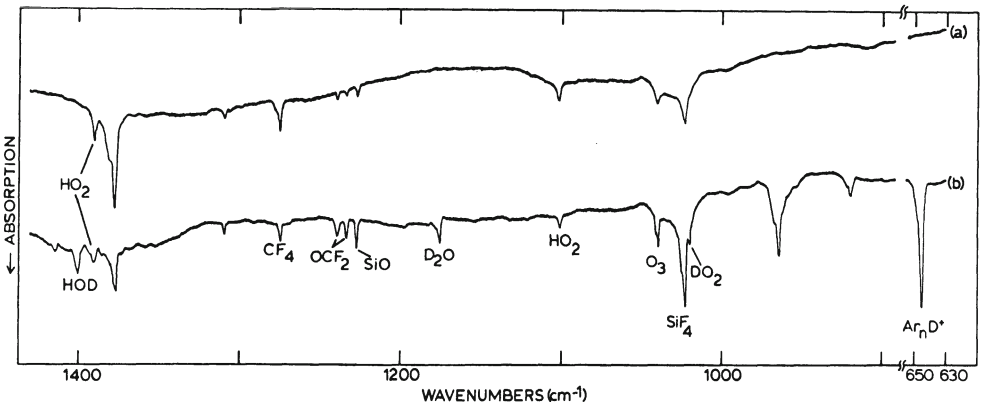

Fig. 5. Infrared spectra of argon-hydrogen fluoride samples subjected to windowless argon discharge photoionization during condensation at 15 K. (a) Ar/HF = 100/1.., (b) Ar/DF, HF = 100/1. Since a comparable amount of argon from the discharge was condensed with the sample, the Ar/HF ratio is greater than 200/1 in the matrix. (McDonald and Andrews Andrews, Ref. 59.)

The most stable member of this series, bifluoride ion, is well-known as a crystalline material with a centrosymmetric $(FHF)^-$ ion [57], and its characterization in matrices completes the case for bihalide ions in matrices. In studies by Ault, the matrix reaction of CsF and HF produced a very strong 1364 absorption and a sharp 1217 cm^{-1} band which were assigned to ν_3 and ν_2 of HF_2^- in the $Cs^+HF_2^-$ species; the 1364/969 = 1.41 ratio indicated the centrosymmetric nature of the bifluoride ion in the ion-pair species [58].

Photoionization experiments in this laboratory using the open discharge tube shown in Fig. 1 and Ar/HF = 100/1 samples produced a strong new absorption at 1377.0 cm^{-1}; the 1377 cm^{-1} band intensity was increased in similar experiments with F_2 and NF_3 added to the argon-hydrogen fluoride sample. The strongest new product band appeared at 965.5 cm^{-1} in the corresponding DF experiment with no new absorption between this new band and the 1377 cm^{-1} feature observed due to HF remaining in the vacuum system. The 1377.0 and 965.5 cm^{-1} absorptions shown in Fig. 5 are assigned to the ν_3 modes of the isolated HF_2^- and DF_2^- ions, respectively. The 1377.0/965.5 = 1.426 ratio shows that HF_2^- is also centrosymmetric as the isolated or "gas-phase" species [59]. Finally, agreement between the 1377 cm^{-1} isolated HF_2^-, the 1364 cm^{-1} "bound" ion-pair $Cs^+HF_2^-$, and the 1450-1550 cm^{-1} crystalline bifluoride stretching fundamentals reinforces the comparison between HCl_2^- and $M^+HCl_2^-$ species [18] and confirms the anion identification of the 696 cm^{-1} absorption as HCl_2^-.

Ar_nH^+ and Ar_nD^+

Bondybey and Pimentel codeposited argon-hydrogen and argon-deuterium mixtures from a coaxial discharge tube and observed photosensitive new absorptions at 904 and 644 cm^{-1} which were assigned to interstitial H-atom and D-atom vibrations, respectively [60]. Although these workers considered the possibility of a charged species, it was rejected at least in part because of the absence of a counter-ion absorption. Milligan and Jacox observed these two absorptions in a number of hydrogen resonance photolysis experiments, noted the increased yield when strong electron acceptors were added, and reassigned the bands to Ar_nH^+ and Ar_nD^+ [61]. In radiolysis experiments performed in this laboratory, the codeposition of deuterons with argon produced the 644 cm^{-1} band in moderate yield; however, with added Cl_2 reagent the very strong DCl_2^- band was observed along with a completely absorbing 644 cm^{-1} band [39]. The observation of the 644 cm^{-1} band with the deuteron beam, coupled with the absence of this absorption when D-atoms were codeposited from an off-axis discharge tube [62] strongly supports the charged species identification.

Wight, et al., passed Ar/D_2 mixtures through a coaxial discharge and observed both DO_2 and the 644 cm^{-1} band in contrast to the off-axis discharge experiments which produced only DO_2 [13]. This suggested that the most probable mechanism for the formation of Ar_nD^+ is direct photoionization of a D atom in the argon matrix with a large solvent shift in the ionization to lower energy owing to the large proton affinity of argon. With this solvent shift, argon resonance (11.6-11.8 eV) and hydrogen resonance (10.2 eV) radiation are energetic enough to photoionize a D atom. The 644 cm^{-1} band has been observed in numerous argon resonance photoionization experiments in this laboratory where deuterium enriched precursors were used, for example, DF, DCl, CDF_3, and CD_2F_2. The requirements for the production of the 644 cm^{-1} band are a D atom in solid argon and ionizing radiation which contribute more evidence for the Ar_nD^+ charged species assignment.

In an interesting series of haloform experiments, which will be described later, Jacox and Andrews and coworkers have observed marked growth of the 904 and 644 cm^{-1} absorptions on mercury arc photolysis of $(CHX_2^+)X$ and $(CDX_2^+)X$ species (X = Cl, Br) [12, 63]. Similar photochemical results have been found for the CH_2Cl_2 and CD_2Cl_2 precursors with the 904 cm^{-1} band reaching A = absorbance units = 0.18 and the 644 cm^{-1} absorption reaching A = 1.2 on 220-1000 nm photolysis [64]. In these examples, mercury arc photolysis affects a transfer of the proton and deuteron from the halocarbon cations to the argon matrix and provides a photochemical synthesis of the Ar_nH^+ and Ar_nD^+ species.

The photochemical stability and yield of the Ar_nH^+ and Ar_nD^+ species depend in general on the nature and abundance of the counterion in the matrix. In experiments depositing only deuterons or D-atoms with vacuum ultraviolet light, the counterion must come from common impurities in the vacuum system such as O_2 and H_2O which could produce anions like O^-, O_2^-, and OH^- by electron attachment to molecular fragments. Counterions like O_2^-, O^-, and OH^- with relatively low energy detachment thresholds are expected to release electrons at comparatively lower energies for neutralization of the Ar_nD^+ ion isolated nearby in the matrix. On the other hand, chlorine present in the sample traps electrons as Cl^- and allows more Ar_nD^+ to be isolated during sample preparation. A photochemical reduction of the positive ion absorption in these experiments requires detachment from Cl^- in the near ultraviolet range, as has been observed in this laboratory. In experiments with CDF_3, the CF_3^+ and Ar_nD^+ cations were each reduced about 10% on 220-1000 nm photolysis for 2 h by photoelectrons detached from fluoride ion electron traps in the argon matrix.

Trihalomethyl Cations

Jacox and Milligan performed hydrogen resonance photolysis of argon/chloroform samples and observed a large yield of CCl_3 radical at 898 cm^{-1} and a new 1037 cm^{-1} absorption. The latter band showed the 3/1 doublet splitting characteristic of three equivalent chlorine atoms and a carbon-13 shift to 1003 cm^{-1} which supported its identification as CCl_3^+ isolated in the matrix [65]. Subsequent radiolysis studies of CCl_4, CCl_3Br, CCl_2Br_2, $CClBr_3$, and CBr_4 in this laboratory produced the 1037 cm^{-1} band, absorptions at 1019 and 957 cm^{-1} for CCl_2Br^+, absorptions at 978 and 894 cm^{-1} for $CClBr_2^+$ and a new band at 874 cm^{-1} for CBr_3^+, each from two of the above precursors, which confirmed the trichloromethyl cation identification of the 1037 cm^{-1} band. Absorptions for trihalomethyl cations are listed in Table 4. The radiolysis experiments with CCl_4 produced major new photosensitive bands at 927, 502, and 374 cm^{-1} in addition to the strong photochemically stable 1037 cm^{-1} band. In order to rationalize the different bulb filament photolysis behavior, the photosensitive bands were assigned to isolated cations and the stable 1037 cm^{-1} band to CCl_3^+ with a nearby chloride ion which would not attract electrons in the photobleaching process [10]. In a following argon resonance photoionization study of CCl_4 using filtered mercury arc photolysis of the deposited sample, the different photochemical behavior of each new absorption was attributed to the photochemical stability of the cation in question. The photosensitive 927 and 374 cm^{-1} bands were assigned to an asymmetric CCl_4^+ species and the 502 cm^{-1} absorption to Cl_3^+. The 1037 cm^{-1} CCl_3^+ band was decreased slightly by prolonged mercury arc photolysis, which required photodetachment from chloride electron traps in the matrix, since CCl_3^+ itself probably does not dissociate in the mercury arc energy range [11]. A small shift of the 1037 cm^{-1} CCl_3^+ band in solid argon to

1035 cm^{-1} in solid krypton suggests that CCl_3^+ does not interact strongly with either matrix. An important conclusion from the mercury arc photolysis studies is that isolated cations in matrices will be of two types: those which photodissociate with mercury arc light and those photochemically stable in the mercury arc range which must exhibit a decrease in intensity from photoneutralization by detachment of electrons from counteranions in the matrix. In this regard, appearance potential data are useful for predicting the photochemical behavior of cations. Clearly, photodetachment will depend on the electron trapping species, as will be discussed below for CF_3^+.

In order to bridge the gap from CCl_3^+ at 1037 cm^{-1} to CF_3^+, photoionization and radiolysis studies were performed in this laboratory on the Freon series $CFCl_3$, CF_2Cl_2, and CF_3Cl [66, 15]. Sharp new bands at 1352 and 1142 cm^{-1} in $CFCl_3$ experiments exhibited appropriate carbon-13 shifts and photolysis behavior for assignment to $CFCl_2^+$. Analogous bands in CF_3Cl experiments at 1415 and 1515 cm^{-1} showed large carbon-13 shifts and slight photolysis with the full mercury arc which indicated assignment to CF_2Cl^+. These vibrations for $CFCl_2^+$ and CF_2Cl^+ are 200-300 cm^{-1} above the corresponding free radical values which predicts that CF_3^+ may absorb above 1600 cm^{-1}.

Photoionization studies were performed on the trifluoromethyl compounds CF_3Cl, CF_3Br, CF_3I, and CHF_3 and the spectrum from the CF_3X studies [67] is shown in Fig. 6. Note the CF_2Cl^+ absorptions at 1514 and 1414 cm^{-1} which shifted to 1483 and 1367 cm^{-1} for CF_2Br^+, as has also been observed by Jacox [68], and the CF_2I^+ absorptions at 1431 and 1320 cm^{-1}. The C-F stretching modes in the CF_2X^+ ions exhibited a pronounced heavy halogen effect. A weak 1665 cm^{-1} band in the CF_3Cl study was produced with greater intensity in the CF_3Br, CF_3I, and CHF_3 experiments at the same frequency [67]. This 1665 cm^{-1} absorption was reduced 10% by full high-pressure mercury arc photolysis for 2 hours in fluoroform experiments. The production of the same 1665.2 cm^{-1} band from four different trifluoromethyl precursors, and the photolysis behavior indicate assignment of the 1665 cm^{-1} band to CF_3^+. The trifluoromethyl cation is formed by photoionization of CF_3 radicals produced in the matrix photolysis process [67].

Infrared spectra for CF_3^+ and $^{13}CF_3^+$ in fluoroform experiments are compared in Fig. 7. The strong absorption produced from $^{13}CHF_3$ at 1599.2 cm^{-1} (A = 0.20) is appropriate for ν_3 of $^{13}CF_3^+$; note the weak $^{12}CF_3^+$ absorption (A = 0.020) at 1665.2 cm^{-1} due to 10% ^{12}C present in the enriched fluoroform precursor. The ^{12}C-^{13}C shift, 66.0 cm^{-1}, is however, greater than expected for the antisymmetric C-F vibration, ν_3, of a planar centrosymmetric species. This unexpectedly large carbon-13 shift can be explained by Fermi resonance between ν_3 and the combination band ($\nu_1 + \nu_4$) for the $^{13}CF_3^+$ species,

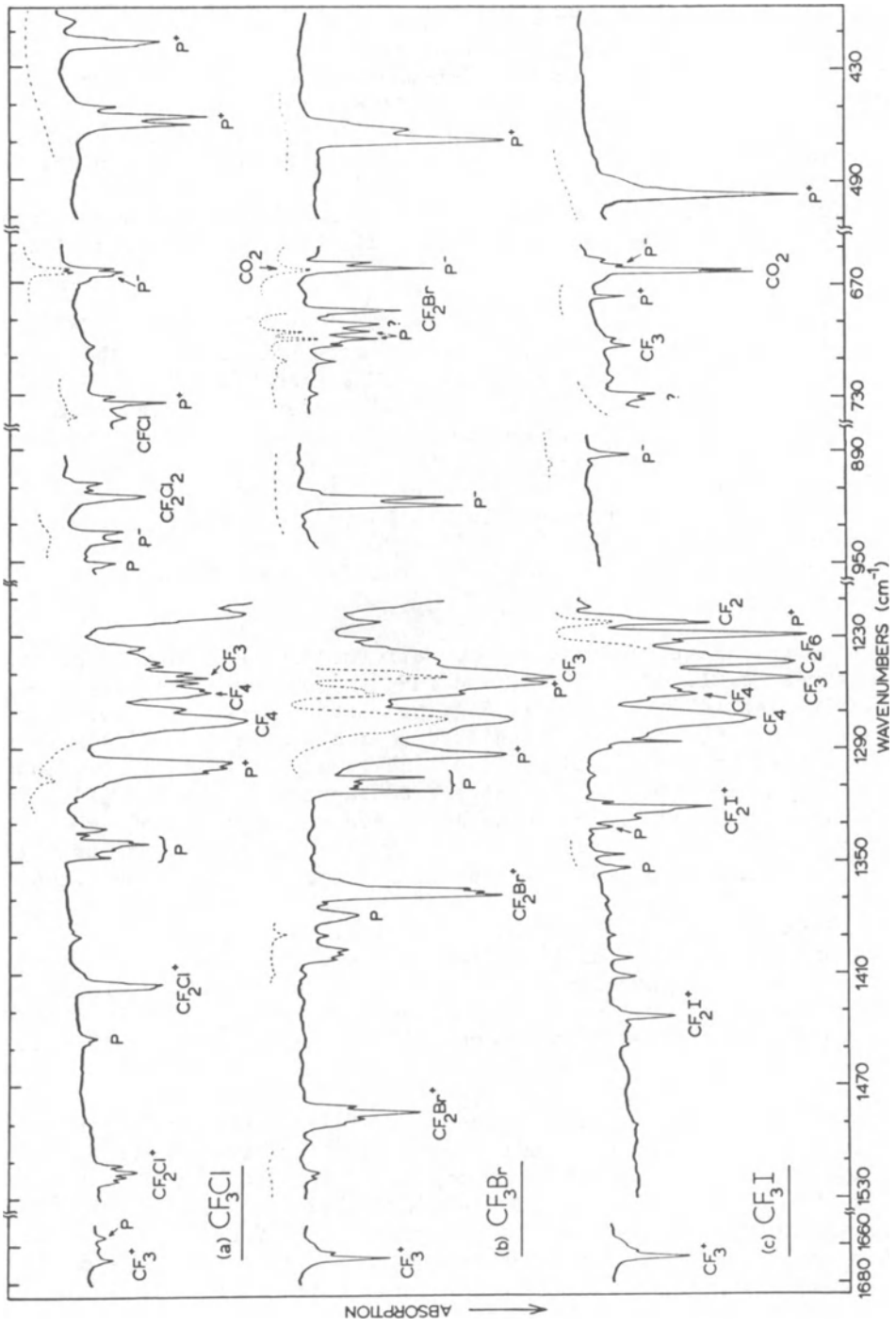
(a) CF_3Cl
(b) CF_3Br
(c) CF_3I
CF_3^+
CF_2Cl^+
CF_2Br^+
CF_2I^+
$CF_3C_2F_6$
CF_4
CF_2Cl_2
$CFCl$
CF_2Br
CO_2
P
P*
P-
P'
P'-
?
ABSORPTION
WAVENUMBERS (cm^{-1})
1680 1660 1530 1470 1410 1350 1290 1230 950 890 730 670 490 430

since the new 1641.7 cm^{-1} product band in the $^{13}CF_3^+$ spectrum can be assigned to the combination band. The calculated position of ν_3 for $^{13}CF_3^+$, 1620 cm^{-1}, appears to coincide with the apparent position of $(\nu_1 + \nu_4)$, and these modes strongly interact and shift ν_3 down to 1599 cm^{-1} and $(\nu_1 + \nu_4)$ up to 1642 cm^{-1}. In the absence of Fermi resonance, the $(\nu_1 + \nu_4)$ combination band for $^{12}CF_3^+$ is expected to be 2-4 cm^{-1} above the $^{13}CF_3^+$ counterpart, in the region of the 1624 cm^{-1} water absorption; the spectrum in Fig. 7b shows the 1624 cm^{-1} band, which may contain additional absorption. The markedly increased CF_3^+ yield in the electric discharge experiment, Fig. 7d, revealed a very strong 1665.2 cm^{-1} absorption (A = 0.84 and 1624 cm^{-1} absorption (A = 0.40) clearly in excess of the other water absorptions present [22]; the latter absorption is assigned to the combination band $(\nu_1 + \nu_4)$ for $^{12}CF_3^+$.

The combination $(\nu_1 + \nu_4)$ for $^{12}CF_3^+$ at 1624 cm^{-1} provides a basis for determining the infrared inactive symmetric C-F bond stretching mode ν_1 of $^{12}CF_3^+$. The intensity of the ν_2 and ν_4 modes of BF_3 are approximately a factor of ten weaker than that of ν_3; the failure to observe these weaker fundamentals of CF_3^+ in the present study is not surprising. However, ν_4 may be estimated to be 500 ± 30 cm^{-1} since ν_4 = 512 cm^{-1} for CF_3 [69] and 480 cm^{-1} for BF_3 [70], which predicts ν_1 = 1125 ± 30 cm^{-1} for $^{12}CF_3^+$.

It is interesting to consider the bonding in CF_3^+ in view of its substantially increased antisymmetric stretching frequency and the increased symmetric stretching frequency deduced from the $(\nu_1 + \nu_4)$ band. This increase is considerable relative to the pyramidal CF_3 species (ν_1 = 1086 cm^{-1}, ν_3 = 1251 cm^{-1}) [69]; and relative to the planar $^{11}BF_3$ molecule (ν_1 = 888 cm^{-1}, ν_3 = 1454 cm^{-1}) [70] as well. From the well-known back-donation of fluorine 2p electron density to the positive carbon, it is readily apparent that CF_3^+ should exhibit extensive π (p-p) bonding, and the markedly increased ν_3 and ν_1 modes are consistent with this bonding model.

Fig. 6. Infrared spectra following open discharge tube photoionization of trifluoromethyl halides during condensation with excess argon at 15 K for 20 h. (a) Ar/CF_3Cl = 300/1; (b) Ar/CF_3Br = 400/1; (c) Ar/CF_3I = 400/1. Since the samples were condensed with a comparable amount of argon, the reagent concentration in the matrix is half the sample value. The dashed inset scan with each trace shows changes caused by 290-1000 nm high-pressure mercury arc photolysis. Parent absorptions are labeled P. (Prochaska and Andrews, Ref. 67.)

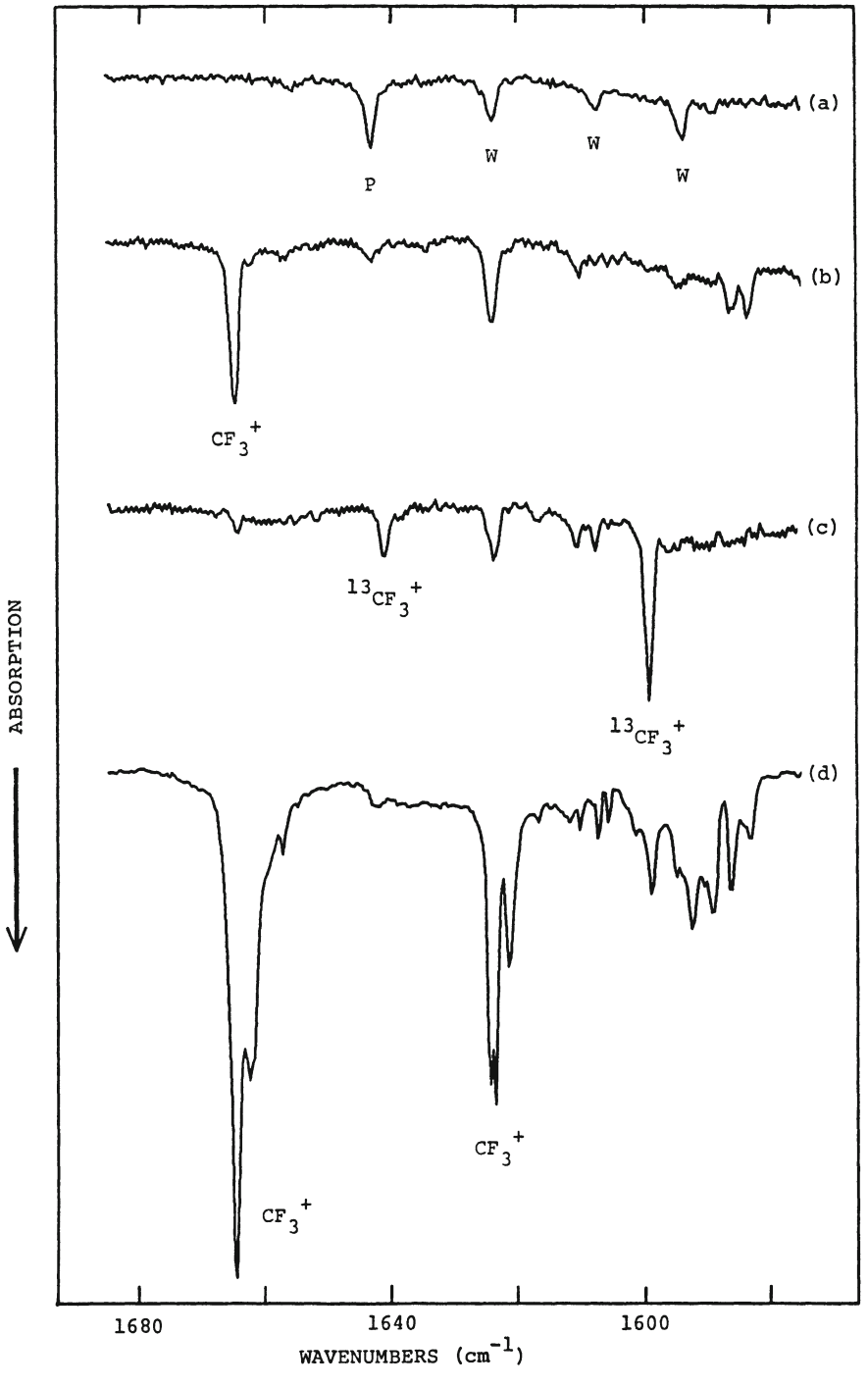
(a)
P
W
W
W
(b)
CF_3^+
(c)
$^{13}CF_3^+$
$^{13}CF_3^+$
(d)
CF_3^+
CF_3^+
ABSORPTION
1680
1640
1600
WAVENUMBERS (cm^{-1})

The photolysis behavior of the 1665 cm^{-1} CF_3^+ absorption in CHF_3, CF_3Cl, CF_3Br, and CF_3I experiments provides evidence for the halide counterion in these studies [67]. Since dissociation of CF_3^+ to $CF_2^+ + F$ requires about 5 eV, which is above the mercury arc range, a photoneutralization mechanism is required for its slight decrease on full mercury arc photolysis. The relative decrease in the CF_3^+ band on 290-1000 and 220-1000 nm photolysis in these experiments was more pronounced in the order $I^- > Br^- > Cl^- > F^-$ where these halide ions are the most likely counterions in photoionization studies with CF_3I, CF_3Br, CF_3Cl, and CHF_3, respectively. This photolysis behavior parallels the expected photodetachment cross section in the halide series and supports the photoneutralization model for the photolysis of CF_3^+ isolated in a matrix containing halide ions.

Parent Cations

Tetrahalomethane parent cations are characterized by their instability with respect to halogen elimination owing in part to the unusual stability of the CX_3^+ daughter cations discussed above. A good example is CCl_4^+, which has escaped gas-phase detection due to the ease of formation of CCl_3^+. The strongest photosensitive band at 927 cm^{-1} and a weaker 374 cm^{-1} band in matrix photoionization studies of CCl_4 have been recently assigned to CCl_4^+ in an asymmetric C_{2v} structure; these absorptions were virtually destroyed by 500-1000 nm photolysis [11]. In a subsequent optical absorption study of the matrix photoionization of CCl_4, a very strong 425 nm band, also destroyed by 500-1000 nm photolysis, was assigned to CCl_4^+ in solid argon [71].

The matrix photoionization studies with $CFCl_3$ produced infrared bands at 1214 and 1041 cm^{-1} and an optical band at 405 nm which were destroyed by 500-1000 nm photolysis; these absorptions were assigned to $CFCl_3^+$ [66, 71]. Similar investigations of CF_2Cl_2 yielded infrared bands at 1234, 1067, 609, and 406 cm^{-1} and an optical band at 310 nm related by their partial photolysis with 290-1000 nm light, which were assigned to $CF_2Cl_2^+$ [15, 71]. Similar spectroscopic ob-

Fig. 7. Infrared spectra in the 1580-1680 cm^{-1} region for fluoroform samples condensed with excess argon at 15 K. Spectrum (a) Ar/CH_3 = 200/1 sample deposited with no discharge, P denotes precursor and W denotes water absorptions; trace (b) Ar/CHF_3 = 800/1 with concurrent argon resonance photoionization. Spectrum (c) $Ar/^{13}CHF_3$ = 800/1 with argon resonance photoionization; trace (d) Ar/CHF_3 = 700/1 with electric discharge on matrix surface during condensation.

Table 4. Carbon-Halogen Stretching Vibrations (cm^{-1}) Observed for Trihalomethyl Cations in Solid Argon

Ion	C-F	C-Cl	C-Br
CF_3^+	1665		
CF_2Cl^+	1514,1414		
$CFCl_2^+$	1351	1142	
CCl_3^+		1037	
CCl_2Br^+		1019,957	
$CClBr_2^+$		978	894
CBr_3^+			874
CF_2Br^+	1483,1367		
CF_2I^+	1432,1320		

servations have been made for the analogous CBr_4^+, $CFBr_3^+$, and $CF_2Br_2^+$ species [11, 71, 72].

Figure 6 shows strong bands labeled P^+ at 1299 cm^{-1} in the CF_3Cl spectrum, 1293 and 1255 cm^{-1} in the CF_3Br scan and 1229 cm^{-1} in the CF_3I spectrum, which along with lower frequency absorptions at 455, 469, and 497 cm^{-1}, respectively, photolysed with 290-1000 nm light that had little effect on the CF_3^+ and CF_2X^+ absorptions. An optical band at 295 nm in the CF_3Cl study showed similar photolysis behavior. These absorptions were assigned to the CF_3X^+ parent cations [67, 71]. It is interesting to note that the matrix photolysis behavior parallels the gas phase stability [73, 74] of these parent cations with more energetic radiation required to dissociate the more stable ion in the order $CF_2Cl_2^+ > CF_3Cl^+ > CFCl_3^+ > CCl_4^+$.

The methylene halide cations provide another interesting series of parent cations for comparison to gas phase studies including photoelectron spectra. Matrix photoionization work on CH_2Cl_2 produced infrared absorptions at 1194 and 764 cm^{-1} which were destroyed by 650-1000 nm photolysis; analogous bands were observed at 1129 and 685 cm^{-1} in CH_2Br_2 studies. Since $CH_2Cl_2^+$ and $CH_2Br_2^+$ require only 0.8 eV for dissociation in the gas phase [73, 75], the photosensi-

tive matrix absorptions were assigned to the $CH_2Cl_2^+$ and $CH_2Br_2^+$ parent ions [64]. Further 290-1000 nm mercury arc photolysis in these experiments produced marked growth in CHX_2 radical, and CHX_2^+ and Ar_nH^+ cation absorptions. The $CHBr_2$ radical and cation absorptions have been observed in both argon and krypton matrices; $CHBr_2$ absorbs at 1166 and 786 cm^{-1} in argon and at 1162 and 782 cm^{-1} in krypton; $CHBr_2^+$ absorbs at 1229 and 897 cm^{-1} in argon and at 1222 and 890 cm^{-1} in krypton. The argon-krypton matrix difference is 7 cm^{-1} for $CHBr_2^+$ and 4 cm^{-1} for $CHBr_2$ suggesting that the cation interacts only slightly more with the matrix than the free radical.

Methylene fluoride provides an interesting contrast to methylene chloride since first ionization in the former involves a C-H bonding electron. Matrix photoionization of CH_2F_2 using the open discharge tube shown in Fig. 1 produced a rich infrared spectrum [76]. Sharp bands at 2854, 2744, 1408, and 1255 cm^{-1} exhibited large carbon-13 displacements, in agreement with the ν_6, ν_1, ν_8, and ν_9 modes of the parent molecule, and photolysed with 420-1000 nm light, which suggests their assignment to the parent cation. The infrared spectrum of $CH_2F_2^+$ is consistent with SCF calculations on the highest occupied orbital for CH_2F_2 which is strongly $C\text{-}H_2$ bonding and $C\text{-}F_2$ antibonding. The removal of an electron from this orbital reduces the $C\text{-}H_2$ stretching fundamentals by 214 and 178 cm^{-1} in the cation and increases the antisymmetric $C\text{-}F_2$ stretching mode by 176 cm^{-1}. An 80-130 cm^{-1} increase in the C-F stretching fundamentals for the CF_3Cl^+, $CF_2Cl_2^+$, and $CFCl_3^+$ parent ions has also been observed [15, 66]. A remaining sharp 1608, 1605 cm^{-1} doublet in the CH_2F_2 studies was reduced only 10-20% by 220-1000 nm photolysis, and its carbon-13 and deuterium isotopic data are consistent with assignment to the CHF_2^+ daughter ion [76].

The fluorohalomethane studies follow the example of methylene fluoride even though a halogen lone pair electron is removed in ionization. In the CH_2FCl experiments, a sharp band at 2902 cm^{-1} and a chlorine isotopic doublet at 874, 869 cm^{-1} exhibited carbon-13 and deuterium shifts similar to the symmetric C-H and C-Cl stretching modes of the neutral molecule and photolysed with 290-1000 nm light, which indicates their assignment to CH_2FCl^+ [77]. The C-H stretching mode for the ion again falls below the 2997 cm^{-1} parent value and the C-Cl stretching mode is above the 750 cm^{-1} neutral value. Similar observations were found for the CH_2FBr^+ and CH_2FI^+ parent ions. With each of the CH_2FX precursors, the $CHFX^+$ daughter ion was characterized by its C-F stretching mode near 1400 cm^{-1} and C-H deformation mode near 1290 cm^{-1} [77].

The boron trichloride and boron tribromide cations have been observed in solid argon following argon resonance photoionization of the molecules during condensation with excess argon at 15 K [78]. The $^{11}BCl_3^+$ and $^{10}BCl_3^+$ absorptions at 1091 and 1133 cm^{-1} were resolved into 9/1/3/1 quartets, as expected for a doubly degenerate

vibration of three equivalent chlorine atoms, identical to that observed for $^{11}BCl_2$ and $^{10}BCl_2$ at 946 and 984 cm^{-1}, respectively. The $^{11}BBr_3^+$ and $^{10}BBr_3^+$ absorptions at 931 and 971 cm^{-1} also appeared above the analogous neutral precursor absorptions at 815 and 850 cm^{-1}. The substantial increases in ν_3 of the BX_3 cations as compared to the neutrals is due to the B-X antibonding nature of the in-plane halogen-lone pair molecular orbital from which the electron is removed upon ionization. Optical absorption studies revealed new ultraviolet bands at 320 and 355 nm in solid argon which were assigned to BCl_3^+ and BBr_3^+, respectively, in excellent agreement with the difference between 1 a_2' and 2e' photoelectron bands corresponding to dipole allowed transitions of the ions at 318 ± 8 and 340 ± 10 nm in the gas phase [79]. The infrared and ultraviolet parent cation absorptions were substantially reduced by 340-600 nm and destroyed by 290-1000 nm photolysis. This behavior is consistent with the dissociation of BCl_3^+ to BCl_2^+ and Cl which is expected from appearance potential data. Boron trihalide and halomethane parent cations are photosensitive species, and their photolysis behavior has facilitated their identification from infrared matrix spectra.

Matrix photoionization studies of CF_2CFCF_3 are of interest for comparison to infrared multiphoton dissociation spectra (IRMPDS) and photoelectron spectra (PES). Experiments with CF_2CFCF_3 produced new photosensitive absorptions at 1543, 1414, and 1062 cm^{-1} which are assigned to the perfluoropropene radical cation [80]. Excellent agreement with 1550 ± 50 cm^{-1} spacing in the first photoelectron band indicates assignment of the 1543 cm^{-1} band to the C-C stretching mode of the radical cation π-bond. Near agreement of the 1062 cm^{-1} band and the 1044 ± 2 cm^{-1} peak from the infrared multiphoton dissociation spectrum supports assignment of these bands to the same vibration, suggested to involve symmetric-CF_2 stretching character. The 1414 cm^{-1} band is assigned to the antisymmetric-CF_2 mode. The C-F vibrations in the molecular cation absorb slightly higher frequency radiation than the neutral molecule, 1062 cm^{-1} compared to 1033 cm^{-1}, and 1414 cm^{-1} compared to 1397 cm^{-1}; however, the C=C vibration is reduced substantially from 1795 cm^{-1} to 1543 cm^{-1}, owing to ionization of a π-bonding electron.

CX_2^+ and CHX_2^+ Cations

Very recent infrared studies of dihalocarbene cations are of interest as the first observation of second daughter cations and the largest increase in a vibrational mode on ionization. In the CH_2Cl_2 experiments described above, a weak 1197, 1194, 1191 cm^{-1} triplet remained after mercury arc photolysis [64]. This same resolved triplet was three-fold stronger in matrix photoionization studies with $CHFCl_2$ and exhibited the 9/6/1 relative intensities expected for a vibration of two equivalent chlorine atoms [81]. No deuterium shift was found in CD_2Cl_2 and $CDFCl_2$ studies. An experiment with a 90% carbon-13 enriched $^{13}CHFCl_2$ sample produced weak carbon-12 absorp-

Table 5. Antisymmetric Carbon-Halogen Stretching Fundamentals (cm^{-1}) for Dihalocarbene Cations, Dihalomethyl Cations and Dihalocarbenes

Species	C-F	C-Cl	C-Br
CF_2^+	1588[a]		
CHF_2^+	1608[b]		
CF_2	1102[c]		
CCl_2^+		1197[d]	
$CHCl_2^+$		1045[e]	
CCl_2		746[f]	
$CClBr^+$		1122[d]	
$CHClBr^+$		993[e]	
$CClBr$		744[g]	
CBr_2^+			1019[d]
$CHBr_2^+$			897[e]
CBr_2			641[g]

[a]Ref. 91. [b]Ref. 76. [c]Ref. 69.

[d]Ref. 81. [e]Ref. 64. [f]Ref. 82. [g]Ref. 83.

tions at 1197 and 1194 cm^{-1} and strong new carbon-13 bands at 1158 and 1155 cm^{-1}, showing that this vibration involves a single carbon atom. The antisymmetric carbon-chlorine stretching absorption of CCl_2 has been well documented at 746 cm^{-1} [82]. The 1197, 1194, 1191 cm^{-1} triplet due to a new (CCl_2) species is higher than $CHCl_2^+$ at 1045 cm^{-1} and $CFCl_2$ at 1142 cm^{-1} [66, 69], which indicates that the new triplet is due to CCl_2^+ [81]. Dichlorocarbene cation was produced in these experiments by photoionization of the CCl_2 intermediate photolysis product. The substantial increase in ν_3 from 746 cm^{-1} for CCl_2 to 1197 cm^{-1} for CCl_2^+ is consistent with removal of an electron from an antibonding C-Cl molecular orbital made up of in-plane chlorine 3p orbitals. Isotopic shifts show that the Cl-C-Cl angle increases 25-30° on ionization to CCl_2^+.

Similar matrix photoionization experiments with CH_2ClBr produced a 3/1 doublet at 1122 and 1118 cm^{-1} and studies with $CHFBr_2$, $CDFBr_2$, CH_2Br_2, and CD_2Br_2 gave a sharp 1019 cm^{-1} absorption. The observation of new products at 1197, 1122, and 1019 cm^{-1} in CH_2Cl_2, CH_2ClBr, and CH_2Br_2 experiments verifies the infrared identification of the dihalocarbene cation species CCl_2^+, $CClBr^+$, and CBr_2^+ [81].

The $CClBr^+$ and CBr_2^+ absorptions are higher than $CHClBr^+$ at 993, 989 cm^{-1} and $CHBr_2^+$ at 897 cm^{-1} [64], and substantially higher than CClBr and CBr_2 at 744, 739, and 641 cm^{-1}, respectively [83], indicating removal of an antibonding electron in the dihalocarbene cations. Antisymmetric C-X_2 stretching fundamentals for CX_2^+, CHX_2^+, and CX_2 species are compared in Table 5.

In recent matrix photoionization experiments with CH_2Cl_2 and high-resolution measurements using a Nicolet Fourier-Transform Infrared Spectrometer, a particularly large yield of $CHCl_2^+$ was produced upon 290-1000 nm photolysis of the CH_2Cl_2 sample subjected to argon resonance photoionization [84]. The intense triplet at 1044.7, 1041.9, and 1039.5 cm^{-1} (A = 0.63, 0.43, 0.08, respectively) has been assigned to the antisymmetric C-Cl stretching mode in $CHCl_2^+$ [64]; these absorption bands are very sharp, with half-widths of 0.3 cm^{-1} using 0.1 cm^{-1} resolution. In addition, a weaker triplet was observed at 945.4, 841.4, 837.7 cm^{-1} (A = 0.054, 0.037, 0.007, respectively) which is assigned to the symmetric C-Cl stretching mode, and a weak band was found at 3033 cm^{-1} (A = 0.03) which is assigned to the C-H stretching mode; these assignments are supported by ^{13}C substitution. It can be seen by comparison with similar molecules (for example, $HBCl_2$ has B-Cl stretching modes at 886 and 740 cm^{-1}) [78] that the 1044 and 845 cm^{-1} values for $CHCl_2^+$ are high for C-Cl stretching fundamentals, and substantial C-Cl pi bonding is indicated. On the other hand, the 3033 cm^{-1} value for the C-H mode in $CHCl_2^+$ is near the 3058 cm^{-1} value for $CHCl_3$; clearly the carbon-hydrogen bond is not affected by the adjacent positive ion center.

Parent Anions

The first infrared spectroscopic evidence for a parent radical anion came from photon radiolysis studies on haloform molecules during condensation [85]. New bands photosensitive to light bulb photolysis were observed at 652, 621, 593, and 570 cm^{-1} in $CHCl_3$, $CHCl_2Br$, $CHClBr_2$, and $CHBr_3$ experiments, respectively. The 652 cm^{-1} $CHCl_3$ product band shifted to 645 cm^{-1} for $^{13}CHCl_3$ and 529 cm^{-1} for $CDCl_3$. The vibrational mode is primarily a carbon-halogen stretch although the large deuterium and small carbon-13 shifts indicate considerable mixing with a hydrogen deformation mode. The observation of four bands from the four different precursors requires the presence of three halogen atoms in the species. These carbon-halogen stretching modes fall 100-120 cm^{-1} below values for the strongest neutral parent modes which, along with their extremely photosensitive nature, suggests assignment to the parent radical anion. The unusual mode mixing also infers that $CHCl_3^-$ is distorted from C_{3v} symmetry.

Spectroscopic evidence has been presented for parent radical anions in the matrix photoionization studies of CF_3Cl, CF_2Cl_2, and $CFCl_3$ systems [15, 66], and in ESR studies following radiolysis [86]. Infrared absorptions assigned to the CF_3X^- species [67] are

identified as P^- in Fig. 6; note that the C-F stretching mode near 900 cm^{-1} for these parent anions is below the neutral parent fundamentals.

The first matrix photoionization studies on $CHCl_3$ by Jacox and Milligan reported new bands at 2723, 2498, 1271, and 838 cm^{-1}, which were also observed following mercury arc photolysis of $Ar/CHCl_3/Na$ samples and assigned to the molecular anion $CHCl_2^-$ [65]. An investigation of the complete mixed chlorobromoform species in this laboratory provided new spectroscopic information and assignments. The $CHCl_2Br$ and $CHClBr_2$ studies each provided two new sets of four product bands and a sixth new set was found with the $CHBr_3$ precursor, which indicates the presence of a third inequivalent halogen atom in the anion product species [63]. The carbon-13 and deuterium isotopic data and the mixed bromochloro spectra have verified the (CHX_2) (X) stoichiometry for the molecular anion product. The heavy halogen substitution behavior requires the intramolecular hydrogen-bonded arrangement X^--HCX_2 formed upon electron capture by CHX_3 in the photoionization experiments. The strong broad 2723 cm^{-1} C-H stretching absorption, ν_S, for Cl^--$HCCl_2$ exhibited a 9 ± 1 cm^{-1} carbon-13 shift and new counterparts absorbed at 2795 cm^{-1} for Br^--$HCCl_2$ and at 2863 cm^{-1} for I^--$HCCl_2$ [87]. This is the expected trend of larger displacement from a 3050 ± 50 cm^{-1} value for the C-H stretching fundamental of $HCCl_2$ radical as the proton affinity of the hydrogen bonding halide increases and the strength of the hydrogen bond increases. The 2498, 1271, and 838 cm^{-1} bands have been assigned to $2\nu_b$, ν_b (hydrogen bending) and ν_X (antisymmetric C-Cl_2 stretching), respectively, for Cl^--$HCCl_2$. These modes demonstrate the expected spectroscopic effect of hydrogen bonding in a type I species involving the perturbation of an existing chemical bond which exhibits the proper change as Cl^- is replaced by Br^- and I^- [87-89]. The bending mode, ν_b, is shifted up from the 1226 cm^{-1} $CHCl_2$ free radical value and the overtone $2\nu_b$ shows the effect of considerable anharmonicity in the bending vibration. The ν_X mode is shifted down from the 902 cm^{-1} $CHCl_2$ value [90] suggesting that hydrogen bonding a Cl^- ion to $CHCl_2$ reduces π bonding in the free radical [87].

Matrix photoionization studies on CHF_3 by Andrews and Prochaska revealed strong new bands at 3599, 1279, 1174, and 603 cm^{-1} in addition to CF_3^+ and free radical absorptions. The 3599 and 603 cm^{-1} bands exhibited 1 ± 1 cm^{-1} carbon-13 and large deuterium shifts which characterize hydrogen vibrations not involving carbon whereas the 1174 and 1279 cm^{-1} bands exhibited large carbon-13 and 1 cm^{-1} positive deuterium shifts, which are in accord with C-F vibrations. These new absorptions have been assigned to the fluoroform electron-capture photolysis product $(F\text{-}H)\text{-}(CF_2)^-$ produced by fluoride rearrangement and proton abstraction [87]. This intramolecular hydrogen bonded anion is a type III species which involves the formation of a new bond with residual perturbation. The similar species $(F\text{-}H)\text{-}(CFCl)^-$ and $(F\text{-}H)\text{-}(CCl_2)^-$ have been observed by Jacox and Milligan

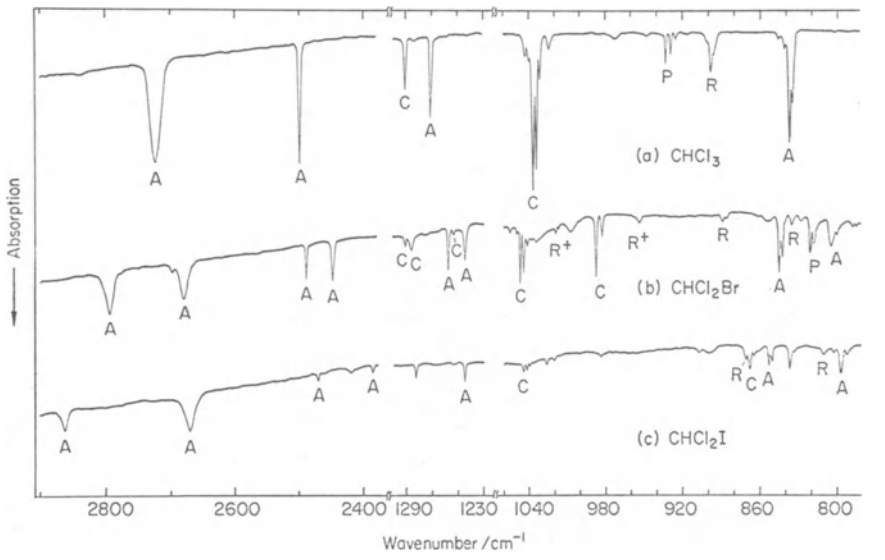

Fig. 8. Expanded-scale infrared spectra of dichlorohaloform matrix samples, $Ar/CHCl_2X$ = 400/1, subjected to argon resonance photoionization during condensation at 15 K. (a) $CHCl_3$, (b) $CHCl_2Br$, (c) $CHCl_2I$. The label R denotes CCl_2X radical and R^+ identifies CCl_2X^+ product absorptions. (Andrews and Prochaska, Ref. 87).

and in this laboratory [91-93] and the corresponding $(Cl-H)-(CF_2)^-$ and $(Cl-H)-(CFCl)^-$ species have also been characterized [91-93].

The nature of the hydrogen bond formed in haloform electron-capture products, i.e., type I or type III, depends on the proton affinities of the halide ion eliminated and the CX_2^- group that can be formed by proton abstraction. Carbon-13 isotopic studies are essential to characterize the hydrogen vibration and identify the new hydrogen bond. Haloform molecular anions rearrange to intramolecular hydrogen-bonded anions in matrix photoionization experiments, which provide interesting subjects for the study of hydrogen bonding.

Conclusions

Molecular ions in matrices maybe classified as "chemically bound" or "isolated" with respect to the counterion. Alkali metal reactions necessarily produce bound ion pairs whereas ionizing radiation is required to produce cation and anions isolated from each other in the matrix. Mercury arc photolysis is an important diagnostic for isolated ions in noble gas matrices; isolated ions should either photodissociate or photoneutralize by electron detachment

from anions for recombination with cations, the latter showing a dependence on the nature of the anion. The ion-matrix interaction is of interest as matrix spectra of ions are related to the gas phase. Although ionization exhibits a substantial shift to lower energy in solid argon, infrared absorption spectra of molecular cations are generally sharp (3 cm^{-1} FWHM) and matrix observations should correspond closely with gas phase vibrational fundamentals.

The effect that removing an electron from a molecule has on the vibrational potential function depends upon the location of the "hole" as can be seen from the examples described here. Halogens bonded to a carbocation center exhibit substantial pi bonding with carbon. The effect of a "hole" in an adjacent bond (C-H in $CH_2F_2^+$) or on an adjacent atom (X in CF_3X^+) is to increase the C-F vibrational frequencies presumably through polarization of the C-F bonding electrons and/or F lone pair electrons by the adjacent "hole." This effect is reduced when the "hole" is delocalized in a pi system as in the case of $CF_2CFCF_3^+$. The bond stretching fundamental is, of course, reduced upon ionization of a bonding electron, as shown by the C-H fundamentals in $CH_2F_2^+$.

References

1. L. Andrews, J. Am. Chem. Soc., 90, 7368 (1968).
2. L. Andrews, J. Chem. Phys., 50, 4288 (1969).
3. P. H. Kasai and D. McLeod, Jr., J. Chem. Phys., 51, 1250 (1969).
4. D. E. Milligan and M. E. Jacox, J. Chem. Phys., 51, 1952 (1969).
5. L. E. Brus and V. E. Bondybey, J. Chem. Phys., 63, 3123 (1975).
6. W. L. S. Andrews and G. C. Pimentel, J. Chem. Phys., 44, 2361 (1966).
7. L. Andrews, J. T. Hwang, and C. Trindle, J. Phys. Chem., 77, 1065 (1973).
8. P. H. Kasai, Acct. Chem. Res., 4, 329 (1977).
9. A. Gedanken, B. Raz, and J. Jortner, J. Chem. Phys., 58, 1178 (1973).
10. L. Andrews, J. M. Grzybowski, and R. O. Allen, J. Phys. Chem., 79, 904 (1975).
11. F. T. Prochaska and L. Andrews, J. Chem. Phys., 67, 1091 (1977).
12. M. E. Jacox, Chem. Phys., 12, 51 (1976).
13. C. A. Wight, B. S. Ault, and L. Andrews, J. Chem. Phys., 65, 1244 (1976).
14. R. R. Smardzewski, Appl. Spectrosc., 4, 332 (1977).
15. F. T. Prochaska and L. Andrews, J. Chem. Phys., 68, 5577 (1978).
16. L. Andrews, D. Tevault, and R. R. Smardzewski, Appl. Spectrosc., 32, 157 (1978).
17. B. S. Ault and L. Andrews, J. Am. Chem. Soc., 97, 3824 (1975).
18. B. S. Ault and L. Andrews, J. Chem. Phys., 63, 2466 (1975).
19. B. S. Ault and L. Andrews, J. Chem. Phys., 64, 4853 (1976).
20. B. S. Ault and L. Andrews, J. Am. Chem. Soc., 98, 1591 (1976); Inorg. Chem., 16, 2024 (1977).

21. J. H. Miller and L. Andrews, Inorg. Chem., 18, 988 (1979).
22. B. J. Kelsall and L. Andrews, J. Phys. Chem., 85, 2938 (1981).
23. D. A. Hatzenbühler and L. Andrews, J. Chem. Phys., 56, 3398 (1972).
24. L. Andrews, Appl. Spectrosc. Rev., 11, 125 (1976).
25. M. E. Jacox, Rev. Chem. Intermed., 1, 1 (1978).
26. L. Andrews, Ann. Rev. Phys. Chem., 30, 79 (1979).
27. L. Andrews, J. Phys. Chem., 73, 3922 (1969); J. Chem. Phys., 54, 4935 (1971).
28. L. Andrews and R. R. Smardzewski, J. Chem. Phys., 58, 2258 (1973).
29. D. E. Tevault and L. Andrews, J. Phys. Chem., 77, 1646 (1973).
30. F. J. Adrian, E. L. Cochran, and V. A. Bowers, J. Chem. Phys., 59, 56 (1973).
31. D. M. Lindsay, D. R. Herschbach, and A. L. Kwiram, Chem. Phys. Letts., 25, 175 (1974).
32. L. Andrews, J. Mol. Spectrosc., 61, 337 (1976).
33. M. H. Alexander, J. Chem. Phys., 69, 3502 (1978) and references therein.
34. R. C. Spiker, Jr., and L. Andrews, J. Chem. Phys., 59, 1851 (1973).
35. L. Andrews and R. C. Spiker, Jr., J. Chem. Phys., 59, 1863 (1973).
36. F. J. Adrian, E. L. Cochran, and V. A. Bowers, J. Chem. Phys., 61, 5463 (1974).
37. M. E. Jacox and D. E. Milligan, J. Mol. Spectrosc., 43, 148 (1972).
38. L. Andrews and D. E. Tevault, J. Mol. Spectrosc., 55, 452 (1975).
39. L. Andrews, B. S. Ault, J. M. Grzybowski, and R. O. Allen, J. Chem. Phys., 62, 2461 (1975).
40. D. M. Thomas and L. Andrews, J. Mol. Spectrosc., 50, 220 (1974).
41. L. Andrews, E. S. Prochaska, and B. S. Ault, J. Chem. Phys., 69, 556 (1978).
42. L. Andrews, J. Chem. Phys., 63, 4465 (1975).
43. W. F. Howard, Jr., and L. Andrews, J. Am. Chem. Soc., 95, 3045 (1973); Inorg. Chem., 14, 409 (1975).
44. L. Andrews, J. Am. Chem. Soc., 98, 2147 (1976).
45. W. F. Howard, Jr., and L. Andrews, J. Am. Chem. Soc., 95, 2056 (1973); Inorg. Chem., 14, 767 (1975).
46. L. C. Lee, G. P. Smith, J. T. Moseley, P. C. Cosby, and J. A. Guest, J. Chem. Phys., 70, 3237 (1979).
47. C. A. Wight, B. S. Ault, and L. Andrews, Inorg. Chem., 15, 2147 (1976).
48. W. F. Howard, Jr., and L. Andrews, J. Am. Chem. Soc., 97, 2956 (1975).
49. L. Andrews, J. Am. Chem. Soc., 98, 2152 (1976).
50. L. Andrews, E. S. Prochaska, and A. Loewenschuss, Inorg. Chem., 19, 463 (1980).

51. W. Kiefer and H. J. Bernstein, Chem. Phys. Letts., 16, 5 (1972).
52. P. N. Noble and G. C. Pimentel, J. Chem. Phys., 49, 3165 (1968).
53. D. E. Milligan and M. E. Jacox, J. Chem. Phys., 53, 2034 (1970).
54. V. E. Bondybey, G. C. Pimentel, and P. N. Noble, J. Chem. Phys., 55, 540 (1971).
55. D. E. Milligan and M. E. Jacox, J. Chem. Phys., 55, 2550 (1971).
56. B. S. Ault and L. Andrews, J. Chem. Phys., 64, 1986 (1976).
57. J. A. Ibers, J. Chem. Phys., 40, 402 (1964).
58. B. S. Ault, J. Phys. Chem., 82, 844 (1978); 83, 837 (1979).
59. S. A. McDonald and L. Andrews, J. Chem. Phys., 70, 3134 (1979).
60. V. E. Bondybey and G. C. Pimentel, J. Chem. Phys., 56, 3832 (1972).
61. D. E. Milligan and M. E. Jacox, J. Mol. Spectrosc., 46, 460 (1973).
62. D. W. Smith and L. Andrews, J. Chem. Phys., 60, 81 (1974).
63. L. Andrews, C. A. Wight, F. T. Prochaska, S. A. McDonald, and B. S. Ault, J. Mol. Spectrosc., 73, 120 (1978).
64. L. Andrews, F. T. Prochaska, and B. S. Ault, J. Am. Chem. Soc., 101, 9 (1979).
65. M. E. Jacox and D. E. Milligan, J. Chem. Phys., 54, 3935 (1971).
66. F. T. Prochaska and L. Andrews, J. Chem. Phys., 68, 5568 (1978).
67. F. T. Prochaska and L. Andrews, J. Am. Chem. Soc., 100, 2102 (1978).
68. M. E. Jacox, Chem. Phys. Letts., 54, 176 (1978).
69. D. E. Milligan and M. E. Jacox, J. Chem. Phys., 48, 2265 (1968).
70. K. Nakamoto, in: Infrared Spectra of Inorganic and Coordination Compounds, John Wiley and Sons, Inc., New York (1963).
71. L. Andrews and F. T. Prochaska, J. Phys. Chem., 83, 368 (1979).
72. F. T. Prochaska and L. Andrews, J. Phys. Chem., 82, 1731 (1978).
73. A. S. Werner, B. P. Tasi, and T. Baer, J. Chem. Phys., 60, 3650 (1974).
74. H. W. Jochims, W. Lohr, and H. Baumgartel, Ber. Bunsenges. Phys. Chem., 80, 130 (1976).
75. T. Baer, L. Squires, and A. S. Werner, Chem. Phys., 6, 325 (1974).
76. L. Andrews and F. T. Prochaska, J. Chem. Phys., 70, 4714 (1979).
77. F. T. Prochaska and L. Andrews, J. Chem. Phys., to be published.
78. J. H. Miller and L. Andrews, J. Am. Chem. Soc., 102, 4900 (1980).
79. P. J. Bassett and D. R. Lloyd, J. Chem. Soc., A 1971, 1551.
80. B. J. Kelsall and L. Andrews, J. Phys. Chem., 85, 1288 (1981).
81. L. Andrews and B. W. Keelan, J. Am. Chem. Soc., 101, 3500 (1979).
82. D. E. Milligan and M. E. Jacox, J. Chem. Phys., 47, 703 (1967); L. Andrews, J. Chem. Phys., 48, 979 (1968).

83. L. Andrews and T. G. Carver, J. Chem. Phys., 49, 896 (1969); A. K. Maltsev, R. H. Hauge, and J. L. Margrave, J. Phys. Chem., 75, 3984 (1971).
84. B. J. Kelsall and L. Andrews, to be published.
85. B. S. Ault and L. Andrews, J. Chem. Phys., 63, 1411 (1975).
86. A. Hasegawa, M. Shiotani, and F. Williams, Far. Disc. Chem. Soc., 63, 157 (1977).
87. L. Andrews and F. T. Prochaska, J. Am. Chem. Soc., 101, 1190 (1979).
88. B. S. Ault, E. Steinbeck, and G. C. Pimentel, J. Phys. Chem., 79, 615 (1975).
89. G. C. Pimentel and A. L. McClellan, in: The Hydrogen Bond, W. H. Freeman, San Francisco (1960).
90. T. G. Carver and L. Andrews, J. Chem. Phys., 50, 4235 (1969).
91. L. Andrews and F. T. Prochaska, J. Phys. Chem., 83, 824 (1979).
92. M. E. Jacox and D. E. Milligan, Chem. Phys., 16, 195, 381 (1976).
93. B. W. Keelan and L. Andrews, J. Phys. Chem., 83, 2488 (1979).

VISIBLE AND ULTRAVIOLET SPECTRA AND PHOTOCHEMISTRY OF MOLECULAR IONS IN SOLID ARGON

Lester Andrews

Chemistry Department
University of Virginia
McCormick Road
Charlottesville, Va. 22901

Introduction

Optical spectroscopic studies of molecular ions in solid argon [1] provide information on electronic states and ion structure which are complementary with studies in rigid organic glasses [2], ultraviolet photoelectron spectra (PES) [3], and photodissociation spectra (PDS) [4]. Spectra in solid argon are generally sharper and provide more vibrational information than glass spectra, and the cryogenic matrix quenches internal energy thus producing sharper bands than PDS and allowing the stabilization of facile molecular ions. The solid argon host also moderates photodissociation and allows isomerization to be a competitive process.

In the first optical observation of an ion in solid argon, Milligan and Jacox produced new 520.6 and 472.5 nm absorptions by the 1216-Å photolysis of C_2H_2 [5]. This study is particularly relevant to the gas-phase spectroscopy of discharge systems. The carrier of a 541.6 nm band system in the flash discharge of methane was tentatively identified as C_2^- [6], and the matrix observation of an appropriate band system provides support for this identification. The C_2^- case illustrates the usefulness of matrix spectroscopy for characterizing new transient species.

Brus and Bondybey provided an explanation for the observation of C_2^- in solid argon using hydrogen resonance (10.2 eV) photoionization which is insufficient to ionize C_2H_2 (11.4 eV) in the gas phase [7]. Owing to solvation of the product ions by the solid argon matrix, which amounts to 1.4 eV for the similar C_2H_4 molecule, the ionizing transition is red-shifted to overlap with hydrogen

resonance radiation. The matrix solvent interaction clearly plays an important role in the formation and stability of ions in noble gas matrices.

Experimental

Optical studies of molecular ions in matrices generally employ photoionization techniques using open-ended discharge tubes [8] (fully open, 8-mm i.d. or partially constricted, 3-mm i.d.) as vacuum ultraviolet lamps or LiF-filtered hydrogen or argon resonance lamps [5]. The former have a higher energy output and a higher total photon flux since no absorbing optic is present, and the argon from the lamp is condensed with the sample, which provides metastable argon atoms that may also contribute to the mechanism of formation of a product ion. The apparatus used in the present studies has been described in a previous chapter on infrared studies, and in earlier work [9-11]. For optical investigations, a sapphire cold window and optical quality quartz vacuum windows are used [9]. The sapphire window is cooled to 20 ± 2 K for sample condensation; this temperature range is optimum for maintaining ultraviolet transmission of the sample while trapping molecular ions in the condensing layer of argon.

Sample preparation is generally done by continuous irradiation of a precursor molecule diluted in argon during condensation for 2 to 7 h; however, strongly absorbing species can be produced by vacuum-ultraviolet irradiation of a cold sample. Here follows a discussion of a number of optical absorption studies of molecular ions in solid argon.

Halomethane Cations

New extremely photosensitive infrared bands at 374 and 927 cm^{-1} in the matrix radiolysis and photoionization of CCl_4 have been assigned to an asymmetric CCl_4^+ species [10]. The ease of photodissociating these infrared bands suggested searching for a visible absorption responsible for the observed dissociation; the spectra shown in Fig. 1 were recorded in this investigation. Carbon tetrachloride diluted in argon was condensed with argon from an open discharge, and the spectrum revealed a very strong broad absorption at 425 nm [11]. This band was virtually destroyed by 500-1000 nm photolysis, as illustrated in Fig. 1d. The optical absorption shifted to 430 nm in solid krypton and 455 nm in solid xenon, showing little interaction with argon but an increasing interaction with xenon. The same 425 nm absorption was produced in lower yield in a cold Ar/CCl_4 = 400/1 sample by radiation from an open argon dischrage tube or from a LiF-filtered argon resonance lamp. Since the matrix cage retards the escape of large atomic fragments, production of the 425 nm absorption by irradiation of a cold sample supports its identification as CCl_4^+.

The observation of CCl_4^+ at 425 nm in solid argon reinforces the earlier interpretation [12, 13] of positive ion absorptions at 480 nm in 3-MP and at 400 nm in polycrystalline CCl_4 produced by radiolysis of CCl_4. Since the positive ion absorptions in 3-MP and solid CCl_4 are near the present argon matrix CCl_4^+ absorption, it is suggested that these absorptions are also due to CCl_4^+.

The CCl_4 PES exhibits three strong bands at 11.6, 12.6, and 13.4 eV, which have been assigned to t, t, and e MO's formed from the chlorine lone-pair orbitals. However, the ion ground state is doubly degenerate due to spin-orbit splitting and susceptible to Jahn-Teller distortion. The strong PES band at 16.7 eV has been assigned to the triply degenerate C-Cl bonding orbital, which is also subject to Jahn-Teller distortion [3]. The difference between the first PES band and the bonding orbital (5.1 eV) clearly does not correspond with the 425-nm absorption observed for CCl_4^+; this disagreement is best explained by significant changes in Franck-Condon factors caused by major geometry changes between the ground state molecule, the ground state ion, and the excited state ion. Here the matrix absorption between the two likely distorted ionic states occurs at considerably less energy than the difference between transitions from the tetrahedral neutral ground state molecule to the ionic states reached in the PES. Comparison of the PES and absorption spectra for CCl_4^+ shows that substantial structural relaxation of CCl_4^+ occurs in the matrix; previous infrared studies suggested an asymmetric C_{2v} structure [10]. To our knowledge, no mass spectrum of the CCl_4^+ molecular ion has been observed owing to the instability of the molecular ion [14]. At thermal energies, CCl_4^+ readily eliminates Cl; however, the matrix effectively quenches internal energy and allows CCl_4^+ to rearrange to a more stable structure.

The strong band at 405 nm in the $CFCl_3$ investigation is assigned to $CFCl_3^+$. This photosensitive band exhibited similar photodestruction to infrared absorptions assigned to $CFCl_3^+$ which yielded an increase in $CFCl_2^+$ absorptions on visible photolysis [15]. Although $CFCl_3^+$ has been detected in the gas phase, the $CFCl_3^+$ ion yield was extremely small and no $CFCl_3^+$ photoion spectrum could be recorded [16]. The detection of $CFCl_2^+$ as the major ion signal shows that $CFCl_3^+$ is of limited stability, a point supported by its matrix photodissociation with red light [15]. The PES of $CFCl_3$ shows four bands between 11.8 and 13.5 eV for the a_1, a_2, and two e lone pair orbitals in C_{3v} symmetry, and a band at 15.0 eV for the e C-Cl bonding orbital [17]. The difference between the ionic ground state at 11.8 eV and the 15.0-eV state corresponds to a 388 ± 10 nm transition, in very good agreement with the present strong 405-nm absorption for $CFCl_3^+$. The transfer of a bonding C-Cl electron to a nonbonding Cl 3p hole is also consistent with chlorine atom photoelimination upon absorption.

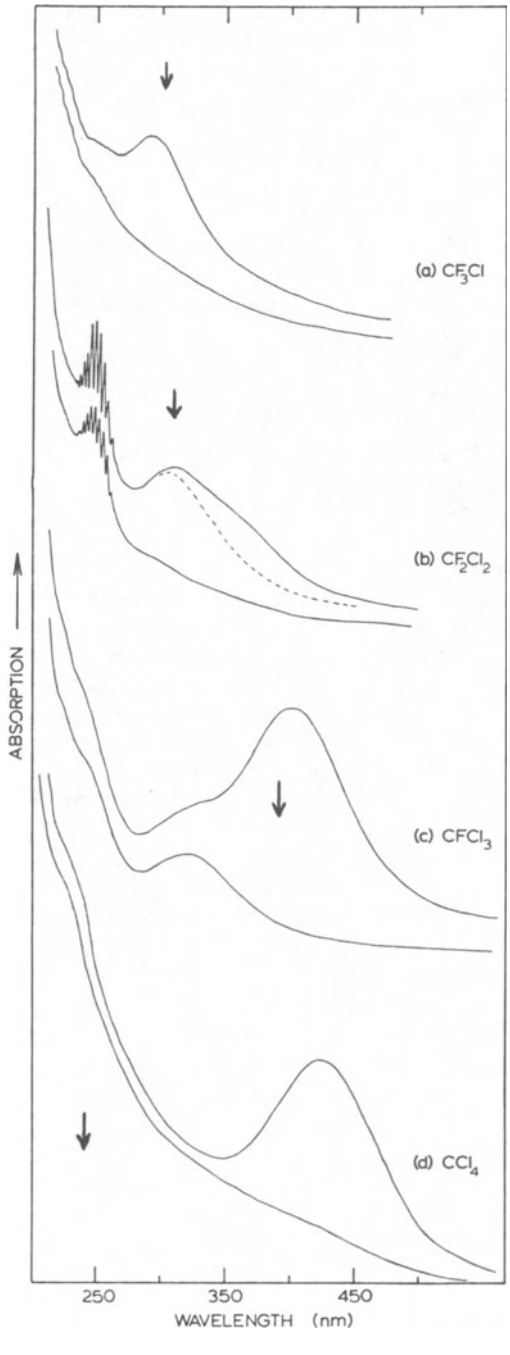
(a) CF_3Cl
(b) CF_2Cl_2
(c) $CFCl_3$
(d) CCl_4
ABSORPTION
250
350
450
WAVELENGTH (nm)

The 310 nm band peak in Fig. 1b from CF_2Cl_2 experiments is assigned to $CF_2Cl_2^+$. The energy difference between the first (12.3 eV) and 16.3-eV PES bands corresponds to an absorption at 310 ± 10 nm, precisely the maximum observed in solid argon. This shows that $CF_2Cl_2^+$ retains the ground state structure. The 295 nm absorption in CF_3Cl experiments exhibits the appropriate photolysis behavior for CF_3Cl^+ from infrared studies [15]. The absorption band is near the 4.1-eV difference between onset of the first (Cl lone pair) and the vertical CF_3 bonding orbital ionizations [17]. Assignment of the 295 nm absorption to a transition form the CF_3 bonding orbital to the Cl lone pair hole is consistent with the growth of CF_2Cl^+ upon 340 nm photolysis of CF_3Cl^+ in infrared studies [15]. The 295 nm absorption probably represents a dissociative transition for CF_3Cl^+.

Figure 1 contrasts optical absorptions for CF_3Cl^+, $CF_2Cl_2^+$, $CFCl_3^+$, and CCl_4^+ and shows an arrow giving the appropriate PES band difference (±10 nm). Structural relaxation of the molecular ion, as determined by the difference between the optical band and the transition predicted from PES, increases with increasing symmetry of the neutral molecule.

The optical spectra for a series of methylene halides subjected to argon resonance photoionization during sample deposition are illustrated in Fig. 2. New absorptions were observed at 342, 362, and 375 nm in the series CH_2Cl_2, CH_2Br_2, and CH_2I_2. These bands were virtually destroyed by visible photolysis (500-1000 nm), as shown in the figure, which supports their assignments to the parent cations [18]. Photoelectron spectra for these compounds exhibited a group of sharp bands from ionization of halogen non-bonding electrons, followed by a broader band from ionization of a C-X bonding electron [3]. The wavelength corresponding to the energy difference between the first sharp lone-pair ionization and the C-X bond ionization is noted with an arrow in each trace of the figure. The agreement between the observed electronic transition for the parent ions in solid argon and the difference between two photoelectron bands is excellent, and it provides strong support for the matrix assign-

Fig. 1. Ultraviolet-visible absorption spectra of chlorofluoromethanes subjected to argon discharge photoionization during condensation with excess argon at 25 ± 2 K using Ar/CX_4 = 400/1 sample concentrations: (a) CF_3Cl, inset scan followed 30 min of 290-1000 nm photolysis; (b) CF_2Cl_2, inset dashed scan recorded after 30 min of 420-1000 nm photolysis and solid inset scan followed 30 min of 290-1000 nm photolysis; (c) $CFCl_3$, inset scan followed 30 min of 420-1000 photolysis; (d) CCl_4, inset scan recorded after 30 min of 500-1000 nm photolysis. Arrows denote the wavelength (±10 mm) of absorption predicted from PES.

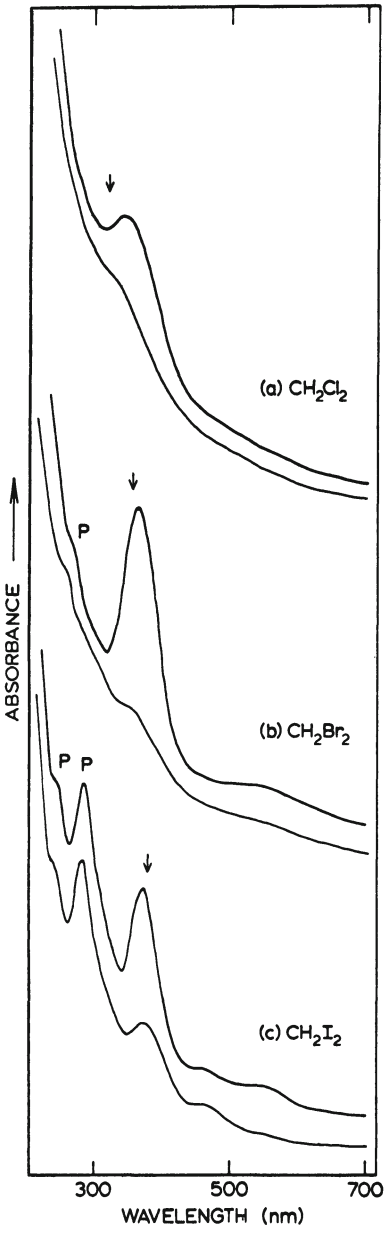

Fig. 2. Absorption spectra from 200-700 nm for methylene halide samples, Ar/CH_2X_2 = 400/1, deposited at 20 K with simultaneous exposure to argon discharge radiation. (a) CH_2Cl_2, (b) CH_2Br_2, (c) CH_2I_2. The trace displaced below each scan was recorded after successive 30 min 650-1000 nm and 500-1000 nm photolysis periods. Arrows denote the wavelength (±10 nm) of transitions from the ground state of the ions to the excited state of the ions determined from PES.

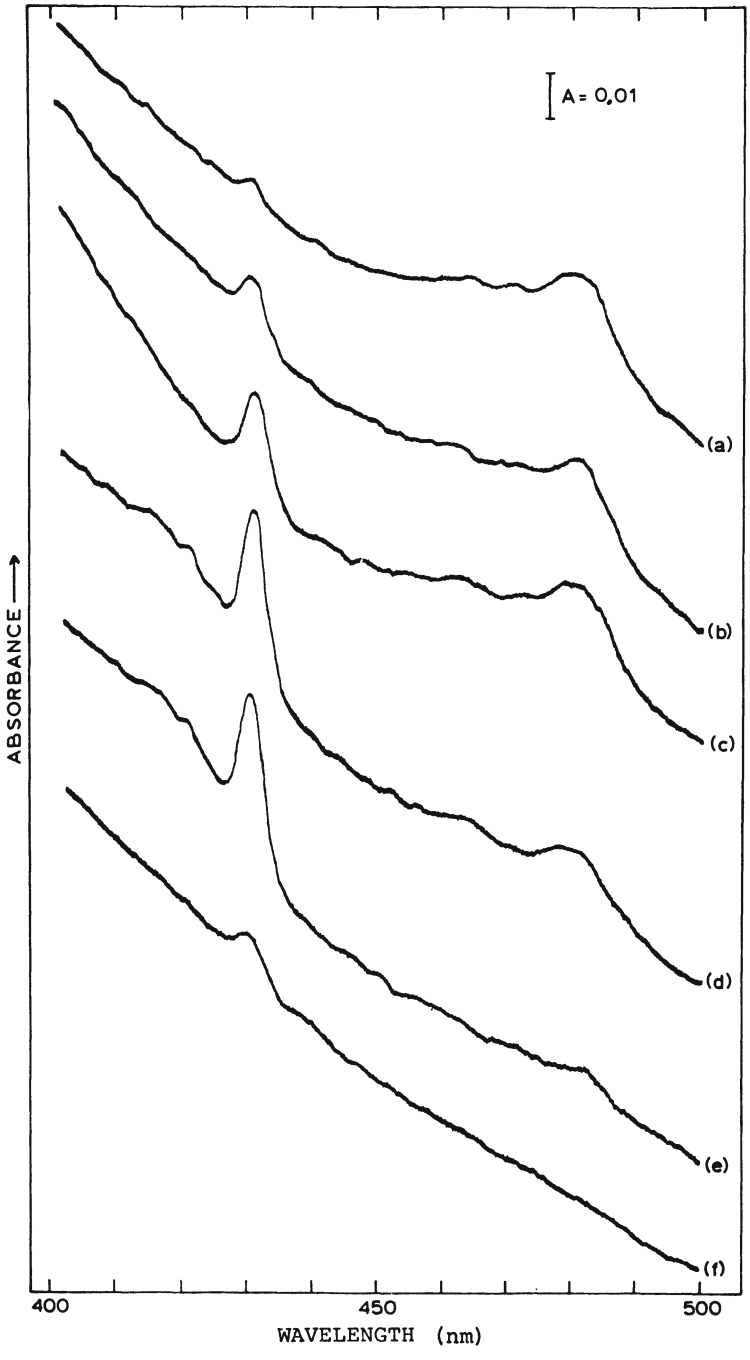

Fig. 3. Absorption spectrum of cycloheptatriene sample subjected to matrix photoionization during condensation, trace (a). Scan (b) recorded after photolysis with 590 nm cut-off filtered high pressure mercury arc light. Trace (c) recorded after photolysis with 520 nm cut-off filter. Spectra (d), (e), and (f) recorded after 450, 420, and 290 nm photolyses, respectively.

ments to these $CH_2X_2^+$ parent ions. Small differences may arise from different Franck-Condon factors between the electronic and ionizing transitions involved, although very good agreement is expected where ionization causes no major change in geometry of the ion compared to the neutral, as is found for the methylene halide cations.

Toluene and Cycloheptatriene Cations

The toluene radical cation and its dissociation products are among the most widely studied ions in mass and photodissociation spectroscopies. The observation of extensive hydrogen scrambling in mass spectra of isotopically-labeled toluene fragmentation products has prompted investigation of the possible isomerization of $C_7H_8^+$ cations produced from toluene and other C_7H_8 compounds. Mass spectroscopic studies with labeled precursors have been explained by isomerization of the parent cations to a common intermediate for toluene, cycloheptatriene and norbornadiene [19-24]. Ion cyclotron resonance (ICR) studies of toluene cation have produced a strong photodissociation spectrum beginning near 538 nm with a peak at 417 nm and have demonstrated that hydrogen randomization before dissociation is almost complete even with energies near the threshold [25-29]. However, an ICR study employing chemical reactions of isomeric $C_7H_8^+$ cation showed that nondissociating cations from toluene and cycloheptatriene do not interconvert on a time scale of milliseconds [30], and another ICR investigation revealed different photodissociation spectra (PDS) for these isomeric cations [31]. Since excess internal energy appears to be the essential prerequisite for interconversion of isomeric $C_7H_8^+$ parent cations, which are thought to be in equilibrium at relatively low internal energies [27, 32, 33], the low temperature matrix isolation technique was employed to trap these cations in their different isomeric structural forms for observation of their characteristic absorption spectra.

Argon/toluene samples were subjected to continuous photoionization and dilution with argon from a 3-mm orifice discharge lamp for 7 h. The spectrum revealed a broad 430 nm band (A = 0.010), a broad weak 480 nm band (A = 0.001), a sharp, weak 449.6 nm absorption, and a strong, sharp 310.5 nm absorption. The sharp bands, stable to photolysis, are due to benzyl radical [34]. Irradiation with 420-1000 nm mercury arc light for 30 m destroyed the 480 nm band and reduced the 430 nm band by 60%.

Identical cycloheptatriene studies were performed using 4 h of simultaneous sample deposition and argon discharge irradiation [35]; the visible spectrum is shown in Fig. 3a. The 480 nm band was stronger (A = 0.030) and the 430 nm band was weaker (A = 0.006) than in the toluene experiment. Photolysis with 590 cut-off light for 15 m reduced the 480 nm band by 10% and doubled the 430 nm band, as can be seen from comparison of traces (a) and (b) in Fig. 3; this trend

continued with 520 and 450 nm photolysis, shown in scans (c) and (d), which also produced a broad 410-422 nm band peaking at 416 nm. At maximum intensity (A = 0.040), the band peaked at 430.5 nm, had a 428-432 nm (220 cm^{-1}) full-width at half-maximum, and a threshold at 436 ± 2 nm (22,940 ± 100 cm^{-1}). As in the previous experiment, 420 nm radiation decreased the 430 nm absorption, trace (e). Irradiation at 290 nm almost destroyed the 430 nm band, as shown in trace (f).

Norbornadiene (bicyclo[2.2.1]hepta-2,5-diene) was studied and the spectrum after matrix photoionization revealed weak broad bands at 430 and 480 nm (A = 0.005) without absorption in the 600 nm region. Photolysis with 590 nm radiation produced a weak, broad 416 nm band (A = 0.002), increased the 430 nm absorption, and decreased the 480 nm absorption. The photolysis sequence described above had the same effect in this experiment.

The 430 nm argon matrix absorption is assigned to the toluene cation, 1, produced by photoionization of toluene molecules (IP = 8.9 eV) [36] with argon resonance radiation (11.6-11.8 eV) and trapped in the condensing argon matrix. This observation of toluene cation is supported by several considerations: (a) the argon matrix absorption energy is in very good agreement with the 3.0 eV energy

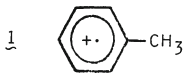

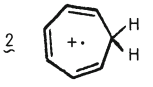

difference between the onset of ionization and the second band in the photoelectron spectrum [36]; (b) the 430 nm band is in excellent agreement with the PDS band peak at 417 nm for toluene cation [26]; and (c) the 430 nm band is photosensitive to 420 nm radiation, as required by the PDS results. The observation of the same 430 nm absorption from three isomeric C_7H_8 precursors provides further evidence for this solid-phase identification of the toluene cation. The marked photochemical growth of the 430 nm absorption (Fig. 3) at the expense of the 480 nm absorption in cycloheptatriene experiments, the latter of which can reasonably be assigned to the isomeric cycloheptatriene cation, 2, confirms assignment of the 430 nm argon matrix absorption to the toluene cation. The 480 nm argon matrix absorption is in excellent agreement with the 470 nm peak in the cycloheptatriene PDS band in ICR studies [31] and with the 2.66 eV energy difference between the first and third photoelectron bands for cycloheptatriene [37] which support the matrix identification 2.

The observation of both 1 and 2 in toluene and cycloheptatriene matrix experiments shows that 2 and 1 rearrange during condensation in the matrix. Upon photo excitation of 2 in solid argon, 1 grows

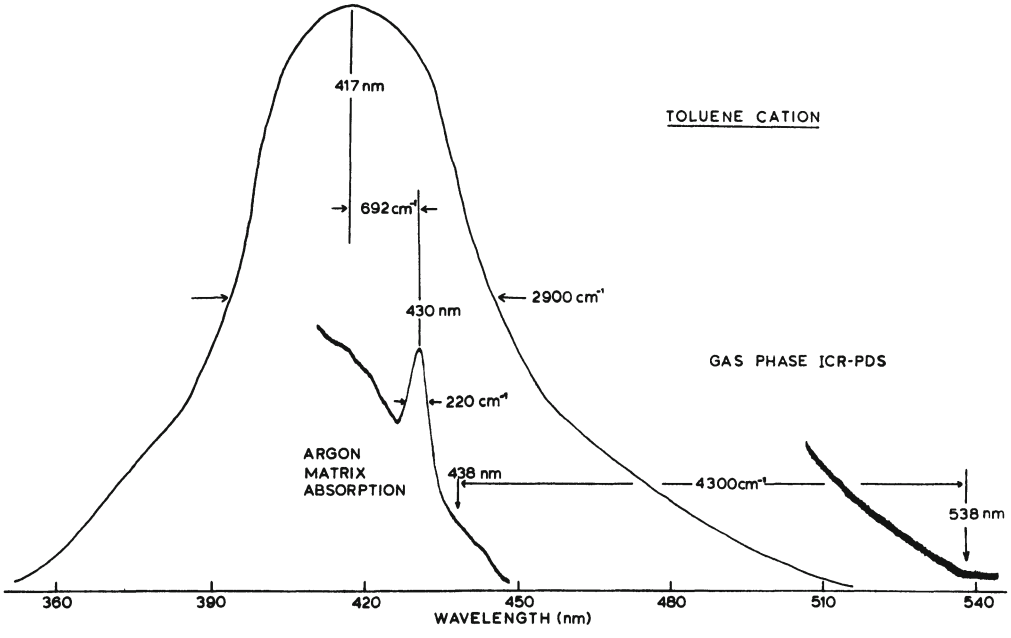

Fig. 4. Comparison of matrix absorption spectrum and ICR photodissociation spectrum of toluene cation on common wavelength scale. The PDS was replotted from Refs. [26] and [29].

at the expense of $\tilde{2}$; this observation demonstrates that rearrangement competes effectively with dissociation in the solid argon host matrix. Final photodissociation of $\tilde{1}$ and $\tilde{2}$ probably gives tropylium ion with absorption at 263 nm, to be discussed in the next section, which is obscured by the strong precursor absorption in this region.

The markedly decreased bandwidth in solid argon is of interest, particularly for the extensively studied $\tilde{1}$ ion. The major difference between gaseous and matrix-isolated $\tilde{1}$ ions is effective quenching of vibrational energy by the matrix, and this will affect the ground state ion and the dissociation dynamics. Even though the dye-laser PDS study in the threshold region used 10 eV electron-impact ionization and retained the ions for 150 ms to undergo approximately 30 collisions with neutrals [29], it is still conceivable that a "few tenths" of an eV of vibrational energy, particularly in totally symmetric modes, might be retained by ions in an ICR cell; the ions in solid argon at 22 K are surely vibrationally quenched. This may account, in part, for the bandwidth and the 4,300 cm^{-1} between the lower energy gaseous and higher energy matrix thresholds for $\tilde{1}$ absorption and dissociation, which are compared in Fig. 4. Since the dissociation of $\tilde{1}$ involves photoexcitation to a bound excited state, followed by rapid internal conversion to the vibrationally hot ground electronic state, which then eliminates a hydrogen atom, the gaseous

PDS may also be lifetime broadened [38]. A very important effect of the solid argon lattice interacting with the guest $\underset{\sim}{1}$ ion is to quench vibrational excitation in the excited electronic state to lower vibrational levels where the density of states for vibronic coupling is less; this may reduce the internal conversion rate which would tend to sharpen the absorption spectrum and retard the photodissociation process. The observation that the matrix $\underset{\sim}{1}$ absorption bandwidth is more than an order of magnitude less than the gaseous PDS bandwidth, as shown in Fig. 4, is consistent with this hypothesis.

The matrix host provides an efficient sink for internal energy which is necessary to stabilize the $\underset{\sim}{1}$ and $\underset{\sim}{2}$ parent cations. Argon resonance radiation (11.6-11.8 eV) exceeds the threshold for production of $C_7H_7^+$ daughter ion from toluene (11.6 eV) and cycloheptatriene (10.1 eV) [39]; however, the matrix quenches internal energy at a rate competitive with unimolecular decomposition and enables the parent cation to be stabilized. While internal energy is being quenched from the original parent cation formed, rearrangements of both $\underset{\sim}{1}$ and $\underset{\sim}{2}$ have been observed as $\underset{\sim}{2}$ was found in toluene studies and $\underset{\sim}{1}$ in cycloheptatriene experiments. The rearrangements $\underset{\sim}{2} \rightarrow \underset{\sim}{1}$ on visible photolysis demonstrates that the balance between internal energy from visible light absorption by the ions and internal energy quenched by the matrix provides sufficient internal energy for rearrangement of the ions without dominant unimolecular decomposition. MINDO/3 calculations of the overall activation energy for $\underset{\sim}{2} \rightarrow \underset{\sim}{1}$ rearrangement gave 39.8 and 39.2 kcal/mole (718 and 729 nm) for two different processes [40]. This is slightly lower than the first absorption detected at 542 nm, although the electronic band could tail to the red. Finally, the $\underset{\sim}{1} \rightleftarrows \underset{\sim}{2}$ isomerization documented here by optical spectroscopy provides support for the conclusion from gas-phase experiments [27, 32, 33] that $\underset{\sim}{1}$ and $\underset{\sim}{2}$ are in equilibrium at relatively low internal energies.

Benzyl and Tropylium Cations

Many investigators have been concerned with the structures of gas-phase $C_7H_7^+$ ions produced from different aromatic compounds [19, 41]. It has been shown by a number of workers that the $C_7H_7^+$ ion population contains reactive and unreactive fractions and that the two populations probably have different structures [25, 32, 33, 42, 43] which have been identified as the benzyl $\underset{\sim}{3}$ and tropylium $\underset{\sim}{4}$ cations, respectively [42, 33].

$\underset{\sim}{3}$ 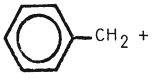 $\underset{\sim}{4}$ 

The first spectroscopic studies of $C_7H_7^+$ ions identified $\underset{\sim}{4}$ in concentrated H_2SO_4 by strong absorptions at 274 and 217 nm [44-46].

Although several methyl-substituted derivatives of 3 have been observed in superacid solutions [47], 3 itself is sufficiently reactive to require pulse radiolysis and submicrosecond observation of a 363 nm absorption in dichloroethane solution [48]. The following matrix photoionization study of benzyl bromide provides ultraviolet absorption spectra and information on the photochemical rearrangement of 3 and 4.

Using a new technique, neat benzyl bromide vapor was condensed with argon from the 3-mm orifice discharge tube in 12 experiments [49]. Codeposition of equilibrium benzyl bromide vapor for 1 h with undischarged argon entering the tube at about 125 m torr pressure produced only a precursor absorption at 220-230 nm (A = 0.15) as a shoulder on the steeply rising sample background. This procedure was continued for 1 more h with the same flow rates and the argon was energized by a microwave discharge. A strong, broad, symmetrical band was observed beginning at 430 nm with a maximum and band center at 353 nm (A = 0.60) and a minimum at 300 nm on a background with little slope (increase 0.15 absorbance units from 430 to 300 nm). A weak shoulder was detected at 263 nm (A = 0.06) on the side of the 225 nm (A = 0.25) precursor absorption. The sample was photolysed with unfiltered mercury arc radiation and the 353 nm absorption was reduced (to A = 0.17) and the 263 nm absorption was destroyed. The next experiment codeposited benzyl bromide vapor neat with argon from a full rich discharge for 2 h; the 353 nm band appeared with increased intensity (A = 0.55) and the 263 nm (A = 0.10) shoulder was observed on the 225 nm precursor absorption superposed on the steeply rising ultraviolet sample background. Pyrex filtered mercury arc photolysis (290 nm short wavelength limit) for 30 min reduced the 353 nm band (to A = 0.10) and increased the 263 nm absorption (to A = 0.20).

Another experiment employed an argon inlet pressure of 140 m torr, and the spectrum after codeposition of benzyl bromide vapor with discharged argon for 1 h is illustrated in Fig. 5a; the product bands were 353 nm (band center, A = 0.36) and 263 nm (A = 0.24). Photolysis with 380 nm cut-off radiation for 10 min markedly reduced the 353 nm band (to A = 0.10) and produced a new maximum at 325 nm (A = 0.10), and increased the 263 nm band (to A = 0.33), Fig. 5b. Irradiation through the 340-600 band pass filter for 10 min further reduced the 353 and 325 nm bands (to A = 0.02) and increased the 263 nm band (to A = 0.37), Fig. 5c. Exposure of this sample to 290 nm light for 10 min destroyed the 353 nm band, reduced the 325 nm absorption (to A = 0.01) and slightly reduced the 263 nm absorption (to A = 0.35), Fig. 5d. A final full arc photolysis for 20 min produced a new absorption centered at 353 nm (A = 0.05), markedly reduced the 263 nm band (to A = 0.06), and destroyed the 325 nm band, Fig. 5e.

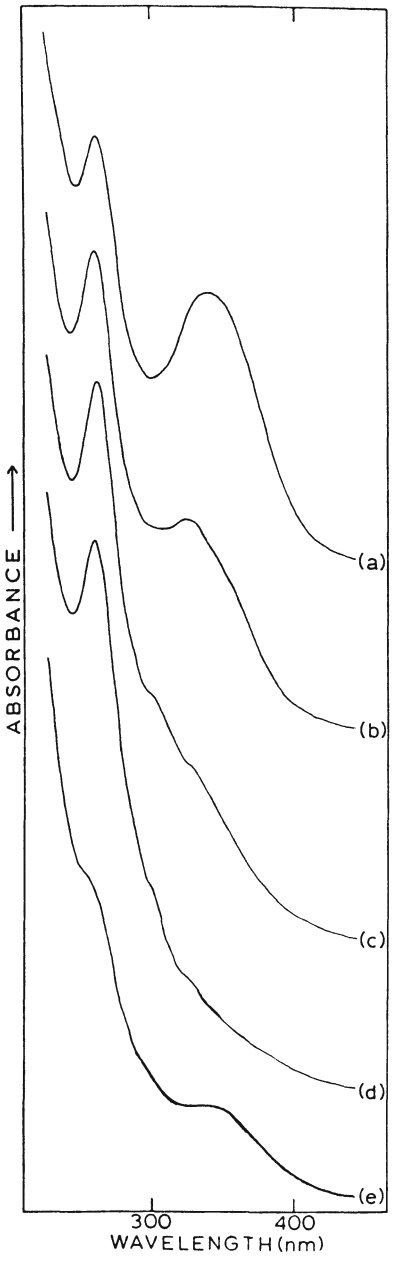

Fig. 5. Ultraviolet spectra of products formed upon 22 K codeposition of benzyl bromide vapor with argon from a microwave discharge. (a) Spectrum after 1 h codeposition with 140 m torr discharge, (b) spectrum after 380 nm cut-off photolysis for 10 min, (c) spectrum after 340-600 nm irradiation for 10 min, (d) spectrum after 290 nm photolysis for 10 min; (e) spectrum after full arc photolysis for 10 min (lamp has no output at shorter wavelength than 220 nm).

The strong 353 nm absorption in solid argon is assigned to the benzyl cation, 3, based on agreement with the 363 nm band produced by pulse radiolysis of several benzyl compounds in 1,2-dichloroethane solution [48]. Typically, solution spectra are red shifted from argon matrix spectra which are in turn red shifted from gas phase spectra. A representative example is benzyl radical observed at 305.3 nm in the gas phase, 310.5 nm in solid argon at 22 K and 318.2 nm in glassy matrices at 77 K [34, 50, 51]. Likewise, the 263 nm band produced on photolysis of the 353 nm absorption is assigned to the tropylium cation, 4, owing to agreement with the 274 nm absorption of tropylium salts in concentrated acid solutions; the stronger 217 nm absorption of 4 in acid solutions is probably displaced to near 208 nm in solid argon where it is obscured by the benzyl bromide absorption and the steeply scattering background in this region. Considering the matrix shift observations for benzyl radical, it is reasonable to expect spectra of 4 to red shift from gas to solid argon to solution phases, particularly in the latter case of a cation in an aqueous acid medium. Since the ionization energies of benzyl radical (7.2 eV) [52] and tropyl radical (6.2 eV) [53] are relatively low compared to argon (15.8 eV), 3 and 4 do not interact significantly with the argon matrix, and the argon matrix spectra should be representative of the gas phase. Further evidence supporting these spectroscopic observations of 3 and 4 is found in their photochemical interconversion.

The figure shows five general photochemical observations that are of interest here: (1) the 353 nm benzyl cation band decreases when the sample is irradiated within the absorption band beginning at 420 nm (the longest wavelength used here), (2) brief photolysis with 420 and 380 nm cut-off radiation produces a new species absorbing at 325 nm, (3) photolysis with 340-600 nm and 290-1000 nm light reduces the benzyl cation band symmetrically and produces the 263 nm tropylium cation absorption, (4) photolysis with 220 nm radiation destroys 4 and regenerates a small yield of 3 without any 325 nm absorption, and (5) continued ultraviolet photolysis decreases both 3 and 4 absorptions owing to neutralization by electrons photodetached from bromide ion electron traps. These observations will be discussed in turn.

(1) The postulated equilibrium between 3 and 4 at relatively low internal energies in the gas phase suggests a ready rearrangement of 3 upon excitation. MINDO/3 calculations predict an activation energy of 33 kcal/mole [54] and experimental energy relationships give approximately the same barrier [32] for the 3 → 4 isomerization, which is exceeded by absorption at 420 nm (68 kcal/mole). The least endothermic dissociation process, $C_7H_7^+$ to $C_5H_5^+$ and C_2H_2, however, requires 95 kcal/mole (300 nm) [32]. The near ultraviolet electronic absorption of 3 provides ample internal energy for rearrangement, but insufficient energy for photodissociation.

(2) The interconversion between 3 and 4 may involve intermediate $C_7H_7^+$ isomeric species with different structures. Calculations have predicted local minima for norcaradienyl cation and 1-cycloheptatrienyl cation (9 and 10 in Ref. 54) with activation energies of 18 and 23 kcal/mole for their formation [54]; these required energies are exceeded by the matrix photolysis. Furthermore, evidence has been presented for norbornadienyl cation as a stable species in the gas phase [32] and in acid solutions [55], and photolysis of 4 in solution has produced norbornadienyl cation with a mechanism suggested to involve a bicyclo[3.2.0]heptadienyl cation intermediate [56]. The 325 nm absorption formed on 380 nm photolysis of 3 (Fig. 5b) is assigned to a $C_7H_7^+$ structure different from 3 and 4. The weak absorption revealed at 300 nm on 340 and 290 nm photolysis (Fig. 5c, d) may be due to a still different structure. Since norbornadienyl cation exhibits no absorption above the 330 nm cut-off of liquid SO_2 [55], it is unlikely that the 325 nm matrix absorption is due to norbornadienyl cation. More likely, the 325 nm argon matrix absorption may be due to norcaradienyl cation 5, which can be readily formed upon photoexcitation of 3 in the matrix.

5 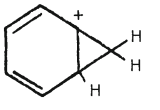

(3) Photolysis with 290-1000 nm radiation gives essentially complete destruction of absorption in the 300 nm region, which results in a maximum yield of the 263 nm absorption due to 4. The 3 → 4 rearrangement is complete insofar as the competitive photoneutralization process will allow.

(4) The full mercury arc provides photon energies up to about 125 kcal/mole which clearly exceed the 95 kcal/mole activation energy [32] for dissociation of 2 to $C_5H_5^+$. Nevertheless, a small amount of 3 is reformed from 4 although dissociation clearly dominates (Fig. 5d). The rearrangement process can be cycled back and forth [49], but both absorptions are reduced in the process owing to the favorably competitive dissociation pathway. The role of the matrix in quenching internal energy makes it possible for some 4 → 3 rearrangement to be observed. This photochemical isomerization of 4 → 3 in solid argon is analogous to the previous matrix observation of the photo isomerization of cycloheptatriene cation to toluene cation.

(5) The final point in these photolysis studies is that when the 369 nm photodetachment threshold [57] of the bromide ion electron trap is exceeded, photoneutralization of all isolated cations will proceed. Experiments with CF_3^+ and Br^- have shown that this is a relatively slow process (approximately 30% reduction in 125 min)

[58], hence the dominant mechanism for the 10 min 220-1000 nm photolysis studies is ion photodissociation.

Recent photodissociation studies have been performed on gaseous $C_7H_7^+$ ions in an ICR trap [59]. Although the method of preparing these $C_7H_7^+$ ions suggested the $\underset{\sim}{3}$ structure, based on reactivity in earlier studies [33], the broad PDS band peak at 290 ± 10 nm is not compatible with the pulse radiolysis observation of $\underset{\sim}{3}$ at 363 nm in solution or the present 353 nm argon matrix absorption. The PDS is not compatible with $\underset{\sim}{4}$ since the gaseous spectrum of $\underset{\sim}{4}$ is expected to the blue of the acid solution (and solid argon) observations. It is suggested that the ions in the ICR cell possess sufficient internal energy upon formation to undergo rearrangements and that the gaseous ion population contains $C_7H_7^+$ ions with a different structure than $\underset{\sim}{3}$.

Halobenzene and Halotoluene Cations

The halobenzene and halotoluene cations have been studied extensively by PES, PDS, and mass spectrometric methods [60-63]. Matrix investigations were performed for comparison to the PDS results.

The maximum at 505 nm in bromobenzene matrix experiments is slightly red-shifted from the 2.50 ± 0.05 eV (490 ± 10 nm) gas-phase PDS maximum; the matrix band position and its photodissociation with 500 nm radiation support assignment of the 505 nm absorption to bromobenzene cation [64]. The 470 nm maximum in similar chlorobenzene studies is also slightly red shifted from the 2.70 eV (459 nm) PDS maximum, and it photolyses substantially with 420 nm radiation, which suggest assignment to the chlorobenzene cation [64]. The 430 nm absorption in fluorobenzene experiments is just lower in energy than the 2.95 eV (420 nm) difference between the onset of ionization and the Franck-Condon maximum in the PES of fluorobenzene [3] and the weak absorption reported near 427 nm in neon matrix photoionization experiments [65]. It is noteworthy that the 430 nm argon matrix band, assigned to fluorobenzene cation, decreased about 10% on 380 nm photolysis and was essentially destroyed by full arc photolysis.

Two-photon dissociation of the heavy halobenzene cations with visible light has been documented in the gas phase [60]. This process involves absorption by the first photon into the excited state, followed by internal conversion to high vibrational levels of the ground electronic state and absorption of a second photon into dissociation. In the present matrix experiments, bromobenzene cation was markedly reduced by 500 nm photolysis, which is below the 355 ± 5 nm one-photon dissociation threshold for bromine atom elimination, and chlorobenzene cation was substantially reduced by 420 nm photolysis, below the 310 ± 5 nm one-photon threshold for chlorine atom detachment [60]. This suggests that sequential two-photon processes can take place in a solid argon matrix when the oscillator strength

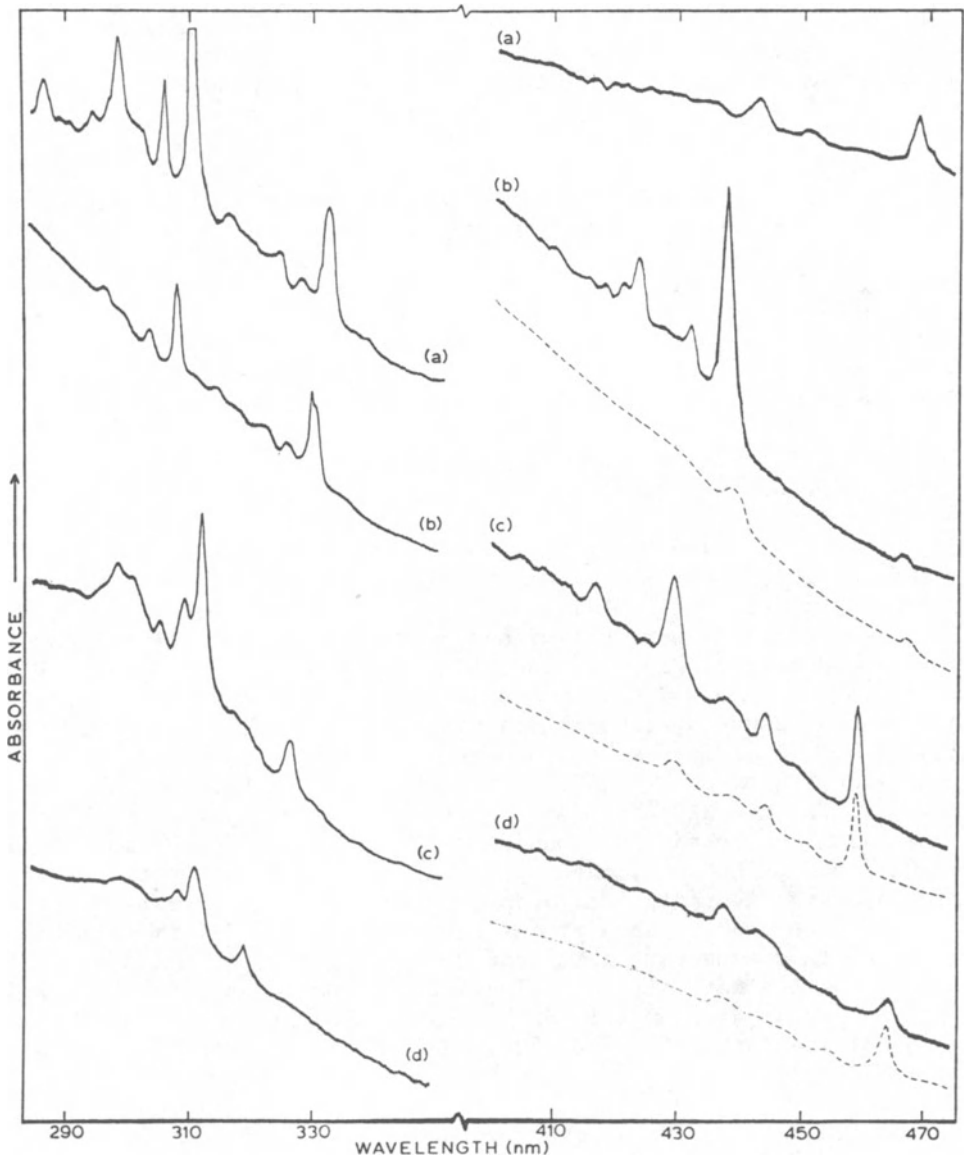

Fig. 6. Absorption spectra of fluorotoluene samples subjected to matrix photoionization during condensation. (a) Kr/p-fluorotoluene, (b) Ar/para, (c) Ar/ortho, (d) Ar/meta. The dashed traces were recorded after visible photolysis.

of the transition is large enough to produce absorption by chlorobenzene and bromobenzene cations before most of their internal energy is removed by the matrix host. A similar two-photon dissociation of styrene cation will be described in the next section. Although the matrix rapidly quenches internal energy from the absorbing species, sequential two-photon processes are possible in a matrix environment when the cross-section for initial photon absorption is particularly large.

In contrast, the fluorobenzene cation was not significantly decreased upon 380 nm photolysis, though it was destroyed with 220 nm radiation, which is above the one-photon threshold. This may be rationalized by the fact that the $\pi \leftarrow n_z$ charge-transfer transition in chlorobenzene and bromobenzene cations have very high oscillator strengths, but due to the small interaction of the fluorine lone pair electrons with the ring π electrons, the visible transition for fluorobenzene is $\pi \leftarrow \pi$, which has a lower oscillator strength.

The optical spectra of fluorotoluenes subjected to matrix photoionization during condensation [66] are contrasted in Fig. 6. The p-fluorotoluene precursor gave a series of sharp absorptions at 437.9, 431.5, and 423.5 nm, which were destroyed by 420 nm light, as indicated by the dashed trace in Fig. 6b. A 329.8 nm band was destroyed by full arc photolysis, whereas bands at 465.4, 308.0, 303.5, and 296.2 nm were not affected by photolysis. The o-fluorotoluene experiment, Fig. 6c, revealed photosensitive bands at 429.5 and 416.6 nm. A new 326.0 nm absorption was destroyed by 220 nm photolysis and new systems beginning at 459.1 and 311.7 nm were decreased by 20%. The m-fluorotoluene study gave lower product yields; a new weak 444 nm band was destroyed by 420 nm light, as shown in Fig. 6d. The new 318.4 nm feature was unaffected by 420 nm photolysis which increased sharp bands at 464.2, 454.8, 310.5, and 307.8 nm. Another p-fluorotoluene experiment was done in krypton using krypton discharge radiation, and the spectrum is illustrated in Fig. 6a. The product absorptions were red shifted 2-4 nm from their argon matrix counterparts, and the relative yields of the several product species were altered. The 441.8 nm band was reduced to 20% of its 437.9 nm argon matrix counterpart, whereas the 332.5 nm band was doubled and the 467, 310, 306, and 298 nm bands were increased four-fold.

The photosensitive absorptions at 437.9, 429.5, and 444 nm in the fluorotoluene matrix studies are near PDS bands for fluorotoluenes in the 420 ± 5 nm [61], and accordingly the matrix absorptions are assigned to the parent cations [66]. The weaker satellite bands in the p- and o-fluorotoluene studies are probably due to vibrational structure. The visible and ultraviolet bands stable to photolysis are due to fluorobenzyl radicals [66]; the ultraviolet band photolysed by the full arc is likely due to a free radical formed upon H atom addition to the aromatic ring [67].

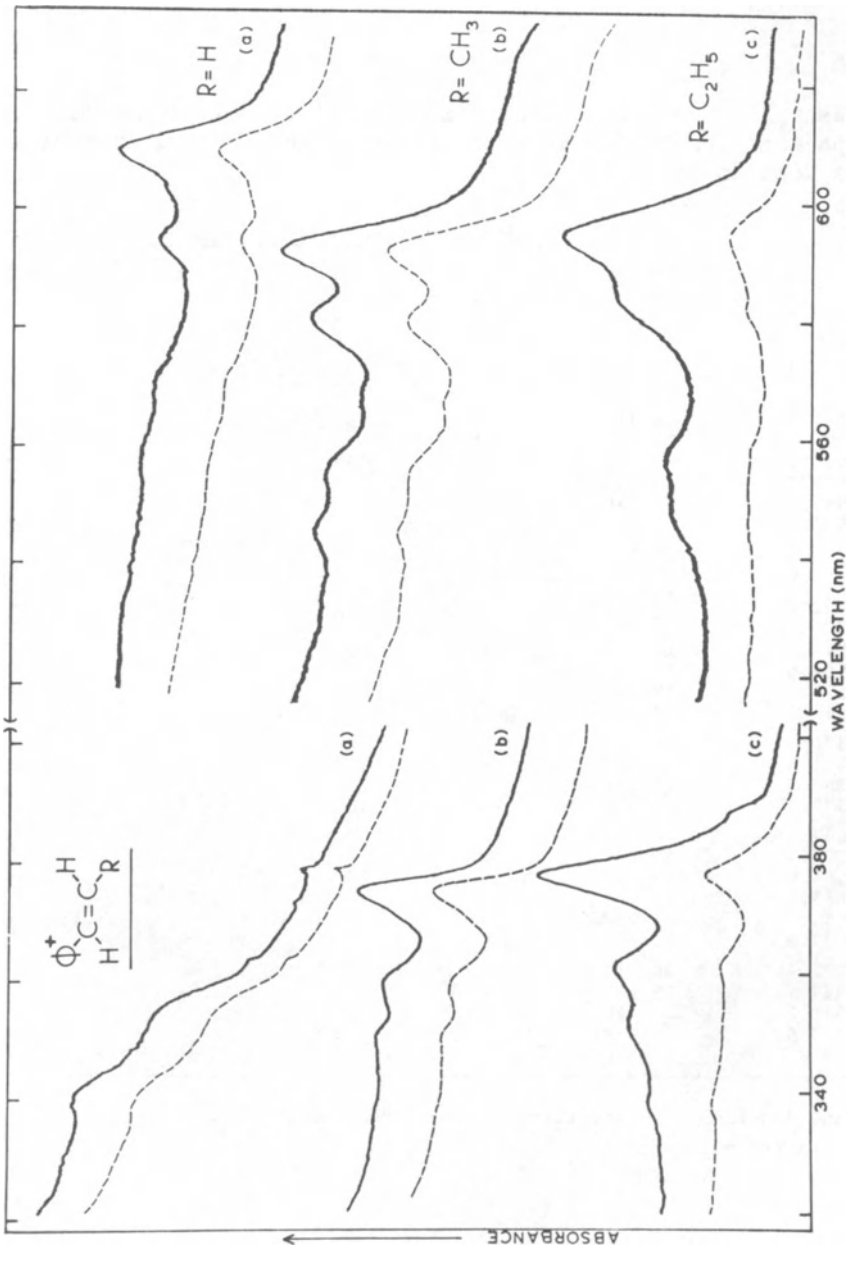

Fig. 7. Absorption spectra of styrene and substituted styrenes subjected to argon resonance photoionization during condensation. (a) Styrene, uV recorded on 0.2 A range, red on 0.1 A range, dashed trace after 500-1000 nm photolysis. (b) β-Methyl styrene, uV recorded on 0.5 A range, red on 0.1 A, dashed trace after 420 nm photolysis. (c) β-Ethyl styrene, uV recorded on 0.5 A range, red on 0.2 A, dashed trace after 500 nm photolysis.

Table 1. Absorption Band Positions (nm and cm^{-1}) and Vibrational Spacings (cm^{-1}) for Styrene, β-Methyl and β-Ethyl Styrene Cations in Solid Argon[a]

	λ (nm)	ν (cm^{-1})	Δ (cm^{-1})	Δ (cm^{-1})	Δ (cm^{-1})	Δ (cm^{-1})
styrene	608.5	16 434	0	0		
R=H	593.0	16 863	429			
	569.0	17 575	0	1141		
	556.0	17 986	411			
	353.0	28 329		0		
	339.0	29 499		1170		
β-methyl	591.1	16 918	0	0	0	0
R=CH_3	579.1	17 268	350			
	565.8	17 647		756		
	553.8	18 057	0		1139	
	543.6	18 396	339			1478
	533.5	18 744	348			
	373.6	26 767		0		
	357.8	27 949		1182		
	349.0	28 653		704		
	337.2	29 656		1003		
β-ethyl	594.2	16 829	0	0		
R=C_2H_5	582.8	17 159	330			
	556.2	17 979	0	1150		
	546.3	18 305	326			
	376.6	26 553		0		
	361.0	27 701		1148		
	350.6	28 523		822		
	337.9	29 595		1072		
β-methyl-d_5	589.4	16 966	0	0	0	0
R=CH_3	578.4	17 289	323			
	564.0	17 730		764		
	553.6	18 064			1098	
	547.0	18 282	0			1316
	537.0	18 622	340			
	372.9	26 817		0		
	357.4	27 980		1163		
	348.2	28 719		739		
	337.0	29 674		955		

[a]Absorption band positions are accurate to better than ± 10 cm^{-1} in the red and ± 25 cm^{-1} in the ultraviolet.

Styrene Cations

The spectroscopic properties of styrene and substituted styrene radical ions are of interest as conjugated aromatic cations. An extensive PDS study [68] on these ions provides a basis for detailed comparison with optical spectra and photochemistry of styrene ions in solid argon.

Figure 7 compares the matrix absorption spectra of (a) styrene, (b) 1-phenyl-1-propene, and (c) 1-phenyl-1-butene and shows similarity in the electronic structure of the absorbing species [69]. The dashed traces, recorded after visible photolyses, demonstrate that the red and near ultraviolet absorption systems are due to the same species since the two absorptions decrease in concert upon irradiation into the red absorption. It can also be seen that β-methyl styrene cation is the most photolytically stable of the styrene cations studied here. The 1-phenyl-d_5-1-propene cation was also prepared and the observed absorptions are given in Table 1.

Styrene cation exhibits a 630 nm absorption with a 590 nm shoulder and a 340 nm absorption in s-butyl chloride glass [70]. Owing to the 518 nm threshold for one-photon dissociation to $C_6H_6^+$ and C_2H_2, the PDS shows only a 330 nm peak with a 315 nm shoulder although some presumably two-photon dissociation was observed at 579 nm [68]. The PES for styrene exhibits three sharp bands for π ionizations before the broad σ orbital ionization [68, 71]; the excitation energy between the first onset and the third vertical ionization energies, 2.13 eV, suggests a red absorption near 582 nm. The matrix spectrum reveals two ultraviolet bands at 353 and 339 nm and a structured red band system beginning at 608.5 nm, which are given in Table 1.

The PDS for 1-phenyl-1-propene cation exhibits peaks at 354 and 579 nm with full-widths at half-maximum of about 3500 and 2000 cm^{-1}, respectively. The origins of the matrix absorptions at 373.6 and 591.1 nm are displaced 1464 and 343 cm^{-1}; however, the matrix bandwidths are less than 600 and 300 cm^{-1}, respectively, and vibrational structure, listed in Table 1, is clearly resolved. The PDS of 1-phenyl-1-butene is indistinguishable from the PDS of 1-phenyl-1-propene; however, Fig. 7 reveals resolvable differences in the matrix band positions, although the data in Table 1 show that the vibrational intervals are almost identical. As discussed in a previous section for toluene cation, the argon matrix bands are substantially sharper than the PDS bands. In the case of β-methyl styrene cation, the matrix bands are a factor of 6 sharper. This difference is again attributed to the quenching of internal energy by the matrix. The PES for styrene and β-methyl styrene [68] predict red absorptions at 2.13 ± 0.02 and 2.20 ± 0.02 eV (582 ± 5 and 563 ± 5 nm), respectively, in the gas phase. The approximately 800 cm^{-1} differences between PES band differences and matrix observations can be attributed to matrix solvent shifts.

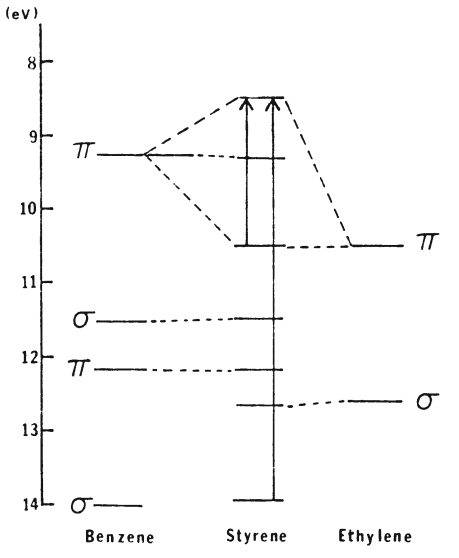

Fig. 8. Molecular orbital energy diagram for benzene, styrene, and ethylene showing the red and ultraviolet $\pi \leftarrow \pi$ transitions.

Assignments for the optical bands of styrene cation have been given by Fu and Dunbar [68] according to the orbital energy diagram in Fig. 8. The red transition moves an olefin π electron into the ring π hole and can be described as $\pi(\text{ring}) \leftarrow \pi(\text{olefin})$. The ultraviolet absorption is analogous to the $^2A_{2u} \leftarrow {}^2E_{1g}$ transition on benzene cation, but it is slightly blue shifted owing to interaction between the olefin and ring π systems; this transition is designated $\pi(\text{ring}) \leftarrow \pi(\text{ring})$.

In two styrene cation experiments, the sample was first photolysed for 30 m through a Corning 2-63 glass filter (cuts off at about 560 nm, 1% transmitting at 585 nm, and 70% transmitting at 608 nm), both band systems were decreased by 15% in each experiment. Since this dissociating radiation is clearly below the 518 nm one-photon threshold [68], it seems possible that styrene ion dissociation in this region involves a sequential two-photon dissociation process. The alternative explanation of photoneutralization requires an electron trap that can undergo absorption and photodetachment with 580 nm radiation. Although a very weak C_2^- band [5] was detected at 520.7 nm in these experiments, vibrationally quenched C_2^- cannot be photodetached with the long wavelength radiation employed here [71].

In spite of the rapid quenching of internal energy by the matrix, this $\pi(\text{ring}) \leftarrow \pi(\text{olefin})$ "charge-transfer" transition is sufficiently strong for the molecular ion to absorb a second photon be-

fore the matrix quenches all of the internal energy provided by the first photon. Although two-photon dissociation of styrene cation in solid argon was observed, photodissociation by one photon in the ultraviolet absorption bands was substantially more efficient, as shown by an 85% reduction in both styrene cation absorptions after 290-1000 nm photolysis.

Perhaps the most interesting aspect of the matrix work on styrene cations is the vibrational structure. Examination of Table 1 reveals two vibrational modes, one near 1150 cm^{-1} and one in the 330-420 cm^{-1} range, which are active in the vibronic absorption bands of the three phenyl alkene cations reported here. Aromatic in-plane C-H bending modes are found at 1178 cm^{-1} for benzene and 1180 cm^{-1} for styrene; in addition, styrene exhibits a polarized Raman band at 1203 cm^{-1}, and phenyl acetylene has a similar band at 1192 cm^{-1}, which are due to ϕ-C stretching vibrations [72, 73, 74]. The small deuterium shift for the latter mode points to assignment of the 1139-1182 cm^{-1} intervals to ϕ-C stretching vibrations as well. This mode should be active in both electronic transitions since conjugation between the two π systems will be different for each electronic state. The lower frequency mode observed twice in each red absorption showed a decrease from about 420 cm^{-1} for styrene cation to 350 cm^{-1} for β-methyl styrene cation and 330 cm^{-1} for β-ethyl styrene cation. The observation of such a pronounced substituent effect indicates that this mode involves a skeletal bending vibration of the alkene group. Styrene itself exhibits a bending mode at 440 cm^{-1} [73]. It is reasonable to expect ϕ-C=C bending vibrations to be active in the π(ring) $\leftarrow$ π(olefin) transition, since an electron from the olefin π bond is promoted to the hole on the aromatic ring, and the ϕ-C=C skeletal angle may change due to reorganization of the conjugation between the two π systems.

1-Phenyl-1-propyne Cation

Absorption spectra of phenyl alkyne cations were investigated as an extension of the foregoing studies on phenyl alkenes. The spectrum of 1-phenyl-1-propyne cation in solid argon is of special interest for the sharp vibrational fine structure, illustrated in Fig. 9a [75]; the strong 586 nm absorption was 125 cm^{-1} wide at half-maximum. Photolysis with the Corning 2-63 filter for 30 m, which transmits 1% in the strong 586 nm peak, reduced all product absorptions (except 348 nm) by 10%, irradiation with 500-1000 nm light reduced the bands by 50% (except 348 nm), and a 290-1000 nm photolysis reduced the product bands by 70% and destroyed the 348 nm feature. Clearly the product bands listed in Table 2 belong to a common photosensitive species and the 348 nm band is due to a different absorber.

Similar experiments performed with phenyl acetylene gave a structured red absorption beginning at 577.5 nm as listed in Table 2,

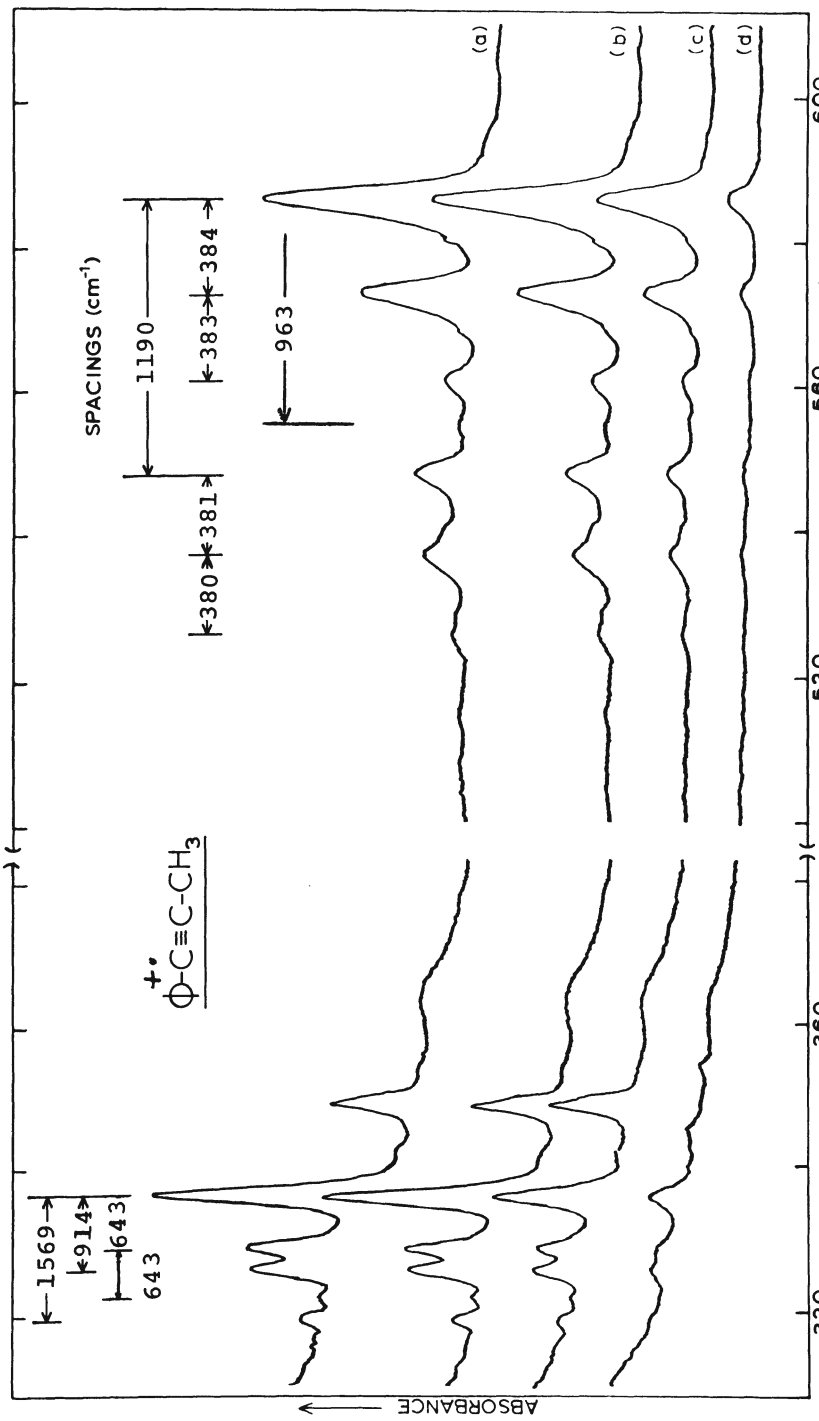

Fig. 9. Absorption spectrum of 1-phenyl-1-propyne codeposited with argon resonance radiation from open discharge lamp, trace (a), both regions recorded on 0.5 A range. Spectrum (b) recorded after 30 m of 580-1000 nm photolysis, trace (c) following 30 m of 50-1000 nm irradiation, and spectrum (d) after 30 m of 290-1000 nm photolysis.

Table 2. Absorption Band Positions (nm and cm^{-1}) and Vibrational Spacings (cm^{-1}) for Phenyl Acetylene and 1-Phenyl-1-propyne Cations in Solid Argon

	λ(nm)	ν(cm^{-1})	Δ(cm^{-1})	Δ(cm^{-1})	Δ(cm^{-1})
phenyl-acetylene[a]	577.5	17 316	0	0	0
	563.3	17 753	437		
	547.2	18 275		959	
	542.4	18 437	0	0	1121
	529.9	18 871	434		
	516.0	19 380		943	
	329	30 395			
1-phenyl-1-propyne[b]	585.9	17 068	0	0	0
	573.0	17 452	384		
	560.7	17 835	383		
	554.6	18 031		963	
	547.7	18 258	0		1190
	536.5	18 639	381		
	525.8	19 019	380		
	514.6	19 433			1175
	335.7	29 789	0	0	0
	328.6	30 432	643		
	325.7	30 703		914	
	321.8	31 075	643		
	318.9	31 358			1569

[a]Absorption band positions are accurate to better than ± 20 cm^{-1}.

[b]Red absorption band positions are accurate to ± 5 cm^{-1} and ultraviolet band positions accurate to ± 10 cm^{-1}.

with bandwidths a factor of two larger than the propyne derivative; no absorption was observed near 800 nm. As in the case of the styrene species, the ultraviolet band was less pronounced for the unsubstituted phenyl alkyne, and only a weak photosensitive 329 nm absorption was observed [75].

The PES of phenyl acetylene contains four sharp bands due to π orbital ionizations before onset of the broad σ orbital ionizations [76, 77]. The strong red matrix band at 577.5 nm is in excellent agreement with the 2.19 ± 0.02 eV (average from two reports) [76, 77] difference between the first and fourth ionization energies which predicts absorption at 566 ± 5 nm. Observation of an intense absorption for this transition of the ion supports an out-of-plane acetylenic π orbital assignment since the π(ring) ← π(alkyne) "charge-transfer" transition is expected to be very strong as found for the styrenes. No absorption appears at 1.50 eV (800 nm) in the matrix spectrum; the 10.38 eV ionization from an orbital identified as π(C≡C) probably involves the in-plane acetylenic π orbital. The phenyl acetylene cation is, therefore, like chlorobenzene cation [36, 60], in that two chlorine lone pair ionizations

were observed in the PES (in-plane 3p and out-of-plane 3p); however, only the out-of-plane lone pair can undergo an allowed optical transition with the ring π system.

The vibrational structure found in the phenyl alkyne cations is similar to that found in the phenyl alkene cations. The intervals in the mid-1100 cm^{-1} region are probably due to the ϕ-C bond stretching modes; this vibration has been observed at 1192 cm^{-1} for the phenyl acetylene molecule. The mid-900 cm^{-1} interval is suggestive of aromatic ring breathing modes, observed at 992 cm^{-1} for benzene [72] and 998 cm^{-1} for phenyl acetylene [74]. The approximately 435 cm^{-1} spacing for phenyl ethyne cation decreases to 384 cm^{-1} for phenyl propyne cation, again demonstrating a substituent effect. This interval, active in the red π(ring) ← π(alkyne) transition, is assigned to the out-of-plane ϕ-C≡C bending mode.

The ultraviolet absorption for 1-phenyl-1-propyne cation is assigned to the π(ring) ← π(ring) transition involving the aromatic ring analogous to the $^2A_{2u} \leftarrow {}^2E_{1g}$ transition of benzene cation. It is immediately recognized that the 643 cm^{-1} vibrational interval is near the Jahn-Teller active [72] $\nu_{18}(e_{2g})$ mode of benzene, 606 cm^{-1}, and PES measurements of 685, 670, and 610 cm^{-1} for this mode of benzene cation [78-80]. The 1569 cm^{-1} spacing is also near $\nu_{16}(e_{2g})$ for benzene at 1585 cm^{-1}. The 914 cm^{-1} interval is slightly lower than the 963 cm^{-1} value ascribed to the aromatic ring-breathing mode for the upper state in the π(ring) ← π(alkyne) transition; it is reasonable for the ring breathing mode to be lower in a state with a hole in the strongly bonding ring π orbital than in a state with the hole primarily in an acetylenic π orbital. Finally, the vibrational fine structure in the π(ring) ← π(ring) transition for 1-phenyl-1-propyne cation is a plausible model for the $^2A_{2u} \leftarrow {}^2E_{1g}$ transition of benzene cation.

Biphenyl Cation

The biphenyl cation is a unique substituted benzene cation. Of particular interest is the extent of π conjugation with variation of the dihedral angle in the neutral molecule, which is 40-45° in the gas phase [81], coplanar in the crystal [82], and intermediate in solid argon [83]. The biphenyl cation has been observed at 380 and 690 nm by pulse radiolysis in solution [84] and at 390 and 700 nm following γ-radiolysis in hydrocarbn glasses [70]. Photoelectron spectra of biphenyl have been observed and assigned to π-orbital ionizations [81, 85]; the first band in the PES is rather broad, indicating some change in geometry between the ground states of the positive ion and neutral molecule.

The argon matrix spectra for samples of $C_{12}H_{10}$ and $C_{12}D_{10}$ subjected to argon resonance photoionization during condensation [86]

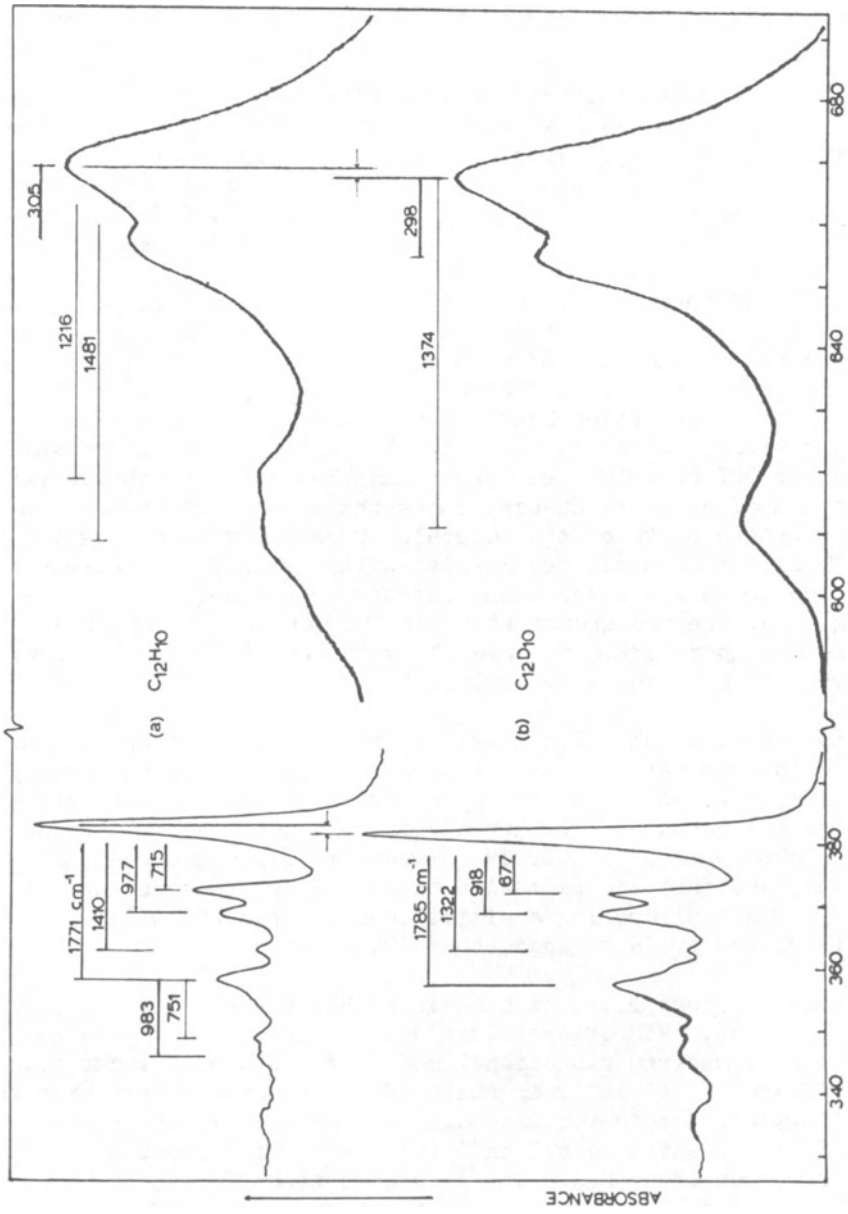

Fig. 10. Absorption spectra of biphenyl vapor codeposited with argon from open discharge lamp. (a) $C_{12}H_{10}$, (b) $C_{12}D_{10}$. Ultraviolet region recorded on 0.5 A range, red on 0.1 A range.

are contrasted in Fig. 10. The strong sharp 382.8 nm and the broad 669 nm absorptions are in excellent agreement with the solution and glass spectra. The 96 and 54 cm^{-1} blue shifts of the most intense features on deuteration are in accord with the 113 cm^{-1} blue shift in the 33 876 cm^{-1} allowed transition for the crystalline molecule [87].

Comparison between the matrix absorption band origin positions at 382.8 and 669 nm for $C_{12}H_{10}^+$ and the PES is limited by selection of the zero point energy position on the PES to represent the quenched ground state ion in solid argon. The first PES band peaks at 8.32 eV and has a width of about 4000 cm^{-1}; and 8.00 ± 0.05 onset [81, 85] was selected for this band. Since the matrix absorptions are band origins, onsets of 9.75 ± 0.05 and 10.95 ± 0.05 eV were selected from PES spectra for the π_3 and π_2 bands, respectively. The differences between these estimated adiabatic ionization energies predict absorption bands at 708 ± 40 and 420 ± 14 nm for $C_{12}H_{10}^+$. The general agreement between PES and matrix absorption supports assignment of the absorption bands to the $\pi_6 \leftarrow \pi_3$ and $\pi_6 \leftarrow \pi_2$ electronic transitions, respectively. The blue shifts from PES to solid argon of about 800 cm^{-1} for the former and 2300 cm^{-1} for the latter are indicative of geometry changes among the several states of the ion and the ground state of the molecule, presumably involving the dihedral angle, since small red matrix shifts are normally observed. The broad 669 nm matrix absorption suggests some change in the dihedral angle between the ground state of the ion and the excited state while the sharp 382.8 nm absorption infers similar structures for the two states of the ion involved in this transition.

The two absorptions and the associated structure belong to the same species as demonstrated by their concerted behavior on photolysis and sample warming. Exposure to 520-1000 nm radiation for 30 m reduced all bands by 15%, irradiation by 380-1000 nm light decreased the absorptions by 20%, 290 nm cut-off light reduced all bands by 35%, and full arc radiation (220-1000 nm) reduced the bands another 10%. Thermal cycling a similar sample from 20 to 40 to 20 K reduced all of the product bands about 30%.

The sharp, strong 382.8 nm band is probably the 0-0 band of the $\pi_6 \rightarrow \pi_2$ transition. Vibrational intervals noted in the figure can be assigned to symmetric vibrational modes of the biphenyl cation. The first interval, 715 cm^{-1}, in the $C_{12}H_{10}^+$ spectrum corresponds to a 739 cm^{-1} symmetric mode for the molecule observed in the Raman spectrum [88]; the shift to 677 cm^{-1} for $C_{12}D_{10}^+$ is compatible with the Raman spectrum of $C_{12}D_{10}$. The second interval for $C_{12}H_{10}^+$, 977 cm^{-1}, is in reasonable agreement with the very strong 1002 cm^{-1} Raman band for $C_{12}H_{10}$, and this interval for $C_{12}D_{10}^+$, 918 cm^{-1}, exhibits a slightly larger deuterium shift than the very strong 965 cm^{-1} Raman band for $C_{12}D_{10}$. The weaker third interval at 1410 cm^{-1}

is probably due to 2 × 715 cm^{-1} = 1430 cm^{-1} with the discrepancy due to anharmonicity.

The peak 1771 cm^{-1} higher energy than the strong origin does not appear to fit a symmetric fundamental of $C_{12}H_{10}$. Furthermore, this interval increases to 1785 cm^{-1} on deuteration; in fact the absolute band position blue shifts 110 cm^{-1}. This suggests that the 358.5 nm band is the origin of another electronic transition. A splitting of 747 cm^{-1} has been reported between the $^1B_{2u}$ and $^1B_{3g}$ excited states of biphenyl in crystals owing to inter-ring resonance interaction [87]. The vibrational intervals of 751 and 983 cm^{-1} built on this new origin are reminescent of the first two intervals described above.

The broad 669.4 nm band is assigned as the origin of the $\pi_6 \leftarrow \pi_3$ transition. The 305 cm^{-1} interval corresponds to the 330 cm^{-1} Raman band of $C_{12}H_{10}$ and the 1216 cm^{-1} and 1481 cm^{-1} spacings are near the very strong 1276 cm^{-1} and medium 1513 cm^{-1} Raman bands [88]. In the $C_{12}D_{10}^+$ spectrum, the origin is blue shifted to 667 nm and the first interval is observed at about 298 cm^{-1} and another interval is found at 1374 cm^{-1}, which are compatible with Raman shifts for the deuterated molecule [88].

Conclusions

Optical spectra of molecular ions in solid argon provide useful comparisons with PES and PDS of gaseous ions and with electronic spectra of ions in glassy matrices. The examples discussed here, with ionization energies in the 6-12 eV range, show small interaction with the argon matrix. In general the argon matrix absorption falls intermediate between the gaseous PDS and glassy matrix values; argon matrix shifts of 0.02 to 0.1 eV to lower energy have been observed in most cases. The fact that argon matrix absorptions are sharper than PDS and glassy matrix bands makes it possible to observe and assign vibrational structure.

The solid argon matrix is an effective trap for particularly facile molecular ions like CCl_4^+, which, if vibrationally relaxed, may be stabilized in a geometry different from the neutral molecule.

A particular advantage of the solid argon medium is rapid quenching of internal energy from the ion after its formation, which gives substantially sharper bands than observed by PDS methods. Vibrational quenching by the matrix is also responsible for changes in photophysical dynamics. Fast relaxation in the excited state results in a reduced internal conversion rate and a reduced dissociation rate which allows rearrangement processes to compete favorably with photodissociation.

Acknowledgements

The research described here was supported by the U. S. National Science Foundation. Helpful discussions with a number of people at the ASI, particularly Sidney Leach, are gratefully acknowledged.

References

1. L. Andrews, Ann. Rev. Phys. Chem., 30, 79 (1970).
2. T. Shida, Y. Nosaka, and T. Kato, J. Phys. Chem., 82, 695 (1978); E. Haselbach, T. Bally, R. Gschwind, U. Klemm, and Z. Lanyiova, Chimia, 33, 405 (1979).
3. D. W. Turner, C. Baker, D. W. Baker, and C. R. Brundle, in: Molecular Photoelectron Spectroscopy, John Wiley, New York (1970).
4. R. C. Dunbar, "Ion Photodissociation," in: Gas Ion Chemistry, Vol. 2, M. T. Bowers, ed., Academic Press, New York (1979).
5. D. E. Milligan and M. E. Jacox, J. Chem. Phys., 51, 1952 (1969).
6. G. Herzberg and A. Lagerqvist, Can. J. Phys., 46, 2363 (1969).
7. L. E. Brus and V. E. Bondybey, J. Chem. Phys., 63, 3123 (1975).
8. L. Andrews, D. W. Tevault, and R. R. Smardzewski, Appl. Spectrosc., 32, 157 (1978).
9. L. Andrews, J. Chem. Phys., 63, 4465 (1975).
10. F. T. Prochaska and L. Andrews, J. Chem. Phys., 67, 1091 (1977).
11. L. Andrews and F. T. Prochaska, J. Phys. Chem., 83, 368 (1979).
12. D. W. Skelly and W. H. Hamill, J. Phys. Chem., 70, 1630 (1966).
13. T. Shida and W. H. Hamill, J. Chem. Phys., 44, 2369 (1966).
14. A. S. Werner, B. P. Tsai, and T. Baer, J. Chem. Phys., 60, 3650 (1974).
15. F. T. Prochaska and L. Andrews, J. Chem. Phys., 68, 5568, 5577 (1978).
16. H. W. Jochims, W. Lohr, and H. Baumgartel, Ber. Bunsenges. Phys. Chem., 80, 130 (1976).
17. J. Doucet, P. Sauvageau, and C. Sandorfy, J. Chem. Phys., 58, 3708 (1973).
18. L. Andrews, F. T. Prochaska, and B. S. Ault, J. Am. Chem. Soc., 101, 9 (1979).
19. R. N. Rylander, S. Myerson, and H. M. Grubb, J. Am. Chem. Soc., 79, 842 (1957).
20. S. Myerson, J. Am. Chem. Soc., 85, 3340 (1963).
21. F. Meyer and A. G. Harrison, J. Am. Chem. Soc., 86, 4757 (1964).
22. K. L. Rinehard, Jr., A. C. Buchholz, G. E. Van Lear, and H. L. Cantrill, J. Am. Chem. Soc., 90, 2983 (1968).
23. A. S. Siegel, J. Am. Chem. Soc., 92, 5277 (1970).
24. I. Howe and F. W. McLafferty, J. Am. Chem. Soc., 93, 99 (1971).
25. R. C. Dunbar, J. Am. Chem. Soc., 95, 472 (1973).
26. P. P. Dymerski, E. Fu, and R. C. Dunbar, J. Am. Chem. Soc., 96, 4109 (1974).

27. R. C. Dunbar, J. Am. Chem. Soc., 97, 1382 (1975).
28. R. C. Dunbar, Chem. Phys. Letts., 32, 508 (1975).
29. J. R. Eyler, J. Am. Chem. Soc., 98, 6831 (1976).
30. M. K. Hoffman and M. M. Bursey, Tetrahedron Letts., 27, 2539 (1971).
31. R. C. Dunbar and E. W. Fu, J. Am. Chem. Soc., 95, 2716 (1973).
32. F. W. McLafferty and J. Winkler, J. Am. Chem. Soc., 96, 5182 (1974); F. W. McLafferty and F. M. Bockhoff, J. Am. Chem. Soc., 101, 1783 (1979).
33. J. A. Jackson, S. G. Lias, and P. Ausloos, J. Am. Chem. Soc., 99, 7515 (1977).
34. L. Andrews, J. H. Miller, and B. W. Keelan, Chem. Phys. Letts., 71, 207 (1980).
35. L. Andrews and B. W. Keelan, J. Am. Chem. Soc., 102, 5732 (1980).
36. A. D. Baker, D. P. May, and D. W. Turner, J. Chem. Soc., B22 (1968).
37. N. Bodor, M. J. S. Deward, and S. D. Worley, J. Am. Chem. Soc., 92, 19 (1970); E. Heilbronner, personal communication (1980).
38. R. C. Dunbar, personal communication (1980).
39. H. M. Rosenstock, K. Draxl, B. W. Steiner, and J. T. Herron, J. Phys. Chem. Ref. Data 6, Supp. 1, I-158 (1977).
40. M. J. S. Deward and D. Landman, J. Am. Chem. Soc., 99, 2446 (1977).
41. J. T. Bursey, M. M. Bursey, and D. G. I. Kingston, Chem. Rev., 73, 191 (1973).
42. J. Shen, R. C. Dunbar, and G. A. Olah, J. Am. Chem. Soc., 96, 6227 (1974).
43. J. M. Abboud, W. J. Hehre, and R. W. Taft, J. Am. Chem. Soc., 98, 6072 (1976).
44. W. E. Doering and L. H. Knox, J. Am. Chem. Soc., 76, 3203 (1954).
45. G. Naville, H. Strauss, and E. Heilbronner, Helv. Chem. Acta, 43, 1221, 1243 (1952). E. Heilbronner and J. N. Murrell, Mol. Phys., 6, 1 (1963).
46. R. B. Medz, Ph.D. Thesis, University of Washington, Seattle, Washington (1964).
47. G. A. Olah, C. U. Pittman, Jr., R. Waack, and M. Dorna, J. Am. Chem. Soc., 68, 1488 (1966).
48. R. L. Jones and L. M. Dorfman, J. Am. Chem. Soc., 96, 5715 (1974).
49. L. Andrews and B. W. Keelan, J. Am. Chem. Soc., 103, 99 (1981).
50. G. Porter and F. Wright, Trans. Far. Soc., 51, 1469 (1955).
51. J. E. Hodgkins and E. D. Megarity, J. Am. Chem. Soc., 87, 5322 (1965).
52. F. A. Houle and J. L. Beauchamp, J. Am. Chem. Soc., 100, 3290 (1978).
53. B. A. Thrush and J. J. Zwolenik, Disc. Far. Soc., 35, 196 (1963).

54. C. Cone, M. J. S. Dewar, and D. Landman, J. Am. Chem. Soc., 99, 372 (1977).
55. P. R. Story and M. Saunders, J. Am. Chem. Soc., 82, 6199 (1960).
56. H. Hogeveen and C. J. Gaasbeek, Recl. Trav. Chim. Pays-Bas, 89, 1079 (1970).
57. R. S. Berry and C. W. Reimann, J. Chem. Phys., 38, 1540 (1963).
58. F. T. Prochaska and L. Andrews, J. Am. Chem. Soc., 100, 2102 (1978).
59. D. A. McCrery and B. S. Freiser, J. Am. Chem. Soc., 100, 2902 (1978).
60. R. C. Dunbar, H. H.-I. Teng and E. W. Fu, J. Am. Chem. Soc., 101, 6506 (1979).
61. E. W. Fu, P. P. Dymerski, and R. C. Dunbar, J. Am Chem. Soc., 98, 337 (1976).
62. A. N. H. Yeo and D. H. Williams, Chem. Comm., 886 (1970).
63. B. J. Stapleton, R. D. Bowen, and D. H. Williams, J. Chem. Soc. Perkin II, 1219 (1979).
64. B. W. Keelan and L. Andrews, J. Am. Chem. Soc., 103, 829 (1981).
65. V. E. Bondybey, T. A. Miller, and J. H. English, J. Chem. Phys., 72, 2193 (1980).
66. B. W. Keelan and L. Andrews, J. Am. Chem. Soc., 103, 822 (1981).
67. T. Shida and W. H. Hamill, J. Am. Chem. Soc., 88, 3689 (1966).
68. E. W. Fu and R. C. Dunbar, J. Am. Chem. Soc., 100, 2283 (1978).
69. L. Andrews, J. A. Harvey, B. J. Kelsall, and D. C. Duffey, J. Am. Chem. Soc., 103, 6415 (1981).
70. T. Shida and W. H. Hamill, J. Chem. Phys., 44, 4372 (1966).
71. W. C. Lineberger and T. A. Patterson, Chem. Phys. Lett., 13, 40 (1972).
72. G. Herzberg, in: Infrared and Raman Spectra, Van Nostrand, Princeton, New Jersey (1945).
73. W. D. Mross and G. Zundel, Spectrochim. Acta, 26A, 1109 (1970).
74. G. W. King and S. P. So, J. Mol. Spectrosc., 36, 468 (1970).
75. L. Andrews, B. J. Kelsall, and J. A. Harvey, J. Chem. Phys. (1982).
76. J. P. Maier and D. W. Turner, Far. Disc. Chem. Soc. II 69, 196 (1973).
77. J. W. Rabalais and R. J. Colton, J. Electron Spectrosc. and Rel. Phen., 1, 83 (1972/73).
78. A. D. Baker, C. R. Brundle, and D. W. Turner, Int. J. Mass. Spectr. and Ion Phys., 1, 443 (1968).
79. L. Asbrink, E. Lindholm, and O. Edqvist, Chem. Phys. Letts., 5, 609 (1970).
80. A. W. Potts, W. C. Price, D. G. Streets, and T. A. Williams, Faraday Discuss. Chem. Soc., 54, 168 (1972).
81. J. P. Maier and D. W. Turner, Far. Disc. Chem. Soc., 54, 149 (1972).
82. A. Hargreaves and C. H. Rivoi, Acta Cryst., 15, 365 (1962).
83. L. LeGall and S. Suzuki, Chem. Phys. Letts., 46, 467 (1977).

84. S. Arai, H. Ueda, R. F. Firestone, and L. M. Dorfman, J. Chem. Phys., 50, 1072 (1969).
85. B. Ruscic, B. Kovac, L. Klasinc, and H. Gusten, Z. Naturforsch., 33a, 1006 (1978).
86. A. C. Puiu, L. Andrews, W. A. Chupka, and S. D. Colson, J. Chem. Phys., 76, 3854 (1982).
87. R. M. Hochstrasser, R. D. McAlpine, and J. D. Whiteman, J. Chem. Phys., 58, 5078 (1973).
88. R. M. Barrett and D. Steele, J. Mol. Struct., 11, 105 (1972); Spectrochim. Acta, 30A, 1731 (1974).

APPLICATION OF DATA FROM PHOTOELECTRON SPECTROSCOPY TO OPTICAL SPECTROSCOPIC STUDIES OF GASEOUS CATIONS

J. M. Dyke, N. Jonathan, and A. Morris

Chemistry Department
University of Southampton
Southampton
United Kingdom

It is now generally accepted that vacuum ultraviolet photoelectron spectroscopy (p.e.s.) can provide valuable information concerning the electronic and geometric structures of molecular cations. In the case of simple species this information can be quite detailed and in many cases may be of considerable assistance to workers in other fields.

The fields where this information is perhaps most appreciated are those of theoretical chemistry and optical spectroscopy.

In the former, the ability to characterize a number of cationic states with relative energies known to an accuracy of perhaps 0.01 eV has proved a great simulus both towards more accurate calculations using ab initio methods beyond the Hartree-Fock limit and refinement of techniques such as the multiple scattering Xα method.

The application of p.e.s. data to optical spectroscopy is perhaps more detailed. At the simplest level, photoelectron spectroscopy pinpoints the spectral region where allowed optical transitions should be observed. This of course presupposes that the ionic states have been correctly identified by p.e.s. In the case of simple molecules the degree of sophistication achieved in molecular orbital calculations is such that identification is normally unambiguous. Optical spectroscopists can also identify experimental spectral by observation of vibrational spacings and other structure which should correspond to that seen in p.e.s. Furthermore the higher accuracy of optical spectroscopy should enable the usual limits of vibrational frequencies obtained in p.e.s. (at least ± 30 cm^{-1})

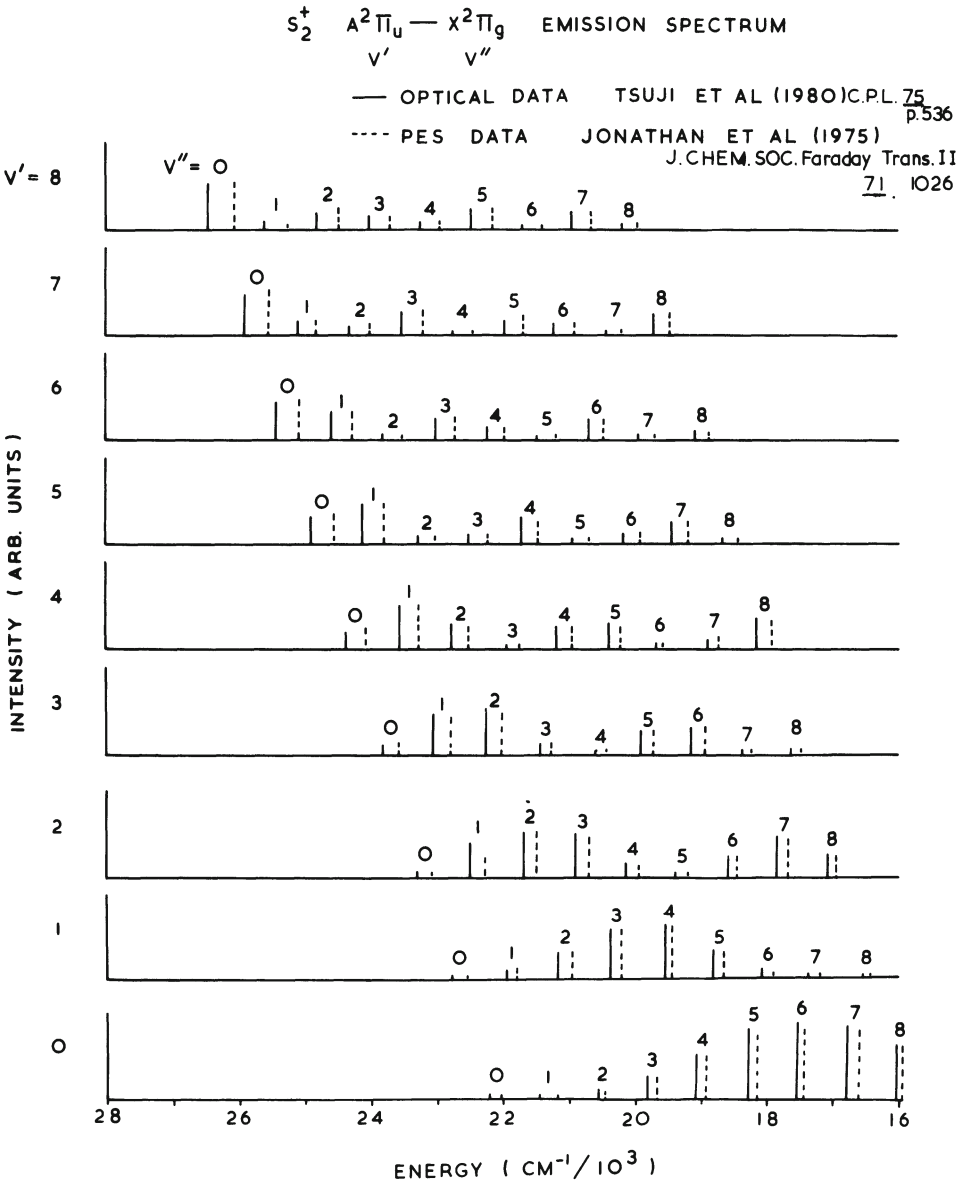

Fig. 1

to be refined. It has now become generally accepted that in spite of this lack of resolution in p.e.s., the equilibrium bond lengths of diatomic cations can usually be determined to an accuracy of ±0.01 Å. By assuming Morse potential functions for both the neutral molecule and cation, using the well-established spectroscopic parameters of the former and the vibrational frequency obtained from p.e.s.

for the latter, the photoelectron spectrum can be predicted for a given equilibrium bond length of the cation. Comparison of the computed envelopes at various ionic equilibrium bond lengths with the observed spectral band then leads to an estimate of the true equilibrium bond length. The only serious approximation made in this method is the assumption that the electronic transition moment is constant over the observed band. Accuracies quoted above have been achieved for some states of CS^+, P_2^+, PN^+, SiO^+ where independent optical measurements are available [1-8].

It is less well appreciated that not only the position but also the form, of the individual band intensities in optical spectra can be predicted from p.e.s. data. This is a logical development of the determination of equilibrium bond lengths and the potential energy curves for two ionic states between which an allowed optical transition may occur. At the simplest level one can therefore predict not only the separation of the zeroth vibrational levels of the two states (the $0 \leftrightarrow 0$ transition) but also the region where the strongest vibrational transition should occur. The obvious extension of this is to predict the entire vibronic band envelope for a molecular ion emission or absorption. The assumptions that must be made are the same as before with again that of invariant electronic transition moment over the band being the most serious. It is also assumed that processes such as predissociation do not occur in the higher parts of the potential energy curves that are not observed directly in the photoelectron spectrum. Since most optical spectra of molecular ions (which may be vibrationally excited) are observed in emission, it will in general be necessary to consider transitions from a reasonable number of vibrational states in the upper electronic state of the ion.

We have adopted the above approach for a number of diatomic cations for which reliable photoelectron data are available. For example, from the electronic states seen in the photoelectron spectrum of S_2, two electronic transitions are electric dipole allowed, i.e., the $b^4\Sigma_g^- \leftrightarrow a^4\Pi_u$ and the $A^2\Pi_u \leftrightarrow X^2\Pi_g$ transitions. The separation of the zeroth vibrational levels for these transitions is predicted as (1.67 ± 0.02) eV and (2.73 ± 0.02) eV respectively, where the latter value refers to a mean of the spin-orbit components in the $X^2\Pi_g(r)$ state. Also, Franck-Condon factors have been computed in each case for vibrational transitions between nine levels in both the upper and lower state. The $b^4\Sigma_g^- \leftrightarrow a^4\Pi_u$ band system has not been observed experimentally but comparison of the relative intensities of vibrational components observed experimentally for the $A^2\Pi_u \leftrightarrow X^2\Pi_g$ transition with those computed from p.e.s. data (Fig. 1) [10] shows good agreement. For S_2^+, the spectroscopic parameters derived from optical data are, as expected, more precise than those obtained by p.e.s., e.g., for S_2^+ $X^2\Pi_g$, $\bar{w}_e$ = (790 ± 30) cm^{-1} from p.e.s. [9] whereas the optical value is (807 ± 3) cm^{-1}. Similarly

the separation of the zeroth vibrational levels for the $S_2^+ A^2\Pi_u \leftrightarrow X^2\Pi_g$, transition was determined as (22,260 ± 160) cm^{-1}, whereas the optical value is (22,452 ± 3) cm^{-1}.

Predictions of this type from photoelectron data should lead to the identification of spectral regions where molecular cationic emissions should occur. Experimental identification and analysis of these optical emission spectra should then lead to improved spectroscopic constants for the cationic state involved.

References

1. D. Gauyacq and M. Horani, Can. J. Phys., 56, 587 (1978).
2. S. Leach, J. C. S. Faraday Disc. Chem. Soc., 54, 68 (1972).
3. N. Jonathan, J. C. S. Faraday Disc. Chem. Soc., 54, 67 (1972).
4. N. Jonathan, A. Morris, M. Okuda, K. J. Ross, and D. J. Smith, J. C. S. Faraday Disc. Chem. Soc., 54, 48 (1972).
5. D. C. Frost, S. T. Lee, and C. A. McDowell, Chem. Phys. Lett., 17, 153 (1972).
6. D. K. Bulgin, J. M. Dyke, and A. Morris, J. C. S. Faraday II, 72, 2225 (1976).
7. D. K. Bulgin, J. M. Dyke, and A. Morris, J. C. S. Faraday II, 73, 983 (1977).
8. E. A. Colbourn, J. M. Dyke, E. P. F. Lee, A. Morris, and I. R. Trickle, Molecular Physics, 35, 873 (1978).
9. J. M. Dyke, L. Golob, N. Jonathan, and A. Morris, J. C. S. Faraday II, 71, 1026 (1975).
10. M. Tsuji, I. Murakami, and Y. Nishimura, Private communication.

ROLE OF CORE HOLE STATE GEOMETRY IN MOLECULAR ELECTRON SPECTROSCOPIES

Jiri Müller[1] and Hans Ågren[2]

[1]Department of Chemistry
University of Bergen
N-5014 Bergen, Norway

[2]Institute of Physics
University of Uppsala
Box 530
S-751 21 Uppsala, Sweden

I. Introduction

The concepts of bonding and antibonding orbitals [1, 2, 3] have played an important role in the qualitative understanding of molecular electronic spectra. This characterization of orbitals was thought to be reserved for valence electron spectra in the UV of optical energy regions, whereas the core orbitals were attributed to a strictly non-bonding function in the formation of the molecule due to their negligible overlap with orbitals of neighboring atoms. This view was also believed to find support in early theoretical investigations indicating only a minor dependence of the core orbital functions on different nuclear configurations.

The improvement in electron and photon spectroscopic techniques significantly increased the prospects for accurate measurements for core hole state energy levels, their chemical shifts, associate satellite structure, and even their intrinsic band shapes [4]. In particular, the introduction of x-ray monochromatization in high energy x-ray excitation sources in photoelectron spectroscopy [5, 6] laid the experimental fundament for band shape analyses in core electron spectra, and even the first studies in this field revealed asymmetric structures of the bands [8, 9]. Simultaneous instrumental improvement in molecular x-ray studies [10-13], viz., high power excitation and high dispersive gratings, rendered the possibility to study fine structure in the emission bands. Such fine structure

was apparent even for transitions pertaining to non-bonding valence electrons. These observations indicated contrary to the earlier assumption that there are substantial differences in potential energy surfaces (referred in this work as potential-energy curves (PECs)) between core ionized species and the ground states of the neutral molecules and this in turn has stimulated ab initio computational investigations for the purpose of explaining the observed features. Such investigations have turned out to be relevant for other types of molecular core electronic experiments, viz., electron energy loss, Auger and autoionization spectroscopy. The first studies of systems related to one-dimensional motions have been extended to polyatomic species and different aspects such as the role of relaxation, exchange interaction and localization on bond length changes and band formation, rationalizations in resonance valence band structures, lifetime vibrational interference effects, have been studied. In this article we would like to review both theoretical and experimental work in this field starting from the first investigations, and ending up with the present state of art.

II. Methods for Vibrational Analysis

Investigations of vibrational intensities in symmetry allowed electronic transitions goes back to solving the Franck-Condon (FC) overlap integral [14]:

$$F(\underline{m},\underline{n}) = \left|\int \Psi''(\underline{m})\Psi'(\underline{n})dQ'\right|^2 \qquad (1)$$

where $\Psi''(\underline{m})$ and $\Psi'(\underline{n})$ are the vibrational wavefunctions of the two states interconnected by the electronic transition. Implicit assumptions of Born-Oppenheimer separability of nuclear and electronic motion and of constancy of the electronic transition moment (crude adiabatic approximation) has then been undertaken. The symmetry forbidden electronic transitions acquire intensity from a vibronic (vibrational-electronic) coupling mechanism. The intensity distribution is then governed by the Herzberg-Teller integrals [15], which constitute matrix elements of the electronic states over one or more normal coordinates. Here we will confine ourselves to the more commonly treated symmetry allowed electronic transitions. For diatomic molecules several methods have been developed for evaluation of the FC integrals using more or less accurate potential energy functions. Reviews of these methods are found in refs. 16 and 17. In the harmonic oscillator (HO) approximation the recurrence relations for FC factors given by Ansbacher [18] have been commonly used. The information used in these relations is confined to separately optimized equilibrium geometries and harmonic frequencies for both ground and ionized states. However, the chief characteristics of the vibrational band profiles emerge if one only considers the difference in bond distances and ignores the change in fre-

quency [19]. With this assumption Smith [20] has shown that the FC factors from the ground state zeroth vibrational level are given by:

$$F(0, n) = \frac{a^n}{n!} \exp(-a) \tag{2}$$

with

$$a = \frac{\pi \cdot \omega \cdot D^2}{h} \tag{3}$$

D denotes the separation of the origins of the ground and ionized state normal coordinates. $\omega = 2\pi\nu$, where ν is the harmonic frequency (h is Planck's constant).

For a molecule possessing M totally symmetric modes the FC factors for the combination bands will then be:

$$F(0, n_1 \cdots n_M) = \exp\left(-\sum_{s=1}^{M} a_s\right) \prod_{s=1}^{M} \frac{a_s^{n_s}}{n_s!} \tag{4}$$

In what follows we will demonstrate how the coupling constants a_s and thereby the FC-factors can be obtained from the gradients of the hole state energy with respect to the symmetry coordinates evaluated at the equilibrium geometry of the ground state.

It is convenient to work with dimensionless normal coordinates (q) which are obtained from the conventional normal coordinates (Q) by multiplying them by $(\frac{\omega}{\hbar})^{1/2}$ ($\hbar = \frac{h}{2\pi}$, $q = (\frac{\omega}{\hbar})^{1/2} Q$). Using atomic units the hole state potential energy is then expressed within the HO approximation as

$$E = \frac{1}{2} \underline{q}'^{+} \underline{\omega}\, \underline{q}' \tag{5}$$

where $\underline{q}'$ is the M dimensional column vector of dimensionless normal coordinates of the ionized molecule, ω is the diagonal matrix of vibrational frequencies. The transformation between symmetry coordinates $\underline{S}$ and the normal coordinates $\underline{q}$ is given by :

$$\underline{L}\, \underline{\omega}^{-1/2} \underline{q} = \underline{S} \tag{6}$$

We define a vector $\underline{R}$ whose components are the changes in equilibrium positions of the ground and ionized states

$$\underline{R} = \underline{S}'' - \underline{S}' \tag{7}$$

The force and kinematic matrices of the ionized state are put equal to the corresponding matrices of the ground state. This implies:

$$\underline{\omega}'' = \underline{\omega}' = \underline{\omega} \tag{8}$$

and

$$\underline{L}'' = \underline{L}' = \underline{L} \tag{9}$$

The normal coordinates for the ground and ionized states are then parallel and related according to

$$\underline{q}'' = \underline{q}' + \underline{d} \tag{10}$$

where

$$\underline{d} = \underline{\omega}^{1/2}\ \underline{L}^{-1}\ \underline{R} \tag{11}$$

If we express the hole state energy expression, (5), in terms of the ground state normal coordinates and evaluate the gradient at the ground state equilibrium geometry we obtain:

$$\left(\frac{\partial E}{\partial q''_s}\right)_0 = \omega_s d_s \tag{12}$$

A useful quantity is the so-called first order coupling constants κ_s, which is defined as:

$$\kappa_s = 2^{-1/2}\left(\frac{\partial E}{\partial q''_s}\right)_0 \tag{13}$$

Combining (12) and (13) in matrix representation yields

$$\underline{\kappa} = 2^{-1/2}\ \underline{\omega}\ \underline{d} \tag{14}$$

We define a matrix $\underline{a}$, the diagonal elements of which are given by the coupling constants a_s in Eq. (3) and (4):

$$\underline{a} = \frac{\pi}{h}\ \underline{\omega}\ \underline{D}\ \underline{D}^{+} = \frac{1}{2}\ \underline{\omega}^{1/2}\ \underline{d}\ \underline{d}^{+}\ \underline{\omega}^{-1/2} \tag{15}$$

where

$$\underline{D} = h^{1/2}\ \underline{\omega}^{-1/2}\underline{d} \tag{16}$$

Substituting (14) into (15) then gives:

$$\underline{a} = \underline{\omega}^{-1/2}\ \underline{\kappa}\ \underline{\kappa}^{+}\ \underline{\omega}^{-3/2}, \tag{17a}$$

or in component form:

$$a_s = (\kappa_s/\omega_s)^2 \tag{17b}$$

It is practical to express the first order coupling constants in terms of the energy gradients of the symmetry coordinates evaluated at the ground state equilibrium geometry $\left(\frac{\partial E}{\partial S_\ell}\right)_o$. From relation (13) and from the transformations between the symmetry coordinates and the dimensionless normal coordinates (6) one obtains:

$$\kappa_s = (2\omega_s)^{-1/2} \sum_\ell L_{\ell s} \left(\frac{\partial E}{\partial S_\ell}\right)_o \tag{18}$$

Relations (17) and (18) give the recipe for calculating the coupling parameters a_s in terms of the hole state energy gradients evaluated at the ground state equilibrium, and from these one can readily obtain the FC factors using expression (4). Note, that relations (1)-(18) correspond to those derived by Cederbaum and Domcke using Greens functions [31]. Thus in this formalism we do not need information on the force field of the excited state. The ground state parameters ($\underline{L}$, $\underline{\omega}$, and Q_o) can often be taken from experiment, otherwise they should be calculated at the same level of approximation as for the calculation of excited state energies.

Using the first order coupling constants κ_s one can obtain a prediction of the excited state equilibrium geometry relative to that of the ground state. Combining (11) and (14) one obtains:

$$\underline{R} = \underline{S}'' - \underline{S}' = 2^{1/2} \; \underline{L} \; \underline{\omega}^{-3/2} \; \underline{\kappa} \tag{19}$$

In a more general treatment of vibrational intensities in polyatomic electronic transitions one must not only account for shifts in origin of the normal coordinates and for shifts in their frequencies, but also for the fact that the normal coordinates of the final state generally are rotated with respect to those of the ground state. That is, one has to consider a Dushinsky [21] rotation:

$$\underline{Q}'' = \underline{A} \; \underline{Q}' + \underline{D} \tag{20}$$

Due to the non-diagonality of $\underline{A}$ it is then also possible to consider the excitations of the antisymmetric modes. The rotation may be large even if the differences in normal harmonic frequencies are small. It should be noted that this linear transformation is an approximation to the more general curvilinear transformation discussed by Lucas [22]. The symmetry coordinates are subject to a similar transformation

$$\underline{S}'' = \underline{Z}\,\underline{S}' + \underline{R} \tag{21}$$

The Z-matrix can be worked out via Cartesian displacement coordinates. Having calculated the L-transformation matrices $\underline{S} = \underline{L}\,\underline{Q}$, from the simultaneous diagonalization of force field and kinetic matrices one obtains $\underline{A}$ and $\underline{D}$ through:

$$\underline{A} = \underline{L}''^{-1}\underline{Z}\,\underline{L}' \tag{22}$$

and

$$\underline{D} = \underline{L}''^{-1}\,\underline{R} \tag{23}$$

Sharp, Rosenstock, and coworkers [7a] have generalized the method of generating functions for calculations of overlap of harmonic oscillators by considering the linear Dushinsky transformation (20). Their method, which thus requires full force field determinations of both ground and ionic states, has been applied to several vibronic spectra of small species [7b, c, d].

A method, suitable for treating symmetric modes and intermediate in accuracy with respect to full optimization and gradient methods, is achieved by assuming parallel normal coordinates ($\underline{Q}'' = \underline{Q}' + \underline{D}$), however, still considering correct ionic frequencies. The FC-integral (1) will then separate into a product of one-dimensional overlap integrals, one for each mode. Coon et al. [23] have used this method to predict excited state geometries via fitting the transformation $\underline{L}'$ matrix to the observed spectrum and using the relation $\underline{R} = \underline{L}'\,\underline{D}$ iteratively.

All molecular calculations of potential energy surfaces reported in this review have been performed using ab initio techniques. In most cases Hartree-Fock calculations have been employed, however, in some cases correlation effects have been taken into account. The use of Hartree-Fock wavefunctions is motivated from the general belief that differences in equilibrium geometries and ratio of force constants between core ionized and neutral species are relatively insensitive to correlation effects. This view is confirmed by those cases when the equilbrium geometries of the core ionized species have been accurately determined from x-ray emission spectra (see Section IV).

Equilibrium geometries and force constants were computed from a mesh of points on the energy surface by a simplex method employing the harmonic approximation. Franck-Condon factors were calculated for diatomic as well as for polyatomic species both by direct optimization of initial and final PECs and by the gradient method described above. The latter method is more computationally cost-effective, but it provides in general a poorer prediction of changes in equilibrium geometry between initial and final states (see Eq. (19)) than does the direct optimization method.

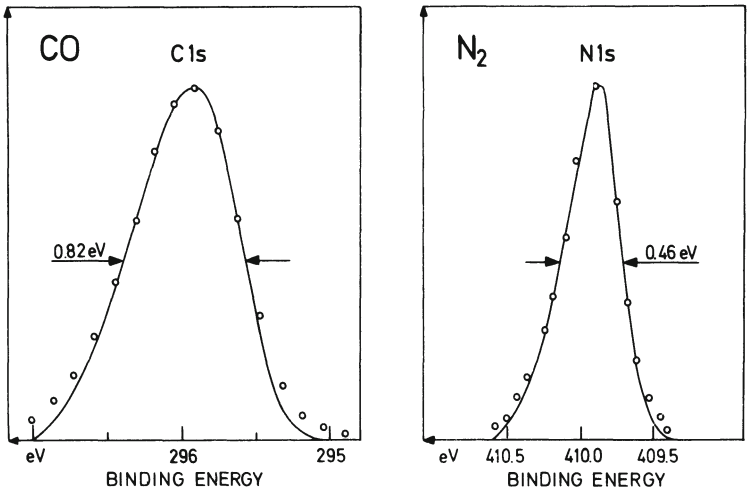

Fig. 1. High resolution ESCA spectra of CO and N_2. (Taken from ref. [8].)

In order to bring out only the important results and the main features in this review we shall leave out further discussion of computational details (such as basis set studies), which an interested reader can find out in appropriate references.

III. Geometrics of Core Hole Containing Species and Their Relation to ESCA Spectra

a) Historical Background and the Results for CO and N_2

As mentioned in the introduction the impetus for calculating PECs of core ionized species by ab initio methods came with the development of high resolution ESCA instrumentation. The first high resolution spectra to be recorded using x-ray monochromatication were C_{1s} of CO, N_{1s} of N_2, and Ne_{1s} of neon atom [5, 8, 9] (Figs. 1 and 2). The line shapes of the core bands in the first two spectra are asymmetrically broadened, whereas the band shape in the spectrum of atomic neon is strictly symmetric. Gelius and coworkers [8] investigated the band shape of the C_{1s} of CO and the N_{1s} of N_2 in terms of FC profiles employing the equivalent core approximation (NO^+) for the potential energy curves (PECs) of the hole state species. Their results explained the FC envelopes of the two spectra with a reasonable accuracy. Apart from the vibrational excitations, the broad features of the spectra are caused by lifetime broadening of the core ionized species and the instrumental resolution. The contribution of the latter is assumed to be Gaussian, whereas the natural linewidth contribution is Lorentzian in shape. However, it should be noted that it is only the vibra-

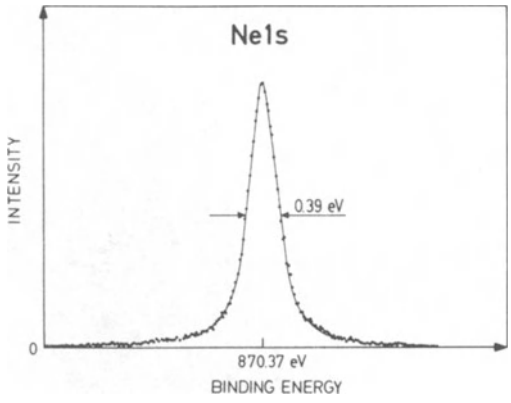

Fig. 2. High resolution ESCA spectrum of neon. (Taken from ref. [5].)

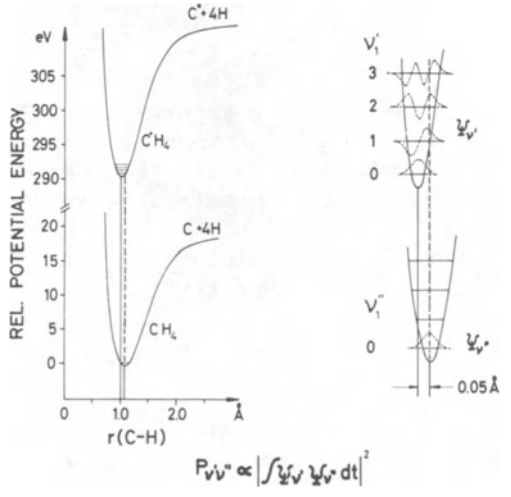

Fig. 3. Franck-Condon schematic representation of vibrational excitations in methane (see text). (Taken from ref. [8].)

tional excitations that causes asymmetricity of ESCA peaks (see Fig. 3), and therefore a final band envelope of photoelectron spectra is given by an incoherent superposition of Voigt lines, each line representing one vibrational component.

Meyer was the first to observe that there is a noticeable difference between PECs of core ionized species and a ground state. In his pioneering work on CEPA (coupled electron pair approxima-

tion), Meyer optimized the geometry of CH_4 and all its ionic species [24]. From these data he constructed the vibrational profile of the band corresponding to the electronic transition between the neutral CH_4 and the C_{1S} ion. His theoretical results fitted very well with the band profile of the experimental spectrum recorded in Uppsala about at the same time (see Table 1 and Fig. 4).

In order to improve the vibrational analysis of the CO and N_2 spectra and due to the lack of experimental data on the equivalent cores species CF^+ of the O_{1S} of CO, Clark and Müller [25] performed ab initio calculations on PECs of the C_{1S}, O_{1S} holes states of CO and the N_{1S} of N_2. The results of these calculations are displayed in Tables 2 and 3. The data in these tables indicate that the C_{1S} and N_{1S} (localized) hole state species have substantially smaller equilibrium geometries and larger force constants than their respective neutral molecules. These findings are in a qualitative agreement with the data for the equivalent core species also displayed in Tables 2 and 3, however, in each case the equivalent core approximation overestimates a given trend for the geometric change.

The results for the O_{1S} core hole state species are rather interesting. The trend is opposite to what was found for the C_{1S} and the N_{1S}, namely the equilibrium geometry is increased and the force constant decreased with respect to the ground state. As we shall show in the next section, these results fit into a general trend observed for PECs of core ionized molecules containing the first row elements. Summary of the results of these calculations are graphically displayed in Figs. 5 and 6.

In order to interpret the band shapes of the ESCA spectra of CO and N_2, FC factors were calculated from the data pertaining to the triple zeta basis set. The FC profiles were then constructed by fitting the various vibrational components to the experimental spectra, the only variable being the linewidth of the individual vibrational components. During the fitting procedure the separation of the vibrational components was put equal to the vibrational frequency of the ionic state in question, and the lineshape was approximated by a Gaussian function. In all cases an excellent agreement with the experimental spectra was achieved (see Figs. 7, 8, 9).

b) Role of Relaxation Accompanying Core Electron Ionization

The effects of relaxation on core binding energies (ionization potentials) have been known for some time. Core binding energies evaluated with frozen orbital approximation (FOA) using Koopmans' theorem [26] are for the first row elements between 10 eV and 20 eV higher than ΔE_{SCF} and experimental values [27, 28].

Table 1. Theoretical and Experimental Results for the C_{1s} State of CH_4

	Theoretical[a]	Experimental[b]
F C Factors	0.62	0.61
	0.31	0.33
	0.06	0.06
Vibrational	0.42	0.43
Frequency[c] (in eV)		
C - H bond length	1.95	
in the ion (in bohrs)		
C - H bond length	2.06	
in the neutral molecule (in bohrs)		

a) Reference 24; b) reference 8; c) totally symmetric vibration.

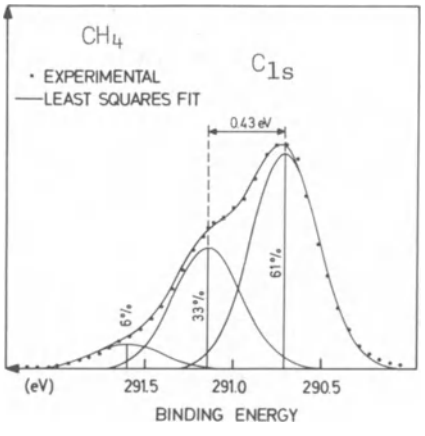

Fig. 4. High resolution ESCA spectrum of CH_4. The least squares fit is made to three Gaussians of equal half width. (Taken from ref. [8].)

Table 2. Geometries of N_2, CO, NO^+, CF^+ Corresponding to Minimum Energies (in atomic units) and Respective Force Constants (in millidynes per angstrom)

Basis	ReN_2	ReCO	$ReNO^+$	$ReCF^+$	ΔRe (N_2-NO^+)	ΔRe $(CO-NO^+)$	ΔRe $(CO-CF^+)$	KeN_2	KeCO	$KeNO^+$	$KeCF^+$
HF 4-31G	2.080	2.164	2.024	2.264	0.056	0.139	-0.100	-	-	-	-
STO 4-31G	2.124	2.167	2.050	2.220	0.074	0.116	-0.053	28.10	22.10	-	-
Double Zeta	2.082	2.155	2.058	2.306	0.024	0.098	-0.151	-	-	-	-
Triple Zeta	2.047	2.123	1.983	2.218	0.064	0.140	-0.095	25.10	19.46	28.90	12.71
Experimental	2.074[a]	2.132[a]	2.007[a]	-	0.067	0.125	-	22.96[b]	19.00[b]	24.85[c]	-

a) Reference 71; b) reference 73; c) reference 74.

Table 3. Geometries of $\overset{*}{N}_2$, $\overset{*}{C}O$, and $C\overset{*}{O}$ Corresponding to Minimum Energies (in atomic units) and Respective Force Constants (in millidynes per angstrom)

Basis	$Re\overset{*}{N}_2$	ΔRe $(N_2-\overset{*}{N}_2)$	$Re\overset{*}{C}O$	ΔRe $(CO-\overset{*}{C}O)$	$ReC\overset{*}{O}$	ΔRe $(CO-C\overset{*}{O})$	$Ke\overset{*}{N}_2$	$Ke\overset{*}{C}O$	$KeC\overset{*}{O}$
HF 4-31G	2.094	-0.014	2.104	0.060	2.316	-0.151	-	-	-
HF 4-31G (Opt.)	2.038	0.043	2.040	0.125	2.281	-0.116	-	-	-
STO 4-31G	2.121	0.004	2.107	0.060	2.266	-0.099	-	-	-
STO 4-31G (Opt.)	2.060	0.064	2.059	0.108	2.237	-0.070	30.70	30.70	15.05
Double Zeta	2.058	0.024	2.052	0.104	2.324	-0.168	-	-	-
Triple Zeta	2.002	0.045	2.010	0.113	2.230	-0.107	29.60	28.90	13.11

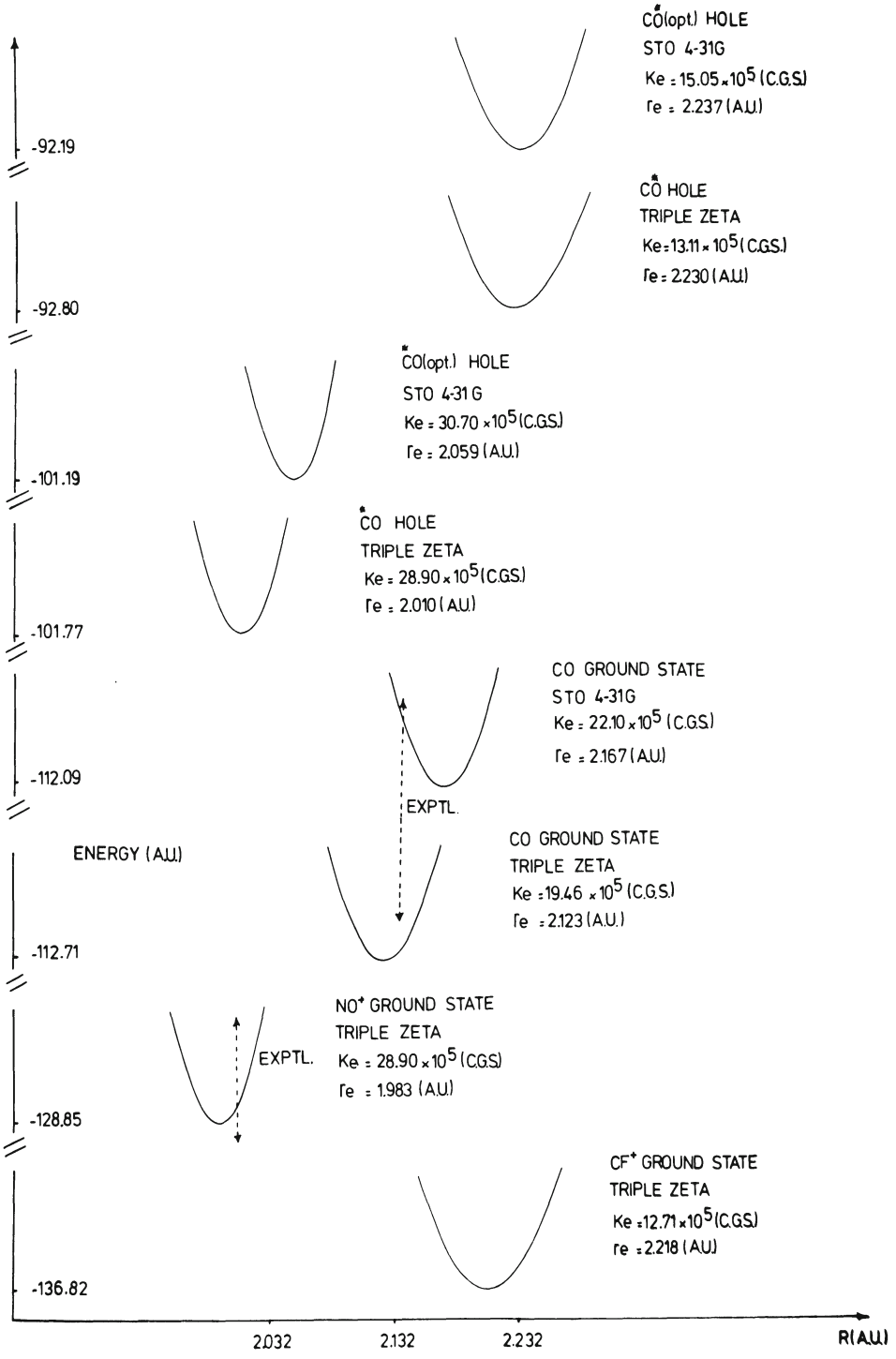

Fig. 5. Calculated potential energy curves, force constants (Ke) and equilibrium geometries (Re) for CO, $\overset{*}{CO}$, $\overset{*}{CO}$, $\overset{+}{NO}$, and $\overset{+}{CF}$ with triple zeta and 'optimized' 4-31G basis sets. (The star indicate a position of the core hole.)

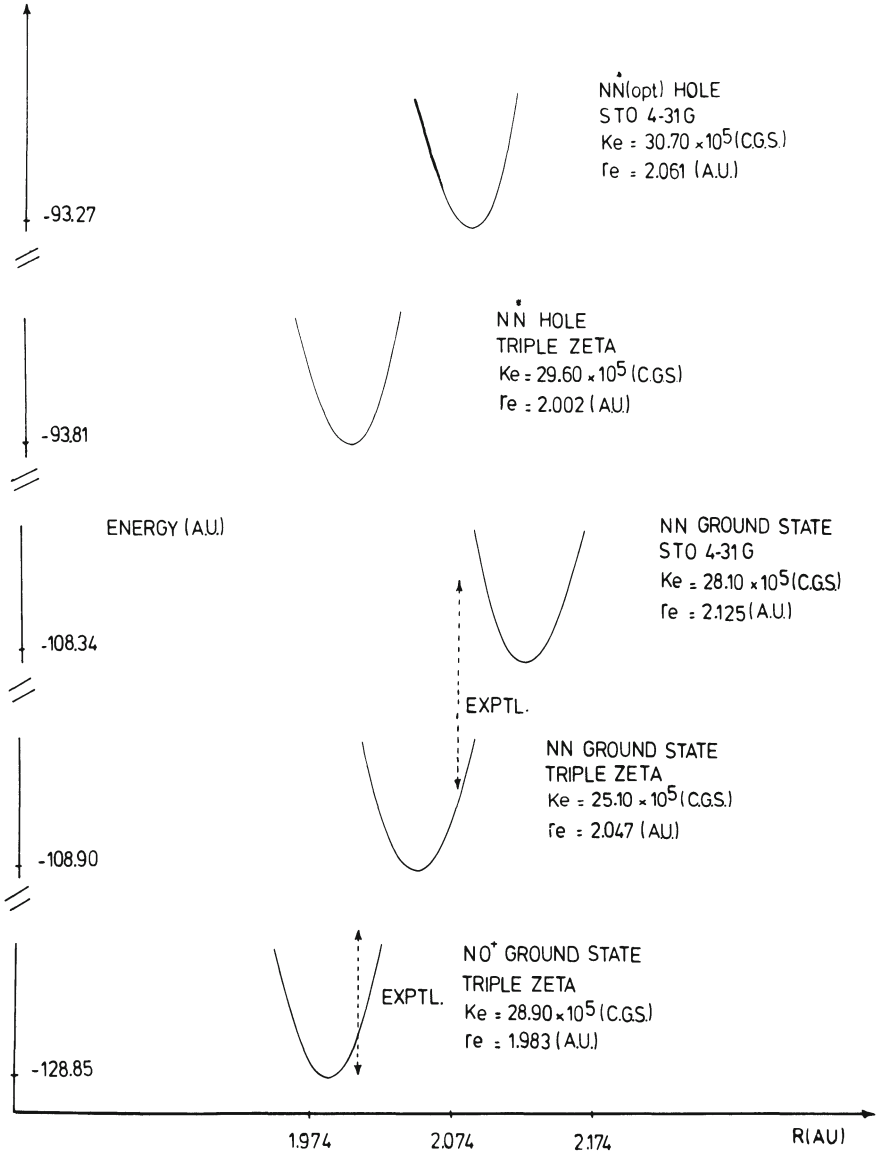

Fig. 6. Calculated potential energy curves, force constants (K_e) and equilibrium geometries (R_e) for N_2, $N\overset{*}{N}$, and $N\overset{+}{O}$ with triple zero and 'optimized' 4-31G basis sets.

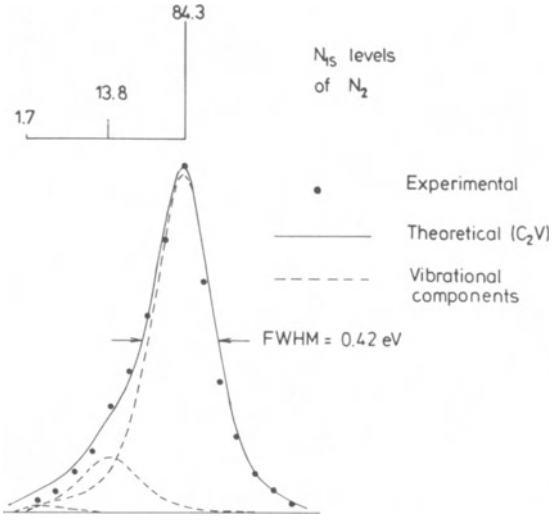

Fig. 7. The N_{1s} spectrum of nitrogen molecule showing three vibrational components of FWHM = 0.39 eV separated by 0.33 eV. (FWHM means full width at half maximum.)

Clark and Müller in their work on CO and N_2 also reported changes of relaxation energies for various ions with respect to the geometry of the neutral molecules. We define relaxation energy for the core hole i as

$$E^r_{i(R)} = - \varepsilon_i(R) - \Delta E_{SCF}(R) \tag{24}$$

where $-\varepsilon_i$ is Koopmans' ionization energy, and ΔE_{SCF} is the difference between the Hartree-Fock energies of the ionic state and the neutral molecule evaluated at internuclear distance R:

$$\Delta E_{SCF}(R) = E^*_i(R) - E_{GS}(R) \tag{25}$$

The result of this study is shown in Fig. 10. It is of interest to note that the relationship is in all cases linear, the slopes being positive. Furthermore, the order of increasing slope C < N < O follows the order of increasing total relaxation energies.

Goscinski and Palma [29] have further shown that relaxation energies have a direct influence on the direction of the geometry changes between core ionized and ground state species, and they were also able to establish a relation between the magnitude of the relaxation slope with the magnitude of the absolute relaxation energy.

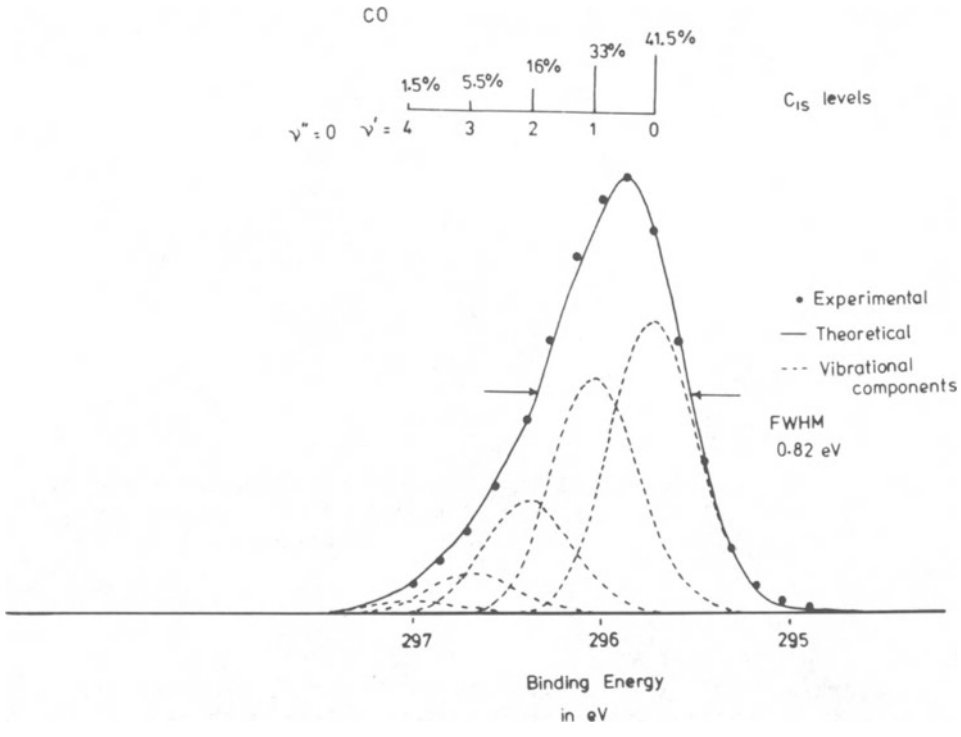

Fig. 8. The C_{1S} spectrum of carbon monoxide showing five vibrational components with FWHM = 0.54 eV separated by 0.33 eV.

Table 4. Changes in Koopmans and Relaxation Energies Following Inner-Shell Ionization (in cV/bohr)

Molecule	$-d\varepsilon_i/dR\|_{\bar{R}}$ [a]	$-dE_i^{Rel}/dR\|_{\bar{R}}$ [b]	$dE_i^*/dR\|_{\bar{R}}$
C*O	6.50	-0.26	6.24
CO*	0.68	-2.40	-1.72
NN*	5.30	-1.26	4.04

a) Reference 72; b) reference 25.

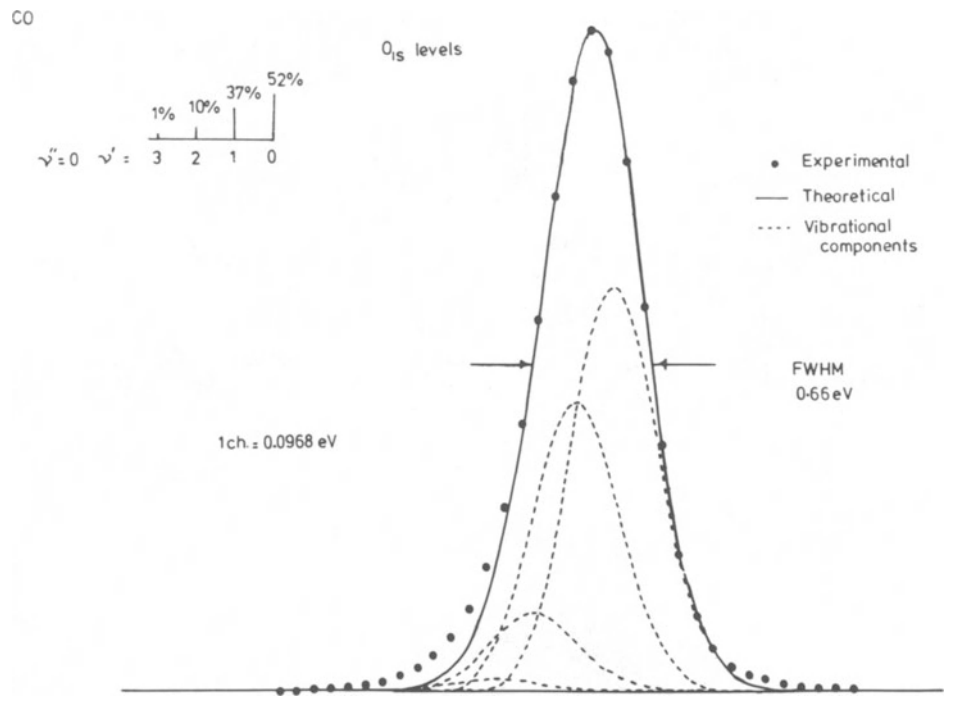

Fig. 9. The O_{1s} spectrum of carbon monoxide showing four vibrational components with FWHM = 0.58 eV separated by 0.22 eV.

The energy gradient for an ionic state i of a diatomic molecule at internuclear distance $\bar{R}$ of the ground state is in the harmonic approximation given by:

$$\left.\frac{dE^*_i}{dR}\right|_{\bar{R}} = K^*_i \, \Delta R_i \tag{26}$$

where $\Delta R_i = \bar{R} - \bar{R}_i$ is the displacement for the equilibrium geometries of the hole and the ground and ionized states and K^*_i is the harmonic force constant of the ionized state. Taking the gradients of Eqs. (24) and (25) one obtains:

$$\left.\frac{dE^*_i}{dR}\right|_{\bar{R}} = - \left.\frac{d\epsilon_i}{dR}\right|_{\bar{R}} - \left.\frac{dE^r_i}{dR}\right|_{\bar{R}} \tag{27}$$

since

$$\left.\frac{dE_{GS}}{dR}\right|_{\bar{R}} = 0$$

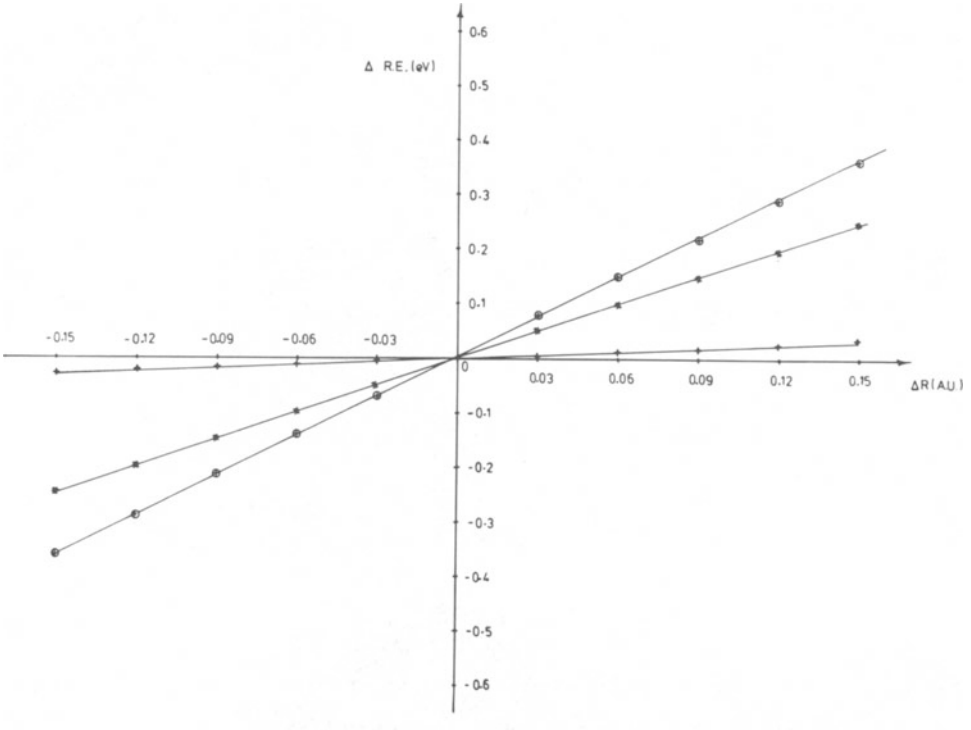

Fig. 10. Plot of differences of relaxation energies for N_2 and CO versus internuclear distance. ⊕ refers to $\overset{*}{CO}$ species. * refers to $\overset{*}{NN}$ species. † refers to $\overset{*}{CO}$ species.

Thus from Eq. (26) one obtains:

$$\Delta R_i = - (K_i^*)^{-1} \left(\frac{d\varepsilon}{dR^i} \Big|_{\bar{R}} + \frac{dE}{dR^i}^r \Big|_{\bar{R}} \right) \tag{28}$$

Equation (28) indicate that there are two terms which determine the value of ΔR_i, namely the gradients of Koopmans' and relaxation energies. For CO, the Koopmans' slopes are -0.68 and -6.50 for oxygen and carbon respectively (in eV/bohr). This implies that a bond length shortening is expected in both cases, though far more pronounced for the carbon hole. However, if one takes into consideration relaxation effects, the picture changes dramatically. This is demonstrated for CO and N_2 in Table 4. For the oxygen hole the relaxation term is dominant, and thus is responsible for the increase of the CO bond length on the O_{1s} hole ionization.

The present results can be readily extended to polyatomic molecules replacing derivatives by gradients. The basic equations have been outlined in Section II, where we have used normal coordinates instead of R.

c) Diatomic Core Hole Species

(i) Geometrices of C_{1s}, N_{1s}, and O_{1s} Core Hole Ions

The early investigation of energy surfaces of the core ionized species of CO and N_2 have led to a series of further investigations, and in the next section we shall try to summarize the main results and their importance on ESCA band shapes.

Clark and co-workers [30] carried out a study on a series of small organic molecules, and they concluded that the C_{1s} ionized species have smaller carbon bonds than the corresponding ground state molecules. They have further shown that the opposite is the case for the O_{1s} systems and that the N_{1s} ionized species can have smaller or larger bonds than the respective neutral molecules depending on the type of the bond. The changes in geometries are of the order 0.1 bohr, they apply for both saturated and unsaturated bonds and are accompanied by appropriate changes in force constants, i.e., larger force constants for shortened bond lengths and vice versa. The results of these calculations are generally in agreement with the studies of Domcke and Cederbaum [31] using Green's function methods.

(ii) Geometries of F_{1s} Core Hole Ions

Goscinski and co-workers [32] carried out a study on PECs of the F_{1s} core hole states of CH_3F and CF_4. From the work on the C_{1s}, N_{1s}, and O_{1s} core hole ions one expected that the F_{1s} ionized species possess larger CF bond lengths than the respective ground state molecules.

To investigate the complete PECs of the two fluoromethanes with three excited symmetric normal modes of vibrations is computationally a difficult task, and therefore a simplified procedure was adopted which consisted of considering only the $\nu_2(a_1)$ mode. The vibration of this mode involves a simultaneous extension of the C-F bond distance (R) and the angle (α) amongst atoms HCF and FCF for CH_3 and CF_4 respectively. This approximation is reasonable, because it involves both changes in C-F distance and in all bond angles.

The results of these two dimensional PEC investigations are graphically displayed in Figs. 11 and 12. It is evident from these data that the PECs of the two F_{1s} core ionized species are disso-

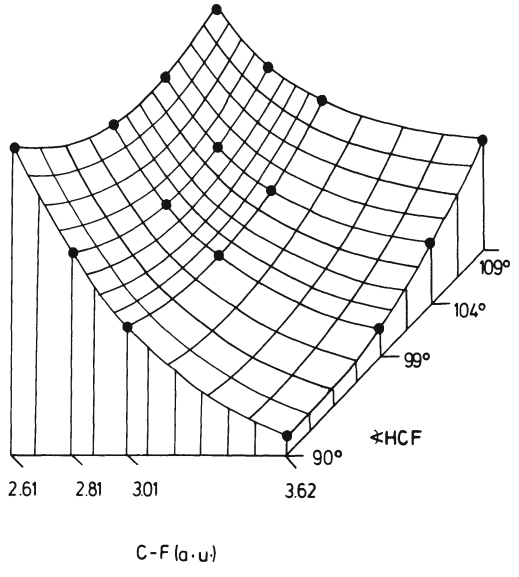

Fig. 11. Potential energy surface for the F_{1s} hole states of CH_3F. The points on the surface marked with dots correspond to the directly computed values, the others have been extrapolated.

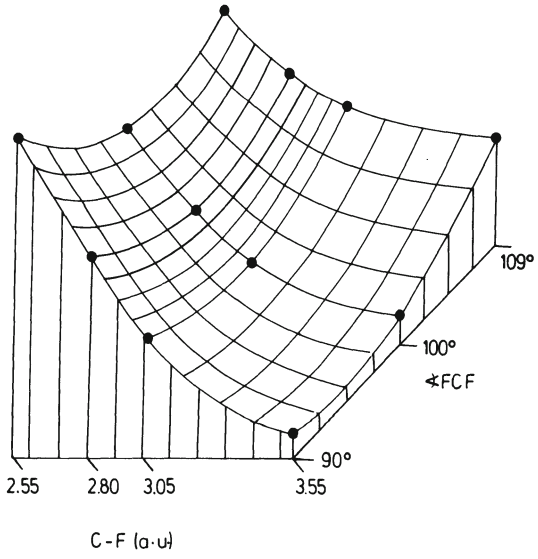

Fig. 12. Potential energy surface for the F_{1s} hole states of CF_4. The points on the surface marked with dots correspond to the directly computed values, the others have been extrapolated.

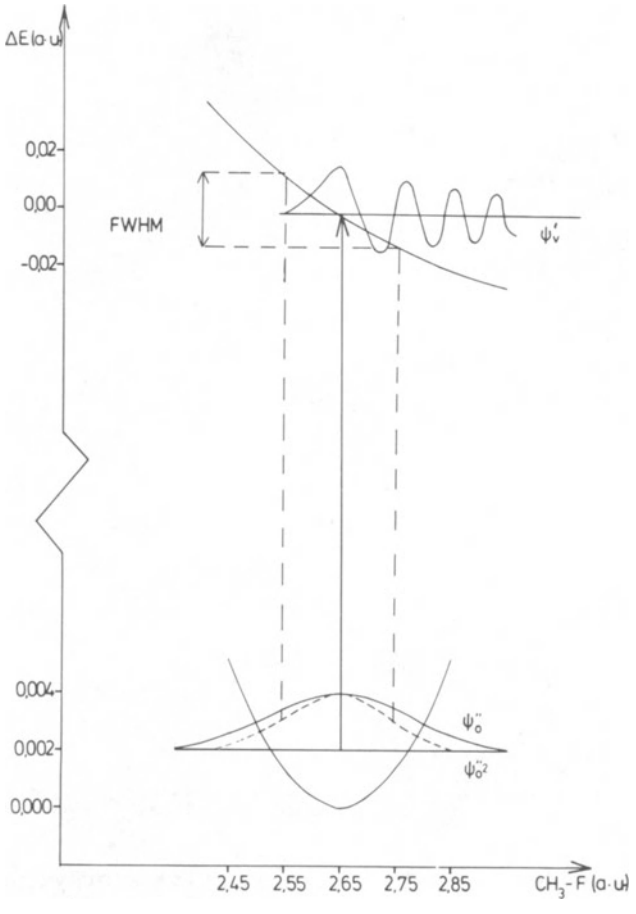

Fig. 13. Ground and F_{1s} hole state potential energy curves for CH_3F in the "two-particle" approximation (see text).

ciative. It is not very likely that the F_{1s} photoionization is directly followed by dissociation, however, because Auger rates of de-excitation are much faster than vibrational frequencies for these systems (10^{-15} s in comparison with 10^{-13} s).

It is appropriate at this stage to mention life-time effects on vibrational profiles of photoelectron spectra, which were investigated in detail by Kaspar [57], Domcke and Cederbaum using S-matrix theory. These authors concluded that for transitions involving short-lived species only in the final state, the spectrum is given by incoherent superposition of Lorentzian lines. We successfully carried out such analyses for CO and N_2 (see Figs. 7-9), however, Gaussian rather than Lorentzian line shapes were used, because the latter take into account instrumental factors. The work

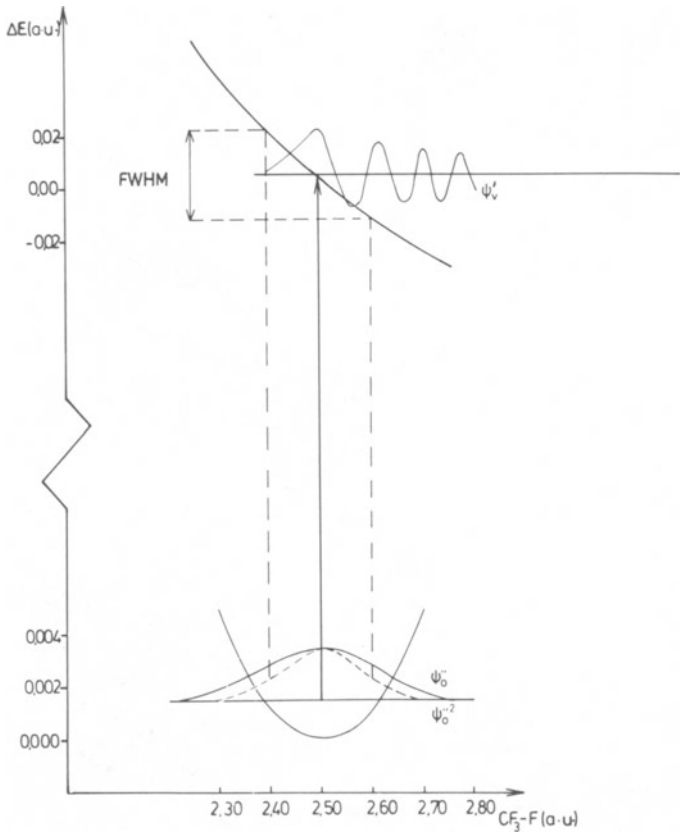

Fig. 14. Ground and F_{1s} hole state potential energy curves for CF_4 in the "two-approximation" (see text).

of Kaspar et al. therefore suggests that short life-times of core hole species do not influence Franck-Condon transitions in a special way. This may however, not be the case for electronic transitions where the initial state species are very short-lived [57]. Such situations arise in soft x-ray emission and Auger spectroscopies, where interference between the vibrational levels of the short-lived electronic state can modify the vibrational structure in a characteristic manner. Such cases will be briefly considered in Section IV.

The ESCA spectrum [33] of CF_4 exhibits larger linewidth than CH_3F, and both are unusually broad in comparison with HF and F_2. Shaw and Thomas [34] suggested that this may be due to transitions to unbound states. The above calculations confirm this view. In order to explain the differences in linewidths of the two spectra one needs to compute Franck-Condon densities, which for these rather

complicated systems possessing several degrees of freedom is a cumbersome task. Therefore Goscinski and co-workers [32] used a rather simplified approach (already successfully used on even more complicated [35] systems) to estimate ratio of the two FWHM. For this purpose they assumed that the vibrational excitation of the "two-particle" systems, consisting of the CX_3 (X = H or F) group and the F atom, is the major factor responsible for the Franck-Condon profiles of the spectra. This is not unexpected in view of the calculations on PECs of CH_3F and CF_4 which show that the energy minima (if they exist) of the ionized systems would occur at very large C-F separation. Potential energy curves for these motions (which are in reality cross sections of the full potential energy surfaces) are displayed in Figs. 13 and 14 for CH_3F and CF_4, respectively. One can then estimate the band envelope through Franck-Condon densities. One imaginable procedure consists simply in projecting the width density [36] at half the maximum associated to the ground state vibrational wavefunction to the upper state, potential curve the latter being approximated as a locally linear function as indicated in Figs. 13 and 14. Simple geometrical considerations lead to the linewidth estimate (in au)

$$\mathrm{FWHM} = 2(\ln 2)^{1/2} m/\gamma^{1/2} \tag{29}$$

where m is the slope of the upper state at ground state equilibrium geometry, and γ is the exponent of the ground state vibrational wavefunction (both in au). Equation (29) can be derived by actually assuming that the uppper state curve is linear, in which case the vibrational functions are Airy functions Ai(-x). One can explicitly evaluate the Franck-Condon density by using known representations of the Airy functions and evaluate the dominant leading term. For this purpose one may use the formulae given by Aspnes [37] and the representation

$$\mathrm{Ai}(a-bx) = \frac{1}{2\pi^{1/2}} \int_{-\infty}^{\infty} ds\, \exp[is^3/s + is(a-bx)] \tag{30}$$

This leads to the Franck-Condon density g(E)

$$g(E) \alpha \exp(-(E + \bar{R}m)^2 \gamma/m^2) \tag{31}$$

which in turn yields Eq. (29). This equation also follows from the work of Schirmer et al. [38]. They derived a general expression for the linewidth associated to an electronic transition, assuming a Poisson distribution which in the case of strong vibrational excitation approaches a Gaussian distribution.

It should be noticed that Eq. (29) includes the crucial final state effects through the slope of the upper state. In the two

cases investigated here, the upper state is dissociating, the only difference between them being the slopes.

The estimated ratio of FWHM values for CF_4:CFH_3 is 0.97 eV/ 0.72 eV = 1.35 with m = 0.196 and 0.127 (in au) together with γ = 84.4 and 62.6 (in au) for CF_4 and CH_3F respectively. These results agree fairly well with the experimental [33, 39] value 1.49 eV/0.85 eV = 1.75. These calculations give only a simplified picture, but nevertheless they seem to account satisfactorily for the experimental results.

d) Role of Localization and Spin Splitting on Geometries and Lineshapes of Core Hole States

(i) Nitrogen Molecule

The problem of localization of core holes in molecular systems, where a possibility of delocalization over equivalent nuclear centers arises, such as the N_{1s} hole in N_2, has been known for some time.

Most of the work performed in this field has been concerned with calculations of ionization potentials [40-44] and the available evidence indicates that ΔE_{SCF} calculations within the Hartree-Fock model give reasonable agreement with experimental values only for a localized hole treatment, a delocalization of a core hole over t centers results in relaxation energy to be 1/t of that for a localized hole [40]. On the other hand, CI calculations carried out either on the basis of delocalized (symmetry adapted) or localized (non-symmetry adapted) molecular orbitals give in both cases the same binding energies. It follows that the relaxation energy of a localized core hole is related to the correlation energy of a delocalized core hole. This has been elegantly shown by Cederbaum and Domcke using the Green's [44] function approach. It goes back to Löwdin's [45] symmetry dilemma.

Müller et al. [46] undertook a vibrational analysis of the N_{1s} state of N_2 in the basis of both the localized and delocalized molecular orbitals (that is in $C_{\infty v}$ and $D_{\infty h}$ molecular point group respectively), and compared the computed ESCA band profiles with the experiment.

As the first step, vibrational contributions to ESCA linewidths for localized and delocalized holes were estimated using Eq. (29). The results are displayed in the first column of Table 5. We can clearly see that there is a striking difference between the two computed bandshapes. The delocalized hole solution, containing contributions from gerade and underade states [47], predicts linewidths twice as large as the localized hole solution, the latter being in a reasonable agreement with the experimental value 0.42 eV.

Table 5. Computed Vibrational Contributions to Linewidths (LW) in eV for Various Core Hole States of N_2, NO, and O_2 using Eq. (29)

N_2		O_2		NO	
N_2		O_2		NO	
State	LW	State	LW	State	LW
$^2\Sigma_g^+$	0.72	$^4\Sigma_g^-$	0.39	$^3\Pi(\overset{*}{N}O)$	0.32
$^2\Sigma_u^+$	0.77	$^2\Sigma_g^-$	0.36	$^1\Pi(\overset{*}{N}O)$	0.18
$^2\Sigma^+$	0.32	$^4\Sigma^-$	0.36	$^3\Pi(N\overset{*}{O})$	0.41
		$^2\Sigma^-$	0.58	$^1\Pi(N\overset{*}{O})$	0.50

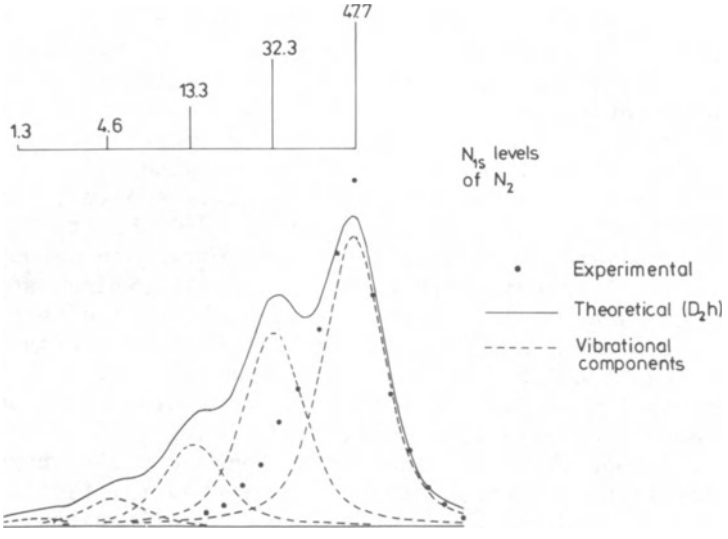

Fig. 15. N_{1s} spectrum of N_2 constructed from gerade delocalized hole solution. The five vibrational components of FWHM = 0.34 eV are separated by 0.37 eV.

As the next step the optimization of the geometries for the ion in the $D_{\infty h}$ symmetry was carried out. The data for the PECs are displayed in the top part of Table 6. The differences between the two cases are striking. This is even more reflected in the theoretical shapes of the two ESCA spectra. The localized spectrum was already shown in Fig. 7 and the delocalized core spectrum is displayed in Fig. 15. Only the spectrum compiled from the localized hole data agrees well with the experiment.

(ii) Oxygen Molecule

The configuration of the O_2 molecule in its ground state possesses two open shells. Therefore, photoionization of a 1s core electron may leave the ion in different states depending on how the remaining 1s electron couples with the unpaired π electrons. The main photoionization band therefore consists of two peaks [4, 48], one corresponding to a quartet and the other to a doublet, which are separated by 1.1 eV with the intensity $^4\Sigma^-/^2\Sigma^-$ equal to 2.47. The reasons for a deviation of this ratio from the "statistical" value 2 has been previously discussed in terms of different total shake-up/off probabilities [48] and in terms of electron correlation effects [49, 50].

The results of the calculations [46] on the energy surfaces of the ground and the localized core hole state species of O_2 (Tables 6 and 7) predict rather large differences in geometries which implies that a theoretical analysis of ESCA spectra must take into account anharmonicity effects. However, Eq. (29) is useful for estimating linewidths of photoelectron spectra in cases where the excited curve cannot be approximated in the region of interest by a harmonic potential which is the situation for the O_{1s} core localized states of O_2. The data obtained using Eq. (29) are displayed in the second column of Table 5. It is apparent from the preceding work on N_2 that the O_{1s} spectrum of O_2 has to be analyzed within the localized state model, but for comparison we have also displayed in Table 5 data pertaining to the delocalized state solutions. The data related to the localized holes indicate an interesting phenomenon, namely that the high binding energy doublet is broader than the low energy quartet, the ratio of the linewidths $^2\Sigma^-/^4\Sigma^-$ is equal to 1.6. The only high resolution spectrum of O_2 which has been available [51] is displayed in Fig. 16. It can be seen that the experimental signal to background ratio, particularly for the less intense doublet, is not high. Several fitting procedures were applied to this spectrum, and in all cases it was found that the doublet is broader than the quartet, the ratio of the linewidths $^2\Sigma^-/^4\Sigma^-$ varied from 0.72 eV/0.61 to 0.65 eV/0.62 eV. It seems that the ratio calculated from Eq. (29) is somewhat too high, however, the significant result of the calculations is clearly the

Table 6. Equilibrium Geometries (in bohrs), Vibrational Excitation Energies (in eV) and Gradients of Total and Relaxation Energies (in eV/bohr) for Core Hole States of N_2, NO, and O_2 in the Hartree-Fock Approximation

	State	$\bar{R}_i^*$	$\Delta\bar{R}_i$	K_i^*	$\frac{dE_i^*}{dR}\Big\vert_{\bar{R}}$	$\frac{-dE_i^{rel}}{dR}\Big\vert_{\bar{R}}$
N_{1s} states	$^2\Sigma_g^+$	1.952	-0.097	0.367	5.20	0.69
of N_2	$^2\Sigma_u^+$	1.942	-0.107	0.359	5.59	0.74
	$^2\Sigma^+$	2.002	-0.047	0.336	2.33	-2.35
N_{1s} states	$^3\Pi$	2.089	-0.007	0.277	2.21	-2.09
of NO	$^1\Pi$	2.121	-0.045	0.241	1.21	-3.71
O_{1s} states	$^3\Pi$	2.279	0.113	0.200	-2.81	-2.93
of NO	$^1\Pi$	2.305	0.139	0.194	-3.40	-2.86
O_{1s} states	$^4\Sigma_g^-$	2.167	-0.091	0.251	2.60	0.48
of O_2	$^2\Sigma_g^-$	2.173	-0.085	0.241	2.40	0.37
	$^4\Sigma^-$	2.410	0.152	0.145	-2.43	-4.51
	$^2\Sigma^-$	2.515	0.257	0.133	-3.85	-5.92

$\bar{R}_i^*$ refers to a computed geometry of hole state species (in bohrs) corresponding to minimum energy.
$\Delta\bar{R} = \bar{R}_i^* - \bar{R}$ (for $\bar{R}$, see Table 7).
K_i^* refers to a computed harmonic vibrational excitation energy around $\bar{R}_i^*$ (in eV).
$\frac{dE_i^*}{dR}\Big\vert_{R}$ refers to a gradient of a core hole state curve E_i^* at $\bar{R}$ computed from the potential energy surface E_i^* (in eV/bohr)
$\frac{dE_i^{rel}}{dR}\Big\vert_{\bar{R}}$ refers a gradient of relaxation energy E_i^{rel} computed at $\bar{R}$ (in eV/bohr).
Relaxation energy is defined as $E_i^{rel} = -\varepsilon_i - \Delta E_{SCF}(i)$.

Table 7. Equilibrium Geometries (in bohrs), Vibrational Excitation Energies (in eV) and Gradients of FOA Ionization Potentials (in eV/bohr) for the Ground State of N_2, NO, and O_2

	N_2	NO	O_2
$\bar{R}$	2.049	2.166	2.258
K	0.322	0.254	0.221
$\left.\frac{-d\varepsilon_i}{dR}\right\|_{\bar{R}}$	N_{1sg} 4.51	$^3\Pi(\overset{*}{NO})$ 0.12	$^4\Sigma_g^-$ 2.12
	N_{1su} 4.85	$^1\Pi(\overset{*}{NO})$ -0.54	
		$^3\Pi(\overset{*}{NO})$ 4.30	$^2\Sigma_g^-$ 2.03
		$^1\Pi(\overset{*}{NO})$ 4.92	
R(exp)	2.074	2.174	2.282
K(exp)	0.293	0.236	0.196

$\bar{R}$ refers to a computed geometry corresponding to minimum energy.
K refers to a computed vibrational excitation energies around $\bar{R}$.
$\left.\frac{-d\varepsilon_i}{dR}\right|_{\bar{R}}$ refers to a gradient of FOA ionization potential computed at $\bar{R}$
R(exp) refers to experimental equilibrium geometry taken from reference 71.
K(exp) refers to experimental vibrational excitation energies taken from reference 73.

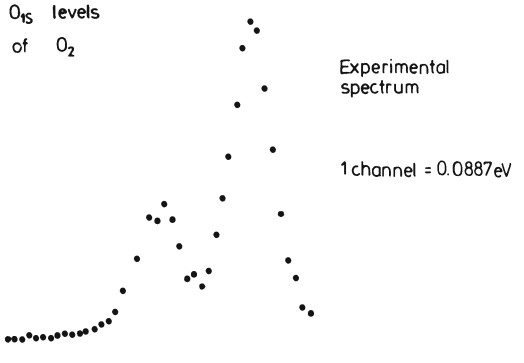

Fig. 16. Experimental spectrum of O_{1S} of O_2.

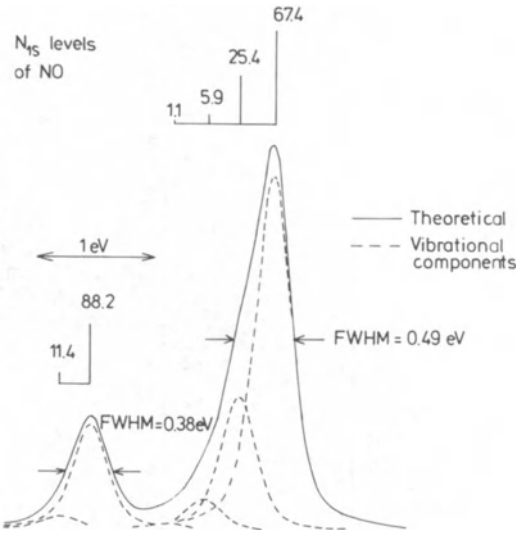

Fig. 17. N_{1S} spectrum of NO. The five vibrational components of the $^3\pi$ state with FWHM = 0.34 eV are separated by 0.277 eV and the two vibrational components of the $^1\Pi$ state with the FWHM = 0.34 eV are separated by 0.24 eV. The energy separation of the two states = 1.48 eV and the intensity ratio $3\pi/1\pi$ = 3.43.

fact that one should not a priori assume that the two spin components should have the same linewidth. This is clearly a consequence of the differences in geometries and force constants between the two spin components (see Tables 6 and 7).

Finally, it is worth pointing out that even if the delocalized hole state model produces linewidths of a comparable magnitude to the localized state solution, it predicts that the doublet should be narrower than the quartet, the ratio $^2\Sigma^-/^4\Sigma^-$ being 0.92.

(iii) Nitric Oxide Molecule

The ESCA spectrum [4, 48] of NO resembles that of O_2 in the sense that it also exhibits a split structure due to the spin induced splitting, which consists of a triplet and a singlet component. The separation of the two components in the main photoionization band of the O_{1S} spectrum is too small (0.07 eV) to allow a complete separation of the two peaks unlike the high resolution spectrum of O_2. However, in the N_{1S} spectrum where the triplet-singlet separation in the main photoionization peak is 1.5 eV [4, 48] and this spectrum therefore lends itself for a theoretical

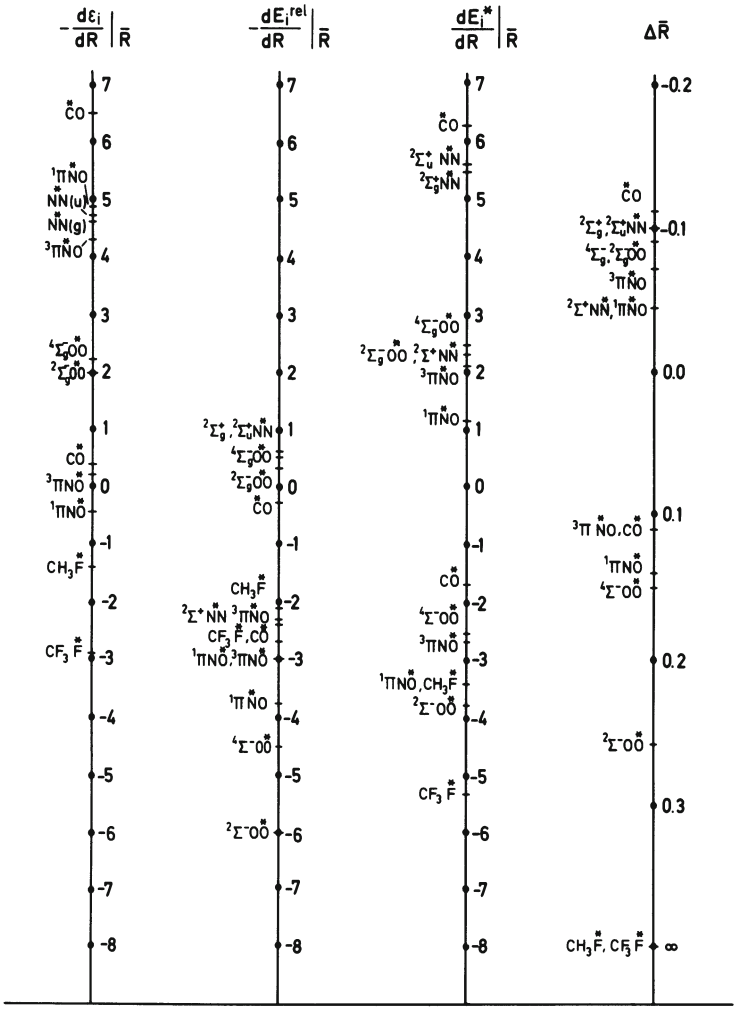

Fig. 18

treatment. The intensity ratio of the two components $^3\Pi/^1\Pi$ is estimated to 3.43 [48].

The values of the linewidths calculated from Eq. (29) are shown in the last column of Table 5. These data again indicate a marked difference in the linewidth of the two spin components, the $^3\Pi/^1\Pi$ ratio for the N_{1s} levels is 0.32 eV/0.18 eV = 1.78. Since the experimental core spectrum of NO is not completely resolved we have resorted to a construction of a high resolution N_{1s} spectrum with the same instrumental resolution as for N_2. Experimental values of the energy difference of two spin components and the experimental itensity ratio [48] were used, the relative intensities

of the vibrational components and their separations were taken from ab initio calculations [46], the results of which are displayed in the middle of Table 6. The resulting "spectrum" with the relevant data is displayed in Fig. 17. Its linewidth $^3\Pi/^1\Pi$ ratio 0.49 eV/ 0.38 eV = 1.29 would seem more realistic than the value obtained from Eq. (29). The difference in the linewidths of the two spin components is again a reflection of the differences in PECs of the two ions.

(iv) Summary

The results for the investigations of the geometry changes on core ionizations for the molecules so far considered in this review are graphically displayed in Fig. 18. The figure in addition shows the values of the slopes of relaxation, frozen orbital approximation and total energies which contribute to the geometry changes, as discussed in Eqs. (27) and (28).

e) Temperature Dependence of Vibrational Fine Structure Profiles

The interpretation of the band profiles for N_{1s}, C_{1s}, and O_{1s} core levels in N_2 and CO as arising from vibrational progessions involving the ground vibrational states of the neutral molecules in each case suggests that a confirmation of this assignment could be made by temperature dependent studies of the band profiles. Unfortunately, the vibrational energy spacings for these molecules are such that significant population of other than $\nu' = 0$ level requires considerably elevated temperatures. One needs to restrict oneself therefore to a theoretical analysis which would correspond to realistic experimental conditions, and therefore the change in band profile for N_2 at 1800 K has been considered. The Boltzmann distribution is such that at this temperature the population of the $\nu'' = 0$ and $\nu'' = 1$ levels are $\sim$87% and $\sim$13% respectively. The vibrational profile arising from transitions from $\nu'' = 0$ to $\nu' = 0$, 1, 2, and from $\nu'' = 0$, 1, 2, and 3 using the theoretically calculated energy separations, force constants and change in bond length previously discussed has therefore been considered and the results are displayed in Fig. 19. The differences with respect to the room temperature spectrum are small but significant and should be detectable with current instrumentation. Thus the FWHM of the high temperature spectrum should be 0.3 eV larger than that at room temperature (see for comparison Fig. 7), and the tails at higher and lower binding energies should also be observable.

An alternative experiment to this direct temperature dependent study would be to investigate the high resolution ESCA spectra of molecular beams where vibrational quanta of the ground state species have been selectively excited by means of a tunable laser. There is

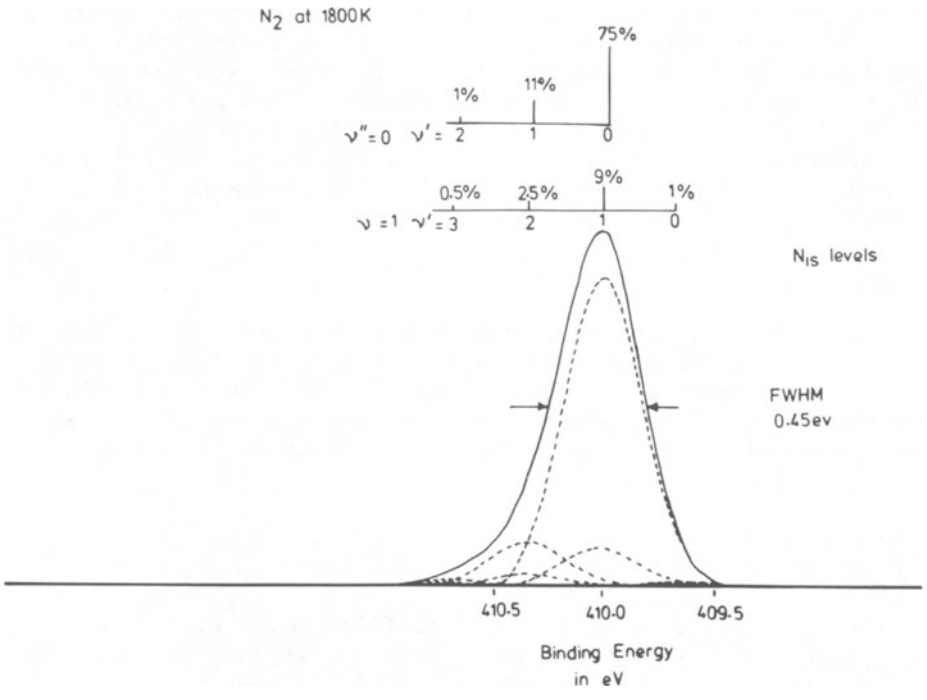

Fig. 19. Theoretically simulated N_{1s} spectrum of nitrogen molecule at 1800 K, showing vibrational excitation from the $\nu'' = 0$ and $\nu'' = 1$ levels. The individual vibrational components have FWHM = 0.39 eV. The vibrational separations being 0.33 eV.

certainly great scope for interesting studies in high resolution temperature dependent and molecular beam studies of x-ray photoelectron spectra.

f) Polyatomic Core ESCA Spectra

As discussed in Section II, the most elaborate methods for calculation of vibrational intensities in polyatomic electronic spectra require force field determinations of both ground and ionic states. Whereas the force field of the ground state for many molecules can be determined quite accurately with aid of experimental values of spectroscopic parameters, such as vibrational frequencies, vibration-rotational interaction constants, etc. (see, ref. 52), a similar determination for the ionized state is seldom possible due to lacking of these experimental data. In particular for core hole species, to which the corresponding experimental spectra experience a considerable instrumental and lifetime broadening, the determination of the force field rests exclusively on

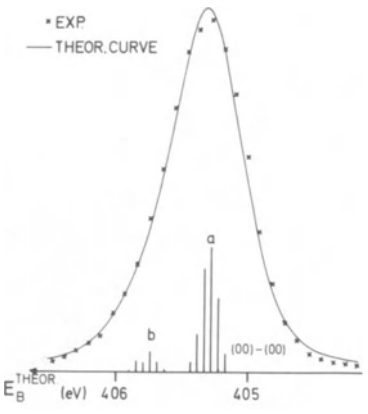

Fig. 20. Experimental and theoretically simultated ESCA N1s band of ammonia. Full width at half maximum (FWHM) of vibrational components is 0.60 eV. FWHM of the experimental band is 0.74 eV. a and b denote the (0, n) and (1, n) progressions respectively. (Taken from ref. [53].)

computational techniques. However, a full polyatomic force field calculation is in general a very cumbersome task to carry out and this fact provides an incitement for adopting the more "cost-effective" gradient approach. The study of smaller molecules like NH_3 and H_2O, however, renders the possibility for direct confrontation of the gradient and full optimization methods.

Ab initio calculations of ground and ionized states of NH_3 have been performed by Ågren et al. [53] in order to interpret the vibrational progressions in its core ESCA and x-ray emission spectra. Both the $3a_1$ hole state and the N1s hole state were found to be planar. This therefore indicates a significant reorganization of the $3a_1$ angle determining orbital upon core ionization. In the planar (D_3h symmetry) the totally symmetric stretching and bending modes decouple, and it is therefore possible to perform a separate anharmonic treatment of the latter mode while retaining a harmonic approximation for the stretching mode. The highly-resolved $3a_1^{-1}$ UV ESCA spectrum [78] has therefore in several works served as a testing ground for anharmonic vibrational calculations as well as for analytic functions describing the double minimum ground state potential. As shown by Domcke et al. [54] the gradient method, although simple to apply, provides the best reproduction of the long progression of the $3a_1^{-1}$ bending mode. This success was traced to the fact that the gradient method gives a more correct behavior of the upper state PEC in the FC region, i.e., at the equilibrium geometry of the ground state, than do various anharmonic approaches.

Table 8. Franck-Condon Factors for the N1s Hole State of NH_3

n_1n_2	00	01	02	03	04	05	10	11	12	13	14	15
$F_A(n_1n_2)$	0.041	0.175	0.299	0.247	0.089	0.006	0.004	0.022	0.046	0.020	0.024	0.001
$F_B(n_1n_2)$	0.046	0.132	0.191	0.183	0.132	0.076	0.009	0.027	0.038	0.037	0.026	0.015

All calculations of the hole state energy surfaces have been performed with OS RHF wavefunctions.
The subscript A indicates calculations of FC factors with direct optimization method.
The subscript B indicates calculations of FC factors with gradient method.

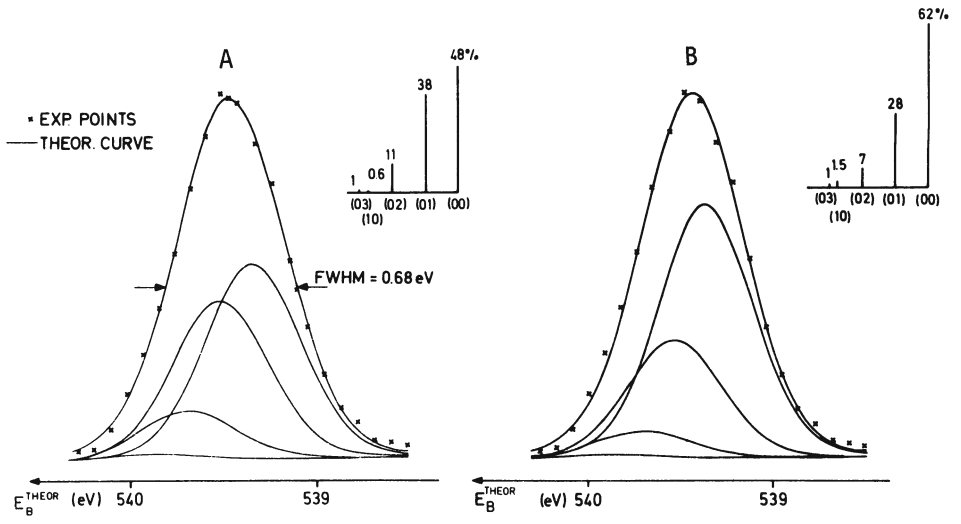

Fig. 21. Experimental and theoretically simulated O_{1s} ESCA of H_2O. FC factors computed with full optimization and gradient methods displayed in spectrum A and B respectively (see text). In both cases full width at half maximum (FWHM) of vibrational components is 0.60 eV. FWHM of the experimental band is 0.68 eV. (Taken from ref. [56].)

In contrast to the $3a_1^{-1}$ state, the formation of the core hole state leads to an N-H bond length shortening and to a significant reduction in the bending force constant and the corresponding N1s ESCA band will therefore appear quite differently than the $3a_1$ band. As seen in Fig. 20 the core ESCA spectrum experiences an asymmetry due to excited stretch-bend combination bands. The influence of the N-H bond shrinkage is more pronounced in the $3a_1$ x-ray emission spectrum which exhibits three distinct shoulders due to stretching excitations (see Section IV). The FC-factors calculated with the gradient and direct optimization methods differ noticeably as displayed in Table 8. This may be due to the anharmonicity correction which to some extent is inherent in the former method but also due to the fact that the stretching excitation influences the bending modes through the stretch-bend coupling constant quite differently for the two states and this is explicitly accounted for in the Sharp-Rosenstock method.

The ionization of the H_2O core electron products a large change in HOH angle (+15.7°) but perturbs the O-H bond length only minorly (+.007 bohrs) [55]. The corresponding ESCA band therefore consists of pure bending excitations as seen in Fig. 21. As for NH_3, a more conclusive comparison of the gradient and direct optimization methods is obtained from the outermost valence levels. The ionization

of the H_2O $1b_1$ electron introduces bond length and angle changes with a subsequent rotation in normal coordinates [56]. In this case the full optimization procedure gives better experimental agreement for the vibrational intensities [56]. Learning from the H_2O and NH_3 examples, we anticipate that the gradient method is suitable for vibrational analysis in quasi one-dimensional cases in which only one vibrational mode is strongly excited, in other cases of small vibrational amplitudes and normal coordinate rotation the direct optimization method is preferable.

IV. Other Molecular Core Electronic Spectra

The properties of the core hole containing state PEC will enter into molecular electronic spectra in quite different fashions for emission and absorption type spectra. In the latter case, the core PEC will directly determine the band shapes through Franck-Condon overlaps with the vibrational functions of the ground state. The most straightforward method is then x-ray photoelectron spectroscopy (XPS or ESCA), described extensively in previous sections, in which the high kinetic energy photoelectron negligibly interferes with the residual core hole ion. Other absorption techniques with inherent high resolution capabilities are electron energy loss and synchrotron x-ray absorption. The band shapes in spectra obtained from those methods will not directly reveal the properties of the PEC of the core hole ion, rather they will be determined by a composition of the bonding properties of the core electron with the bonding properties of an electron in the excited orbital. In emission, the core hole will form an intermediate state in the excitation – deexcitation process, and its PEC will therefore have a crucial influence on the final band profile. Especially the grazing incidence x-ray emission method is a powerful tool for determination of the core hole PEC and results from this method will therefore be described in some detail. Examples of Auger and autoionization radiationless emission spectra will also be given in the next section.

Molecular core electronic spectra will have a clear-cut division into absorption and emission type also with respect to the influence of the finite lifetime of the core hole. This aspect has recently been brought up by the Kaspar et al. [57] who founded a formulation of vibrational motion in the presence of a finite lifetime in a single scattering treatment of the excitation – deexcitation process. In absorption type core electron spectra the bands will consist of incoherent superpositions of Lorentzian lines convoluted with instrumental broadening, as shown in the spectra in the previous sections. The finite lifetime will not appear more than as an additional broadening as long as it is negligibly dependent on nuclear geometry. In emission type core spectra, however, the contributions from different vibrational levels of the short-lived core hole state will in general interfere.

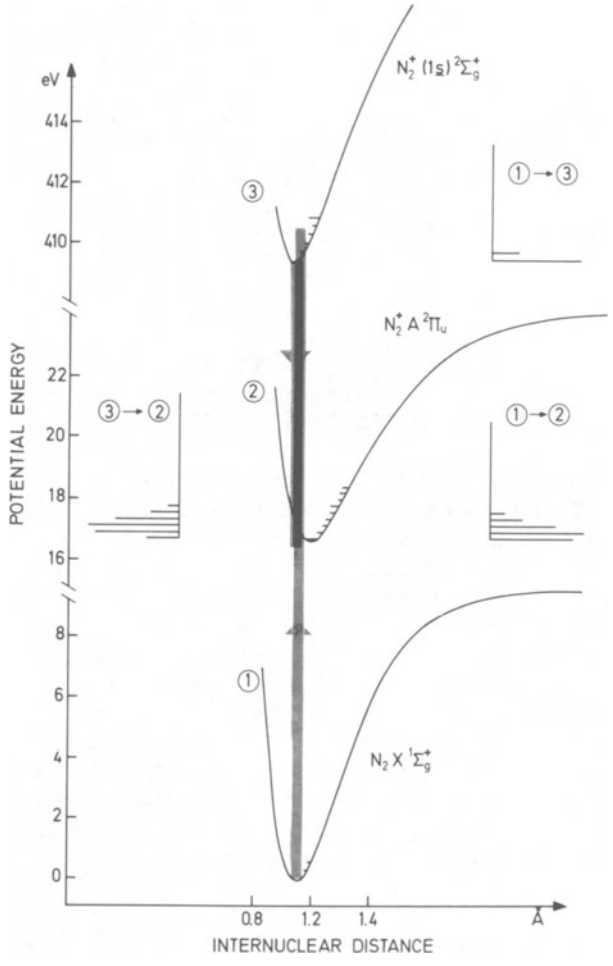

Fig. 22. Potential energy curves for the core, valence $A^2\Pi_u$ and ground $X^1\Sigma_g$ states of N_2. The shaded strip pointing upwards represents transitions from the neutral molecule to the ionic states. The bar diagrams to the right show the vibrational structure in such transitions. The downward pointing strip shows the deexcitation of an $N_2^+(1s)$ molecule to the $N_2^+A^2\Pi_u$ state. The bar diagram to the left shows the expected vibrational structure. (Taken from ref. [11].)

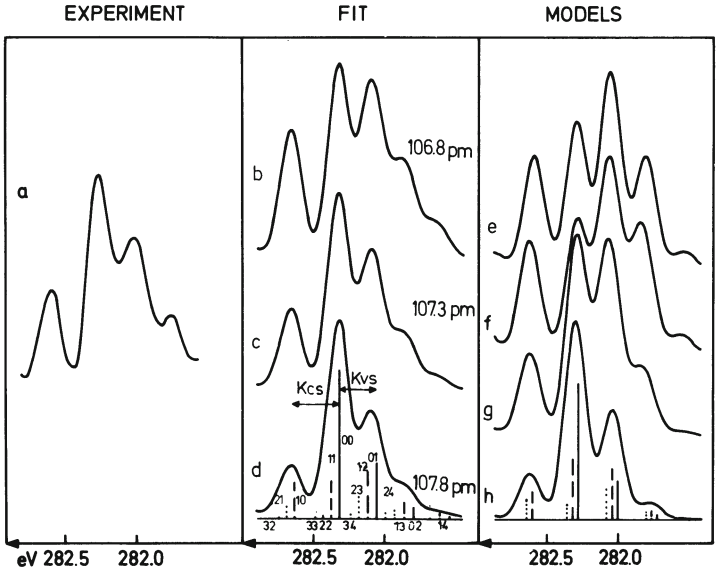

Fig. 23. CK emission in CO, 5σ band. 1) The CO 5σ-C_{1s} x-ray band. a: Third order experimental spectrum. b-d) Anharmonic Franck-Condon analysis for different R_{CS}. The best fitted value of K_{CS} is used (see Table 9). Experimental values for GS and VS parameters are used (anharmonic force constant of the core hole state is taken from the equivalent core species). e-h) Theoretical results in the harmonic approximation. Experimental values are used for parameters not stated. e) R (CS) and K_{CS} from the equivalent core; f) ΔR (CS-GS) from gradient of Koopmans energies (K_{CS} from SCF optimization); g) ΔR (CS-GS) and K_{CS} from SCF optimizations; h) SCF calculated parameters used for all three states (GS, CS, and VS). GS = Ground State; CS = Core State; VS = Valence State.

a) Emission Type Spectra

The advent of high resolution dispersion techniques in soft x-ray emission experiments introduced new means for studying core and valence levels in molecules [10-13]. In particular it became possible to combine accurate UV photoelectron and x-ray emission data to obtain core binding energies and shifts in correlation with x-ray photoelectron data.

Such a correlation from vertical (defined as center of gravity of respective bands) x-ray emission, UV and core ESCA energies have in general provided good overall agreement, but slight deviations of the order of 0.5 eV have been observed and these deviations were

Table 9. Harmonic Core Hole State Force Constants (eV) Difference of Core Hole State and Ground State Equilibrium Bond Lengths for CO and N_2 (bohrs)

$\Delta\bar{R}\ \overset{*}{CO}$	-0.125	-0.130	-0.111	-0.104
$\Delta\bar{R}\ \overset{*}{CO}$	0.087	-0.030	.108	>0
$\Delta\bar{R}\ \overset{*}{N_2}$	-0.066	-0.104	-0.045	-0.045
$K\ \overset{*}{CO}$	.29		.33	.34
$K\ \overset{*}{CO}$	.22		.22	
$K\ \overset{*}{N_2}$	.29		.34	.31

a) From the equivalent core; b) from Koopman's approximation; c) from SCF-calculations; d) from soft x-ray spectra.

found to alter between different valence or core levels for a given molecule [58, 59]. The situation is explained by Fig. 22 in which the formation of the N_2 $3\sigma_g$ x-ray emission band is displayed. It is evident that the position and shape of the intermediate core hole state PEC will have a crucial influence on the final x-ray emission vibrational envelope. Since refinements in the high resolution grazing incidence grating technique made it capable also of recording fine structure it has been possible in some cases to deduce information on the core hole state PECs by means of a vibrational analysis [60]. Such an analysis for the CO 5σ band employing FC-calculations on directly optimized PECs of all states involved is displayed in Fig. 23. A consideration of anharmonicity in these analyses was found rather crucial for the degree of experimental agreement that could be attained and was found to change the best fitted values for the core hole state bond lengths by about 0.01 bohrs. Thus deduced values for core hole state force constants and differences between ground and core hole state equilibrium geometries are compiled for N_2 and CO in Table 9 and are shown to be in quite good agreement with SCF calculations. Frozen orbital or equivalent core models do not reproduce the measured profiles very well, see, e.g., the theoretical curves f and g in Fig. 23, although the

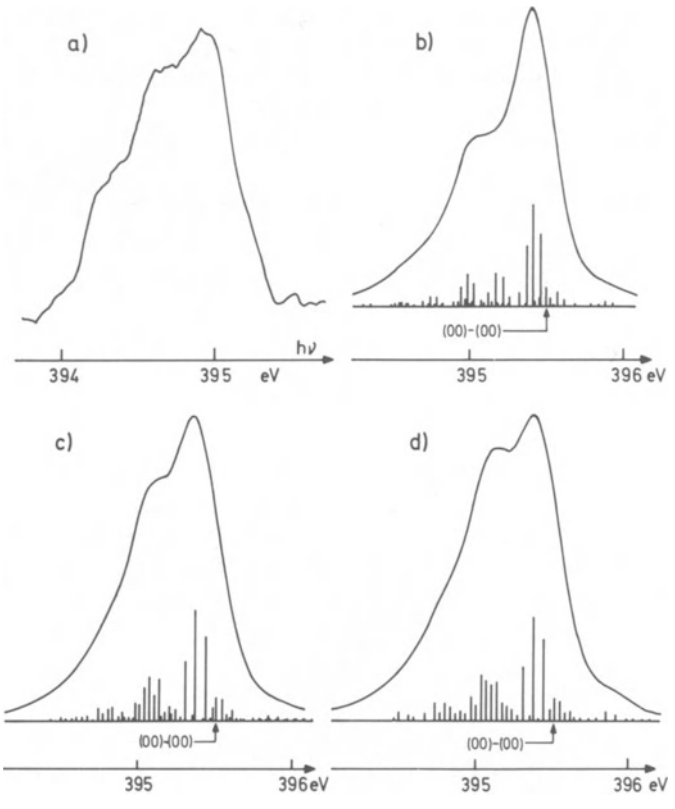

Fig. 24. The NH_3 $3a_1$ x-ray emission band. a) Experimental densitometer curve. b) Theoretically simulated band profile using ab initio results for force constants and equilibrium geometries (see text). FWHM of individual components is 0.25 eV. c) Same parameters used as in b) except for the frequencies of $3a_1^{-1}$-state for which experimental values obtained from the the UV-ESCA spectrum [78] are used. d) Parameters chosen as in c), but the N1s N-H bond length is shortened by .015 a.u. to 1.814 a.u. (Taken from ref. [53].)

equivalent core model gives the correct trends for bond length changes in all cases.

The accuracy of this type of analysis when extended to polyatomic species is limited by the large number of parameters to be determined due to the increased number of vibrational degrees of freedom. As an example of a polyatomic x-ray band the $3a_1$ band of NH_3 is shown in Fig. 24a [59]. It is observed to be composed of three shoulders separated by approximately 0.3 eV. This is a clear

indication of stretching mode excitations, and is in qualitative agreement with the theoretical prediction of a rather significant bond length shortening following core ionization. However, in spite of this excitation, the resulting $3a_1$ x-ray band seems to be somewhat narrower than the corresponding UV ESCA band which is composed of a long vibrational progression of the pure bending mode. This can again be rationalized from the theoretical findings in that the $N1s^{-1}$ bending energy curve is very shallow, implying closely spaced peaks (frequency 0.054 eV), and in that the equilibrium bending normal coordinate coincides for the $1s^{-1}$ and $3a^{-1}$ states connected in the x-ray transition. Figures 24b, c, d clearly display the sensitivity of the x-ray band envelope on choice of bond lengths and frequencies. These figures indicate a somewhat larger bond length shrinkage than the theoretically predicted of 0.062 bohrs.

In the above described analyses the excitation and deexcitation vibrational spectra were convoluted from incoherent superpositions of Lorentzian lines and the contributions from interference of the different vibrational levels of the short-lived core states were thus neglected. The influence of this interference due to lifetime broadening in x-ray vibrational band envelopes have subsequently been investigated by Kontradenko et al. [61] and by Kaspar et al. [57] using Green's function techniques. A previous investigation by Gelmukhanov et al. employed frozen orbital coupling constants [62]. The strength for a x-ray transition of energy ω_p to the final vibrational quantum n will be expressed within the gradient approach [57] as:

$$\sigma(n,\omega_p)\alpha\left|\sum_m A_{nm}/\{\omega_p - E_r + E_c + (n-m)\omega - K_r^2/\omega + K^2/\omega + 1/2i\Gamma\}\right|^2 \quad (32)$$

Here A_{nm} are vibrational amplitudes expressed in exponentials and Laguerre polynomials with the core (K) and valence hole state (K_r) coupling constants as arguments, ω is the vibrational frequency and Γ is the core hole decay width. Kaspar et al. [57] treated recently the CO 5σ and N_2 $3\sigma_g$ x-ray bands using formula (32). They assumed the decay width Γ to be independent of nuclear coordinates Q and set the absolute value of this quantity equal to that for the core excited state in the electron energy loss (EEL) spectra [63, 64]. They found a rather negligible lifetime effect on these spectra, clearly smaller than e.g., anharmonicity effects, and the previously obtained good agreement for the experimentally deduced core hole bond lengths with SCF optimizations was thus preserved. In a more recent calculation on the NO 2π-N1s x-ray transition by Kondratenko et al. [61] the lifetime-effects seem to be more prominent, and these authors were able to resolve a previous ambiguity concerning the interpretation of the band [59]. The NO spectrum, however, still needs a more advanced experimental attention.

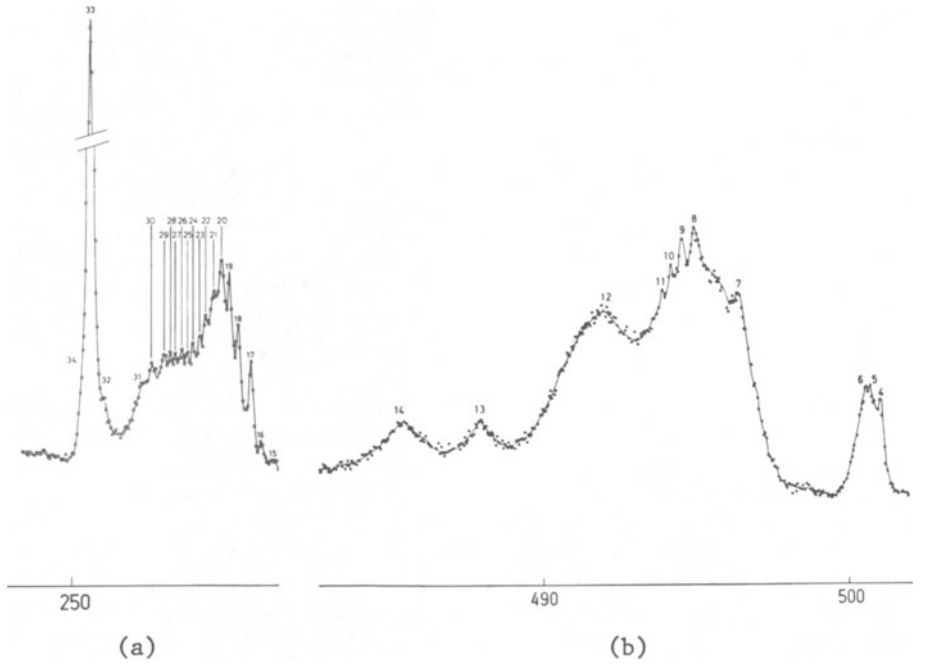

Fig. 25. Details of the high kinetic energy part of carbon and b) oxygen Auger electron spectrum of CO. (Taken from ref. [4].)

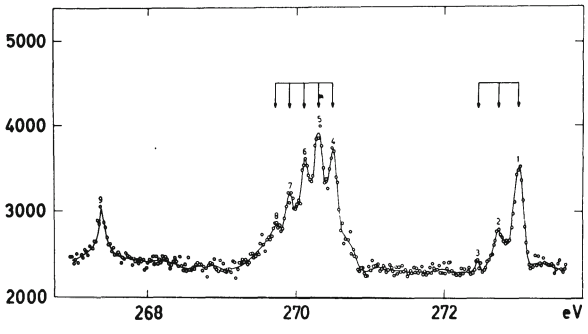

Fig. 26. Part of autoionization spectrum of CO. The bands correspond to transitions to, from left to right, $4\sigma^{-1}$, $1\pi^{-1}$, $5\sigma^{-1}$ final states. (Taken from ref. [4].)

Broad band electron excitations produce discrete core excited states in the neutral molecule which can also be studied in x-ray emission. Especially interesting are bands corresponding to identical initial and final state, namely the ground state, in the excitation-deexcitation process, leaving the vibrational profile to depend solely on the core excited PEC. Such a band was recorded from the CO $C1s^{-1}$ 2π state by Werme et al. [11], and it was found to be very narrow. This feature may qualitatively be understood from the fact that both C1s and 2π orbitals are antibonding, the latter being populated while the former is depopulated during the excitation of the $C1s^{-1}$ 2π state.

The X-emission from core ionized and core excited states has its nonradiative counterparts in Auger respectively autoionization emission. Vibrational fine structure in these spectra have only been observed for the CO and, to a less extent, for the N_2 molecules and was firstly reported in the second ESCA book [4]. Valence Auger spectra are most difficult to analyze since they involve doubly ionized final states, which in turn leads to substantial geometric distortions or in many cases to dissociation. The most detailed vibrational Auger bands, namely the outermost carbon and oxygen bands of CO, are shown in Fig. 25a and b. According to a recent ab initio calculation [75] the band at 500 eV corresponds to an $O1s^{-1}$-$5\sigma^1 1\pi^3$ $^1\Pi$ transition and is comparatively narrow, whereas the corresponding carbon band (also overlapped by $5\sigma^{-2}$) seems to be broader. The band at 250 eV, assigned to the 4σ 5σ $^1\Sigma$ state, is, however, sharp in the carbon spectrum. These differences in the two spectra may thus be explained from the quite different characteristics at the $C1s^{-1}$ and $O1s^{-1}$ PECs.

Further up in the high kinetic energy part, the CO Auger spectrum exhibits bands due to autoionization with resolved vibrational progressions [4]. Figure 26 displays the three outer valence bands, 4σ, 1π, and 5σ, originating from radiationless deexcitation of the $C1s^{-1}2\pi$ state. In accordance with observations in X-emission and electron energy loss (EEL, see next section), the PEC of this state will be only minorly displaced, and we would therefore expect its autoionization spectrum to be quite similar to the direct UPS spectrum [75], which indeed is the case. These bands have furthermore been analyzed by Kaspar et al. [57] with the intention of revealing vibrational interference effects. It was established that these effects were in general weak although noticeable at the high energy tails of the bands, acting constructively in the 1π band but destructively in the 5σ band. Kaspar et al. furthermore analyzed autoionization from the $N1s^{-1}1\pi_g^1$ $^1\Pi$ state, the PEC of which is substantially displaced. In this case vibrational interference was found to be pronounced although this assertion can not be met by the experiment due to lack of resolution. As proposed by these authors, precise high resolution X-emission or autoionization measure-

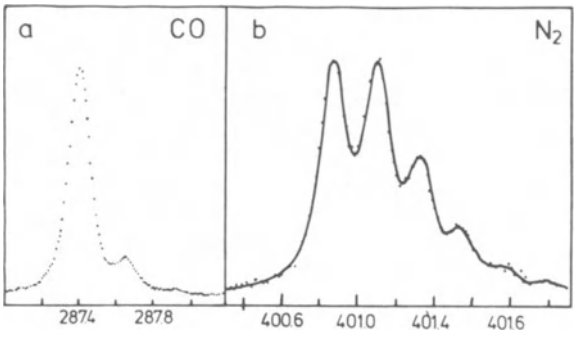

Fig. 27. Electron energy loss spectra at a) $Cls^1\ 2\pi^1\ ^1\Pi$ state of CO; b) $Nls^1\ 1\pi_g^1\ ^1\Pi$ state of N_2. (Taken from Refs. [63] and [64].)

ments of the deexcitation of this state would perhaps constitute the best test of vibrational interference due to the short lifetime of core hole containing states and eventually also provide some estimate of the imaginary part of the core hole vibrational coupling constant, i.e., the variation of lifetime with nuclear coordinates.

b) Absorption Type Spectra

The technical conditions in electron energy loss experiments have now reached the point where it is possible to study vibrational fine structure. Figures 27a and b shows the GS-$Cls^{-1}2\pi^1$ transition in CO and GS-$Nls^{-1}1\pi g^1$ transition in N_2, respectively, recorded by Tronc, King et al. [63, 64]. From fitting procedures, based on FC-calculations computed from Morse potential energy curves, these authors were able to deduce values for harmonic and anharmonic frequencies, equilibrium bond length and lifetime width for the $Nls^{-1}1\pi g^1\ ^1\Pi$ state. The determination of the latter quantity (to 128 meV) is rather unique in the case of electronic spectra of free molecules containing core holes. With respect to bond distance and frequencies this core excited state was found to constitute a compromise of the relevant properties of the N_2^+ Nls^{-1} and the N_2^- $1\pi g^1$ ions, however, the properties of the latter being favored. Thus, the formation of the $Nls^{-1}\ 1\pi g^1$ state increased the bond distance by 0.130 bohrs and decreased the harmonic frequency by 58 meV. These observations were found to correlate well with data obtained from the ground state of the equivalent core molecule NO. The $Cls^{-1}2\pi^1$ band in CO, Fig. 27a is only slightly vibrationally excited, and this is thus in agreement with findings in X-emission and autoionization CO spectra.

As an example of an x-ray photoabsorption experiment, we show the synchrotron radiation K-absorption spectrum of N_2 by Nakamura

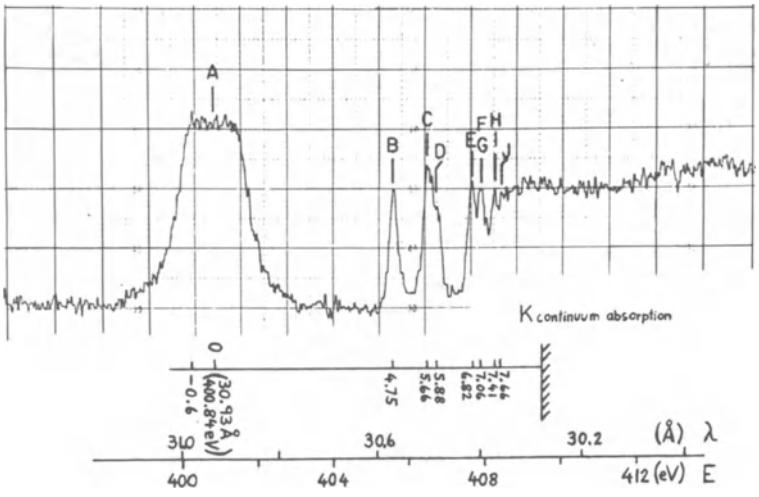

Fig. 28. K-Absorption spectrum of N_2. (Taken from ref. [65].)

et al. [65] in Fig. 28. It has several features in common with the pseudophoton EEL experiment [66, 67], evidently concerning excited discrete energies, but also concerning band widths and cross sections. The relatively large momentum transferred to the molecule by the scattered electron in the EEL process implies though that also optically forbidden excitations occur in that experiment [67]. One striking feature, common for both spectra, is the very intense representation of the $N1s^{-1}1\pi g^{1}$ level in comparison with other discrete levels. This has later been attributed to a localized confinement of the $1\pi g$ 2p orbital to the core and this feature has in turn been rationalized as a centrifugal barrier effect due to the shape resonance induced by the molecular field [68]. Concerning the width of the corresponding x-ray absorption band, it seems to confirm the high resolution EEL observation of a significant vibrational excitation, although no asymmetry could be discerned due to the truncation effect in the photographic detection technique. This band as well as the $C1s^{-1}2\pi^{1}$ band in the x-ray absorption spectrum of CO [69] have subsequently been analyzed by means of non-empirical MO SCF calculations by Kondradenko et al. [70].

V. Conclusions

The role of core hole state potential energy surfaces in molecular electronic spectra is reviewed in this article. The experimental and theoretical conditions for their study respectively analysis are described. Computational methods for diatomic and polyatomic vibrational analyses are briefly analyzed.

Firstly, results from x-ray monochromatized core hole ESCA measurements of 1st row molecular species and their theoretical investigations in LCAO MO SCF calculations are reviewed. It is shown that the results for these species fit into a nice trend; namely significant bond length shortening for Cls^{-1} species, slight shortening for Nls^{-1}, lengthening for Ols^{-1} and dissociation of Fls^{-1} species. The influence of relaxation on bond length changes following core ionization as well as on formation of the relevant ESCA bands are clarified and in that context the range of applicability of frozen orbital and equivalent core approximations is investigated. The role of exchange induced interaction in many open shell species and of core hole localization/delocalization on bond length changes and on formation of band shapes are investigated, and it is found that a correct account of these effects is of crucial importance. The relevance of core hole PECs in temperature dependent or molecular beam experiments are commented. The investigations of core hole state PECs are also extended to polyatomic species and in that context different methods for vibrational intensity calculations are tested and their relationship between these methods and their dependence on accuracy of computed wavefunctions is investigated.

The role of core hole PEC's in other types of molecular electronic techniques, viz., x-ray absorption and emission, electron energy loss, Auger and autoionization spectroscopy are discussed and examplified with a collection of spectra. In particular, the very high-resolution capability inherent in current x-ray emission dispersion techniques allows accurate determination of core ionic state PEC's, and the electron energy loss experiment correspondingly lends the possibility of determining the properties of the core excited state PEC's. The recent studies by Kaspar et al. [57] on the influence of finite core hole lifetime on emission type spectra are commented.

We conclude by asserting that from the technical achievements, molecular electronic spectroscopy is by now capable of providing information on several parameters of the core hole state PEC's, such as vertical transition energies, harmonic and anharmonic frequencies, decay widths and presumably also dependence of lifetime on nuclear geometry. The theoretical methods involved need further refinement, especially in the case of polyatomic species, and, ultimately, in the case of breakdown of Born-Oppenheimer separability of nuclear and electron motion.

References

1. G. Herzberg, Ann. Physik, 57, 616 (1929).
2. F. Hund, Z. Physik, 63, 731 (1930).
3. R. S. Mulliken, Rev. Mod. Phys., 4, 1 (1932).

4. K. Siegbahn, C. Nordling, G. Johansson, J. Hedman, P. F. Heden, K. Hamrin, U. Gelius, T. Bergmark, L. O. Werme, R. Manne, and Y. Baer, ESCA applied to free molecules, Amsterdam, North Holland (1969).
5. U. Gelius, E. Basilier, S. Svensson, T. Bergmark, and K. Siegbahn, J. Electron Spectry, 2, 405 (1974).
6. a) K. Siegbahn, Conference Proceedings, Namur (1974); J. Electron Spectry, 5, 3 (1974).
b) H. Fellner-Feldegg, U. Gelius, B. Wamberg, A. G. Nilsson, E. Basilier, and K. Siegbahn, Conference Proceedings, Namur (1974), J. Electron Spectry, 5, 64 (1974).
7. a) T. E. Sharp and H. M. Rosenstock, J. Chem. Phys., 41, 3453 (1964).
b) V. Dibler, J. Walker, and H. M. Rosenstock, J. Res. Ntal. Bur. Std., 70A, No. 6, 459 (1966).
c) R. Botter and H. M. Rosenstock, J. Res. Natl. Bur. Std., 73A, No. 3, 313 (1969).
d) R. Botter and H. M. Rosenstock, Adv. Mass Spectrom., 4, 579 (1968).
8. U. Gelius, S. Svensson, H. Siegbahn, E. Basilier, A. Faxälv, and K. Siegbahn, Chem. Phys. Letters, 28, 1 (1974).
9. U. Gelius, Conference Proceedings, Namur (1974), J. Electron Spectry, 5, 985 (1974).
10. L. O. Werme, B. Grennberg, J. Nordgren, C. Nordling, and K. Siegbahn, Phys. Letter., 41A, 113 (1972).
11. L. O. Werme, J. Nordgren, H. Ågren, C. Nordling, and K. Siegbahn, Z. Physik, A272, 131 (1975).
12. J. Nordgren, H. Ågren, C. Nordling, and K. Siegbahn, Ann. Acad. Reg. Sci. Ups, 21, 23 (1978).
13. J. Nordgren, H. Agren, L. Petterson, L. Selander, S. Griep, C. Nordling, and K. Siegbahn, Physica Scripta 00, 000 (1979).
14. J. Franck, Trans. Faraday Soc., 21, 536 (1925), E. U. Condon, Phys. Rev., 28, 1182 (1926), 32, 858 (1928).
15. C. Herzberg and E. Teller, Z. Phys. Chem. Leipzig, B21, 410 (1933).
16. P. Steele, E. R. Lippincott, and J. T. Vanderslice, Rev. Mod. Phys., 34, 329 (1962).
17. B. Chakaborthy and Y. K. Pan, Appl. Spectrosc. Rev., 7, 283 (1977).
18. F. Ansbacher, Z. Naturforsch., 14a, 889 (1959).
19. M. Wagner, Z. Naturforsch., 14a, 81 (1959).
20. W. L. Smith, J. Phys., B 1, 89 (1968), W. L. Smith, J. Phys. B 2, 1, 908 (1969).
21. F. Dushinsky, Acta Physicochim. URSS, 7, 551 (1937).
22. N. J. D. Lucas, J. Phys., B 6, 155 (1973).
23. J. B. Coon, R. E. DeWames, and C. M. Loyd, J. Mol. Spectroscopy, 8, 8285 (1962).
24. W. Meyer, J. Chem. Phys., 58, 1017 (1973).
25. D. T. Clark and J. Muller, Theoret. Chim. Acta, 41, 193 (1976).
26. T. A. Koopmans, Physica, 1, 104 (1933).
27. P. Bagus, Phys. Rev., 139A, 619 (1965).

28. D. T. Clark, I. W. Scanlan, and J. Muller, Theoret. Chim. Acta, 35, 341 (1974).
29. O. Goscinski and A. Palma, Chem. Phys. Lett., 47, 322 (1977).
30. a) D. T. Clark and J. Muller, Chem. Phys., 23, 429 (1977).
b) D. T. Clark and L. Colling, Nouv. J. Chem., 2, 225 (1978).
c) D. T. Clark and L. Colling, J. Electron Spectrosc., 13, 317 (1978).
d) D. T. Clark and L. Colling, J. Electron Spectrosc., 12, 343 (1977).
e) D. T. Clark, Physica Scripta, 16, 307 (1977).
31. L. S. Cederbaum and W. Domcke, Adv. Chem. Phys., 36, 205 (1977) and references therein.
32. O. Goscinski, J. Muller, E. Poulain, and H. Siegbahn, Chem. Phys. Lett., 55, 407 (1978).
33. T. D. Thomas, J. Am. Chem. Soc., 92, 4184 (1970).
34. R. W. Shaw and T. D. Thomas, Chem. Phys. Lett., 22, 127 (1973).
35. L. J. Saethre, S. Svensson, N. Mårtensson, U. Gelius, P. Å. Malmquist, E. Basilier, and K. Siegbahn, Chem. Phys., 20, 431 (1977).
36. J. G. Winans and E. C. G. Stuckelberg, Proc. Nat. Acad. Amer., 14, 867 (1928).
37. D. E. Aspnes, Phys. Rev., 147, 554 (1966).
38. J. Schirmer, L. S. Cederbaum, W. Domcke, and W. von Niessen, Chem. Phys., 26, 149 (1977).
39. The experimental ratio 1.75 takes into consideration corrections for instrumental resolution. For details see reference 12.
40. L. S. Snyder, J. Chem. Phys., 55, 95 (1971).
41. P. S. Bagus and H. F. Shaefer, J. Chem. Phys., 56, 224 (1972).
42. A. Denis, J. Langlet, and J.-P. Malrieu, Theoret. Chim. Acta, 38, 49 (1975).
43. a) H. T. Jonkman, G. A. van der Velde, and W. C. Nieupoort, Proceedings of SRC Atlas Symposium No. 4, St. Catherine's College, Oxford, April 1975.
b) H. T. Jonkman, Broken Orbital Symmetry in Excited and Ionized State Molecules, Ph. D. Thesis, University of Groningen, The Netherlands (1975).
44. L. S. Cederbaum and W. Domcke, J. Chem. Phys., 66, 5084 (1977).
45. P. O. Löwdin, Rev. Mod. Phys., 35, 469 (1963).
46. J. Müller, H. Ågren, and O. Goscinski, Chem. Phys., 38, 349 (1979).
47. The difference between minimum energies of the gerade and ungerade states is 0.15 eV. The overall linewidth of two Gaussians with FWHM = 0.75 eV separated from each other by 0.15 eV is another Gaussian with FWHM = 0.82 eV.
48. P. S. Bagus, M. Schrenk, D. W. Davis, and D. A. Shirley, Phys. Rev., A9, 1090 (1974).
49. T. Darko, I. H. Hillier, and J. Kendrick, J. Chem. Phys., 67, 1702 (1977).

50. T. Darko, I. H. Hillier, and J. Kendrick, Chem. Phys. Lett., 45, 188 (1977).
51. S. Svensson, P. Å. Malmquist, E. Basislier, and U. Gelius, Private communication.
52. J. L. Duncan and I. M. Mills, Spectrochimica Acta, 20, 523 (1964).
53. H. Ågren, J. Muller, and J. Nordgren, J. Chem. Phys., 72, 4078 (1980).
54. W. Domcke, L. S. Cederbaum, H. Köppel, and W. von Niessen, Molecular Physics, 34, 1759 (1977).
55. J. A. Smith, P. Jorgenssen, and Y. Öhrn, J. Chem. Phys., 62, 1285 (1974).
56. H. Ågren and J. Müller, J. Electron Spectrosc., 19, 285 (1980).
57. F. Kaspar, W. Domcke, and L. S. Cederbaum, Chem. Phys., 44, 33 (1979).
58. L. O. Werme, B. Grennberg, J. Nordgren, C. Nordling, and K. Siegbahn, J. Electron Spectrosc., 2, 435 (1973).
59. J. Nordgren, H. Ågren, L. O. Werme, C. Nordling, and K. Siegbahn, J. Phys., B 9, 295 (1976).
60. H. Ågren, L. Selander, J. Nordgren, C. Nordling, and K. Siegbahn, Chem. Phys., 37, 161 (1979).
61. a) A. V. Kondratenko, L. N. Mazalov, F. Kh. Gelmukhanov, V. I. Avdeev, and E. A. Saprykina, J. Struct. Chem., 18, 494 (1978).
b) A. V. Kondratenko, L. N. Mazalov, and B. A. Kornev, Theoret. Chim. Acta, 52, 311 (1979).
62. a) F. K. Gelmukahanov, L. N. Mazalov, A. V. Nikolajev, A.V. Kondratenko, V. G. Smirnoj, P. I. Vadasj, and A. P. Sadovskij, Dokl. Akad. Nauk SSSR, 225, 597 (1975).
b) F. K. Gelmukahnov, L. N. Mazalov, and A. V. Kondratenko, Chem. Phys. Lett., 46, 133 (1977).
63. M. Tronc, G. C. King, R. C. Bradford, and F. H. Read, J. Phys., B 9, 1555 (1976).
64. G. C. King, F. H. Read, and M. Tronc, Chem. Phys. Lett., 72, 498 (1977).
65. M. Nakamura, M. Sasanuma, S. Sato, M. Wanatabe, H. Yamashita, Y. Iguchi, S. Yamaguchi, T. Sagawa, Y. Nakai, and T. Oshio, Phys. Rev., 178, 80 (1969).
66. G. R. Wright, C. E. Brion, and M. J. van der Wiel, J. Electron Spectrosc. Relat. Phenom., 1, 457 (1973).
67. M. Inokuti, Rev. Mod. Phys., 43, 297 (1971).
68. J. L. Dehmer and D. Dill, J. Chem. Phys., 65, 5327 (1976).
69. M. Nakamura, Y. Morioka, T. Hayaishi, E. Ishiguro, and M. Sasanuma, Conference Proceedings of the Third International Conference on Vacuum Ultraviolet Radiation Physics, Tokyo, Japan (1971).
70. A. V. Kondratenko, L. N. Mazalov, F. Kh. Gelmukhanov, V. I. Avdeev, and E. A. Saprykina, J. Struct. Chem., 18, 437 (1977).
71. L. E. Sutton (ed.), Tables of Internuclear Distances and Configurations in Molecules and Ions. Chem. Soc. Spec. Publ., 18 (1965).

72. A. D. McLean, M. Yoshimine, Supplement of "Computation of molecular properties and structures," IBM Journal of Research and Development (November 1967).
73. G. Herzberg, Molecular spectra and molecular structure, Vol. 2, Van Nostrand, New York (1950).
74. Yu. Ya. Kharitonov, I 3v. Akad. Nauk SSR, Otd. Khim. Nauk, 1953 (1962).
75. H. Ågren and H. Siegbahn, Chem. Phys. Lett., 72, 489 (1980).
76. D. W. Turner, C. Baker, A. D. Baker, and C. R. Brundle, Molecular Photoelectron Spectroscopy, Wiley-Interscience, Wilson and Sons, London (1970).
77. A. P. Hitchcock and C. E. Brion, J. Electron Spectrosc., 18, 1 (1980).
78. J. W. Rabalais, L. Karlsson, L. O. Werme, T. Bergmark, and K. Siegbahn, J. Chem. Phys., 58, 3370 (1973).

ELECTRONIC FLUORESCENCE SPECTRA OF GAS-PHASE POSITIVE IONS

A. Carrington and R. P. Tuckett

Department of Chemistry
University of Southampton
Hampshire, England

We describe here a novel technique to observe electronic spectra of gas-phase positive ions. The ions are formed by electron impact on a supersonic beam of neutral molecules, and the fluorescent radiation from the ions is dispersed. The two particular properties of supersonic beams that we exploit are:

(a) The density of molecules in a beam can be high, yet they all travel in the same direction in a collision-free environment. Collisional deactivation of the ion by fast ion-molecule reactions is therefore absent.

(b) In the expansion, random motion of the molecules is converted into forward directed flow, producing a beam of internally cold molecules; the rotational temperature can be less than 1°K.

We assume that electron impact does not substantially change the rotational angular momentum of the molecule. When only its lowest rotational levels are populated in the beam, this means that only the lowest rotational levels of the parent ion will be populated by electron impact; the fluorescence spectrum of the ion will then be very simple, as the number of rotational lines will be very small. The populations of vibrational levels of the ion, however, will be no different from conventional electron impact studies, as they are governed only by the Franck-Condon factors with the neutral molecule. By working with supersonic beams, therefore, we hope to simplify dramatically electronic spectra of polyatomic cations such that a very large number of normally unresolved rotational components in a given vibronic band will now be condensed into a very few. This simplification is

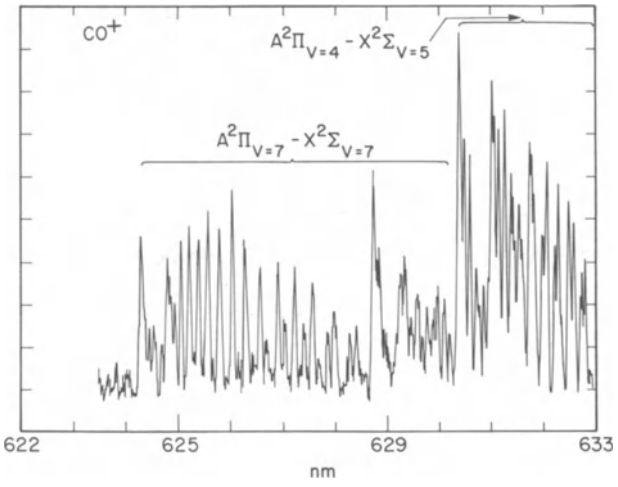

Fig. 1. Part of the fluorescence spectrum of the CO^+ ion.

only predicted for the parent ion, and not for secondary ions, formed by decomposition of the parent.

The apparatus and some preliminary results are described in a recent paper [1]. We obtained N_2^+ (B-X) with a rotational temperature of 23°K, N_2O^+ (A-X) at 25°K, and CO_2^+ also at a low temperature. The last spectrum is particularly revealing as the different vibronic bands of CO_2^+ ($A^2\Pi_u \rightarrow X^2\Pi_g$) stand out very clearly in isolation to each other, as the complications of rotational structure have, in effect, been removed.

We now describe some very recent results on several fluorobenzene cations. Visible emission spectra in the gas-phase were first observed by Maier et al. [2] in 1975 using electron impact excitation of the parent neutral molecule. More recently, Cossart-Magos et al. [3] have photographed emission spectra of these ions from a d.c. discharge source at higher resolution, and made some vibrational analyses. Both techniques, however, suffer the great disadvantage that the different vibrational bands are superimposed on a large continuous rotational envelope (the species being rotationally hot), greatly hindering analysis. Miller's group [4] have observed these spectra both in the gas-phase, but more especially in a Ne matrix at 5°K. They then use, for example, LIF to probe vibrational levels in the upper electronic state. Such experiments do, however, suffer the disadvantage that the band origin is shifted substantially by the matrix.

We have recorded these fluorescence spectra under supersonic beam conditions. The different vibronic bands are rotationally very

cold, so unlike the spectra of Maier and Cossart-Magos, they stand out clearly on a true baseline, thus greatly simplifying analysis. [In effect, such experiments perform matrix-like studies in the gas-phase without any shift in band origin due to the matrix.] Their spectra contain vibrational information on both ground and excited electronic states. Our spectra, unfortunately, only contain ground state information as nearly all the fluorescence is to low frequency of ν^{00}. This is a consequence of extensive vibrational cooling of the neutral molecules in the supersonic expansion. Following electron impact, Franck-Condon factors populate only low vibrational levels of the upper ionic electronic state (mostly the zero level), so dispersed fluoresence is to low frequency of ν^{00}.

The spectra fall into two groups. Those with non-degenerate ground electronic state (e.g., $C_6F_5H^+$, all isomers of $C_6F_4H_2^+$) have well-behaved spectra, consisting of an origin (ν^{00}) and progressions involving only totally symmetric vibrations (i.e., a_1 vibrations in molecules of C_{2v} symmetry). Little anharmonicity is observed in these vibrations. No other vibrations are observed, suggesting planarity is preserved in both electronic states of the ion.

The second group have doubly-degenerate ground electronic states. $C_6F_6^+(X^2E_{1g})$, for example, has D_{6h} symmetry, and is a candidate for Jahn-Teller distortion. In strict D_{6h} symmetry, $C_6F_6^+$ has only two a_{1g} totally symmetric vibrations, and only these bands or combinations should appear in the fluorescence spectrum. This is not the case, and 'forbidden' bands are observed 284, 406, and 497 cm^{-1} to low frequency of ν^{00}. They are assigned to vibrations of e_{2g} symmetry (ν_{18}, ν_{17}, and $2\nu_{18}$ respectively) which become allowed as the molecule lowers its symmetry from D_{6h} through Jahn-Teller distortion. The huge apparent anharmonicity in ν_{18} is a direct consequence of the Jahn-Teller effect. We stress that these forbidden vibrations are only observed due to the very extensive rotational cooling (probably a few Kelvin, only) of each vibronic band. Full details of all these spectra will be described in a future publication [5].

REFERENCES

1. A. Carrington and R. P. Tuckett, Chem. Phys. Letters, 74, 19 (1980).
2. M. Allan and J. P. Maier, Chem. Phys. Letters, 34, 442 (1975).
3. C. Cossart-Magos, D. Cossart, and S. Leach, Mol. Phys., 37, 793 (1979).
4. V. E. Bondybey, J. H. English, and T. A. Miller, J. Mol. Spectrosc., 81, 455 and references therein (1980).
5. R. P. Tuckett, Chem. Phys., 58, 151 (1981).

HeI PHOTOELECTRON SPECTROSCOPY OF TRANSIENT AND UNSTABLE SPECIES

N. P. C. Westwood

Department of Chemistry
University of Columbia
Vancouver, B.C., Canada

Photoelectron (PE) spectroscopy is a technique involving ejection of electrons from molecules by radiation (in this case, HeI, 21.2 eV). The ejected electron carries away information about the electronic, vibrational, and rotational states of the resultant ion, the first providing information on a manifold of ionic states, and the second giving the vibrational frequencies in the ion. Rotational structure is not usually resolved.

As such, the technique provides via Koopmans theorem [1] a relationship between the measured ionization energies (IE's) and the orbital energies. Thus, within the HeI energy range, a molecule will show a series of bands which may, to a first approximation, be interpreted within the single particle picture.

In the particular case described here, we are interested in generating unstable molecules direct into the PE spectrometer under fast pumping conditions using a variety of experimental techniques including microwave discharge, pyrolysis, atom-molecule reactions, etc. Unlike other forms of spectroscopy where certain selection rules are appropriate, the PE technique detects all species present within a mixture and thus extremely complicated spectra can result. However, by means of judicious experimental procedures, transient/unstable molecules can be generated directly into the PE spectrometer in relatively high yield and their PE spectra obtained. Spectrometer deterioration and species identification constitute the main problems in this area. The former can be minimized by using a spectrometer specifically designed to study such deleterious and short lived compounds [2], and the second can be circumvented by a choice of different preparative routes, quantum mechanical calculations and comparison with known appearance potentials. In our

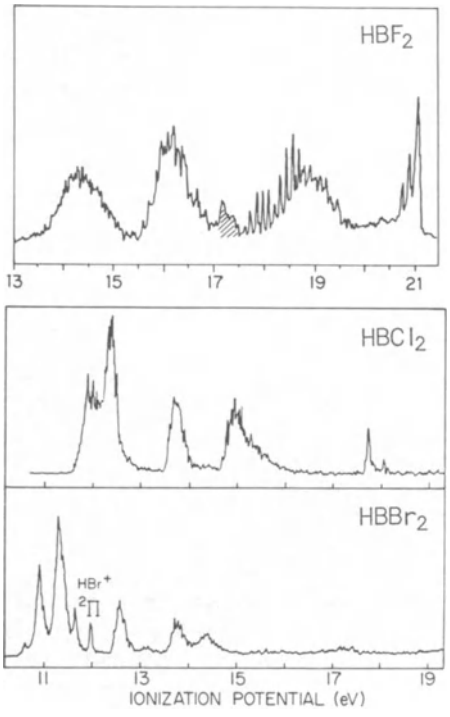

Fig. 1

particular case, the parent ion can usually be observed by means of a quadrupole mass spectrometer coupled to the PE spectrometer.

We are particularly interested in small molecules for a number of reasons since they occur as reaction intermediates, interstellar and upper atmosphere molecules, etc. They are readily recognized amongst the spectra of precursors, they usually possess resolved vibrational structure which can be of assistance in the subsequent analysis, and they are tractable by sophisticated calculations.

A particularly good example of such a molecule is trans-diazene, N_2H_2[3], which shows four IE's with extensively resolved vibrational structure. Assignment of the first IE to the n_+N lone pair combination (^2A_g) is unequivocal. However, the relative positions of the π and n_- levels can only be determined from a deuteration experiment when the N=N and NNH(D) vibrational frequencies can be distinguished on the $\pi(^2A_u)$ and $n_-(^2B_u)$ cationic states. Additionally, the resolved fine structure on the ground ionic state can be analyzed to provide an estimate of the ionic geometry [4].

More recently, we have prepared the unstable HBX_2 molecules (X=F, Cl, and Br) in the pure state by reaction of BX_3 with solid $NaBH_4$. The spectra (Fig. 1) illustrate that the technique is very efficient for formation of these molecules which under normal equilibrium conditions, decompose to B_2H_6 and BX_3. A comparison can be made with the corresponding BX_3 molecules from which they are derived, illustrating the correspondence upon lowering the symmetry from D_3h to C_2v by replacement of X by H. The sequence of ionic states for $HCBl_2$ is $\tilde{X}^2B_2$, $\tilde{A}^2A_1$, $\tilde{B}^2A_2$, $\tilde{C}^2B_1$, $\tilde{D}^2B_2$, $\tilde{E}^2A_1$, $\tilde{F}^2A_1$, ..., although it is conceivable that a switch of the first two could occur since they are close in energy. Resolved vibrational structure gives the ionic frequencies for several of the states.

In HBF_2, the ground ionic state can be unequivocally established from a comparison with the isoelectronic CF_2 molecules [5] and calculations involving perturbation corrections to Koopman's theorem. The $^2A_1$ ground ionic state shows a broad Franck-Condon envelope but no resolved vibrational structure. The other states can be assigned in correspondence with those for $HBCl_2$. The $^2A_1$ state right at the cut-off corresponds to the B2s orbital which in BF_3 occurs at 21.4 eV. In this case the resolved vibrational structure is 1050 cm^{-1}, the Franck-Condon envelope suggesting some bonding character.

The absence of structure on the first band (cf. CF_2 [5]) suggests a dissociative process. This orbital is strongly B—H bonding, B—F antibonding and F...F bonding. A geometry calculation for the ion using the semiempirical MNDO, and *ab-initio* (STO-3G basis set) methods shows a large increase in the B—H bond length (up to $\sim$1.4 Å) and a widening ($\sim$20°) of the FBF angle. This approaches the geometry of the linear 16 electron system BF_2^+. In this connection it is interesting to note that HBF_2 does not show a parent peak in the mass spectrum [6].

The final example involves investigation of the $(FBS)_n$ system (n = 1, 2, and 3). Monomer and dimer are generated by passing SF_6 over B at 1370°K; the ratio of the two varies with pumping speed. Trapping of the mixture and revaporization into the spectrometer produces solely the trimer. All three species can be characterized by the in-situ quadrupole. FBS^+ has a sequence of ionic states, $\tilde{X}^2\Pi$, $\tilde{A}^2\Sigma^+$, $\tilde{B}^2\Pi$, $\tilde{C}^2\Sigma^+$ ... . The first two are readily observed at 10.91 and 14.21 eV with associated vibrational structure of 1550 and 1670 cm^{-1} respectively. There is some evidence for spin-orbit coupling in the Π state. These are therefore analogous to the similar states observed in the isoelectronic FCP^+ system [7]. The second excited state is hidden by BF_3, the third is observed at 19.62 eV. The analysis of the dimer and trimer spectra is at present underway.

In conclusion, it may be said that UPS has now moved away from the general cataloguing of spectra and IE's, and in its maturity now provides detailed information on the ionic states of small novel molecules, such species being generated directly into the spectrometer. An additional bonus is the development of experimental routes to new molecules. The prognosis for this line of development is certainly very favorable, since it provides a link between synthetic chemistry, spectroscopy, and quantum mechanical methods.

ADKNOWLEDGEMENTS

This work was funded by the NSERC of Canada. The contributions of Colin Kirby and Woon Ming Lau are gratefully acknowledged. D. C. Frost and C. A. McDowell are thanked for their interest in this work.

REFERENCES

1. T. Koopmans, 1, 104 (1934).
2. D. C. Frost, S. T. Lee, C. A. McDowell, and N. P. C. Westwood, J. Electron Spectrosc. Relat. Phenon., 12, 95 (1977).
3. D. C. Frost, S. T. Lee, C. A. McDowell, and N. P. C. Westwood, J. Chem. Phys., 64, 4719 (1976).
4. J. Berkowitz Invited paper, NATO ASI, Kos, Greece (1980).
5. J. M. Dyke, L. Golob, N. Jonathan, A. Morris, and M. Okuda, J. Chem. Soc. Farad. Trans., 2, 1828 (1974).
6. J. H. Wilson and H. A. McGee, J. Chem. Phys., 46, 1444 (1967).
7. H. W. Kroto, J. F. Nixon, N. P. C. Simmons, and N. P. C. Westwood, J. Am. Chem. Soc., 100, 446 (1978).

AUTOIONIZATION PROCESSES IN CARBONYL SULFIDE INVESTIGATED BY THRESHOLD PHOTOELECTRON SPECTROSCOPY

M.-J. Hubin-Franskin,* J. Delwiche*
L.U.R.E., Bâtiment 209c, Université de Paris-Sud,
F-91405 Orsay Cédex, France
and Institut de Chimie, Batiment B6,
Université de Liège, Sart Tilman par 4000 Liège I,
Belgium

P.-M. Guyon
Laboratoire des Collisions Atomiques et Moléculaires
Université de Paris-Sud, Orsay, France

and

I. Nenner
C.E.N. Saclay, Département de Physicochimie
Service de Photophysique et de Photochimie
B.P.2, 91190 Gif-sur-Yvette, France

The recent development of the threshold photoelectron spectroscopy [1] showed that the photoionization of small polyatomic molecules produces threshold energy electrons in Franck-Condon gap regions where direct excitation probability is vanishingly small.

For N_2O, Baer et al. [2, 3] observed that autoionization processes producing threshold photoelectrons are greatly enhanced in some regions of the photoionization spectrum. It was shown that the photoelectron energy distribution was sharply peaked at zero kinetic energy. The phenomenon was called resonant autoionization. Furthermore, Guyon et al. [4] suggested that such resonant autoionization was enhanced for Rydberg levels coupled to a neutral dissociation continuum.

We report here a threshold photoelectron spectroscopic study of OCS.

---

*"Chercheur qualifié" of the "Fonds national de la Recherche Scientifique" of Belgium.

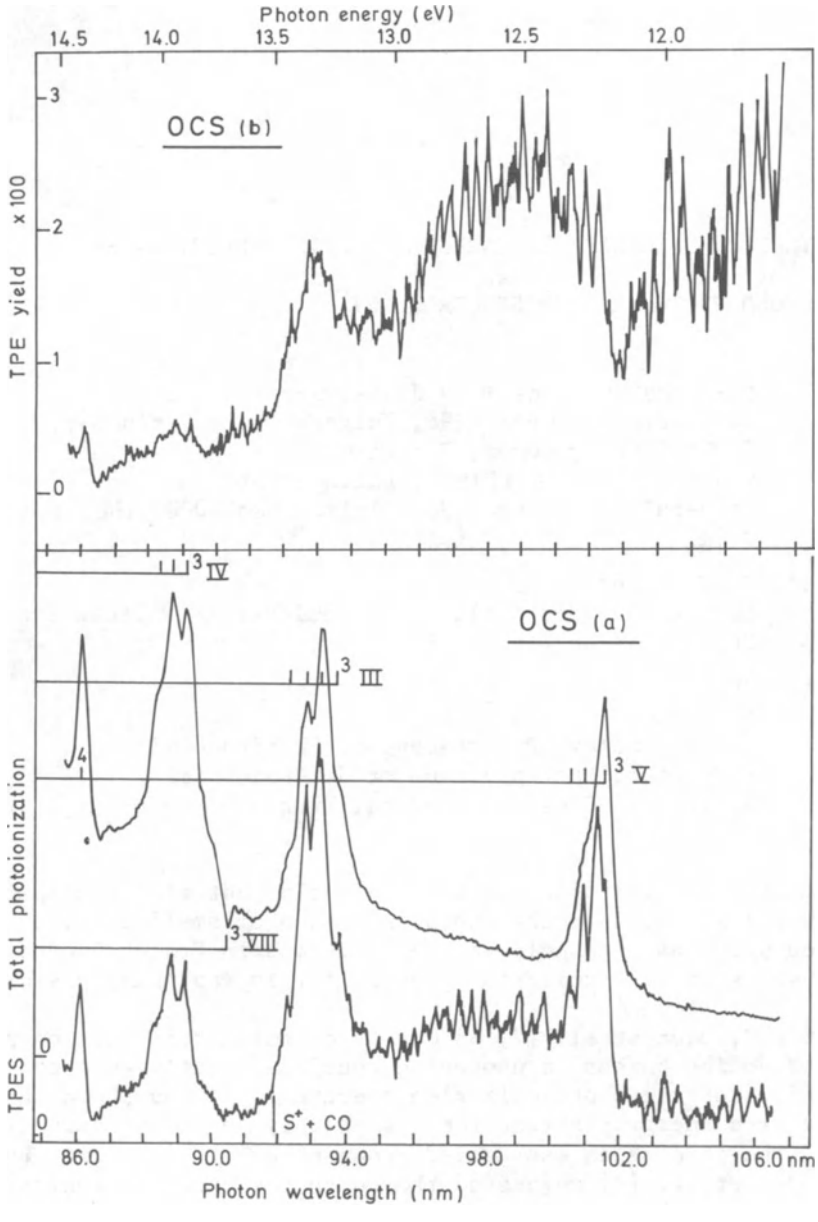

Fig. 1. a) The TPES and the total photoionization spectrum in the energy region corresponding to the gap $\tilde{A}$-$\tilde{X}$. b) TPE yield curve in the energy region corresponding to the gap $\tilde{A}$-$\tilde{X}$.

The detailed description of the experimental set up and the complete analysis of the experimental data will be given elsewhere [5]. We shall present here only the results for the 86-106 nm range, i.e., the processes occurring in the Franck-Condon gap between the $\tilde{A}^2\Pi$ and the $\tilde{X}^2\Pi$ states.

In Fig. 1, we present (part a) the threshold photoelectron spectrum (TPES) of OCS between 86 and 106 nm together with the total photoionization curve (PIS) and (part b) the threshold photoelectron yield curve.

The prominent structures of the TPES are produced by Rydberg series (R_B) converging to the 000 level of the $\tilde{B}^2\Sigma^+$ state at 77.29 nm (16.041 eV).

In addition, we observe between 95 and 105 nm a broad band with a maximum at 98 nm. We attribute it to a Rydberg state (R_A), member of a series converging to the $\tilde{A}^2\Pi$ state at 82.25 nm (15.075 eV). The effective quantum number would be 2.2.

As we are here in the Franck-Condon gap between $\tilde{A}^2\Pi$ and the $\tilde{X}^2\Pi$ states, we would expect small TPE yield in that region. It is not the case.

Moreover, the time-of-flight (TOF) photoelectron spectra recorded between 95 and 100 nm all show a bimodal energy distribution for the electrons, with a sharp peak at zero kinetic energy and a large distribution corresponding to the population of the lowest vibrational levels of the $\tilde{X}$ state.

As the Franck-Condon factors for R_B are unfavorable for the production of zero kinetic energy electrons in this energy range, only R_A is expected to contribute significantly to the TPES. One would expect, however, a large kinetic energy distribution of the electrons in the TOF photoelectron spectrum. As it is not the case, we are lead to conclude that here, as well as in N_2O, we have autoionization mechanisms that deviate from the classical model.

A detailed discussion, based on an extension of the Smith's formalism [6] will be presented elsewhere [5].

We are grateful to the LURE and the "Laboratoire de l'Accélérateur Linéaire" staff for operating the ACO storage ring. We (M.-J. H.-F., J.D.) thank the "Fonds National de la Recherche Scientifique" of Belgium for a research position.

REFERENCES

1. P. M. Guyon, R. Spohr, W. A. Chupka, and J. Berkowitz, J. Chem. Phys., 65, 1650 (1976).
2. T. Baer, in: Gas Phase Ion Chemistry, M. T. Bowers (ed.), Academic Press (1979), pp. 153-196.
3. T. Baer, P. M. Guyon, I. Nenner, A. Tabché-Fouhaillè, R. Botter, L. F. A. Ferreira, and T. Govers, J. Chem. Phys., 70, 1585 (1979).
4. Comments to C. Jungen, J. Chim. Phys., 77, 32 (1980), edited by J. Jortner and S. Leach. P. M. Guyon, I. Nnner, T. Baer, and A. Tabche-Fouhaille (to be published).
5. J. Delwiche, M.-J. Hubin-Franskin, P. M. Guyon, and I. Nenner (to be published in J. Chem. Phys.).
6. A. L. Smith, J. Quant. Spect. Radiat. Transfer, 10, 1129 (1970); Phil. Trans. Roy. Soc. London, A268, 169 (1970).

CORRELATION AND SELF-REPULSION IN STUDIES OF MOLECULAR IONS WITH THE HAM METHOD

E. Lindholm, L. Åsbrink, and C. Fridh

Physics Department
The Royal Institute of Technology
S-100 44 Stockholm
Sweden

In the study of positive and negative molecular ions the primary data can be said to be the energies which are required to produce them from the molecules. The ionization energies are usually calculated using Koopmans' theorem, which means, that the accuracy depends upon the extent to which the correlation energy change and the reorganization energy cancel each other. For electron affinities there is no such cancellation, and the calculation of electron affinities is therefore difficult and only few such studies have been published.

It would therefore be of importance to have access to a method in which the correlation energy has been incorporated already in the construction of the method. The reorganization can then be calculated correctly and good results for both ionization energies and electron affinities can be expected.

It will be shown that the exploitation of the idempotency property of density matrices in the Hartree-Fock method seems to make possible the construction of such a method [1, 2].

The total energy of a molecule is the sum of the LCAO Hartree-Fock total energy and the pair correlation energy

$$E = -\frac{1}{2}\sum_{\mu\nu} P_{\mu\nu}\int \phi_\mu^* \nabla^2 \phi_\nu d\tau - \sum_{\mu\nu} P_{\mu\nu}\int \phi_\mu^* \phi_\nu \sum_B Z_B \gamma_B^{-1} d\tau +$$

$$\frac{1}{2}\sum_{\mu\nu\lambda\sigma} P_{\mu\nu}P_{\lambda\sigma}[(\mu\nu/\lambda\sigma) - \tfrac{1}{2}(\mu\sigma/\lambda\nu)] + \sum_{A>B} Z_A Z_B R_{AB}^{-1} +$$

$$\frac{1}{2}\sum_{\mu} N_\mu(N_\mu - 1)\varepsilon_{\mu\mu}^{corr} + \frac{1}{2}\sum_{\substack{\mu}}\sum_{\substack{\nu \\ \mu\neq\nu}} N_\mu N_\nu \varepsilon_{\nu\mu}^{corr}$$

with $N_\mu = \sum_{\nu} P_{\mu\nu}S_{\mu\nu}$.

We will now transform the total energy expression in a way which is fully described in [2]. Here only the main principles will be suggested.

The diagonal element of the idempotency property of density matrices in the ZDO approximation is

$$2P_{\mu\mu} = \sum_{\nu} P_{\mu\nu}P_{\nu\mu}$$

In the full overlap basis we obtain

$$0 = -\frac{1}{2}\sum_{\mu} N_\mu(\mu\mu/\mu\mu) + \frac{1}{4}\sum_{\mu\nu\lambda\sigma} P_{\mu\nu}P_{\sigma\lambda}S_{\lambda\mu}S_{\nu\sigma}(\mu\mu/\mu\mu)$$

which can be added to the total energy without changing it.

We can further use Mulliken's approximation

$$\int\phi_\mu{}^*\nabla^2\phi_\nu d\tau = \frac{1}{2}S_{\mu\nu}[\int\phi_\mu{}^*\nabla^2\phi_\mu d\tau + \int\phi_\nu{}^*\nabla^2\phi_\nu d\tau] + \beta_{kin}^{\mu\nu}(\mu, \nu, R_{AB})$$

where β is a correction term which compensates for the inaccuracy of the approximation.

If we introduce

$$\gamma_{\nu\mu} = (\nu\nu/\mu\mu) + \varepsilon_{\nu\mu}^{corr}$$

which means that <u>all</u> pair-correlation energies are combined with the electron-electron repulsions, we obtain the total energy as

$$E = -\sum_{A}^{A}\sum_{\mu} N_\mu[+\frac{1}{2}\int\phi_\mu{}^*\nabla^2\phi_\mu d\tau + Z_A\int\phi_\mu^2\gamma_A^{-1}d\tau - \frac{1}{2}(N_\mu - 1)\gamma_{\mu\mu} -$$

$$\frac{1}{2}\sum_{\nu\neq\mu}^{A} N_\nu\gamma_{\nu\mu}] - \sum P_{\mu\nu}\cdot\beta_{\mu\nu} + \sum_{A>B} Q_AQ_B\gamma_{AB}$$

+ penetration terms + small terms

We observe that the mechanism for the compensation of self-repulsion in the HAM model is different from that in the Hartree-Fock model. In the latter model the compensation is performed with

the exchange integral, which is often difficult to handle (cf. the Xα method). In the HAM model we have instead a simple term, -1, obtained from the exploitation of the idempotency.

If we here introduce the shielding efficiency $\sigma_{\nu\mu}$ which was called "shielding constant" by Slater

$$\sigma_{\nu\mu} = \frac{(\nu\nu/\mu\mu) + \varepsilon_{\nu\mu}^{corr}}{2\int \phi_\mu^2 \gamma_A^{-1} d\tau}$$

and if we assume that the atomic orbitals ϕ_μ are hydrogen-like with orbital exponent ζ_μ the main part of the total energy becomes

$$E = -\frac{1}{2}\sum_\mu N_\mu \zeta_\mu^2 - \sum_{\mu_A \nu_B} P_{\mu\nu}\beta_{\mu\nu} + \sum_{A>B} Q_A Q_B \gamma_{AB}$$

This total energy expression can be handled using *ab-initio* methods if the pair-correlation energies are neglected. If not, semiempirical methods must be used. The "Slater shielding constants" $\sigma_{\nu\mu}$ must then be replaced by the shielding efficiencies $\sigma_{\nu\mu}$ given above. The proof here shows that in such a semiempirical method the parametrization will take care of all correlation energy in the total energy expression, supposed that a "single-determinant" wavefunction is enough. If not, a limited CI must be performed.

From these principles a parametrized method, HAM/3, was constructed [3] and submitted to QCPE [4]. Although the model behind HAM/3 is only an approximation to the theory presented here, and therefore the inclusion of the correlation energy is only partial, the method has appeared to give results in good agreement with experiment, not only for ionization energies but, as expected, also for electron affinities. The last feature is important due to the recent experimental methods to measure electron affinities.

We are now working to construct an improved version, HAM/4, from the theory presented here, extending it to molecules with heavier atoms than those in the first line of the periodic table. It is our hope that the exploitation of the idempotency in Hartree-Fock theory will open up new possibilities to study positive and negative molecular ions, since it in this way seems to be possible to handle the correlation energy in a very simple and correct way without wasting computer time.

REFERENCES

1. L. Åsbrink, C. Fridh, E. Lindholm, and S. de Bruijn, Chem. Phys. Letters, 66, 411 (1979).

2. L. Åsbrink, C. Fridh, E. Lindholm, S. de Bruijn, and D. P. Chong, Phys. Scripta, 22, 475 (1980).
3. L. Åsbrink, C. Fridh, and E. Lindholm, Chem. Phys. Letters, 52, 63, 69, 72 (1977).
4. L. Åsbrink, C. Fridh, and E. Lindholm, QCPE No. 393 (1980).

THEORETICAL STUDIES OF THE STRUCTURES OF MOLECULAR IONS

J. A. Pople

Department of Chemistry

Carnegie-Mellon University
Pittsburgh, Pennsylvania 15213

Theoretical Studies of the Structures of Molecular Ions

1. Introduction

The prediction of the equilibrium geometries and stabilities of molecular ions is a major challenge to quantum chemistry. Although many ions are detectable by experimental techniques such as mass spectroscopy and although some information may be available on their heats of formation, experimental determination of structure is more difficult because of low concentrations and the amount of good data is relatively small. The techniques of ab initio molecular orbital theory, on the other hand, are as easily applied to ionic as neutral systems and, if they can be documented for reliability, such studies provide an independent approach to structural problems. In these lectures, the current level of development of molecular orbital theory will be described and some recent application to structural problems for small ions, particularly cations, will be reviewed.

There is considerable advantage in using a certain well-defined level of theory uniformly over as wide a range of chemical problems as possible. If a mathematical procedure is uniquely defined for obtaining a total energy as a function of nuclear coordinates for any number of nuclei and electrons, such a procedure constitutes a theoretical model chemistry. Given an efficient computer algorithm, such a technique can be used to explore the potential surfaces of any molecular system to determine (a) the positions of stationary points and (b) the energies at these points. If the stationary points are established to be local minima on the potential surface,

then the corresponding geometrical parameters define the equilibrium structures of the possible isomers of the system. In addition, the model will predict relative energies of such isomers. Other stationary points will be saddle points on the potential surface and will predict transition structures for intramolecular rearrangements connecting the isomers.

In recent years, we have developed a number of theoretical models and have tested them extensively against experimental data on neutral systems. This has led to a fairly clear recognition of the level of theoretical model necessary to achieve adequate reproduction of experimental structural parameters. Application of the same procedures to ionic systems leads to prediction of structures, often in the absence of experimental data. Such predictions have some reasonable validity, given the documentation of the success of the same theoretical models for neutral systems.

In Section 2, an outline is given of the theoretical models used in our current investigations of the structures of ions. These are all based on molecular orbital theory at the Hartree-Fock level, followed by studies of the effects of electron correlation using Møller-Plesset perturbation theory. This is followed in Section 3 by a computer-generated tabulation of data on small cations containing carbon, hydrogen, nitrogen, and oxygen. Finally, Section 4 illustrates application of the theory by surveying recent investigations of small carbocations.

2. Theoretical Models Appropriate for Studies of Ions

Most ab initio quantum chemistry studies start with the single-determinant, Hartree-Fock wavefunction. This is simplest for a closed-shell system, that is, a system with an even number of electrons in a singlet (zero net spin) state which is represented by the assignment of electrons to orbitals in pairs,

$$(\psi_1)^2(\psi_2)^2 \ \ldots \ (\psi_n)^2 \tag{2.1}$$

The corresponding many-electron wavefunction is the Hartree-Fock determinant,

$$\Psi_o = \det \{(\psi_1\alpha)(\psi_1\beta)(\psi_2\alpha) \ \ldots \ (\psi_n\beta)\} \tag{2.2}$$

apart from normalization. Here $(\psi_1\alpha)$, $(\psi_1\beta)$ ... are spin orbitals or one-electron functions involving both Cartesian and spin coordinates of one electron.

In practical applications, the individual molecular orbitals, ψ_1, ψ_2, ... ψ_n are further expanded as linear combinations of basis functions,

$$\psi_i = \sum_{\mu}^{N} C_{\mu i}\, \phi_\mu \tag{2.3}$$

The basis functions ϕ_μ are prescribed as a set of functions centered at the various nuclei of the molecule and depending only on the element (i.e., only on the nuclear charge). The set of N such functions constitutes the basis set and its specification is part of the description of a theoretical model chemistry.

The expansion coefficients $C_{\mu i}$ in the molecular orbital ψ_i are initially unknown. In Hartree-Fock theory, they are determined by the variational method. This means that $C_{\mu i}$ are varied until the energy computed from the wavefunction Ψ_o,

$$\xi = \int \ldots \int \Psi_o\, H\, \Psi_o d\tau \tag{2.4}$$

is minimized. According to the variational theorem, such a computed energy must lie higher than the energy corresponding to exact solution of the Schrödinger equation

$$H\Psi = \mathcal{E}\Psi \tag{2.5}$$

It follows that the minimum value of (2.4) is the closest possible approach to the exact $\mathcal{E}$ subject to the limitations imposed by the the choice of a single-determinant wavefunction (2.2) and a limited basis set of N functions ϕ_μ.

The above technique applies only to closed-shell singlet states. If there is a resultant spin, as in radicals or triplet states, it is still usual to begin with a single-determinant Hartree-Fock wavefunction. Here there are two possibilities. The first is to take a set of molecular orbitals and populate some with two electrons and others with only one. For a triplet state with two more α and β electrons, the electron configuration would be

$$(\psi_1)^2(\psi_2)^2 \ldots (\psi_{n-1})^2(\psi_n\alpha)(\psi_{n+1}\alpha) \tag{2.6}$$

ψ_n and ψ_{n+1} being single occupied with α-electrons. If such spin orbitals are arranged inside a single determinant, we obtain a spin-restricted Hartree-Fock wavefunction (RHF). Such a wavefunction is an eigenfunction of the total spin operator and therefore represents a pure spin state (triplet in this case). The second possibility is to take a completely different set of molecular orbitals for the α and β electrons. The corresponding single-determinant wavefunction then has the form

$$\Psi = \det\{(\psi_1^\alpha\alpha)(\psi_1^\beta\beta)(\psi_2^\alpha\alpha) \ldots (\psi_n^\alpha\alpha)(\psi_{n+1}^\alpha\alpha)\} \tag{2.7}$$

where ψ_1^α, ψ_2^α ... are the α molecular orbitals and ψ_1^β, ψ_2^β ... are the β molecular orbitals. This is the spin-unrestricted Hartree-Fock wavefunction (UHF). If the α- and β-orbitals are constrained to be identical, the wavefunction (2.7) reverts to the RHF case. The general UHF function (2.7), however, is no longer necessarily an eigenfunction of the total spin operator and, in this example, may contain 'contamination' from states of other multiplicities such as quintets.

The orbitals in open-shell systems are still written as linear combinations of basis functions. For the UHF case, there will be two sets of coefficients,

$$\psi_i^\alpha = \sum_\mu^N C_{\mu i}^\alpha \phi_\mu \tag{2.8}$$

$$\psi_i^\beta = \sum_\mu^N C_{\mu i}^\beta \phi_\mu \tag{2.9}$$

Since the coefficients are determined variationally and since RHF corresponds to a constraint $C_{\mu i}^\alpha = C_{\mu i}^\beta$, it follows that the UHF energy will generally lie below the RHF value.

We next turn to the specification of basis sets. These are chosen as gaussian functions or linear combinations thereof. This permits analytic integration of the energy expression (2.4). The simplest type of basis used in molecular orbital studies is minimal and consists of one basis function for each atomic orbital in the inner and valence shells of the atoms involved. Thus there is one ϕ per hydrogen atom (1s), five ϕ's per carbon atom (1s, 2s, 2px, 2py, 2pz) and so forth. The minimal basis used in most of our studies is denoted by STO-3G and consists of linear combinations of three gaussian functions least-squares fitted to individual Slater-type atomic orbitals [1].

A minimal basis has the disadvantage that it does not allow for expansion or contraction of atomic structure in going from one molecular environment to another. This is best overcome by expansion of the basis set including two basis functions for each valence atomic orbital, retaining one for each inner shell. Such a basis is termed split-valence. The split-valence basis principally used in our work [2] is 3-21G (3 gaussians for inner shell functions, 2 for the inner parts of valence functions and 1 for the outer parts of valence functions). A corresponding 4-31G basis was used in earlier work [3] but 3-21G has been found to give comparable results at lower cost. The split valence basis has two functions for hydrogen (1s', 1s"), nine for carbon (1s, 2s', 2s", 2px', 2px", 2py', 2py", 2pz', 2pz") and so forth.

For further refinement of the basis set, functions of higher orbital angular quantum numbers have to be added to the basis set. These make better allowance for the polarization of the atomic structure and are usually referred to as polarized basis sets. The polarized basis mostly used in our work [4] is denoted by 6-31G* and consists of a split-valence 6-31G set together with a single set of second-order gaussian functions on each non-hydrogen atom. This means fifteen basis functions for each such atom. A corresponding basis denoted by 6-31G** also has polarization (p type) functions on each hydrogen atom. These larger basis sets become more expensive to use and are normally applied following preliminary studies with the smaller sets.

The other aspect of a theoretical model concerns the way that electron correlation is handled. It can be shown that the Hartree-Fock wavefunction makes some allowance for the correlation in space between electrons of parallel spin (by virtue of the antisymmetric nature of Ψ_o) but fails to take any account of the tendency of electrons of opposite spin to be kept apart by their coulomb repulsion. This can only be done by going beyond the Hartree-Fock single-determinant level of theory.

The simplest way to allow for electron correlation is by a perturbation technique originally introduced by Møller and Plesset (MP) [5]. If the correct Hamiltonian is H and H_o is a Hamiltonian for which the Hartree-Fock wavefunction is an eigenfunction, then we may introduce a Hamiltonian H_λ by

$$H_\lambda = H_o + \lambda(H-H_o) \qquad (2.10)$$

H_λ is the correct Hamiltonian if $\lambda = 1$. If $\lambda = 0$, then H_λ is identical with H_o and Ψ_o (Eq. (2.1)) would be the correct eigenfunction. The MP perturbation procedure is to expand in powers of λ, taking the expansion as far as practicable, and then put $\lambda = 1$ in the truncated series. The theory at second order (MP2) gives a simple correction for electron correlation but corrections at third and fourth orders are practical and give reasonable estimates of energy changes due to electron correlation.

A theoretical model may be designated by a compound symbol showing both the procedure used for handling electron correlation and the basis set. Thus MP2/6-31G* denotes second order Møller-Plesset theory with the polarized 6-31G* basis set. The whole set of models may be displayed on a two-dimensional chart as shown in Table 1. Improvement of basis occurs going down on such a chart, the highest level of basis approaching complete flexibility for the molecular orbitals. In conjunction with HF, this is called the Hartree-Fock limit. Each basis may be associated with various levels of perturbation theory, increasing from left to right. In principle,

Table 1. Two-Dimensional Chart of Theoretical Model Chemistries

Procedure / Basis	HF	MP2	MP3	MP4	Full
Minimal STO-3G					
Split-Valence 3-21G					
Polarized 6-31G*					
Fully Polarized 6-31G**					
Infinite					

such a series converges towards full treatment (full configuration interaction) for the particular basis. At the bottom right of such a chart, full treatment of electron correlation with an infinite basis would correspond to exact solution of the Schrödinger equation.

As the cost of computation increases rapidly as the level of theory is improved, a common practice is to use the optimized geometry obtained at one (lower) level to carry out single-point computations at another (higher) level. The notation used for this procedure is, for example:

MP3/6-31G**//HF/6-31G*

This denotes a single MP3/6-31G** point carried out at the HF/6-31* optimized geometry.

In conclusion, mention should be made of a more extended basis set (6-31G*) recently introduced for studies with correlated wavefunctions [6]. This has been used for single-point calculations with some of the ions discussed in later sections.

3. Archival Listing of Structures

The techniques described in the previous section can be used to generate structures and energies of molecular systems in a highly automated form. Once a theoretical model has been selected, the search for the stationary points on a potential surface can be carried out directly from any given initial geometry. The GAUSSIAN 80 computer program [7] is used in our work in this area.

One important feature of the program is the archival listing of structures. On completion of an optimization run, the GAUSSIAN 80 program can be modified to generate an archival entry describing the final geometry and energy. This is kept on a permanent, expanding disc file which may then be used to generate extensive tables of structures. Such tables have recently been published in the Carnegie-Mellon Quantum Chemistry Archive (CMQCA) [8].

To illustrate the use of archival structure listings, a set of cationic structures and energies is given in the Appendix to this paper. This consists of all polyatomic entries in CMQCA which use the HF/6-31G* model and have:

1) one or two atoms in the set C, N, O,

2) at least one atom of hydrogen,

3) a single positive charge.

The entries are extracted from the full archive by an automatic procedure.

Some explanation of the format used is appropriate. The table in the appendix consists of a summary table followed by a listing of the full archive entries. Each entry is identified by a sequence number. The summary table lists the following:

1) The composition of the molecule with the charge and multiplicity following in parentheses. Thus N1H2(1+,3) identifies the N_1H_2 cation which is a triplet. If the electronic state is a singlet, the multiplicity is not given. If the molecule is neutral, the charge is not given. However, this does not apply to any of the entries given here which are all single-charged cations.

2) The point group imposed as a constraint in the symmetry optimization.

3) The first 40 characters in the title identifying the nature of the species being investigated.

4) The total energy at the stationary point in hartrees.

5) The sequence number of the entry.

At the end of the summary table, the full archive entries are listed in compressed form. These contain complete specifications of the geometries at the stationary points.

To extract the geometry from the full archive entry, it should first be expanded into a more readable form. The backslash symbol '\' is used to denote the end of a line. The expanded form of entry 1728 therefore is as follows:

```
1728
CMU
FOPT
RHF
6-31G*
H2N1(1+)
DEFREES
28-MAR-1979
1

# OPT 6-31G*

NH2(1+) ... SINGLET ... GEOMETRY OPTIMIZATION ... 6-31G*

1,1
N
H,1,R
H,1,R,2,A

R = 1.02942
A = 110.00334

HF = -55.1272915
RMSD = 0.287D-08
RMSF = 0.532D-05
PG = C02V
```

This material is divided into sections, each section being terminated by a blank line. The initial section contains identifying information used for sorting purposes - the sequence number, the site of the calculation (CMU for Carnegie-Mellon University), the type of run (FOPT for full optimization), the procedure (RHF for restricted Hartree-Fock), the basis (6-31G*), the composition, the name of the person who carried out the optimization, the date and a further code number.

The next four sections constitute the input deck for the GAUSSIAN 80 program which would reproduce the optimization starting at the final geometry. This entry in the archive is therefore self-reproducing if submitted to the program. The section beginning with the '#' sign identifies the type of calculation, here OPT for optimization with the 6-31G* basis. The third section is the title card which is for description purposes only.

The fourth section specifies the molecular composition in detail. The first line of this section '1,1' gives the charge and multiplicity. The third line identifies the second nucleus as hydrogen, attached to nucleus 1 and separated from it by a distance R. The fourth line of the section identifies the third nucleus as hydrogen, again attached to nucleus 1 at the distance R and the positioned so that the angle from nucleus 3 to nucleus 1 to nucleus 2 is A. R and A are then the two variables in the optimization. Since the two NH distances are both R, the molecule is contrained to C_{2v} symmetry.

The next section gives the final values of the variables (angstroms for distances and degrees for angles). The final section gives the total energy at the stationary point (in hartrees), data specifying the degree of convergence and finally the point group.

Other entries in the table are more complex. If there are more than three nuclei, all nuclei after three have to be identified by a dihedral angle or a second bond angle as well as by the distance and first bond angle. A fourth nucleus defined by the line

H,1,R,2,A,3,B,0

implies that nucleus 4 is hydrogen, at a distance R from nucleus 1, with an angle A for 4-1-2 and a dihedral angle B for 4-1-2-3. If +1 is used as the final entry on the line, the nucleus is defined by two bond angles, 4-1-2 (A) and 4-1-3 (B) rather than by a dihedral angle.

Some entries use a 'dummy atom' X which has no charge and no basis functions but is used for ease of geometrical specification. Full details of the format can be found in the CMOCA publication [8] or in the GAUSSIAN 80 documentation [7].

4. Small Carbocations

An important set of ions that have been studied extensively by the techniques described above is that of carbocations $C_mH_n^+$. The set with m = 1,2 was originally studied by Lathan et al. [9] at the STO-3G and 4-31G levels, but since that time the structures have been refined at higher levels. To illustrate the application of the theory, we shall describe some results of a recent full investi-

gation of these ions using high-level theoretical models incorporating electron correlation [10, 11].

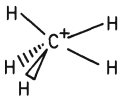

1

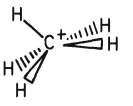

2

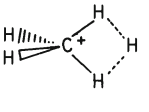

3

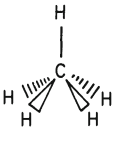

4

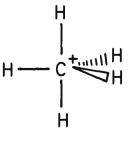

5

CH_5^+

Protonated methane has been investigated extensively by a number of authors [10]. In our recent work, we have examined the structures 1 - 5. 1 and 2 are C_S forms, 3 is a C_{2V} form corresponding to protonation of methane at the center of an edge of the tetrahedron, 4 is a square pyramid and 5 a trigonal biyramid. Geometries for all of these structures were optimized at the MP2/6-31G* level and single-point calculations were then carried out with the 6-311G** basis. The relative energies obtained in this way are listed in Table 2.

At the Hartree-Fock level the C_S structure 1 (corresponding to a three-center complex between CH_3^+ and H_2) is most stable. Structure 2 is very close, indicating nearly free rotation of the CH_3 and H_2 groups. When correlation corrections are made, the energies of 1 to 5 are compressed into a smaller range. In particular, 3 falls to only about 1 kcal/mole above 1 or 2. This close proximity has been noted previously [12] and implies a low activation barrier for interchange or 'scrambling' of the hydrogen nuclei.

The dissociation process

$$CH_5^+ \rightarrow CH_3^+ + H_2$$

is exothermic and may be compared with experimental data. At the MP4(SDQ)/6-311G**//MP2/6-31G* level, the theoretical value is 41.7

Table 2. Relative Energies (kcal/mole) of CH_5^+ Structures Using the 6-311G** Basis and MP2/6-31G* Geometries

Structure		HF	MP2	MP3	MP4(SDQ)
C_s	1	0.0	0.0	0.0	0.0
C_s	2	0.1	0.1	0.1	0.1
C_{2v}	3	3.0	0.6	0.9	1.1
C_{4v}	4	7.5	2.8	3.2	3.7
D_{3h}	5	16.4	10.8	11.2	11.7

Table 3. Structures and Energies for C_2H^+ States[a]

Electronic State	HF/6-31G*			MP3/6-31G*		
	R_{CC}	R_{CH}	ΔE	R_{CC}	R_{CH}	ΔE
$^1\Sigma^+$	1.73	1.075	105.3	1.206	1.090	67.7
$^1\Delta$	1.356	1.079	36.9[b]			
$^3\Sigma^-$	1.345	1.080	7.6	1.372	1.093	2.4
$^3\Pi$	1.253	1.074	-	1.237	1.085	-

[a]Distances in angstroms, relative energies ΔE in kcal/mole

[b]Based on complex molecular orbitals

kcal/mole. This may be compared with an experimental number of 40.0 kcal/mole [13]. However, the latter has not been corrected for zero-point vibrational energies.

The ethynyl cation C_2H^+ has been the subject of a number of theoretical studies [9, 14]. Early work with the STO-3G and 4-31G basis sets suggested that it had a triplet ground state $^3\Pi$ with three π-electrons. This is a little surprising in view of the fact that the C_2 molecule has a singlet ground state with four π-electrons. However, the multiplicity of the ground state may not be

predicted correctly at the Hartree-Fock level, since electron correlation corrections are normally larger for singlet states than for triplets.

A recent study of C_2H^+ by Krishnan, Frisch, Pople, and Schleyer has examined singlets and triplets at a higher level of theory [11]. The states studied are:

$1\sigma^2 2\sigma^2 3\sigma^2 4\sigma^2 1\pi^4$ $^1\Sigma^+$

$1\sigma^2 2\sigma^2 3\sigma^2 4\sigma^2 5\sigma^2 1\pi^2$ $^1\Delta$

$1\sigma^2 2\sigma^2 3\sigma^2 4\sigma^2 5\sigma^2 1\pi^2$ $^3\Sigma^-$

$1\sigma^2 2\sigma^2 3\sigma^2 4\sigma^2 5\sigma 1\pi^3$ $^3\Pi$

The HF/6-31G* results show the energy order to be

$$^1\Sigma^+ > {}^1\Delta > {}^3\Sigma^- > {}^3\Pi$$

the gap between $^1\Sigma^+$ and the $^3\Pi$ ground state being as large as 105 kcal/mole. For this system, geometries were optimized at the MP3/6-31G* level. This theoretical model is known to reproduce experimental geometries of neutral molecules with high precision. Results are summarized in Table 3 which gives some indication of geometry changes caused by allowance for correlation.

To test the conclusion about the multiplicity of the ground state, additional single-point calculations were carried out at the MP4(SDQ)/6-311G*//MP3/6-31G* level. The results again showed $^3\Pi$ to be the ground state with $^3\Sigma^-$ being only slightly higher (2.4 kcal/mole) and $^1\Sigma^+$ much higher (by 59.4 kcal/mole).

$C_2H_3^+$

The vinyl cation is of interest as the simplest carbocation for which classical (6) and non-classical, bridged structures (7) may be compared.

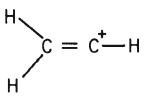

6

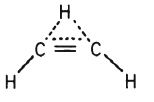

7

Early work with the STO-3G and 4-31G basis sets gave lower energies for the classical form by around 20 kcal/mole [9]. However, the introduction of d-type functions makes a major difference and at the HF/6-31G* level, the difference between 6 and 7 is reduced to 7.0 kcal/mole. Zurawski et al. [12] later found that electron cor-

Table 4. Relative Energies (kcal/mole) E(6) - E(7) for $C_2H_3^+$

Basis//Geometry	HF	MP2	MP3	MP4(SDQ)
6-31G**//HF/6-31G*	-5.4	5.2	1.9	0.6
6-311G**//MP2/6-31G*	-4.6	7.9	4.1	3.0

relation led to greater energy lowerings for the bridged structure. When such corrections were included, 7 became more stable than 6.

Table 4 reports results from a recent study in which this and other carbocations are carried to a higher level of theory [10]. Møller-Plesset studies with the 6-31G** basis produced additional stabilization of the bridged form. However, the MP2 level clearly overestimates the effect and the correlation effect is moderated at higher orders of perturbation theory. At the MP4(SDQ)/6-31G**//HF/6-31G* level, the two structures have almost identical energies. This parallels closely results of Weber et al. [15] using configuration interaction techniques and a similar basis. Further extension of the basis to 6-311G** produces a further lowering of 7 relative to 6. At the highest level of theory considered, 7 is more stable than 6 by 3.0 kcal/mole [10].

$C_2H_5^+$

The ethyl cation also has possible classical and non-classical structures. In its classical form, it may have one of the two C_s rotameric forms 8 or 9, while the bridged form 10 has C_{2v} symmetry. As with the

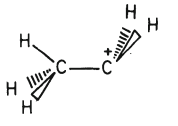

8

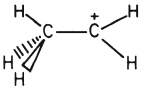

9

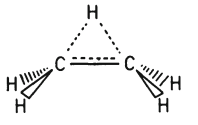

10

vinyl cation, HF/STO-3G and HF/3-21G theory predicts the classical forms to be more stable by a substantial amount. A full study including addition of d-functions reduces the gap substantially and,

at the HF/6-31G* level, 9 is more stable than 10 by only 0.8 kcal/mole. Again, addition of correlation further favors the bridged form [16]. Optimization of geometry at the MP2/6-31G* level leads to a collapse of the classical form 8 to the bridged form 10. The bridged form is then the global minimum on the potential surface and 9 is a transition structure for rearrangement.

$C_2H_7^+$

Protonated ethane is believed to have two isomeric forms. One corresponds to protonation of the CC bond and the other is a weak complex between the classical form of the ethyl cation and a hydrogen molecule. Results at the HF/6-31G* level are included in the Appendix and show that the most stable structure is the C-C protonated form with asymmetric structure of C_1 symmetry. Inclusion of electron correlation reduced the gap between the energies of the two structures. At the MP4(SDQ)/6-31G**//HF/6-31G* level, the C-C protonated form is the more stable by 6.9 kcal/mole [10]. It is of interest to note that significant binding of the $C_2H_5^+$ and H_2 fragments does not occur until correlation is included in the theory (at the MP2/6-31G* level) [10].

APPENDIX

X.TAB;2 23-OCT-1980 11:21:36.69 PAGE 1

HF/6-31G* CATION STRUCTURES AND ENERGIES
22-OCT-80 17:43:53

MOLECULE	SYMM	TITLE	ENERGY	SEQ
CH(1+)	C*V	CH (+). SINGLET. 6-31G* OPTIMIZATION.	-37.89554	6077
CHN(1+,2)	C*V	HCN+ 2-SIGMA+	-92.42077	9112
		HNC+ 2-SIGMA+ 6-31G* OPTIMIZATION	-92.46507	9111
CHO(1+)	C*V	HOC+ LINEAR 6-31G* OPTIMIZATION	-112.91439	3598
		HCO+ LINEAR 6-31G* OPTIMIZATION	-112.96592	3599
CH2N(1+)	C*V	HCNH+ LINEAR 6-31G* OPTIMIZATION	-93.15904	3600
CH2O(1+,2)	CS	HCOH+ TRANS 6-31G* OPTIMIZATION	-113.50367	9125
	C2V	FORMALDEHYDE CATION PLANAR C2V 6-31G* OP	-113.52144	9124
CH3(1+)	D3H	CH3+. D3H. 6-31G* OPTIMIZATION.	-39.23064	1087
CH3(1+,3)	C2V	CH3+ METHYL CATION TRIPLET 3B1 6-31G*	-39.09016	8435
		CH3+ METHYL CATION TRIPLET 3A2 6-31G*	-39.09095	8446
CH3N(1+,2)	CS	H2CNH+ PLANAR 6-31G* OPTIMMIZATION	-93.71748	9144
		H2N-CH+ 2-A'	-93.72539	9115
CH3O(1+)	CS	PROTONATED FORMALDEHYDE CS 6-31G* OPTIMI	-114.15643	8317
CH4(1+,2)	C3V	METHANE RADICAL CATION ... C3V ... GEOME	-39.74759	1486
	D2D	CH4+ D2D 2-B2 FLATTENED 6-31G* OPTIMIZAT	-39.75044	6624
CH4N(1+)	C2V	H2CNH2(1+) PLANAR C2V 6-31G* OPTIMIZATIO	-94.38318	8577
CH4O(1+,2)	CS	H3COH+ STAGGERED 6-31G* OPTIMIZATION	-114.68722	9145
		H2O--CH2+ TRANS 2-A'	-114.69401	9123
CH5(1+)	D3H	CH5+. 6-31G* OPTIMIZATION. D3H.	-40.36763	1084
	C4V	CH5+ C4V STRUCTURE	-40.37782	1066
	C2V	CH5+ OPTIMIZATION C2V SYMMETRY	-40.38241	1063
	CS	CH5+ OPTIMIZATION CS(II) SYMMETRY	-40.38844	1074
		CH5+. CS(I). 6-31G* OPTIMIZATION.	-40.38850	1085
CH5N(1+,2)	CS	H3N-CH2+ STAGGERED 2-A'	-94.93081	9154
		H2NCH3+ STAGGERED 6-31G* OPTIMIZATION	-94.93223	9153
CH5O(1+)	CS	PROTONATED METHANOL STAGGERED 6-31G* OPT	-115.33899	8678
CH6N(1+)	C3V	H3CNH3+ STAGGERED C3V 6-31G* OPTIMIZATIO	-95.57349	5198
C2H(1+)	C*V	CCH+ LINEAR C*V. SINGLET SIGMA (+).	-75.61775	4425
		CCH+ LINEAR C*V. SINGLET DELTA (+).	-75.70657	4521
		CCH+ LINEAR C*V. SINGLET DELTA (+). COMP	-75.72678	5826
C2H(1+,3)	C*V	CCH+ LINEAR C*V. TRIPLET SIGMA MINUS. 6-	-75.77350	8945
		CCH+ TRIPLET LINEAR C*V 6-31G* OPTIMIZAT	-75.78555	3795
C2H2(1+,2)	C2V	H2CC+ VINYLIDENE CATION 2-A1	-76.39991	9114
	D*H	HCCH+ 2-PI-U LINEAR 6-31G* OPTIMIZATION	-76.46287	9085
C2H3(1+)	C2V	BRIDGED VINYL CATION 6-31G* OPTIMIZATION	-77.07556	2887
		CLASSICAL VINYL CATION 6-31G* OPTIMIZATI	-77.08673	2885
C2H5(1+)	C2V	ETHYL CATION,BRIDGED NON-CLASSICAL 6-31G	-78.30994	3552
	CS	ETHYL-CATION,STRUCTURE II,CLASSICAL 6-31	-78.31021	3551
		ETHYL-CATION,STRUCTURE I,CLASSICAL. 6-31	-78.31123	3527
C2H7(1+)	CS	C2H7+ CS (ETHYL+H2 IN PLANE) 6-31* OPT.	-79.43918	3611
	D3D	C2H7+ D3D 6-31* OPT.	-79.45287	3585
	C2V	C2H7 (+). C2V. 6-31G* OPT.	-79.45300	7637
	CS	C2H7 (+). D3D -> CS. 6-31G* OPT.	-79.45511	4007
	C1	C2H7 (+). C1 SYMMETRY. 6-31G* OPT.	-79.45524	7732
HN(1+,2)	C*V	NH+ DOUBLET-PI 6-31G* OPTIMIZATION	-54.48706	9003
HN2(1+)	C*V	HNN+ LINEAR 6-31G* OPTIMIZATION	-109.13193	9006
HO(1+,3)	C*V	OH+ TRIPLET SIGMA- 6-31G* OPTIMIZATION	-74.96875	9004
HO2(1+)	CS	PROTONATED O2 SINGLET 6-31G* OPTIMIZATIO	-149.73403	9007

```
X.TAB;2                    23-OCT-1980 11:21:36.69          PAGE 2

H2N(1+)      C2V   NH2(1+) ... SINGLET ... GEOMETRY OPTIMIZ    -55.12729  1728

H2N(1+,3)    C2V   NH2(1+) ... TRIPLET ... GEOMETRY OPTIMIZ    -55.20852  1729

H2NO(1+)     CS    HNOH+ O-PROTONATED HNOH C(S) 6-31G* OPT    -130.04016  8796
             C2V   H2NO+ C2V 6-31G* OPTIMIZATION              -130.06412  8824
             CS    N-PROTONATED HNO (H2NO)+ C(S) HF/6-31G*    -130.06412  8853

H2N2(1+,2)   C2H   HN=NH+ TRANS 2-AG                          -109.67241  9116
             C2V   H2N-N+ PLANAR 2-B2                         -109.69694  9117

H2O2(1+,2)   C2V   H2OO+ PLANAR C2V 2-B1                      -150.39991  9118
             C2H   HOOH+ TRANS 6-31G* OPTIMIZATION            -150.41175  9113

H3N(1+,2)    D3H   PLANAR AMMONIA CATION OPTIMIZATION 6-31G    -55.87324  8997

H3N2(1+)     CS    H2NNH+ PLANAR CS 6-31G* OPTIMIZATION       -110.30594  9064

H3O(1+)      D3H   HYDRONIUM ION PLANAR D3H 6-31G* OPTIMIZA    -76.28656  3437
             C3V   HYDRONIUM ION 6-31G* OPTIMIZATION          -76.28934  2880

H3O2(1+)     CS    H2OOH+ TRANS 6-31G* OPTIMIZATION           -151.03296  9050

H4N(1+)      TD    AMMONIUM ION 6-31G* OPTIMIZATION            -56.53077  2879

H4NO(1+)     CS    O-PROTONATED HYDROXYLAMINE C(S) HF/6-31G   -131.26158  9041
                   N-PROTONATED HYDROXYLAMINE 6-31G* OPTIMI   -131.30677  9043

H5N2(1+)     CS    PROTONATED HYDRAZINE STAGGERED 6-31G* OP   -111.51833  9047
                   ------------------------

 FULL ENTRIES.
 -------------

1063\CMU\FOPT\RHF\6-31G*\C1H5(1+)\POPLE\21-DEC-1978\1\\#P RHF/6-31G* OPT\\CH5+ OPTIMIZATION C2V SYMMETRY\\1,1\C\H,1,CH1\H,1,CH2,2,A1\H,1,CH2,2,A1,3,180.,0\H,1,CH4,2,A2,3,90.,0\H,1,CH4,2,A2,3,-90.,0\\CH1=1.14957\CH2=1.12719\CH4=1.0804\A1=61.4677\A2=119.37981\\HF=-40.3824061\RMSD=0.265D-08\RMSF=0.431D-03\PG=C02V\\

1066\CMU\FOPT\RHF\6-31G*\C1H5(1+)\POPLE\22-DEC-1978\1\\#P RHF/6-31G* OPT\\CH5+ C4V STRUCTURE\\1,1\C\H,1,CH1\H,1,CH2,2,HCH\H,1,CH2,2,HCH,3,90.,0\H,1,CH2,2,HCH,4,90.,0\H,1,CH2,2,HCH,5,90.,0\\CH1=1.07547\CH2=1.11497\HCH=115.12458\HF=-40.3778214\RMSD=0.450D-07\RMSF=0.236D-03\PG=C04V\\

1074\CMU\FOPT\RHF\6-31G*\C1H5(1+)\POPLE\23-DEC-1978\1\\#P RHF/6-31G* OPT\\CH5+ OPTIMIZATION CS(II) SYMMETRY\\1,1\C\X,1,1.,\H,1,CH1,2,A1\H,1,CH2,2,A2,3,PH,0\H,1,CH2,2,A2,3,-PH,0\H,1,CH4,2,A3,3,90.,0\H,1,CH4,2,A3,3,-90.,0\\CH1=1.07726\CH2=1.08554\CH4=1.22956\A1=107.57838\A2=104.22672\A3=20.27664\PH=122.98991\\HF=-40.3884408\RMSD=0.779D-08\RMSF=0.922D-03\PG=CS\\

1084\CMU\FOPT\RHF\6-31G*\C1H5(1+)\KRISHNAN\24-DEC-1978\1\\#P OPT 6-31G* NOPOP\\CH5+. 6-31G* OPTIMIZATION. D3H.\\1,1\C\H,1,R1\H,1,R1,2,120.\H,1,R1,2,120.,3,180.,0\H,1,R2,2,90.,3,90.,0\H,1,R2,2,90.,3,-90.,0\\R1=1.10191\R2=1.11605\\HF=-40.3676348\RMSD=0.221D-08\RMSF=0.208D-03\PG=D03H\\

1085\CMU\FOPT\RHF\6-31G*\C1H5(1+)\KRISHNAN\24-DEC-1978\1\\#P OPT 6-31G* NOPOP\\CH5+. CS(I). 6-31G* OPTIMIZATION.\\1,1\C\H,1,R1\H,1,R2,2,THETA1\H,1,R3,2,THETA2,3,180.,0\X,1,1.,4,THETA3,2,180.,0\H,1,R4,5,THETA4,4,90.,0\H,1,R4,5,THETA4,4,-90.,0\\R1=1.22832\R2=1.22805\R3=1.08906\R4=1.07964\THETA1=40.63043\THETA2=82.45701\THETA3=133.71537\THETA4=58.76755\\HF=-40.3885022\RMSD=0.144D-07\RMSF=0.146D-02\PG=CS\\

1087\CMU\FOPT\RHF\6-31G*\C1H3(1+)\KRISHNAN\24-DEC-1978\1\\#P OPT 6-31G* NOPOP\\CH3+. D3H. 6-31G* OPTIMIZATION.\\1,1\C\H,1,R1\H,1,R1,2,120.\H,1,R1,2,120.,3,180.,0\\R1=1.07837\\HF=-39.2306399\RMSD=0.737D-07\RMSF=0.451D-04\PG=D03H\\

1486\CMU\FOPT\UHF\6-31G*\C1H4(1+,2)\DEFREES\22-FEB-1979\1\\# OPT 6-31G*\\METHANE RADICAL CATION ... C3V ... GEOMETRY OPTIMIZATION ... 6-31G*\\1,2\C\H,1,A\H,1,B,2,HAH\H,1,B,2,HAH,3,120.,0\H,1,B,2,HAH,3,240.,0\\A=1.39403\B=1.08194\HAH=95.3959\\HF=-39.7475863\S2=0.757\RMSD=0.118D-07\RMSF=0.158D-04\PG=C03V\\

1728\CMU\FOPT\RHF\6-31G*\H2N1(1+)\DEFREES\28-MAR-1979\1\\# OPT 6-31G*\\NH2(1+) ... SINGLET ... GEOMETRY OPTIMIZATION ... 6-31G*\\1,1\N\H,1,R\H,1,R,2,A\\R=1.02942\A=110.00334\\HF=-55.1272915\RMSD=0.287D-08\RMSF=0.532D-05\PG=C02V\\

1729\CMU\FOPT\UHF\6-31G*\H2N1(1+,3)\DEFREES\28-MAR-1979\1\\# OPT 6-31G*\\NH2(1+) ... TRIPLET ... GEOMETRY OPTIMIZATION ... 6-31G*\\1,3\N\H,1,R\H,1,R,2,A\\R=1.02083\A=151.30675\\HF=-55.2085224\S2=2.022\RMSD=0.881D-07\RMSF=0.10
```

X.TAB;2 23-OCT-1980 11:21:36.69 PAGE 3

6D-02\PG=C02V\\

2879\CMU\FOPT\RHF\6-31G*\H4N1(1+)\POPLE\16-MAY-1979\1\\# RHF/6-31G* OPT\\AM
MONIUM ION 6-31G* OPTIMIZATION\\1,1\N\H,1,R\H,1,R,2,109.471\H,1,R,2,109.471
,3,120.,0\H,1,R,2,109.471,3,-120.,0\\R=1.01345\\HF=-56.5307714\RMSD=0.130D-
08\RMSF=0.118D-04\PG=TD\\

2880\CMU\FOPT\RHF\6-31G*\H3O1(1+)\POPLE\16-MAY-1979\1\\# RHF/6-31G* OPT\\HY
DRONIUM ION 6-31G* OPTIMIZATION\\1,1\O\H,1,R\H,1,R,2,A\H,1,R,2,A,3,A,1\\R=0
.96885\A=113.08513\\HF=-76.2893384\RMSD=0.325D-07\RMSF=0.708D-04\PG=C03V\\

2885\CMU\FOPT\RHF\6-31G*\C2H3(1+)\POPLE\17-MAY-1979\1\\# RHF/6-31G* OPT\\CL
ASSICAL VINYL CATION 6-31G* OPTIMIZATION\\1,1\C\C,1,CC\X,1,1.,2,90.,\H,1,CH1
,3,90.,2,180.,0\H,2,CH2,1,HCC,3,180.,0\H,2,CH2,1,HCC,3,0.,0\\CC=1.26224\CH1
=1.07237\CH2=1.08531\HCC=120.02814\\HF=-77.0867339\RMSD=0.604D-07\RMSF=0.13
5D-03\PG=C02V\\

2887\CMU\FOPT\RHF\6-31G*\C2H3(1+)\POPLE\17-MAY-1979\1\\# RHF/6-31G* OPT\\BR
IDGED VINYL CATION 6-31G* OPTIMIZATION\\1,1\X\C,1,HALFCC\H,1,HC12,2,90.\C,1
,HALFCC,3,90.,2,180.,0\H,2,CH,4,HCC,3,180.,0\H,4,CH,2,HCC,3,180.,0\\HALFCC=
0.60346\HC12=1.11738\CH=1.07071\HCC=179.12107\\HF=-77.0755599\RMSD=0.425D-0
7\RMSF=0.124D-03\PG=C02V\\

3437\CMU\FOPT\RHF\6-31G*\H3O1(1+)\POPLE\2-JUN-1979\1\\# RHF/6-31G* OPT\\HYD
RONIUM ION PLANAR D3H 6-31G* OPTIMIZATION\\1,1\O\H,1,R\H,1,R,2,120.\H,1,R,2
,120.,3,120.,1\\R=0.96513\\HF=-76.286564\RMSD=0.393D-08\RMSF=0.773D-05\PG=D
03H\\

3527\CMU\FOPT\RHF\6-31G*\C2H5(1+)\KRISHNAN\6-JUN-1979\1\\# OPT 6-31G* NOPOP
\\ETHYL-CATION,STRUCTURE I,CLASSICAL. 6-31G* OPTIMIZATION.\\1,1\C\C,1,RCC\H
,1,RCH3,2,AH3CC\X,2,1.,1,X4CC,3,0.,0\H,2,RC2H,4,HC2X,1,90.,0\H,2,RC2H,4,HC2
X,1,-90.,0\X,1,1.,2,X7CC,4,180.,0\H,1,RC1H,7,HC1X,2,90.,0\H,1,RC1H,7,HC1X,2
,-90.,0\\RCC=1.43229\RCH3=1.11528\RC2H=1.0786\RC1H=1.08139\AH3CC=98.17827\X
4CC=175.97123\HC2X=58.47634\X7CC=140.60556\HC1X=57.31744\\HF=-78.3112266\RM
SD=0.151D-07\RMSF=0.133D-02\PG=CS\\

3551\CMU\FOPT\RHF\6-31G*\C2H5(1+)\KRISHNAN\6-JUN-1979\1\\# OPT 6-31G* NOPOP
\\ETHYL-CATION,STRUCTURE II,CLASSICAL 6-31G* OPTIMIZATION.\\1,1\C\C,1,RCC\H
,1,RCH3,2,H3CC\H,2,RC2H4,1,H4CC,3,0.,0\H,2,RC2H5,1,H5CC,3,180.,0\X,1,1.,2,X
6CC,4,180.,0\H,1,RC1H,6,HC1X,2,90.,0\H,1,RC1H,6,HC1X,2,-90.,0\\RCC=1.44071\
RCH3=1.07761\RC2H4=1.07884\RC2H5=1.07857\RC1H=1.09686\H3CC=114.8837\H4CC=12
2.80469\H5CC=120.37154\X6CC=118.64326\HC1X=51.38684\\HF=-78.3102088\RMSD=0.
767D-07\RMSF=0.558D-03\PG=CS\\

3552\CMU\FOPT\RHF\6-31G*\C2H5(1+)\KRISHNAN\6-JUN-1979\1\\# OPT 6-31G* NOPOP
\\ETHYL CATION,BRIDGED NON-CLASSICAL 6-31G* OPTIMIZATION.\\1,1\X\C,1,RXC\X,
2,1.,1,XCX\H,2,RCH,3,HCX,1,90.,0\H,2,RCH,3,HCX,1,-90.,0\H,1,RXH,2,90.,3,180
.,0\C,1,RXC,6,90.,2,180.,0\X,7,1.,1,XCX,6,180.,0\H,7,RCH,8,HCX,1,90.,0\H,7,
RCH,8,HCX,1,-90.,0\\RXC=0.60588\RCH=1.07668\RXH=1.11255\XCX=178.32329\HCX=5
9.2867\\HF=-78.3099429\RMSD=0.813D-07\RMSF=0.232D-03\PG=C02V\\

3585\CMU\FOPT\RHF\6-31G*\C2H7(1+)\KRISHNAN\8-JUN-1979\1\\# OPT RHF 6-31G* N
OPOP\\C2H7+ D3D 6-31* OPT.\\1,1\H\X,1,1.\C,1,R1,2,90.\C,1,R1,2,90.,3,180.,0
\H,3,R2,1,THETA1,2,0.,0\H,3,R2,1,THETA1,5,120.,0\H,3,R2,1,THETA1,5,-120.,0\
H,4,R2,1,THETA1,2,180.,0\H,4,R2,1,THETA1,8,120.,0\H,4,R2,1,THETA1,8,-120.,0
\\R1=1.24119\R2=1.0763\THETA1=101.23431\\HF=-79.4528739\RMSD=0.516D-07\RMSF
=0.466D-04\PG=D03D\\

3598\CMU\FOPT\RHF\6-31G*\C1H1O1(1+)\POPLE\9-JUN-1979\1\\# 6-31G* OPT\\HOC+
LINEAR 6-31G* OPTIMIZATION\\1,1\O\C,1,CO\X,1,1.,2,90.\H,1,OH,3,90.,2,180.,0
\\CO=1.14149\OH=0.98066\\HF=-112.9143934\RMSD=0.173D-07\RMSF=0.520D-03\PG=C
*V\\

3599\CMU\FOPT\RHF\6-31G*\C1H1O1(1+)\POPLE\9-JUN-1979\1\\# 6-31G* OPT\\HCO+
LINEAR 6-31G* OPTIMIZATION\\1,1\C\O,1,CO\X,1,1.,2,90.\H,1,CH,3,90.,2,180.,0
\\CO=1.08696\CH=1.08609\\HF=-112.9659192\RMSD=0.314D-08\RMSF=0.970D-04\PG=C
*V\\

3600\CMU\FOPT\RHF\6-31G*\C1H2N1(1+)\POPLE\9-JUN-1979\1\\# 6-31G* OPT\\HCNH+
 LINEAR 6-31G* OPTIMIZATION\\1,1\C\N,1,CN\X,1,1.,2,90.\H,1,CH,3,90.,2,180.,
0\X,2,1.,1,90.,3,180.,0\H,2,NH,5,90.,1,180.,0\\CN=1.11734\CH=1.07343\NH=1.0
0385\\HF=-93.1590423\RMSD=0.259D-07\RMSF=0.140D-03\PG=C*V\\

3611\CMU\FOPT\RHF\6-31G*\C2H7(1+)\KRISHNAN\9-JUN-1979\1\\# OPT RHF 6-31G* N
OPOP\\C2H7+ CS (ETHYL+H2 IN PLANE) 6-31* OPT.\\1,1\C\C,1,R1\H,1,R2,2,THETA1
\X,1,1.,3,THETA2,2,180.,0\H,1,R3,4,THETA3,2,90.,0\H,1,R3,4,THETA3,2,-90.,0\
X,2,1.,1,THETA4,3,0.,0\H,2,R4,7,THETA5,1,90.,0\H,2,R4,7,THETA5,1,-90.,0\H,2
,R5,1,THETA6,3,180.,0\H,10,R6,2,THETA7,1,180.,0\\R1=1.43439\R2=1.11439\R3=1
.08103\R4=1.0781\R5=2.67591\R6=0.73279\THETA1=97.99406\THETA2=121.31945\THE
TA3=57.27267\THETA4=174.85535\THETA5=58.48697\THETA6=98.6033\THETA7=86.7833
2\\HF=-79.4391832\RMSD=0.618D-07\RMSF=0.309D-03\PG=CS\\

X.TAB;2 23-OCT-1980 11:21:36.69 PAGE 4

3795\CMU\FOPT\UHF\6-31G*\C2H1(1+,3)\KRISHNAN\25-JUN-1979\1\\# 6-31G* OPT SC
FCYC=64 NOPOP\\CCH+ TRIPLET LINEAR C*V 6-31G* OPTIMIZATION\\1,3\C\C,1,CC\X,
2,1.,1,90.,H,2,CH,3,90.,1,180.,0\\CC=1.25265\CH=1.07355\\HF=-75.7855508\S2=
2.237\RMSD=0.629D-07\RMSF=0.327D-03\PG=C*V\\

4007\CMU\FOPT\RHF\6-31G*\C2H7(1+)\KRISHNAN\18-JUL-1979\1\\# OPT 6-31G* NOPO
P\\C2H7 (+). D3D -> CS. 6-31G* OPT.\\1,1\H\C,1,R1\C,1,R2,2,THETA1\H,2,R3,3,
THETA2,1,0.,0\H,2,R4,5,THETA3,1,180.,0\H,2,R4,5,THETA4,1,90.,0\H,2,R4,5,THE
TA4,1,-90.,0\H,3,R5,2,THETA5,1,180.,0\H,3,R6,2,THETA6,1,0.,0\H,3,R6,9,THETA
7,1,90.,0\H,3,R6,9,THETA7,1,-90.,0\\R1=1.24062\R2=1.23799\R3=1.08079\R4=1.0
7432\R5=1.07279\R6=1.07814\THETA1=123.15114\THETA2=119.93557\THETA3=98.0144
1\THETA4=58.08672\THETA5=85.78285\THETA6=132.50296\THETA7=57.85226\\HF=-79.
4551087\RMSD=0.215D-07\RMSF=0.174D-03\PG=CS\\

4425\CMU\FOPT\RHF\6-31G*\C2H1(1+)\KRISHNAN\25-AUG-1979\1\\# OPT RHF 6-31G*\
\CCH+ LINEAR C*V. SINGLET SIGMA (+).\\1,1\C\C,1,CC\-,2,1.,1,90.\H,2,CH,3,90
.,1,180.,0\\CC=1.17337\CH=1.07498\\HF=-75.6177549\RMSD=0.496D-07\RMSF=0.477
D-05\PG=C*V\\

4521\CMU\FOPT\RHF\6-31G*\C2H1(1+)\KRISHNAN\29-AUG-1979\3\\# OPT RHF 6-31G*
ALTER\\CCH+ LINEAR C*V. SINGLET DELTA (+).\\1,1\C\C,1,CC\-,2,1.,1,90.\H,2,C
H,3,90.,1,180.,0\\CC=1.35631\CH=1.07946\\6 7\\HF=-75.7065703\RMSD=0.366D-08
\RMSF=0.414D-04\PG=C*V\\

5198\CMU\FOPT\RHF\6-31G*\C1H6N1(1+)\POPLE\24-SEP-1979\1\\# 6-31G* OPT\\H3CN
H3+ STAGGERED C3V 6-31G* OPTIMIZATION\\1,1\C\N,1,CN\H,1,CH,2,HCN\H,1,CH,2,H
CN,3,120.,0\H,1,CH,2,HCN,3,-120.,0\H,2,NH,1,HNC,3,180.,0\H,2,NH,1,HNC,3,60.
,0\H,2,NH,1,HNC,3,-60.,0\\CN=1.50749\CH=1.07806\NH=1.0115\HCN=108.13934\HNC
=111.58892\\HF=-95.5734912\RMSD=0.642D-07\RMSF=0.503D-05\PG=C03V\\

5826\CMU\FOPT\RHF\6-31G*\C2H1(1+)\KRISHNAN\12-SEP-1979\3\\# OPT=FP RHF COMP
LEX 6-31G* ALTER\\CCH+ LINEAR C*V. SINGLET DELTA (+). COMPLEX.\\1,1\C\C,1,C
C\-,2,1.,1,90.\H,2,CH,3,90.,1,180.,0\\CC=1.35167\CH=1.07919\\5 7\\HF=-75.72
6776\S2=0.\RMSD=0.982D-07\RMSF=0.126D-03\PG=C*V\\

6077\CMU\FOPT\RHF\6-31G*\C1H1(1+)\POPLE\2-DEC-1979\1\\# OPT 6-31G* NOPOP\\C
H (+). SINGLET. 6-31G* OPTIMIZATION.\\1,1\C\H,1,CH\\CH=1.10453\\HF=-37.8955
373\RMSD=0.604D-09\RMSF=0.135D-04\PG=C*V\\

6624\CMU\FOPT\UHF\6-31G*\C1H4(1+,2)\POPLE\1-JAN-1980\1\\# 6-31G* OPT\\CH4+
D2D 2-B2 FLATTENED 6-31G* OPTIMIZATION\\1,2\C\X,1,1.\X,1,1.,2,90.\X,1,1.,3,
90.,2,180.,0\H,1,CH,2,HCX,3,180.,0\H,1,CH,2,HCX,3,0.,0\H,1,CH,4,HCX,3,90.,0
\H,1,CH,4,HCX,3,-90.,0\\CH=1.11113\HCX=69.94767\\HF=-39.7504353\S2=0.754\RM
SD=0.114D-07\RMSF=0.231D-04\PG=D02D\\

7637\CMU\FOPT\RHF\6-31G*\C2H7(1+)\KRISHNAN\25-MAR-1980\1\\# OPT 6-31G* NOPO
P\\C2H7 (+). C2V. 6-31G* OPT.\\1,1\X\H,1,HQ\C,1,CQ,2,90.\C,1,CQ,2,90.,3,180
.,0\H,3,H1C,1,H1CQ,2,180.,0\H,4,H1C,1,H1CQ,2,180.,0\X,3,1.,1,QCQ,5,180.,0\H
,3,H2C,7,H2CQ,2,90.,0\H,3,H2C,7,H2CQ,2,-90.,0\X,4,1.,1,QCQ,6,180.,0\H,4,H2C
,10,H2CQ,2,90.,0\H,4,H2C,10,H2CQ,2,-90.,0\\HQ=0.45607\CQ=1.15615\H1C=1.0726
3\H1CQ=89.17873\QCQ=126.87781\H2C=1.07758\H2CQ=57.96283\\HF=-79.4529964\RMS
D=0.170D-08\RMSF=0.115D-05\PG=C02V\\

7732\CMU\FOPT\RHF\6-31G*\C2H7(1+)\KRISHNAN\5-APR-1980\1\\# OPT=READFC RHF 6
-31G* NOPOP SAVE=FC\\C2H7 (+). C1 SYMMETRY. 6-31G* OPT.\\1,1\H\C,1,R1\C,1,R
2,2,THETA1\H,2,R3,1,THETA2,3,DIH1,0\H,2,R4,1,THETA3,4,DIH2,0\H,2,R5,1,THETA
4,4,DIH3,0\H,3,R6,1,THETA5,2,DIH4,0\H,3,R7,1,THETA6,7,DIH5,0\H,3,R8,1,THETA
7,7,DIH6,0\\R1=1.23931\R2=1.23921\R3=1.08045\R4=1.07557\R5=1.07335\R6=1.073
33\R7=1.08042\R8=1.07557\THETA1=121.70221\THETA2=92.49101\THETA3=103.96907\
THETA4=112.40178\THETA5=112.4211\THETA6=92.5109\THETA7=103.94186\DIH1=155.0
3725\DIH2=116.64146\DIH3=-117.40724\DIH4=37.47205\DIH5=117.41764\DIH6=-125.
93482\\HF=-79.455238\RMSD=0.539D-07\RMSF=0.567D-05\PG=C01\\

8317\CMU\FOPT\RHF\6-31G*\C1H3O1(1+)\DELBENE\20-JUN-1980\1\\# 6-31G* OPT\\PR
OTONATED FORMALDEHYDE CS 6-31G* OPTIMIZATION\\1,1\C\O,1,CO\H,1,CH0,2,H0CO\H
,1,CH3,2,H3CO,3,180.,0\H,2,OH,1,HOC,3,0.,0\\CO=1.23203\CH0=1.07897\H0CO=121
.67771\CH3=1.07631\H3CO=116.18618\OH=0.96475\HOC=117.42783\\HF=-114.1564259
\RMSD=0.286D-07\RMSF=0.124D-03\PG=CS\\

8435\CMU\FOPT\UHF\6-31G*\C1H3(1+,3)\POPLE\26-JUL-1980\1\\# 6-31G* OPT\\CH3+
 METHYL CATION TRIPLET 3B1 6-31G*\\1,3\C\H,1,CH1\H,1,CH2,2,HCH\H,1,CH2,2,HC
H,3,180.,0\\CH1=1.30456\CH2=1.08414\HCH=99.24457\\HF=-39.0901624\S2=2.018\R
MSD=0.278D-07\RMSF=0.566D-04\PG=C02V\\

8446\CMU\FOPT\UHF\6-31G*\C1H3(1+,3)\POPLE\26-JUL-1980\1\\# 6-31G* OPT\\CH3+
 METHYL CATION TRIPLET 3A2 6-31G*\\1,3\C\H,1,CH1\H,1,CH2,2,HCH\H,1,CH2,2,HC
H,3,180.,0\\CH1=1.0742\CH2=1.15678\HCH=141.9762\\HF=-39.0909493\S2=2.016\RM
SD=0.514D-07\RMSF=0.404D-04\PG=C02V\\

8577\CMU\FOPT\RHF\6-31G*\C1H4N1(1+)\DELBENE\20-AUG-1980\1\\# HF/6-31G* OPT\

X.TAB;2 23-OCT-1980 11:21:36.69 PAGE 5

\H2CNH2(1+) PLANAR C2V 6-31G* OPTIMIZATION\\1,1\C\N,1,CN\H,1,CH,2,HCN\H,1,CH,2,HCN,3,180.,0\H,2,NH,1,HNC,3,0.,0\H,2,NH,1,HNC,3,180.,0\\CN=1.26326\CH=1.07463\HCN=119.85455\NH=1.00561\HNC=121.85121\\HF=-94.3831772\RMSD=0.998D-08\RMSF=0.876D-04\PG=C02V\\

8678\CMU\FOPT\RHF\6-31G*\C1H5O1(1+)\DELBENE\26-AUG-1980\1\\# 6-31G* OPT\\PROTONATED METHANOL STAGGERED 6-31G* OPTIMIZATION\\1,1\C\O,1,AB\H,1,AH3,2,H3AB\X,2,1.,1,ABH78,3,0.,0\H,2,BH7,4,H7BH8,1,90.,0\H,2,BH7,4,H7BH8,1,-90.,0\X,1,1.,2,BAH12,3,180.,0\H,1,AH1,7,H1AH2,2,90.,0\H,1,AH1,7,H1AH2,2,-90.,0\\AB=1.51112\AH1=1.07475\AH3=1.07568\BH7=0.96227\BAH12=116.37474\H3AB=107.68555\ABH78=141.31261\H1AH2=56.07901\H7BH8=55.34452\\HF=-115.3389926\RMSD=0.812D-08\RMSF=0.307D-04\PG=CS\\

8796\CMU\FOPT\RHF\6-31G*\H2N1O1(1+)\DELBENE\7-SEP-1980\1\\# HF/6-31G* OPT SCFCYC=100\\HNOH+ O-PROTONATED HNOH C(S) 6-31G* OPT\\1,1\N\O,1,NO\H,1,NH,2,OHN\H,2,OH,1,NOH,3,180.,0\\NO=1.19879\NH=1.02417\OHN=106.92404\OH=0.97751\NOH=111.31997\\HF=-130.040157\RMSD=0.233D-07\RMSF=0.109D-03\PG=CS\\

8824\CMU\FOPT\RHF\6-31G*\H2N1O1(1+)\DELBENE\8-SEP-1980\1\\# OPT,RHF/6-31G*\\H2NO+ C2V 6-31G* OPTIMIZATION\\1,1\N\O,1,AB\H,1,AH,2,HAB\H,1,AH,2,HAB,3,180.,0\\AB=1.14891\AH=1.02385\HAB=119.64853\\HF=-130.0641201\RMSD=0.621D-07\RMSF=0.139D-04\PG=C02V\\

8853\CMU\FOPT\RHF\6-31G*\H2N1O1(1+)\DELBENE\9-SEP-1980\1\\# HF/6-31G* OPT\\N-PROTONATED HNO (H2NO)+ C(S) HF/6-31G* OPT\\1,1\N\O,1,NO\X,1,1.,2,90.\X,1,1.,3,X3NX4,2,180.,0\H,1,NH,4,NHAF,2,90.,0\H,1,NH,4,NHAF,2,-90.,0\\NO=1.14898\X3NX4=90.00758\NH=1.02386\NHAF=60.34116\\HF=-130.0641201\RMSD=0.334D-07\RMSF=0.553D-04\PG=CS\\

8945\CMU\FOPT\UHF\6-31G*\C2H1(1+,3)\KRISHNAN\16-SEP-1980\1\\# OPT HF 6-31G* NOPOP SCFCYC=100\\CCH+ LINEAR C*V, TRIPLET SIGMA MINUS, 6-31G* OPT.\\1,3\C\C,1,CC\X,2,1.,1,90.\H,2,CH,3,90.,1,180.,0\\CC=1.34494\CH=1.08016\\HF=-75.7735036\S2=2.015\RMSD=0.807D-07\RMSF=0.133D-04\PG=C*V\\

8997\CMU\FOPT\UHF\6-31G*\H3N1(1+,2)\POPLE\26-SEP-1980\1\\# HF 6-31G* OPT\\PLANAR AMMONIA CATION OPTIMIZATION 6-31G*\\1,2\N\H,1,RNH\H,1,RNH,2,120.\H,1,RNH,2,120.,3,180.,0\\RNH=1.01242\\HF=-55.8732355\S2=0.76\RMSD=0.814D-07\RMSF=0.502D-05\PG=D03H\\

9003\CMU\FOPT\UHF\6-31G*\H1N1(1+,2)\POPLE\27-SEP-1980\1\\# 6-31G* OPT\\NH+ DOUBLET-PI 6-31G* OPTIMIZATION\\1,2\N\H,1,R\\R=1.04489\\HF=-54.4870623\S2=0.756\RMSD=0.230D-07\RMSF=0.150D-03\PG=C*V\\

9004\CMU\FOPT\UHF\6-31G*\H1O1(1+,3)\POPLE\27-SEP-1980\1\\# 6-31G* OPT\\OH+ TRIPLET SIGMA- 6-31G* OPTIMIZATION\\1,3\O\H,1,R\\R=1.01329\\HF=-74.9687493\S2=2.013\RMSD=0.734D-07\RMSF=0.358D-05\PG=C*V\\

9006\CMU\FOPT\RHF\6-31G*\H1N2(1+)\POPLE\27-SEP-1980\1\\# 6-31G* OPT\\HNN+ LINEAR 6-31G* OPTIMIZATION\\1,1\N\N,1,NN\X,1,1.,2,90.\H,1,NH,3,90.,2,180.,0\\NN=1.07083\NH=1.0255\\HF=-109.1319301\RMSD=0.406D-08\RMSF=0.143D-03\PG=C*V\\

9007\CMU\FOPT\RHF\6-31G*\H1O2(1+)\POPLE\27-SEP-1980\1\\#P 6-31G* SCFCYC=64 OPT\\PROTONATED O2 SINGLET 6-31G* OPTIMIZATION\\1,1\O\O,1,OO\H,1,OH,2,OOH\\OO=1.15986\OH=0.9953\OOH=111.49272\\HF=-149.7340294\RMSD=0.695D-07\RMSF=0.162D-03\PG=CS\\

9041\CMU\FOPT\RHF\6-31G*\H4N1O1(1+)\DELBENE\29-SEP-1980\1\\# OPT HF/6-31G*\\O-PROTONATED HYDROXYLAMINE C(S) HF/6-31G*\\1,1\N\O,1,NO\X,1,1.,2,ANB1\H,1,NH,3,ANHAF,2,90.,0\H,1,NH,3,ANHAF,2,-90.,0\X,2,1.,1,AOB1,3,180.,0\H,2,OH,6,HOHAF,1,90.,0\H,2,OH,6,HOHAF,1,-90.,0\\NO=1.49044\ANB1=108.26445\NH=1.00842\ANHAF=53.38461\AOB1=122.91862\OH=0.96673\HOHAF=53.76915\\HF=-131.2615754\RMSD=0.518D-07\RMSF=0.625D-04\PG=CS\\

9043\CMU\FOPT\RHF\6-31G*\H4N1O1(1+)\DELBENE\29-SEP-1980\1\\# OPT,RHF/6-31G*\\N-PROTONATED HYDROXYLAMINE 6-31G* OPTIMIZATION\\1,1\N\O,1,AB\H,1,AH3,2,H3AB\H,2,BH9,1,H9BA,3,180.,0\X,1,1.,2,BAH12,3,180.,0\H,1,AH1,5,H1AH2,2,90.,0\H,1,AH1,5,H1AH2,2,-90.,0\\AB=1.37393\AH1=1.01406\AH3=1.01328\BH9=0.9577\H1AH2=55.30568\BAH12=130.99794\H3AB=105.12305\H9BA=108.67214\\HF=-131.3067703\RMSD=0.182D-07\RMSF=0.429D-04\PG=CS\\

9047\CMU\FOPT\RHF\6-31G*\H5N2(1+)\DELBENE\29-SEP-1980\1\\# HF/6-31G* OPT\\PROTONATED HYDRAZINE STAGGERED 6-31G* OPTIMIZATION\\1,1\N\N,1,AB\H,1,AH3,2,H3AB\X,2,1.,1,ABH78,3,0.,0\H,2,BH7,4,H7BH8,1,90.,0\H,2,BH7,4,H7BH8,1,-90.,0\X,1,1.,2,BAH12,3,180.,0\H,1,AH1,7,H1AH2,2,90.,0\H,1,AH1,7,H1AH2,2,-90.,0\\AB=1.42824\AH1=1.01227\AH3=1.01441\BH7=1.00306\BAH12=121.80754\H3AB=115.96737\ABH78=123.72129\H1AH2=53.19545\H7BH8=54.84066\\HF=-111.5183302\RMSD=0.706D-07\RMSF=0.620D-04\PG=CS\\

9050\CMU\FOPT\RHF\6-31G*\H3O2(1+)\DELBENE\30-SEP-1980\1\\# HF/6-31G* OPT\\H2OOH+ TRANS 6-31G* OPTIMIZATION\\1,1\O\O,1,AB\X,1,1.,2,BAH12\H,1,AH1,3,QH1A

```
X.TAB;2                    23-OCT-1980 11:21:36.69          PAGE 6

H2,2,90.,,0\H,1,AH1,3,QH1AH2,2,-90.,,0\H,2,BH6,1,ABH6,3,180.,,0\\AB=1.41005\AH
1=0.97083\BH6=0.96493\BAH12=122.38601\ABH6=101.28629\QH1AH2=55.69817\\HF=-1
51.032957\RMSD=0.522D-08\RMSF=0.332D-04\PG=CS\\

9064\CMU\FOPT\RHF\6-31G*\H3N2(1+)\DELBENE\5-OCT-1980\1\\# HF/6-31G* OPT\\H2
NNH+ PLANAR CS 6-31G* OPTIMIZATION\\1,1\N\N,1,NN\H,1,NH0,2,HONN\H,1,NH3,2,H
3NN,3,180.,,0\H,2,NH,1,HNN,3,0.,,0\\NN=1.20428\NH0=1.01424\HONN=124.30159\NH3
=1.0123\H3NN=117.55299\NH=1.01518\HNN=112.40886\\HF=-110.305942\RMSD=0.736D
-07\RMSF=0.441D-04\PG=CS\\

9085\CMU\FOPT\UHF\6-31G*\C2H2(1+,2)\POPLE\15-OCT-1980\1\\# 6-31G* OPT NOSYM
\\HCCH+ 2-PI-U LINEAR 6-31G* OPTIMIZATION\\1,2\H\C,1,CH\X,2,1.,1,90.,\C,2,CC
,3,90.,1,180.,,0\X,4,CC,2,90.,3,180.,,0\H,4,CH,5,90.,,2,180.,,0\\CH=1.0711\CC=1
.22888\\HF=-76.4628717\S2=0.754\RMSD=0.536D-07\RMSF=0.189D-04\PG=D*H\\

9111\CMU\FOPT\UHF\6-31G*\C1H1N1(1+,2)\POPLE\17-OCT-1980\1\\# 6-31G* OPT SCF
CYC=64\\HNC+ 2-SIGMA+ 6-31G* OPTIMIZATION\\1,2\H\N,1,NH\X,2,1.,1,90.,\C,2,NC
,3,90.,,1,180.,,0\\NH=1.00914\NC=1.134\\HF=-92.4650681\S2=1.037\RMSD=0.968D-0
7\RMSF=0.119D-03\PG=C*V\\

9112\CMU\FOPT\UHF\6-31G*\C1H1N1(1+,2)\POPLE\17-OCT-1980\1\\# OPT SCFCYC=64
6-31G*\\HCN+ 2-SIGMA+\\1,2\H\C,1,CH\X,2,1.,1,90.,\N,2,CN,3,90.,,1,180.,,0\\CH=
1.0786\CN=1.13732\\HF=-92.4207736\S2=1.053\RMSD=0.993D-07\RMSF=0.188D-03\PG
=C*V\\

9113\CMU\FOPT\UHF\6-31G*\H2O2(1+,2)\POPLE\17-OCT-1980\1\\# 6-31G* OPT\\HOOH
+ TRANS 6-31G* OPTIMIZATION\\1,2\O\O,1,OO\H,1,OH,2,HOO\H,2,OH,1,HOO,3,180.,,
0\\OO=1.25681\OH=0.97822\HOO=106.412\\HF=-150.4117493\S2=0.766\RMSD=0.842D-
07\RMSF=0.895D-05\PG=C02H\\

9114\CMU\FOPT\UHF\6-31G*\C2H2(1+,2)\POPLE\17-OCT-1980\1\\# 6-31G* OPT SCFCY
C=64\\H2CC+ VINYLIDENE CATION 2-A1\\1,2\C\C,1,R(C-C)\H,1,R(C-H),2,A(H-C-C)\
H,1,R(C-H),2,A(H-C-C),3,180.,,0\\R(C-C)=1.28971\R(C-H)=1.0861\A(H-C-C)=118.9
1101\\HF=-76.3999108\S2=0.981\RMSD=0.848D-07\RMSF=0.501D-04\PG=C02V\\

9115\CMU\FOPT\UHF\6-31G*\C1H3N1(1+,2)\POPLE\17-OCT-1980\1\\# 6-31G* OPT SCF
CYC=64\\H2N-CH+ 2-A'\\1,2\N\C,1,NC\H,2,CH,1,HCN\H,1,NH1,2,H1NC,3,0.,,0\H,1,N
H2,2,H2NC,3,180.,,0\\NC=1.25136\CH=1.07524\HCN=131.85552\NH1=1.01246\NH2=1,0
1044\H1NC=122.43058\H2NC=121.05096\\HF=-93.7253869\S2=0.809\RMSD=0.369D-07\
RMSF=0.149D-03\PG=CS\\

9116\CMU\FOPT\UHF\6-31G*\H2N2(1+,2)\POPLE\17-OCT-1980\1\\# 6-31G* OPT\\HN=N
H+ TRANS 2-AG\\1,2\N\N,1,NN\H,1,NH,2,HNN\H,2,NH,1,HNN,3,180.,,0\\NN=1.1409\N
H=1.02523\HNN=126.34667\\HF=-109.6724069\S2=0.76\RMSD=0.150D-07\RMSF=0.646D
-04\PG=C02H\\

9117\CMU\FOPT\UHF\6-31G*\H2N2(1+,2)\POPLE\17-OCT-1980\1\\# 6-31G* OPT SCFCY
C=64\\H2N-N+ PLANAR 2-B2\\1,2\N\N,1,NN\H,1,NH,2,HNN\H,1,NH,2,HNN,3,180.,,0\\
NN=1.20771\NH=1.02302\HNN=120.23011\\HF=-109.696942\S2=0.953\RMSD=0.810D-07
\RMSF=0.501D-04\PG=C02V\\

9118\CMU\FOPT\UHF\6-31G*\H2O2(1+,2)\POPLE\17-OCT-1980\1\\# 6-31G* OPT SCFCY
C=64\\H2OO+ PLANAR C2V 2-B1\\1,2\O\O,1,OO\H,1,OH,2,HOO\H,1,OH,2,HOO,3,180.,,
0\\OO=1.33471\OH=0.97369\HOO=118.04115\\HF=-150.3999089\S2=0.757\RMSD=0.145
D-07\RMSF=0.987D-05\PG=C02V\\

9123\CMU\FOPT\UHF\6-31G*\C1H4O1(1+,2)\POPLE\18-OCT-1980\1\\# 6-31G* OPT\\H2
O--CH2+ TRANS 2-A'\\1,2\C\O,1,AB\X,1,1.,,2,BAH12\H,1,AH1,3,QH1AH2,2,90.,,0\H,
1,AH1,3,QH1AH2,2,-90.,,0\X,2,1.,1,ABH78,3,180.,,0\H,2,BH7,6,QH7BH8,1,90.,,0\H,
2,BH7,6,QH7BH8,1,-90.,,0\\AB=1.45859\AH1=1.06989\BH7=0.96478\BAH12=138.79941
\QH1AH2=62.54732\ABH78=141.65525\QH7BH8=55.65209\\HF=-114.6940081\S2=0.758\
RMSD=0.812D-07\RMSF=0.162D-04\PG=CS\\

9124\CMU\FOPT\UHF\6-31G*\C1H2O1(1+,2)\POPLE\18-OCT-1980\1\\# 6-31G* OPT SCF
DM SCFCYC=128\\FORMALDEHYDE CATION PLANAR C2V 6-31G* OPTIMIZATION\\1,2\C\O,
1,AB\H,1,AH,2,HAB\H,1,AH,2,HAB,3,180.,,0\\AB=1.21152\AH=1.08743\HAB=117.8033
1\\HF=-113.5214436\S2=0.786\RMSD=0.892D-07\RMSF=0.973D-04\PG=C02V\\

9125\CMU\FOPT\UHF\6-31G*\C1H2O1(1+,2)\POPLE\18-OCT-1980\1\\# 6-31G* OPT\\HC
OH+ TRANS 6-31G* OPTIMIZATION\\1,2\C\O,1,AB\H,1,AH0,2,BAH0\H,2,BH6,1,ABH6,3
,180.,,0\\AB=1.20964\AH0=1.08402\BH6=0.97215\BAH0=125.31131\ABH6=118.74981\\
HF=-113.5036714\S2=0.759\RMSD=0.916D-07\RMSF=0.156D-03\PG=CS\\

9144\CMU\FOPT\UHF\6-31G*\C1H3N1(1+,2)\POPLE\19-OCT-1980\1\\# 6-31G* OPT SCF
CYC=64\\H2CNH+ PLANAR 6-31G* OPTIMMIZATION\\1,2\C\N,1,AB\H,1,AH3,2,H3AB\H,1
,AH0,2,BAH0,3,180.,,0\H,2,BH6,1,ABH6,3,0.,,0\\AB=1.24292\AH0=1.08003\AH3=1.08
351\BH6=1.0101\BAH0=119.23789\H3AB=119.31362\ABH6=148.6348\\HF=-93.717479\S
2=0.857\RMSD=0.135D-07\RMSF=0.175D-03\PG=CS\\

9145\CMU\FOPT\UHF\6-31G*\C1H4O1(1+,2)\POPLE\19-OCT-1980\1\\# 6-31G* OPT\\H3
COH+ STAGGERED 6-31G* OPTIMIZATION\\1,2\C\O,1,AB\H,1,AH3,2,H3AB\H,2,BH9,1,H
```

X.TAB;2 23-OCT-1980 11:21:36.69 PAGE 7

9BA,3,180.,,0\X,1,1.,,2,BAH12,3,180.,,0\H,1,AH1,5,H1AH2,2,90.,,0\H,1,AH1,5,H1AH
2,2,-90.,,0\\AH=1.47723\AH1=1.0822\AH3=1.07386\BH9=0.9775\H1AH2=55.91872\BAH
12=118.39217\H3AB=105.02188\H9BA=114.86693\\HF=-114.6872181\S2=0.76\RMSD=0.
719D-07\RMSF=0.217D-04\PG=CS\\

9153\CMU\FOPT\UHF\6-31G*\C1H5N1(1+,2)\POPLE\19-OCT-1980\1\\# 6-31G* OPT\\H2
NCH3+ STAGGERED 6-31G* OPTIMIZATION\\1,2\N\C,1,AB\X,1,1.,,2,HALXAB\X,1,1.,,3,
HALXAB,2,180.,,0\H,1,AH,4,HAX,2,90.,,0\H,1,AH,4,HAX,2,-90.,,0\H,2,BH,1,HBA,3,0
.,,0\X,2,1.,,1,YBA,3,180.,,0\H,2,BHP,8,HBY,1,90.,,0\H,2,BHP,8,HBY,1,-90.,,0\\AB=
1.45815\HALXAB=88.80941\AH=1.01023\HAX=58.15212\BH=1.08699\HBA=107.07378\YB
A=125.30401\BHP=1.07898\HBY=55.94574\\HF=-94.9322253\S2=0.763\RMSD=0.186D-0
7\RMSF=0.731D-04\PG=CS\\

9154\CMU\FOPT\UHF\6-31G*\C1H5N1(1+,2)\POPLE\20-OCT-1980\1\\# 6-31G* OPT SCF
CYC=64\\H3N-CH2+ STAGGERED 2-A'\\1,2\N\C,1,AB\H,1,AH3,2,H3AB\X,1,1.,,2,BAH12
,3,180.,,0\H,1,AH1,4,QH1AH2,2,90.,,0\H,1,AH1,4,QH1AH2,2,-90.,,0\X,2,1.,,1,ABH78
,3,0.,,0\H,2,BH7,7,QH7AH8,1,90.,,0\H,2,BH7,7,QH7AH8,1,-90.,,0\\AB=1.46984\AH1=
1.01301\AH3=1.01572\BH7=1.07006\BAH12=127.9411\H3AB=112.2472\ABH78=158.2362
1\QH1AH2=53.61057\QH7AH8=62.15294\\HF=-94.9308101\S2=0.761\RMSD=0.838D-07\R
MSF=0.627D-04\PG=CS\\

Acknowledgement

The research described in this paper was supported in part by the Natonal Science Foundation (Grant CHE 79-01061-01).

References

1. W. J. Hehre, R. F. Stewart, and J. A. Pople, J. Chem. Phys., 51, 2657 (1969).
2. J. S. Binkley, J. A. Pople, and W. J. Hehre, J. Amer. Chem. Soc., 102, 939 (1979).
3. W. J. Hehre and J. A. Pople, J. Chem. Phys., 54, 724 (1971).
4. P. C. Hariharan and J. A. Pople, Theoretica Chimica Acta, 28, 213 (1973).
5. (a) C. Møller and M. S. Plesset, Phys. Rev., 46, 618 (1934); (b) J. A. Pople, J. S. Binkley, and R. Seeger, Int. J. Quant. Chem., 510, 1 (1976).
6. R. Krishnan, J. S. Binkley, R. Seeger, and J. A. Pople, J. Chem. Phys., 72, 650 (1980).
7. GAUSSIAN 80, J. S. Binkley, R. A. Whiteside, R. Krishnan, R. Seeger, D. J. DeFrees, H. B. Schlegel, S. Topiol, L. R. Kohn, and J. A. Pople, Quantum Chemistry Program Exchange, Indiana University (1980).
8. Carnegie-Mellon Quantum Chemistry Archive, R. A. Whiteside, J. S. Binkley, R. Krishnan, and D. J. DeFrees, H. B. Schlegel, and J. A. Pople, Department of Chemistry, Carnegie-Mellon University, Pittsburgh, PA 15213.
9. W. A. Lathan, W. J. Hehre, and J. A. Pople, J. Amer. Chem. Soc., 93, 808 (1971).
10. R. Krishnan, H. B. Schlegel, J. A. Pople, and P. v. R. Schleyer, to be published.
11. R. Krishnan, M. J. Frisch, J. A. Pople, and P. v. R. Schleyer, to be published.

12. V. Dyczmons and W. Kutzelnigg, Theor. Chim. Acta, 33, 239 (1974).
13. Based on available heats of formation.
14. J. A. Montgomery and C. E. Dykstra, J. Chem. Phys., 71, 1380 (1979).
15. J. Weber, M. Yoshimine, and A. D. McLean, J. Chem. Phys., 64, 4159 (1976).
16. B. Zurawski, R. Ahlrichs, and W. Kutzelnigg, Chem. Phys. Lett., 21, 309 (1973).

MRD-CI METHOD FOR THE STUDY OF LOW-LYING ELECTRONIC STATES. APPLICATION TO SECOND-ROW MOLECULAR IONS OF TYPE AH_2^+, AH^+, AB^+, AND HAB^+

Pablo J. Bruna, Gerhard Hirsch,
Robert J. Buenker and Sigrid D. Peyerimhoff

Lehrstuhl für Theoretische Chemie
der Universität Bonn
Bonn, West Germany

Lehrstuhl für Theoretische Chemie
Gesamthochschule Wuppertal
Wuppertal, West Germany

I. INTRODUCTION

From the point of view of the Schrödinger equation the theoretical description of molecular ions is not essentially different than that for neutral systems. The corresponding Hamiltonian operator simply needs to be approximately adjusted to reflect the number of electrons in the ionic species and the problem is reduced to obtaining the associated eigenvectors and eigenvalues theoreof to a suitably good approximation. Furthermore for molecules containing relatively light atoms there is good reason to believe that a non-relativistic approach to electronic structure calculations suffices in virtually all types of applications, and thus a purely electrostatic Hamiltonian operator is all that is required. In addition in most situations the Born-Oppenheimer Approximation can be safely assumed in such calculations, which is to say the nuclear and electronic motion can be treated in a basically uncoupled manner (the field of fixed or clamped nuclei). In this case the nuclear kinetic energy is temporarily ignored in the calculations and the first step in the overall treatment is to solve the so-called electronic Schrödinger equation for a series of fixed nuclear conformations (clamped-nuclei approximation). As long as the resulting electron energy surfaces are well separated for states of the same symmetry, the nuclear motion of each such species can be treated separately by combining the appropriate rovibrational kinetic energy operator with the above potential energy terms.

For our purposes in this lecture then the main objective in formulating a completely general theoretical treatment of molecular ions is to develop effective computational techniques for solving the electronic Schrödinger equation to a useful approximation. Because of the different natures of various ionic species it is necessary that such procedures can be applicable to a wide variety of electronic structures, particularly if attention is directed beyond the study of just the ground states of such systems, and at the same time it is highly desirable that they are also equally effective for all types of nuclear conformations and not simply that preferred by the system at equilibrium. In the following sections a method of calculation designed to achieve these objectives will be presented and numerous applications thereof will be considered to illustrate its effectiveness in actual practice.

II. THEORETICAL TREATMENT

Exact analytical solution of the electronic Schrödinger equation has only been possible for systems containing a single electron, and thus to date the most fruitful approach to this general problem has involved the use of computationally straightforward methods which are capable of obtaining approximate solutions. Conceptually the simplest way to proceed is to assume a basis of one-electron functions or spin orbitals, and from these to construct appropriate many-electron species in the form of Slater determinants using energy minimization as a criterion for optimization in accordance with the variation principle. If only a single determinant is employed to describe the wavefunction the treatment is referred to as the self-consistent field (SCF) method, and in the past calculations of this type have been quite useful in predicting a number of ionic or molecular properties such as bond lengths and bond angles, but this procedure has not proven to be sufficiently reliable on a general basis to qualify as fulfilling the objectives set forth in the Introduction.

To go beyond the SCF approximation it is necessary to assume a less restrictive form of the electronic wavefunction than just a single Slater determinant in which only the most stable spin orbitals are populated. An easy generalization is thus to form a series of Slater determinants involving distributions of the various one-electron functions without regard to their individual stabilities and to obtain the optimum linear combination thereof via energy minimization (the CI method); specifically the Hamiltonian matrix over all such many-electron species needs to be formed and subsequently diagonalized through solution of the corresponding secular equation. If all possible Slater determinants which can be formed from a given AO basis are taken in such a treatment, it is referred to as a full CI, and it might well be said that the goal in electronic structure calculations is to obtain results at this level for a sufficiently flexible choice of one-electron

functions. Calculations at this level can realistically be expected to be satisfactory for all types of ionic and molecular systems, in both ground and excited states, without regard to the nature of the associated nuclear conformation. The difficulty with this approach, however, is that with m spatial orbitals and n electrons in the problem the dimension of a full CI is equal to $\binom{2m}{n}$ and thus the corresponding secular equations rapidly become too large to be treated by conventional diagonalization methods.

In order to proceed further it thus becomes necessary to settle for an approximation to the full CI treatment and essentially two different approaches have been investigated to this end. The first idea has simply been to introduce a truncation scheme to reduce the CI matrices to manageable size while still employing a good AO basis [1]. Alternatively other authors have used various forms of high-order perturbation theory to improve the degree of accuracy beyond some initially simple level of approximation such as an SCF wavefunction. In the first case there has been considerable effort expended in trying to develop a generally effective truncation scheme, usually involving the choice of a few key (reference) electronic configurations and then supplementing these with all species differing from them by some minimal level of excitation (substitution). If all singly and doubly excited species are to be considered it has become popular to divide the individual configurations into strongly and weakly interacting categories and thereby afford a simple criterion for further reduction of the CI space. The major difficulty with such an approach is that because of the extremely large numbers of configurations, even very weakly interacting species are capable of combining to produce significant changes in the energy and property results obtained thereby.

In the second type of approach it has been demonstrated that the use of higher-order perturbation theory can lead to a very good approximation to the desired full CI results, but the major difficulty in this instance has been that such treatments have only been feasible when the system under consideration is characterized by a well-defined single (Hartree-Fock) configuration. As a result such methods are far from generally applicable, being restricted to particular types of electronic states (most often only the ground state) and then not always for the entire range of nuclear conformations of interest. A well-known example of the latter type is the N_2 ground state, which is reasonably well described as a simple closed-shell species near the equilibrium bond distance but which assumes a more complex representation as the bond-breaking process begins, at which point the accuracy of the perturbation methods rapidly degrades.

The theroetical technique employed in the calculations of molecular ions to be discussed subsequently is best looked upon as a

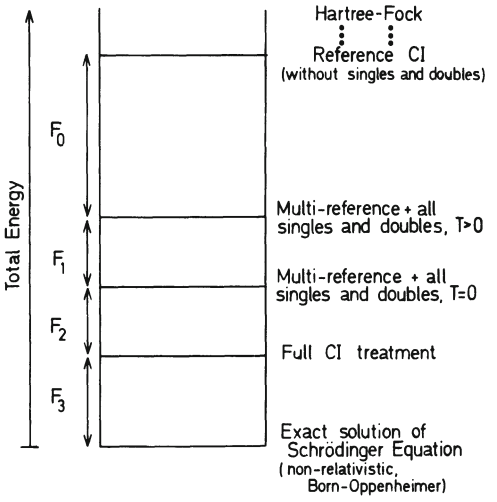

Fig. 1. Schematic diagram showing the variation of the total energy of a system with level of CI treatment.

combination of both of the above approximate procedures. In practice it consists of truncated CI calculations where only a selected sample of singly and doubly excited configurations relative to a series of reference species are treated via explicit diagonalization methods, but it also makes use of a simple perturbation theory approach to go beyond this level of treatment and thereby achieve a significantly better approximation to the true Schrödinger equation results than would other be possible [1-3]. Details of this general computational technique have recently been discussed in another NATO ASI [4], but its main features can be conveniently summarized with reference to a simple diagram in which the CI energies obtained at various levels of treatment are indicated (Fig. 1) [5]. The energy which is not accounted in such a multi-reference double-excitation (MRD-CI) treatment at a given level of configuration selection is divided into three parts therein, labelled F_1-F_3, representing the errors introduced successively by a) employing a selection of the generated CI space, b) not including enough reference species to attain the full CI, and c) not including enough AO basis functions to solve the Schrödinger equation exactly. Rather than simply accept these errors, as is done in conventional CI treatments, however, the present methods attempts to make accurate estimates of their magnitudes via perturbation theory and thereby achieve an effective reduction in the uncertainty associated with the overall energy results.

The key point which distinguishes this approach from conventional many-body perturbation theory treatments (MBPT) [6] is that

because the starting point for such computations is already a relatively large CI wavefunction the order to which the subsequent perturbation expansions need to be taken to achieve high accuracy is relatively small. In addition with the help of individual CI calculations it has become possible to make the resulting perturbation scheme self-correcting in nature. The basic idea is to estimate a given energy discrepancy F_i as being proportional to a simple perturbation quantity K_i, which in the case of F_i is simply a sum of the individual energy lowerings achieved by each of the unselected test configurations in the MRD-CI treatments: $K_i = \sum_j^1 \Delta E_j$. The value of the proportionality constant λ_i which when multiplied with K_i gives the true value for F_i can then be estimated to good accuracy by comparing results at two or more levels of truncation [2]. For example, the ratio of the actual CI energy lowering in going from one selection threshold to another divided by the corresponding change in $K_i = \sum_j^1 \Delta E_j$ can be used to predict the value of λ_i in estimating the F_i quantity. Alternatively a family of energy vs. selection threshold curves can be formed for various values of the weighting factor λ_i for the perturbation sum and the desired zero-threshold result can be obtained by a simple plotting procedure [2, 5]. Especially because of the self-correcting nature of this procedure it is not necessary to go to high orders of perturbation theory to obtain quite accurate results, particularly when the CI starting point is well advanced so that the ensuing perturbation expansion is quickly converging.

The same type of innovation can be applied to obtain the full CI correction F_2. In this case the perturbation quantity K_2 is taken as $(1 - \sum_j^{ref} c_j^2) \cdot (E_{MRD-CI} - E_{ref})$, in analogy to a formula given by Davidson [7], and the self-correcting feature of the technique is realized by carrying out a series of MRD-CI calculations for several different sets of reference configurations. An example of how this procedure works in the case of the diatomic ion CN^+ [8] is shown in Fig. 2. As the sum of the squares of the coefficients for the reference species in the final CI expansion approaches 1.0, both the corresponding MRD-CI energy and the same quantity augmented by the K_2 term must approach the full CI limit and a clear pattern of convergence is in fact noted in the calculated results for both the low-lying $^1\Sigma^+$ and $^3\Pi$ states of this molecular ion. In addition it is possible to go one step further and obtain an estimate for the AO basis error F_3 by such a perturbative scheme but no results are available as yet in this case [5].

The point which needs to be emphasized is that by implementing perturbation theory in the above manner it is still possible to retain the essential generality with respect to different types of electronic states and nuclear conformations associated with the

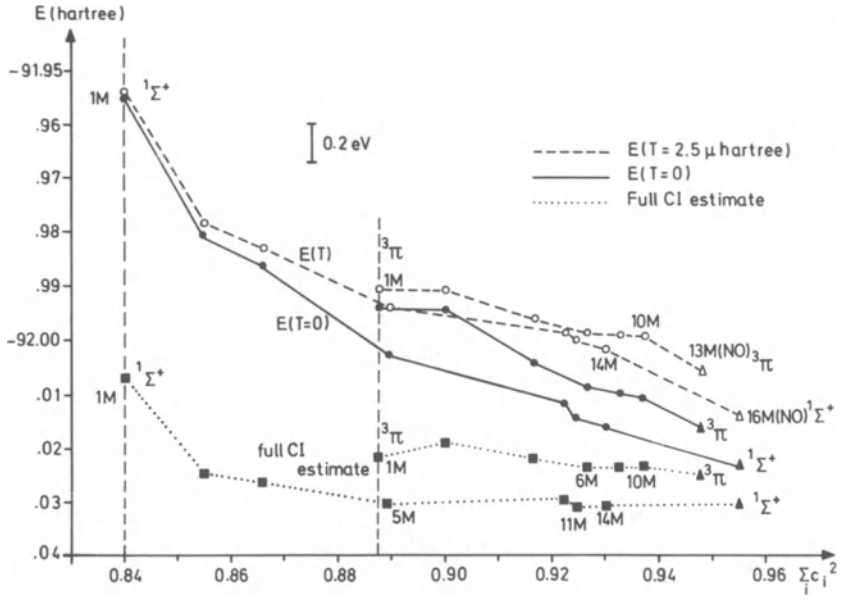

Fig. 2. Illustration of a full-CI extrapolation procedure for several electron states of CN^+ (for more details see Ref. 8).

Schrödinger equation itself, which property distinguishes it to a large degree from MBPT or CEPA techniques, which can only be applied when certain specific conditions on the electronic wavefunction are fulfilled. At the same time the general applicability does not have to be paid for at the price of reduced accuracy, by reason of the fact that the simple perturbation technique employed is quite effective because the starting point in the expansion is already a good CI wavefunction and thus rapid convergence is assured. In addition such calculations are relatively inexpensive because the extra work required over and above a truncated CI treatment to obtain the F_1 correction is minimal and the cost of obtaining the corresponding full CI energy estimate is not substantially greater, especially since no additional four-index integral transformation is required in the process.

In the next sections explicit calculations will be presented to illustrate how such techniques perform effectively in practical applications involving molecular ions at general electronic structure and nuclear conformation. We shall concentrate on species including the second-row atoms silicon, phosphorus and sulfur; in studying the mono- and dihydrides a comparison with the isovalent compounds from the first will be made too (Sections III and IV). In the AB^+ and HAB^+ systems especial attention has been paid to those species containing one atom from the first-row and the other from

Table 1. Low-Lying States of the AH_2^+ under Discussion

System	$D_{\infty h}$	$D_{\infty h}$	C_{2v}		C_s	Approximate bond angle
	$\sigma_u^2\ \pi_u^3$	$^2\Pi_u$	$2b_2^2\ 5a_1^2\ 2b_1^1$	$^2B_1$	$^2A''$	90°
H_2S^+			$2b_2^2\ 5a_1^1\ 2b_1^2$	$^2A_1$	$^2A'$	120°
7 ve	$\sigma_u^1\ \pi_u^4$	$^2\Sigma_u^+$	$2b_2^2\ 5a_1^2\ 2b_1^2$	$^2B_2$	$^2A'$	30°
	$\sigma_u^2\ \pi_u^2$	$^3\Sigma_g^-$	$2b_2^2\ 5a_1^1\ 2b_1^1$	$^{1,3}B_1$	$^{1,3}A''$	120°
		$^1\Delta_g$	$2b_2^2\ 5a_1^2\ 2b_1^0$	$^1A_1$	$^1A'$	90°
		$^1\Sigma_g^+$	$2b_2^2\ 5a_1^0\ 2b_1^2$	$^1A_1$	$^1A'$	180°
PH_2^+	$\sigma_u^1\ \pi_u^3$	$^{1,3}\Pi_g$	$2b_2^1\ 5a_1^2\ 2b_1^1$	$^{1,3}A_2$	$^{1,3}A''$	30°
6 ve			$2b_2^1\ 5a_1^1\ 2b_1^2$	$^{1,3}B_2$	$^{1,3}A'$	90°
	$\sigma_u^0\ \pi_u^4$	$^1\Sigma_g^+$	$2b_2^0\ 5a_1^2\ 2b_1^2$	$^1A_1$	$^1A'$	30°
	$\sigma_u^2\ \pi_u^2$	$^2\Pi_u$	$2b_2^2\ 5a_1^1\ 2b_1^0$	$^2A_1$	$^2A'$	120°
			$2b_2^2\ 5a_1^0\ 2b_1^1$	$^2B_1$	$^2A''$	180°
	$\sigma_u^1\ \pi_u^2$	$^{2,4}\Sigma_u^-$	$2b_2^1\ 5a_1^1\ 2b_1^1$	$^{2,4}A_2$	$^{2,4}A''$	60°
		$^2\Delta_u$	$2b_2^1\ 5a_1^2\ 2b_1^0$	$^2B_2$	$^2A'$	30°
SiH_2^+		$^2\Sigma_u^+$	$2b_2^1\ 5a_1^0\ 2b_1^2$	$^2B_2$	$^2A'$	
	$\sigma_u^0\ \pi_u^3$	$^2\Pi_u$	$2b_2^0\ 5a_1^1\ 2b_1^1$	$^2B_1$	$^2A''$	30°
5 ve			$2b_2^0\ 5a_1^1\ 2b_1^2$	$^2A_1$	$^2A'$	60°

Bond angles are only given in general classes (i.e., 180°, 120°, 90°, 60°, 30°) in order to demonstrate qualitatively the influence of the $2b_1$ and $5a_1$ occupation.

the second-row. These compounds will be discussed in Sections V and VI.

In the concluding Chapter VII reference will be given to other molecular-ions studied with the MRD-CI method but not treated explicitly in this report. It should be called that the theoretical procedures employed are by no means restricted to charged systems.

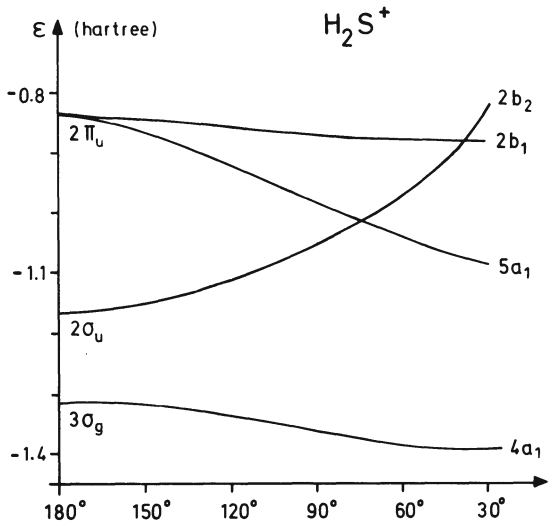

Fig. 3. Walsh diagram for AH_2 systems exemplified by the $3\sigma_g$, $2\sigma_u$, and $2\pi_u$ MOs of H_2S^+.

III. MOLECULAR IONS OF TYPE AH_2^+

As an example of *ab initio* studies on molecular ions we want to discuss in the following various molecular ions of type AH_2^+. We shall concentrate on systems with A belonging to the second row of the periodic table (i.e., A = S, P, Si) and compare our results with information available for their corresponding first-row counterparts H_2O^+, NH_2^+, and CH_2^+. The general trends found in all these systems will be discussed and structural information will be given.

Table 1 gives a survey of the electronic configurations as well as the corresponding states for AH_2^+ in the linear ($D_{\infty h}$), bent (C_{2v}), and asymmetric (C_s) arrangements. All possibilities involving the $2\sigma_u$ and $2\pi_u$ orbitals are listed with $3\sigma_g$ ($4a_1$) always being doubly occupied. Thus we shall refer to the 7-valence-electron system H_2S^+ by its ground state configuration $2\sigma_u^2 2\pi_u^3$, to PH_2^+ with 6 valence electrons by $2\sigma_u^2 2\pi_u^2$ and to SiH_2^+ with 5 valence electrons by $2\sigma_u^2 2\pi_u^1$. The C_{2v} configurations are described in terms of the orbitals $2b_2$, $5a_1$, and $2b_1$. An additional column in Table 1 gives very generalized information about the geometric features of the various states by indicating a rough equilibrium angle. One finds minima for angles from 180° (linear) down to extremely small values around 30° among all the systems discussed, which behavior can be explained by the character of the molecular orbitals forming the various states. The use of Walsh's rules for the description of molecular structure has been applied earlier to AH_2 and AH_3 molecules by Peyerimhoff and Buenker [9, 10]. Recently, Casida et al.

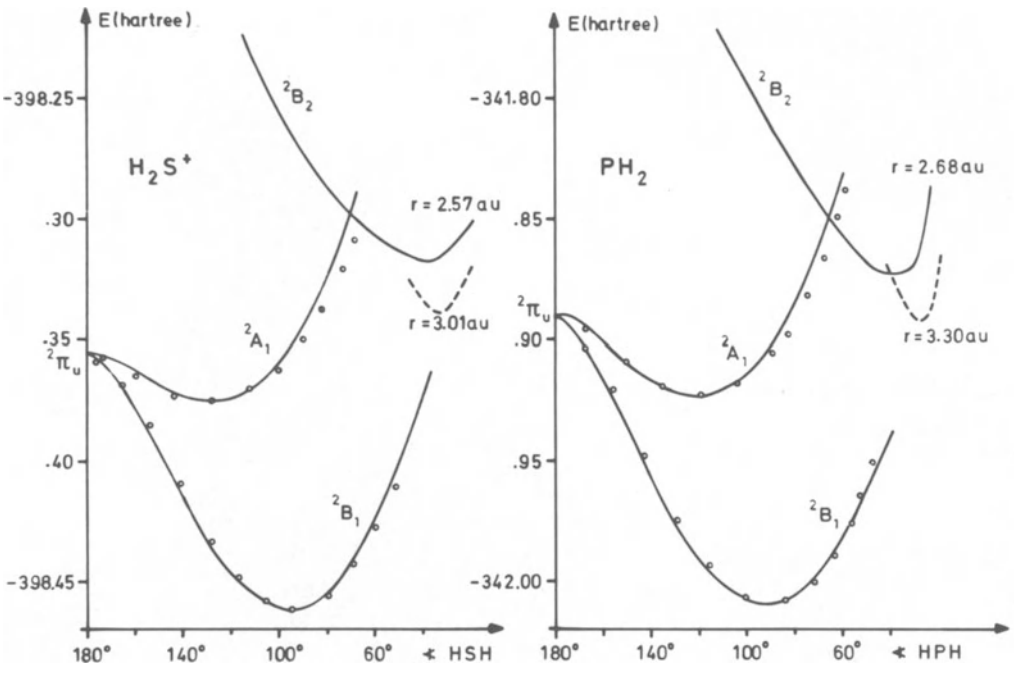

Fig. 4. Calculated MRD-CI potential energy curves for the three lowest states in H_2S^+ and PH_2. The dashed lines indicate the $^2B_2$ curves for the optimized XH distance. The circles are data which are obtained by fitting experimental results.

[11] have applied Walsh's rules to study small bond angle states of AH_2 and AH_2^+ molecules with A standing for a first-row atom. We shall extend this description to the second-row systems H_2S^+, PH_2^+, and SiH_2^+ and deduce from the results information concerning the behavior after photoionization of the corresponding neutral molecules. Figure 3 shows the Walsh diagram for the relevant orbitals as obtained by SCF calculations on H_2S^+. The same picture is also valid qualitatively for the systems PH_2^+ and SiH_2^+.

Starting from the linear arrangement of the atoms a destabilization of the $2b_2$ orbital is seen upon decreasing the molecular bond angle along with a complementary stabilization of the $5a_1$ orbital, while the $2b_1$ component of the π_u remains quite unaffected by changes in this quantity. Thus on decreasing this angle the $2b_2$ orbital first undergoes a crossing with the $5a_1$ and then for rather small angles even with the $2b_1$. It has been shown by Casida et al. [11] for the first-row systems — as is equally valid for the second-row AH_2^+ discussed here — that the equilibrium bond angle is deter-

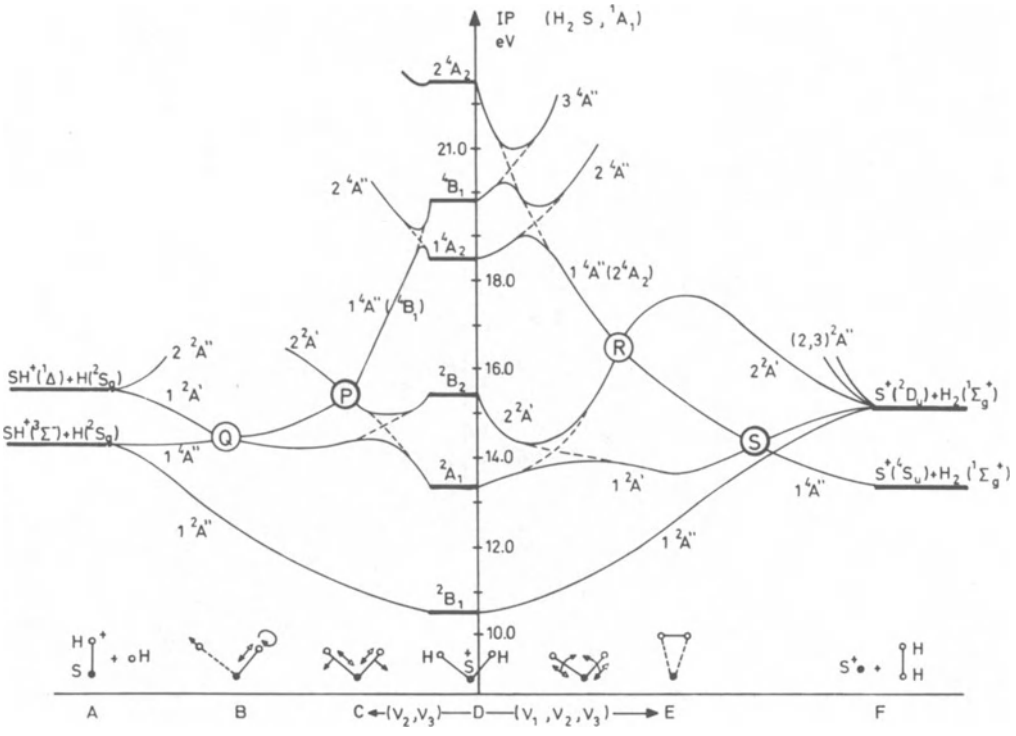

Fig. 5. Correlation diagram for the lowest electronic states of H_2S^+ and their different dissociation products (for more details see Ref. 13).

mined by the relative occupation of the $2b_2$ and $5a_1$ orbitals. Table 1 demonstrates this clearly: a $b_2^2a_1^0$ occupation favors the linear arrangement, $b_2^2a_1^1$ leads to ca 120°, $b_2^2a_1^2$ to ca 90° and $b_2^1a_1^2$ to very small bond angles less than 50°. A $b_2^1a_1^1$ configuration is stabilized around 90° similar to the $b_2^2a_1^2$ occupation.

In the following we want to discuss the different systems in greater detail. Table 2 gives a survey of our calculated data on excitation energies and the barrier to linearity for the three lowest states (two for SiH_2^+) together with the vertical ionization potentials from the ground state of the neutral system. Together with the following Figs. 2, 3, 4, and 5 this serves as a basis for the discussion of the behavior of the system after photoionization of the neutral molecule. The technical details of the calculations such as AO basis set or dimension of the configuration space are given in the publications dealing with the various molecules explicitely. In general the basis used is of double zeta quality (Huzinaga's for the first row, Veillard's for the second row), if necessary augmented by polarization functions and such of d- or f-type.

Table 2. Relative Energies (in eV) for Some Low-Lying States of the AH_2^+ Systems under Discussion

H_2S^+	(7 valence electrons) [12]		
	X $^2B_1$	0.0	
	$^2A_1$	3.02	(2.34)[a]
	$^2B_2$	5.34	(3.37)[a,b]
	$^2\Pi_u$ ($D_{\infty h}$)	2.91	
PH_2^+	(6 valence electrons)[c]		
	X $^1A_1$	0.0	
	$^3B_1$	1.26	(0.59)[a]
	$^1B_1$	2.68	(2.05)[a]
	$^1\Delta_g$ (D_∞)	2.83	
	$^3\Sigma_g^-$ ($D_{\infty h}$)	1.43	{0.84}[d]
SiH_2^+	(valence electrons)[c]		
	X $^2A_1$	0.0	
	$^2B_1$	1.90	(1.08)[a]
	$^2\Pi_u$ ($D_{\infty h}$)	1.08	

a) Values in parentheses correspond to T_e.
b) This value is obtained with the system restrained to C_{2v}.
c) Results of this laboratory.
d) Barier to linearity for the $^3B_1$ state.

A) The 7-Valence-Electron Systems H_2S^+

The first example for the study of molecular ions using the MRD-CI technique will be the positive ion of hydrogen sulfide. A more detailed discussion of low-lying states of H_2S^+ as well as of the dissociation behavior has been published elsewhere [12, 13] and

only a summary will be given here. The ionization of $H_2S(^1A_1)$ will lead to $H_2S^+(^2B_1)$ by excitation out of the $2b_1$ orbital. As can be seen in Fig. 3 the occupation of this MO has very little influence on the molecular geometry and thus both the neutral molecule and the positive ion have a very similar equilibrium geometry ($\alpha \simeq 90°$, $r \simeq 2.58\ a_0$). The first and second excited states of H_2S^+ are obtained by ionizing out of the $5a_1$ and $2b_2$ orbitals. A single occupation of the $5a_1$ instead of the double occupation in the neutral system favors a larger bond angle for the resulting $^2A_1$ state, while the opposite direction is preferred for the $^2B_2$ state with only one electron in the $2b_2$ orbital. For these three lowest states the calculated CI potential energy curves for $(HSH)^+$ bending are given in Fig. 4 together with those for the isovalent PH_2.

The energy levels of the ν_2 bending vibration have been calculated for the $^2A_1$ and $^2B_2$ states of H_2S^+ as well as the corresponding Franck-Condon factors [12]. The potential minima for the two states differ by about 30° and hence for the transitions the maximum intensity is found for $v_2' = 5$ and $v_2' = 6$, in accordance with the experimental results of Dixon et al. [14] in the ionization process $A^2A_1 \leftarrow X^1A_1(H_2S)$. Using the available experimental data these authors have deduced an analytical potential function for the $^2A_1$ and $^2B_1$ states, leading to the curves indicated in Fig. 4 by circles, whereby an excellent agreement between the calculated and experimentally obtained curves is observed.

As discussed above the $^2B_2$ state in general prefers a strongly bent nuclear arrangement and optimization of the geometrical parameters yield an equilibrium geometry of $\alpha \simeq 32°$ and $r \simeq 3.01\ a_0$ as indicated in Fig. 4 by the dashed lines (the S-H distance in the $^2B_1$ ground state being $r \simeq 2.58\ a_0$). Since vertical ionization out of the $2b_2$ orbital reaches the $^2B_2$ in a highly excited vibrational state, a broadened irregular vibrational progression towards the adiabatic IP is expected and actually observed experimentally [15].

In order to describe the dissociative behavior of the first two excited states of H_2S^+ ($^2A_1$ and $^2B_2$) — examined experimentally by Eland [16] — a study on the basis of MRD-CI calculations [13] has shown clearly that it is absolutely necessary to treat the problem in C_S symmetry throughout, since even small asymmetric motions of the molecular frame prevent us from applying the C_{2V} point group in general. In the lower symmetry then both $5a_1$ and $2b_2$ belong to the a' irreducible representation and we have an avoided crossing between the resulting two $^2A'$ states. Its importance for the dissociation of H_2S^+ as well as for the appearance of metastable peaks and irregular vibronic lifetimes for the $^2A_1$ state (see [13] and references to the experimental works given therein) is demonstrated by the correlation diagram given in Fig. 5, which is the result of a strict analysis in the lower symmetry. This procedure allows a correct description of the known facts that the $^2A_1$ state leads to

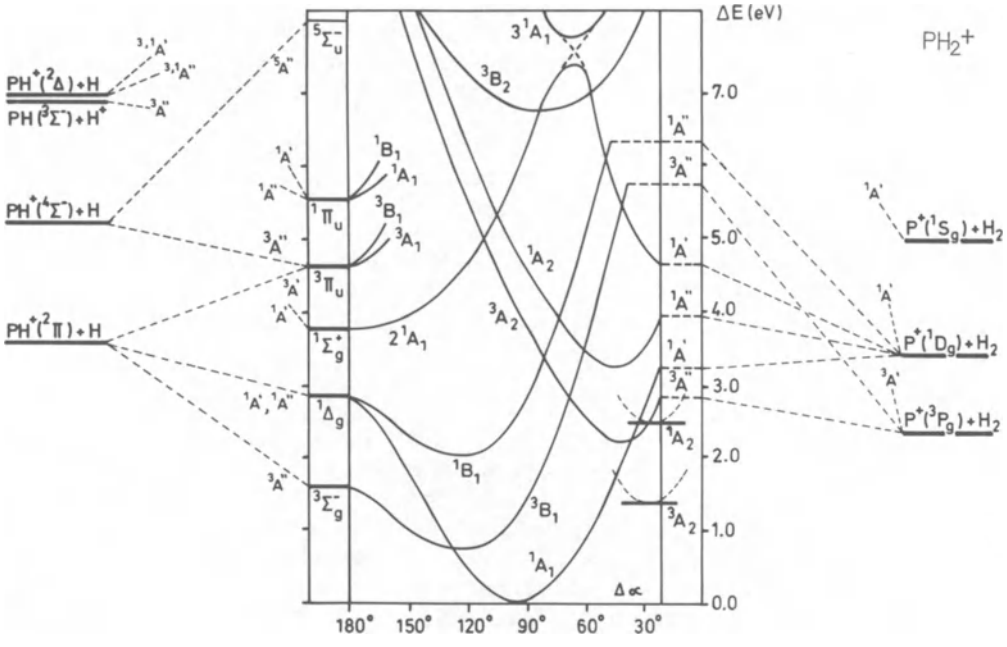

Fig. 6. Calculated MRD-CI bending potential curves for PH_2^+ together with a correlation in C_S-symmetry to the lowest dissociation products $P^+ + H_2$ and $[PH + H]^+$.

S^+ and H_2 while the $^2B_2$ state dissociates into SH^+ and H. Additionally, the large discrepancy between measured and calculated adiabatic ionization energies into the $^2B_2$ state can be explained: because of an avoided crossing in C_S the effective minimum accessible from the vertical ionization lies at higher energies than the minimum of the $^2B_2$ potential surface calculated in C_{2v}.

The same observation on the third adiabatic IP has been made for the H_2O^+ molecular ion by Meyer [17] and Smith et al. [18], but their speculation that the 0-0 transition has not been detected seems to be invalid. A more detailed comparison between the first- and second-row systems H_2O^+/H_2S^+ is given in [12]: the adiabatic energy lowering for the $^2A_1$ and $^2B_2$ states in comparison to their vertical position is roughly the same in both systems, but the barrier to dissociation, i.e., mainly the relative position of $^2B_2$ minimum and the $^2A_1$ reached by vertical excitation, is considerably higher for the first-row systems, thus preventing us from also applying to H_2O^+ the dissociation mechanism outlined for H_2S^+ into $H_2 + S^+$.

B) The 6-Valence-Electron System PH_2^+

Similar conclusions can also be drawn for PH_2^+ with one valence electron less than the sulfur compound. Figure 6 gives the calculated potential energy curves for $(HPH)^+$ bending motion (from the linear arrangement down to angles of ca. 30°) in its central part. The P-H distance is kept fixed at 2.647 a_0 and only for the important $^{3,1}A_2$ states is the optimized potential minimum indicated as well. Left and right of this rectangle the correlation of the different states to the dissociation products $(P + H_2)^+$ and $(PH + H)^+$ is shown in a strictly C_s scheme. Thus in most cases a change in the character of the wavefunctions is required to yield the correlation indicated, e.g., the $^3\Sigma_g^-$ state itself leads to $PH^+(^4\Sigma^-)$ + H, while only a $^3\Pi_u$ state dissociates to $PH^+(^2\Pi)$ + H, both via $^3A''$ states.

Many features discussed for the H_2S^+ are valid for this system as well: a) similar geometrical structures of PH_2 and PH_2^+ (ground states) as a result of a $2b_1$ ionization ; b) the minimum of the B_1 states $(b_2^2a_1^1b_1^1)$ around 120° and the small bond angles for the A_2 states $(b_2^1a_1^2b_1^1)$; c) a crossing between the A'' states (B_1 and A_2). Thus the following predictions can be made for the dissociation after photoionization of PH_2: $2b_1 \rightarrow \infty$ leads to the stable ground state $^1A_1$, while the second ionization $5a_1 \rightarrow \infty$ reaches the $^3B_1$ state which — with some additional excess energy and the participation of all vibrational modes — can reach the $^3A_2$ minimum and dissociate into $P^+(^3P_g) + H_2$. The energetic situation seems to be less balanced than in H_2S^+, however, for which $^2A_1$ vertical, the $1^2A'$ minimum and the $S^+ + H_2$ products all possess approximately the same energy.

There is one important difference compared with the situation in H_2S^+, however: it can be seen from Fig. 5 that for the final dissociation of the $^2A'$ state a spin-orbit interaction with $^4A''$ is obligatory. In PH_2^+ (Fig. 6) the $^3A_2$ state possesses the configuration $2b_2^15a_1^22b_1^1$, thus itself describing the H_2 molecule via the doubly occupied $5a_1$MO and the $2b_2^12b_1^1$ occupation corresponding to the phosphorus ion in its ^3P_g state. Photoionization from the $2b_2$ orbital leads to $^3A_2$, a state having (in C_s symmetry) a local minimum due to the non-adiabatic crossing with the lower $^3A''$ ($^3B_1$) state. Due to this equivalence with the H_2S^+ molecular ion we expect a dissociation into $PH^+(^2\Pi)$ + H following this ionization process.

The upper part of the potential curve diagram in Fig. 6 reveals another interesting feature. The $5a_1/2b_2$ interchange previously discussed only for the lowest states of the molecular ions also causes another crossing area in this instance. Because of the energetic equivalence of the $5a_1$ and $2b_2$ orbitals near their crossing region three states are found close together, namely two $^1A_1$ states ($2b_2^22b_1^2$ and $5a_1^22b_1^2$) experiencing an avoided crossing in the

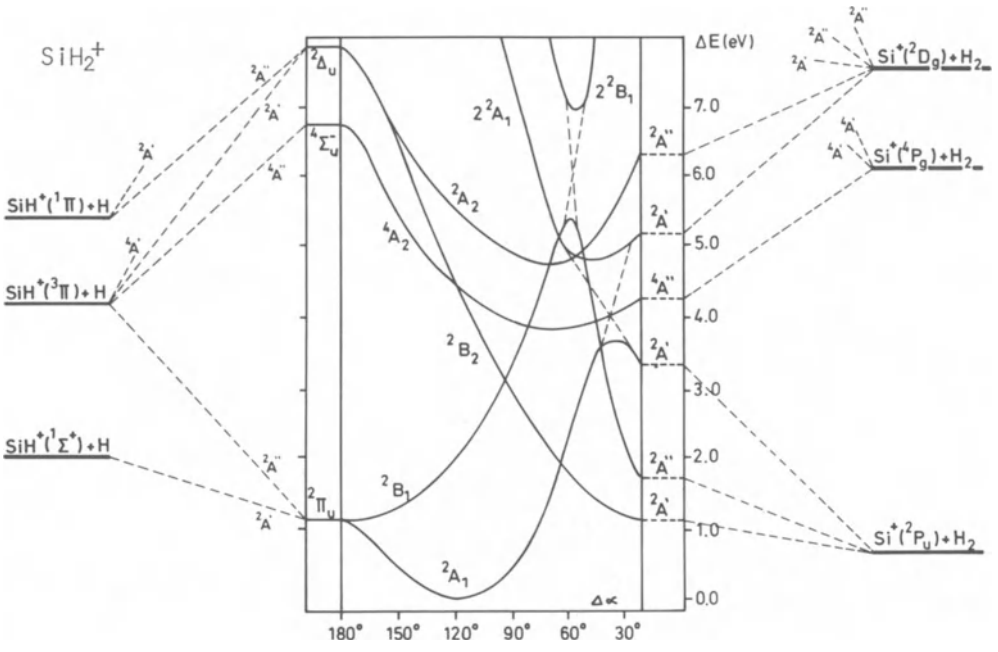

Fig. 7. Calculated MRD-CI bending potential curves for SiH_2^+ together with a correlation in C_s-symmetry to the lowest dissociation products $Si^+ + H_2$ and $SiH^+ + H$.

neighborhood of a $^1B_2$ state ($2b_2^1 5a_1^1 2b_1^2$). (Please note that only the corresponding $^3B_2$ species is included in Fig. 6.)

For NH_2^+, the corresponding molecule of the first rwo, MRD-CI calculations have been reported by Peyerimhoff and Buenker [19] giving potential energy curves and oscillator strengths for transitions between low-lying states. The ground state is found to be $^3B_1$ (quasilinear with a very shallow minimum near 150°), since the $^1A_1$ state does not experience a stabilization as strong as in PH_2^+. The crossings between the A" states, for example $^{3,1}B_1$ and $^{3,1}A_2$, are found to be similar in both ions, but the dissociation products lie at considerably higher energies than in the case of PH_2^+. In addition, in NH_2^+ the avoided crossing between the two higher $^1A_1$ states in the region of the $^1B_2$ have been also found.

C) The 5-Valence-Electron System SiH_2^+

The last example of AH_2^+ molecular ions to be discussed is the silicon compound SiH_2^+; Fig. 7 follows the same scheme as been given for PH_2^+ in Fig. 6. From the neutral molecules SiH_2, with its ground state $2b_2^2 5a_1^2$ configuration and an equilibrium bond angle of ca. 90°,

the first ionization occurs out of the $5a_1$MO, shifting the equilibrium bond angle of the $^2A_1$ ground state of SiH_2^+ to larger values near 120°. The other component of the linear $^2\Pi_u$, the $^2B_1$ state $(2b_2^2 2b_1^1)$ is not accessible directly by (simple) ionization out of the SiH_2 ground state. Finally, the $2b_2$ ionization process gives rise to the $^2B_2$ state $(2b_2^1 5a_1^2)$, which prefers a very small bond angle.

There are two obvious differences to the other AH_2^+ systems treated above. First, the ground state is component of a linear $^2\Pi_u$ state as in H_2S^+ (π_u^3), but in SiH_2^+ we have the inverted case (π_u^1) with the $^2A_1$ component being more stabilized than the $^2B_1$ branch. Secondly, in SiH_2^+ it is the ground state which now corresponds to the lowest $^2A'$ surface finally leading to $Si^+(^2P_u) + H_2$ (with the hydrogen molecule being described by the $5a_1$MO again). There is no experimental information about the photoionization of SiH_2, but by a theoretical interpretation of the calculated potential curves such a dissociation is to be expected as well as the formation of $SiH^+ + H$ from the $2b_2$ ionization reaching the $^2B_2$ surface. The second mixing region due to the $5a_1/2b_2$ interchange involves here two $^2B_1$ states and the $^2A_2$ with three open shells $(2b_2^1 5a_1^1 2b_1^1)$.

A comparison with data available for CH_2^+ [20] shows once again the general difference between the first- and second-row systems discussed in this work: the dissociation products $(C^+ + H_2)$ lie at much higher energies than in SiH_2^+, for which the $Si^+(^2P_u) + H_2$ fragments are found less than 1 eV above the $^2A_1$ minimum. This value represents about the same height as the levels reached on the $^2A_1$ surface by vertical ionization of $SiH_2(^1A_1)$, which fact makes the existence of a long-lived SiH_2^+ molecular ion after ionization $^1A_1 \rightarrow {}^2A_1$ doubtful — an interesting object for experimental research.

IV. MOLECULAR IONS OF TYPE AH^+

In addition to those for the dihydrides AH_2^+ of the second row of the periodic table, further MRD-CI calculations have also been carried out for the diatomic AH^+ systems, A standing again for a second-row atom (S, P, Si). Table 3 gives a survey on the various states treated together with their electronic configurations. In order to study the ionization of the neutral AH molecules, their electronic configurations are given as well, together with the ionization potentials.

It can be seen from this table, that the lowest-lying states of the 6- and 5-valence-electron systems SH^+ and PH^+ are characterized by variable occupation of the 5σ and 2π orbitals only, with the 4σ orbital always being doubly occupied. In SiH^+ with only 4 valence electrons, however, excitations from the 4σ orbital have to be included in the study. It should be noted that in some cases

Table 3. Low-Lying States of the AH^+ Systems under Discussion and Correspondingly Vertical Excitation Energies (in eV)

System	$C_{\infty v}$		ΔE calculated	ΔE experimental
	$4\sigma^2\ 5\sigma^2\ 2\pi^2$	$^3\Sigma^-$	(a) 0.0 (IP=10.19)	(b) 0.0 (IP=10.37)
		$^1\Delta$	1.34	1.28
		$^1\Sigma^+$	2.39	1.84 / 2.39[c]
SH^+	$4\sigma^2\ 5\sigma^1\ 2\pi^3$	$^3\Pi$	3.98	3.74
6 ve		$^1\Pi$	5.22	5.32
	$5\sigma^1\ 2\pi^2\ 6\sigma^1$	$^5\Sigma^-$	9.09	
	$4\sigma^2\ 5\sigma^0\ 2\pi^4$	$^1\Sigma^+$	10.49	
	SH: $5\sigma^2\ 2\pi^3$	$^2\Pi$		
	$4\sigma^2\ 5\sigma^2\ 2\pi^1$	$^2\Pi$	(d) 0.0 (IP=10.06)	(d) 0.0
	$4\sigma^2\ 5\sigma^1\ 2\pi^2$	$^4\Sigma^-$	1.66	---
		$^2\Sigma^-$	3.38	---
PH^+		$^2\Delta$	3.43	3.25
5 ve		$^2\Sigma^+$	4.50	
	$5\sigma^1\ 2\pi^1\ 6\sigma^1$	$^4\Pi$	8.21	
	$4\sigma^2\ 5\sigma^0\ 2\pi^3$	$^2\Pi$	8.21	
	PH: $5\sigma^2\ 2\pi^2$	$^3\Sigma^-$		
	$4\sigma^2\ 5\sigma^2\ 2\pi^0$	$^1\Sigma^+$	(a) 0.0 (IP=7.70)	
	$4\sigma^2\ 5\sigma^1\ 2\pi^1$	$^3\Pi$	2.23	
SiH^+	$4\sigma^2\ 5\sigma^1\ 6\sigma^1$	$^3\Sigma^+$	7.24	
4 ve	$4\sigma^2\ 5\sigma^0\ 2\pi^2$	$^3\Sigma^-$	6.13	
	$4\sigma^1\ 5\sigma^2\ 2\pi^1$	$^3\Pi$	7.62	
	SiH $5\sigma^2\ 2\pi^1$	$^2\Pi$		

a) Results of this laboratory

b) Reference 21

c) Reference 22

d) Reference 23

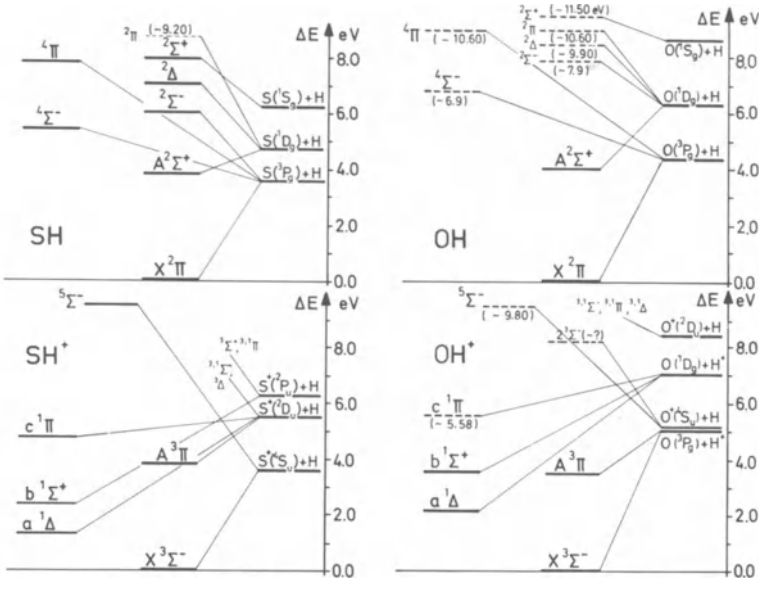

Fig. 8. Comparison of energy levels for the isovalent pairs SH/OH and SH^+/OH^+ and their relative position with respect to the lowest dissociation limits.

only the lowest-lying multiplet derived from a given configuration is given explicitly in the table.

A comparison of the first- and second-row systems (to be given in more detail in the following for the different molecules) is determined by the fact that the ionization potential of the second-row atoms is considerably smaller than the IP of their first-row counterparts and of hydrogen as well. Thus the lowest dissociation products for the AH^+ second-row hydrides are always $A^+ + H$, while in the first-row dissociation there will be a competition between $A^+ + H$ and $A + H^+$.

For SH^+ (Fig. 8) the following features are of special interest. Ionization out of the 2π orbital of SH gives rise to three states with a $5\sigma^2 2\pi^2$ configuration, $^3\Sigma^-$, $^1\Delta$, $^1\Sigma^+$, and a comparison with the experimental results of Dunlavey et al. [21] shows excellent agreement in the positioning of the excited states (cf. the data given in Table 3) except in one instance. The $^1\Sigma^+$ species is placed by our calculations at a relative energy of 2.39 eV, while Dunlavey et al. [21] give 1.84 eV. Additional work by these authors, however, [22] has led to a new assignment of their photoelectron spectrum and a corrected value for the relative energy of $SH^+(^1\Sigma^+)$ of 2.39 ± 0.01 eV, thus improving the agreement with

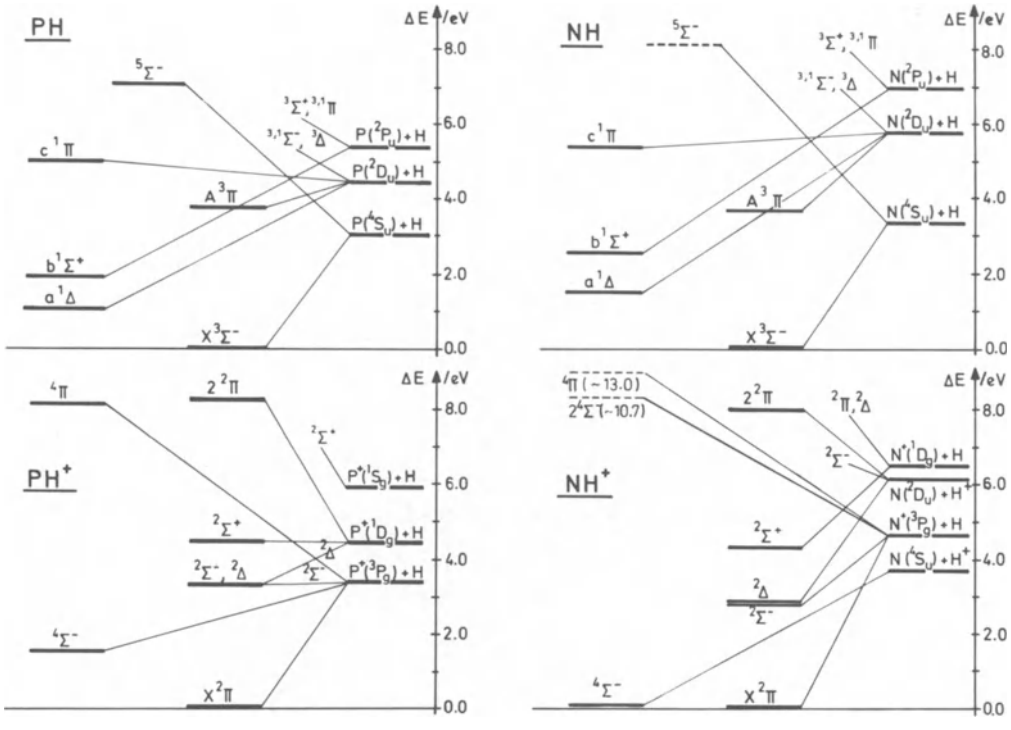

Fig. 9. Comparison of energy levels for the isovalent pairs PH/NH and PH^+/NH^+ and their relative position with respect to the lowest dissociation limits.

our calculated results significantly. The next ionization $5\sigma \rightarrow \infty$ leads to $^{3,1}\Pi$ states. Both of these are only slightly bound, the triplet state slightly more so than the singlet. The $^5\Sigma^-$ state, obtained by $2\pi \rightarrow 6\sigma$ excitation from $^3\Sigma^-$ and strongly repulsive to $S^+(^4S_u) + H$ dissociation (since the 6σ orbital describes the H atom), crosses with the Π states and should cause predissociation. In the photoelectron spectrum [21] only four vibrational components have been observed for the $^3\Pi$ and only one for the $^1\Pi$, thus confirming the shallow and/or predissociated character of their potential curves.

A comparison with OH^+ (Fig. 8) shows a rather different shape for the correlation diagram. The $O(^3P_g) + H^+$ dissociation limit is slightly lower than the $O^+(^4S_u) + H$ reached by the repulsive $^5\Sigma^-$. The $^3\Pi$ state on the other hand correlates with the lower products and hence there is no comparable predissociation as in SH^+.

The PH^+/NH^+ systems are compared in Fig. 9, while a more detailed study of PH/PH^+ is published elsewhere [23]. While 2π ionization in PH gives the PH^+ ground state $^2\Pi$, with a dissociation

Table 4. Spectroscopic Constants for the Low-Lying States of PH^+[a)]

State	r_e (Å)	B_e (cm^{-1})	ω_e (cm^{-1})	
$X\ ^2\Pi$	1.4246	8.509	2354	MRD-CI
	1.4352 (r_o)	8.3851 (B_o)	22.996 ($\Delta G_{1/2}$)	exp.
	1.431	8.420	2376	CEPA
$^4\Sigma^-$	1.4899	7.7803	1781	MRD-CI
$^2\Delta$	1.5465	7.2224	1458	MRD-CI
	1.5726 (r_o)	6.9833 (B_o)	1398.8 ($\Delta G_{1/2}$)	exp.

a) See reference 23 for a more detailed discussion.

energy to the first limit of separated atoms $P^+(^3P_g)$ + H of about 3.4 eV, the next set of states derived from the $5\sigma \rightarrow \infty$ ionization is much less bound. The $^4\Sigma^-$ dissociation energy can be estimated to be about 1.4 eV, while the $^2\Sigma^-$ and $^2\Sigma^+$ states are almost repulsive. The $^2\Delta$ shows a shallow minimum, but it is strongly predissociated by the repulsive $^4\pi$ state with a $5\sigma^1 2\pi^1 6\sigma^1$ configuration, leading directly to dissociation $P^+(^3P_g)$ + H. The shape of the potential curves [23] is reflected in the spectroscopic constants calculated for the three bound states of PH^+ and given in Table 4. There is good agreement with the experimental data with a deviation of about 30 cm^{-1} for the vibrational frequencies assigned to the $^2\Pi$ and $^2\Delta$ states, while the spectroscopic constants calculated for the $^4\Sigma^-$ state await experimental verification. The internuclear distance predicted for this state is somewhat larger than for the ground state (since it is reached by ionization of the P-H bonding 5σ orbital this is quite understandable) and there is a consistent lowering in the respective vibrational frequencies compared to the ground state $^2\Pi$.

In the first-row parallel NH^+ the dissociation pattern is again opposite to the PH^+ case: a neutral nitrogen atom plus a proton are the first dissociation fragments, instead of a phosphorus ion plus a hydrogen atom. The energy gap between $^4\Sigma^-$ and $X^2\Pi$ (only the first one correlating with the lowest dissociation channel) is notably smaller in NH^+ (0.07 eV) than in its second-row counterpart

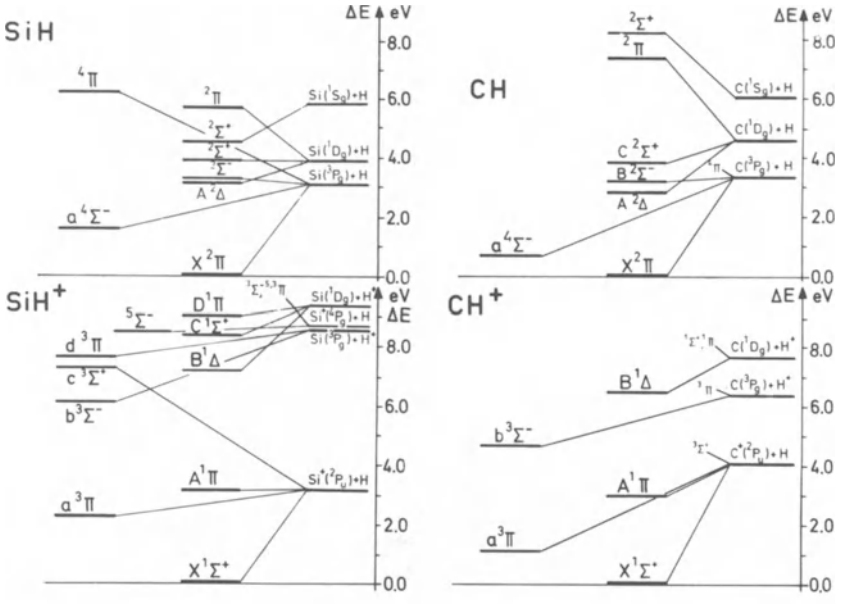

Fig. 10. Comparison of energy levels for the isovalent pairs SiH/CH and SiH^+/CH^+ and their relative position with respect to the lowest dissociation limits.

PH^+ (1.6 eV). The predissociation of the $^2\Delta$ and $^2\Sigma^+$ states via the $^4\Pi$ species might be present in NH^+ too, but another interaction of predissociative nature could occur for these states because of the presence of a repulsive second $^4\Sigma^-$ species, which is in the $^2\Pi$ vertical region lower-lying than does the $^4\Pi$. Both predissociations lead to the second NH^+ dissociation channel, but nonetheless a larger vibrational excitation is necessary to reach the interaction region in NH^+ compared to PH^+.

In the case of the SiH^+ molecular ion (Fig. 10) only four valence electrons are available, whereby 2π ionization of neutral SiH results in its closed-shell ground state $^1\Sigma^+(4\sigma^2 5\sigma^2)$. The $^{3,1}\Pi$, obtained by 5σ ionization, follow in the vertical region. While the $^3\Pi$ state shows a minimum at a slightly larger Si-H bond length, the singlet is almost dissociative. Ionization out of the strongly Si-H bonding 4σ gives rise to another pair of Π states to be found at considerably higher energies and with an equilibrium bond length almost 1.0 a_o larger than in the neutral system or the $^1\Sigma^+$ ground state. Again the singlet is much less bound than the triplet curve.

Because of the large difference in the IP's of Si and H as well as that between $Si(^2P_u)$ and the first excited state ^4P_g (both more

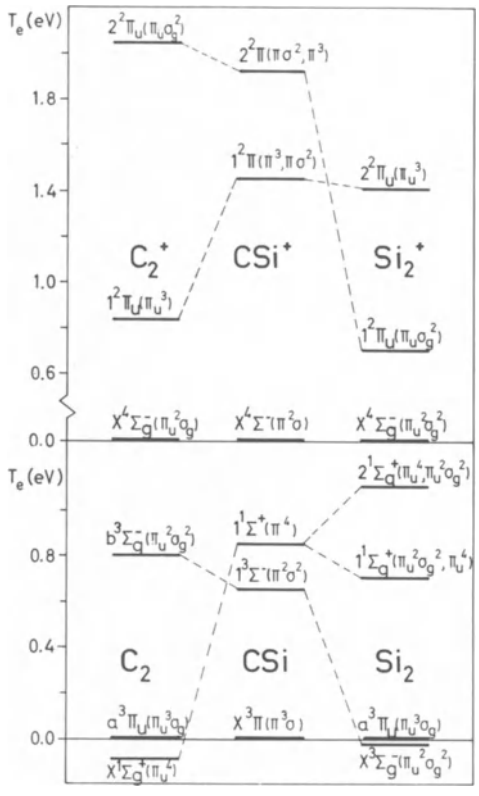

Fig. 11. Relative stabilities of the isovalent molecules C_2, CSi, and Si_2 and their corresponding positive ions in various low-lying electronic states. The data for the neutral species are taken from Ref. 25.

than 5 eV), and also the large energies required for 4σ ionization (ca. 5 eV more than necessary to ionize 5σ), there is a rather 'empty' region in the potential diagram between lowest states/dissociation products and the higher excited species. This area is crossed only by the strongly repulsive $^3\Sigma^+$ state ($4\sigma^2 5\sigma^1 6\sigma^1$), leading to $Si^+(^2P_u)$ + H dissociation. This is not the case in the CH^+ molecular ion for which the second and third dissociation channels are given by a neutral carbon plus a proton. Hence the correlation pattern for an energy region higher than ca. 4 eV above the corresponding AH^+ ground state is quite different in both systems in contrast to the similarity in the lower region.

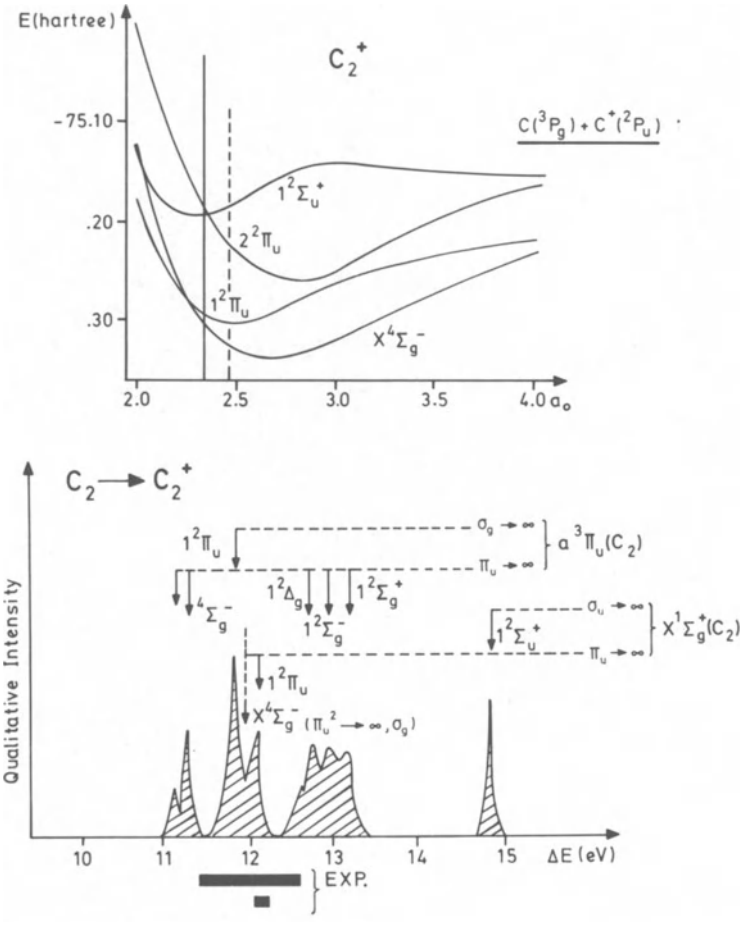

Fig. 12. Calculated potential energy curves of C_2^+ and schematic diagram for the energy and intensity distribution in the ionization process. The vertical lines in the upper diagram refer to the equilibrium bond length in the C_2 ground state (solid vertical line) and in its $a^3\Pi_u$ excited state (dashed vertical lines).

V. DIATOMIC IONS

A) C_2^+, CSi^+, and Si_2^+ (Systems with 7 Valence Electrons)

Before one analyzes the positive ions it is convenient to consider the isovalent neutral systems C_2, CSi, and Si_2, all possessing 8 valence electrons. Although the two homonuclear molecules have been studied spectroscopically [24], there is no such data available for the mixed CSi molecule. A recent MRD-CI *ab initio* study [25]

Table 5. Important Low-Lying Electronic States in the Isovalent Diatomic Molecules C_2, CSi, and Si_2 and their Positive Ions; the Calculated Vertical Ionization Potentials and the Change in Geometry upon Ionization are also Given

Species	Neutral state/ R_e (a_o)	Ionization	Ionic state	ΔR_e (a_o)	IP vert. (eV) [a]	Experim. (eV)
C_2	$X\ ^1\Sigma_g^+$	$\pi_u^2 \rightarrow \sigma_g, \infty$	$X\ ^4\Sigma_g^-$	+0.33	12.16(11.25)	12.0±0.6
	2.348	$\pi_u \rightarrow \infty$	$1\ ^2\Pi_u$	+0.18	12.16(11.97)	12.15 ± 0.05
		$\sigma_u \rightarrow \infty$	$1\ ^2\Sigma_u^+$	-0.02	15.01(15.01)	
	$a\ ^3\Pi_u$	$\pi_u \rightarrow \infty$	$X\ ^4\Sigma_g^-$	+0.20	11.45(11.16)	
	2.479	$\sigma_g \rightarrow \infty$	$1\ ^2\Pi_u$	+0.05	11.89(11.88)	
CSi	$X\ ^3\Pi$	$\pi \rightarrow \infty$	$X\ ^4\Sigma^-$	+0.16	8.82(8.62)	9.0±0.4
	3.307					9.2±0.4
		$\sigma \rightarrow \infty$	$1\ ^2\Pi$	~0.0	9.94(9.94)	
Si_2	$X\ ^3\Sigma_g^-$	$\sigma_g \rightarrow \infty$	$X\ ^4\Sigma_g^-$	+0.13	7.62(7.61)	7.3±0.3
	4.328	$\pi_u \rightarrow \infty$	$1\ ^2\Pi_u$	+0.49	8.48(8.24)	7.4±0.3
	$a\ ^3\Pi_u$	$\pi_u \rightarrow \infty$	$X\ ^4\Sigma_g^-$	+0.30	7.69(7.59)	
	4.157	$\sigma_g \rightarrow \infty$	$1\ ^2\Pi_u$	+0.66	8.53(8.14)	

a) values in parentheses refer to the corresponding adiabatic ionization potential.

has shown that each one of these molecules possesses a characteristic ground state and that three electronic configurations are important to describe the low-lying electronic states, namely $\pi_u^4(^1\Sigma_g^+)$, $\pi_u^3\sigma_g(^{3,1}\Pi_u)$ and $\pi_u^2\sigma_g^2(^3\Sigma_g^-,\ ^1\Delta_g,\ ^1\Sigma_g^+)$ which are carried over to CSi if one omits the subscripts u and g respectively. These calculations have pointed out that the $^3\Pi_u$ state is invariably low-lying in each system: it is the ground state in the mixed molecule CSi while it is located at only 0.089 eV above the $^1\Sigma_g^+$ ground state in the case of C_2 [24] and is also very close to the ground $X^3\Sigma_g^-(\pi_u^2\sigma_g^2)$ state in Si_2 whereby it should be pointed out that the $^3\Pi_u$ state in Si_2 has not yet been observed experimentally.

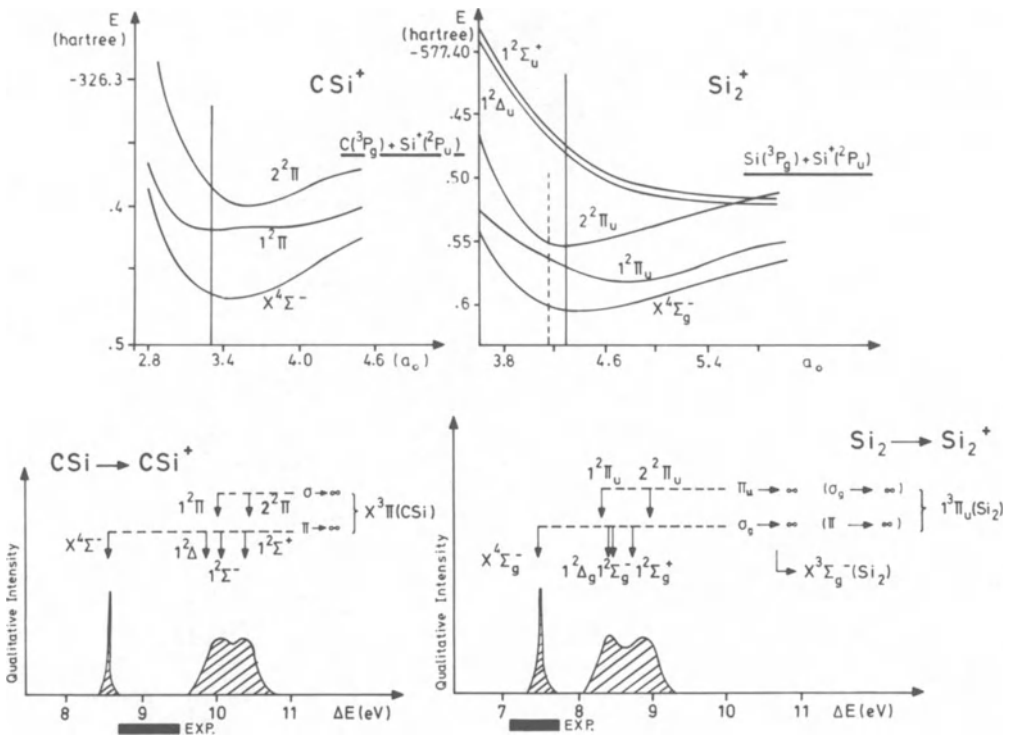

Fig. 13. Calculated potential energy curves for CSi^+ and Si_2^+ and schematic diagram for the energy and intensity distribution in the ionization processes. The vertical solid lines in the upper diagrams indicate the equilibrium bond length of the neutral systems while the dashed vertical line in Si_2^+ corresponds to R_e in $^3\Pi_u$ of Si_2.

As diagrammatically indicated in Fig. 11, one observes that in the series C_2, CSi, and Si_2 the energy gap between the $^3\Pi_u$ and the $^3\Sigma_g^-$ states is reduced from 0.8 eV in C_2 to a value practically equal to zero in Si_2. The ground state configuration π_u^4 of C_2 undergoes a complementary shift towards higher energies: it describes the second excited state in CSi while at the vertical region of Si_2 it mixes with the $^1\Sigma_g^+(\pi_u^2\sigma_g^2)$ multiplet.

All these findings indicate that the gradual substitution of a C atom by the homolog Si is accompanied by a tendency toward double occupany of the σ_g (slightly antibonding) species rather than the bonding π_u MO's. In accordance with the corresponding orbital features, the respective internuclear distances increase in the order $^1\Sigma_g^+ < {}^3\Pi_u < {}^3\Sigma_g^-$.

Under these circumstances the interesting question arises as to what extent the different stability pattern of these electronic configurations is carried over to the corresponding positive ions C_2^+, CSi^+, and Si_2^+. At present there are no photoelectron spectra available for these species to the best of our knowledge and therefore experimental efforts in this direction are welcome. Table 5 summarizes the most important electronic configurations involved and the respective calculated relative positions.

Recent calculations have shown that the ground state is invariably $^4\Sigma_g^-(\pi_u^2\sigma_g)$ for C_2^+ and Si_2^+ [26], while in the case of CSi^+ it is in analogy described by the $^4\Sigma^-(\pi^2\sigma)$ symmetry; these findings imply that the distinctions observed in the neutral species with respect to their ground state descriptions are not present in the corresponding ground states of the charged systems. Taking as reference the $^3\Pi_u(\pi_u^3\sigma_g)$ states in the neutral molecules, which have been observed to be of larger stability upon Si substitution, the present results also indicate a preferred ionization from the π_u MOs in the $\pi_u^3\sigma_u$ configuration and leading to the $\pi_u^2\sigma_g$ occupation in the ionized molecules.

With respect to other excited states, it is possible to describe two $^2\Pi_u$ states by the configurations π_u^3 or $\pi_u\sigma_g^2$. As indicated in Figs. 11-13, the first $^2\Pi_u$ state prefers the π_u^3 occupation in C_2^+ while in the homologous Si_2^+ the $\pi_u\sigma_g^2$ configuration dominates in the lowest state. The corresponding 2 $^2\Pi_u$ state is described in each case by the other configuration. This behavior again reflects the stabilization of those electronic configurations in which the σ_g MO is doubly occupied when carbon is replaced by silicon. As result of these orbital stability features it is found that an avoided crossing between the $^2\Pi_u$ states takes place in different regions relative to the equilibrium bond lengths of the ionic ground state. As shown in Figs. 12 and 13, the crossing in CSi^+ occurs approximately at the vertical region close to the minimum of 1 $^2\Pi$ while in C_2^+ the equilibrium distance of 1 $^2\Pi_u(\pi_u^3)$ is much shorter than that of $^4\Sigma_g^-$; finally, in the case of Si_2^+ the 1 $^2\Pi_u(\pi_u\sigma_g^2)$ state is characterized by a larger internuclear distance.

The tendency to occupy the π_u MO in the case of C_2 (or C_2^+) is also reflected in the 1 $^2\Sigma_u^+(\sigma_u\pi_u^4)$ state, with an equilibrium distance very similar to the neutral ground state, while in Si_2^+ by contrast the above configuration does not contribute at all to the lowest $^2\Sigma_u^+$ state.

After these general considerations each systems will be discussed in more detail:

a) C_2^+

As seen in Table 5, the transition between the neutral and the ionic ground states requires a double excitation ($\pi_u^2 \rightarrow \infty$, σ_g) and therefore is expected to appear with very low intensity in the experimental spectrum, a situation which is enhanced by the unfavorable Franck-Condon factors arising from the relatively large difference in the interatomic distance in these two states (Fig. 12). On the other hand, the transition $X^1\Sigma_g^+(C_2) \rightarrow 1\ ^2\Pi_u(C_2^+)$ involves a single ionization process $\pi_u \rightarrow \infty$ and is accompanied by a smaller change in the bond length as before. The vertical IP's for the last two mentioned processes are practically the same (i.e., 12.16 eV, vertical, Table 11) because the $^4\Sigma_g^-$ and $1\ ^2\Pi_u$ potential curves cross approximately at the equilibrium distance of C_2. The third IP relative to $X^1\Sigma_g^+$ is connected with a σ_u ionization, leading to the $1\ ^2\Sigma_u^+$ state, placed vertically at about 15.01 eV and possessing practically the same geometrical features as the $^1\Sigma_g^+$ state.

It is experimentally known that in C_2 the first excited $^3\Pi_u$ state is placed only 0.089 eV above the ground state and therefore it can be populated to some extent when the temperature is raised, as has already been done in some of the experimental measurements. Under these conditions the ionization $\pi_u \rightarrow \infty$ from the $^3\Pi_u$ leads directly to $X\ ^4\Sigma_g^-$, and as indicated in Table 11, with a vertical IP lying at 11.45 eV and a bond length change Δr_e of 0.20 a_o. The next ionization from σ_g in $^3\Pi_u$ yields the $1\ ^2\Pi_u(\pi_u^3)$ state, which is placed at 11.89 eV in the vertical region and this ionization is characterized by the smallest change in the C-C distance.

On the basis of these results, one can explain the experimentally reported IP of C_2 lying at 12.0 ± 0.6 eV [27] or 12.15 ± 0.05 eV (28) as resulting from the overlap of two ionization processes, namely the $X\ ^1\Sigma g^+ \rightarrow 1\ ^2\Pi_u$ and a $^3\Pi_u \rightarrow 1\ ^2\Pi_u$, respectively, as shown schematically in the lower part of Fig. 12. These ionization process leading to the $X\ ^4\Sigma_g^-$ is also accompanied by possible multiplets $^2\Delta_g$, $^2\Sigma_g^-$, and $^2\Sigma_g^+$, all of them corresponding to $\pi_u^2\sigma_g$ occupation. These states are placed approximately in the 13 eV energy region.

b) CSi^+

In this case both the neutral and the ionic ground states are simply related by a π ionization. The calculated value of 8.82 eV for the vertical process agrees well with the experimental results lying in the 9.0 ± 0.4 eV ionization region [29] (Table 5).

The second ionization process involving the σ MO could be more complicated because upon ionization the portion of the potential curve is reached in which the avoided crossing between the $^2\Pi$ states

occurs and therefore a broad structure in the PES can be expected. The last observation is reinforced by the fact that the other multiplets $^2\Delta$, $^2\Sigma^+$, and $^2\Sigma^-$ with the same electronic configuration as the X $^4\Sigma^-$ ground state are found in the same energy region: they are placed in the 9.7-10.5 eV ionization region, while the ionization into 1 $^2\Pi$ is found at 9.94 eV.

c) Si_2^+

The X $^4\Sigma_g^-$ state is derived from X $^3\Sigma_g^-$ (Si_2) upon direct $\sigma_g \rightarrow \infty$ ionization. The theoretical value of 7.61 eV is comparable with the experimental inference of 7.4 ± 0.3 eV [29]. The other multiplets $^2\Delta_g$, $^2\Sigma_g^-$, and $^2\Sigma_g^+$ are clustered in the 8.4-8.8 eV photoionization region. The second process $\pi_u \rightarrow \infty$ leads to 1 $^2\Pi_u$, with an adiabatic value of 8.24 eV and therefore almost superimposed over the mentioned doublet states.

Because of the isoenergetic position of the X $^3\Sigma_g^-$ and $^3\Pi_u$ states in Si_2, it is also possible to detect ionizations from the latter neutral species. The final ionic levels are the same as when one ionizes from the ground state, but the MO's involved are exchanged. In accordance with the results in Table 5, it is found that the variations in the respective equilibrium distances are larger when one considers the excited $^3\Pi_u$ state.

In general, more resemblance is expected between the photoelectron spectra of CSi and Si_2, while in C_2 a quite different structure must be observed (see Figs. 12 and 13). This point also awaits the corresponding experimental verification.

B) CN^+, CP^+, and NSi^+ (Systems with 8 Valence Electrons)

Another interesting group of diatomic molecules are the isovalent CN, CP, and NSi radicals with 9 valence electrons, which are invariably described by a X $^2\Sigma^+(\pi^4\sigma)$ and a first $^2\Pi(\pi^3\sigma^2)$ excited state. As indicated in Fig. 14, substitution of each one of the first-row atoms by the corresponding isovalent atom of the second row leads to a reduction of the energy gap between $^2\Pi$-$^2\Sigma^+$: in CN a T_e of 1.15 eV [24] is experimentally reported (i.e., with a T_e (calc.) = 1.09 eV), while in CP it is slightly lowered (T_e (exp) = 0.86 eV [24] versus T_e (calc.) = 0.94 eV), and the analogous energy difference is drastically reduced when one replaces the C atom in CN by Si (T_e (calc.) = 0.28 eV; experimental data are yet not available). The tendency toward double occupation of the σ species is again observed in the silicon compound and runs parallel with the findings pointed out in the last section A.

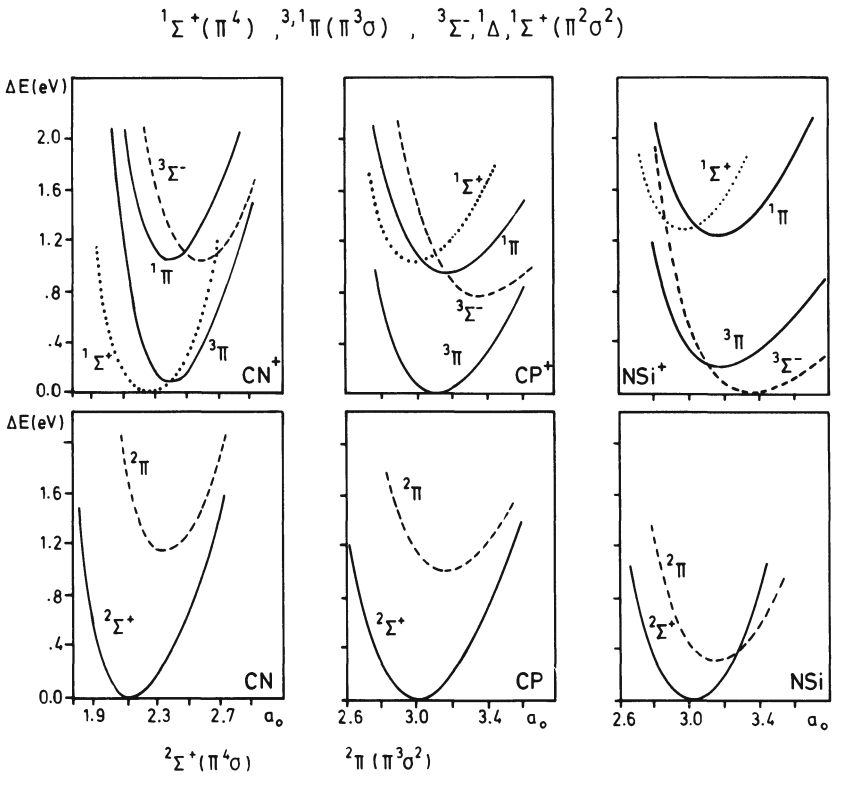

Fig. 14. MRD-CI potential energy curves calculated for the isovalent radicals CN, CP, and NSi and their respective positive ions. More details for the charged systems are given in Ref. [25].

We now consider possible ionizations from the $^2\Sigma^+$ neutral ground state

$$^2\Sigma^+(\pi^4\sigma) \rightarrow {}^1\Sigma^+(\pi^4) \qquad \sigma \rightarrow \infty$$
$$^{3,1}\Pi(\pi^3\sigma) \qquad \pi \rightarrow \infty,$$

whereas if one considers the formal ionization from the excited $^2\Pi$ state, the following manifold of ionic states is expected:

$$^2\Pi(\pi^3\sigma^2) \rightarrow {}^{3,1}\Pi(\pi^3\sigma) \qquad \sigma \rightarrow \infty$$
$$\rightarrow {}^3\Sigma^-, \ {}^1\Delta, \ {}^1\Sigma^+(\pi^2\sigma^2) \qquad \pi \rightarrow \infty$$

Extensive calculation on CN^+, CP^+, and NSi^+ [25] have indicated that each one of these isovalent species possesses a particular ground state, namely $^1\Sigma^+(CN^+)$, $^3\Pi(CP^+)$, and $^3\Sigma^-(NSi^+)$, in very close analogy with the isovalent molecules C_2, CSi, and Si_2, respectively.

Table 6. Calculated Relative Positions (in eV) for the Various Adiabatic Ionization Peaks in the Isovalent Radicals CN, CP, and NSi. The Corresponding Increase in the Bond Length is also Given

Species	Neutral state/ R_e (a_o)	Ionization	Ionic state	ΔR_e (a_o)	Relative position[a] in eV
CN	X $^2\Sigma^+$	$5\sigma \rightarrow \infty$	X $^2\Sigma^+$	0.05	0.0 (13.76)[b]
	2.21	$1\pi \rightarrow \infty$	$^3\Pi$	0.17	0.1-0.15
			$^1\Pi$	0.19	1.03
		$1\pi^2 \rightarrow (5\sigma, \infty)$	$^3\Sigma^-$	0.36	0.91
CP	X $^2\Sigma^+$	$2\pi \rightarrow \infty$	X $^3\Pi$	0.17	0.0 (10.9)[b]
	2.95		$^1\Pi$	0.22	0.91
		$7\sigma \rightarrow \infty$	$^1\Sigma^+$	0.04	0.98
		$2\pi^2 \rightarrow (7\sigma, \infty)$	$^3\Sigma^-$	0.41	0.74
NSi	X $^2\Sigma^+$	$2\pi^2 \rightarrow (7\sigma, \infty)$	X $^3\Sigma^-$	0.45	0.0 (9.8)[b]
	2.97	$2\sigma \rightarrow \infty$	$^3\Pi$	0.26	0.21
			$^1\Pi$	0.22	1.25
		$7\sigma \rightarrow \infty$	$^1\Sigma^+$	0.0	1.22

a) T_e values taken from reference 25.
b) Energy differences between the respective minima in the neutral and positive diatomic.

a) CN^+

There is no experimental information concerning the electronic description of the ground state of this radical, although some intercombination lines are found in the literature [24, 30]. A detailed study [8] of the relative stability of the $^1\Sigma^+$ and $^3\Pi$ states with respect to different theoretical treatments has indicated that the use of an extended AO basis and an adequate set of reference configurations yields as a result that the ground state is almost certainly $^1\Sigma^+$ (π^4) state, while the $^3\Pi$ ($\pi^3\sigma$) is placed about 0.1-0.15

eV higher in energy. Earlier calculations from the literature were ambiguous on the relative position, however [8].

As indicated in Table 6 there is practically no change in the bond length when one ionizes the 5σ MO in CN to give $^1\Sigma^+$ (CN^+). On the other hand the second IP (1π removal) for the $^3\Pi$ state corresponds to an increase of 0.17 a_o in bond length and therefore a vibrational progression is expected for this process.

Ab initio calculations carried out in this laboratory at the equilibrium geometry of CN ($^2\Sigma^+$) (r_e = 2.21 a_o) give values of 13.77 eV and 14.07 eV for the transition into $^1\Sigma^+$ and $^3\Pi$ respectively, which are expected to underestimate the experimental results by about 0.2-0.3 eV; therefore the corresponding vertical IP's are predicted to lie in the 14.0 eV and 14.3 eV energy region. The small energy difference of 0.3 eV between the first two ionization processes is further reduced to 0.1-0.15 eV if one considers the corresponding adiabatic transitions. Various experimental results place the first ionization region within the 14.0-14.2 eV interval [24, 31]. The question thus arises to what extent the experimental measurements are actually a combination of the superposition of the first two ionization processes.

A possible formal way to elucidate this question could be the ionization of CN in its excited $^2\Pi$ state. As indicated before, the first IP in this case only originates from the $^3\Pi$ state, and this information combined with the corresponding IP's from the ground state and the well-known $^2\Pi$-$^2\Sigma^+$ excitation energy in CN can be used to characterize the nature of the CN^+ ground state. The $^1\Pi$ state, also derived from 1π ionization is predicted to be placed at 1.03 eV above the ground state (adiabatically), also in good agreement with spectroscopic measurements [30].

b) CP^+

The first ionization of CP ($^2\Sigma^+$) is associated with the 2π MOs, leading to the CP^+ ($^3\Pi$) ground state and underscores the stabilization of the σ MO on going from CN to CP. In the present CI calculations an adiabatic value of 10.9 eV is predicted, which in turn suggests that the corresponding experimental results are expected to lie around 11.2 eV, although this expectation awaits experimental investigation.

The $^1\Pi$ counterpart is placed 0.91 eV above the ground state and, as shown in Table 6, lies very close to the $^1\Sigma^+$ state obtained by ionization from the 7σ MO CP ($^2\Sigma^+$). Finally, it should be pointed out that the first excited state $^3\Sigma^-$ in CP^+ is not connected directly with the CP ground state; it implies a $\pi^2 \rightarrow (\infty, 7\sigma)$ transition and a relatively larger increase in internuclear distance, a situation which suggests a very low photoionization cross-section.

c) NSi^+

The ground state of this ion is precisely a $^3\Sigma^-$ state and therefore, the last observation made for CP^+ (namely weak intensity) is also valid here. The first ionization from 2π leads to the $^{3,1}\Pi$ states, with a multiplet splitting predicted to be of the order of 1 eV and an elongation of the NSi bond of about 0.25 a_o. The $^3\Sigma^-$ ground state, which is placed 0.21 eV below the $^3\Pi$ minimum [25] crosses the upper state at $r_e \simeq 3.1$ a_o and therefore perturbations are expected to be present in the first ionization region. The ionization from the 7 σ MO has a favorable Franck-Condon factor and is expected to lie (adiabatically) in the 11 eV energy region. As indicated in Table 6, the T_e values for $^1\Pi$ and $^1\Sigma^+$ are practically the same and this suggests a broad structure in the corresponding spectrum.

Because the energy difference between the $^2\Pi$-$^2\Sigma^+$ is predicted to be very small, it maybe of interest to ionize the excited $^2\Pi$ state; in this case both the $^3\Sigma^-$ ground state and $^3\Pi$ are accessible and as discussed above for CN, experiments of this kind could be appropriate for the determination of the correct ordering for the electronic states of the respective molecular-ions.

VI. Molecular-Ions of the Type HAB^+ and ABH^+

We now wish to direct our attention to those HAB^+ isomers pairs containing the following heavy atoms, namely one coming from the first and the other from the second row, respectively:

CSi	NSi	OSi
CP	NP	OP
CS	NS	OS

If one considers the corresponding neutral HAB, ABH species (18 in total), it is found that only four isomers are actually known experimentally, namely HCP ($^1\Sigma^+$), HNSi ($^1\Sigma^+$), HPO ($^1A'$), and HSO ($^2A''$). On going to the respective 18 positive ions, one finds that there is no experimental information, with the exception of the appearance potentials in some cases.

In recent times some theoretical work has been carried out on these mixed first/second-row systems [32-35] and it was observed that the isomerization energies are larger than the corresponding values assigned to those systems containing first-row atoms only, at least for those species possessing a linear equilibrium geometry. As an example of this behavior it can be mentioned that the isomerization energy of 68 kcal/mole and of 110.9 kcal/mole predicted for HNSi-NSiH and HCS^+-CSH^+, respectively, are much greater than the

Table 7. Survey of the HAB^+ Ions Treated in the Present Work and Information on Their Low-Lying Electronic States

Valence electrons/ species	Electronic configuration	States	Geometry	Equiv. systems from first row
8				
$HCSi^+$, $CSiH^+$	$7\sigma^2\ 2\pi^2$	$^3\Sigma^-$, $^1\Delta$, $^1\Sigma^+$	$C_{\infty v}$	HC_2^+
	$7\sigma^1\ 2\pi^3$	$^3,^1\Pi$		
$HNSi^+$, $NSiH^+$	$7\sigma^2\ 2\pi^3$	$^2\Pi$	$C_{\infty v}$	HCN^+, CNH^+
HCP^+, CPH^+	$7\sigma^1\ 2\pi^4$	$^2\Sigma^+$	$C_{\infty v}$	
10				
$HOSi^+$, $OSiH^+$	$7\sigma^2\ 2\pi^4$	$^1\Sigma^+$	$C_{\infty v}$	HCO^+, COH^+
HNP^+, NPH^+				HN_2^+
HCS^+, CSH^+				
11				
HOP^+, OPH^+	$9a'^2 2a''^2 10a'$	$^2A''$	C_s	HNO^+, NOH^+
HNS^+, NSH^+	$(7\sigma^2\ 2\pi^4\ 3\pi)$	$(^2\Pi)$	$(C_{\infty v})$	
12				
HOS^+, OSH^+	$\ldots 10a'3a''$	$^3,^1A''$	C_s	HO_2^+
	$\ldots 10a'^2$	$^1A'$		
	$(7\sigma^2\ 2\pi^4\ 3\pi^2)$	$(^3\Sigma^-, ^1\Delta, ^1\Sigma^+)$	$C_{\infty v}$	

values of 10 kcal/mole and 36 kcal/mole assigned to the HCN-CNH and HCO^+-COH^+ counterparts respectively. In addition, a recent MRD-CI study [34] carried out at the linear geometries of $HCSi^+$-$CSiH^+$ and HNP^+-NPH^+ has pointed out that the relative energies are of the order of 70-90 kcal/mole respectively, while on going to those species for which a bent structure is preferred as, for example, in HNP,

Table 8. Equilibrium Geometries and Relative Stability for Various HAB^+ Systems Obtained from the MRD-CI Calculations

System	R_{AB} (a_o)	R_{AH} (a_o)	Angle (degr)	Rel. stability (kcal/mole)	Isoval. syst. of first row Rel. stability (kcal/mole)
$HCSi^+$ $^3\Sigma^-$	3.42	2.10	180	0.0	$HC_2^+(^3\Pi)\Delta E = 0$
$CSiH^+$ $^3\Sigma^-$	3.53	2.88	(180)[a]	68.8	(Ref. 41)
$HNSi^+$ $^2\Pi$	3.17	1.93	180	0.0	$HNC^+(^2\Sigma^+)$ 0.0
$NSiH^+$ $^2\Pi$	3.16	2.78	(180)[a]	72.6	$HCN^+(^2\Pi)$ 20.7
HCP^+ $^2\Pi$	3.06	2.04	180	0.0	(Ref. 40)
CPH^+ $^2\Sigma^+$	2.91	2.66	(180)[a]	83.2	
$HOSi^+$ $^1\Sigma^+$	2.95	1.82	180	0.0	$HCO^+(^1\Sigma^+)$ 0.0
$OSiH^+$ $^1\Sigma^+$	2.86	2.79	(180)[a]	70.0	$COH^+(^1\Sigma^+)$ 36.0
HNP^+ $^1\Sigma^+$	2.79	1.92	180	0.0	$HN_2^+(^1\Sigma^+)\Delta E = 0$
NPH^+ $^1\Sigma^+$	2.87	2.67	(180)[a]	87.4	
HCS^+ $^1\Sigma^+$	2.81	2.06	180	0.0	
CSH^+ $^1\Sigma^+$	3.10	2.60	(180)[a]	110.9	
HOP^+ $^2A'$	2.94	1.86	126	0.0	$HNO^+(^2A')$ 0.0
OPH^+ $^2A'$	2.86	2.73	100	32.4	$NOH^+(^2A')$ 17.5
HNS^+ $^2A'$	2.87	1.96	131	0.0	(Ref. 37)
NSH^+ $^2A'$	2.99	2.62	98.8	36.4	
HOS^+ $^3A''$	2.97	1.85	120	0.0	$HO_2^+(^3A'')\Delta E = 0$
OSH^+ $^1A'$	2.81	2.61	102	15.4	(Ref. 52)

a) No angular geometry search has been undertaken in these cases, a bent structure or even a preferred energy path to the more stable isomer as well-known for HCS^+-HSC^+ for example is expected.

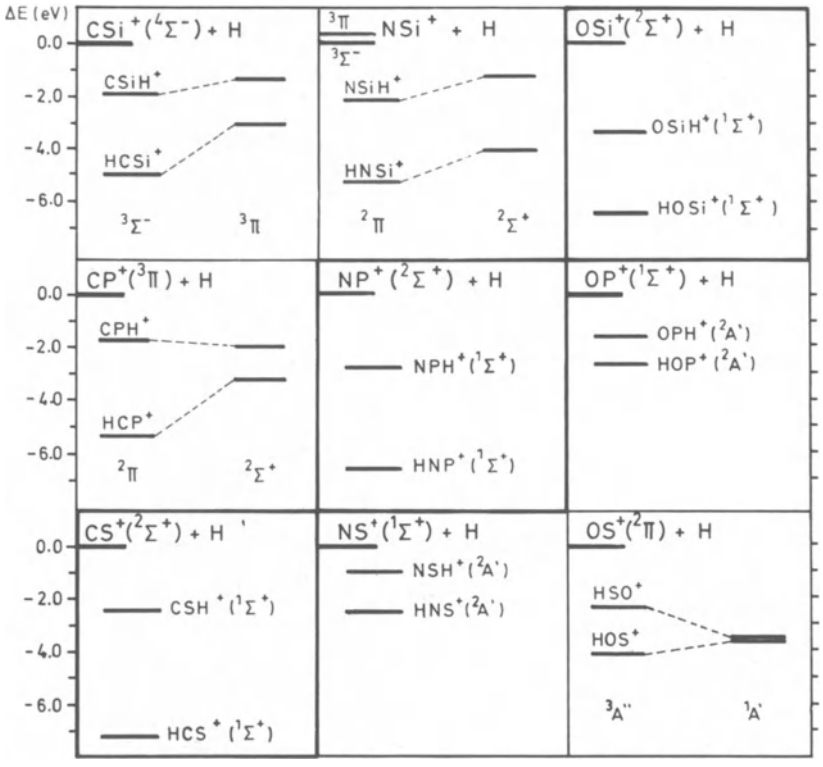

Fig. 15. Comparison of various HAB^+ isomers pairs in their lowest electronic states and correlation to the parent diatomic AB^+ ion.

HOS^+, HOS, $HOCl^+$, and the respective isomers, values ranging from 10-40 kcal/mole for the relative stability are obtained.

Finally, for these HAB systems it is expected that the most stable isomer is that in which the heavy atom is located at the terminal position of the molecule. In this connection it should be pointed here that although the HOS isomer is predicted to be lowest lying, the fact is that only the other isomer OSH has as yet been isolated. At the same time in the case of HPO one finds a true exception to this general rule in the relative stabilities, i.e., with phosphorous slightly preferred in the central position, as will be discussed subsequently.

The aim of the present investigation is the theoretical determination of the equilibrium geometries and the relative energies of all the remaining molecular-ions not yet explicitly studied. The electronic character of the ground state was also investigated in

those cases in which more than one electronic configuration is expected to be important. Table 7 summarizes the electronic structure for the molecular-ions considered while the geometrical parameters at equilibrium and the corresponding relative energies are listed in Table 8 while a diagram showing the relative energies between the various HAB^+ isomers pairs and their respective dissociation limits $AB^+ + H$ is given in Fig. 15.

a) HOS^+ and OSH^+ (12 Valence Electrons)

In all HAB molecules possessing 12 ve one has a π^2 occupation in the linear geometry, which correlates with the configurations (a' a"), (a'^2), and ($a"^2$) in the lower C_s symmetry. In general the various a' MO's acquire stabilization upon bending through hydrogen admixture, but the degree of such energy stabilization depends on the nature of the H-A bond involved. For the present systems under consideration, the last π MO in the diatomic AB is more concentrated on the second-row atom, while the lowest π MO is complementarily shifted toward the first-row center. In other words, it is expected that the last a' MO acquires a larger stabilization upon bending if the hydrogen atom is bonded to a second-row element, while if the A-H bond involves one of the atoms, C, N, or O, other low-lying a' species rather than the highest occupied species are affected by the bending motion.

In each isomer the natural ordering of states in the linear geometry is $^3\Sigma^-(^3A")$ and $^1\Delta(^1A', {}^1A")$. Upon bending both $^{3,1}A"$ components run quite parallel to each other, while the $^1A'$ state, with double occupation of the last stable a' MO, has the possibility of acquiring a larger or a smaller stabilization, depending on the character of the AH bond involved. For example, it is known that while the most stable HNO possesses a $^1A'$ ground state, its NOH counterpart prefers $^3A"$ electronic character (single occupation of the a' MO) [36]. However, according to results from this laboratory, the HPO-POH pair is an exception of the feature of relative stability: while the POH ($X\ ^3A"$) state is more stable than the equivalent state of HPO, the larger stabilization of the 10 a' MO in HPO leads finally to a $^1A'$ ground state, placed 0.3 eV <u>below</u> the ground state of POH.

In the present case of HOS^+ and OSH^+ one notes that the most stable species is the $^3A"$ (HOS^+), while the ground state of OSH^+ is a $^1A'$, placed at 15.4 kcal/mole above the other isomer. The corresponding $^1A'$ level in HOS^+ is practically isoenergetic with the ground state of OSH^+, as given by a T_e of 13.2 kcal/mole [34].

Taking as reference the results published elsewhere [34] for the neutral and positive ions in both the HOS and OSH nuclear arrangements, it is possible to derive the various adiabatic ionization potentials, and such values are summarized in Table 9. In HOS

Table 9. Adiabatic Ionization Potentials Predicted for HOS, HNP, HCSi and Their Corresponding Isomers Obtained from the MRD-CI Calculations

Neutral system	Ionization	Ionic system	IP (eV)	Remarks
HOS (^{2}A") 10a'^{2}3a"	10a' → ∞	HOS^+ (^{3}A")	9.31	
E = 0	3a" → ∞	HOS^+ (^{1}A')	9.88	
	10a' → ∞	HOS^+ (^{1}A")	10.37	
OSH (^{2}A") 10a'^{2}3a"	3a" → ∞	OSH^+ (^{1}A')	9.55	
ΔE = +9.7 kcal/mole	10a' → ∞	OSH^+ (^{3}A")	10.65	
	10a' → ∞	OSH^+ (^{1}A")	11.19	
HNP (^{2}A') 10a'	10a' → ∞	HNP^+ ($^1\Sigma^+$)	7.05	Very long progression in the bending motion due to an opening of 60° in HNP and 80° in HPN. The vert. IP can be 0.5-0.8 eV higher.
E = 0				
NPH (^{2}A') 10a'	10a' → ∞	NPH^+ ($^1\Sigma^+$)	9.75	
ΔE = 25.3 kcal/mole				
HCSi ($^2\Pi$) $2\pi^3$ $7\sigma^2$	2π → ∞	$HCSi^+$ ($^3\Sigma^-$)	8.51	$^1\Delta$ (9.48)
E = 0				$^1\Sigma^+$ (10.03)
	7σ → ∞	$HCSi^+$ ($^3\Pi$)	10.31	$^1\Pi$ (10.92)
CsiH ($^2\Pi$) $2\pi^3$ $7\sigma^2$	2σ → ∞	$CSiH^+$ ($^3\Sigma^-$)	8.83	$^1\Delta$ (9.50)
ΔE = 61.4 kcal/mole				$^1\Sigma^+$ (9.73)
	7σ → ∞	$CSiH^+$ ($^3\Pi$)	9.42	$^1\Pi$ (10.70)

it is observed that an energy difference of 0.5 eV exists between the first (10 a' → ∞) and the second (3a" → ∞) ionization potentials and this contrasts with an inverted ordering and a larger ΔE (1.0 eV) between the first two ionization peaks in the OSH counterpart. The last observation is in agreement with a larger stabilization of the 10 a' component (SH bond) in comparison with the 3a" MO.

Finally, it should be emphasized that these systems with 12 ve can only be treated realistically by means of a theoretical method which considers correlation effects. As discussed in detail elsewhere for the HNO-NOH isomers [36], the SCF method leads to excessively larger stabilities for triplet states.

b) HOP^+-OPH^+ and HNS^+-NSH^+ (11 Valence Electrons)

In these systems the ground state is invariably a $^2A'$ (10 a'), with equilibrium angles varying in the 125-130 degree region if the first-row atom is placed in the middle of the molecule, while it has a value around 100 degree if the central atom comes from the second row of the periodic table. The same observation is valid for HOS^+ ans OSH^+ (see Table 8).

The HOP^+ isomer is found to be more stable than OPH^+ by 32.4 kcal/mole and this result is in accordance with the general tendency of attributing larger stability to that isomer in which the hydrogen atom is bonded with a first-row atom. Because in this case one has only a single configuration to be considered, this point is clearly apparent, while in the neutral species this rule is somewhat less clear because of the possibility of choosing between the two configurations $^1A'$ (10 a'^2) or $^3A''$ (10a' 3a"), the first of which is effectively preferred in the HPO arrangement.

The other isomers HNS^+ and NSH^+ also fit into this general scheme, with an isomerization energy of 36.4 kcal/mole having been calculated. It should be noted that these two isomerization energies are twice the corresponding value predicted theoretically for the HNO^+-NOH^+ isomers (ΔE = 17.5 kcal/mole, Ref. [37]).

c) $HOSi^+$-$OSiH^+$, HNP^+-NPH^+, and HCS^+-CSH^+ (10 Valence Electrons)

As indicated in Table 8, the isomerization energies are very large for such systems; it is around 70 kcal/mole for the silicon compound and it increases successively by roughly 20 kcal/mole when one goes to the phosphorus and finally to the sulfur atom, with the highest isomerization energy of 110.9 kcal/mole observed for these mixed HAB species.

According to Walsh's rules, it is expected that these molecular ions possess a linear $^1\Sigma^+$ ground state, but because of the greater difference in their respective stabilities, one can suppose that the high-lying isomer is slightly or even strongly unstable relative to the bending motion, that is without showing any kind of energy restriction for a total conversion into the most stable isomer. It is of interest to note that the isovalent HNSi-NSiH and HCP-CPH systems are also characterized by quite different total energies at each of their equilibrium nuclear conformations, as compared with the smaller distinctions assigned to HCN-CNH or HCO^+-COH^+, as discussed previously.

A very interesting aspect which requires corresponding experimental verification is the following. The neutral radicals HOSi, HNP, and HCS, and their isomers follow similar trends as those ions with 11 valence electrons, especially as regards their geometry and relative stabilities. This fact implies that ionization from the most stable (neutral) nuclear conformation must be characterized by a long progression in the bending mode (i.e., the molecular angle is opened by about 50-60 degree upon ionization), and therefore a larger difference between the vertical and adiabatic IPs must be present, which can be roughly estimated to be of the order of 0.5-0.8 eV. By contrast in the case of the less stable neutral conformation, the corresponding ionization must necessarily be accompanied by a drastic nuclear rearrangement towards the other low-lying positive ion; upon ionization the ionic potential surface is reached at a portion in which the more stable HAB^+ system is strongly favored. Finally, it should be pointed out that a recent determination of the ionization potential in HCO leads to an energy gap of about 1 eV between the vertical and adiabatic peaks, while the band intensity is distributed over at least twenty vibrational components [38].

d) $HNSi^+$-$NSiH^+$ and HCP^+-CPH^+ (9 Valence Electrons)

While in the last section the electronic configurations $\pi^4\sigma^2$ was the only one to be considered, in going to species with 9 ve one must study both the $^2\Pi$ ($\pi^3\sigma^2$) and $^2\Sigma^+$ ($\pi^4\sigma$) species. In the case of HCP^+ it is found that the lowest state is the $^2\Pi$, while the $^2\Sigma^+$ is placed 2.13 eV above it, in good agreement with an experimental difference between the two first IP's of 2.07 eV [39]. The less stable isomer CPH^+ is found to lie 83.2 kcal/mole higher in its $^2\Sigma^+$ state, while the $^2\Pi$ (CPH^+) state is placed only 3.7 kcal/mole above the latter species. This small energy difference between the two low-lying states in CPH^+ suggests that a very complicated picture must be obtained if one considers a coupling among the stretching and the bending motions in this relatively unstable system.

Both $HNSi^+$ and $NSiH^+$ possess $^2\Pi$ ground states, the first one being favored by 72.6 kcal/mole. According to the present calculations, the second IP in HNSi leading to $^2\Sigma^+$ should be found at 1.25 eV higher than the first one, while the relative energy between the $^2\Sigma^+$ states in both nuclear arrangements is also rather high, namely 65.5 kcal/mole. As discussed before for the phosphorus compounds, it is suggested here that a slight perturbation of the less stable species leads directly to the $HNSi^+$ isomer.

Recent calculations on HCN^+ and CNH^+ [40] have pointed out that the ground state of CNH^+ is a $^2\Sigma^+$, which is placed 20.7 kcal/mole below HCN^+ (X $^2\Pi$). These results indicate that after ionization the relative stability of the HCN and CNH conformations is reversed.

One observes in this case that for the mixed HAB molecules always the conformation with the second-row atom at the terminal position of the molecules are prefered for both the neutral and the positive ions.

e) $HCSi^+$-$CSiH^+$ (8 Valence Electrons)

There are here two configurations to be considered, namely $\pi^2\sigma^2$ ($^3\Sigma^-$, $^1\Delta$, $^1\Sigma^+$) and $\pi^3\sigma$ (^{3},$^1\Pi$). The MRD-CI calculations indidicate that both isomers possess a $^3\Sigma^-$ ground state [34], but the $HCSi^+$ compound is placed 86.8 kcal/mole below the $CSiH^+$ counterpart, a value which is comparable with the stability difference of 61.4 kcal/mole predicted for the corresponding neutral states [34]. By contrast the ground state of HC_2^+ is a $^3\Pi_u$ ($\pi_u{}^3\sigma_g$) state [41], again denoting the preferred tendency to occupy the π_u MO in those compounds containing atoms of the first row.

The ionization potential associated with the process HCSi ($^2\Pi$) → $HCSi^+$ ($^3\Sigma^-$) of 8.51 eV compares with a value of 8.61 eV calculated in the case of the CSi ($^3\Pi$) → CSi^+ ($^4\Sigma^-$) transition. The other peaks associated with ionization from the 2π in HCSi are placed at 9.48 eV ($^1\Delta$) and 10.03 eV ($^1\Sigma^+$), while both the triplet and singlets states obtained after ionization from the 7 σ MO are found at 10.35 eV and 10.92 eV, respectively (see Table 9).

VII. Summary

The present contribution has demonstrated in numerous examples the feasibility of present-day theoretical methods for the calculation of structural data for positively charged molecular-ions as well as their relative energetics in a variety of electronic states and nuclear conformations. In addition it has provided numerous predictions of the characteristics of various molecular-ions which await experimental verification. The applications chosen have been restricted to rather small ions with at most two hydrogen and no more than two non-hydrogenic atoms, for which a variety of qualitative interrelationships have been underscored, but it should be emphasized that the same theoretical techniques can also be employed effectively to study larger systems and also for multiply ionized species, especially when special features which make use of a simple form of perturbation theory to correct the raw CI results are taken into account, as discussed at the beginning of the paper.

In the present context it will suffice to give a brief summary of such results for some larger molecular-ions. MRD-CI calculations for selected nuclear conformations of CH_4^+ [42] and for different dissocation paths into $CH_3^+ + H$ and $CH_2^+ + H_2$ have confirmed the experimentally observed low photodissociation cross sections, arising because of the existence of either barriers, ineffective state correlation or low oscillator strengths for all available reaction

paths. In the case of $C_2H_6^+$ [43] the ground state is a pure $^2A_{1g}$ species with a larger CC distance than in the neutral C_2H_6, but at shorter R_{CC} values it becomes a mixture of $^2A_{1g}$ and ^2E_g character through reduction in the molecular symmetry. The first excited ^2B_g species (C_{2h} structures) correlates with ^2E_g in D_{3d} symmetry but is Jahn-Teller distorted. A Franck-Condon analysis of the calculated potential curves indicates that the spectrum for ionization to the lowest ^2A_g species is too diffuse and of wrong characteristic frequency to be attributed to the fairly regular fine structure of the ethane PES within the 11.5-12.6 eV energy region. By contrast the analogous results for ^2B_g ionization do compare quite well with the latter experimental system. In addition the calculations of vertical IPs have been extended [44] to include ionization out of the $1e_u$, $2a_u$, and $2a_{1g}$ (14-25 eV region), which agree well with the location of the three ionization maxima in this spectral range. A very interesting result was the analysis of the proper Rydberg states of the positive $C_2H_6^+$ ion. In general, it was found that the quantum defects for such species are from 0.4-0.5 units smaller than for their counterparts in neutral systems, in agreement with a decrease in the core penetrability of the Rydberg electron resulting from the increased effective nuclear charge in this system. It is of interest to point out that there is little experimental and/or theoretical information on the general features of Rydberg states in positive ions and therefore more experimental effort in this direction would be a welcome development.

The capability of the MRD-CI method to give reliable ionization potentials can be demonstrated on the basis of two examples, namely for the valence ionization of C_2H_4 and H_2S. On comparing the results for the vertical ionization of ethylene obtained with the present theoretical treatment and those derived by the Green function technique, it has been verified that both methods give similar values for the ionization potentials if one works with exactly the same AO basis, as discussed in detail in the original references (Table of Ref. 4b and 45). The experimental ionization out of the $4a_1$ MO in H_2S corresponds to a broad band covering the 19.5-33 eV energy region and the indication is that quite extensive configuration mixing exists in this excitation region of H_2S^+, with a relative larger number of electronic states in which the contribution of the electronic configuration $4a_1 2b_2{}^2 5a_1{}^2 2b_1{}^2$ is non-negligible. An MRD-CI treatment [46] for this ionization process fits in quite well with the experimental findings, as pointed out by calculating a lowest $^2A_1$ state at 19.67 eV above the neutral system, whereby the first pole obtained by a MBPT study is placed at higher energies (i.e., 21.33 eV, Ref. 47). The next two states are found in the MRD-CI treatment at 22.62 eV and 23.63 eV, respectively, and just within the energy region in which the strongest absorption is experimentally observed, thereby supporting the supposed existence of two (superposed) electronic states in the corresponding experimental peak.

Finally, it can be remarked that the MRD-CI method (or analogous theoretical technique) possesses a more general range of application than the Green function treatments because firstly, the latter method only can be used to predict IPs in the case that the equilibrium geometry of a (as yet unknown) molecule has been previously determined by another ab-initio method, and secondly, it is incapable of making a direct prediction of the adiabatic IP if the geometries of the ionic states are quite different than for the corresponding neutral ground state.

Another interesting aspect of molecular ions which has received special attention in the last years concerns inner-shell phenomena (core ionizations, core-valence excitations, shake-up states, etc.). As discussed in the literature for the case of N_2 [35, 48], while excitations from the core $1\sigma_u$ or $1\sigma_g$ MOs into the valence π_g or 3s species show deviations of about 2 eV with respect to the absolute experimental transition energies of the order of 400 eV (please note that this represents a 0.5% error in this case), the relative position between those high-lying excited states has been predicted within the usual error limits of the method of about 0.1-0.2 eV (Refs. 4b, 35).

The $1\sigma_g$ ionization potential of 291.2 eV and 291.1 eV calculated for C_2H_2 and C_2H_4 [49] respectively, fit in well with the experimental results, in this case the worse deviation being of only 0.5 eV. With respect to the strong $1s \rightarrow \pi^*$ valence transition in both molecules, it is found that the vibrational structure corresponds to the symmetric CH stretching mode in each case, while the term values derived for the transitions into Rydberg-like MO's (which are more contracted than for the neutral species) of the type 3s, 3p, etc., are in accordance with laboratory inferences. In the case of C_2H_2 good agreement with experiment is also observed for those shake-up states involving 1s ionization plus excitations from π into π^* or low-lying Rydberg species, and a quite similar pattern is calculated for C_2H_4, for which no measurements are as yet available. In analogy to Rydberg states in positive ions, the upper orbital of a shake-up state of Rydberg type is found to be considerably more contracted than its counterpart in neutral systems because of the influence of the additional positive charge in the inner shell, but the entire pattern of Rydberg states is quite similar to that which has been noted previously for the valence-shell spectra of both these molecules.

For negative molecular-ions the number of experimental and theoretical studies is still rather small in comparison with the positive systems, but some results are available. The C_2^- radical is one of the most studied species, for example, for which an MRD-CI investigation [50] has obtained an EA(C_2) of 3.43 eV compared with a value of 3.54 eV measured in photo-detachment experiments. It should be pointed out that the ground state is found to be $^2\Sigma_g^+$

($\pi_u^4\sigma_g$), while the other $^2\Pi_u$ ($\pi_u^3\sigma_g^2$) and $^2\Sigma_u^+$ ($\sigma_u\pi_u^4\sigma_g^2$) states are placed at 0.40 eV (T_e value experimentally unknown) and 2.33 eV (exptl. T_e = 2.28 eV), respectively. These results thus raise the interesting question as to the identity of the ground state in the isovalent CSi^- and Si_2^- ions. On the basis of the general features discussed in Section V, namely, the larger stabilization of the σ_g species in comparison with the π_u MOs, it can therefore be expected that the ground state of Si_2^- could be $^2\Pi_u$ rather than $^2\Sigma_g^+$, contrary to the case of C_2^-, but this point clearly needs a quantitative investigation using both theoretical and experimental methods. Finally, it has been found experimentally that dissociative attachment in $CFCl_3$ is possible at essentially zero electron kinetic energy. MRD-CI potential curves calculated for C-Cl bond stretch [51] indicate a definite minimum for the neutral species along this reaction coordinate, while the corresponding curve for $CFCl_3^-$ is clearly dissociative with respect to release of chloride ion. In addition the negative ion potential curve crosses the corresponding neutral species only slightly to the right of the $CFCl_3$ minimum (and only 0.05-0.1 eV above the neutral minimum), thereby explaining on a good quantitative basis the fact that very low kinetic energy is necessary to initiate dissociative electron attachment of this halocarbon.

Perhaps more important than the results for such larger molecular-ions which have already been obtained, however, is the realization that the numerical accuracy of the theoretical methods discussed in this work is still improving at the present time, so that there is good reason to believe that their range of applicability will greatly expand in the future. Even though in many situations the level of accuracy which can now be achieved is still not competitive with the degree of resolution which can be obtained experimentally, the fact that these theoretical techniques can be applied on such a general basis insures their continued usefulness, and at the same time emphasizes the need for increased cooperation between experimentalists and theoreticians in future investigations on this general subject.

Acknowledgements

The authors want to thank Prof. C. Petrongolo for helpful discussions and Cand. Chems. M. Lewerenz, W. Quade, and W. Wald for help in carrying out the calculations of the silicon hydrides. G. H. expresses his gratitude to the Studienstiftung des deutschen Volkes for a fellowship. The computer time made available by the Bonn Computer Center (RHRZ) is gratefully acknowledged.

References

1. R. J. Buenker and S. D. Peyerimhoff, Theor. Chim. Acta, 35, 33 (1974).
2. R. J. Buenker and S. D. Peyerimhoff, Theor. Chim. Acta, 39, 217 (1975).
3. R. J. Buenker, S. D. Peyerimhoff, and W. Butscher, Mol. Phys., 35, 771 (1978).
4. a) R. J. Buenker and S. D. Peyerimhoff, in: "Excited States in Quantum Chemistry," NATO ASI Series C46, C. A. Nicolaides and D. R. Beck, eds., D. Reidel Publ. Co., Dordrecht, Holland (1979), p. 45.
   b) S. D. Peyerimhoff and R. J. Buenker, in: "Excited States in Quantum Chemistry," NATO ASI Series C46, C. A. Nicolaides and D. R. Beck, eds., D. Reidel Publ. Co., Dordrech, Holland (1979), p. 79.
5. R. J. Buenker, S. D. Peyerimhoff, and P. J. Bruna, in: "Proc. NATO ASI Series C 67," Menton, France (1980).
6. a) W. Meyer, J. Chem. Phys., 58, 1017 (1972); R. Ahlrichs, H. Lischka, V. Staemmler, and W. Kutzelnigg, J. Chem. Phys., 62, 1225 (1974).
   b) L. S. Cederbaum, Theor. Chim. Acta, 31, 329 (1973); W. V. Niessen, G. H. F. Diercksen, L. S. Cederbaum, and W. Domcke, Chem. Phys., 18, 469 (1976).
   c) R. J. Bartlett and C. D. Purvis, Int. J. Quantum Chem., 14, 561 (1978).
7. E. R. Davidson, in: "The World of Quantum Chemistry," R. Daudel and B. Pullman, eds., D. Reidel Publ. Co., Dordrecht, Holland (1974), p. 17.
8. P. J. Bruna, S. D. Peyerimhoff, and R. J. Buenker, Chem. Phys. Lett., 72, 278 (1980).
9. S. D. Peyerimhoff, R. J. Buenker, and L. C. Allen, J. Chem. Phys., 45, 734 (1966).
10. R. J. Buenker and S. D. Peyerimhoff, Chem. Rev., 74, 127 (1974).
11. M. E. Casida, M. M. L. Chen, R. D. MacGregor, and H. F. Schaeffer, III, Israel J. Chem., 19, 127 (1980).
12. P. J. Bruna, G. Hirsch, M. Perić, S. D. Peyerimhoff, and R. J. Buenker, Mol. Phys., 40, 521 (1980).
13. G. Hirsch and P. J. Bruna, Int. J. Mass Spectrom. Ion Phys., 36, 37 (1980).
14. R. N. G. Duxbury, M. Horani, and J. Rostas, Mol. Phys., 22, 977 (1972).
15. a) J. Delwiche, P. Natalis, and J. E. Collin, Int. J. Mass Spectrom. Ion Phys., 5, 443 (1970); J. Delwiche and P. Natalis, Chem. Phys. Lett., 5, 564 (1970).
   b) D. W. Turner, C. Baker, A. D. Baker, and C. R. Brundle, 'Molecular Photoelectron Spectroscopy," Wiley Interscience, London (1970).

16. J. H. D. Eland, Int. J. Mass Spectrom. Ion Phys., 31, 161 (1979).
17. W. Meyer, Int. J. Quantum Chem. Symp., 5, 341 (1971).
18. J. A. Smith, P. Jorgensen, and Y. Öhrn, J. Chem. Phys., 62, 1285 (1975).
19. S. D. Peyerimhoff and R. J. Buenker, Chem. Phys., 42, 167 (1979).
20. B. H. Mahan and T. M. Sloane, J. Chem. Phys., 59, 5661 (1973); D. H. Liskow, C. F. Bender, and H. F. Schaeffer, III, J. Chem. Phys., 61, 2507 (1974); D. Gervy and G. Verhaegen, Int. J. Quantum Chemistry, 12, 115 (1977).
21. S. J. Dunlavey, J. M. Dyke, N. K. Fayad, N. Jonathan, and A. Morris, Mol. Phys., 38, 729 (1979).
22. Ibidem, Mol. Phys., 44, 265 (1981).
23. P. J. Bruna, G. Hirsch, S. D. Peyerimhoff, and R. J. Buenker, Mol. Phys., 42, 875 (1981).
24. K. P. Huber and G. Herzberg, Molecular Spectra and Molecular Structure IV, Constants of Diatomic Molecules, van Nostrand Reinhold Co., New York (1979).
25. P. J. Bruna, S. D. Peyerimhoff, and R. J. Buenker, J. Chem. Phys., 72, 5437 (1980).
26. C. Petrongolo, P. J. Bruna, S. D. Peyerimhoff, and R. J. Buenker, J. Chem. Phys., 74, 4594 (1981); 74, 4611 (1981).
27. J. Drowart, R. P. Burns, G. De Maria, and M. G. Inghram, J. Chem. Phys., 31, 1131 (1959).
28. V. H. Dibeler and S. K. Liston, J. Chem. Phys., 47, 4548 (1967).
29. a) J. Drowart, G. De Maria and M. G. Inghram, J. Chem. Phys., 29, 1015 (1958).
b) G. Verhaegen, F. E. Stafford, and J. Drowart, J. Chem. Phys., 40, 1622 (1964).
30. B. L. Lutz, Astrophys. J., 163, 131 (1971).
31. J. Berkowitz, J. Chem. Phys., 36, 2533 (1962).
32. a) R. Preuß, R. J. Buenker, and S. D. Peyerimhoff, J. Mol. Struct., 49, 171 (1978).
b) H. W. Kroto, J. N. Murrell, A. Al-Derzi, and M. F. Guest, Astrophys. J., 219, 886 (1978).
c) J. N. Murrell, H. W. Kroto, and M. F. Guest, J. Chem. Soc. Chem. Comm., 619 (1977).
d) R. Preuß, R. J. Buenker, and S. D. Peyerimhoff, Chem. Phys. Lett., 62, 21 (1979).
e) P. J. Bruna, G. Hirsch, S. D. Peyerimhoff, and R. J. Buenker, Can. J. Chem., 57, 1839 (1979).
33. P. J. Bruna, S. D. Peyerimhoff, and R. J. Buenker, Chem. Phys., 27, 33 (1978).
34. R. J. Buenker, P. J. Bruna, and S. D. Peyerimhoff, Israel J. Chem., 19, 309 (1980).
35. P. J. Bruna, Gazz. Chim. Ital., 108, 395 (1978).
36. P. J. Bruna and C. M. Marian, Chem. Phys. Lett., 67, 109 (1979); P. J. Bruna, Chem. Phys., 49, 39 (1980).

37. P. J. Bruna and C. M. Marian, Chem. Phys., 37, 425 (1979).
38. J. M. Dyke, N. B. H. Jonathan, A. Morris, and M. J. Winter, Mol. Phys., 39, 629 (1980).
39. D. C. Frost, S. T. Lee, and C. A. McDowell, Chem. Phys. Lett., 23, 472 (1973).
40. J. N. Murrell and A. Al-Derzi, J. Chem. Soc. Faraday II, 76, 319 (1980).
41. S. K. Shih, S. D. Peyerimhoff, and R. J. Buenker, J. Mol. Spectrosc., 64, 167 (1977).
42. E. F. van Dishoeck, W. J. van der Hart, and M. van Hemert, Chem. Phys., 50, 45 (1980).
43. a) A. Richartz, Progress in Theor. Org. Chem., 2 (1977).
b) A. Richartz, R. J. Buenker, P. J. Bruna, and S. D. Peyerimhoff, Mol. Phys., 33, 1345 (1977).
44. A. Richartz, R. J. Buenker, and S. D. Peyerimhoff, Chem. Phys., 28, 305 (1978).
45. K. H. Thunemann, R. J. Buenker, S. D. Peyerimhoff, and S. K. Shih, Chem. Phys., 35, 35 (1978).
46. P. J. Bruna, to be published.
47. L. S. Cederbaum, J. Schirmer, W. Domcke, and W. von Niessen, J. Electron Spectrosc., 16, 59 (1978).
48. W. Butscher, R. J. Buenker, and S. D. Peyerimhoff, Chem. Phys. Lett., 52, 449 (1978).
49. A. Barth, R. J. Buenker, S. D. Peyerimhoff, and W. Butscher, Chem. Phys., 46, 149 (1980).
50. M. Zeitz, S. D. Peyerimhoff, and R. J. Buenker, Chem. Phys. Lett., 58, 487 (1978).
51. S. D. Peyerimhoff and R. J. Buenker, Chem. Phys. Lett., 65, 434 (1979).
52. S. K. Shih, S. D. Peyerimhoff, and R. J. Buenker, Chem. Phys., 28, 299 (1978).

GREEN'S FUNCTION CALCULATIONS OF IONIZATION SPECTRA OF MOLECULES IN THE OUTER AND INNER VALENCE REGION

W. von Niessen

Institut für Physikalische Chemie
Technische Universität Braunschweig
D - 3300 Braunschweig, West Germany

Introduction

The study of ionic states has become a very important field of research containing an enormous amount of chemical and physical information which can be extracted by different experiments and by calculations. It is a field of research where experiment and theory work hand in hand in order to obtain this information. Among the most important pieces of information are the ionization energies, i.e., the transition energies to the different ionic states. Their calculation will preoccupy us in the sections below. It is generally assumed that the most prominent bands in a photoelectron spectrum (PES) arise from transitions to electronic states that are obtained by ejection of a single electron out of a molecular orbital in the ground state. In addition to these "simple" one-electron transitions two-electron transitions can sometimes be observed, i.e., processes which are ionization of one plus simultaneous excitation of another electron. They appear as satellite lines in a PES and borrow their intensity from the simple transitions. In the outer valence region and in the core region their intensity is small compared to the main line; i.e., a one-electron picture of the ionization process is valid. In the inner valence region, however, this need not be the case as we are going to see. The one-electron picture of ionization can break down completely.

The electronic excitation can be accompanied by the excitation of vibrations and rotations. The vibrational structure can be resolved or - due to its complexity and the limited experimental resolution - appear only as a broadening of the bands. In case it is resolved this adds significantly to the information one can deduce from a spectrum. The main questions are: which normal vibrations

become excited in a given electronic transition, how strongly are they excited and what are their frequencies. This also leads to the question of geometry changes upon ionization. Closely connected with the vibrational structure are vibronic coupling effects between different electronic states, i.e., the effects which result from the breakdown of the Born-Oppenheimer approximation. We will discuss these topics also in the sections below. The rotational structure is, except for the case of the hydrogen molecule, not resolvable at present and thus does not play a significant role yet.

Further pieces of information are the ionization cross sections, branching ratios, angular dependencies, line widths, the coupling of shape resonances, but also the different chemical reaction pathways of the ionic species in their different states and the associated branching ratios. More and more activity is going into the study of these topics. Thus, e.g., the measurement and the calculation of the ionization cross sections is a very active area of research. In the normal case of photoelectron spectroscopy these quantities are properties of the apparatus, in particular the analyzer, and sometimes show little relation to the physical quantities. But new types of experiments can yield this and other information. The use of synchrotron radiation, coincidence measurements (e, 2e)-techniques as well as new theoretical tools have opened the door to new developments. In the present article we will be preoccupied with the calculation of the ionization energies and vibrational phenomena - i.e., the fundamental quantities used to assign a given PES. The computational tool is the Green's function method.

Koopmans' Approximation

The simplest method to calculate ionization energies is based on Koopman's theorem and is called Koopmans' approximation [1]. The method is simple to apply and reasonably successful in that it permits to assign experimental ionization spectra. In the Hartree-Fock (HF) approximation the wave function consists of a Slater determinant built from molecular spin orbitals $|\phi_i\rangle$

$$\Psi_o = \det |\phi_1\bar{\phi}_1 \ldots \phi_i\bar{\phi}_i \ldots \phi_n\bar{\phi}_n| . \qquad (1)$$

($|\phi_i\rangle$ without the bar denotes that the orbital is associated with a spin function with $m_s = + {}^1/_2$, and with the bar that the orbital is associated with a spin function with $m_s = - {}^1/_2$) which are solutions of the HF equations

$$F|\phi_i\rangle = \varepsilon_i|\phi_i\rangle \qquad (2)$$

with ε_i the orbital and F the HF operator

$$F = h + \sum_i 2\,J_i - K_i, \qquad (3)$$

where h is the one-electron operator, $J_i = \langle \phi_i(2) | 1/r_{12} | \phi_i(2) \rangle$ the Coulomb and $K_i = \langle \phi_i(2) | 1/r_{12} | \rangle | \phi_i(1) \rangle$ the exchange operator. The HF operator contains only an average interaction between the electrons resulting from the integration over the coordinates of the other electrons. Because of this approximate interaction one has neglected an energy contribution, the so-called correlation energy. If one approximates the ionic wave function by

$$\Psi_i = \det |\phi_1\bar{\phi}_1 \ldots \phi_i \ldots \phi_n\bar{\phi}_n|, \tag{4}$$

where the electron has been taken out of the spin orbital $|\bar{\phi}_i\rangle$ leaving all other orbitals unchanged one obtains for the energy difference

$$E_i(\Psi_i) - E_o(\Psi_o) = I_i = -\varepsilon_i. \tag{5}$$

The i-th ionization energy is thus approximately given by the negative of the i-th orbital energy. This is Koopmans' approximation which has proved to be very useful. With the Ansatz Eq. (4) for the ionic wave function, in which the molecular orbitals of the neutral groundstate are used for the ionic state one has neglected the so-called reorganization energy of the electrons. Ejection of an electron will always lead to a charge rearrangement and the ionic wave function should be constructed from orbitals appropriate for the ion. Thus Koopmans' approximation involves the neglect of the correlation energy both in the ion and the neutral state and the neglect of the reorganization energy in the ion. In the outer valence region of many molecules this approximation is quite acceptable as these two neglected effects tend to cancel to a certain degree, but there can be no guarantee that the approximation is reliable. There are quite a number of molecules and there are whole classes of molecules where Koopmans' approximation fails badly in supplying the correct ordering of ionic states. Ionic states can be quite close together in energy and thus one needs more accurate means of calculating the ionization energies which take into account the effects of electron correlation and reorganization. The reorganization energy can be obtained by separate SCF calculations and the correlation energy by performing separate configuration interaction (CI) calculations for the ionic states and the ground state. These methods appear as a logically consistent improvement in the calculation of ionization energies. There is, however, also a direct way to calculate ionization energies, the method of Green's functions [2, 3]. (For a general text on Green's functions see, e.g., Ref. 4.)

Before discussing the method of Green's functions let us point out another consequence of Koopmans' theorem, which we would like to call Koopmans' hypothesis. This will clarify the physical model underlying Koopmans' approximation. In a closed shell molecule and in the SCF approximation each electron pair occupies one of the

orbitals $|\phi_i\rangle$ once with $m_s = {}^1/_2$, once with $m_s = -{}^1/_2$. The total energy, the electron density, many properties are reasonably well described by this model. In this respect it can be said that the model - the molecular orbital (MO) model - acquires a certain degree of reality. One can now take an electon out of each orbital. A photoelectron spectrum should thus consist of as many lines as there are orbitals. The reason for this is that the photon interacts only with one electron at a time, the transition operator is a one particle operator. It is not implied that the orbital energies are (aside from the sign) accurate approximations to the ionization energies - reorganization and correlation effects will necessarily modify the values - but it is implied in using Koopmans' approximation that to each orbital corresponds one line in the PES. This has well been borne out in many PES in the outer valence region and in ESCA spectra for the core region. The physical model thus appears to be sound. The MO scheme and the resulting schematic PES are sketched in Fig. 1. It is, however, long known in photoelectron spectroscopy that in addition to the one-electron transitions mentioned above two-electron transitions can also be observed which are ionization combined with simultaneous excitations. This process is also sketched in Fig. 1. These processes lead to the so-called satellite lines. They usually have small intensities and borrow this intensity from the main - transitions via many - body effects. If their intensities are small the physical model underlying Koopmans' approximation is a valid one, but if their intensities become large this model becomes shaky and must be abandoned. Koopmans' approximation then burns down to pure mathematics. One still calculates an orbital energy but it has little relation to an ionization energy. A relation may still be thought of to exist if the intensities of the two-electron transitions are borrowed from the simple one-electron transitions. This shows that a discussion of ionization spectra and Koopmans' approximation cannot be based on the energetics alone, but should take the intensities into consideration.

It has been found in the studies of atoms (in particular the interpretation of the Xe ESCA spectrum by Wendin and Ohno [5]) and in calculations on a large number of molecules (see, e.g., Refs. 6-13; Ref. 13 contains a fairly complete list) that the satellite lines acquire a considerable intensity in the inner valence region. A main line frequently ceases to exist and the intensity becomes distributed over a large number of lines. Things may become even worse. It may occur that the intensity of a satellite line is not borrowed from a single simple transition but from several. In this case neither the energetics nor the intensity borrowing can be understood in a MO model. (In addition, interference effects can be observed.) Extremely strong effects of this type have recently been found in several molecules and even for the first ionization processes [14]. A one-to-one correspondence between lines in the PES and the MO's seems to exist but a MO interpretation of the PES is

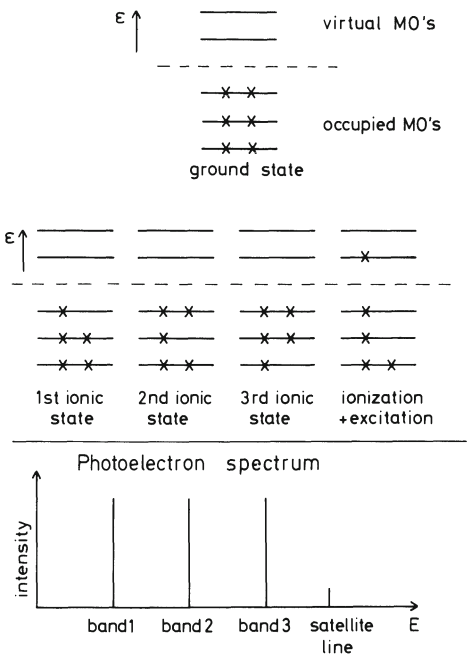

Fig. 1. MO scheme for the ground state, for the ionic states obtained by simple one - electron ejection processes and for ionization plus excitation processes together with the corresponding schematic photoelectron spectrum.

totally impossible. There are also other effects such as vibronic coupling which can lead to complications in a PES. Koopmans' hypothesis may thus frequently fail to meet reality or even if it seems to be in agreement with reality it may be so for the wrong reason.

More accurate methods such as CI or the Green's function method will lead to a correct interpretation in a complete calculation but will only lead to it in an incomplete calculation if the approximation is based on a correct physical model. In the absence of the evidence shortly mentioned above there is no guarantee that this will be the case. For numerical reasons the more accurate methods are cast into a restricted form (e.g., limited CI of various kinds or low order perturbation methods) which may in some instances not be capable of coping with reality. One then obtains a number but this number is meaningless. One certainly would like to have a method where one can foresee the failure of a given approximation. The Green's function method is one example. But still it is not clear without a calculation in which energy range a given approximation is valid and where it is not, as this depends on the system.

Let us discuss some of the effects which may be possible to observe in PES. This will not be a complete list to avoid too many complications. In particular, we will be mainly concerned with energetic phenomena and less with intensity phenomena. The list certainly depends on the present state of knowledge. Several effects have not been expected or have even been declared as impossible prior to their verification. When we increase the energy of the radiation incident on the atom or molecule we will first excite electrons to valence and to Rydberg states, the latter forming the so-called Rydberg series which converge to the various ionization thresholds. When ionization occurs the electron is no longer bound but is excited into the continuum. Ionization is not a resonance phenomenon as absorption so any energy beyond the ionization energy will be absorbed and will appear as kinetic energy of the ejected electron. The first ionization process is expected to be a simple one-electron transition; but as Hilbert space can be segmented into the different symmetry spaces one expects that the first ionization of each symmetry should be a simple one-electron process and Koopmans' approximation and hypothesis should be valid. This is, however, not correct as has been found recently [15]. Exceptions can be expected for molecules which have a bound negative ion state of the same symmetry or which have very low lying valence excited states (see below). It is certainly incorrect to assume that where ionization starts excitation stops. Bound neutral excited states may lie in the ionization continuum. These superexcited states do not in general disturb a PES from an energetic point of view but may do so from the intensities. If the superexcited state does not decay into an ionic state it will not be observed; if it does decay - this is called autoionization - it will enhance the intensity of the ionization band. This may sometimes lead to gross distortions.

If two ionic states of different or of the same symmetry are separated by an energy about equal to the energy of vibrational quanta the Born-Oppenheimer approximation may break down. Vibrations of the appropriate symmetry couple the electronic states. This may lead to great complications which manifest themselves in a very complicated vibrational structure or even in the appearance of new bands.

For the further discussion we shall denote a configuration where an electron has been ejected from the MO p by p^{-1} and a configuration where one electron has been ejected from MO k and another one simultaneously excited from MO l to a virtual MO j by $k^{-1}l^{-1}j$. If two configurations p^{-1} and q^{-1} of the same symmetry are fairly close together in energy one would not expect a configuration mixing because of the content of Koopmans' theorem which is a stability theorem for the ionic wavefunctions. And in fact to the authors' knowledge this has not been found until recently. In propynol and in propiolic acid this configuration mixing does occur [14]. The number of bands is unchanged but instead of being described by con-

figurations p^{-1} and q^{-1}, the ionic states have to be described in the simplest approximation by $ap^{-1} + bq^{-1}$ and $bp^{-1} - aq^{-1}$, where $a \sim b$. It is clear that this configuration mixing is mediated via two-hole-one particle configurations, because the Hamiltonian matrix element between p^{-1} and q^{-1} is zero, but these are found to be quantitatively unimportant. With increasing ionization energy other processes become possible. In addition to ionizing one electron, another one may be simultaneously excited. If the energy of configuration p^{-1}, $E(p^{-1})$, is far away from the energy of other configurations then one line will be found in the PES. If, however, $E(p^{-1})$ is close to $E(k^{-1}l^{-1}j)$ for some configuration $k^{-1}l^{-1}j$ then there will be configuration mixing and a redistribution of intensity. Thus several lines of roughly equal intensities may appear in the PES for ionization out of the orbital p. For molecules consisting of first row atoms $E(k^{-1}l^{-1}j)$ is larger than the energy of the neutral ground state by 15 to 25 eV. Thus these effects will be found at higher energies affecting mainly 2s lines of the first row atoms. An important factor which enters $E(k^{-1}l^{-1}j)$ is the excitation energy of the molecule. If a molecule has very low lying excitations these many-body effects will appear at lower energy. The spectrum will depend on two other quantities; the first one is the interaction matrix element between the configuration p^{-1} and $k^{-1}l^{-1}j$. This is approximately given by V_{pjkl}. Such a matrix element is expected to be large only if the virtual orbital j is localized in space as the occupied orbitals are. Therefore sufficiently large interaction between the relevant configurations can be expected especially for those molecules that possess low lying valence type excited states. If V_{pjkl} is nearly zero for some reason, no many-body effects will be observable in spite of the quasidegeneracy of p^{-1} and $k^{-1}l^{-1}j$. The second factor which enters is the density of the $k^{-1}l^{-1}j$ configurations in energy space. If the density is low in the energy region of the single hole configuration, p^{-1}, the breakdown phenomenon will only occur if there is an accidental quasidegeneracy. The intensity is then distributed only over a few lines. If the density is high on the other hand the intensity becomes distributed over numerous lines each having only a few percent of the total intensity. Since larger molecules have a high density of configurations the breakdown phenomenon will dominate their ionization spectra in the inner valence shell. In the neighborhood of the double ionization threshold the density of the configurations is very high and the configurations $k^{-1}l^{-1}j$ may constitute a continuum. In case this continuum is structureless in the range of ε_p its interactions with p^{-1} will mainly lead to a broadening of the main line. In the energy region not high above the double ionization threshold the continuum usually has pronounced structures (resonances) and these lead not only to a lifetime effect but also to intensity distributions as discussed above.

To explain in more detail what is happening in the mixing of single hole configurations with two-hole-one-particle configurations,

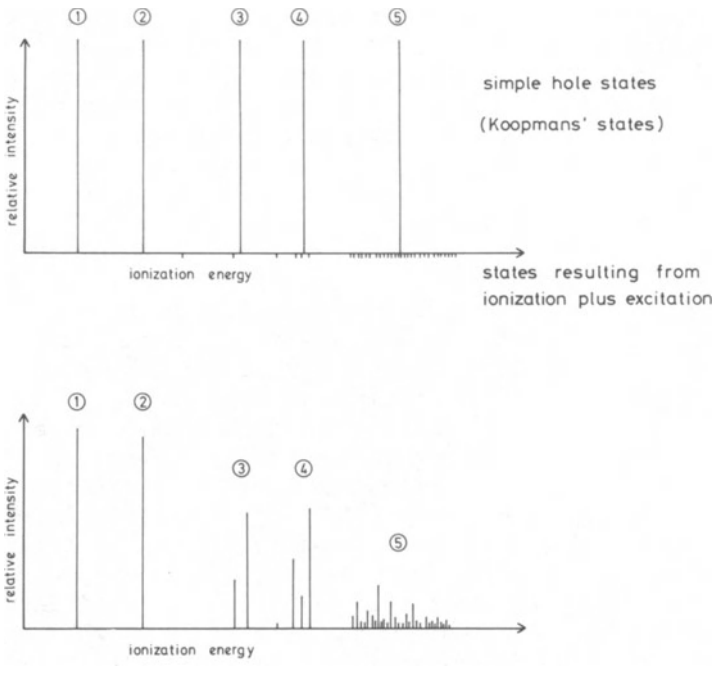

Fig. 2. Artifical schematic ionization spectrum separated into simple hole states and states resulting from ionization plus excitation (upper part) and resulting schematic ionization spectrum obtained by including configuration mixing (lower part).

we have plotted in Fig. 2 an artificial schematic ionization spectrum. In the upper spectrum the simple hole states (Koopmans' states) are separated from the states resulting from ionization plus excitation. The transitions to the former states are allowed in a one-particle model, and the lines have unit relative intensities, whereas the transitions to the latter ones are forbidden, and the states have thus only been marked by the energies. The density of these states is low in the low energy region and high in the high energy region. When we permit configuration mixing the schematic spectrum drawn in the lower part of Fig. 2 results. The lines become first split into few lines (due to occurring near degeneracies) in the lower energy part and at higher energies are completely smashed to pieces.

From this overview we conclude that ionization spectra of molecules are not as simple as may be tought on the basis of Koop-

mans' hypothesis. A great number of complications arise. These are a source of information on the electronic and vibronic structure of molecules and present a challenge to the spectroscopist and to the theoretician. PE spectroscopy would perhaps become boring if it were not for these complications and for additional chemical and physical applications.

The Green's Function Method

The necessity to assign PES and to analyze the physical background of the complications which have been discussed and thus to understand them demands theoretical developments. This can be done using CI techniques, perturbation techniques or the method of Green's functions. We will describe some aspects of the method of Green's functions as they are relevant for the calculation of ionization energies in the outer and inner valence region.

The one-particle Green's function is defined in time, state space as the expectation value with respect to the exact ground state wave function of a time-ordered product of annihilation and creation operators for electrons in one-particle states

$$G_{kl}(t, t') = - i < \Psi_o^N | T\{a_k(t) a_l^+(t')\} | \Psi_o^N >. \qquad (6)$$

$a_k(t)$, $a_k^+(t')$ are operators in the Heisenberg representation with H the full Hamiltonian of the system.

$$a_k^+(t) = e^{iHt}\, a_k^+\, e^{-iHt}. \qquad (7)$$

They annihilate (create) electrons in one-particle states $|k>$. The operators fulfill the anticommutation relations $[a_k, a_l^+]_+ = \delta_{kl}$ with all other anticommutators vanishing. T is Wick's time ordering operator which orders the operators so that time increases from right to left. A permutation of the operators from the original ordering by the action of T is accompanied by a change of sign. With the help of the Fourier transformation one can go over from time, state space to energy, state space

$$G_{kl}(\omega) = \int_{-\infty}^{\infty} G_{kl}(t, t') e^{i\omega(t-t')} d(t-t'). \qquad (8)$$

By inserting the decomposition of unity and performing the integration one arrives at the spectral representation of the Green's function

$$G_{kl}(\omega) = \lim_{\eta \to +o} \{ \sum_n \frac{<\Psi_o^N | a_k | \Psi_n^{N+1}> <\Psi_n^{N+1} | a_l^+ | \Psi_o^N>}{\omega + A_n + i\eta} \qquad (9)$$

$$+ \sum_m \frac{\langle \Psi_o^N | a_l^+ | \Psi_m^{N-1} \rangle \langle \Psi_m^{N-1} | a_k | \Psi_o^N \rangle}{\omega + I_m - i\eta} \}$$

with $A_n = E_o^N - E_n^{N+1}$ the vertical electron affinity and $I_m = E_o^{N-1} - E_o^N$ the vertical ionization energy. By calculating the poles of the Green's function one thus obtains directly the ionization energies and the electron affinities. The ionization energies and electron affinities are best calculated from the Dyson equation which is formally equivalent to the spectral representation but more amenable to numerical calculations

$$G(\omega) = G^o(\omega) + G^o(\omega)\Sigma(\omega)G(\omega). \tag{10}$$

The Dyson equation connects the Green's function with the HF Green's function $G^o_{kl} = \delta_{kl}/(\omega-\varepsilon_k)$ and the quantity $\Sigma(\omega)$ which is called the self-energy potential. $\Sigma(\omega)$ is the exact potential seen by an electron due to the interaction with its surroundings. The Green's functions have inverses

$$G^{-1} = (G^o)^{-1} - \Sigma(\omega). \tag{11}$$

Thus instead of calculating the poles of G we calculate the zeros of G^{-1}. In a diagonal approximation this takes the form

$$G^{-1}_{mm} = o = \omega - \varepsilon_m - \Sigma_{mm}(\omega). \tag{12}$$

The energies ω fulfilling this equation are the ionization energies and electron affinities. They can be calculated by obtaining the intersection points of the straight line $y = \omega - \varepsilon_m$ with $\Sigma_{mm}(\omega)$. This and the structure of Σ is represented schematically in Fig. 3.

$\Sigma(\omega)$ itself has poles and is a monotonically decreasing function of ω between the poles. For closed shell systems Σ has always a large interval free of poles. In this interval the outer valence ionization energies are found and for their calculation high accuracy is required. In this region far away from the poles a perturbation expansion of Σ in the electron-electron interaction is justified. We include all terms up to and including the third order terms. Higher order terms are taken into account by a renormalization procedure.

$$\Sigma = \Sigma^{(1)} + \Sigma^{(2)} + \Sigma^{(3)} + \Sigma^{(R)}. \tag{13}$$

$\Sigma^{(1)}$ is zero if one starts from HF solutions.

As seen from Fig. 3 there are many intersections of the straight line $y = \omega - \varepsilon$ with $\Sigma(\omega)$. Thus one obtains many ionization energies (in principle infinitely many) for ionization out of a given orbital. Which of the energies corresponds closest to Koopmans' approximation

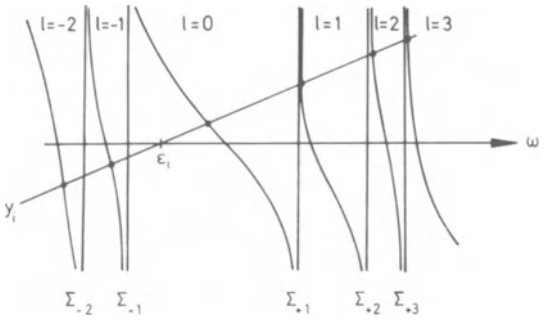

Fig. 3. A schematic plot of Σ_{mm} as a function of ω and of the solution of the Dyson equation.

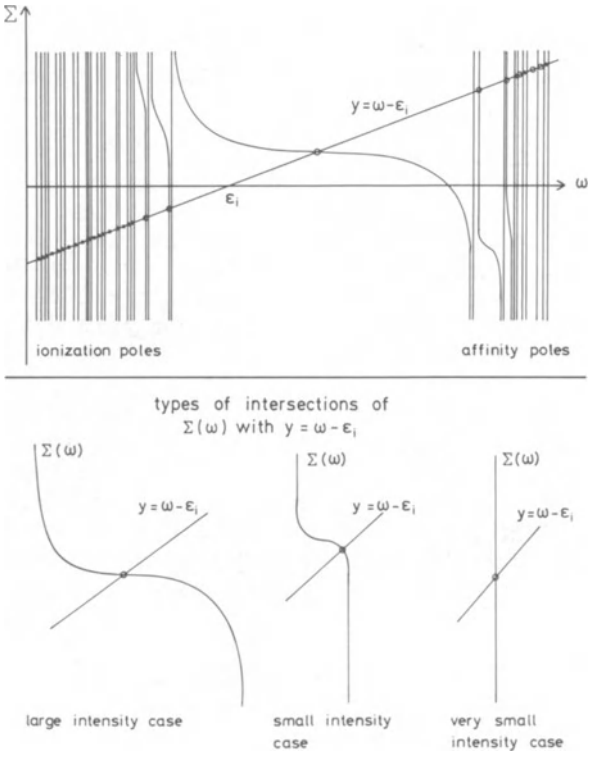

Fig. 4. Schematic solution of the Dyson equation exhibiting the high density of states outside the principal interval and the types of intersections which lead to high, medium, or small intensities. In the upper part only the intervals are drawn in general and the self-energy is plotted only for the first few intervals.

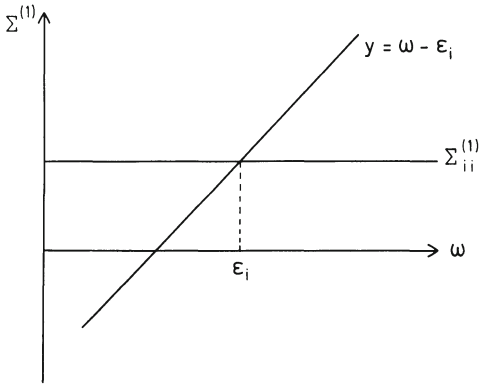

Fig. 5. Schematic solution of the Dyson equation with a Hartree-Fock (first order) approximation to the self-energy potential Σ.

cannot be decided by the energy alone but require the relative intensities, the pole strengths. These relative intensities are given by

$$P^{(s)} = (1 - \frac{\partial}{\partial\omega} (\varepsilon + \Sigma(\omega))\big|_{Is})^{-1} \tag{14}$$

If the pole strength of one solution is close to unity this will be the main line. The other intersections will have small intensities and correspond to the mentioned satellite lines. But it may also happen that there is no solution with a pole strength close to unity.

The schematic solution of the Dyson equation is drawn again in Fig. 4. In this case the high density of intervals which results in a high density of states is exhibited. The first few intervals to the right and left of the main interval are in general broader than the other ones. The possible types of intersections of the self-energy with the straight line $y = \omega - \varepsilon_i$ are plotted in the lower half. The first case is in general only encountered in the principal interval.

In Figs. 3 and 4 we have plotted schematically a section of the exact self-energy of which it can be shown that it has only simple poles. It is, however, also quite useful to plot the self-energy in the simplest approximation. This first order approximation is the HF approximation. If one starts from free particles then

$$\Sigma^{(1)}_{ii} = \sum_k (V_{ikik} - V_{ikki})\, n_k, \tag{15}$$

where $n_k = 1$ if k is occupied and $n_k = 0$ if k is unoccupied.

$$V_{ijkl} = \int\int \phi_i(1)\phi_j(2) \frac{1}{r_{12}} \phi_k(1)\phi_l(2) d\tau_1 d\tau_2 \qquad (16)$$

(If one starts from HF particles then $\Sigma_{ij}^{(1)} = 0$ and the first order electron-electron interaction effect is contained in the orbital energies themselves [3, 11].) This self-energy potential is independent of the energy and thus has no poles. It is sketched in Fig. 5 together with the schematic solution of the Dyson equation in this case. Because of the constancy of the self-energy one obtains only one solution of the Dyson equation, the Koopmans' value of the ionization energy. This figure demonstrates how simple the HF approximation is, but also that the essential physics is absent from it if the ionization energy happens to be situated in the pole region of the self-energy. Koopmans' approximation is only meaningful far away from the poles.

As mentioned above the finite perturbation can only be used for the calculation of outer valence ionization energies which are far from the poles of the self-energy. These ionization energies have pole strengths close to unity. A consequence is that there is one line in the PES for each MO. Satellite lines will accompany these main lines, but they have only small relative intensities. These solutions lie in the pole region of the self-energy. The inner valence ionization will lie in this region too. To calculate these ionization energies and the satellite lines a method is required which takes the pole structure of the self-energy into account. Quite new phenomena may occur in this energy range. We are going to see that in the inner valence region the one-particle picture of ionization may break down completely. The familiar concepts useful in the outer valence region and in the core are without validity here. The method used for these calculations is the 2-particle-hole Tamm-Dancoff approximation (2ph-TDA) [3, 16].

The exact self-energy has a constant and an energy-dependent term which we denote by $M(\omega)$

$$\Sigma(\omega) = \Sigma(\infty) + M(\omega). \qquad (17)$$

As $\Sigma(\infty)$ can be obtained from $M(\omega)$ (see Ref. 3) we investigate only $M(\omega)$ here. The straightforward perturbation expansion of the self-energy is certainly limited to low orders because of the rapidly increasing effort involved in calculating higher orders. The lowest order energy-dependent term is the second order term $M^{(2)}(\omega)$

$$M^{(2)}{}_{pq}(\omega) = \frac{1}{2} \sum_{jkl} V_{pj[kl]} V_{qj[kl]}$$

$$\times \{\frac{\bar{n}_j n_k n_l}{\omega + \varepsilon_j - \varepsilon_k - \varepsilon_l - i\eta} + \frac{n_j \bar{n}_k \bar{n}_l}{\omega + \varepsilon_j - \varepsilon_k - \varepsilon_l + i\eta}\}$$

$$= M^{I}_{pq} + M^{II}_{pq}. \qquad (18)$$

with $V_{ij[kl]} = V_{ijkl} - V_{ijlk}$ and $\bar{n}_i = 1 - n_i$. This expansion up to second order has the analytical structure of the exact $M(\omega)$. Unfortunately $M^{(2)}$ has, in general, proved to provide only a poor approximation. The extension to the third order or any higher finite order will destroy the simple spectral structure of the second order expression, since quadratic poles are added already by $M^{(3)}(\omega)$. It is thus clear that an expansion up to a finite order will completely fail to describe $M(\omega)$ in the neighborhood of its poles, whereas it might be useful if a region far from the poles is only of interest. The latter is the case for the outer valence ionization energies of closed shell systems.

We have to look for a structure conserving approximation, that is, an approximation for $M(\omega)$ exhibiting the spectral form reflected by the exact self-energy. Such an approximation can only be obtained by some kind of infinite partial summation.

Let us consider the second order expression Eq. (18). The poles of M^{I} describe ionic states where one electron is removed from the occupied MO k(1) and another one is excited from the occupied MO 1(k) into the unoccupied orbital j. Analogously the poles M^{II} correspond to an electron attachment process to an unoccupied orbital accompanied by a simultaneous particle-hole excitation. The corresponding states have the configuration $k^{-1}l^{-1}j$ and $j^{-1}kl$, respectively. By solving the Dyson equation, with $M^{(2)}$ these configurations are allowed to interact with the one-hole and one-particle configurations p^{-1} and p which are described by G^{o}. The resulting ionic states now include correlation effects. At this place we wish to mention that in some cases two (or more) one-hole configurations p^{-1} and p'^{-1} interact indirectly via a configuration of the type $k^{-1}l^{-1}j$. As a consequence the Green's function becomes nondiagonal and the resulting line corresponding to the ionic state which develops from the $k^{-1}l^{-1}j$ configuration cannot be thought of as arising from the ionization of a specific MO.

We do not wish to discuss in any detail the TDA method as for this discussion diagrammatic techniques are required. We only wish to make some general comments. The TDA method is the simplest method which gives the correct analytical form of the self-energy. Certain classes of diagrams (those which have two hole and one particle line as well as those which have two particle and one hole line between any two interaction vertices) have been summed to infinite order. The self-energy is defined by this selective summation. Recently the energy independent terms which are ground state correlation

terms have also been included [17]. This leads to an improved description of the ground state which is of particular importance in the lower energy region and for the calculation of electron affinities. In the Dyson equation the single hole, two-hole-one-particle, single particle and two-particle-one-hole terms are coupled together. The solution then gives the ionization energies. Particle number is not conserved in this equation but this trick is used in the Green's function method to include ground state correlation energy. An explanation in a wave function picture is not possible. If, however, one leaves out the one particle and the two-particle-one-hole components, then the solution of the Dyson equation is equivalent to a CI with single excitations included for all possible single hole states. The TDA method appears to be a necessary first step in the calculation of ionic states in the inner valence region. It can be improved in a number of ways (e.g., by the inclusion of the energy independent diagrams, by making it correct to third order in the electronic interaction) and work is in progress along these lines.

In its present version the TDA method is inferior in its accuracy to the outer valence Green's function (GF) method based on the perturbation expansion with renormalization. This creates some problems in those cases where the TDA and the GF method have to be used in the same energy range, i.e., where ionization spectra calculated with these two methods have to be welded together. This occurs, e.g., when the TDA method has to be used for a state of one symmetry and the GF method for a neighboring state of a different symmetry. As the TDA method gives a qualitatively correct spectrum over the entire energy range (valence region) this calculation has always preceded a GF calculation. It determines where the GF method is applicable and only for these states is the GF calculation performed. Both calculations cover the entire valence region and nicely complement each other because in the inner valence region a qualitatively correct description of the spectrum is required (the details being beyond observability at present) and in the outer valence region high accuracy is needed.

Vibrational Structure in Photoelectron Spectra

The vibrational structure is a prominent feature of molecular PES and it reflects the bonding properties of the electrons. The Green's function method has been extended to include vibrational effects [3, 18]. In the derivation use has been made of the Born-Oppenheimer, Franck-Condon and harmonic approximation (for methods which go beyond these approximations, see the section on vibronic coupling), but it should be mentioned from the outset that the harmonic approximation used here is not identical to the harmonic approximation generally used. The philosophy behind the approach is, that the neutral ground state of the molecules is well characterized, but little or no information is available on the ionic states. We use this information on the ground state, in particular

the force field and the harmonic frequencies and calculate the properties of the ion.

In the one-particle approximation the Hamiltonian is given by

$$H = V_o + \sum_s \omega_s (b_s^+ b_s + \frac{1}{2}) + \sum_i \varepsilon_i(Q)(a_i^+(Q) a_i(Q) - n_i), \qquad (19)$$

where V_o is a constant, ω_s are the ground state frequencies, b_s^+ and b_s are boson creation and destruction operators, Q_s the normal coordinates and

$$n_i = \begin{cases} 1 \text{ for i occupied} \\ 0 \text{ for i unoccupied} \end{cases}$$

The orbital energies and electronic operators depend on the normal coordinates. The neglect of this dependence in the electronic operators corresponds to the Born-Oppenheimer approximation which amounts to setting the commutators $[b_s^{(+)}, a_i^{(+)}] = 0$. $\varepsilon_i(Q)$ is expanded in a Taylor series where we include only the first order term (for a more complete derivation, see Refs. 3 and 18; for a simplified derivation Ref. 11).

$$\varepsilon_i(Q) = \varepsilon_i(0) + \Sigma_s \left(\frac{\partial \varepsilon_i}{\partial Q_s}\right)_o Q_s + \ldots, \qquad (20)$$

where "0" denotes the equilibrium geometry of the neutral ground state. Introducing the first order coupling constants

$$\kappa_s^{(o)}(i) = -\frac{1}{\sqrt{2}} \left(\frac{\partial \varepsilon_i}{\partial Q_s}\right)_o \qquad (21)$$

we obtain for the Hamiltonian

$$H = V_{NN}(0) + \sum_s \omega_s (b_s^+ b_s + \frac{1}{2}) + \Sigma \varepsilon_i(0)\, a_i^+ a_i$$

$$- \sum_i \sum_s \kappa_s^{(o)}(i)\,(a_i^+ a_i - n_i)\,(b_s + b_s^+) \qquad (22)$$

where $V_{NN}(0) = V_o - \sum_i \varepsilon_i n_i$. Many-body effects are included by replacing ε_i by E_i and $\kappa_s^o(i)$ by $\kappa_s(i) = -1/\sqrt{2}\,(\partial E_i/\partial Q_s)_o$, where E_i is the exact pole of the Green's function. The spectrum is given by the transition probability per unit time and unit energy. For ionization out of orbital $|i\rangle$ and for one vibrational mode this is given by

$$P_i(\omega) = \sum_{n=o}^{\infty} e^{-a} \frac{a^n}{n!} \delta\,(\omega - E_i - a\omega + n\omega) \qquad (23)$$

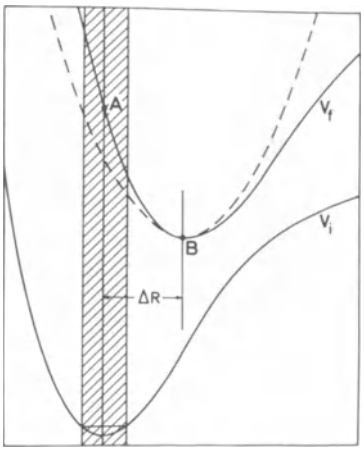

Fig. 6. A schematic one-dimensional drawing of the initial (i) and final (f) potential surfaces. The Franck-Condon region is indicated by the shaded area. The harmonic expansion of V_f about its equilibrium geometry is represented by a broken line.

with $a = (\kappa/\omega)^2$. The first part is the Franck-Condon factor and the δ-function gives the position of the lines. $E_i + a\omega$ is except for the sign the adiabatic ionization energy (0-0 transition).

The Hamiltonian has been obtained by expanding all Q-dependent terms with the exception of the electronic operators about the equilibrium geometry of the electronic ground state. The calculation of the spectral function implies that the ground state and the ionic state potential surfaces are expanded about the ground state equilibrium geometry. It must be emphasized at this point that the traditional approach to calculate Franck-Condon factors within the harmonic approximation is to expand both potential surfaces up to second order about their respective minima. That this expansion is inappropriate is easily understood from an inspection of Fig. 6 which shows schematically the initial and final state potential surfaces. The initial state vibrational function can be assumed to be well described within the harmonic approximation. The minimum of the upper potential surface, however, may lie considerably outside the Franck-Condon region as indicated by the shaded area in Fig. 6. The overall shape of the spectrum depends only on the behavior of the final state potential surface within the Franck-Condon region. It is advantageous therefore to expand the final state potential surface about a point within the Franck-Condon region, i.e., the ground state equilibrium configuration, point A, in Fig. 6. An expansion about the final state equilibrium configuration (point B) will give a poor description of the final state energy surface

within the Franck-Condon region if the coupling is strong. In contrast to the intensities the vibrational energy levels in the final state depend on the potential surface as a whole. Therefore its harmonic expansion about the initial state equilibrium geometry does not necessarily lead to accurate line spacings in the calculated spectrum. It is our opinion, however, that for interpretative purposes the accurate calculation of intensities is more valuable than the accurate calculation of line spacings as the intensities are necessary to assign the spectrum. The calculated intensities are, as should be noted, independent of the line spacings. In drawing the spectra the ionic frequencies may be taken as those of the ground state or from the PES.

The success of this method can clearly be demonstrated in the calculation of the vibrational structure in the first band in the PES of NH_3 [19]. The calculation of the vibrational structure of some Rydberg transitions and of the first band in the PES of NH_3 has presented a problem. These transititions show an extended progression in the bending mode ν_2. The intensity maximum occurs at n = 6 in the UV absorption spectrum and at n = 7 in the PES. The strong excitation of the bending mode is in qualitative agreement with the transition from a pyramidal ground state to a planar final state. Calculations in the traditional way have been performed within the harmonic approximation and employing anharmonic potentials for the bending vibration. In the harmonic approximation the intensity maximum was found to occur for n = 4 in the excitation spectrum in rather poor agreement with experiment. The use of anharmonic potentials did surprisingly not improve the agreement with experiment. If the vibrational structure in the PES is calculated according to the procedure outlined above very good agreement with experiment is obtained as can be seen from Fig. 7. The intensity maximum is calculated to occur at the n = 7 line as is indeed observed in the high resolution spectrum of Rabalais et al. [20]. The calculation presented here is an absolute one including the calculation of the position of the band of the energy scale. The potential in the case of NH_3^+ is rather anharmonic. But as the Franck-Condon zone is narrow a second order Taylor expansion about the center of the zone gives a fairly accurate description of the final state potential surface within the zone. In the traditional approach this part of the potential surface is poorly described and a high order Taylor expansion would have been necessary.

Applications

For the calculations the MUNICH integral, SCF, and transformation package written by G. Diercksen and W. P. Kraemer [21] has been used. The Green's function and TDA calculations have been performed with programs written by the author. All calculations have been performed on the IBM 360/91 and the Amdahl 470/V6 computers at the Max-Planck-Institutes in Garching (Germany).

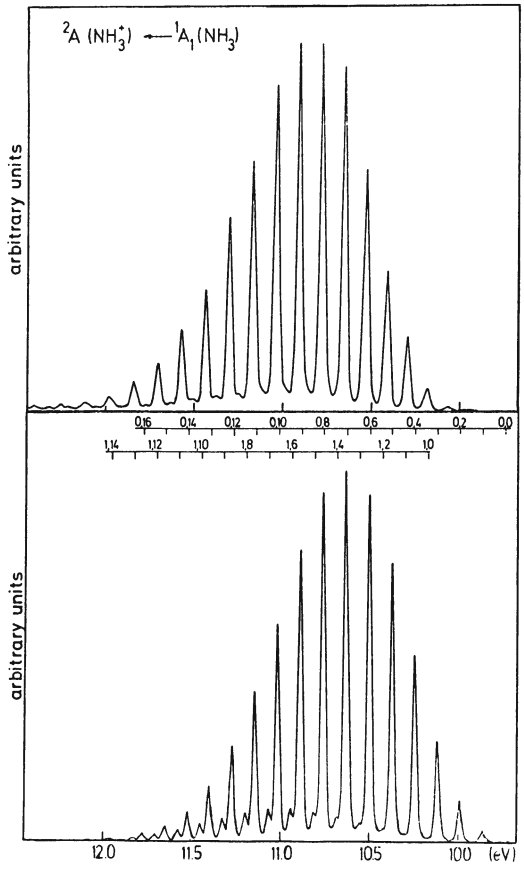

Fig. 7. The first band in the PES of NH_3 as recorded by Rabalais et al. [20] (upper part) and the calculated spectrum (lower part).

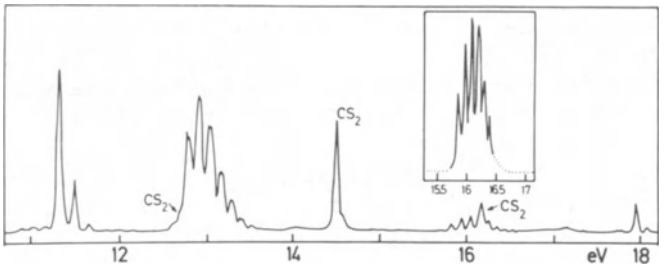

Fig. 8. The PES of CS [22].

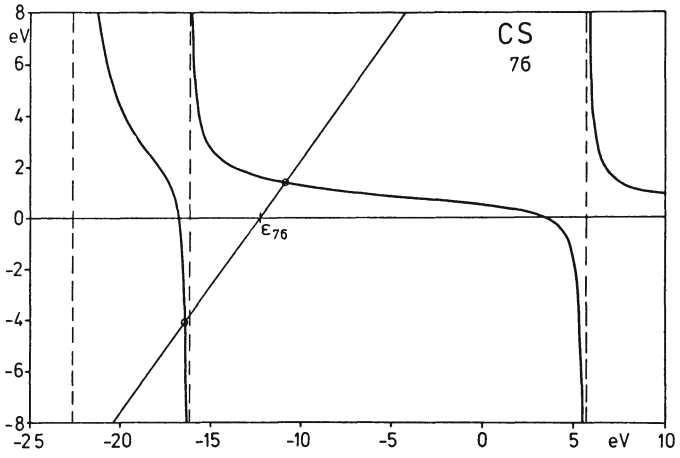

Fig. 9. Schematic plot of $\Sigma_{7\sigma 7\sigma}$ as a function of ω for CS.

Application to the CS Molecule

As the first example we discuss the CS molecule [8]. This will illustrate clearly the structure of the self-energy and the different possibilities that can arise in solving the Dyson equation. The calculations have been performed with the TDA method and without the inclusion of the constant diagrams. It should be mentioned that in the outer valence region much more accurate results can be obtained by using the Green's function method especially adapted to this energy range. But such a calculation should be preceeded by a TDA calculation as the TDA method gives a qualitatively correct spectrum over the entire energy range and its results then determine for which ionization processes the GF calculation should be performed. The GF calculations have been performed for CS but they will not be discussed here. We will return to the question of accuracy below.

The PES of CS (Fig. 8) contains four bands [22] below 20 eV instead of three bands (due to ionization from 7σ, 2π, and 6σ; ionization of 5σ electrons occurs above 20 eV), i.e., there is one band too many. This phenomenon can be explained by looking at the schematic self-energy potentials in Figs. 9-11. The solution for the 7σ ionization energy occurs in the main interval and leads to a large pole strength (Fig. 9); the same is the case for 2π ionization.

In the case of the 6σ orbital (Fig. 10) one solution is still found in the main interval but close to the first pole and another solution of approximately equal pole strength in the first interval. These two solutions explain the experimental finding. The 6σ line is split into two lines at about 16 and 18 eV by final state correlation effects. None of these lines corresponds to simple ionization from the 6σ orbital.

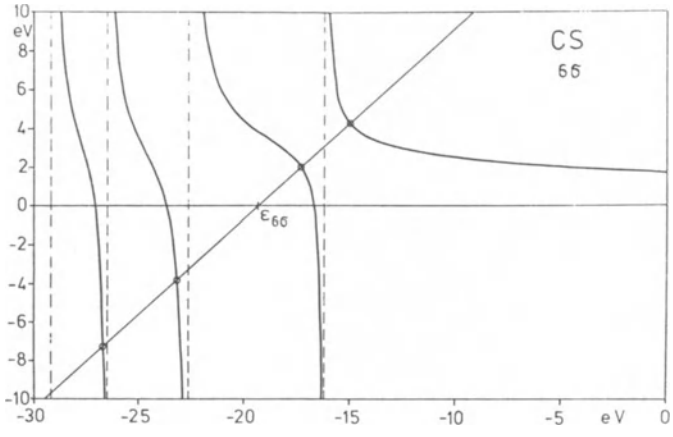

Fig. 10. Schematic plot of $\Sigma_{6\sigma 6\sigma}$ as a function of ω for CS.

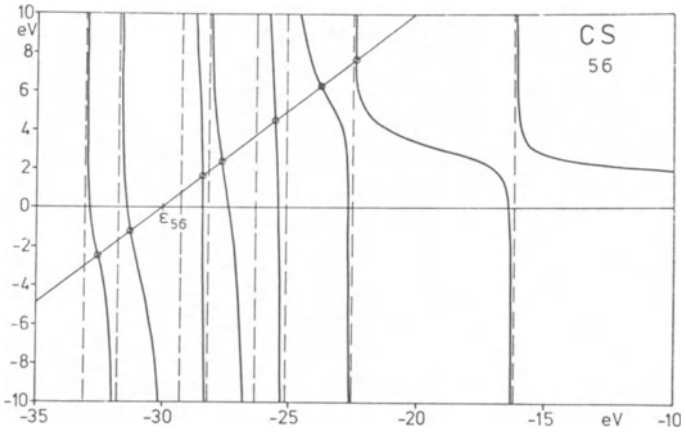

Fig. 11. Schematic plot of $\Sigma_{5\sigma 5\sigma}$ as a function of ω for CS.

The 5σ orbital energy lies in the midst of many poles of the self-energy (Fig. 11). Here we find many solutions of about equal intensity. The orbital picture of ionization thus breaks down for ionization out of the 6σ and 5σ orbitals. The line spectra for 7σ, 6σ, and 5σ ionization are given in Fig. 12.

Application to CS_2 [24]

As the next example we consider CS_2; the PES of this molecule contains two intense satellite lines at very low energy (about 14.1

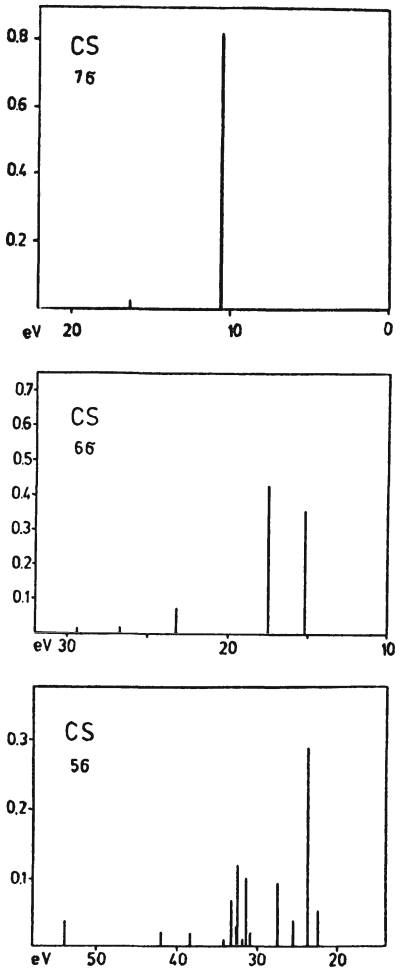

Fig. 12. The calculated ionization spectra of CS (7σ, 6σ, and 5σ orbitals). Note the different ordinate scale for the 5σ spectrum.

and 17.0 eV) [23, 24]. Both arise from $2\pi_u$ ionization, but their intensity (about 4% and 16%) is still small compared to the main line. We will not discuss this point in detail) but turn to the energy region above 20 eV. The ESCA spectrum [25] is reproduced in Fig. 13. It shows a broad band extending over about 20 eV which contains little structure.

In the orbital model two bands ($4\sigma_u$ and $5\sigma_g$) should be found in this energy range. But this clearly cannot explain the observed structure. Vibrational broadening cannot account for it either. The explanation is given by the calculated spectrum (Fig. 14). The $4\sigma_u$ and $5\sigma_g$ lines are smashed to pieces by many-body effects and

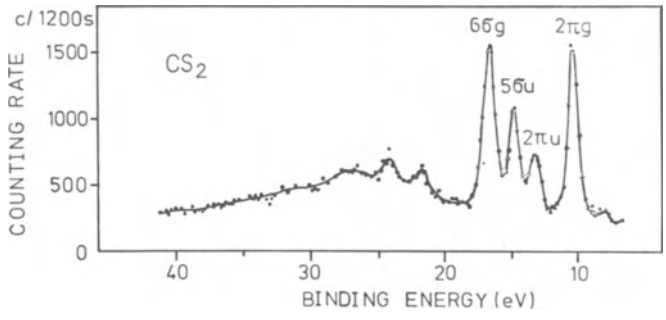

Fig. 13. Mg K_αPES of CS_2 as recorded by Allan et al. [25].

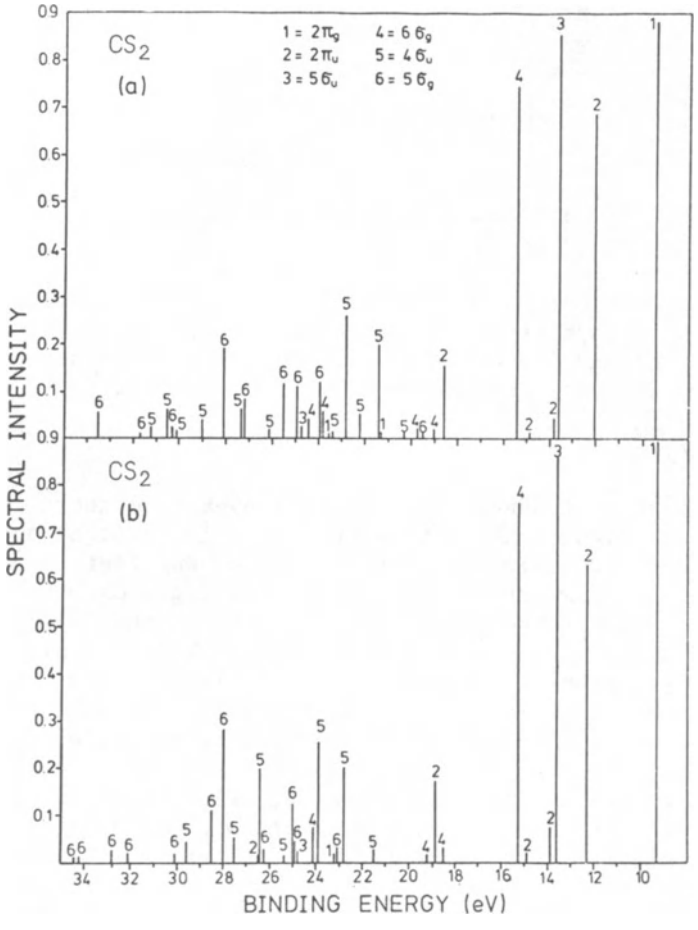

Fig. 14. Calculated positions and relative intensities for the ionic states arising from valence ionization of CS_2. a) Basis set (12s 9p/9s 5p); b) basis set (12s 9p 2d/9s 5p 1d).

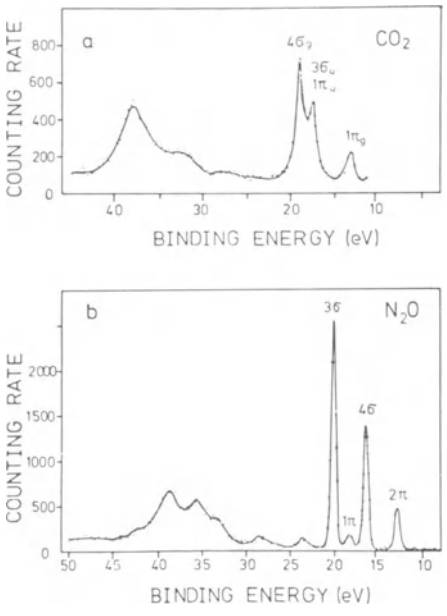

Fig. 15. ESCA spectra of CO_2 and N_2O (from Refs. 25, 26).

numerous lines appear instead of the expected two lines. The two calculated spectra differ in some details which is to be expected, because of the complicated nature of these resonance states, but both explain the observed spectrum in a very satisfactory way.

CO_2, N_2O [12]

It is a general tendency that the many-body effects (satellite lines and breakdown of the orbital model of ionization) are stronger for the heavier atoms in a homologous series and that they are stronger if the symmetry is lowered. Thus, e.g., many-body effects in CO occur mainly for the 3σ lines but not for the 4σ line in contrast to CS where the 5σ line (corresponding to the 3σ line of CO) is completely smashed to pieces and the 6σ line (corresponding to the 4σ line of CO) is split into essentially two components. In this respect it is interesting to examine the molecules CO_2 and N_2O which are valence isoelectronic with CS_2. The ESCA spectra of CO_2 and N_2O are given in Fig. 15 and the (e, 2e) spectra are given in Fig. 16. Both groups of spectra show below about 20 eV the four main outer valence lines and a lot of structure in the region from about 20 to 45 eV. The CO_2 ESCA spectrum appears to contain less structure than the spectrum of CS_2. The spectra calculated with the TDA method for CO_2 are plotted in Fig. 17. Below 20 eV there are no satellite lines in contrast to the case of CS_2. But the breakdown

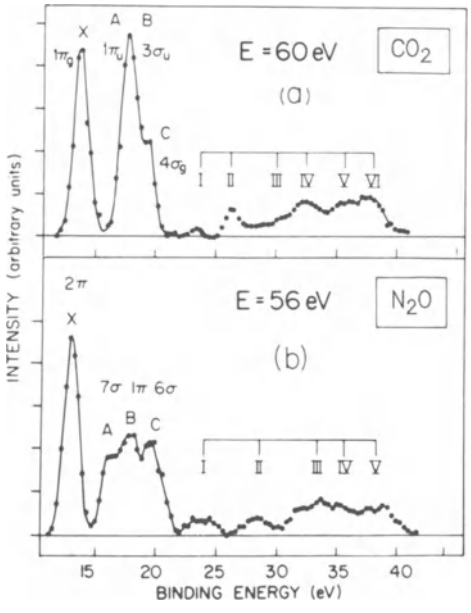

Fig. 16. (e, 2e) spectra of CO_2 and N_2O (from Refs. 27, 12).

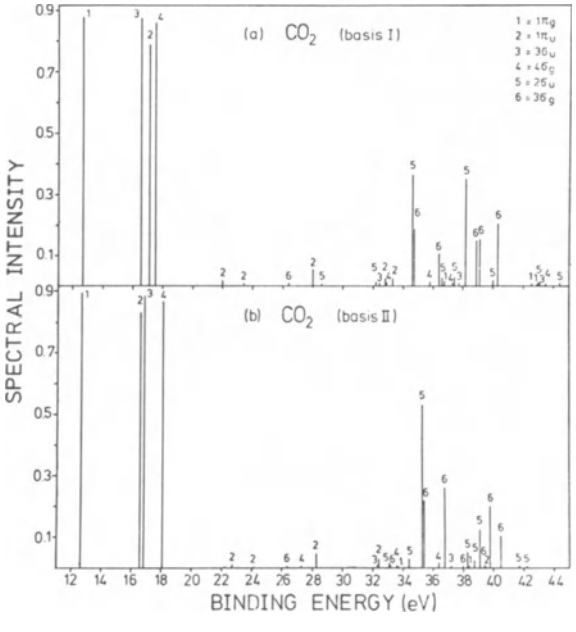

Fig. 17. Ionization spectrum of CO_2 calculated with the TDA method and two different basis sets (upper part: basis (9s5p/4s2p), lower part: basis (11s7p1d/5s3p1d).

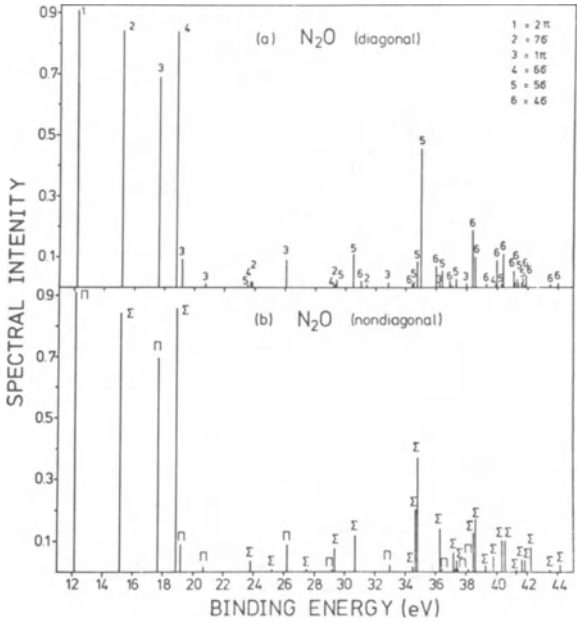

Fig. 18. Ionization spectrum of N_2O calculated with the TDA method (upper part: diagonal approximation to the self-energy; lower part: nondiagonal approximation to the self-energy).

of the orbital model of ionization occurs as in the case of CS_2 for ionization from the two innermost valence orbitals, although there is somewhat less structure than calculated for CS_2. The two calculations exhibit some quantitative differences but the qualitative effects are the same. The spectrum calculated with the TDA method for N_2O with a (9s5p1d/4s2p1d) basis is plotted in Fig. 18. There is one intense low energy satellite line at about 19 eV borrowing its intensity from 1π ionization. The breakdown of the molecular orbital model of ionization occurs for the two innermost valence orbitals as found for CO_2 and CS_2. We thus observe that many-body effects are stronger for heavier atoms in a molecule and for less symmetric molecules.

HF, HCl, HBr, and HI

We would like to pursue this question a bit further and consider the molecules HF, HCl, HBr, and HI. Their (e, 2e) spectra have been recorded by Brion and Weigold et al. [28-30] and they are given together with the theoretical spectra in Fig. 19. The theoretical spectra have been combined from the GF calculation on the 1π and 2σ lines and the TDA calculation. The spectra of HCl, HBr,

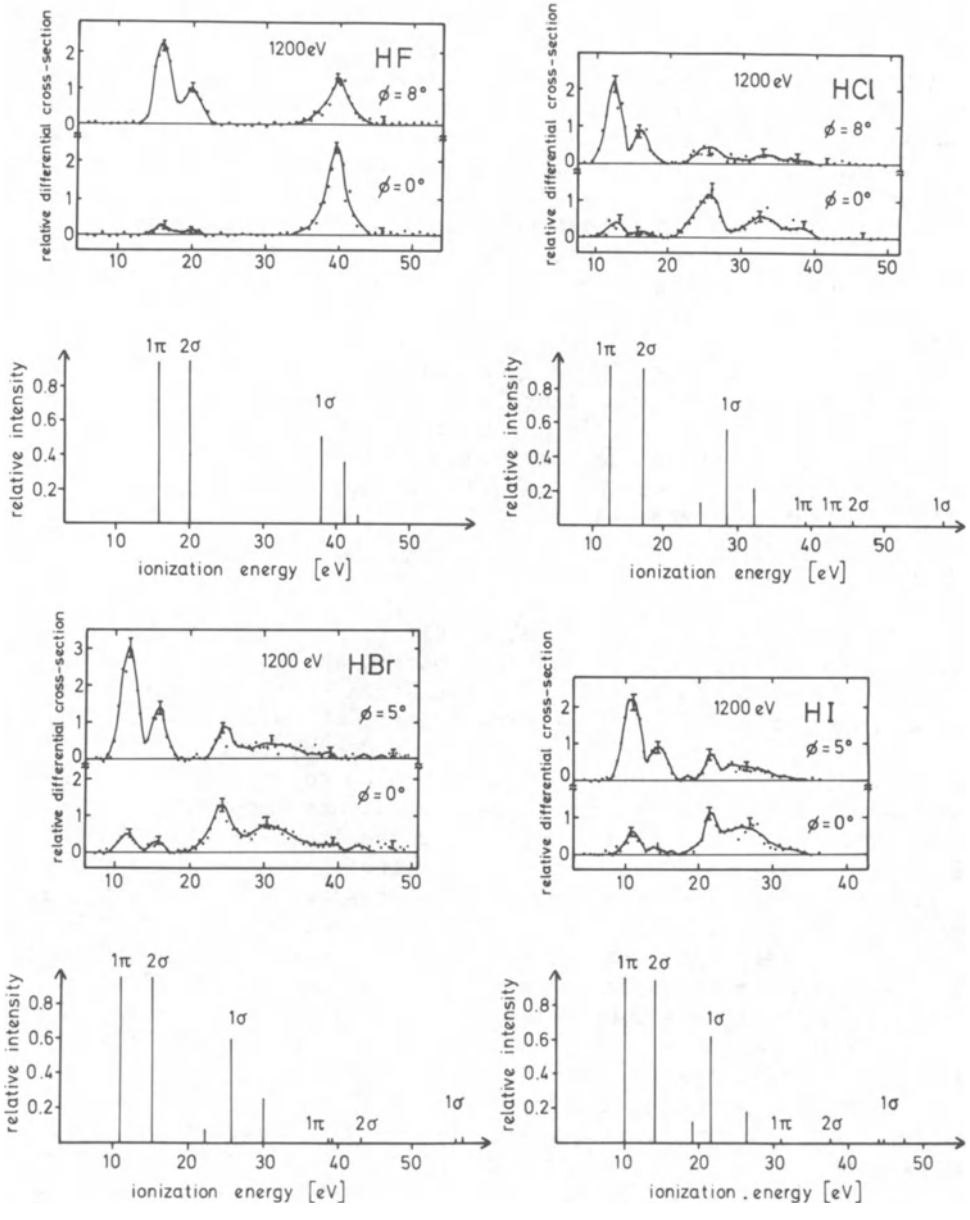

Fig. 19. (e, 2e) spectra of HF, HCl, HBr, and HI (from Refs. 28-30) and theoretical spectra.

and HI are rather similar both from experiment and from the calculation but they differ from the spectrum of HF. The 1σ line of HF is rather symmetric. The calculations predict that it should consist of two lines of about equal pole strength. One would expect this to lead to a more unsymmetrical band shape which is not found in the experiment, but the experiment does not exclude that the band does consist of two lines of nearly equal intensity. The experimental resolution is not sufficient to decide this. The spectra of HCl, HBr, and HI are all very similar. The 1σ line is broken into several lines. A line with about 60% of the intensity survives. An intense satellite line is observed at lower energy and another even more intense one at higher energy to the "main" line. This explains the unsymmetrical shape of the first part of the 1σ band and the next maximum towards higher energy. A number of smaller satellite lines are calculated at higher energies but their intensity is not in agreement with the experimentally found structure at higher energies. The reasons for this may be the basis set deficiencies in the higher energy range and continuum contributions. On the whole the TDA calculations become inadequate once one is close to the double ionization threshold.

s-Tetrazine [13]

The breakdown of the orbital model of ionization becomes more dramatic for larger molecules. The spectra above about 20 eV begin to look like a continuum, but this breakdown also occurs at very low energies, i.e., for lines which are not of 2s origin for first row atoms. The experimental and calculated spectra for s-tetrazine are given in Fig. 20 for the energy range up to about 24 eV. In the case of the azabenzenes the use of Koopmans' approximation to assign the PES is a real disaster. The results have no relation to reality, whereas the Green's function method proves to be a very powerful calculation tool [13]. In Koopmans' approximation the ordering of ionic states is (with increasing ionization energy) 1, 2, 3, 4, 5, 6 where the detailed symmetry labels can be deduced from Fig. 20. The correct ordering of states is, however, 1, 5, 2, 4, 6, 3, i.e., there is a complete reordering necessary. Beyond the sixth ionization energy the one-particle picture of ionization breaks down and Koopmans' approximation is intrinsically inapplicable. Above about 15 eV the orbital model breaks down and the lines become split into two to four components. These orbitals are not of 2s character. As a consequence the concept of orbital ordering is inapplicable here. The spectrum in the energy range from 20 to 50 eV is given in Fig. 21. The spectrum is considered only as a qualitative one due to basis set limitations. A huge number of lines is found instead of the six lines postulated by Koopmans' hypothesis. The maximum pole strength is as small as 0.1 in some cases. This corresponds in a CI language to the case that the "dominant" configuration has only a coefficient of 0.3!

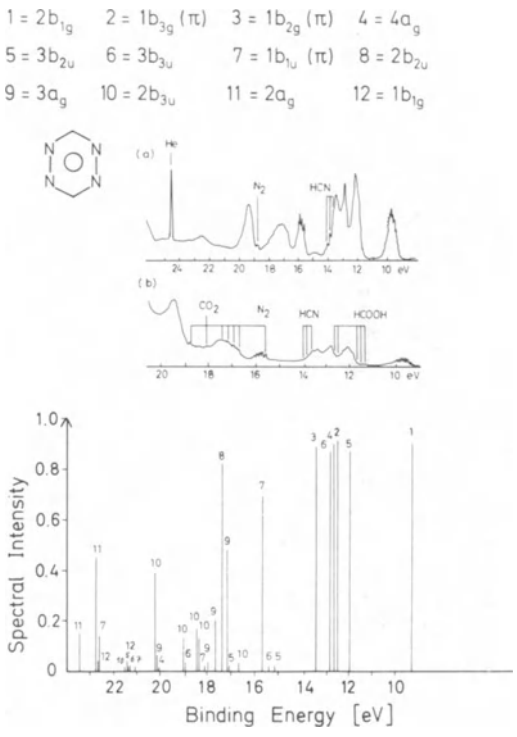

Fig. 20. Ionization spectrum of s-tetrazine up to about 24 eV. The experimental spectra are taken from Ref. 31. The numbering of the orbitals is according to the HF sequence.

The Accuracy of the GF Calculations [32]

The main interval, i.e., the interval between the first affinity pole and the first ionization pole of the self-energy contains the outer valence ionization energies. A PES in general consists in the low energy range of many closely spaced bands. One thus needs high accuracy in the computed ionization energies in order to reliably assign a PES. This is a requirement to both the computational method and to the basis set. But besides accuracy one needs stability of the results - stability with respect to basis set variations. One could call this stability if large basis sets are used and one would better call it basis set insensitivity if one is dealing with smaller basis sets. A double zeta basis will be called a small basis set to avoid misunderstanding. The accuracy which can be achieved and the stability with respect to basis set extension and variation has been examined with the Green's function method and the results are published in Ref. 32 and compared with litera-

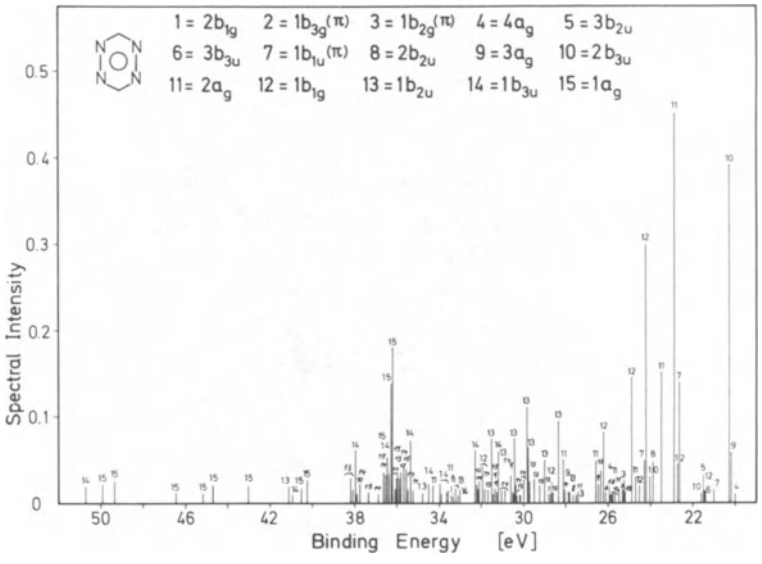

Fig. 21. Ionization spectrum of s-tetrazine from 20 to about 50 eV calculated with the TDA method.

Table 1. Absolute Errors in the Ionization Energies of N_2 Calculated with the GF Method and with Different Basis Sets (all values in eV)

	9s5p	11s7p1d	11s7p2d	11s7p3d	11s7p2d1f	exp [23]
$3\sigma_g$	0.75	0.29	0.15	0.07	0.08	15.60
$1\pi_u$	0.64	0.18	0.22	0.23	0.15	16.98
$2\sigma_u$	0.41	0.23	0.13	0.18	0.20	18.78

ture values (see also Refs. 33-35). We would like to discuss the results for N_2, H_2O, and HCl.

The N_2 molecule represents a good test case since Koopmans' approximation predicts an incorrect ordering for the $^2\Pi_u$ and $^2\Sigma_g$ states [36]. This incorrect ordering persists in ΔE_{SCF} calculations and only by including the electronic correlation energy can the correct ordering of states be obtained. Calculations have been performed with the (11s7p)/[5s4p] basis set [37] supplemented with 1,2 and 3 d-type functions and with 2 d-type and 1 f-type functions. All basis sets have been exhausted completely in the many body calculations except for the last one, where the six virtual orbitals of largest orbital energy were left out. The experimental values

Table 2. Absolute Errors in the Ionization Energies of H_2O Calculated with the GF Method and with Different Basis Sets (all values in eV)

	9s5p	11s7p1d	11s7p2d	11s7p3d	11s7p4d	11s7p3d1f	exp [23]
$1b_1(\pi)$	0.41	0.0	0.09	0.05	0.03	0.12	12.78
$3a_1$	0.51	0.05	0.02	0.02	0.01	0.02	14.83
$1b_2$	0.23	0.22	0.26	0.22	0.20	0.19	18.72

of the errors in the GF calculations are given in Table 1. The results obtained with a double zeta basis set are given as well.

For the large basis sets the maximum error is approximately 0.2 eV, for the double zeta basis set the errors are exceptionally large, but N_2 represents a very critical case.

Until recently CI-type calculations did not achieve quite the same accuracy for the ionization energies of N_2. The CI calculations of Ermler and Wahl [38] gave a maximum error of 0.9 eV, the CEPA-PNO calculations of Meyer [39] gave a maximum error of 0.4 eV, the MRD-CI calculations of Peyerimhoff, Buenker, and coworkers [40] gave a maximum error of 0.47 eV, but recently Ermler and McLean [35] performed CI-type calculations with large basis sets and included single, double, and quadruple substitutions with unlinked cluster corrections to obtain a maximum error of 0.22 eV.

Similar results are obtained for the H_2O molecule. Five calculations have been performed with the (11s7p/6s1p)/[5s4p/3s1p] basis set supplemented with 1,2,3 and 4 d-type functions and with 3 d-type and 1 f-type functions. All basis sets have been completely exhausted. Table 2 lists the absolute errors in the calculated ionization energies and the experimental values (centroids) [23].

The maximum error is again about 0.2 eV. The results of a calculation with a double zeta basis is enclosed as well; again this basis is insufficient for obtaining accurate results. We thus conclude (see also Ref. 20) that the GF method gives accurate and stable results. The data obtained with the double zeta basis set are, however, somewhat disappointing. But it should be mentioned that in particular N_2 is among the worst representatives (for F_2 the maximum error is only about 0.1 eV, although such a good result can only be pure chance).

It has been occasionally observed that the ionization energies calculated theoretically are lower than the experimental ones al-

Table 3. Ionization Energies of HCl Calculated with the GF Method and Different Basis Sets

	(12s9p/4s)	(12s9pld/4slp)	(12s9p2d/4slp)	(12s9p5dlf/4slp)	exp[a]
1π	12.19	12.29	12.52	12.66	12.79
2σ	16.27	16.44	16.50	16.67	16.72

a) Centroids estimated from the spectra in Ref. 23 and Ref. 45.

though large basis sets including polarization functions have been used (e.g., H_2S [41], C_2H_4 [42, 43]). In such a case the neutral ground state is less well described than the ionic state and ground state correlation energy is lacking. It has been found that a large number of polarization functions including very diffuse ones are required to alleviate this situation (for a detailed discussion, see Ref. 41). This is also the case for HCl [44] (see Table 3).

Using a basis set of double-zeta quality one obtains a rather large error both for the 1π and the 2σ ionization energy. Both energies are calculated too small. Addition of a polarization function on each center only slightly improves the situation. Adding another d-type function on the Cl atom (with a rather small exponential parameter) gives a more substantial improvement. The calculation with 5 d- and 1 f-type function proves to be in very good agreement with experiment.

For other molecules and in particular for larger molecules the errors are in general smaller. In the latter case the reason presumably is the larger effective number of basis functions available due to the larger number of centers. It has been found in comparison both with experimental results and with calculations involving polarization functions that a double zeta basis set can be reliably used to assign PES, i.e., the ordering of states is claimed to be reliable without the claim for quantitative agreement with experiment for all ionization energies. One remark should be added. With increasing ionization energy the errors tend to become larger. There are two principal reasons for this. Satellite lines become more pronounced for these ionization processes and the GF method inherently will give lower accuracy in general; the other reason is that the basis sets appear not to be sufficiently flexible for calculations in this energy range.

Application to C_2N_2 [46], C_4N_2 [47, 48], and Some Nitriles [47]

We turn now to the outer valence region and discuss mainly the GF calculations as well as the calculation of the vibrational structure.

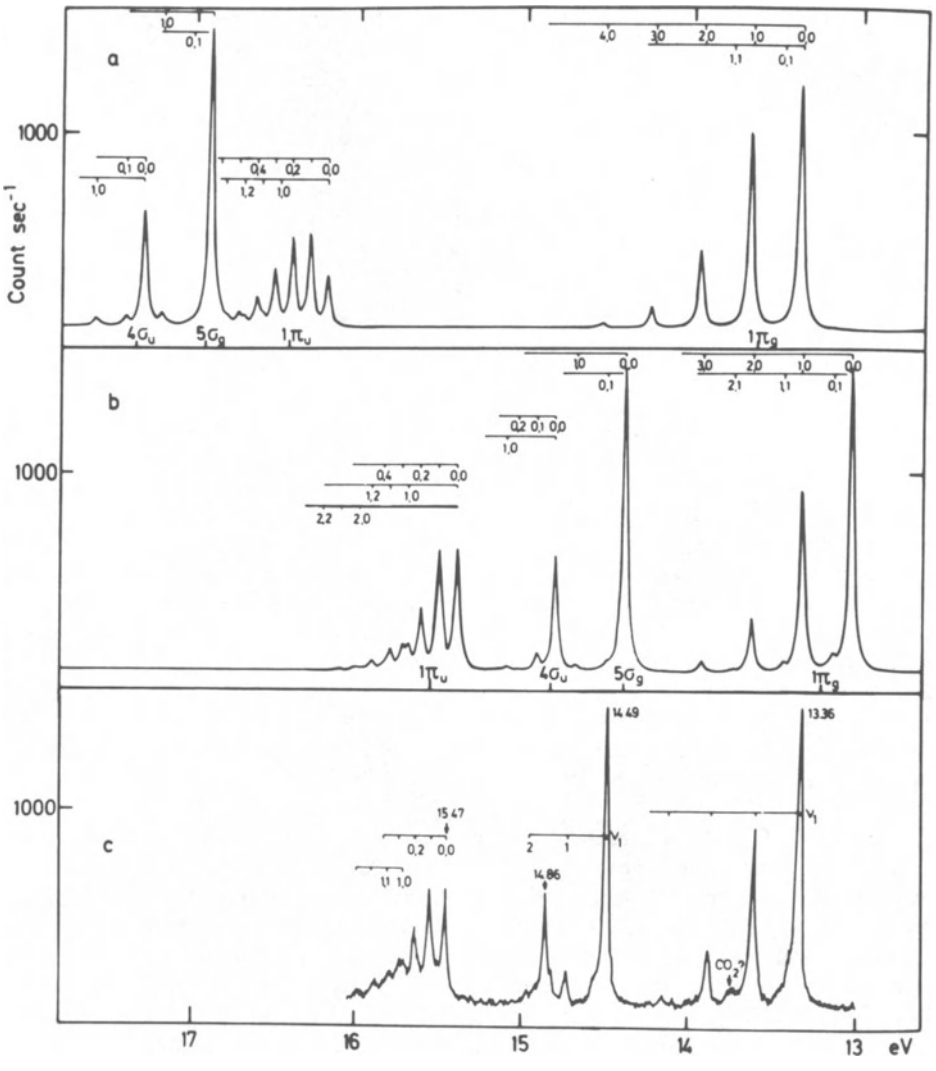

Fig. 22. A comparison of the calculated and experimental PES of C_2N_2. a) Spectrum calculated on the HF level, b) spectrum calculated by including many-body effects, c) experimental spectrum.

It has been mentioned in the beginning that Koopmans' approximation supplies in many cases a reasonable ordering of ionic states and reasonable estimates for the ionization energies. We wish to discuss here a few cases where Koopmans' approximation fails badly. Actually these cases belong to a whole class of molecules, where this method is useless. These are molecules containing N atoms in

Table 4. Ionization Energies of C_2N_2 Calculated with a (9s 5p 1d) Basis Set. The P are the Pole Strengths. All Energies in eV

Symmetry	$-\varepsilon_i$	$I_i^{theor.}$	P_i	$I_i^{exp.}$
$1\pi_g$	13.60	13.20	0.91	13.36
$3\sigma_g$	16.93	14.40	0.90	14.49
$2\sigma_u$	17.35	14.80	0.89	14.86
$1\pi_u$	16.42	15.56	0.88	15.6

an aromatic ring, one example of which has been discussed above, or the C≡N group in a conjugated molecule. The HeI spectrum of C_2N_2 exhibits four bands which have been assigned in order of increasing binding energy as $1\pi_g$, $3\sigma_g$, $2\sigma_u$, and $1\pi_u$ [23]. The assignment has been based on the vibrational structure. The σ-orbitals are the N-lone pair orbitals and ionization out of these orbitals should lead to little vibrational excitation; whereas ionization out of the π-orbitals (CN and CC bonding) should show strong vibrational excitation. Koopmans' approximation on the other hand leads to the following sequence of ionization energies $1\pi_g$, $1\pi_u$, $3\sigma_g$, $2\sigma_u$. (The calculations have been performed with a (9s 5p 1d) basis set.) Thus this approximation fails badly. The experimental and calculated spectra are reproduced in Fig. 22.

In addition it is seen that the vibrational structure of the $1\pi_u$ band is not given correctly in the SCF approximation. The spectrum calculated with the Green's function method is given in Fig. 22 as well [46]. The large frequency mode, ν_1, couples to the π_g ionization and the small frequency mode, ν_2 couples to the π_u ionization process. For $3\sigma_g$ and $2\sigma_u$ ionization the vibrational excitation is only minor. Only three points on the potential surface are required to calculate this PES. A double interchange of the two σ-ionization energies with the $1\pi_u$ ionization energy occurs in the many-body calculation and the computed spectrum is in quantitative agreement with the experimental one. The calculated ionization energies of C_2N_2 are given in Table 4. It is seen that the maximum error is 0.16 eV which is very satisfactory.

In the same way as for C_2N_2 Koopmans' approximation fails for dicyanoacetylene, C_4N_2. In this case the calculations have been performed only with a double-zeta basis set. The agreement with experiment is thus not as good as for C_2N_2 [47, 48]. Again the correct assignment is $2\pi_u$, $4\sigma_g$, $3\sigma_u$, $1\pi_g$, whereas Koopmans' approximation gives $2\pi_u$, $1\pi_g$, $4\sigma_g$, $3\sigma_u$ and a double interchange is necessary to obtain the correct ordering of ionic states as can be seen from Fig. 23.

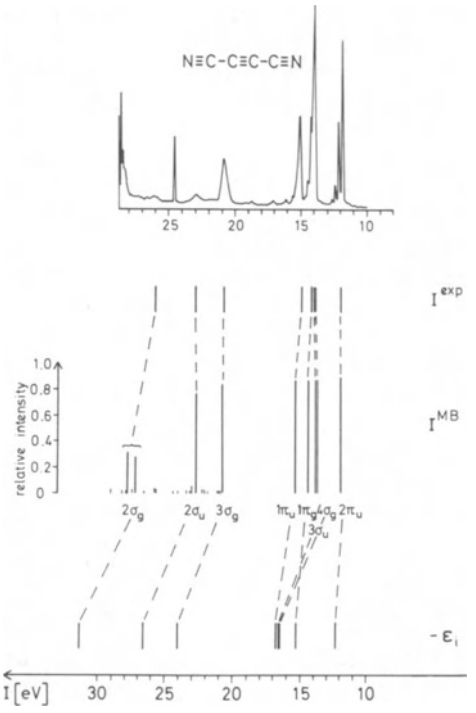

Fig. 23. HeII photoelectron spectrum of C_4N_2 from Ref. 48 and calculated main ionization energies combined from the outer valence GF and the TDA method; the small dots indicate satellite lines.

For a fairly large number of nitriles it has been found that Koopmans' approximation fails consistently in predicting the correct ordering of ionic states [47]. But for this class of molecules it fails also in another respect and this may be even worse. It has been found that in an X-C≡N molecule the ionization energy for ejection of an electron from the N-lone pair orbital increases in the sequence X = CH_3, H, CF_3, and F. This sequence is found from experiment and the many-body calculations but Koopmans' approximation produces a different sequence (CH_3, H, F, CF_3). In molecules of the type X-C≡C-C≡N one would have expected based on the known qualitative rules of organic chemistry and of substituent effects in photoelectron spectroscopy the same trend in the n(N) ionization energies, although with reduced shift sizes. However, this is not the case. The n(N) ionization energy in F-C≡C-C≡N is found at lower ionization energy than that of CF_3-C≡C-C≡N, namely at the same position as in H-C≡C-C≡N. The n(N) ionization energy thus increases in the sequence X = CH_3, H ≃ F, CF_3. This is reproduced by the many-body calculation (the molecule CF_3-C≡C-C≡N

has not been calculated), but Koopmans' approximation again fails. This ordering also contradicts the rules of the perfluoro-effect. Thus, it is dangerous to use Koopmans' approximation to predict such trends. Even in such instances the inclusion of many-body effects is necessary.

There is a simple model which permits rationalization when Koopmans' approximation fails [49, 50]. If a molecule possesses low-lying virtual orbitals or non-diffuse character it is an indication that considerable non-uniform many-body corrections can be expected and thus the ordering of ionic states obtained from Koopmans' approximation may not be the correct one. More precisely, for a linear or planar molecule the existence of a low-lying $\pi(\sigma)$-type unoccupied orbital of non-diffuse character and of an outer valence $\pi(\sigma)$-type occupied orbital leads to large many-body corrections for outer valence ionization energies of $\sigma(\pi)$-type orbitals. The change of ordering occurs in the RCN-type molecules so easily because then n(N) and π-type ionization energies are close together in energy.

Application to Benzene [51]

Owing to the fundamental importance of the benzene molecule in chemistry it has been extensively investigated. Many investigations by photoelectron spectroscopy do exist (see Ref. 51 for a list of references). But in spite of all this work a few points in the assignment of the spectrum remained controversial for a long time. The overlapping of bands and the possibility of Jahn-Teller splitting in the ionic states rendered the assignment of the bands difficult. It was agreed that 8 IP's should lie in the energy range up to 21.21 eV and that the first IP of benzene is due to ionization from the degenerate $e_{1g}(\pi)$ orbital. The next two IP's are attributed to the degenerate $e_{2g}(\sigma)$ and the nondegenerate $a_{2u}(\pi)$ orbitals, but the relative order could not be unambiguously established. The convergence of Rydberg series, the perfluoro effect, deuterium substitution, the vibrational structure and many other data were used to assign the spectrum, but agreement could not be reached; the assignment remained a matter of interpretation. Another controversy concerned the relative ordering of the $2a_{1g}$ and $1b_{1u}$ IP's at 15.45 eV and 16.85 eV (the MO's are again numbered starting with the first valence orbital). This problem was settled by Gelius using intensity arguments to interpret the ESCA spectrum [26]. As the $1b_{1u}$ MO has strong C 2s character in contrast to the $2a_{1g}$ MO it should appear with higher intensity in the ESCA spectrum. This is the case for the band at 15.45 eV.

Theoretical calculations on the SCF level of approximation were of little help in the clarification of these problems as they gave rather divergent results. Only the ab initio calculations employing larger basis sets gave acceptable results. But as the

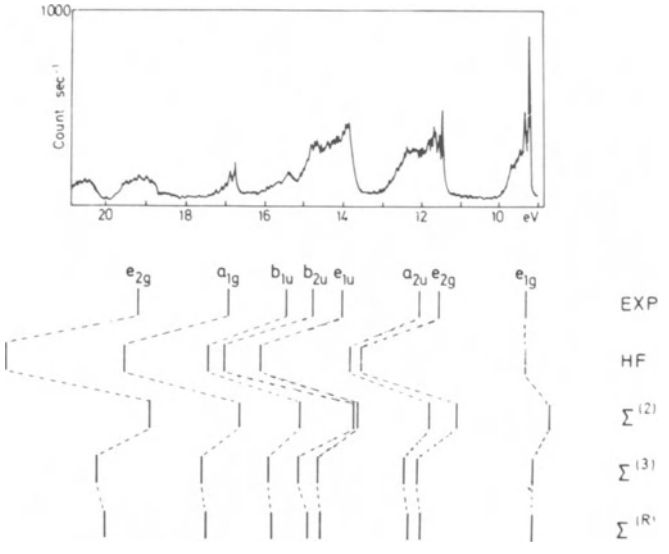

Fig. 24. HeI PES of benzene from Ref. 23 and calculated vertical ionization energies.

$e_{2g}(\sigma)$ and $a_{2u}(\pi)$ MO's are quite close together the inclusion of many-body effects is necessary. The results are given in Fig. 24.

In this case there is no change of ordering in going from the Koopmans' approximation result to the final results. The e_{2g} IP is smaller than the $a_{2u}(\pi)$ IP and the $1b_{1u}$ IP is smaller than the $2a_{1g}$ IP to mention only the two most controversial points.

But due to these basis set deficiencies it might still be argued that the ordering of the second and third IP's is open to some debate as they are separated by only 0.3 eV. In this case the calculation of the vibrational structure of the two bands could bring the decision. Due to the high symmetry of benzene and as only totally symmetric vibrations couple in first order to the electronic motion the vibrational structure in the PES can be computed. This has been done for the e_{2g} and a_{2u} bands neglecting, however, the Jahn-Teller effect in the e_{2g} band. The results are given in Fig. 25. Comparing with the experimental spectrum in Fig. 24 it becomes obvious that the onset of the second band system cannot be due to the a_{2u} band which shows strong vibrational structure. As the a_{2u} band cannot show a Jahn-Teller effect we can make a definite assignment.

Actually every chemist should have argued for the present assignment. The $a_{2u}(\pi)$ MO is the lowest occupied π-orbital and must be strongly C-C bonding and thus should show strong vibrational ex-

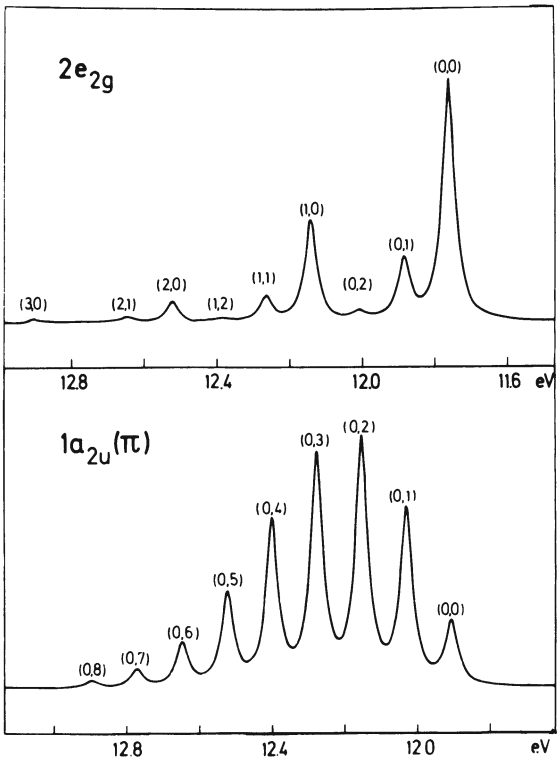

Fig. 25. The calculated vibrational structure of the $2e_{2g}(\sigma)$ and $1a_{2u}(\pi)$ bands of benzene.

citation. This is not the case for the onset of the second band system. Instead, it was argued that the onset of the second band system shows weak vibrational excitation and thus the $a_{2u}(\pi)$ MO is nonbonding!

Novel Breakdown Effects [14, 52]

We have above encountered cases where the orbital model of ionization breaks down completely and cases where Koopmans' approximation completely fails to supply a reasonable ordering of ionic states, although a one-particle picture of ionization is valid. But there exist new and quite unexpected many-body effects. These were discovered in calculating the spectra of propynal, propynol and propiolic acid [14, 52]. We will not discuss their PES in any detail but only pick out the novel part. The HeII PES of propynal is given in Fig. 26 together with the main theoretical results. According to Koopmans' approximation the ordering of ionic states is 2a", 8a', 7a' (with increasing binding energy) but in the many-body calculation (both the GF and the TDA calculation) this changes

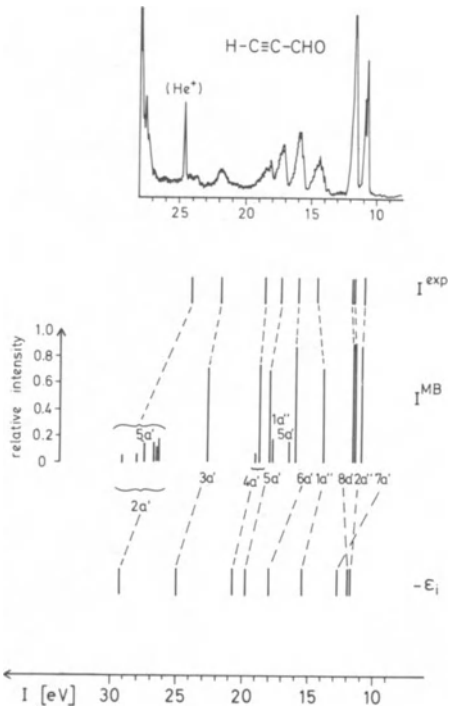

Fig. 26. HeII PES of propynal (from Ref. 52) and calculated main ionization energies (combined from the GF and the TDA calculation).

to 7a', 2a", 8a'. There is thus a change of ordering within a given symmetry species. The node rule becomes violated by many-body effects. It is well-known that the node rule holds only in a one-particle approximation but until now there have been - to the knowledge of the author - no cases of its violation reported. Another case, however, occurs for CH_3NO_2, but this one is not as clear cut [53]. In the presence case there is an easily understandable explanation for the effect. The 7a' orbital is essentially the lone pair orbital on the O atom and the 8a' orbital is the in-plane π orbital of the CC triple bond. If the 7a' ionization energy becomes interchanged with the 2a" ionization energy due to many-body effect it also has to become interchanged with the 8a' ionization energy. The 2a" out of plane and the 8a' in plane CC π-orbitals are quite similar in their structure.

In propynol another type of many-body effect is observed (Fig. 27). The Green's function is strongly nondiagonal in the 4a' and 5a' orbitals. This is denoted by the circle between the correlation lines in Fig. 27 connecting the many-body results with the orbital energies. One obtains two ionization energies. Let the correspond-

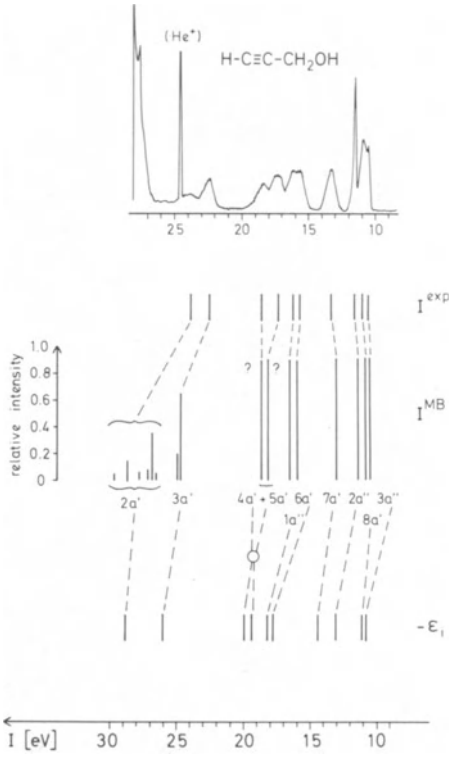

Fig. 27. HeII PES of propynol (from Ref. 52) and calculated main ionization energies (combined from the GF and TDA calculation).

ing ionic states be Ψ_I and Ψ_{II}. These two lines seen in the spectrum obtain their intensities in nearly equal amounts from the simple processes of electron ejection from the 4a' and the 5a' orbital. In a CI picture the wave functions take the following approximate form:

$$\Psi_I = a\ 4a'^{-1} + b\ 5a'^{-1} + c\ \text{2-hole-1-particle terms}$$
$$\Psi_{II} = b\ 4a'^{-1} - a\ 5a'^{-1} + d\ \text{2-hole-1-particle terms},$$

where $|a| \approx |b|$ and $|c|, |d| \ll |a|, |b|$. This looks like a CI between the configurations $4a'^{-1}$ and $5a'^{-1}$. The two-hole-one-particle terms turn out to be very unimportant with respect to their magnitude but they cannot be omitted because otherwise the mixing of the configurations $4a'^{-1}$ and $5a'^{-1}$ would not take place because the matrix element

$$\langle 4a'^{-1}|H|5a'^{-1}\rangle = \langle 4a'|F|5a'\rangle = 0,$$

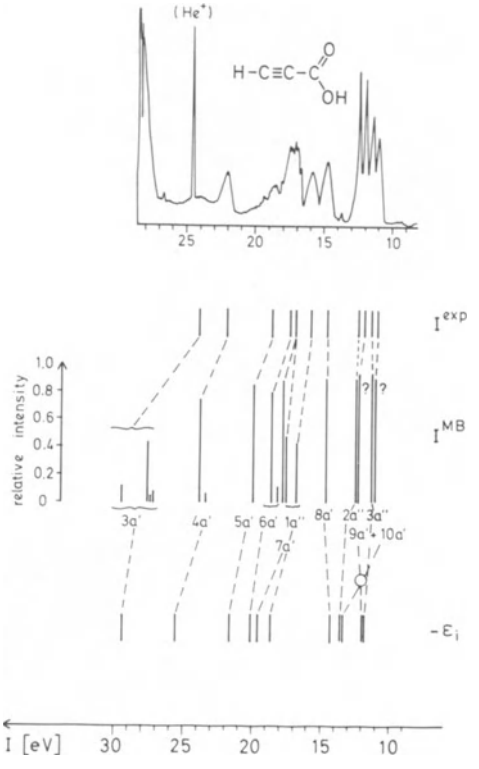

Fig. 28. HeII PES of propiolic acid (from Ref. 52) and calculated main ionization energies (combined from the GF and the TDA calculation).

where H is the Hamiltonian and F the HF operator. A similar although more complicated case is encountered for propiolic acid (Fig. 28). Here the $9a'^{-1}$ and $10a'^{-1}$ configurations mix to give two new states where the mixing is again mediated via two-hole-one-particle terms which in magnitude are quite unimportant. In addition, there is a reordering of one of these a' ionization energies with the 3a" ionization energy. In effect what happens is even more complex and is discussed in detail in Ref. 14.

Vibronic Coupling in the PES of Butatriene [54]

The adiabatic approximation relies on the fact that the energy difference between electronic states is large compared to the spacing of the vibrational energies. A breakdown of this approximation may therefore occur when two electronic states become degenerate or nearly degenerate. The Jahn-Teller effect represents just one example. But vibronic coupling effects are more general. We have

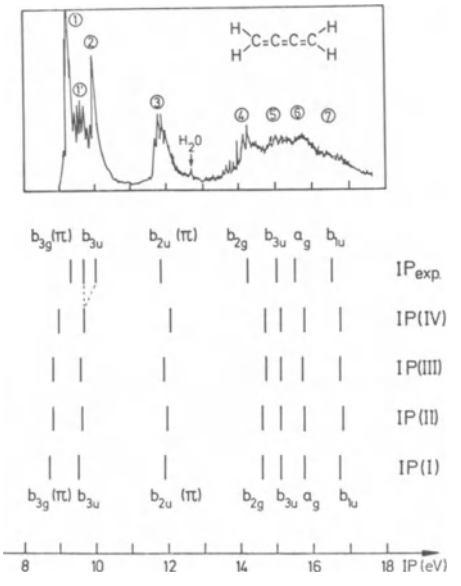

Fig. 29. Photoelectron spectrum of butatriene from Ref. 57 and ionization energies calculated by the GF method with different bases.

dealt with these effects in the PES of butatriene [54], where vibronic coupling is responsible for the appearance of an additional band in the PES, in ethylene, where the strong excitation of the torsional mode in the first band arises from vibronic coupling [55] and in the case of HCN where the complex vibrational structure of the first band system arises from vibronic coupling [56]. Here we would like to deal with the butatriene molecule [54].

The first band system in the PES of butatriene has presented a mystery [57, 42], see Fig. 29. In the energy range from about 9 to 10.5 eV two bands should be found, but the spectrum does contain three. This first band is shown enlarged in Fig. 30. Band (1') is referred to as the mystery band. The calculations with the GF method and different basis sets are shown in Fig. 29 as well. It is seen that only two ionization processes ($1b_{3g}(\pi)$ and $2b_{3u}$) can be assigned to this band system. The clue to the mystery band lies in the fact that the $^2B_{3g}(\pi)$ and $^2B_{3u}$ states are quite close in energy so that the Born-Oppenheimer approximation breaks down. The two states are coupled by a vibration of a_u symmetry which is the torsional vibration.

In the treatment of the vibrational motion as presented above we have neglected the Q-dependence of the electronic operators.

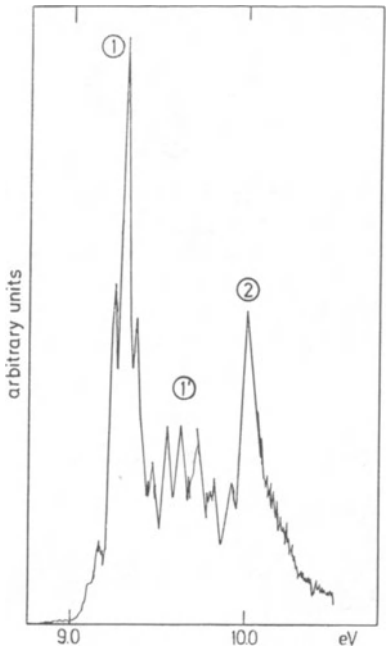

Fig. 30. The first band system in the photoelectron spectrum of butatriene [57]. The band (1') is referred to as the mystery band.

This is not permitted if the energy difference between the electronic states is not large compared to the vibrational spacings. We start from the Hamiltonian Eq. (22), where it is assumed that the electronic operators still depend on the normal coordinates. We transform the $a_i(Q)$ to a Q-independent basis:

$$a_i(Q) = \sum_j \langle \phi_i(Q) | \phi_j(0) \rangle \, a_j(0) \tag{24}$$

We insert this expansion in Eq. 22, expand $|\phi_i(Q)\rangle$ in a Taylor series and collect all terms linear in Q to obtain

$$\begin{aligned} H = & \sum_s \omega_s (b_s^+ b_s + \tfrac{1}{2}) + \sum_i \varepsilon_i(0)\, a_i^+ a_i \\ & - \sum_{i,s} k_s^o(i)[a_i^+ a_i - n_i](b_s + b_s^+) \\ & + \sum_{i<j} \sum_s \lambda_s^o(i,j)[a_i a_j^+ + a_j a_i^+](b_s + b_s^+). \end{aligned} \tag{25}$$

For the vibronic coupling constants $\lambda_s^o(i,j)$ the following expression is obtained

$$\lambda_s^o(i,j) = \frac{1}{4}\left\{\left(\frac{\partial^2(\varepsilon_i(Q)-\varepsilon_j(Q))}{\partial Q_s^2}\right)_o\right\}^{1/2} \tag{26}$$

From the form of the Hamiltonian one can deduce the following selection rules for nonvanishing adiabatic coupling constants $\kappa_s(i)$: $\Gamma_i \times \Gamma_i \times \Gamma_s \supset \Gamma_A$ and for the nonvanishing nonadiabatic ones (λ_s): $\Gamma_i \times \Gamma_j \times \Gamma_s \supset \Gamma_A$, where Γ_i is the representation of orbital $|\phi_i\rangle$, Γ_s the representation of Q_s and Γ_A the totally symmetric representation. Vibronic coupling thus takes place between different electronic states by vibrations of appropriate symmetry (not necessarily totally symmetric ones).

For the spectrum one obtains the expression

$$P(\omega) = \int dt\, e^{i\omega t}\, \underline{\tau}^{+}\langle \underline{0}|e^{i\mathcal{H}t}\,\underline{0}\rangle\underline{\tau} \tag{27}$$

where $\underline{\tau}$ is the matrix of the electric dipole operator between the initial and final state.

$$|\underline{0}\rangle = \begin{pmatrix} |0\rangle & 0 \\ 0 & |0\rangle \end{pmatrix} \tag{28}$$

$|0\rangle$ is the vibrational ground state of the neutral molecule. The dimension of $|0\rangle$ is two as in butatriene we are dealing with two electronic degrees of freedom, the $^2B_{3g}(\pi)$ and the $^2B_{3u}$ states. $\mathcal{H}$ is a matrix Hamiltonian free of electronic operators. For butatriene it is given by

$$\mathcal{H} = \mathcal{H}_1 + \mathcal{H}_2 \tag{29}$$

$$\mathcal{H}_1 = [\omega_\alpha(b_\alpha^{+}b_\alpha + \tfrac{1}{2})]\underline{1} + \begin{pmatrix} -\varepsilon_1 + k_1^o(b_\alpha + b_\alpha^{+}) & 0 \\ 0 & -\varepsilon_2 + k_2^o(b_\alpha + b_\alpha^{+}) \end{pmatrix} \tag{30}$$

$$\mathcal{H}_2 = [\omega_\beta(b_\beta^{+}b_\beta + \tfrac{1}{2})]\underline{1} + \begin{pmatrix} 0 & -\lambda^o(b_\beta + b_\beta^{+}) \\ -\lambda^o(b_\beta + b_\beta^{+}) & 0 \end{pmatrix}. \tag{31}$$

Here $k_i^o \equiv k_\alpha^o(i)$. We have assumed that only one totally symmetric vibration α and one non-totally symmetric vibration β couple to the

electronic motion (that this is correct results from the calculation of all coupling constants). The above Hamiltonian is given in the one-particle approximation. As discussed above many-body effects can be taken into account by using renormalized poles of the Green's function and renormalized coupling constants.

$$\varepsilon_i \rightarrow E_i \tag{32}$$

$$k_s^0(i) \rightarrow k_s(i) = -\frac{1}{\sqrt{2}}\left(\frac{\partial E}{\partial Q_s}\right)_0 \tag{33}$$

$$\lambda_s^0(1,2) \rightarrow \lambda_s(1,2) = \frac{1}{4}\left\{\left(\frac{\partial^2 (E_1(Q)-E_2(Q))}{\partial Q_s^2}\right)_0\right\}^{1/2}, \tag{34}$$

where the E_i are the exact poles of the Green's function. The Hamiltonian describes the vibrational motion in the ionic states as well as the vibronic coupling between these states. It should be noted that unless $k_1 = k_2$ the two parts $\mathcal{H}_1$ and $\mathcal{H}_2$ do not commute and therefore the totally symmetric and non-totally symmetric motions cannot be treated separately. The non-totally symmetric vibration is in the case of the first two electronic states of butatriene a torsional vibration of a_u symmetry, as $b_{3g} \times b_{3u} \times a_u = a_g$. It turns out that the coupling to the totally symmetric modes is very important. Fortunately it is only one totally symmetric mode (one of the CC stretching modes) which couples strongly to the electronic motion in this particular case. One mode modulates the potential for the other one; thus the two modes cannot be separated. This effect is of fundamental importance (see also C_2H_4 [55] and HCN [56]) and has practically been overlooked in the literature on vibronic coupling. To be able to compare with experiment we have drawn the calculated spectra in Fig. 31A-D representing the vibrational lines by Lorentzians of width (fwhm) 0.025 eV and have assumed $|\tau_{e1}|^2 = |\tau_{e2}|^2$. The spectra in Figs. 31A and B have been computed using the HF and many-body results, respectively. It is seen that the vibronic coupling effects influence the first band only little, i.e., the individual vibrational lines of mode α show only little structure due to interaction with mode β. This is due to the large energy difference E_1-E_2 obtained in the HF approximation. By including many-body effects this difference becomes smaller, the modes α and β interact stronger and the more complex structure shown in Fig. 31B results. The distance between the most intense peaks is still too large in the calculated spectrum. This is mainly due to basis set deficiences as discussed in Ref. 41. In particular, E_1 will be lowered by using extended basis sets. In Fig. 31C we have thus chosen $E_1 = -9.4$ eV and $E_2 = -9.9$ eV and otherwise taken the many-body results. The fine structure of the first band in the experimental spectrum is well reproduced and it is seen that a third band emerges between the two bands. This band clearly represents the mystery band.

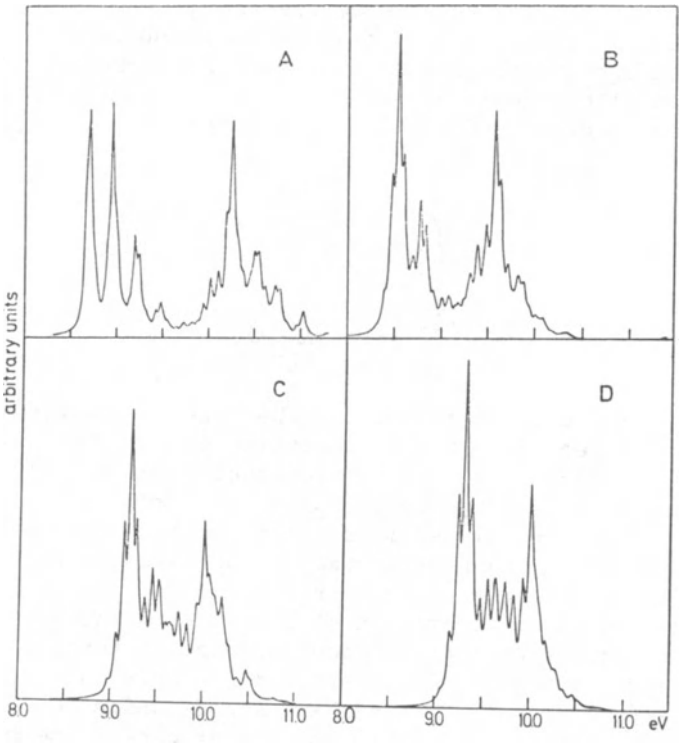

Fig. 31. The calculated PES of butatriene (see text).

In order to find out how accurately the experimental spectrum can be reproduced with the Hamiltonian [29] we have varied the energies and coupling constants to obtain the best fit. This best result is plotted in Fig. 31D. The result is very satisfactory. The number of peaks in bands 1 and 1' is accurately reproduced as is also the onset of band 2 and the peculiar diffuse structure of this band. A 5% variation only from the calculated coupling constants gives the nearly quantitative fit to the experimental spectrum. With the experience gained at present it appears hopeless to determine all parameters purely by ab initio means and get quantitative agreement with experiment. The parameters should be calculated in an ab initio manner to understand the physics underlying the observed phenomenon, i.e., which vibrations are involved and how strong; but to obtain quantitative agreement requires a fitting.

To gain some further insight into the coupling mechanism we have performed three more calculations whose results are plotted in Fig. 32A-C. In the first calculation the best parameters are used, but λ is set to zero, i.e., no vibronic coupling is allowed for. Neglecting κ_1 and κ_2 but including λ leads to the spectrum in Fig. 32B. Both spectra have little in common with the experimental one.

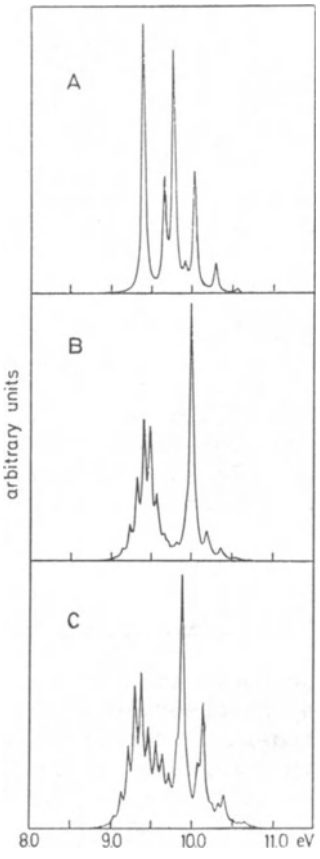

Fig. 32. Investigation of the influence of the individual coupling constants on the first band system of butatriene.

In the last calculation the sign of κ_1 is reversed (Fig. 32C). Again a rather different spectrum results. These results underline the fact that the mystery band arises from a rather subtle interplay between the totally and nontotally symmetric vibrations.

The case of the first band in butatriene is the case of very strong vibronic coupling. The Born-Oppenheimer and the Franck-Condon approximations break down completely. Individual lines can in general no longer be associated with the individual electronic states or with the individual vibrational modes. The lines are of combined electronic and vibrational origin and are a mixture of totally and nontotally symmetric modes.

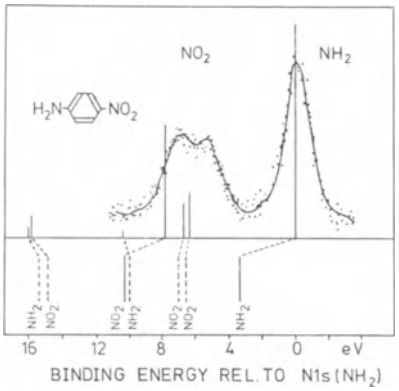

Fig. 33. N1s energy region of the Al Kα ESCA spectrum of paranitroaniline (from Ref. 58) together with the calculated ionization spectrum. The energies of the corresponding unperturbed states are shown in the lower panel.

Splitting of the Line in the Case of Core Ionization [59]

As a final example we would like to turn to ionization of core electrons. In most cases one observes a main line with satellite lines of much smaller intensity. But in some cases one encounters a different situation, e.g., for para-nitroaniline [58]. This molecule has been treated in detail in Ref. 59. The N1s energy region of the Al Kα ESCA spectrum of this molecule is shown in Fig. 33. The N1s lines resulting from nitrogen atoms in the NH_2 and NO_2 groups, respectively, are clearly separated because of the large chemical shift in this highly polar molecule. The N1s (NO_2) line shows a double peak structure, the N1s (NH_2) line, on the other hand, appears as a single line. One might now assume that ionization out of the N1s (NH_2) orbital leads to satellite lines at higher energy which then couple with the N1s (NO_2) ionization leading to a splitting of this latter line. But this is not the case. Because of the extreme and different localization characteristics the coupling matrix element V_{pjkl} is zero. The N1s (NH_2) satellite lines do not couple with the N1s (NO_2) main line. The $k^{-1}l^{-1}j$ configurations which lie energetically below and interact with the N1s (NO_2) single hole configuration involve a hole in the N1s (NO_2) orbital itself plus a valence $\pi \rightarrow \pi^*$ excitation. The shake-up energies in para-nitroaniline are thus negative. The calculated spectra are included in Fig. 33. The specific properties which are responsible for the negative shake-up energies for N1s (NO_2) ionization are easily rationalized considering the charge distribution of the highest occupied and lowest unoccupied orbitals. A schematic picture of these orbitals is given in Fig. 34. From Fig. 34 it is seen that in the highest occupied π orbital most of the charge re-

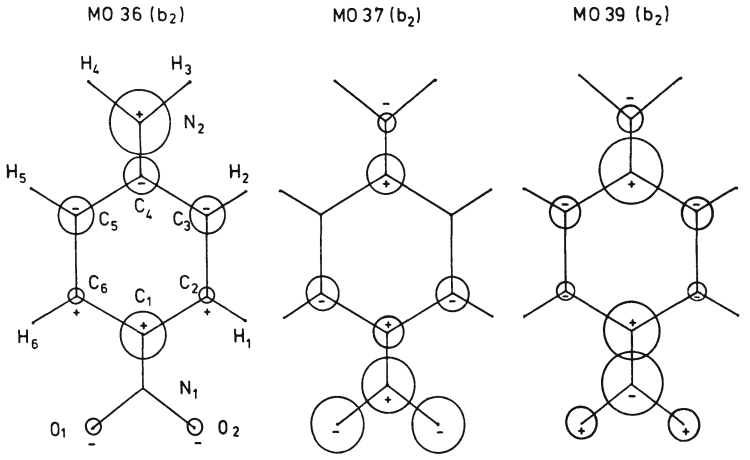

Fig. 34. Schematic picture of the molecule orbitals involved in the low-lying shake-up transitions of para-nitroaniline. Orbital 36 is the highest occupied one, orbitals 37 and 39 are virtual orbitals, all of $b_2(\pi)$ symmetry. The radii of the circles represent the absolute magnitudes of the coefficients of the atomic p-type functions in the LCAO expansion of the molecular orbital.

sides on the NH_2 part of the molecule, the charge on the N atom of the NO_2 group is negligibly small. In the π^* orbital on the other hand most of the charge is concentrated on the NO_2 part of the molecule. Thus the $\pi \rightarrow \pi^*$ excitation involves considerable charge transfer from the NH_2 part to the NO_2 part of the molecule. It is now clear that the presence of a core hole on the N atom of the NO_2 group lowers the $\pi \rightarrow \pi^*$ excitation energy since the core hole is effectively screened by the charge flowing towards this N atom. A core hole on the N atom of the NH_2 group, on the other hand, must increase the $\pi \rightarrow \pi^*$ excitation energy since negative charge is pulled away from the positive core hole in the excitation. The energy gain through the screening of the N1s (NO_2) core hole is large enought to make the $\pi \rightarrow \pi^*$ shake-up energy negative.

Conclusions

We have presented a number of applications of the Green's function method to phenomena in the field of molecular photoelectron spectroscopy and have demonstrated that even some of the complicated effects can be calculated with the help of this Green's function method. With higher resolution and new types of measurements being made in the field of photoelectron spectroscopy more information on molecular structure will become available. The Green's function method is a powerful tool for the interpretation of measurements as well as for predictions.

Acknowledgements

The author would like to acknowledge the close cooperation with L. S. Cederbaum, W. Domcke, J. Schirmer, H. Köppel, G. Diercksen, and W. P. Kraemer and the permission to use the MUNICH SCF and transformation program.

1. T. Koopmans, Physica, 1, 104 (1933).
2. L. S. Cederbaum, Theor. Chim. Acta, 31, 239 (1973); J. Phys., B8, 290 (1975).
3. L. S. Cederbaum and W. Domcke, Adv. Chem. Phys., 36, 205 (1977).
4. A. L. Fetter and J. D. Walecka, Quantum Theory of Many-Particle Systems, McGraw-Hill, New York (1971).
5. G. Wendin and M. Ohno, Phys. Scripta, 14, 148 (1976).
6. L. S. Cederbaum, J. Schirmer, W. von Niessen, and W. Domcke, J. Phys., B10, L549 (1977).
7. J. Schirmer, L. S. Cederbaum, W. Domcke, and W. von Niessen, Chem. Phys., 26, 149 (1977).
8. J. Schirmer, W. Domcke, L. S. Cederbaum, and W. von Niessen, J. Phys., B11, 1901 (1978).
9. W. von Niessen, W. Domcke, L. S. Cederbaum, and J. Schirmer, J. Chem. Soc. Faraday Trans., II 74, 1550 (1978).
10. L. S. Cederbaum, W. Domcke, J. Schirmer, W. von Niessen, G. H. F. Diercksen, and W. P. Kraemer, J. Chem. Phys., 69, 1591 (1978).
11. W. von Niessen, L. S. Cederbaum, and W. Domcke, Proceedings of the NATO Advanced Study Institute, Kos, Greece (1978); C. A. Nicolaides and D. R. Beck, eds., D. Reidel Publ. Co., Dordrecht (1978), p. 183.
12. W. Domcke, L. S. Cederbaum, J. Schirmer, W. von Niessen, C. E. Brion, and K. H. Tan, Chem. Phys., 40, 171 (1979).
13. W. von Niessen, W. P. Kraemer, and G. H. F. Diercksen, Chem. Phys., 41, 113 (1979).
14. W. von Niessen and G. Bieri, in press.
15. W. von Niessen, Unpublished results.
16. J. Schirmer and L. S. Cederbaum, J. Phys. B11, 1889 (1978).
17. J. Schirmer, L. S. Cederbaum, and W. von Niessen, in press.
18. L. S. Cederbaum and W. Domcke, J. Chem. Phys., 60, 2878 (1974); 64, 603, 612 (1976).
19. W. Domcke, L. S. Cederbaum, H. Köppel, and W. von Niessen, Mol. Phys., 34, 1759 (1977).
20. J. W. Rabalais, L. Karlsson, L. O. Werme, T. Bergmark, and K. Siegbahn, J. Chem. Phys., 58, 3370 (1973).
21. G. H. F. Diercksen and W. P. Kraemer, MUNICH, Molecular Program System, Reference Manual, Special Technical Report, Max-Planck-Institut für Physik und Astrophysik (in press); G. H. F. Diercksen, Theor. Chim. Acta, 33, 1 (1974).
22. N. Jonathan, A. Morris, M. Okuda, D. Smith, and K. J. Ross, Chem. Phys. Lett., 13, 334 (1972).

23. D. W. Turner, C. Baker, A. D. Baker, and C. R. Brundle, "Molecular Photoelectron Spectroscopy," Wiley-Interscience, New York (1970).
24. J. Schirmer, W. Domcke, L. S. Cederbaum, W. von Niessen, and L. Åsbrink, Chem. Phys. Lett., 61, 30 (1979).
25. C. J. Allan, U. Gelius, D. A. Allison, G. Johansson, H. Siegbahn, and K. Siegbahn, J. Electron Spectry, 1, 131 (1972).
26. U. Gelius, J. Electron Spectrosc., 5, 983 (1975).
27. C. E. Brion and K. H. Tan, Chem. Phys., 34, 141 (1978).
28. C. E. Brion, I. E. McCarthy, I. H. Suzuki, and W. Weigold, Chem. Phys. Lett., 67, 115 (1979).
29. C. E. Brion, S. T. Hood, I. H. Suzuki, and E. Weigold, in press.
30. E. Weigold, Private communication.
31. C. Fridh, L. Åsbrink, B. Ö. Jonsson, and E. Lindholm, Intern. J. Mass. Spectrom. Ion. Phys., 8, 85 (1972).
32. W. von Niessen, L. S. Cederbaum, and G. H. F. Diercksen, J. Chem. Phys., 67, 4124 (1977).
33. D. P. Chong and S. R. Langhoff, Chem. Phys. Lett., 59, 397 (1978).
34. G. B. Bacskay, Chem. Phys., 48, 21 (1980).
35. W. C. Ermler and A. D. McLean, in press.
36. P. E. Cade, K. D. Sales, and A. C. Wahl, J. Chem. Phys., 44, 1973 (1966).
37. C. Salez and A. Veillard, Theor. Chim. Acta, 11, 441 (1968).
38. W. C. Ermler and A. C. Wahl, Unpublished results cited in M. F. Herman, D. L. Yeager, K. F. Freed, and V. McKoy, Chem. Phys. Lett., 46, 1 (1977).
39. W. Meyer, in: Modern Theoretical Chemistry, Vol. 3. Methods of Electronic Structure Theory, H. F. Schaeffer, III, ed., Plenum Press, New York (1977), Chapter 11.
40. S.-K. Shih, W. Butscher, R. J. Buenker, and S. D. Peyerimhoff, Chem. Phys., 29, 241 (1978).
41. W. von Niessen, L. S. Cederbaum, W. Domcke, and G. H. F. Diercksen, J. Chem. Phys., 66, 4893 (1977).
42. W. von Niessen, G. H. F. Diercksen, L. S. Cederbaum, and W. Domcke, Chem. Phys., 18, 469 (1976).
43. K.-H. Thunemann, R. J. Buenker, S. Peyerimhoff, and S.-K. Shih, Chem. Phys., 35, 35 (1978).
44. W. von Niessen, Unpublished results.
45. M. J. Weiss, G. M. Lawrence, and R. H. Young, J. Chem. Phys., 52, 2867 (1970).
46. L. S. Cederbaum, W. Domcke, and W. von Niessen, Chem. Phys., 10, 459 (1975).
47. G. Bieri, E. Heilbronner, V. Hornung, E. Kloster-Jensen, J. P Maier, F. Thommen, and W. von Niessen, Chem. Phys., 36, 1 (1979).
48. L. Åsbrink, W. von Niessen, and G. Bieri, J. Electron Spectrosc., in press.

49. L. S. Cederbaum, Chem. Phys. Lett., 25, 562 (1974).
50. D. P. Chong, F. G. Herring, and D. Mc Williams, J. Electron Spectry., 7, 445 (1975).
51. W. von Niessen, L. S. Cederbaum, and W. P. Kraemer, J. Chem. Phys., 65, 1378 (1976).
52. W. von Niessen, G. Bieri, and L. Åsbrink, J. Electron Spectrosc., in press.
53. W. von Niessen, Unpublished results.
54. L. S. Cederbaum, W. Domcke, H. Köppel, and W. von Niessen, Chem. Phys., 26, 169 (1977).
55. H. Köppel, W. Domcke, L. S. Cederbaum, and W. von Niessen, J. Chem. Phys., 69, 4252 (1978).
56. H. Köppel, L. S. Cederbaum, W. Domcke, and W. von Niessen, Chem. Phys., 37, 303 (1979).
57. F. Brogli, E. Heilbronner, E. Kloster-Jensen, A. Schmelzer, A. S. Manocha, J. A. Pople, and L. Radom, Chem. Phys., 4, 107 (1974).
58. S. Tsuchiya and M. Senō, Chem. Phys. Lett., 54, 132 (1978).
59. W. Domcke, L. S. Cederbaum, J. Schirmer, and W. von Niessen, Phys. Rev. Lett., 42, 1237 (1979); Chem. Phys., 39, 149 (1979).

CALCULATIONS OF ELECTRIC DIPOLE TRANSITION PROBABILITIES IN THE ELECTRONIC GROUND STATES OF THE NeH^+, ArH^+, and KrH^+ IONS

P. Rosmus, E. A. Reinsch, H. J. Werner

Fachbereich Chemie der Universität

6000 Frankfurt, Germany

In systematic studies on the first- and second-row hydrides AH [1,2], AH^+ [3], and AH^- [4] we have shown previously that *ab initio* quantum-chemical calculations using highly correlated electronic wavefunctions are capable of producing rotational transition energies within about 0.1 to 0.2cm^{-1} [1-4], vibrational transition energies within about 20 to 30cm^{-1} [1-4], proton affinities within ±0.05eV and dipole transition matrix elements within about 5 to 10 percent [1,2]. Molecular parameters of this quality have so far not been available from experiments for the strongly bound protonated rare gas atoms NeH^+, ArH^+, and KrH^+, whereas for the two electron system HeH^+ experimental [5] and theoretical [6,7] data of an outstanding accuracy have been reported recently.

We have performed calculations of the potential energy and the dipole moment functions for the ground states of the NeH^+, ArH^+, and KrH^+ ions using highly correlated PNO/CEPA or SCEP/CEPA electronic wavefunctions. (For details, see Refs. 8 and 9.) Our theoretical spectroscopic constants for NeH^+ and ArH^+ (cf. Table I) have been used by Lorenzen et al [10] for the interpretation of the electron spectra observed in associative ionization experiments. The $\Delta G_{1/2}$ value for NeH^+ has been determined to be 2563 $\pm$ 200cm^{-1} [10] and calculated to be 2670cm^{-1}. For ArH^+ these values amount to 2564 $\pm$ 200cm^{-1} [10] and 2611cm^{-1}, respectively.

The equilibrium distances of NeH^+, ArH^+, and KrH^+ are so far experimentally known only from model potentials derived from scattering experiments [11,12]. They are less reliable than our theoretical values (cf. Table I), which are expected to be accurate within about ±0.005Å. The theoretical proton affinities of Ne and

Table I. Calculated spectroscopic constants, proton affinities, and dipole moments

Molecule	R_e (Å)	B_e (cm^{-1})	α_e (cm^{-1})	ω_e (cm^{-1})	$\omega_e x_e$ (cm^{-1})	D_o (eV)	μ_o* (D)
NeH^+	0.996	17.72	1.096	2896	113	2.10	3.004
ArH^+	1.286	10.36	0.364	2723	56	3.89	2.229
KrH^+	1.419	8.41	0.256	2561	49	4.65	1.944

Ar agree nicely with the values derived by Lorenzen et al. [10]. The corresponding experimental values are 3.856 ± 0.03 eV for ArH^+ and 2.096 ± 0.03 eV for NeH^+. For KrH^+, however, the value of 4.29 eV derived from scattering experiments [11] deviates strongly from our calculated value of 4.65 eV. The proton affinities can be used for the derivation of the heat of ion-molecule reactions like $Ar + H_2^+ \rightarrow ArH^+ + H$, etc. For this reaction we calculate a heat of reaction of 120kJ/mole. Assuming small activation energies and using our spectroscopic constants this is sufficient to populate rotational-vibrational levels up to v = 4 of ArH^+.

Even though the protonated rare gas atoms are usually produced in excited rotational-vibrational states, so far no infrared emission systems have been detected experimentally. In such experiments the transition probability coefficients of spontaneous emission are of considerable interest. They can easily be calculated once the potential energy and the dipole moment functions are known. The calculated dipole moment functions for NeH^+, ArH^+, and KrH^+ are presented in Figure 1. For comparison, the functions of the isoelectronic hydrogen halides are also shown.

In hydrogen halides for the limiting cases R = 0 and R = ∞ the dipole moment vanishes. Thus, the shapes of the dipole moment functions reflect the ionic or covalent characters of the chemical bonds in these molecules. For ions a different situation is observed: the dipole moments are zero for R = 0, but go to infinity for $R \rightarrow \infty$. The first derivative of the dipole moment function, which mainly determines the magnitude of the transition matrix elements, approaches always the maximum value one for large R (in atomic units, heavy atom in origin of the coordinate system, values are to be corrected for the center of mass). For smaller R the curvature of the functions depends on the size and polarizability of the valence shell of the rare gas atoms. Especially for

*center of mass as origin

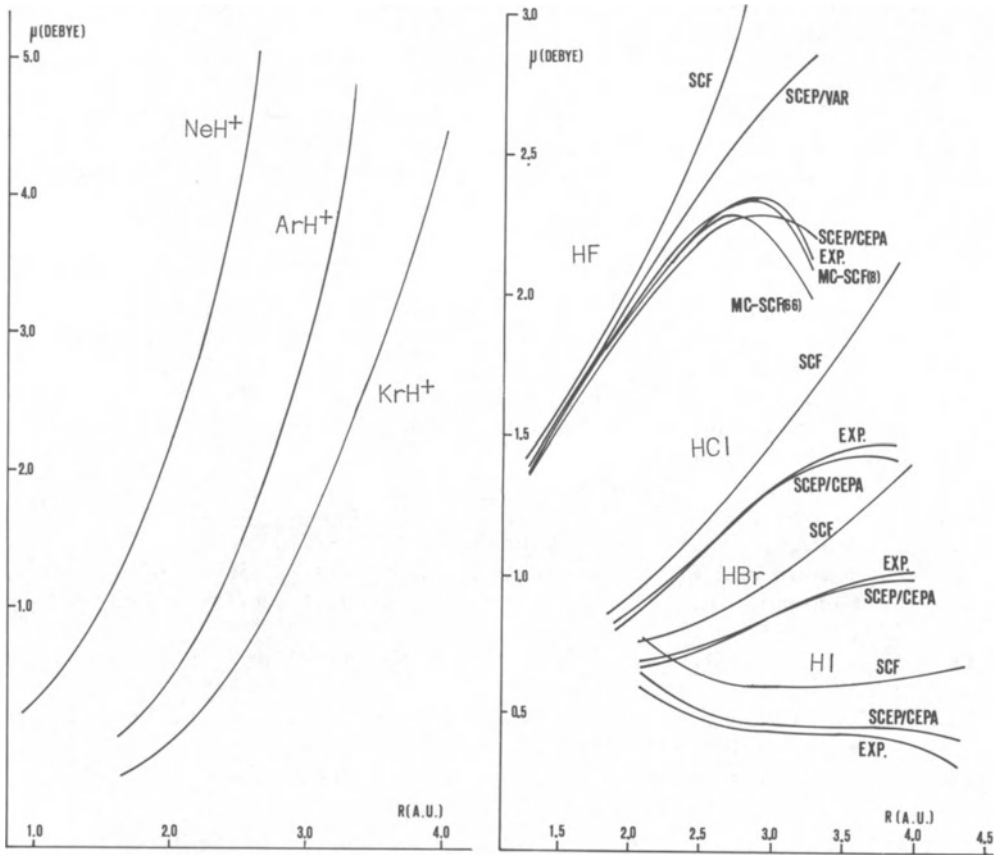

Fig. 1. Comparison of the dipole moment functions of hydrogen halides and protonated rare gas atoms (see Refs. 2, 8, 9, 13).

the heavier ions the dipole moment functions near the equilibrium distances are much steeper than those of the hydrogen halides. This means that the ions emit considerably better than the neutral counterparts even if somewhat smaller vibrational transition energies of the ions are considered. In Table II several transition probability coefficients of hydrogen halides and protonated rare gas atoms are compared. Details of this work can be found in References 2, 8, 9, and 13.

Table II. Transition probability coefficients of spontaneous emission of the first vibrational levels (J = 0) in sec^{-1}.

HF	HCl	HBr	HJ	NeH^+	ArH^+	KrH^+
189	34.6	5.6	0.11	756	438.4	284.9

REFERENCES

1. W. Meyer and P. Rosmus, J. Chem. Phys. 63, 2356 (1975).
2. H. J. Werner and P. Rosmus, J. Chem. Phys. 73, 2319 (1980).
3. P. Rosmus and W. Meyer, J. Chem. Phys. 66, 13 (1977).
4. P. Rosmus and W. Meyer, J. Chem. Phys. 69, 2745 (1978).
5. D. E. Tolliver, G. A. Kyrala, and W. H. Wing, Phys. Rev. Lett. 43, 1719 (1979).
6. W. Kolos and J. M. Peek, Chem. Phys. 12, 381 (1976).
7. D. M. Bishop and L. M. Cheng, J. Mol. Spectrom. 75, 462 (1979).
8. P. Rosmus, Theor. Chim. Acta 51, 359 (1979).
9. P. Rosmus and E. A. Reinsch, Z. Naturforsch. 35a, 1066 (1980).
10. J. Lorenzen, H. Hotop, M. W. Ruf, and H. Morgner, Z. Physik A 297, 19 (1980).
11. A. Henglein, J. Phys. Chem. 76, 3883 (1972) and references therein.
12. W. B. Rich, S. M. Bobbio, R. L. Champion, and L. D. Doverspike, Phys. Rev. A4, 2253 (1971).
13. H. J. Werner, E. A. Reinsch, and P. Rosmus, Chem. Phys. Lett. 78, 311 (1981).

AB INITIO POTENTIAL ENERGY FUNCTIONS AND VIBRATIONAL STATES OF THE FLUORONIUM AND CHLORONIUM IONS

Peter Botschwina

Fachbereich Chemie der Universität Kaiserslautern

West Germany

The cations FH_2^+ (fluoronium ion) and ClH_2^+ (chloronium ion) have been investigated by beam experiments and mass spectroscopy [1, 2], ion cyclotron resonance spectroscopy [3] and the molecular beam photoionization method [4]. These experimental techniques yielded rather accurate values for the proton affinities of the hydrogen halides, but gave no information on molecular structure and vibrational states of the fluoronium and chloronium ions.

A larger number of *ab initio* calculations has been performed in order to determine the equilibrium geometry of FH_2^+ and some quadratic force constants. Most of them were carried out within the Hartree-Fock Self-Consistent-Field approximation. Only the calculations of Lischka [5], which made use of the independent electron pair approximation, covered a large fraction of the valence shell correlation energy, but this approximation tends to overestimate correlation effects even for molecules with well localizable electrons. The chloronium ion has so far been only investigated by Jörgensen [6] using minimal basis sets (*ab initio* STO-3G and semiempirical MINDO/3).

In the present *ab initio* calculations, the Self-Consistent Electron Pairs method (SCEP, ref. 7) is employed in connection with the Coupled Electron Pair Approximation (CEPA, ref. 8). Basis sets of Gaussian type orbitals are used which recover about 80% of the valence correlation energy for hydrogen fluoride and about 73% for hydrogen chloride. The calculations performed for these hydrogen halides yield errors of +0.005 Å (HF) and +0.001 Å (HCl) in the equilibrium bond lengths and errors of -28 cm^{-1} (HF) and $+36$ cm^{-1} (HCl) in the fundamental vibrational frequencies, and similar accuracy is expected for the protonated molecules.

Table 1. Potential Energy Functions for FH_2^+ and ClH_2^+(a)

PEF terms (b)	FH_2^+	ClH_2^+
r_e	0.966	1.306
α_e	112.7	94.9
rr	6.929	4.518
$\alpha\alpha$	0.552	0.764
rr´	0.202	0.010
rα	0.064	0.042
rrr	-50.0	-25.7
$\alpha\alpha\alpha$	-0.76	-0.23
rrr´	0.15	-0.08
rrα	-0.28	-0.04
rr´α	-0.28	-0.25
r$\alpha\alpha$	-0.37	-0.32
rrrr	330	125
$\alpha\alpha\alpha\alpha$	-0.7	-1.7
rrrrr	-2337	-589
$\alpha\alpha\alpha\alpha\alpha$	-2	-1
rrrrrr	17892	2754
$\alpha\alpha\alpha\alpha\alpha\alpha$	17	33

(a) Values are obtained by the SCEP-CEPA-1 method except for the cubic coupling terms, which were calculated by the SCF/gradient method. Basis sets employed are: F: 11s,7p,2d contracted to [8, 5, 2] Cl: 13s,8p,2d contracted to [9, 6, 2] H: 6s,1p contracted to [4, 1].

(b) Equilibrium bond lengths are given in Å, bond angles in degrees. PEF terms ("force constants") are designated by their respective coordinate, e.g. (rrα) corresponds to the partial differential quotient $(\partial^3 V/\partial r^2 \partial\alpha)_e$. Units are aJ $Å^{-n}$, where n is the number of stretching coordinates involved in the partial differential quotient of the potential energy V.

Table 2. Harmonic and Anharmonic Vibrational Frequencies (in cm^{-1}) for Isotopes of the Fluoronium and Chloronium Ions

	FH_2^+	FHD^+	FD_2^+	ClH_2^+	$ClHD^+$	ClD_2^+
ω_1 (symm.)	3519	3503	2527	2797	2006	2003
ω_2 (bend)	1460	1278	1065	1247	1085	894
ω_3 (asymm.)	3487	2539	2550	2798	2797	2009
ν_1	3355	3331	2440	2676	1944	1941
ν_2	1373	1212	1021	1212	1058	876
ν_3	3315	2450	2455	2679	2677	1947
$2\nu_2$	2681	2376	2009	2407	2103	1743
ZPE[a]	4157	3601	3031	3372	2907	2428

[a] zero-point energy

The pointwise calculated potential energy surfaces (PES) for FH_2^+ and ClH_2^+ are analytically approximated by a polynomial expansion in curvilinear internal displacement coordinates around the calculated equilibrium geometries. This expansion is chosen such that up to sextic "diagonal" and up to cubic "off-diagonal" terms are included. The parameters of the PES are given in Table 1. Vibrational energies are calculated by means of the author's "vibrational CI" program [9, 10]; results are given in Table 2. The stretching fundamental vibrations of FH_2^+ are calculated at considerably smaller wavenumbers than in HF, the difference amounting to about 600 cm^{-1}, while the corresponding difference between ClH_2^+ and HCl amounts to only 250 cm^{-1}. There is a relatively large anharmonicity effect on the bending vibration in FH_2^+, the ratio between harmonic and anharmonic value amounting to as much as 1.063 (usual values $\sim$1.03). In contrast to isoelectronic water, the fundamental with largest wavenumber in FH_2^+ corresponds to the symmetric stretching vibration, which is due to a positive stretch-stretch coupling force constant $f_{rr'}$ of 0.20 aJ $Å^{-2}$. The order is reversed for FD_2^+, and this may be easily explained by a simple model [10], which is based on the harmonic approximation and neglects the small couplings between bending and symmetric stretching vibrations. In this model, ω_1 (symm.) is larger than ω_3 (asymm.) if

$$f_{rr'} > -\frac{f_{rr} \cos \alpha_e}{1 + m_F/m_{H'}}$$

This inequality if fulfilled for FH_2^+, but not for FD_2^+.

REFERENCES

1. M. A. Haney and J. L. Franklin, J. Phys. Chem., 73, 4328 (1969).
2. C. W. Polley and B. Munson, Int. J. Mass Spectrom. Ion Phys., 26, 49 (1978).
3. M. S. Foster and J. L. Beauchamp, Inorg. Chem., 14, 1229 (1975).
4. P. W. Tiedemann, S. L. Anderson, S. T. Ceyer, T. Hirooka, C. Y. Ng, B. H. Mahan, and Y. T. Lee, J. Chem. Phys., 71, 605 (1979).
5. H. Lischka, Theoret. Chim. Acta, 31, 39 (1973).
6. W. L. Jörgensen, J. Amer. Chem. Soc., 100, 1057 (1978).
7. W. Meyer, J. Chem. Phys., 64, 2901 (1976).
8. W. Meyer, Int. J. Quantum Chem., S5, 341 (1971); J. Chem. Phys., 58, 1017 (1973); Theoret. Chim. Acta, 35, 277 (1974).
9. P. Botschwina, Chem. Phys., 40, 33 (1979).
10. P. Botschwina, Dissertation, Kaiserslautern (1980).

AB INITIO CALCULATION OF POTENTIAL ENERGY CURVES OF THE CO_2^+ ION

M.-Th. Praet, J.-C. Lorquet, and G. Raseev

Département de Chimie Générale et de Chimie Physique

Université de Liège, Sart Tilman
B-4000 Liège, Belgium

There are numerous examples in the present volume of experimental determinations of the geometry of positive ions. All of the excited electronic states of the ions however are not necessarily experimentally detectable: the transition is sometimes forbidden by selection rules. However, these "forbidden states" may play an important role, e.g., in predissociation processes. Such a behavior has been recently reported by Eland and Berkowitz [1] in the case of the predissociation of the $\tilde{C}(^2\Sigma_g^+)$ state of CO_2^+. The theoretical determination of the potential energy surfaces for all of the electronic states in the energy range of interest is then of great help in the analysis of the dissociation mechanisms.

We wish to report here preliminary results regarding the *ab initio* calculation of various electronic states of CO_2^+ as a function of the OCO angle.

As far as we know, the only theoretical work on the same subject is a SCF calculation by England et al. [2]. As shown in Table 1, they obtained a reversed order for the $\tilde{A}$ and $\tilde{B}$ states when compared with the photoelectron spectroscopy results [3].

Here, we use the MOLALCH system of programs [4] and we proceed in two steps. The first one is a SCF calculation with the Huzinaga's cartesian GTO 9s 5p [5a] with Dunning's contraction 4s 3p [5b] on the C and O atoms. Preliminary calculations showed that Rydberg type orbitals had a negligible influence on the energy of low-lying states; they were therefore not included in the calculations reported below. This step is followed by a CI calculation including all of the monoexcited and a part of the diexcited con-

Table 1. Excitation Energies Relative to $\tilde{X}(^2\Pi_g)$ in eV

	Experimental	Calculated	
	Ref. 3	Ref. 2	This work
$\tilde{A}$ $^2\Pi u$	3.54	5.77	3.81
$\tilde{B}$ $^2\Sigma u^+$	4.30	5.46	4.81
$\tilde{C}$ $^2\Sigma g^+$	5.61	7.24	5.69
$^4\Pi u$	–	7.24	6.95
$^2\Pi u$	–	11.84	8.18
$^4\Sigma g^-$	–	–	10.68

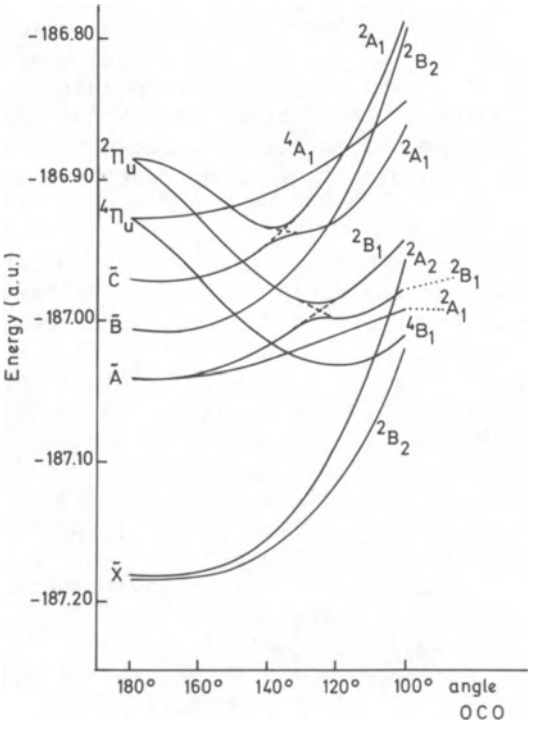

Fig. 1. Energy of the low-lying states of CO_2^+ as a function of the valence angle (C_{2v} point group). The CO length is frozen at a value of 1.1612 Å (2.1944 au).

figurations derived from the reference configuratins chosen to represent the various states which we wanted to calculate. The size of the CI matrices range from 300 to 1850 CSF.

The molecular orbitals we use in the CI calculations are obtained from an intermediate configuration. This technique [6] provides a homogeneous level of approximation when we are faced with problems linked to degeneracy or near-degeneracy of orbitals or states.

The calculations are performed in the C_{2v} point group of symmetry with a bond length of 1.1612 Å (2.1944 au), i.e., the CO equilibrium distance in the ground state of the neutral molecule. In its linear geometry ($D_{\infty}h$), the ground state of CO_2^+ has the electronic configuration

$$(1\sigma_g)^2(1\sigma_u)^2(2\sigma_g)^2(3\sigma_g)^2(2\sigma_u)^2(4\sigma_g)^2(3\sigma_u)^2(1\pi_u)^4(1\pi_g)^3$$

which becomes, in C_{2v} symmetry

$$(1a_1)^2(1b_2)^2(2a_1)^2(3a_1)^2(2b_2)^2(4a_1)^2(3b_2)^2(5a_1)^2(1b_1)^2$$

$$(4b_2)^2(1a_2)^1 \text{ or } (4b_2)^1(1a_2)^2$$

The lowest lying states of CO_2^+, ($^2\Pi_g$), ($^2\Pi_g$), $\tilde{A}(^2\Pi_u)$, $\tilde{B}(^2\Sigma_u^+)$, and $\tilde{C}(^2\Sigma_g^+)$ are observed experimentally since they result from the removal of one electron from the first four valence orbitals.

Other states can be obtained by excitation of the π_g electron either in the $2\pi_u$ orbital or into the $5\sigma_g$ orbital. This gives rise to a number of spectroscopically inactive states, among which the $^2\Pi_u$, $^4\Pi_u$, and $^4\Sigma_g^-$ are expected to be the lowest in energy.

The energy of the $^2\Pi_u$ and $^4\Pi_u$ states was calculated by England and coworkers [2]: the $^4\Pi_u$ is found to lie close to the $\tilde{C}$ state in a linear geometry and to predissociate all the lower excited states. In Table 1, we give the excitation energies for different electronic states in their linear geometry. The agreement between the experimental and our calculated values is very good.

In Fig. 1, we present the potential energy curves of these states. We see that the $^4B_1$ component of the $^4\Pi_u$ state crosses the $\tilde{A}$, $\tilde{B}$, and $\tilde{C}$ states before reaching its equilibrium angle at 120°.

We have optimized the bond length of the $^4B_1$ and of $\tilde{C}$ and we find values of 1.3 Å and 1.16 Å respectively; therefore the $^4B_1$ ionic state is more stable with increased CO distances.

The crossing between the $^4B_1$ and the $\tilde{C}(^2A_1)$ state takes place near 160°. The $^2A_1$ state is therefore expected to interact

with the $^4B_1$ via a spin orbit coupling. We calculate a value of 0.9 cm^{-1} for the $\langle {}^2A_1 | H^{SO} | {}^4B_1 \rangle$ matrix element using the semi-empirical method described in Ref. 7.

This low value is due to the fact that the predominant electronic configurations of these two states differ by more than one molecular orbital.

The crossing with the $\tilde{B}(^2B_2)$ state gives rise to a value of 2 cm^{-1} for the $\langle {}^2B_2 | H^{SO} | {}^4B_1 \rangle$ matrix element.

A low value is also expected for the $\tilde{A}$ state for similar reasons. On the other hand, the interaction between the $\tilde{X}(^2A_2)$ and $^4B_1$ states at near 110° was found to be much stronger; a value of 37 cm^{-1} was obtained for the matrix element.

The value of the spin orbit matrix elements can be used to estimate rate constants for the intersystem crossings. This work is in progress and will be reported later.

REFERENCES

1. J. H. D. Eland and J. Berkowitz, J. Chem. Phys., 67, 2782, (1977).
2. W. B. England, B. J. Rosenberg, P. J. Fortune, and A. C. Wahl, J. Chem. Phys., 65, 684 (1976).
3. D. W. Turner, C. Baker, A. D. Baker, C. R. Brundle, Molecular Photoelectron Spectroscopy (1970), Wiley Interscience, London.
4. The program system MOLALCH incorporates the MOLECULAR Gaussian integral program and the ALCHEMY SCF and CI wavefunction generator programs. MOLECULE was written by Dr. Almlöf of the University of Uppsala, Sweden. ALCHEMY was written at the IBM San Jose Research Laboratory. The interfacing of these programs was performed by P. S. Bagus and U. I. Wahlgren. For a description of MOLECULE, see J. Almlöf, Proceedings of the Second Seminar on Computational Problems in Quantum Chemistry (Max Planck Institut, München, 1973), p. 14. For a description of ALCHEMY see P. S. Bagus, in Selected Topics in Molecular Physics (Chemie, Weinheim, 1972), p. 187.
5a. S. Huzinaga, J. Chem. Phys., 42, 1293 (1965).
5b. J. H. Dunning, J. Chem. Phys., 53, 2823 (1970).
6. R. McWeeny, Mol. Phys., 28, 1273 (1974). L. Salem, C. Leforestier, G. Segal, and R. Wetmore, J. Am. Chem. Soc., 97, 479 (1975). J. Liévin and G. Verhaegen, Theor. Chim. Acta, 42, 42 (1976).
7. A. J. Lorquet, J. C. Lorquet, H. Wankenne, and J. Momigny, J. Chem. Phys., 55, 4053 (1971).

DENSITY FUNCTIONAL APPROACH TO MOLECULAR STRUCTURE AND ATOMIC SCATTERING

E. K. U. Gross, A. Toepfer, B. Jacob,
M. Horbatsch, H. J. Lüdde,
and R. M. Dreizler

Institut für Theoretische Physik der Universität
6000 Frankfurt am Main
Federal Republic of Germany

We discuss density functional methods as alternatives to stationary two-center Hartree Fock (HF) and time dependent HF (TDHF) calculations.

The exact quantitative formulation of the two-center Coulomb problem is given by the full time dependent Schrödinger equation (SE) for two nuclei and a number of N electrons

$$i\partial_t \Psi(\underline{r}_1 \ldots \underline{r}_N, \underline{R}, t) = H \Psi(\underline{r}_1 \ldots \underline{r}_N, \underline{R}, t).$$

The nonrelativistic Hamiltonian of such a system in the nuclear center of mass frame consists of a nuclear and an electronic part, where the nuclear part contains the kinetic energy of the relative motion and the nuclear Coulomb-Potential

$$H = H_n + H_e, \quad H_n = -\frac{1}{2\mu} \nabla_R^2 + \frac{Z_1 Z_2}{R}.$$

The electronic part consists of the kinetic energy of the electrons, the electron-nucleus potential and the mutual electron-electron interaction

$$H_e = -\frac{1}{2} \sum_i \nabla_i^2 - \sum_i \left(\frac{Z_1}{\left| \underline{r}_i + \frac{M_2}{M} \underline{R} \right|} + \frac{Z_2}{\left| \underline{r}_i - \frac{M_1}{M} \underline{R} \right|} \right) + \frac{1}{2} \sum_{i \neq j} \frac{1}{\left| \underline{r}_i - \underline{r}_j \right|}$$

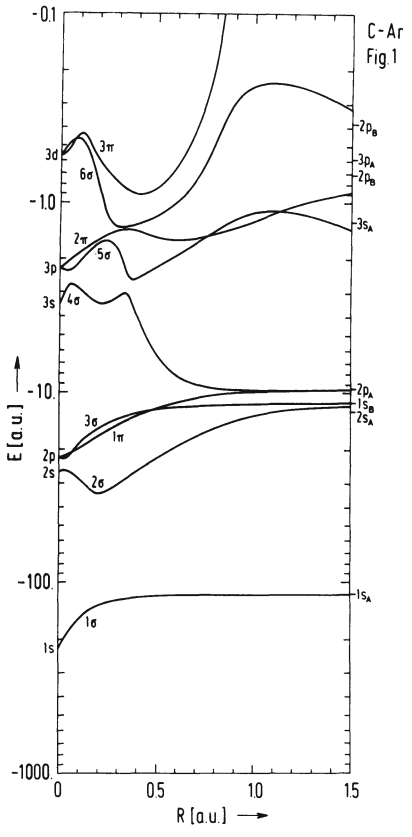

Fig. 1

In order to make the problem tractable a decoupling of the nuclear and the electronic motion must be achieved. This aim can be reached by two fundamentally different methods. The first one is the Born-Oppenheimer approximation which essentially leads to a stationary SE for the electronic system

$$H_e(\underline{R})\phi_\alpha(\underline{r}_1 \ldots \underline{r}_N, \underline{R}) = E_\alpha(\underline{R})\phi_\alpha(\underline{r}_1 \ldots \underline{r}_N, \underline{R}) \qquad (1)$$

which contains the internuclear distance $\underline{R}$ as a parameter. In addition one obtains a SE for the nuclear motion. This approximation is adequate in the case of adiabatic situations as e.g., low energy collisions and molecular structure problems. For collisions at higher energies one has to rely on another method, the so-called impact parameter approximation, leading to a time dependent SE for the electronic system

$$i\partial_t\, \phi(\underline{r}_1 \ldots \underline{r}_N, \underline{R}(t), t) = H_e(\underline{R}(t))\phi(\underline{r}_1 \ldots \underline{r}_N, \underline{R}(t), t) \qquad (2)$$

which contains the internuclear separation $\underline{R}(t)$ as a given function of time.

The stationary SE (1) for the ground state ($\alpha = 0$) can be written as a variational equation

$$\frac{\delta}{\delta\phi}\,(E - E_o\,\langle\phi|\phi\rangle) = 0 \text{ with } E = \langle\phi|H_e|\phi\rangle$$

In the same way the time dependent SE (2) can be expressed in terms of a variational principle

$$\frac{\delta\Omega}{\delta\phi} = 0 \text{ with } \Omega = \int dt\,\langle\phi|i\partial_t - H_e|\phi\rangle$$

If the electronic many particle wave function is approximated by a Slater determinant of single particle orbitals $\phi := \det(\varphi_\mu(\underline{r}_\nu))$, one obtains the ground state energy or the quantity Ω in the so-called single particle approximation, i.e., as a functional of the single particle orbitals

$$E_{sp} = E[\varphi_\mu],\ \Omega_{sp} = \Omega[\varphi_\mu]$$

Variation of these functionals with respect to the single particle orbitals φ_μ yields the stationary or time dependent HF equations. As the numerical solution of these equations is extremely tedious (in the case of stationary HF) or even not feasible so far (in the case of TDHF) we offer the following program

Step (1):

The ground state energy E_{sp} is approximated by a functional of the single particle density $\rho(\underline{r})$. In the same way Ω_{sp} is approximated by a functional of the single particle density $\rho(\underline{r}, t)$ and a velocity potential $\chi(\underline{r}, t)$.

$$E_{sp} \to E[\rho],\ \Omega_{sp} \to \Omega[\rho, \chi]$$

This can be done in a systematic fashion by so-called gradient expansion techniques.

Step (2):

The corresponding variational equations

$$\frac{\delta}{\delta\rho}\,(E - \lambda\int\rho(\underline{r})d^3r) = 0 \quad \Big| \quad \frac{\delta\Omega}{\delta\chi} = 0,\ \frac{\delta\Omega}{\delta\rho} = 0$$

are solved with appropriate boundary conditions. As solution one obtains an effective single particle density. By use of this

density an effective single particle Hamiltonian is constructed from the prescription $h_{eff} = t + v_{eff}$

with $v_{eff} := -\frac{Z_1}{r_1} - \frac{Z_2}{r_2} + \int \frac{\rho(\underline{r}')}{|\underline{r} - \underline{r}'|} d^3r' + V_{ex}[\rho]$ + asymptotic

$1/r$ − self energy-correction.

Step (3):

The effective single particle SE

$$h_{eff}(R)\varphi_\mu = \varepsilon_\mu(R)\varphi_\mu \quad | \quad i\partial_t \varphi_\mu(\underline{r}, t) = h_{eff}\varphi_\mu(\underline{r}, t)$$

is solved. In the time dependent case one obtains time dependent single particle orbitals $\varphi_\mu(\underline{r}, t)$ from which cross sections can be extracted. In the stationary case one obtains R-dependent single particle orbitals and energies, i.e., correlation diagrams $\varepsilon_\mu(R)$. Figure 1 shows such a correlation diagram for the system C-Ar.

The essential point in this program lies in the fact that Step (1) and Step (2) are completely independent of the number of particles, and in Step (3) the increase of computer time and storage goes only linear with the number of electrons. For this reason arbitrary two-center systems become tractable.

Finally, the same program can be carried through for relativistic systems by use of the Dirac-Hamiltonian in place of the non-relativistic Hamiltonian H_e.

GEOMETRIC AND ELECTRONIC STRUCTURES OF MOLECULAR IONS FROM HIGH ENERGY COLLISIONS*

K. O. Groeneveld

Institut für Kernphysik der J. W. Goethe-Universität

Frankfurt/Main, Germany

1. Introduction

Collision processes are an important tool to study both reaction mechanisms and stationary states of the systems involved. It is common that the collision energies are in the order of the binding or excitation energies of the particles of the system (e.g., electrons in the atom, nucleons in the nucleus). We discuss here, however, the advantages of studies of molecular ions for which the collision energies exceed by far the binding or excitation energies of molecular ions.

Until very recently it was a credo that particles from accelerators with typical energies per mass unit >1 MeV/nucleon are only useful for atomic or nuclear physics experiments if the particles are monoatomic. In particle accelerator ion sources, however, molecular ions are generated in large quantities and in great varieties which can be used for studies. In addition, quite a few particle accelerators originally designed for nuclear physics experiments have been abandoned by nuclear physicists because of higher energy requirements: those already existing machines became very valuable tools in atomic and molecular research.

This volume contains three articles on accelerator based molecular ion research. The present paper gives first an introduction to the characteristics of heavy ion collision and of beam foil spectroscopy including a discussion of the kinematic consequences

*Supported by Bundesministerium für Forschung und Technologie, Bonn/Germany and GSI, Darmstadt.

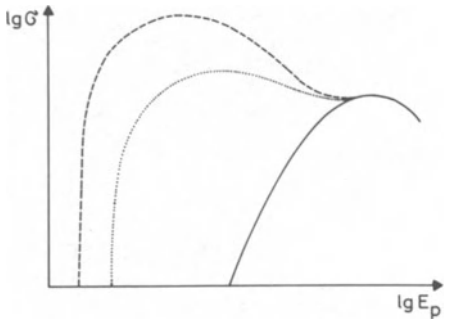

Fig. 1. Schematic of ionization cross section σ (normalized) vs. collision energy E (normalized) for Coulomb ionization (Cb) and for "molecular orbital" ionization.

of the high energies. Finally we present results from "Coulomb explosion" and structure determination of molecular ions. The two subsequent articles give details of structure studies of molecular ions penetrating solids (ref. 1) and of molecular ions in excited states (ref. 2).

2. Characteristics of Heavy Ion Collisions

It is only very recently that we find in the literature a survey of heavy ion collision processes. The reader is referred to [3] and to references quoted there. For the present purpose we summarize some important characteristics.

Collision processes at specific energies $\gtrsim$1 Mev/nucleon are associated with the creation of inner shell vacancies, the removed electron being promoted either to excited states or to the ionization continuum of either collision partner. With higher Z_p-projectiles there is a high probability for creating multiple vacancies (e.g., $1s^{-1}$, $2s^{-1}$, $2p^{-4}$) in a single collision [3, 4]. For each charge state formed in the collision we find a different system of excited states and, consequently, in general very complex Auger- or x-ray spectra from deexciting excited states. There are several mechanisms for inner shell vacancy production: Coulomb excitation, Molecular Orbital excitation (MO), charge exchanges, etc. [3].

Coulomb excitation dominates for $Z_p/Z_T \lesssim 50$ and high velocities ($\eta \gtrsim 0.1$) while MO-excitation is most important at $Z_p/Z_T \sim 1$ and low velocities ($\eta \lesssim 0.1$). The index p refers to the projectile, the index T to the target; atomic number Z). The parameter $\eta = (v_p/u)^2$ defines the adiabaticity and distinguishes between high and low projectile velocities v_p (u refers to the mean electron orbital velocity prior to the vacancy production). The resulting reaction

Table 1. Processes in High Energy (MeV), Molecular Heavy Ion Collisions

	Single collision with atoms [T]	Single colision with molecules [T]	Multiple collision in solids [T]
Projectile:	Energy transfer	Energy transfer	Energy transfer
- Charge:q=: ± n e	Deflection	Deflection	Deflection
n = -1, 0, 1...Zp	Charge change	Charge change	Charge change
- metastable	Excitation	Excitation	Excitation
- monatomic		Dissociation	Coulomb Explosion
- molecular ions		Coulomb Explosion	Beam Foil Spec-troscopy
			Implantation
			Channeling
Reaction Products of Target [T] or Projectile [P]			
1. Electromagnetic Radiation	Bremsstrahlung	Bremsstrahlung	Beam Foil Spec-troscopy
	charact. x-rays	charact. x-rays	Beam-in-Foil Spec-troscopy
	Photons	Photons	Absorption
			Secondary Electrons
2. Electrons (e)	Ionization Electr.	Ionization Electr.	Beam Foil Spec troscopy
	Auger Electrons	Auger Electrons	Radiation Damage
	Coster Kronig	Coster Kronig	Secondary Electrons
	Electrons	Electrons	Delta Electrons
3. Atoms or Molecules	Recoil	Recoil	Displacement
	- charge q'= ± ne	-charge'q'= ± ne	Radiation damage
	- Excitation	- Excitation	
	- metastable	- metastable	
		Dissociation	
		Coulomb Explosion	

cross sections are in the order of the geometric n-shell area and are schematically illustrated in Fig. 1. The high energy maximum can also be envisioned as a consequence of the Massey- or Bohr-Lamb-criterion; this explains that energy-per-unit-mass arguments, i.e., velocity arguments, rather than energy arguments are the relevant ones. For example, experiments with electrons of 1 keV impact energy (i.e., 1.836 MeV/nucleon) must be compared with ex-

periments with protons of 1.836 MeV/nucleon impact energy. It is important to note that in one single collision, say Ar^{+12} (56 MeV) → Ne, all target electrons but two or three can be removed with high probability and with impact parameters larger than the neon-K-shell radius [4, 5].

Another important distinction must be made between inner shell vacancy production in a heavy projectile ion, when interacting with a gaseous target like Ne under single collision conditions on the one hand and when interacting with thin solid targets like carbon foils (e.g., 100 Å thickness) under multiple collision conditions on the other hand. Heavy particles penetrating thin solid foils suffer one- or a few-small impact parameter collisions but many large impact parameter collisions [see Refs. 6, 7] the net effect being small straggling effects in angle and energy. The collision frequency, however, in the solid is so high (typically: 10^{16} Hz) that an ion excited in the n^{th} collision does not have time to deexcite into its ground state before the $(n + 1)^{st}$ collision. One consequence is that a solid is more effective in removing electrons from penetrating heavy (molecular) ions.

A survey of some of the various processes accompanying the passage of charged particles through matter is given in Table 1.

3. Characteristics of Beam-Foil-Spectroscopy

In Beam-Foil (BF) experiments [8] particles of known velocity v_p :typically: $v_p = 10^9$ cm/s) pass through thin (typically 2 or 3 $\mu g/cm^2$ or 100 Å) carbon foils. By this rather violent interaction are created particles in different stages of ionization and various excited states. The foil density is about 10^5 times larger than in gaseous light sources of gaseous targets. 1) Because of the large number of collisions in the solid, 2) because of the rapid succession of collisions (typically $t = s/v \approx 10^{-16}$ s elapse between two successive collisions, see above) and 3) because of the violence of the collisions (small impact parameters, large charge product $(q_1 \cdot q_2)$), there can occur with high probability several excitation, or ionization processes (multiple excitation/ionization), including inner shell vacancy production (even before the projectiles have time to relax before the next collision).

Characteristic properties of the beam-foil technique are:

1. High chemical and isotopic purity;
2. Short excitation time typical 10^{-15} s, which allows to measure decay rates with high time resolution;
3. Perturbation-free deexcitation;
4. Coherent excitation of ions in terms of linear superposition of eigenstates ("quantum beat" arrangement);

5. Population of otherwise unaccessible states (high excitation/ionization);
6. Non-statistical population.

Electronic deexcitation via photon-, x-ray, or Auger electron emission of the projectiles thus excited is measured.

The typical experimental set-up is illustrated schematically in Fig. 2. Particles are ionized in the ion source and after acceleration interact with the target. The targets are thin solid foils in most cases, but target gases are used as exciter as well [8, 9].

After the target interaction projectiles can deexcite via emission of x-rays, photons or electrons (compare Table 1).

Collision induced electrons with their energy and angular distribution are the primary source of information on the collision process itself. Electrons, however, from very different production mechanisms are superimposed in the energy spectra [10]. For electron beam-foil spectroscopy care must be taken, that experimental parameters such as incident energy E_p, observation angle ϑ_e etc., are chosen properly. These conditions are elucidated in Fig. 3: Beam-foil excited KLL-Auger electron from neon ($E_{e,lab} \sim 1$ keV) can be studied here only at incident Ne-projectile energies $2 < E_p < 15$ MeV.

Intensity of the radiation (x-rays, photons, Auger electrons) from the electronically deexciting projectile after leaving the interaction region with the target is measured as a function of the distance x between the acceptance point of the radiation and the exit surface of the target foil. The intensity dependence $I(x) = I(x = t \cdot v_p)$ at v_p = const allows to calculate the life-time τ of metastable states. An example is given in Fig. 4 which presents the decay rate τ^{-1} of the iso-electronic sequence of the metastable three electron state $(1s\ 2s\ 2p)\,^4P^o_{5/2}$ for elements $3 \leqslant Z_p \leqslant 18$ [11]. It is interesting to note, that the life time range accessible by the beam foil technique can be extended from $\tau > 10^{-10}$s to $\tau \gtrsim 10^{-14}$ or 10^{-15}s by the "beam-in-foil"-technique first applied by Betz et al. [12] for the projectile and by Groeneveld et al. [13] for the target. The dwell time t of an ion, say, with 1 MeV/nucleon pene-

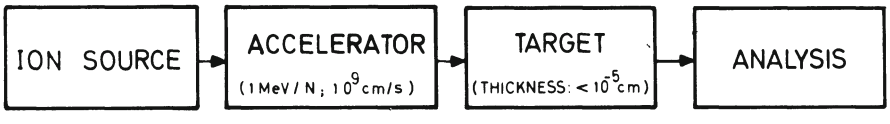

Fig. 2. Schematic of molecular ion accelerator experiment.

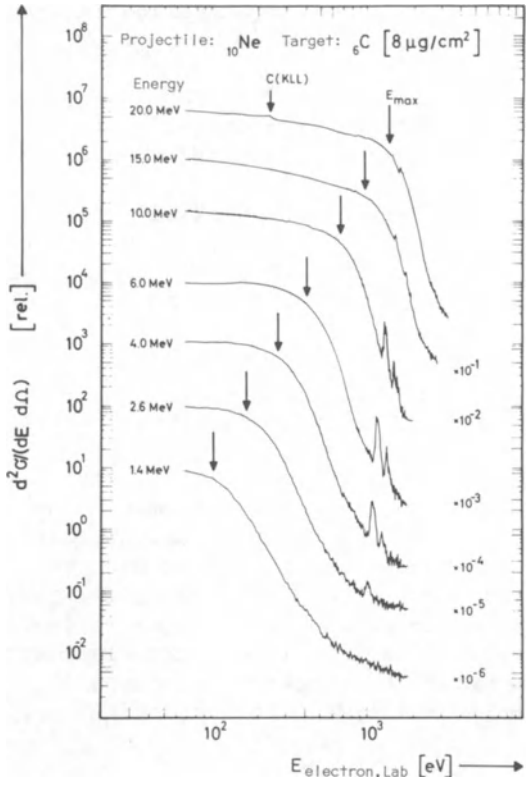

Fig. 3. Electron energy spectra from Ne → carbon (solid) collisions at different incident Ne-energies (observation angle 45°). From ref. [10].

trating a thin carbon foil (10 µg/cm² or 400 Å) is $t \lesssim 10^{-14}$s; the decay time τ of inner shell excited states is also $\tau_{th} \sim 10^{-14}$s. One observes the growth of projectile resp. target x-ray intensity with target thickness, i.e., dwell time t and calculates the life time τ_{exp} of inner shell excited states. The use of the "beam-in-foil" spectroscopic technique has thus extended the range of the beam-foil-life time measurements to 10^{-14} s.

Thus, Beam Foil Spectroscopy yields information on the following quantities:

1. transition energies and thereby the term energy of a particular electronic configuration;
2. line widths ($\Delta E \sim \hbar/\Delta t$);
3. life-time τ of states with $\tau > 10^{-10}$ s resp. 10^{-14} s.

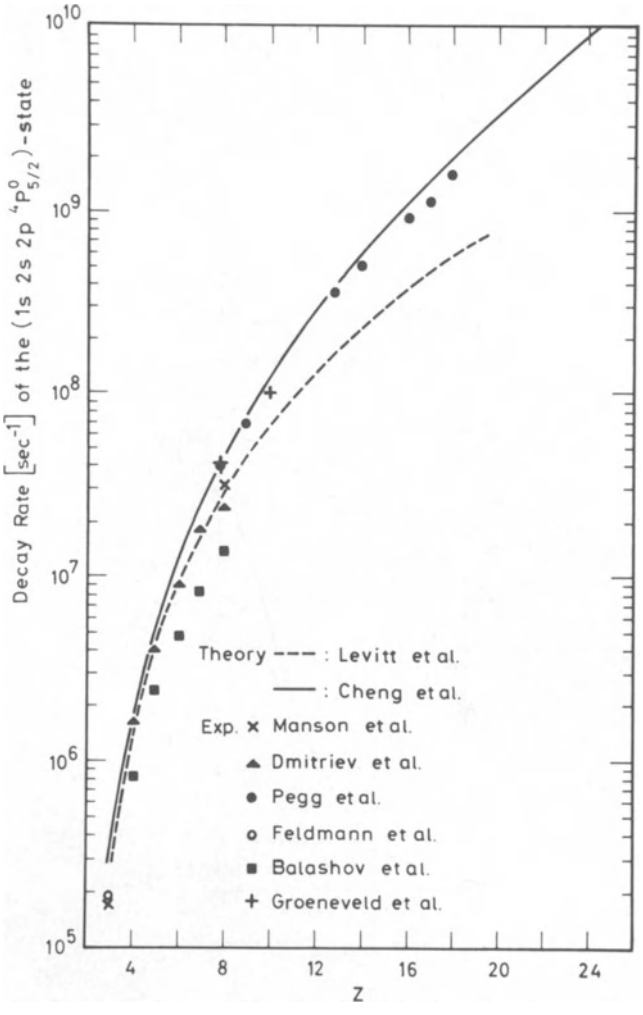

Fig. 4. Decay rate W of the (1s 2s 2p)$^4P_{5/2}$-state in Li-like systems versus the atomic number Z. From ref. 11 (see also [3]).

Both 2 and 3 can be compared with relative absolute transition probabilities or oscillator strengths. This provides a critical test of wave functions, of theoretical approximations and interactions causing the transitions.

Some comments on the kinematics are important in this context: In Electron Beam Foil Spectroscopy [3, 8] Auger electrons (velocity v_A) are emitted from the moving projectile system (velocity v_p).

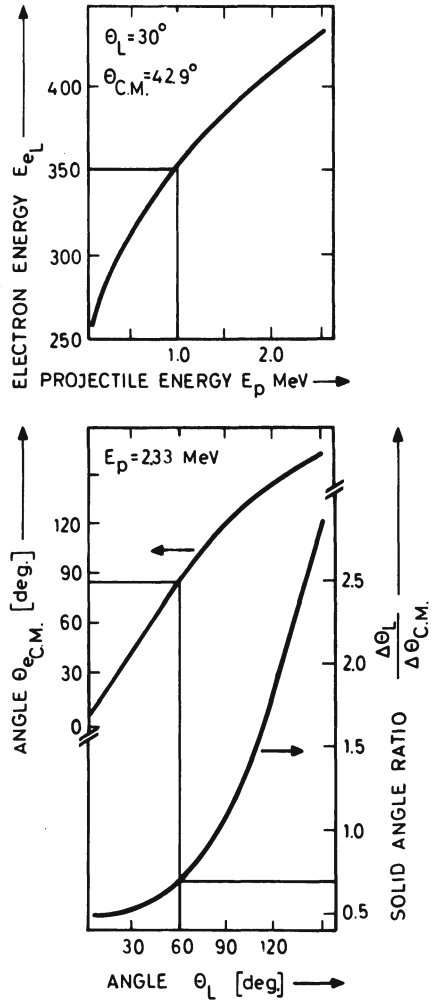

Fig. 5. Kinematic transformation of (Auger) electron energy and angles from projectile frame of reference to laboratory system. From ref. [14].

The Auger electrons measured in the laboratory system suffer a Doppler-like velocity shift to $\vec{v}_e = \vec{v}_p + \vec{v}_A$. From this vector equation can be deduced relations between velocity and angle of emission in the particle rest frame and the corresponding velocity and detection angle in the laboratory frame [9, 14].

An example of the consequences is given in Fig. 5: Carbon KLL-Auger electrons are shifted, e.g., at E_p = 1 MeV from an Auger electron energy $E_A \approx 250$ eV in the particle rest frame to $E_e \sim 350$

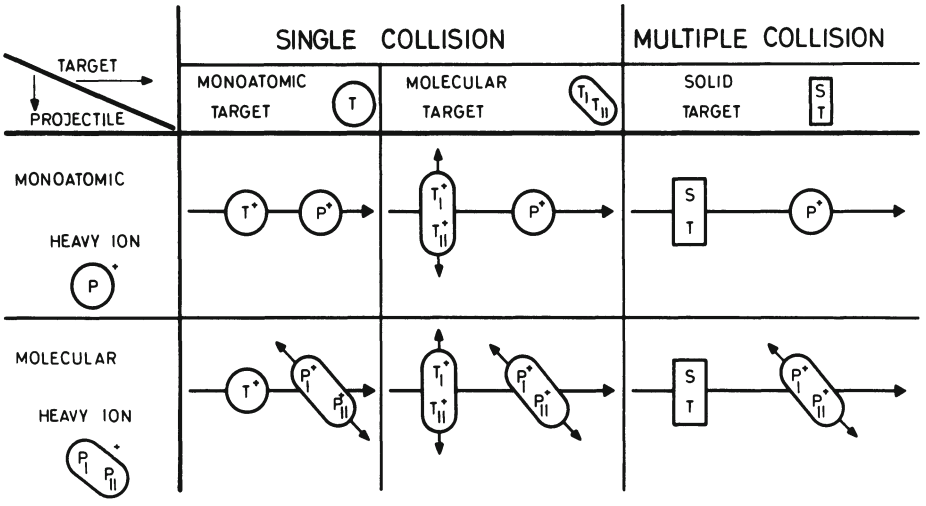

Fig. 6. Different heavy ion collision processes between monoatomic and polyatomic projectiles (P) and targets (T).

eV in the laboratory frame (Fig. 5, top, compare also Ne-KLL Auger electrons in Fig. 3); at E_p = 2.33 MeV, C-KLL-Auger electron emitted under $\vartheta_{e,cm} \simeq 80°$ are observed under $\vartheta_L = 60°$; similarly strong influence is exerted on the solid angle ratio R of the laboratory to the projectile rest-frame solid angle. These rest-frame laboratory transformations impose also stringent requirements on the magnitude of the projectile divergence $\delta\vartheta$ and the magnitude of the projectile energy distribution δE_p, because the observed Auger-line width depends very sensitively on these quantities [9, 14].

4. "Coulomb Explosion"

As has been discussed in Chapter 2, collisions of heavy ions (several MeV/nucleon) with gaseous or solid matter create highly excited and highly ionized collision partners. In the case of molecular collision partners — either as target molecule or as projectile molecular ion — most electrons are removed during the collision; the molecular fragment ions are repelled by the mutual Coulomb force or by other forces associated with this process. Because of the high charge states (q_1, q_2) of the fragment ions we find high charge-products ($q_1\ q_2\ e^2$) creating high repulsion energies (typically hundred eV). Therefore, the term "Coulomb explosion" is used frequently instead of dissociation.

A view on Fig. 6 presents schematically the variety of heavy ion collisions involving (— for simplicity here, diatomic —) molecules (e.g., N_2) or molecular ions (e.g., HeH^+). It is quite obvious, that the right hand column represents a typical beam foil

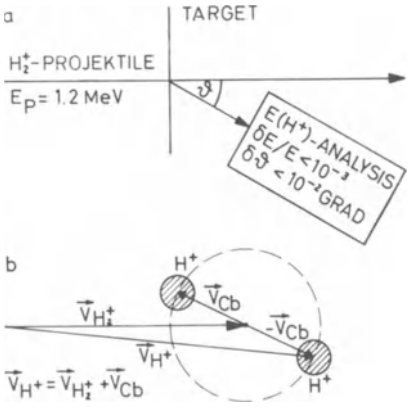

Fig. 7. Coulomb explosion of molecular ions, example H_2^+. a) Schematic of experiments where the energy- and angular-distribution of the exploding fragment (here: H^+) is measured. b) Velocity vectors $\vec{v}$ involved in the explosion.

experiment. In fact, all requirements on beam quality (parallelity, energy homogeneity, etc.) and all characteristic properties listed in Chapter 3 apply again. A scheme of the experimental arrangement is given again by Fig. 2; analyzed here are:

1. Molecular ions
2. Fragment ions
   with such quantities as
   a) Transmission probability
   b) Trajectories (i.e., angular and energy distribution)
   c) Electronic deexcitation (photon, x-rays, Auger electrons)
   d) Secondary processes (e.g., nuclear reactions)

More specifically, transmission studies are discussed in this volume by Remillieux [1], energy- and angular-distributions of fragments are explained by Kanter [2]. Electronic deexcitation from fragments in exploding molecular systems [15, 16, 17] are presented in this chapter. Energy loss and nuclear reaction data are reviewed, e.g., in Ref. [17].

4a. Kinematic Studies of Molecular Projectiles

Molecular ions (e.g., HeH^+, $C_2H_6^+$) of many different species [2] are copiously produced in ion sources and can be accelerated to, say, MeV energies. For simplicity, let us first consider the diatomic molecular ion H_2^+ [18] with kinetic energy E_p = 1.2 MeV

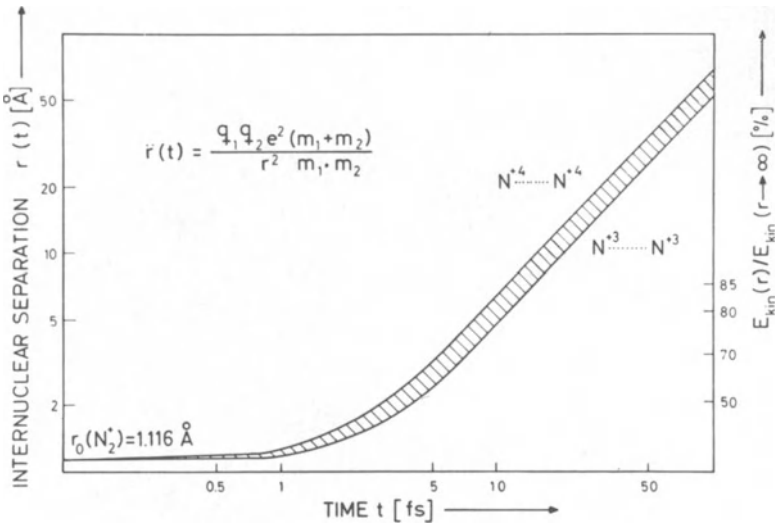

Fig. 8. Internuclear separation r(t) of the diatomic molecular ion N_2^q with charge product $q_1 = q_1 \cdot q_2 = 12$ under unscreened Coulomb repulsion [9].

(Fig. 7). When penetrating a solid foil (typically carbon, 100 Å thick) H_2^+ will loose its binding electron within the first few atomic layers. The fragment ions H^+ with charges q_1 and q_2 and mass m_{H^+} at internuclear separation r_0 (bond length) are repelled by their mutual Coulomb force F_{cb} (or forces from other potentials associated with the break-up). Their potential energy $E_{cb} = q_1 q_2 e^2/r(t)$ is transformed into kinetic energy $E_{kin} = m_{H^+} v_{cb}^2/2$ in the projectile frame of reference within a few 10^{-14}s according to

$$\mu \ddot{r}(t) = q_1 q_2 e^2 / r^2(t)$$

where μ is the reduced mass of the fragments. Figure 8 gives a quantitative example of r(t) for N_2^{+q} [9].

If the internuclear axis is parallel to the projectile velocity $\vec{v}_{H_2^+}$ one observes under an observation angle $\vartheta = 0°$ (see Fig. 7) exploding fragments H^+ with $|\vec{v}_{H^+}| = |\vec{v}_{H_2^+}| \pm |\vec{v}_{cb}|$, i.e., a velocity spectrum with two maxima. They are separated by an energy

$$\Delta E = 4(1/4 \; E_p \; E_{cb})^{1/2}$$

(the factor 1/4 is required by two equal mass particles sharing the available energy E_{cb}).

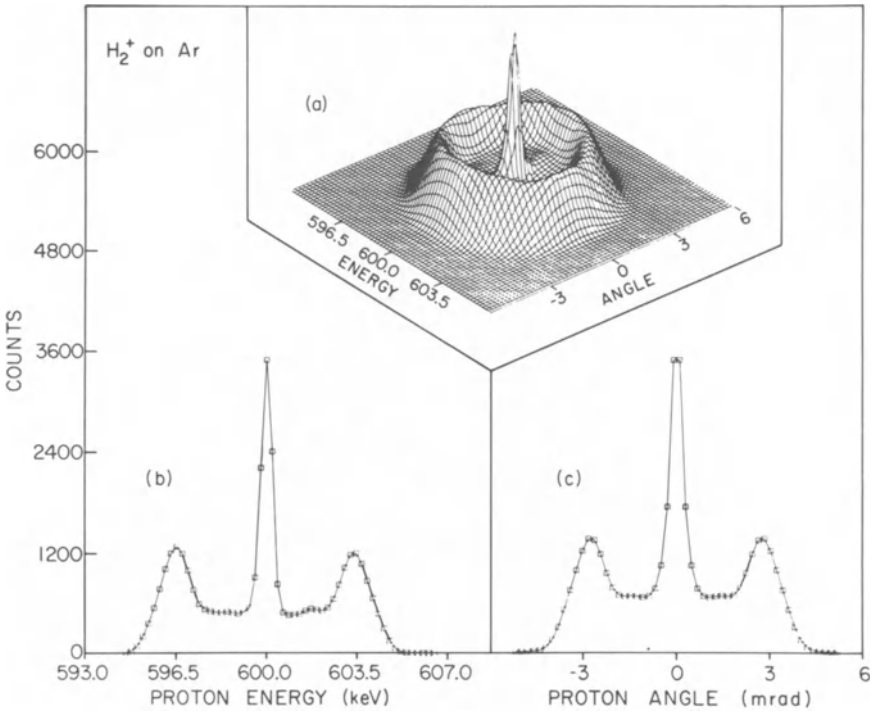

Fig. 9. Angular- and energy-distribution of H^+-fragments from the break-up of H_2^+-projectiles (1.2 MeV) in a Ar-gas-target (pressure ca. 8 m Torr). From ref. [18].

For the paradigmatic case H_2^+ (1.2 MeV) the dissociation energy amounts to E_{cb} = 14.4 eV and is transformed into the laboratory system to ΔE = 8.3 keV. The accelerator acts like an amplifier which transforms the small projectile frame dissociation energies ($\sim$eV) into large laboratory energies (keV). They are measurable easily and with high precision with accelerator-based instrumentation devices.

Beautiful experiments have been performed at Argonne National Laboratory [18] which illustrate the just stated findings. The experimental set-up is displayed schematically in Fig. 7 and will be discussed in more detail by E. Kanter [2]. Figure 9 presents the joint angular- and energy-distributions of H^+-fragments from H_2^+ break-up in collisions with Ar gas targets. The intensity is independent of the direction of the explosion ("ring"-pattern), indicating random orientation previous to the collision. Also, the dissociation energy is transformed from several eV in the projectile frame of reference into (ΔE) several keV in the laboratory system. We assume — for the sake of argument — a mere Coulomb

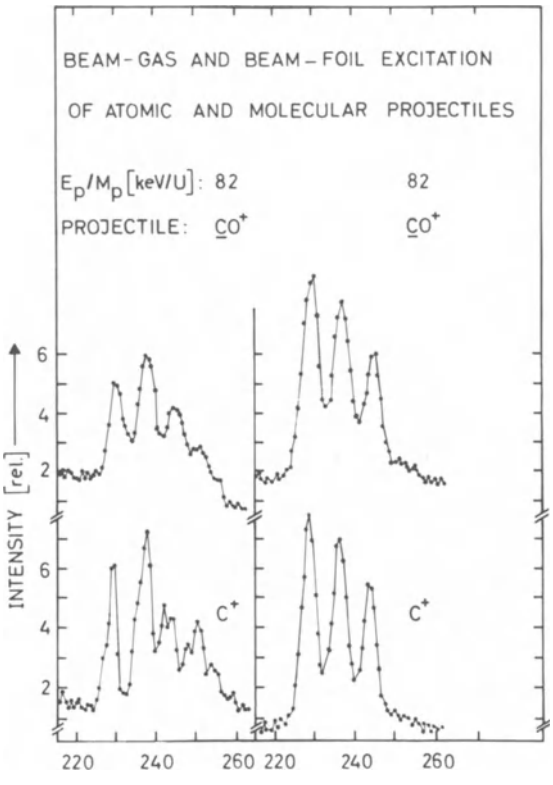

Fig. 10. Shapes of Auger lines from the decay of the metastable (τ = 88 ns) (1s 2s 2p)^{4}P-state in lithium-like carbon (83 keV/nucleon) in carbon monoxide (top) and in carbon alone (bottom), excited by a gas target (left) and by a solid target (right). From ref. [22].

potential between the two exploding fragments; the quantity $\Delta E = 4\,(1/4\ E_p\ E_{cb})^{1/2}$ can be determined experimentally with high accuracy and thus allows to calculate the bond length $r_0 (= q_1\ q_2\ e^2/E_{cb})$ of the molecular ion.

There are two further very interesting aspects: 1) the shape of the joint angular- and energy-distributions including the central peak after collision with gases which reveal, e.g., details of the excited states associated with the dissociation, which is discussed in detail by E. P. Kanter [2], and 2) these distributions after penetration through solids which are affected by the wake-potential, which is discussed in detail by J. Remillieux [1].

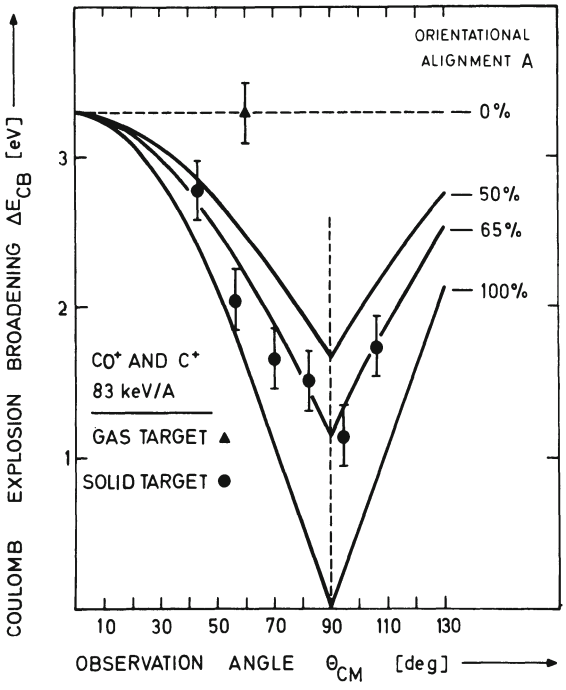

Fig. 11. Coulomb explosion line broadening ΔE_{cb} for the decay of the (1s 2s 2p) $^4P^o$-state as a function of the observation angle ϑ_{cm}. Ref. [14, 19].

4b. Electronic Deexcitation of Molecular Ions

Fragment ions from exploding molecular projectiles can have inner shell vacancies and can have electrons in highly excited states as has been discussed in Chapters 2 and 3. The kinematics of the exploding fragments is imposed on such deexcitation processes as Auger electron emission. This causes an additional line broadening in the observed spectra. The contribution by the Coulomb explosion ΔE_{cb} alone to the total line width can be determined quantitatively without knowing any other line broadening contributions, simply by comparing the width of the lines from well separated transitions in both atomic and molecular projectiles of equal velocity [9]. The kinematics of this process is more complicated as the kinematics of the electron beam foil spectroscopy of monoionic systems discussed in Chapter 3. Electron beam foil spectroscopy of exploding molecular fragments have to deal with three velocities affecting the Auger electron velocity $\vec{v}_e = \vec{v}_p + \vec{v}_A + \vec{v}_{cb}$ observed in the laboratory frame of reference (for details see [9, 14, 19]).

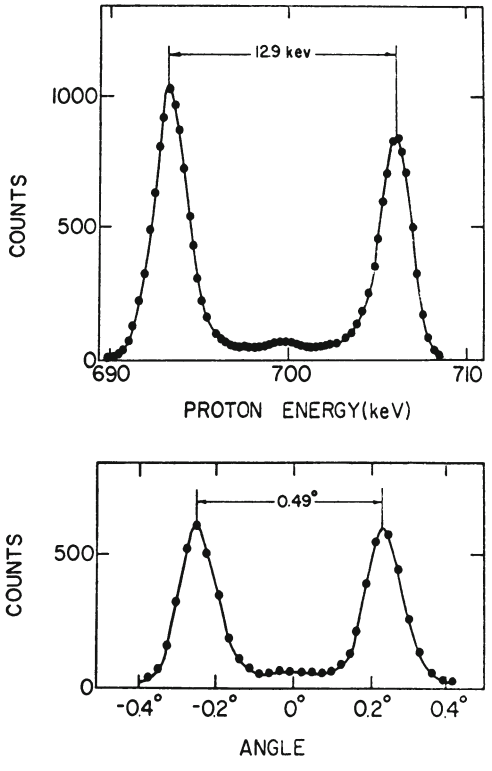

Fig. 12. Zero angle ($\vartheta = 0°$) energy spectrum (above) and zero energy shift ($\Delta E = 0$ eV) angular distribution (below) of H^+ fragments from break-up of H_3^+ (0.7 MeV/nucleon) in a carbon (2.5 g/cm^2) foil. From [20].

It is advantageous to distinguish three different times:

Time A: The collision time in single collision experiments is in the order of $t = d/v_p = 10^{-17}$s (spacial diameter d of a molecule, say N_2; projectile velocity v_p)

Time B: Life time of inner shell vacancies are in the order of 10^{-14}s (compare Chapter 3). An inspection of Fig. 8 shows that we can define a characteristic "explosion time" $t_{expl} = t(r = 2r_o)$. For most cases discussed here we find $t_{expl} = 10^{-14}$s.

Time C: Life-time τ of metastable states, like the $(1s\ 2s\ 2p)^4P \rightarrow (1s^2)^1S + e^-$ Auger transition $\tau > 10^{-9}$s (see Chapter 3).

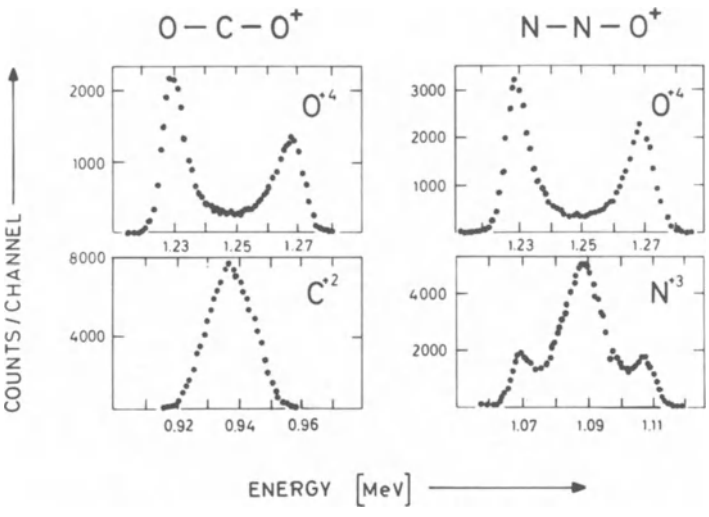

Fig. 13. Energy spectra of molecular fragments from the Coulomb explosion of CO_2^+ (left) and N_2O^+ (right) at 80 keV/nucleon (from [21]).

Studying Coulomb explosion via Auger electron spectroscopy, in particular, Auger electrons from the decay of metastable states (Time C) are affected; the reason is that in this case most of the initial potential energy E_{pot} is converted into kinetic energy E_{kin} before most of these decays can take place. For example, exploding nitrogen molecules gain a value of $E_{kin}/E_{pot} = 0.85$ already after only $t = 10$ femto seconds (compare Fig. 8, right hand ordinate).

An example of electron beam foil spectroscopy of the exploding molecular fragments C from CO in Fig. 10 will be briefly discussed [9, 14]. The study is done in the range of time C; the measured quantity is ΔE_{cb} (defined at the beginning of this chapter) as a function of the observation angle ϑ (Fig. 11). As is discussed in more detail by J. Remillieux [1] the wake-potential trailing charged particles penetrating a solid tends to align the linear CO-molecular axis into the beam-direction; this yields a kinematic broadening ΔE_{cb} which originates only from the projection of the molecular fragment velocity vectors $\vec{v}_F$ in the direction of the electron detector. The solid lines in Fig. 10 are calculations for different fractions of molecules aligned in the beam direction. For beam gas excitation an alignment is neither expected nor found. For beam foil excitation is deduced a surprisingly high alignment of $A \sim 65\%$, surprising in view of much smaller alignments calculated from energy and angular distributions of fragments from similar systems [18]. The result may be caused by selective excitation of the par-

Table 2. Auger Transitions in Li-Like Carbon; A Comparison of Monoionic Carbon and Carbon in $(CH_4)^{+7}$ (see Ref. [23] and [24]).

Transition in carbon	$(1s\ 2s^2)^2\ S_{1/2} \rightarrow (1s^2)^1S_0$	$(1s\ 2s\ 2p)^4P_{3/2} \rightarrow (1s^2)^1S_0$
Energy [eV]		
C^{+++} calc.	227.3	229.9
C^{+++} exp.	227.5 $\Delta E = (4 \pm 0.3)$ eV	229.9
$(CH_4)^{+7}$ exp	223.5	230.0
Life time [s]		
calc.	$14\ 10^{-15}$	$8.8\ \ 10^{-9}$
exp.	—	$(11 \pm 2.5)\ 10^{-9}$

ticular electronic state analyzed in this experiment. The data demonstrate in this paradigm that very detailed information can be obtained from individual electronic configurations of fragments from Coulomb explosion.

5. Structure Studies of Molecular Ions

With the procedure described in Chapter 4a it is possible to determine the bond length r_0 of diatomic molecular ions. This method, however, is not restricted to diatomic systems, it can in principle be used with any polyatomic molecular ion — eventually with coincidence techniques [2]. The structure of H_3^+ has been clarified experimentally by a collaborative study between Argonne National Laboratory, the University of Lyon, and the Weizmann Institute in Rehovot [20]. It has been shown that H_3^+ is predominantly of equilateral triangular shape as an inspection of Fig. 12 reveals with its only two strong maxima. The most probable length of the side of the triangle is found to be $r_0 = (0.97 \pm 0.03)$ Å. A linear structure would yield an energy and angular distribution with three maxima in contrast to the experimental result. Structure information from more complex molecular ions, namely, CO_2^+ and N_2O^+, is easily extracted from the energy spectra in Fig. 13: The two upper spectra indicate that oxygen in both molecular ions is in the outside position of the two molecules and that the oxygen atoms in CO_2^+ occupy equivalent positions. The right-bottom spectrum show two non-equivalent positions for the nitrogen atom in N_2O^+,

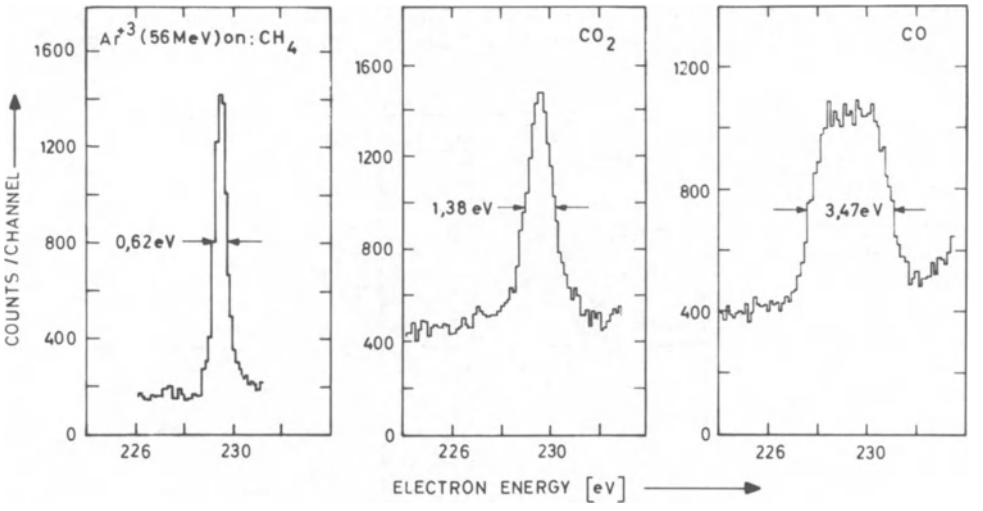

Fig. 14. Line shapes of $[(1s\ 2s\ 2p)^4P_{5/2} \rightarrow (1s^2)^1S + e]$ Auger electrons in carbon in different molecules (CH_4, CO_2, CO) after Ar^{+12} (56 MeV) impact. From R. Mann et al. [4].

namely one on the outside and one roughly in the center. The left-bottom spectrum indicates, however, that the carbon is roughly in the center of CO_2^+ [21, 22]. A more detailed analysis of such studies is discussed by E. Kanter [2].

Another source of information on molecular structure via "Coulomb explosion" experiments is the study of Auger electrons from exploding molecular fragments. The basic idea for the simple case of CO^+ has already been given by Fig. 10 in Chapter 4b. Instead of using molecular ions as projectiles as in Fig. 10, it is also possible to analyze Auger electrons from fragment ions from molecular targets (see Fig. 6) [4, 5]. Auger electrons emitted in the time range C (see above) from lithium-like carbon bound in three different compounds, CH_4, CO_2, and CO, are observed with quite different line shapes, which are understood quantitatively [4] in terms of the molecular structure: carbon in a central, symmetric position (CH_4, CO_2) gives a small line width (close to the instrumental resolution of 0.6 eV) because of lack of a recoil partner to impose Doppler-like broadening on the Auger line; on the other hand, carbon in CO has a recoil partner of almost equal mass so that the Auger lines show the full Doppler-like broadening. These data show that it is possible to obtain molecular ion structure information from fragments in a particular electronic configuration.

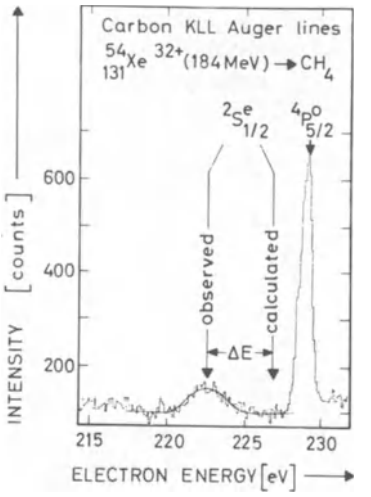

Fig. 15. Auger electrons from carbon in $(CH_4)^{+7}$ [$(1s\ 2s^2)^2S_{1/2}$-state] and in C^{+3} [$(1s\ 2s\ 2p)^4P$-state] after Xe (184 MeV) impact. From R. Mann et al., ref. [23] and [24].

A very exotic molecular ion is the $(CH_4)^{+7}$, which is formed transiently from CH_4 under Xe (184 MeV) impact and is studied by R. Mann et al. [23, 24]. The highly charged Xe removes immediately (range time A) 7 of the 10 electrons of the target CH_4. The four H^+-fragments dissociate similarly to the time scale in Fig. 8. Auger electrons from the metastable $(1s\ 2s\ 2p)^4P_{5/2}$-state emitted in the range of time C are unaffected both in energy and in line width (see Fig. 15 and Table 2). Prompt transitions, however, which occur from states with life times τ in the range of time B, i.e., $\tau \sim 10^{-14}$s, are roughly affected by the field of the exploding H^+-fragments. They did not have time to travel away from the central carbon atom for more than $r = 2r_0$ in the explosion time $t_{expl}(r = 2r_0) \simeq 10^{-14}$s (see above). The effect on the prompt Auger transition from the $(1s\ 2s^2)^2S_{1/2}$ state is a significant shift (about 4 eV) in energy and a broadening of the observed line (see Table 2).

6. Conclusions

We have demonstrated that studies of molecular ions with accelerators are indeed a very promising tool to provide electronic and geometric structure information of molecules or molecular ions. The use of this tool is a rather recent development, which has not yet been fully exploited in instrumental refinement [1, 2]. Also, the understanding of the microscopic processes at such high energies is incomplete and needs both further experimental and further theoretical efforts [3, 8, 10, 25].

The author is indebted in particular to his colleagues at Frankfurt University, GSI Darmstadt, and Argonne National Laboratory for their elucidating comments and fruitful collaboration.

References

1. J. Remillieux, in: "Molecular Ions," J. Berkowitz and K. O. Groeneveld, eds., Plenum Publishing Corporation, New York, N. Y., USA, p. 445 (1983).
2. E. P. Kanter, in: "Molecular Ions," J. Berkowitz and K. O. Groeneveld, eds., Plenum Publishing Corporation, New York, N. Y., USA, p. 463 (1983).
3. I. A. Sellin, ed., Structure and Collisions of Ions and Atoms, Springer, Heidelberg (1978).
4. R. Mann, F. Folkmann, R. S. Peterson, Gy. Szabó, and K. O. Groeneveld, J. Phys. B 11, 3045 (1978).
5. R. Mann, F. Folkmann, and K. O. Groeneveld, Phys. Rev. Lett., 37, 1674 (1976).
6. P. Sigmund and K. B. Winterbon, Nucl. Instr. Meth., 119, 541 (1974).
7. G. Spahn and K. O. Groeneveld, Nucl. Instr. Meth., 123, 425 (1975).
8. S. Bashkin, ed., Beam-Foil-Spectroscopy, Springer, Heidelberg (1976).
9. H. J. Frischkorn, S. Schumann, R. Kluge, and K. O. Groeneveld, Physica Scripta, 21, 63 (1980).
10. K. O. Groeneveld, in: "Beam-Foil-Spectroscopy," I. A. Sellin, and D. J. Pegg, eds., Plenum Publishing Corporation, New York, N. Y., USA, p. 593 (1976). K. O. Groeneveld, R. Mann, G. Nolte, S. Schumann, R. Spohr, and B. Fricke, Z. Phys., A274, 191 (1975).
11. K. O. Groeneveld, R. Mann, G. Nolte, S. Schumann, and R. Spohr, Phys. Lett., 54A, 335 (1975).
12. H.-D. Betz, F. Bell, H. Panke, G. Kalkolten, M. Welz, and D. Evers, Phys. Rev. Lett., 33, 807 (1974).
13. K. O. Groeneveld, B. Kolb, J. Schader, and K. D. Sevier, Z. Phys., A277, 13 (1976).
14. G. Reichardt, H.-J. Frischkorn, S. Schumann, and K. O. Groeneveld, to be published.
15. K. O. Groeneveld, G. Astner, S. Hultberg, S. Mannervik, and P. S. Ramanujam, J. Phys., B13, L205 (1980).
16. T. J. Gay and G. Berry, J. Phys., B13, L199 (1980); J. Phys., B13 L (1980).
17. D. S. Gemmel, ed., Proc. of the Conf. on the Physics with Molecular Ion Beams, Argonne Nat. Lab., ANL/PHY, 79-3 (1979).
18. E. P. Kanter, P. J. Cooney, D. S. Gemmell, K. O. Groeneveld, W. J. Pietsch, A. J. Ratkowski, Z. Vager, and B. J. Zabransky, Phys. Rev., A20, 834 (1979).

19. H. J. Frischkorn, K. O. Groeneveld, G. Reichhardt, and S. Schumann, Proc. of the Intern. Conf. on Inner Shell Ions, Stirling/Scotland, August 1980, to be published.
20. M. J. Gaillard, D. S. Gemmell, G. Goldring, I. Levine, W. J. Pietsch, J. C. Poizat, A. J. Ratkowski, J.- Remillieux, Z. Vager, and B. J. Zabransky, Phys. Rev., A17, 1797 (1978).
21. D. S. Gemmell, E. P. Kanter, W. J. Pietsch, Chem. Phys. Lett., 55, 33 (1978).
22. K. O. Groeneveld, H. J. Frischkorn, S. Schumann, D. S. Gemmell, P. J. Cooney, E. P. Kanter, and W. J. Pietsch, J. of Molecular Structure, 60, 85 (1980).
23. R. Mann, I. A. Sellin, F. Folkmann, H. J. Frischkorn, K. O. Groeneveld, D. Rosich, S. Schumann, and Gy. Szabó, Bull. Am. Phys. Soc., 22, 1320 (1977).
24. K. O. Groeneveld, IEEE Transactions, NS26, 1033 (1979).
25. K. O. Groeneveld, E. Schopper, and S. Schumann, J. Solid State Nucl. Track Det., S2, 81 (1980).

GEOMETRIC AND ELECTRONIC STRUCTURE OF MOLECULAR IONS PENETRATING THROUGH SOLIDS

J. Remillieux

Institut de Physique Nucléaire (and IN2P3)
Université Lyon-I
43 Bd du 11 Novembre 1918
69622 Villeurbanne Cedex, France

Introduction

This lecture has to be read in conjunction with the preceding one by K. O. Groeneveld [1] who introduced the principle of the determination of molecular ion structure by beam-foil methods, and also in conjunction with the following paper by E. Kanter [2] who describes many applications of these methods not only in beam-foil but also in beam-gas configurations.

This paper will concentrate on two aspects of the physics of the break-up of fast molecular ions in foil target: i) the penetration of a fast incident ion cluster into the solid matter, and ii) the use of a molecular orbital picture to describe the post foil evolution of the ion cluster after emergence.

The discussion will be restricted to the case of fast projectiles, with velocities much larger than the Bohr velocity ($v_o = e^2/h$) and typically of the order of 1 MeV/nucleon, which penetrate through thin amorphous foils with thicknesses typically of the order of a few 100 Å. Carbon foils are used in most of the experiments because homogeneous films can be obtained rather easily with thicknesses ranging from 1 to 50 $\mu g/cm^2$. Such foils exhibit no channeling effects, a characteristic which proves that they are amorphous.

In the velocity range considered here the cross section for the loss of the projectile electron inside the solid is much larger than the cross section for an electron capture. As a consequence most of the incident molecules explode inside the foil into ionic fragments. Information on the structure of the incident molecular ion can be

obtained from the knowledge of the dynamics of the projectile explosion which initiates inside the foil and then is completed in the vacuum.

In the first section will be considered the most probable case where the weakly bound electrons of the incident molecular ion are stripped off within the first few atomic layers of the front surface of the foil. As the electron capture probability by each of the fragments is very small inside the foil one deals with fragments which are bare nuclei, or which carry only few inner shell electrons. As a consequence the fragments behave during the explosion as point charge particles, with an average charge inside the foil and a fixed charge in the vacuum.

In the second section we will consider the much less probable case where the weakly bound electrons can survive to the traversal of the foil. In that case the projectile behaves like a molecular ion not only in the post foil vacuum but also during the penetration of the foil.

In the last section will be considered the intermediate case where the cluster penetrates the foil as point charge fragments which then collectively capture a target electron at the back surface of the foil to reconstitute a molecular ion in a bound or unbound state.

I. Explosion between Point Charge Fragments

1. Pure Coulomb Explosion

If one assumes that the valence electrons of the incident molecule are immediately stripped away, each fragment reaches an average charge $Z_{eff} < Z$ which represents the screening of the nuclear charge Z by a fluctuating number of electrons which are bound to the fragment. In a diatomic cluster of velocity V the two fragments interaction at distance R should be simply governed by a screened Coulomb potential

$$U(R) = (Z_1 Z_2)_{eff} \, (e^2/R) \, \exp(-R\omega_p/V),$$

where it is assumed that the perturbation caused by the solid to a free Coulomb explosion is only due to the target electron gas, characterized by its plasmon frequency ω_p, which screens the mutual Coulomb force between the separating fragments. After the foil the ionic fragments achieve their separation in the vacuum under non-screened Coulomb forces.

For a given incident diatomic projectile, with an internuclear separation R_o and a negligible internal motion, one can easily calculate the dynamics of the explosion in the center of mass frame and

then in the laboratory frame. This is described in the preceding paper by Groeneveld [1]. The fragments of randomly oriented projectiles have a momentum distribution which can be characterized by a ring with a diameter inversely proportional to the bond length R_o. The momentum distribution of fragments of MeV molecules can be accurately measured since an explosion which liberates a few eV in the projectile frame can shift the total energy of the fragments by a few KeV and deviate their trajectories by few tenths of degrees.

In real experiments the momentum distribution of the fragments is broadened by the vibrational-rotational excitation of the projectiles. In some cases that can be used to measure the distribution of vibrational excitations in a molecular ion beam. An example is given in the next paper by Kanter [2] for H_2^+ and HeH^+ beams accelerated from ion sources of various types.

2. Application to Simple Structure Determination

A simple Coulomb picture of the foil break up of molecules, although it neglects many aspects of the ion-solid interaction, can be useful to get some information on molecular structures when the following conditions are fulfilled: the dwell time of the projectile inside the foil is small, the fragments have a well defined ionic charge in the foil, the fragments are fully stripped when they emerge from the foil.

An example of that is the method we used in Lyon [3] to study the structure of H_3^+ (in Ref. 3 are also described the other methods which were developed simultaneously at Rehovot and at Argonne). 2.2 MeV H_3^+ ions were broken up in a thin carbon foil. A tightly collimated detector was used to measure the angular distribution of two types of events among the proton fragments: events corresponding to the simultaneous detection of two and three protons issued from the same triproton cluster. The observed absence of 3 proton events was the proof of the absence of an observable fraction of linear H_3^+ ions in the incident beam. On the other hand the presence in Fig. 1 of pairs of protons which emerge along a cone centered on the beam axis proves the triangular structure of H_3^+. Furthermore, the opening angle $\theta_o \sim 0.115°$ of this cone can be directly related to the mean internuclear separation R_o in the molecule. This value was found to be R_o (H_3^+) = 0.95 ± 0.06 Å.

3. Manifestation of Ion-Solid Effects

The interest of using a foil stripper rather than a gas stripper for structure studies is to get heavily stripped fragments which separate under simple Coulomb forces. Nevertheless, in most of the molecular beam-foil experiments the cluster-foil interaction strongly perturbs the dynamics of the explosion. This perturbation was unexpected and was recognized to be due to the close proximity of the

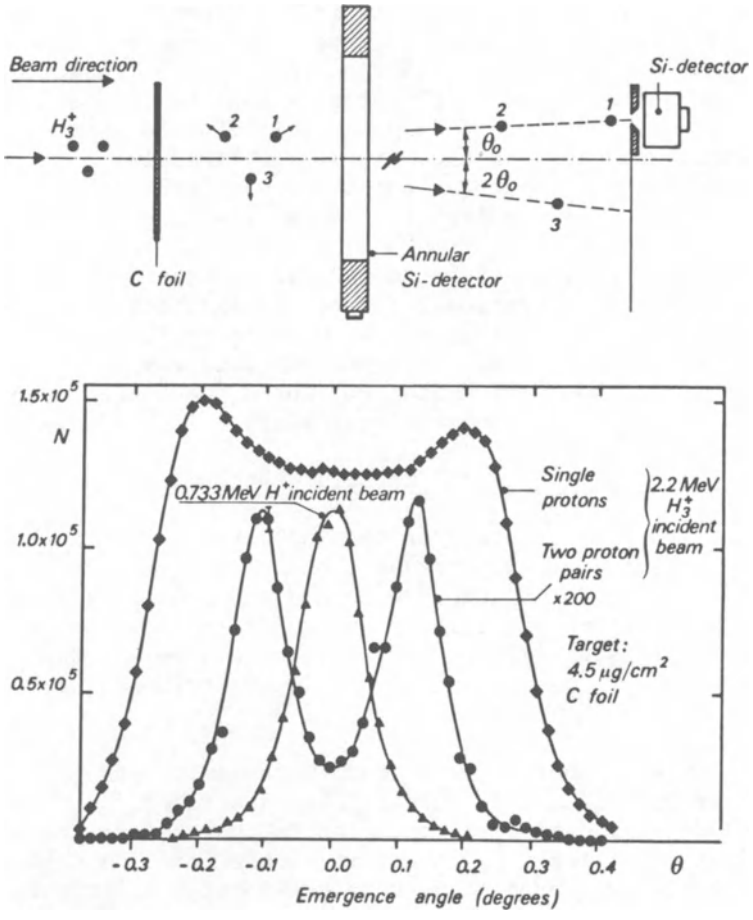

Fig. 1. Schematic description of the Lyon experiment designed for the study of the H_3^+ structure. Angular distribution of single protons and pairs of protons detected within an angular acceptance of ±0.019°, transmitted through a 4.5 µg/cm^2 carbon foil bombarded by 2.2 MeV H_3^+ ions (from Gaillard et al., Ref. 3).

fragments during the foil penetration. That was unexpected because the closely correlated penetration of ions into matter had never been observed before (the mean distance between the break-up fragments is by several orders of magnitude shorter than the mean distance between two ions in the most intense ion beams). Proximity effects during the penetration make more difficult the interpretation of the molecular break-up for structure studies; nevertheless

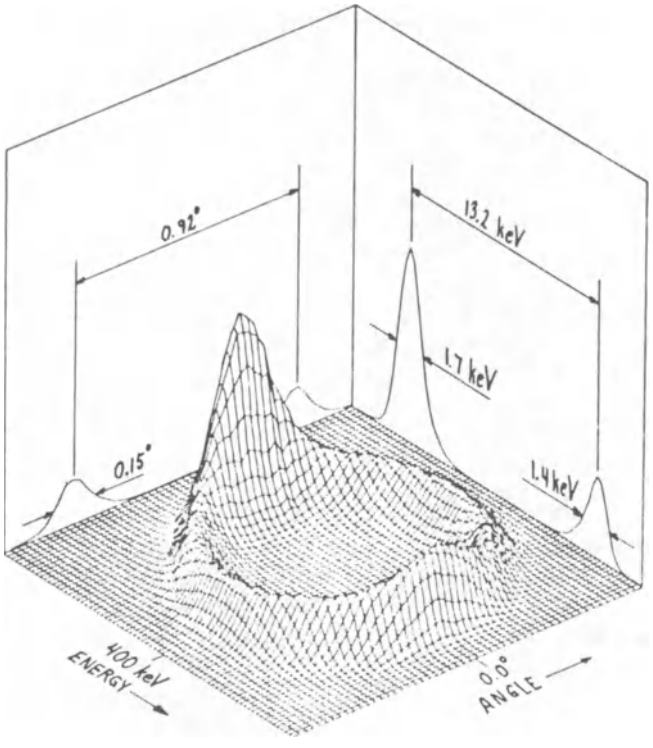

Fig. 2. Experimental distribution in energy and angle for protons emerging from a 85 Å C foil bombarded by 2 MeV HeH^+ ions. (Taken from Vager et al., Ref. 9).

these effects revealed novel aspects of the ion-solid interaction such as the local electron polarization of the medium in a fast ion track.

a) Electron Polarization Wake

In 1975 was observed a strong break down of the spherical symmetry in the distribution of the fragments around the cluster center of mass [4]. That was the first evidence for the existence of a non-central force, the wake-force, which exists only inside a solid, and which tends to align the fragments along the beam axis. This force originates from the non spherical distribution of the target electrons around a fast moving ion. Neelavathi and Ritchie [5] predicted in 1973 that the electron density of the medium should oscillate along an ion track. The amplitude and the wavelength of this oscillation depends on the ionic charge and on the velocity of the penetrating ion, but also on the dielectric response of the

penetrated medium through its plasmon frequency ω_p and the rate of damping of the plasmon oscillations. The fluctuation of the electron density sets up a potential distribution in the medium which moves at the projectile velocity. Wake potentials induced by MeV light ions are typically of the order of a few tens of eV, with a wavelength of a few tens of Å. In molecular beam-foil experiments the distance between the fragments is typically of the order of 1-10 Å, a distance which is short when compared to the spatial extension of the wake potential. Then inside the foil the fragments interact between them not only through Coulomb forces but also through polarization wake forces. Coulomb and wake potentials can develop forces of the same order of magnitude on a given fragment. Wake forces perturb the symmetry which is expected from a pure Coulomb explosion, since wake forces are not directed along the internuclear axis but tend to align the fragments along the beam axis. Furthermore wake effects are stronger on the trailing ion than on the leading ion in the cluster. Such an effect is clearly observable in Fig. 2 which shows that a large number of fragments emerge along the beam axis, with a stronger effect for the low energy fragments than for the high energy fragments.

The discovery of wake effects in molecular ion experiments stimulated many theoretical works devoted to a better description of the wake potential and of wake effects in various ion-solid interactions [6].

The various plasmon wake models [7-12] differ from each other by the degree of complexity of the dielectric function $\varepsilon(k, \omega)$ which is used and by the way close electronic collisions are taken into account if at all. The fact that close collisions with the target electrons have to be included in a full description of the wake potential is evident when one considers that in the case of an isolated projectile the wake potential at the ion creates a retarding force on the projectile itself which has to be compared with the well known predictions of energy loss theories. Now most of the momentum distributions of fragments observed in molecular beam-foil experiments can be correctly interpreted in the frame work of the plasmon wake model.

Nevertheless some recent experiments performed in Lyon and Rehovot cannot be explained by the usual plasmon wake models.

In Lyon [13] it was observed with H_3^+ projectiles that the lifetime for the non-dissociation of an H_2^+ ion inside a solid is much shorter when H_2^+ trails behind the third proton of the projectile, whereas this lifetime is "normal" when it is H_2^+ which leads the cluster. This reduced lifetime revealed that the electron density in the proton track is much higher than the predictions of simple plasmon wake models. In Rehovot [14] experiments with OH^+ ions revealed also that the distribution of the break-up protons deviates

from the predictions of plasmon wakes. The conclusion was that in some cases the wake at close proximity from the moving charge can be better described by reducing the interaction of the moving ion with the medium to the Coulomb scattering of the target electrons, which increases the electron density in the ion track. Since this "Coulomb wake model" [15] neglects the plasma aspects of the medium it cannot describe the wake potential at long distance, but it should be noticed that the observation of long distance interactions between the fragments in the solid is usually not accessible to beam-foil type experiments. More experiments and theoretical works are now necessary to unify the plasma and Coulomb aspect of the electron polarization wake in a solid medium.

b) Cluster Stopping Power

In the concept of electron wakes the electronic stopping power of the medium for a fast ion is related to the derivative of the wake potential at the ion. Then the energy loss of an ion cluster will be determined by the interference of the individual wakes of each fragment in the cluster. This concept was first developed by Brandt and Ritchie [16] in terms of a "vicinage function" calculated from interference effects between plasmon wakes. Due to the close proximity of the fragments in molecular beam-foil experiments with fast projectiles the interference is always constructive. As a consequence the cluster stopping power is generally enhanced by proximity effect. Indeed such an enhancement has been observed in various experiments [17].

One can also give another interpretation of the observed excess of energy loss for an ion cluster by dividing the electronic energy loss into two parts: the energy loss due to close collisions with individual target electrons, this part involves too small distances to be concerned by any proximity effects, and the energy loss due to distant excitation of the target electrons by collective modes, only this last process involves distances large enough to exhibit proximity effect. This interpretation allows a quick estimation of the stopping power for an ion cluster but the theoretical limits between close and distant collisions are not accurate enough to allow a full quantitative description of the observed stopping power.

c) Statistical Fluctuations

The interaction of a fast ion with a solid is characterized by a very large number of individual interactions. It is then of interest to consider at which level the statistical fluctuations of these individual interactions can perturb the momentum distribution of the fragments in a molecular beam-foil experiment.

The effect of the fluctuations due to the statistical aspect of the plasmon wake, and consequently of the energy straggling of

an ion cluster, has been theoretically investigated by Echenique, et al. [12]. They conclude that wake fluctuations are of negligible effect in most of the experiments.

Much more severe is the effect of the multiple-scattering suffered by the break-up fragments in the foil. Escovitz, et al. [18] calculated the relative momentum dispersion between the fragments in the two extreme cases where the companion ions of a cluster suffer totally correlated and totally uncorrelated multiple scattering effects. The first case is not realistic as it could concern only linear projectiles perfectly aligned with the beam axis. In the second extreme case, which seems to be applicable to the majority of the ion clusters, uncorrelated multiple scattering effects are easy to calculate. The net result is a very large broadening in the distribution of the relative momentum of the fragments. Then multiple scattering effects severely limit the accuracy of the beam-foil techniques for structure determination in the cases where one cannot use foils thin enough or when the fragments have a too large ionic charge.

II. Survival of Fast Molecular Ions Inside a Solid

It was assumed in the preceding section that the break-up of all the incident molecules initiates at the front surface of the foil. In fact various experiments performed in Lyon show that the survival probability of the incident molecules inside the solid can play an important role in beam-foil experiments performed with very thin targets.

We first investigated the lifetime of fast atoms in solids by measuring non-equilibrated charge state distributions emerging from thin foils [19]. We observed that the fraction of neutral H atoms emerging from foils of various thicknesses bombarded with incident H atoms exponentially decreases with the target thickness for very short dwell times in the foil and then reaches an equilibrated value, independent of the foil thickness, for longer dwell times. The characteristic time of the exponential decay was interpreted as the lifetime of fast hydrogen atoms inside the foil.

Such a measurement shows that an H atom emerging from a foil can be either a reconstituted atom, resulting from the capture of a target electron (we call them for simplicity the "blue atoms"), or H atoms which survived to the traversal of the foil (we call them the "red atoms"), the latter being observable only when the dwell time is of the order of one femtosecond. Then this type of measurement was extended to other atomic systems with one and two electrons, such as He^+, He^0, and H^- (Fig. 3).

It was tempting to extend this type of measurement to molecular projectiles, and that is also shown on Fig. 3 for H_2^+ and H_3^+

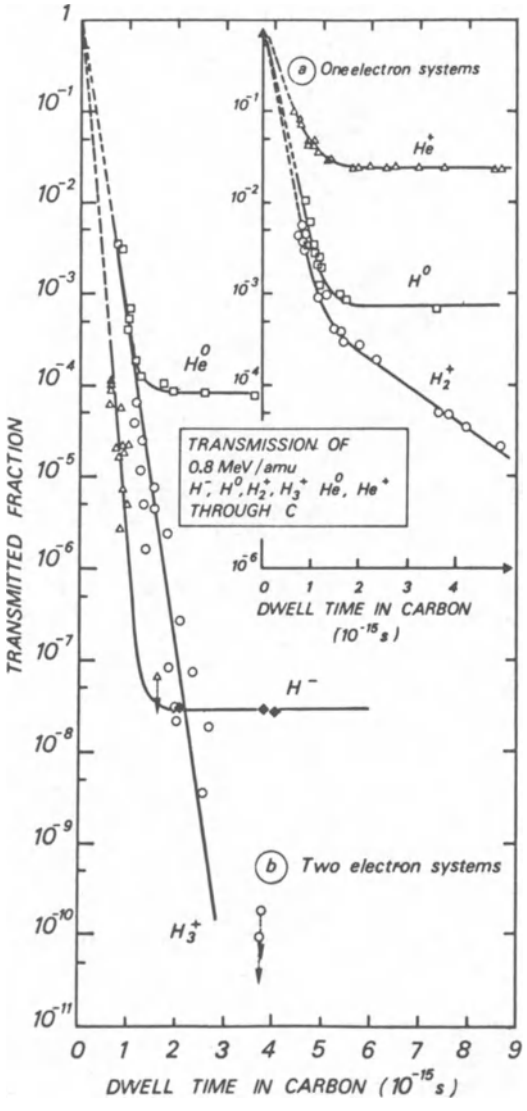

Fig. 3. Transmitted fraction of atomic and molecular 800 KeV/amu projectiles through carbon foils as a function of the projectile dwell-time: (a) one - electron H^0, $^3He^+$, and H_2^+; (b) two - electron H^-, $^3He^0$, and H_3^+ (from Cue et al., Ref. 21).

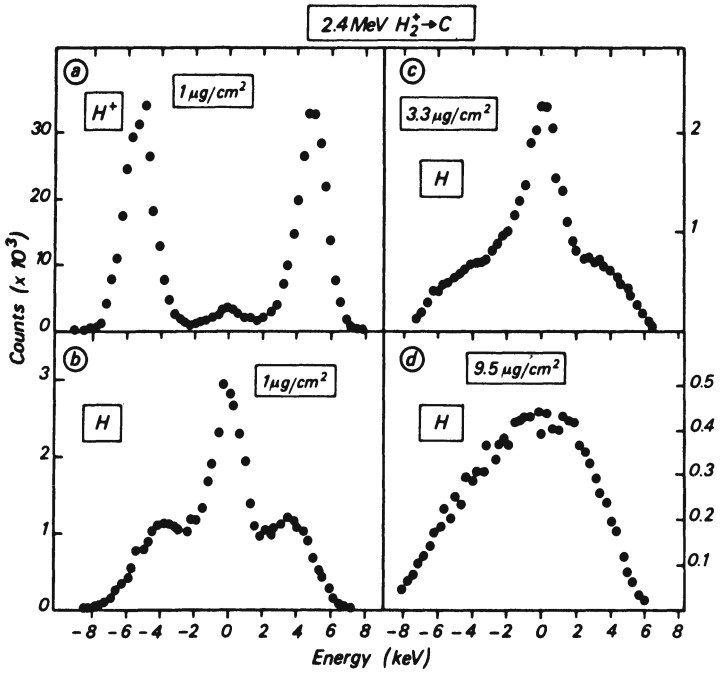

Fig. 4. The energy distribution of (a) protons and (b)-(d) neutral H atoms emerging at 0° when 2.4 MeV H_2^+ are incident on (a), (b) 1 - (c) 3.3, and (d) 9.5 μg/cm² carbon foils (from Gaillard et al., Ref. 22).

projectiles. It appeared that molecules can emerge from the foil, a phenomenon which is known for H_2^+ since 1971 [20] and has been observed later with other molecular ions. Their yield exhibits also an exponential decrease with target thickness for very short dwell times. As for atoms, it was the proof that "red molecules" can survive to the traversal of a foil. For longer dwell times, reconstituted "blue" H_2^+ molecules are observed with a probability which decreases slowly with the target thickness and that will be discussed in Section III. In the case of H_3^+ we have no evidence for the existence of blue H_3^+, since the reconstitution of a molecule is much less probable for a triatomic system than for a diatomic one. From this study of the lifetime of fast atoms and molecules in solids we conclude [21] that the solid medium introduces a strong perturbation on the electronic state of red atoms and molecules, more particularly, this perturbation induces a level width upon the electronic state.

During the traversal of the foil the internal motion of the red molecules is also strongly perturbed by the solid. Due to the more or less independent multiple-scattering suffered by its nuclei

a red molecule gets more and more excited as it penetrates the foil, and this can lead to the vibrational dissociation of the red molecule. That has been clearly observed by measuring the overproduction of neutral H atoms emerging from very thin foils bombarded with H_2^+ and H_3^+ beams [19]. This overproduction exhibits also a red regime due to the transmission of the projectile electrons. The momentum analysis of the red H^0 atoms [22] showed that the majority of them are produced via the formation of unbound excited states of H_2^+, but some of them have not been repelled by their proton partner (see the central peak in the spectra of Fig. 4). We believe that this central peak indicates that some incident molecules have been vibrationally dissociated by the foil without suffering any electronic excitation.

III. Reconstitution of Atoms and Molecules by Target Electron Capture - A Molecular Orbital Picture

1. Enhanced Electron Capture Probability by a Fast Ion Cluster

It was shown many years ago by Meggitt et al. [23] that the production per incident proton of neutral H atoms of a given velocity was higher with H_2^+ and H_3^+ incident beams than with H^+ beams. In the preceding section it was demonstrated that this overproduction can be explained for very short dwell times by the transmission of some projectile electrons (Fig. 3) which leads to the formation of "red atoms." After subtracting this red contribution one observes an overproduction of "blue atoms," due to target electron capture, which decreases slowly when the dwell-times increases. This H^0 overproduction is plotted on Fig. 5 as a function of the emergent interproton separation. One observes that protons which are at a distance larger than $\sim$10 Å from their partner behave like individual particles. Two types of models can be advanced to interpret the enhancement of the capture probability by an ion cluster. Our first model [19] is based on the predominant role played by the target electrons which emerge from the solid along the beam axis and with a velocity close to the ion velocity. In the case of H_2^+ and H_3^+ projectiles we calculated the probability of forming a H^0 atom in the following two step process: a target electron is first accelerated to the velocity of the cluster center of mass by collision with one of the protons in the cluster and then this electron is captured by another proton of the same cluster. The predictions of this model correspond to the lines on Fig. 5.

One can also make another attempt to describe collective effects in the electron capture probability by calculating what should be the effective charge Z_{eff} of a point particle having the same capture cross section as the ion cluster. Z_{eff} is then a function of the separation between the fragments when the collective capture of a target electron occurs. Generally the calculation of

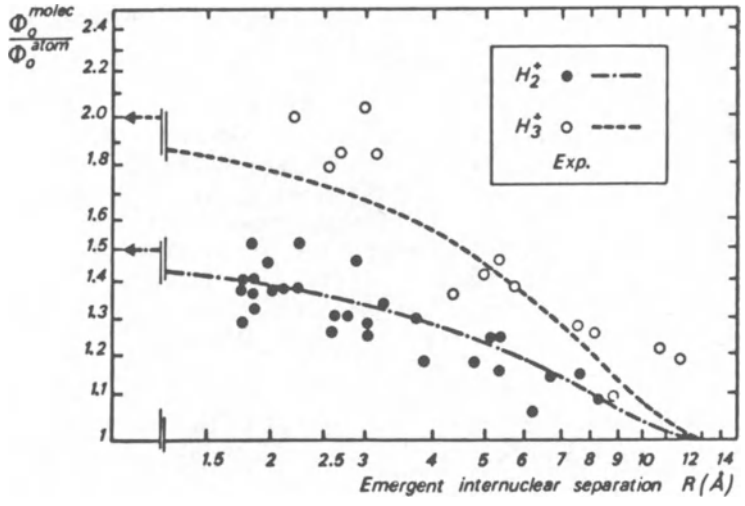

Fig. 5. Variation of the overproduction of neutral H atoms for H_2^+ and H_3^+ projectiles as a function of the mean internuclear separation in the proton clusters when they emerge from the foil (from Gaillard et al., Ref. 19).

Z_{eff} is difficult because one has to know the final state of the capture which can be any electronic state of the molecular ion in formation. Indeed a molecular orbital picture has to be used to describe the electronic state of atoms at so close a distance.

We calculated the capture cross section of a diproton cluster [24] by the Z_{eff} model, for that we used the work of Mc Caroll et al. [25] concerning the 1s σ_g and 2p σ_u final states of H_2^+. Then for each final state the capture cross section at velocity V and separation R was expressed as:

$$\sigma_c(R, V) = [Z_{eff}(R)]^5 \, \sigma_c^H(V),$$

where σ_c^H is the corresponding cross section for an isolated proton. We simply used here the Z^5 scaling which is well established for atomic projectiles. Although this method cannot be considered as a general theory for capture into molecular orbital states, it allows us to reduce the problem of the electron capture by many centers of charges to the case of a capture by a single charge. We applied this Z_{eff} model to the production of blue H_2^+ and H^o species and the results are in good quantitative agreements with our data.

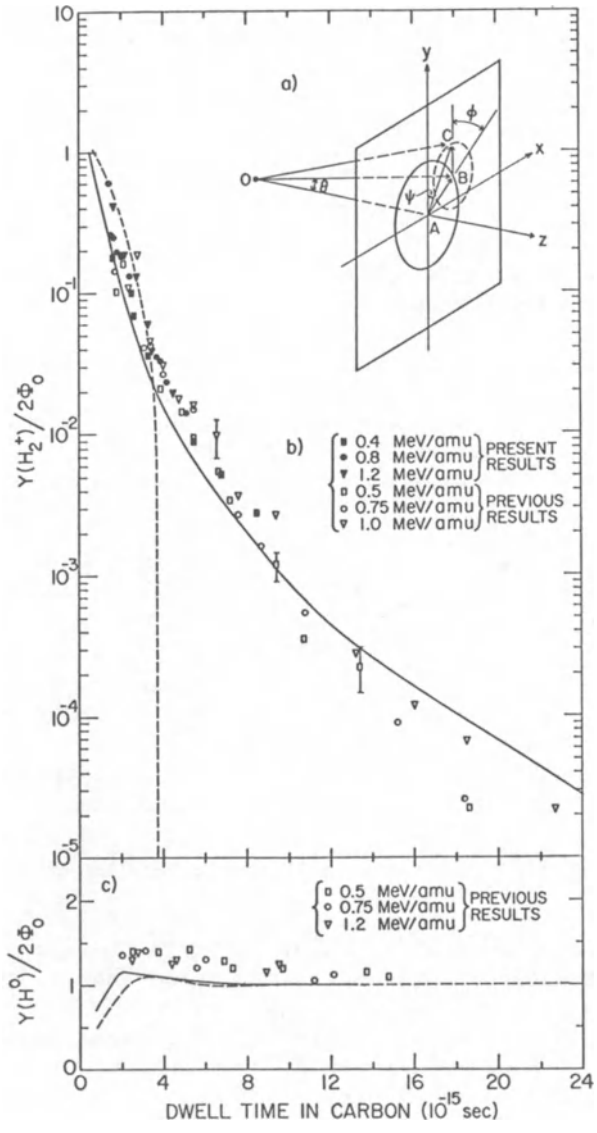

Fig. 6. (b) Measured yields of transmitted H_2^+ fraction $Y(H_2^+)$ through C foils in the blue regime, normalized to twice the equilibrium neutral fraction Φ_0 of protons of the corresponding velocities. (c) Yields of H^0 and H_2^+ break-up in C foils in the blue regime (from Cue et al., Ref. 24).

2. Total Energy of the Molecular System After a Capture Event

In the preceding discussion we assumed that the cross section for capturing an electron into a given diatomic molecular orbital state is only a function of the internuclear separation R of the fragments at the time of the capture event, whatever is their relative kinetic energy. One should notice at this point that there is now some experimental evidences that for a given R the capture cross section depends also on the respective angle θ between $\vec{R}$ and the beam direction. In Ref. 26 it is suggested that the capture probability reaches a maximum for $\theta = 90^{\circ}$. To our knowledge this anisotropy is not yet understood.

The fact that we assumed the non dependence of the capture cross section on the relative momentum of the fragments reflects the very short time scale which is associated with any electronic transition. But it is clear that the relative momentum of the fragments just before the capture event will determine the final state of the system at infinity.

Let us, for instance, discuss the case of a capture event into a 1s σ_g (H_2^+) molecular orbital. A given H_2^+ projectile, with internuclear separation R_o, which explodes inside the solid under wake and Coulomb forces will emerge from the foil as a pair of proton fragments with a relative kinetic energy ε_c and a separation R_e. A capture event into the 1s σ_g state will lead to the formation of a bound H_2^+ only when $\varepsilon_c < U(R_e)$, where $U(R_e)$ is the electronic binding energy of the H_2^+ ion at separation R_e. When this condition is not fulfilled the fragments at infinity constitute an ($H^+ + H^o$) pair.

3. Calculation of the Absolute Yield of Blue Atoms and Molecules

In order to calculate the absolute yield of reconstituted H atoms and H_2^+ molecular ions we first consider the distribution $D(R_o)$ of initial separation R_o in the incident H_2^+. We will not discuss this point since this distribution is studied in detail in the lecture of E. Kanter [2]. After assuming that the molecular break-up occurs at the front surface of the foil one can calculate the distribution of distances $D(R_e)$ and relative energies $D(\varepsilon_c)$ for the fragments when they emerge from the foil. The capture probability into 1s σg and 2p σ_u states is then calculated in the Z_{eff} approximation described above. Capture events into higher excited states have been neglected. Finally the binding criterion $\varepsilon_c < U(R_e)$ is applied to separate the H_2^+ channel from the (H^o + H^+) channel. Figure 6 shows that the calculated yields are in good agreement with the data over a wide range of dwell-times. The dotted line corresponds to a calculation where multiple-scattering effects are neglected inside the foil. It is clear in that case, as mentioned in Section I - 3, that multiple-scattering effects have

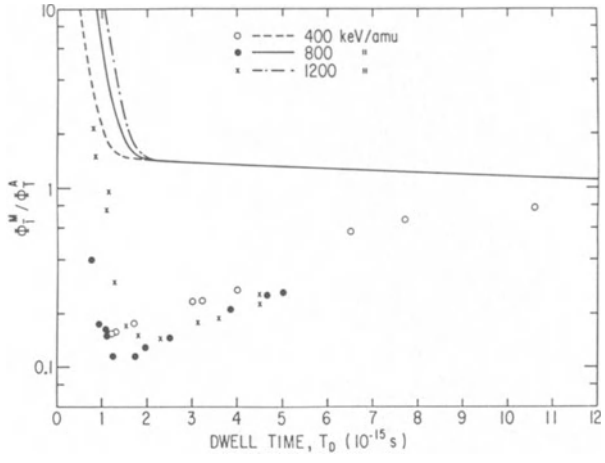

Fig. 7. Total yields of emergent H^- per proton $\Phi_{\bar{1}}^{M}$ from H_2^+ incident on C foils, normalized to the corresponding yields $\Phi_{\bar{1}}^{A}$ from incident H^+ of the same velocity displayed as a function of the dwell-time t_D in the target (from Cue et al., Ref. 27).

to be taken into account in molecular beam-foil experiments. It is remarkable to notice that blue molecules should not exist after 4 fs, whereas due to multiple-scattering they can be observed for dwell-times longer than 20 fs.

Transmission of molecular ions in the blue regime has now been observed with a number of simple molecular ions. Nevertheless most molecular ions have an unobservable transmission yield in the blue regime. That can be explained by many reasons: the capture cross section into molecular states can be too small, the criterion $\varepsilon_c < U(R_e)$ can be too severe, or the experimental conditions can be complicated by the presence in the beam of isotopes which have the same mass and charge as the expected molecular ion.

4. Long Range Charge Exchange Effects between Separating Fragments

In some cases the knowledge of the electronic state and of the internal kinetic energy of a blue cluster at emergence from a foil is not sufficient to predict the electronic state of the fragments at infinity. That is the case of a study we did in Lyon [27] of the production of H^- ions in the foil break-up of fast H_2^+. We observed that, in opposition with the production of H^0 atoms discussed before, the production of H^- ions is over a wide range of dwell-times lower with H_2^+ projectiles than with H^+ projectiles of the same velocity.

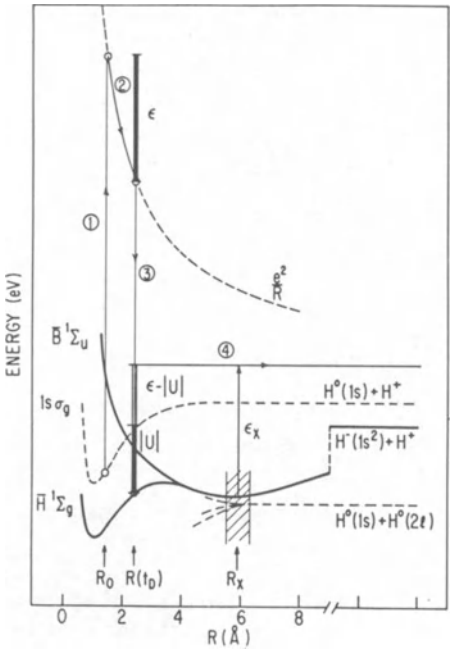

Fig. 8. Schematic diagram for the various molecular orbitals relevant to the inhibition mechanisms of H^- (from Cue et al., Ref. 27).

Figure 7 shows the data and the predictions of the model discussed in the preceding section when one considers only the molecular orbitals of H_2 which correlate with an (H^- + H^+) final state.

It was recognized that the observed H^- inhibition could be due to the pseudo-crossing of molecular orbitals which occur far away from the foil, when the fragments are a few Å apart. Figure 8 shows the H_2 molecular orbitals relevant with the charge exchange effect occurring at the pseudo-crossing point R_X. A detailed calculation of the crossing probability was performed by using the Landau-Zener model. The results of the calculation are that the observed inhibition can be quantitatively attributed to this effect. Inhibited H^- yields have subsequently been observed with other projectiles such as H_3^+ and HeH^+. We believe that the study of charge exchange effects between distant atoms can be examined in great detail in molecular beam-foil experiments, because the fragments separate gently in the cluster frame from a well defined initial state which is prepared by the foil interaction, to infinity where the fragments are detected.

Conclusions

We have described some aspects of the penetration of fast molecular ions in a solid target which can be useful to extract molecular structures from beam-foil experiments. The future developments of the method depend largely on a deeper understanding of the basic processes involved in the interaction of a fast ion cluster with a solid medium.

This Advanced Study Institute stimulated contacts between chemists and physicists who use a very large variety of techniques to observe the same objects, namely molecular ions, but wo do not use the same language and obviously do not read the same scientific Journals.

The author is indebted to Dr. J. C. Poizat for his critical remarks on the manuscript.

References

1. K. O. Groeneveld, These Proceedings.
2. E. Kanter, These Proceedings.
3. M. J. Gaillard, D. S. Gemmell, G. Goldring, I. Levine, W. J. Pietsch, J. C. Poizat, A. J. Ratkowski, J. Remillieux, Z. Vager, and B. J. Zabranski, Phys. Rev., A 17, 1797 (1978).
4. D. S. Gemmell, J. Remillieux, J. C. Poizat, M. J. Gaillard, R. E. Holland, and Z. Vager, Phys. Rev. Lett., 34, 1420 (1975).
5. V. N. Neelavathi and R. H. Ritchie, in: "Atomic Collisions in Solids," Plenum, New York (1975), p. 289.
6. For a discussion of wake effects in other fields, see for example, J. Remillieux, Nucl. Instr. and Methods, 170, 31 (1980).
7. M. H. Day, Phys. Rev., B 12, 514 (1976).
8. R. H. Ritchie, W. Brandt, and P. M. Echenique, Phys. Rev., B 14, 4808 (1976).
9. Z. Vager and D. S. Gemmell, Phys. Rev. Lett., 37, 1352 (1976).
10. M. Kitagawa and Y. H. Ohtsuki, Phys. Rev., B 16, 5321 (1977).
11. W. Schafer, H. Stocker, B. Muller, and W. Greiner, Z. Phys., A 288, 349 (1978).
12. P. M. Echenique, R. H. Ritchie, and W. Brandt, Phys. Rev., B 20, 2567 (1979).
13. N. Cue, M. J. Gaillard, J. C. Poizat, J. Remillieux, and J. L. Subtil, Phys. Rev. Lett., 42, 959 (1979).
14. A. Breskin, A. Faibis, G. Goldring, M. Hass, R. Kaim, Z. Vager, and N. Zwang, Nucl. Instr. and Methods, 170, 93 (1980).
15. A. Faibis, R. Kaim, I. Plesser, and Z. Vager, Nucl. Instr. and Methods, 170, 99 (1980).
16. W. Brandt and R. Ritchie, Nucl. Instr. and Methods, 132, 43 (1976).

17. See for example: W. Brandt, A. Ratkowski, and R. H. Ritchie, Phys. Rev. Lett., 33, 1329 (1974); J. W. Tape, W. M. Gibson, J. Remillieux, R. Laubert, and H. Wegner, Nucl. Instr. and Methods, 132, 75 (1976).
18. W. H. Escowitz, T. R. Fox, and R. Levi-Setti, IEEE Trans. Nucl. Sci., 26, 1395 (1979).
19. M.J. Gaillard, J. C. Poizat, A. Ratkowski, J. Remillieux, and M. Auzas, Phys. Rev., A 16, 2323 (1977).
20. J. C. Poizat and J. Remillieux, Phys. Lett., 34 A, 53 (1971).
21. N. Cue, N. V. de Castro-Faria, M. J. Gaillard, J. C. Poizat, and J. Remillieux, Nucl. Instr. and Methods, 170, 67 (1980).
22. M. J. Gaillard, J. C. Poizat, and J. Remillieux, Phys. Rev. Lett., 41, 159 (1978).
23. B. T. Meggitt, K. G. Harrisson, and M. W. Lucas, J. Phys., B 6, L 362 (1973).
24. N. Cue, N. V. de Castro-Faria, M. J. Gaillard, J. C. Poizat, J. Remillieux, D. S. Gemmell, and I. Plesser, Phys. Rev. Lett., 45, 613 (1980).
25. R. Mac Carroll, R. D. Piacentini, and A. Salin, J. Phys., B 3, 137 (1970).
26. P. J. Cooney, D. S. Gemmell, E. P. Kanter, W. J. Pietsch, and B. J. Zabranski, Nucl. Instr. and Methods, 170, 73 (1980).
27. N. Cue, N. V. de Castro-Faria, M. J. Gaillard, J. C. Poizat, and J. Remillieux, Phys. Rev., A 22, 388 (1980).

THE ROLE OF EXCITED STATES OF MOLECULAR IONS IN STRUCTURE STUDIES WITH HIGH ENERGY COLLISIONS

E. P. Kanter

Argonne National Laboratory

Argonne, IL 60439

I. Introduction

As a result of the efforts of several experimental groups, a very large amount of data has been accumulated in studies of the interactions of energetic (several MeV) molecular-ion beams with solid and gaseous targets [1, 2]. A fairly detailed (though by no means complete) picture of these interactions is now evolving. We have reached the point of sophistication where it is apparent that one of the crucial factors in successfully interpreting the available data is an equally detailed knowledge of the geometric structures of the incident molecular-ions [3]. More importantly, if experimental conditions are properly controlled, these data can be used to determine uniquely such structures with a fair degree of accuracy [4]. Though the accuracy achievable in these measurements is not as high as through standard photon emission or absorption techniques, they do provide an important starting point for the usually more difficult photon measurements. In this presentation, we will describe the use of such "Coulomb explosion" measurements to gain important structural information about various molecular ions.

To begin, let us first review some of the basic details of "Coulomb explosions."

II. High Velocity "Coulomb Explosions"

The collision-induced dissociation of molecular ions has been extensively studied with gaseous targets and with ion-beam energies in the keV range (for a recent review, see Ref. 5). In this field, the term "high energy" has come to mean beam energies of a few tens

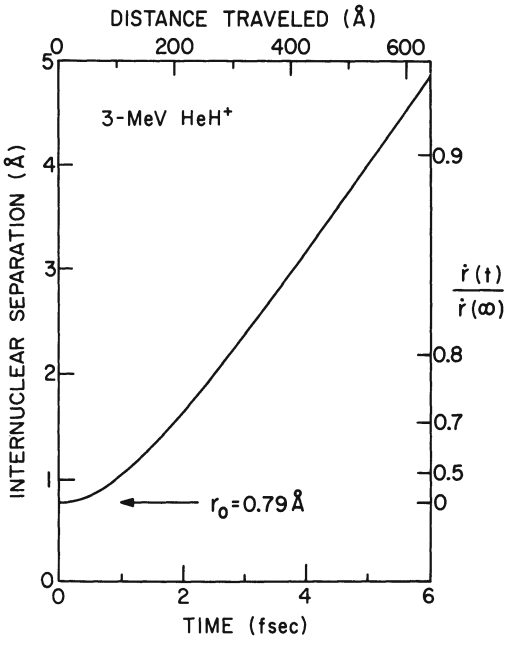

Fig. 1. The dependence upon time of the internuclear separation between the α-particle and the proton of a HeH^+ ion whose internuclear separation at t = 0 is 0.79 Å. The nuclei are assumed to be stationary at t = 0 in the projectile rest frame. The right-hand ordinate gives the fractional growth of the Coulomb-explosion velocity as a function of time. The scale at the top shows the distance travelled in the LAB frame by the projectile assuming the beam energy to be 3 MeV.

of keV. There are however some definite advantages in extending such studies to ion velocities an order of magnitude higher — i.e., beam energies in the MeV range. For light projectiles at these energies, the time for a typical collision with a target atom is short enough ($\sim 10^{-17}$ sec) compared with the times for molecular vibration ($\sim 10^{-14}$ sec) and rotation ($\sim 10^{-12}$ sec) that during the collision the nuclei of an incident molecular ion may be considered to be stationary in the projectile frame. Furthermore, the collision time is short compared with the characteristic times for the possible dissociation modes. As is shown in Fig. 1, these times extend down to about a femtosecond (10^{-15} sec) for those dissociations that arise from "Coulomb explosions" (i.e., the rapid flying apart of the nuclear constituents of a molecular projectile when all or most of its electrons are stripped away in a collision). Thus for high projectile velocities ($V_0 \gg e^2/\hbar$) it can be expected that, to an excellent approximation, collision-induced dissociation may be treated

as a two-step process. First there occurs a rapid collision with a target atom during which the projectile's nuclei do not move in their center-of-mass (COM) frame. Because of their low mass the electrons associated with the projectile reconfigure themselves in a time comparable with the collision time (this process includes the possibility of removal by ionization of some or all of the electrons). There then follows, on a much longer time scale, a dissociation of the resultant excited molecular state into two or more atomic or molecular fragments. At these projectile velocities, excitation mechanisms other than electronic excitation (e.g., rotational/vibrational excitation due to large momentum transfer to one of the projectile nuclei) can be expected to play relatively minor roles [6].

There are several other approximations that acquire improved validity at MeV bombarding energies. For example, energy losses (typically a few eV) due to inelastic collision processes may be neglected. Deflection of the projectile's COM during the collision may be neglected. A Born-approximation treatment of the collision is expected to be more fully justified at high projectile velocities. (For detailed discussions concerning these and other approximations, see Refs. 7 and 8 and references contained therein.)

As a result of the preceding considerations, we anticipate that electronic, or ro-vibrational excitations in the beam will only affect our observations as changes in the geometry of the initial molecule. For a diatomic molecule, this will be reflected in the distribution of internuclear separations $D(r_o)$. We shall be observing the breakup of an ensemble of molecules, each of which enters our target with a unique geometry. We shall return to this point later.

The main difficulty in studying collision-induced dissociation at MeV energies is the technical one of obtaining adequate angular resolution. The fragments emerging from a collision are contained within narrow cones centered on the beam direction. The angular widths of these cones are approximately inversely proportional to the projectile velocity. At MeV energies the width of such a cone is typically a few milliradians and thus an overall angular resolution of $\sim 10^{-4}$ radians is usually required. In the work described here, an angular resolution of 3×10^{-4} radians was employed. A corresponding resolution in measuring the momenta of the collision fragments is also needed, but in practice that is not as difficult to achieve. The relative momentum resolution used in this work was also 3×10^{-4} (a relative energy resolution of 6×10^{-4}).

A significant advantage in using MeV bombarding energies lies in the fact that the measurements can be readily extended to include thin solid targets. At keV energies, use of even the thinnest and lightest foils (e.g., $\sim$100-Å thick carbon) introduces a serious worsening in resolution because of energy-loss straggling and multi-

ple scattering. Of these, the effects of multiple scattering are the most crippling. However, as the projectile velocity V_0 is raised, there is a decline not only in the absolute values of the multiple scattering angles (which may vary as V_0^{-2}) but also in the values relative to the fragments' cone angles (which vary as V_0^{-1}). As an example, the full width at half maximum (FWHM) of the multiple scattering distribution for 1-MeV protons traversing a 100-Å thick carbon foil is 7×10^{-4} radians, while the average energy loss of these protons is ∿500 eV and the straggling width is only a few tens of eV.

For light projectiles (H_2^+, HeH^+, He_2^+, etc.) incident at these energies upon a foil, the electrons that bind the projectile are almost always totally stripped off within the first few Ångstroms of penetration into the solid target. This is a consequence of the large cross sections (∿10^{-16} cm^2) for electron loss [9] and of the fact that close collisions with target electrons cannot be avoided in a solid. There then follows a "Coulomb explosion" in which the bare (or nearly bare) nuclei of the projectile fly apart by virtue of their mutual Coulomb repulsion. The characteristic time for this explosion is typically ∿10^{-15} sec which is on the same order as the dwell time of the projectile in the foil if the latter is about 100 Å thick. It is therefore to be expected that much of the Coulomb explosion takes place inside the foil and that it then runs to completion in the vacuum downstream after the fragments emerge from the target. Inside the target the individual fragments' trajectories are also influenced by multiple scattering and by effects due to the electron polarization "wakes" induced behind each of the fragments traversing the foil. These wake effects have been shown [10, 11] to give rise to easily observable modifications to the pattern of trajectories measured downstream from the target.

For dilute gaseous targets, on the other hand, it has been found that many collisions are much less violent than those in foil targets [3]. On the average, fewer electrons are removed from the projectile and correspondingly, one finds a greater probability for dissociation into less highly charged, though electronically excited fragments. There are no observable effects due to wakes or to multiple scattering.

III. A Simple Model

After the Coulomb explosion has run to completion, the excess kinetic energy released by the explosion produces sizeable energy and angle shifts which are easily measured in the laboratory distributions of dissociation fragments observed downstream of the target.

Consider the case of a dissociative fragment which in the rest frame of the projectile molecule acquires a velocity $\vec{u}$ oriented at

an angle ϕ relative to the projectile velocity V_o. In the laboratory, this fragment will be observed at an angle

$$\theta = \frac{u \sin\phi}{V_o} = \frac{u_\perp}{V_o} \tag{1}$$

relative to the beam direction. Likewise, there will also be a shift in lab energy of this particle given by:

$$\Delta E = \frac{1}{2} m (\vec{V}_o + \vec{u})^2 - \frac{1}{2} m V_o^2 \cong m\vec{V}_o \cdot \vec{u} = m V_o u \cos\phi = m V_o u_\parallel \tag{2}$$

The approximation in Eq. (2) amounts to ignoring terms of relative magnitude $\sim u/V_o$ (typically $u/V_o \approx 5 \times 10^{-3}$ for the cases we will be treating).

If we consider only those fragments which acquire a given velocity u_o in the projectile rest frame, then we see that there is a maximum laboratory $\theta_{max} = u_o/V$ such that no fragments are observed beyond this angle. For $\theta < \theta_{max}$, there are two groups of these fragments: one shifted up in energy and the other with an equal downward energy shift. At $\theta = \theta_{max}$, ($\phi = 90°$), these two groups coalesce into a single energy corresponding to the beam velocity. The other extreme orientation ($\phi = 0°$ or $180°$) is observed at $\theta = 0$. These fragments suffer no angular shift; however, they are observed with the maximal energy shifts $\Delta E_{max} = \pm m V_o u_o$.

To get a feel for magnitudes, let us concentrate on a very simplified model for the explosion of 3 MeV HeH^+ ions, each molecule having a fixed initial internuclear separation $r_o = 0.79$ Å. If such an ion is instantaneously stripped of its electrons to leave a bare α-particle-proton pair, then as the Coulomb explosion develops, the Coulomb energy $\varepsilon = 2e^2/r_o = 36.5$ eV will be converted into kinetic energy in the center of mass. Since this Coulomb energy ε is so much larger than the fragment energies due to vibration or rotation we may neglect any fragment COM motion prior to stripping.

Under these conditions, the separating fragments would asymptotically achieve a final relative recession velocity of 0.94 Å/fsec (for comparison, the beam velocity is 108 Å/fsec). The resulting shifts for the protons are $\Delta E_{max} = 8.4$ keV and $\Delta\theta_{max} = 7.0$ mrad (0.40°). The corresponding energy shift for the α-particles is the same while the angular shift is reduced a factor of 4. As a result of the amplification caused by the large beam velocity, the eV c.m. energy is observed as a large and easily measurable keV shift in the lab frame.

IV. Refinements

This model is of course an oversimplification of the problem and requires further refinements for rigorous interpretations of the experimental data. As was detailed in the preceding paper of Remillieux [12], the effects of multiple scattering, energy loss and energy straggling, electron polarization wakes, and charge exchange each to varying extents, modify the outgoing velocities of the explosion fragments when solid targets are used to initiate the Coulomb explosion.

The treatment of energy loss and straggling is usually straightforward. Energy loss produces a small energy decrease for all particles. For 600-keV protons traversing 100 Å of carbon, the energy loss is 0.7 keV. Because the energy loss process is statistical, there is a finite width to the loss distribution which in this case would be only a few tens of eV. This is usually referred to as the energy straggling width.

For slowly moving ions, the influence of screening by target electrons could be important. If we treat the target as a sea of free electrons, then the internuclear potential while in the target can be approximated by an exponentially screened Coulomb potential with a screening length given by

$$a = V_o/\omega_p \tag{3}$$

where ω_p is the plasma frequency for the contributing target electrons. For carbon, $\hbar\omega_p$ = 25.9 eV. Hence for our 600 keV/amu particles a≃3 Å. This is much larger than the internuclear separations of the ions while in the target and so we may neglect the spatial dependence of the screening, though we recognize that the nuclear charges will be characterized by an effective charge $Z_{eff} \lesssim Z$. As the ion velocity decreases, so does the screening length. Thus for 1-MeV carbon ions we find a = 1.0 Å, comparable to the bond lengths of the molecular ions we will be considering. Hence screening must be dealt with more rigorously at low velocities. We thus desire a high velocity and short dwell time in the target.

For heavy ionic fragments, charge exchange processes in the target are also important. Because of the large cross sections involved, capture and loss of electrons take place very rapidly ($\sim 10^{-17}$ sec) in the target and thus combine to produce a well-defined mean effective charge which governs large impact parameter processes. In particular both the electronic stopping power and the Coulomb explosion should be determined by the same Z_{eff}. At high velocities, ($V_o^2 > e^4/\hbar^2 \sim 25$ keV/amu) the effective charge for an ion can be determined by:

$$Z_{eff} = \sqrt{S/S_p} \tag{4}$$

where S is the electronic stopping power of the foil for the ion and S_p the corresponding quantity for a proton of the same velocity [13]. Once outside the foil the ionic fragments adopt integral charge states which appear to be independent of the history of the ion in the solid [14].

The subject of electron polarization wakes remains an open and very interesting subject despite a long history dating back to Bohr's 1948 paper [9]. The wake represents the response of target electrons to the presence of a moving charged particle. The resulting oscillations in charge density along the path of the ion yields an oscillating electric potential stationary in the rest frame of the ion. For a single ion, the spatial derivative of this potential at the site of the ion is simply the electronic stopping power of the medium. For a molecular ion, the wakes of the individual exploding fragment ions must be superimposed to find the net potential. In addition to the longitudinal stopping forces, the superposition of wakes can also produce orientation-dependent radial forces which tend to rotate the molecule. For diatomic molecules, this is observed as a tendency for trailing fragments to align more closely behind their leading partners. For light ions, this effect is fairly well described by a model proposed by Vager and Gemmell [11]. A more general description seems to be required to explain some subtler effects seen with heavy ions and there is still a considerable amount of work to do in this area [14, 15].

The remaining problem of multiple scattering can be quite serious in that it is relatively large and it can determine the effective overall angular resolution. One tries to minimize the effect by utilizing thin target foils of low atomic number and high velocity ions (multiple scattering widths vary as the square root of target thickness over the square of velocity). For our 3 MeV HeH^+ example the proton multiple scattering width in 100 Å of carbon would be about 0.6 mrad, nearly 10% of the angular shift produced by Coulomb explosion.

Insofar as each of these effects can be accounted for by calculation, the remaining question of incident-ion geometry dominates the velocity profiles for Coulomb explosions from solid targets. This is quite fortunate for us since molecular-ion structure is the subject of this conference. Before we look at this question, however, let's first discuss the complementary measurements of Coulomb explosions in gaseous targets.

V. Gas Targets

In studying Coulomb explosions of molecular ions initated by collisions in gas, one avoids many of the complicating effects discussed above for solid targets. The resulting explosions are dramatically different and are determined not only by the structure of

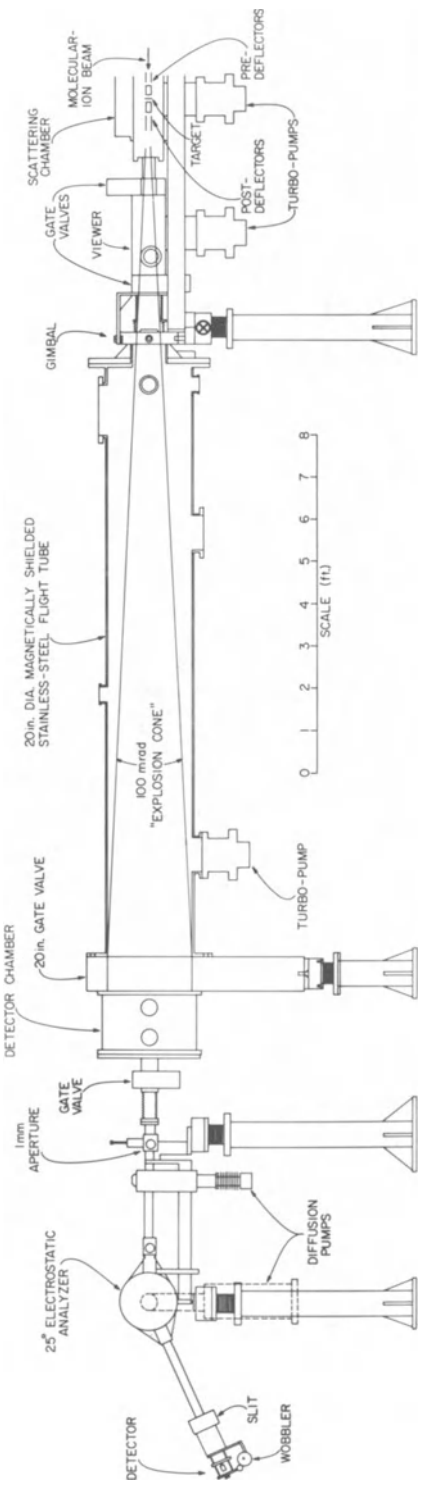

Fig. 2. Schematic diagram of the experimental arrangement at Argonne's 4-MV Dynamitron accelerator.

the incident ion (which is usually in the ground electronic state) but also by the structures of electronically excited states formed during the collision in the target.

We have seen that for foil-induced dissociations, well-defined Coulombic potentials determine the explosion characteristics. When dilute gas targets are used, one finds that to a considerable degree, large impact parameter collision processes dominate the excitation process and a much lower probability for multi-electron ionization results. Instead, one promotes electrons to dissociative states which can produce charged as well as neutral fragments. The ensuing fragment velocity distributions result not so much from a Coulomb explosion as from a fizzle. These distributions are sensitive to the shapes of the appropriate screened potentials for these excited states [3].

The explosion data with gas and solid targets are in a sense complementary. The solid target data probes the structure of the ensemble of incident ions, while the gas data gives information about excited state structures.

VI. Apparatus for High-Resolution Measurements

To carry out high-resolution measurements of Coulomb explosion fragments at MeV energies, experimental resolution widths at least an order of magnitude smaller than the energy and angle shifts are desirable. A system which was designed to achieve such resolution has been used at Argonne for several years and is extensively described in previous publications (Refs. 1, 3, 16-19). Figures 2 and 3 show the current experimental arrangement.

Molecular-ion beams are produced in either a duoplasmatron or an rf ion source and then accelerated by the Argonne 4-MV dynamitron accelerator. After being magnetically analyzed, the ion beams are collimated to have a maximum angular divergence of ±0.09 mrad and a 1-mm spot size at the position of the target. A set of "pre-deflector" plates permits electrostatic deflection of the beam incident on the target. A similar set of "post-deflectors" is used to deflect charged dissociation fragments emerging from the target. The pre- and post-deflectors are used in combination so as to avoid the detection of particles arising from spurious incident beams (e.g., fragments arising from collisional dissociation of the primary beam along the long flight path through residual gas between the beam collimators).

A 25° electrostatic analyzer, having a relative energy resolution of 6×10^{-4} (FWHM), is located several meters downstream from the target. An aperture placed ahead of the analyzer accepts a 1-mm diameter group of fragment trajectories originating at the target position. The entrance axis of the analyzer is offset 2 mrad from

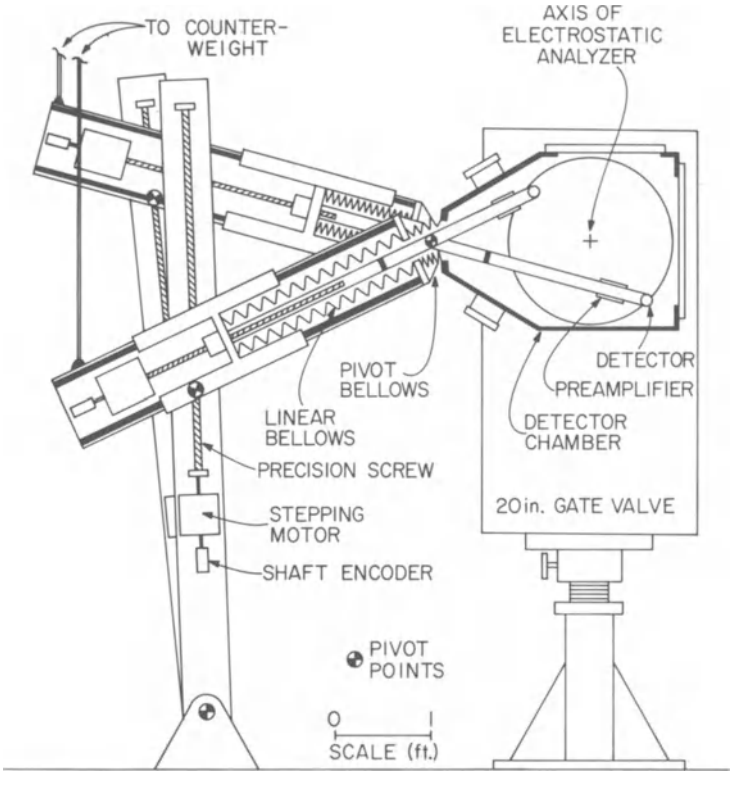

Fig. 3. Schematic diagram showing a cross-sectional view of the detector chamber and movable detector systems at Argonne's 4-MV Dyanmitron accelerator.

the direction defined by the collimators for the incident beam. This offset eliminates interference of neutral beam contaminants and permits certain classes of measurements on neutral fragments. [Neutrals are detected by applying a high field across the horizontal, or "X" post-deflectors to remove charged fragments and then by stripping the neutrals at the analyzer entrance aperture using a thin (~100 Å) carbon foil insertable for that purpose.]

Distributions in energy and angle are made for particles emerging from the target by varying the voltages on the horizontal predeflectors and/or the post-deflectors in conjunction with that on the electrostatic analyzer. (The vertical, or "Y" deflectors are normally used only for "trimming" purposes.) The overall angular resolution is 0.30 mrad (FWHM).

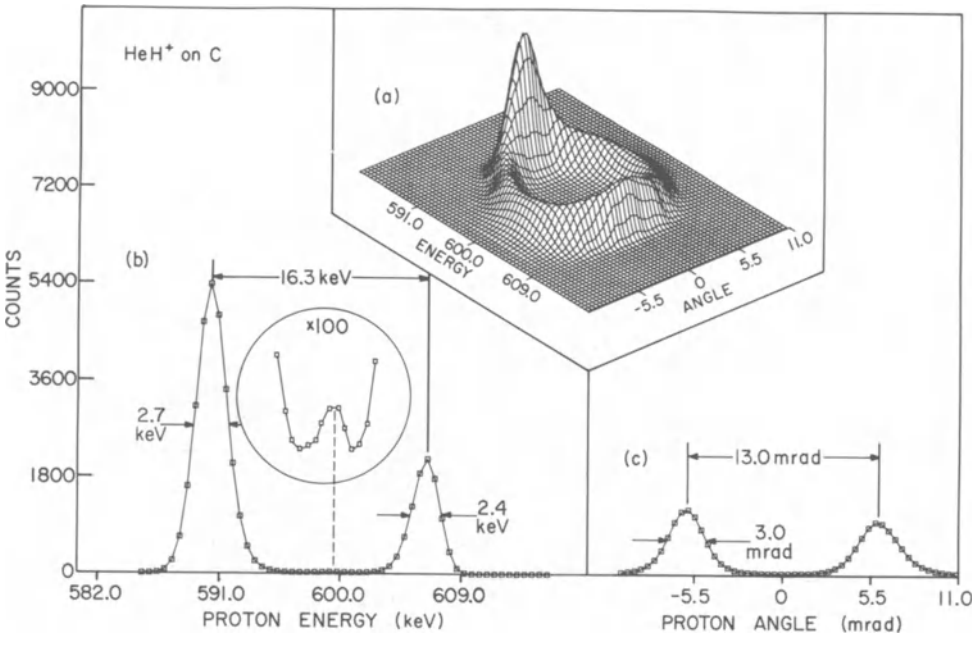

Fig. 4. (a) "Ring pattern" and (b), (c) "cross" for protons from 3.0-MeV HeH^+ dissociating in a 195-Å thick carbon foil.

The 20" diameter flight tube (Fig. 2) and associated detector chamber (Fig. 3) were recently added to permit the coincident detection of multiple dissociation fragments. The chamber houses two movable detectors which can be independently positioned to an accuracy of ∿0.001 in. anywhere on a 20-in. diameter circular plane (perpendicular to the beam direction) subtending an angle of ±50 mrad at the target.

With our apparatus resolutions quoted above, we are able to measure the center of mass velocities $u_\perp$ and $u_\parallel$ with equal accuracy

$$(\delta u_\perp = \delta u_\parallel = \pm 1.5 \times 10^{-4}\ V_o).$$

Most of our data on fragments arising from molecular-ion dissociation take the form of measurements of a complete "ring pattern" [a complete joint angle-energy distribution] or of a "cross" [i.e., an energy distribution for zero angular shift together with an angular distribution for zero energy shift].

VII. Measurements for Diatomic Projectiles

a. Dissociation in Solids

Figure 4 shows a typical joint energy-angle distribution measured for protons from 3 MeV HeH^+ incident upon a 195-Å thick carbon foil [3]. The most obvious feature to be noted in this distribution is that it is a "ring pattern" as is to be exected on the basis of the simple Coulomb explosion picture of the dissociation process. The diameter of the ring is determined primarily by the bond length in the projectile. The width of the "rim" of the ring reflects the range of internuclear distances present in the projectiles as they enter the target. Wake effects manifest themselves through slight distortions of the ring. The ring is thereby stretched along the energy axis and contracted along the angle axis. The stretching along the energy axis is actually the result of two effects — a contraction of the energy shift on the high-energy side coupled with a (larger) stretching of the energy shift on the low-energy side. This asymmetry along the energy axis is further accentuated by the pronounced increase in proton intensity on the low-energy side of the ring as compared with the smaller increase on the high-energy side. For more detailed discussions of all of these effects the reader is referred to the other work noted above. In particular, the influence of wake effects is treated more fully in Ref. 11.

Most of our data on the fragments arising from molecular-ion dissociation take the form of measurements either of a complete "ring pattern" or of a "cross" [i.e., an energy distribution for zero angular shift together with an angular distribution for zero energy shift (allowing for the usually trivially small energy loss due to the stopping power of the target)]. A "cross" thus represents the two distributions obtained by cuts along the energy and angle axes of the ring pattern. In Fig. 4 we show both a "ring" and a "cross." The central peak in Fig. 4 arises from the dissociations in the target producing He° and a proton. It is discussed in detail in Ref. 3.

By choosing beam energies and target thicknesses to minimize simultaneously the influence of both non-equilibrium charge state effects and multiple scattering, such data can be used to determine the initial distribution of internuclear separations, $D(r_o)$, for light diatomic beams such as H_2^+ and HeH^+. Calculations on the influence of wake forces have shown that they modify the Coulomb explosion least when the projectile's internuclear vector is perpendicular to the beam direction. This can be seen clearly in Fig. 5 which shows the wake potential derived by Vager and Gemmell [11]. Because this potential is the effect of a line of charge following the moving ion, it falls off rapidly in the direction transverse to the beam velocity. Other wake models display quite similar behavior in this respect [15]. For 3 MeV H_2^+ for instance, incident upon a 160 Å carbon foil, these calculations show that the spacings and

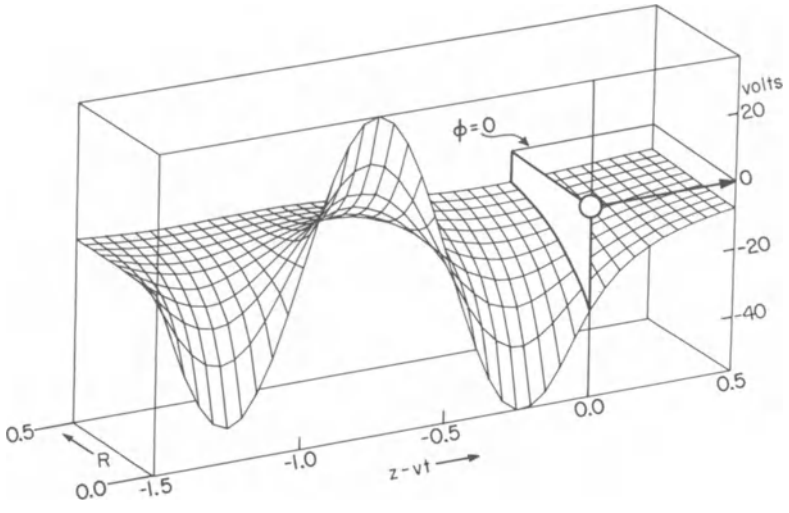

Fig. 5. Potential distribution associated with the polarization wake of a 400-keV proton traversing carbon ($\hbar\omega_{p_o}$ = 25.0 eV). Distances are shown in units of $\lambda = 2\pi a$ = 14.5 Å (from Ref. 11).

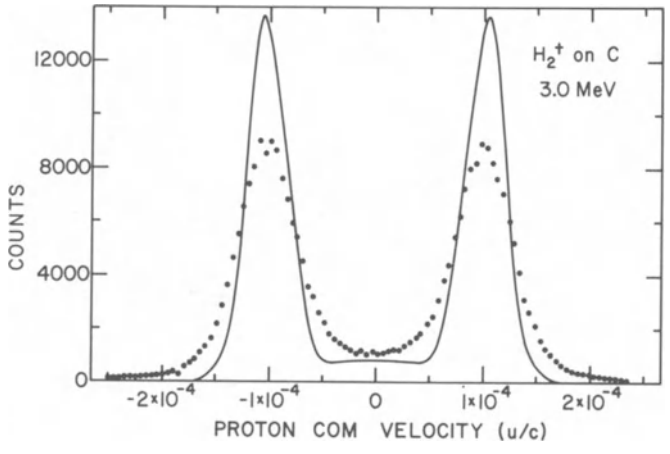

Fig. 6. Velocity spectrum for outgoing H^+ from the dissociation of 3.0-MeV H_2^+ in a 172-Å thick carbon foil. The points are the data, transformed to center-of-mass velocity from a lab angular distribution at zero energy shift. The solid curve results from the deconvolution of multiple scattering from these data, as discussed in Ref. 3.

peak widths in the angular part of a "cross" are modified by less than 0.5% by wake forces. By concentrating on these angular distributions at zero energy shift, we therefore avoid the complication of wake effects.

In order to extract a $D(r_o)$ distribution from an angular distribution one needs to deconvolute the non-negligible effects of multiple scattering and (to a lesser extent) of the experimental angular resolution. The deconvolution procedure that we have used for this has been described in Ref. 3. Figure 6 shows the result of this unfolding procedure for the case of an H_2^+ beam (the abscissa in Fig. 6 has been converted from an angle scale to a COM velocity scale). Because the functional form used for the multiple scattering distribution has a long tail, there is a region corresponding to high COM velocities (near the extreme wings of the data) where the deconvolution is not valid. This translates into a cutoff at small internuclear separations (at about r = 0.5 Å) in the derived distribution $D(r_o)$.

In our analysis, we assume that in a dissociative collision the molecular projectile makes a sudden electronic rearrangement while its nuclear constituents remain unperturbed. That is, we consider the projectile as undergoing a sudden vertical transition up to some excited electronic state which then dissociates liberating a total COM kinetic energy of $U(r_o)-U(\infty)$, where U(r) is the potential energy at an internuclear separation r for the particular final electronic state involved. The relation

$$u = (1/m_f)\ \{2\mu[U(r_o)-U(\infty)]\}^{1/2}, \tag{5}$$

where μ is the reduced mass of the projectile and m_f the fragment mass, then serves as a mapping function relating the COM velocity of a fragment to the potential and to the initial internuclear separation. For the case of solid targets, U(r) is assumed to be a simple Coulomb potential.

If we further assume that the cross section for the electronic excitation is independent of the spatial orientation of the projectile and also independent of its internuclear spacing, then we can readily derive the relationship between the distribution functions for u and r_o.

$$G(u) = (4\pi u^2)^{-1}\ D(r_o)dr_o/du, \tag{6}$$

where u and r_o are related via Eq. (5) and the distribution functions are normalized by

$$\int_0^\infty D(r)dr = 1, \tag{7}$$

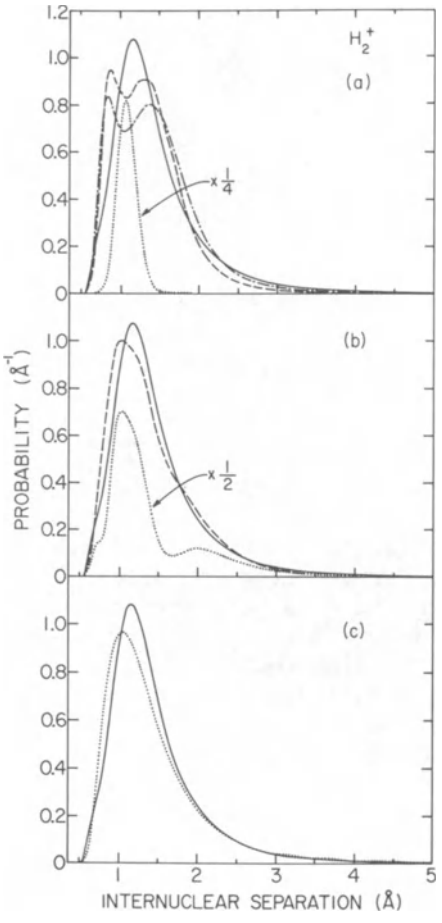

Fig. 7. Radial distribution functions for incident 3.0-MeV H_2^+ ions. The solid curve in (a), (b), and (c) is obtained from the deconvoluted angular distribution given in Fig. 6. In (a), the dashed curve is the radial distribution based on the vibrational state distribution derived by von Busch and Dunn [20] from the ionization of the ground-vibrational state of H_2; the chained curve is a similar result based on Itikawa's calculations [21]; the dotted curve is the distribution for the ground-vibrational state of H_2^+ only. In (b), the dotted curve is the radial distribution resulting from ionization of the first excited-vibrational state in H_2, as calculated by von Busch and Dunn, while the dashed curve represents a best fit to our data using a linear combination of the distributions expected from the ionization of the two lowest-lying vibrational states of H_2. The dotted curve in (c) is a best fit to our data using a linear combination of all 19 vibrational states of the ground-electronic state of H_2^+.

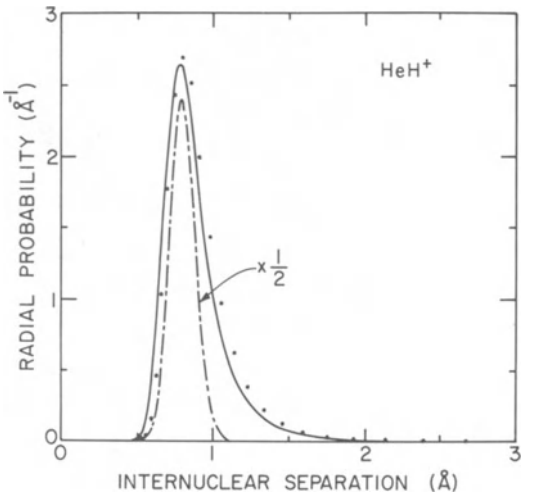

Fig. 8. Radial distribution for incident 3.63-MeV HeH^+ ions. The points are derived from the data. The solid curve is the best fit to the data, obtained by adjusting the fractional contribution of each of the nine lowest-lying vibrational levels of the electronic ground state. The chained curve is the distribution for the ground-vibrational state only.

and

$$4\pi \int_0^\infty G(u)u^2du = 1. \tag{8}$$

Another way of viewing Eq. (6) is simply to note that for fragments whose COM velocities are greater than the limits imposed by our resolution, the contribution of a given r-value to our measured distributions is spread out over the phase space $4\pi u^2du$. For a detailed discussion of the validity and limitations of the reflection method see Ref. 7.

In this manner, and using a pure Coulomb potential in Eq. (5), we have derived the distributions shown in Figs. 7 and 8 for $D(r_o)$ in H_2^+ and HeH^+, respectively. Also shown in each figure is the calculated distribution for the ground vibrational and electronic state. For H_2^+, where it was thought to be reasonable to assume that the molecular ion is formed by direct ionization of H_2 we show additional distributions $D(r_o)$. These were calculated on the basis of H_2^+ vibrational populations given by (1) the (approximate) Franck-Condon factors of Von Busch and Dunn [20], (2) the parameters of Itikawa [21] (these are parameters used in a computation that gives excellent agreement with the observed [22] photoelectron intensities

from H_2) and (3) a mixture of H_2^+ level populations obtained assuming the initial H_2 to be 58% in the ground state and 42% in the first excited vibrational state.

The derived distributions $D(r_0)$ show the most probable values of r_0 to be 1.17 Å for H_2^+ and 0.80 Å for HeH^+. These may be compared with values of 1.08 Å and 0.79 Å obtained for the ground states alone in H_2^+ and HeH^+, respectively. For HeH^+ the derived $D(r_0)$ is about 1.5 times wider than expected from the ground state alone. This fact, together with the small overall shift of the distribution towards higher r values, indicates that most of the HeH^+ ions are incident in the ground vibrational state with a relatively small fraction in the first one or two vibrationally excited states. For H_2^+ on the other hand, excited vibrational levels are clearly much more involved, although the population of these levels is significantly lower than has been assumed by other authors [23, 24] in analyzing Coulomb explosion experiments. This difference between the results for HeH^+ and H_2^+ is not very surprising in view of the very different formation process involved. Since neutral HeH is not stable, HeH^+ is formed by ion-molecule reactions rather than direct ionization.

We believe that the factors most likely responsible for the deviation of our derived $D(r_0)$ for H_2^+ from a Franck-Condon-like distribution [20] are firstly, the fact that in the ion source the initial H_2 is not always in its ground state and secondly, the higher vibrational states of H_2^+ are depleted either in the high-pressure ion-source region or in the accelerator and flight-tube enroute to the target. In the ion-source, the high vibrational states may be preferentially collisionally de-excited and enroute to the target, the now swift ions may have their high vibrational states preferentially dissociated by collisions with residual gas in the vacuum system. The results we obtain are not observably dependent upon the ion-source parameters that are presently at our disposal to vary with our duoplasmatron source. In addition, autoionization of high Rydberg states and rotational effects may play a role in the ion source [20].

Attempts to fit vibrational-state populations to our measured radial distributions (Fig. 7c and 8) are only moderately successful. A histogram of the resulting population for H_2^+ is shown in Fig. 9. The best fit to the HeH^+ radial distribution gives relative population intensities of 53%, 22%, 11%, and 6% for the four lowest-lying vibrational levels in the incident beam. It is worth noting that our derived distributions can be expected to be in error for internuclear separations large compared with the characteristic electronic screening distance for fast ions traversing carbon. From Eq. (3) we find a = 4.3 Å and a = 3.0 Å for 3.0 MeV H_2^+ and 3.63 MeV HeH^+, respectively. We have not made any correction for screening effects in our derivation of $D(r_0)$ (such effects would produce a very slight

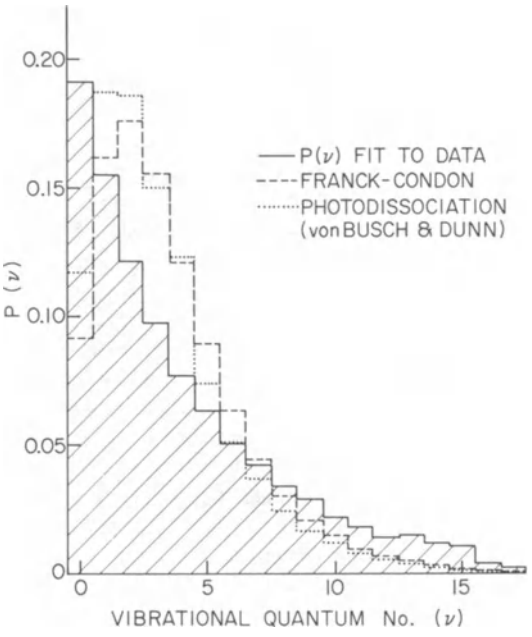

Fig. 9. A histogram of the vibrational-state population of the H_2^+ electronic ground state derived from the fit to the radial distribution in Fig. 7b.

shift to lower r_0). Another possible explanation for our failure to obtain a better fit to the H_2^+ vibrational population may be the presence in the incident beam of bound H_2^+ molecules in higher electronic states. This would produce a shift toward somewhat larger internuclear separations.

While both of these distributions are apparently independent of the range of conditions we can attain with our duoplasmatron ion source, changing to an rf source yields a dramatic change in $D(r_0)$ for HeH^+. Figure 10 shows rings measured for neutral hydrogen fragments from 2-MeV HeH^+ beams dissociating after passage through a carbon target. Neutral fragments are particularly sensitive to the r_0-distribution at large internuclear distances. At these energies, the fragment ions are essentially bare while transiting the solid target and thus acquire velocities characteristic of a simple Coulomb explosion in the foil. Electron capture upon exit effectively truncates the explosion as the ions are screened and little further kinetic energy is acquired outside the foil. Those ions that enter the target with initially large internuclear separations transform a significantly smaller fraction of the available Coulomb energy to kinetic energy than do those molecules with small separations and correspondingly higher accelerations. By truncating the explosion

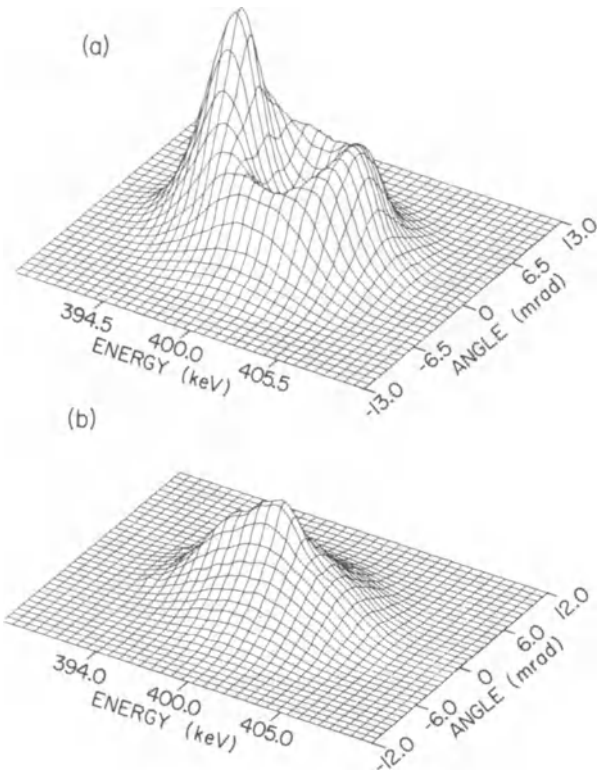

Fig. 10. The joint energy-angle distributions ("ring patterns") for neutral hydrogen fragments arising from the dissociation of 2-MeV HeH^+ in a 108 Å carbon foil. The distribution in (a) is measured when the beam is prepared in a duoplasmatron ion source fed with a gas mixture of 90% He and 10% H_2 while (b) shows the distribution obtained with an rf source using the same gas mixture.

at exit from the foil we limit the velocity acquired by these large r_o ions. The ring in Fig. 10a is measured for the duoplasmatron-prepared HeH^+ beam and though the explosion ring diameter is smaller, the distribution is similar to the full explosion of protons (as seen in Fig. 4). By contrast, Fig. 10b shows a similar measurement performed with the beam prepared in an rf ion source. Here we see a ring collapsed to smaller COM velocities (large r_o). This is characteristic of a hotter population of vibrational states in the incident beam.

This modification of the H^o ring distribution for HeH^+ produced by changing ion sources is similar to what is observed by comparing H^o from H_2^+ and HeH^+ from the same (duoplasmatron) source

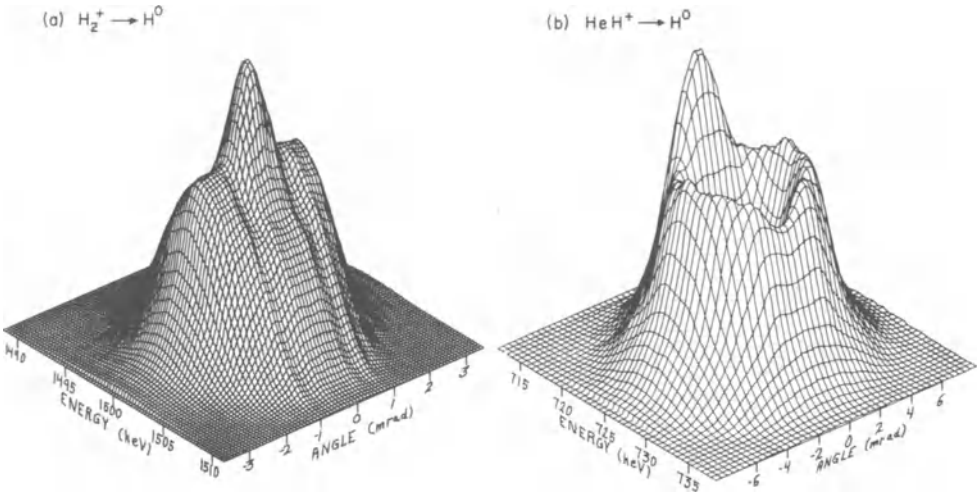

Fig. 11. Ring patterns for (a) 3.0-MeV $H_2^+ \rightarrow H^0$ in a 132-Å carbon foil, and (b) 3.63-MeV $HeH^+ \rightarrow H^0$ in a 144-Å carbon foil. The incident beams are prepared in a duoplasmatron ion source.

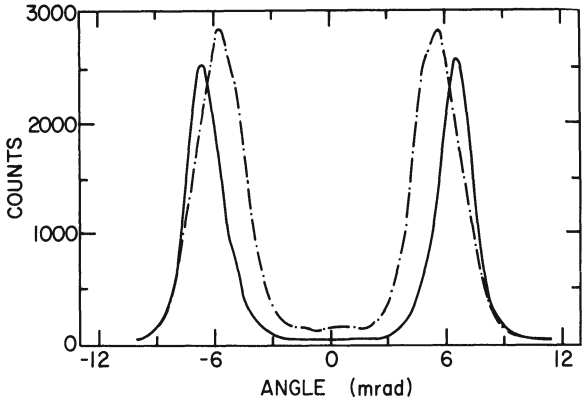

Fig. 12. Angular distributions, measured at zero energy shift, for outgoing H^+ from the dissociation of 3.0-MeV HeH^+ in a 108-Å carbon foil (similar to Fig. 6). The solid curve was observed when the HeH^+ beam was prepared in a duoplasmatron ion source while the chained curve resulted from a similar measurement using an rf source.

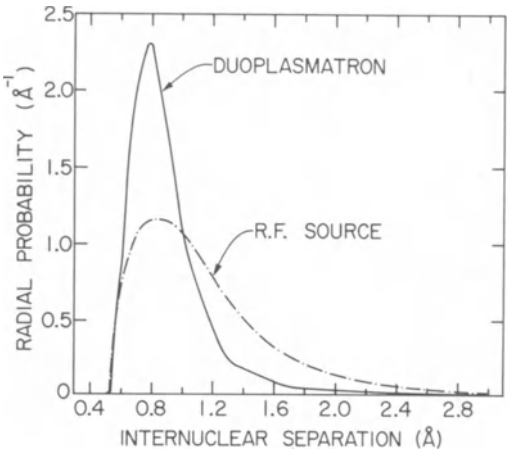

Fig. 13. Radial distribution functions for incident 3.0-MeV HeH^+ ions. These curves are derived from the data shown in Fig. 12 using the methods described in Ref. 3. The solid curve is the distribution observed from a duoplasmatron source while the chained curve is the result of measurements utilizing an rf source.

(see Fig. 11). Whereas the cooler HeH^+ shows a characteristic distribution (Fig. 11b), the vibrationally excited H_2^+ gives a dramatically different profile indicative of a significantly smaller energy release. It is worth noting that unlike HeH^+, the already hot H_2^+ r_o-distribution does not observably change when the ring is remeasured for an rf source.

Though not strikingly evident as in the case of H^o, the rf-duoplasmatron difference is also observed with the proton fragments from HeH^+ as shown in the measured angular distributions of Fig. 12. Again, one clearly sees a smaller explosion when the HeH^+ beam is produced in the rf source, suggesting longer internuclear separations. Using the reflection model, we can again unfold the r_o-distributions for each beam (Fig. 13).

Another very sensitive probe of the large-r_o component of the incident beam, is the measured yield of transmitted molecules. The transmission phenomenon, as discussed in the preceding paper by Remillieux [12], has now been well described quantitatively by a recent model proposed by Cue et al. [25]. According to this model, transmission probability increases with increasing internuclear separation and hence transmission yields are most sensitive to the tail of the r_o-distribution of the incicent ions. As in the case of the neutral fragments, this is a consequence of the very weak explosion experienced by large-r_o molecules. Comparing the radial distribu-

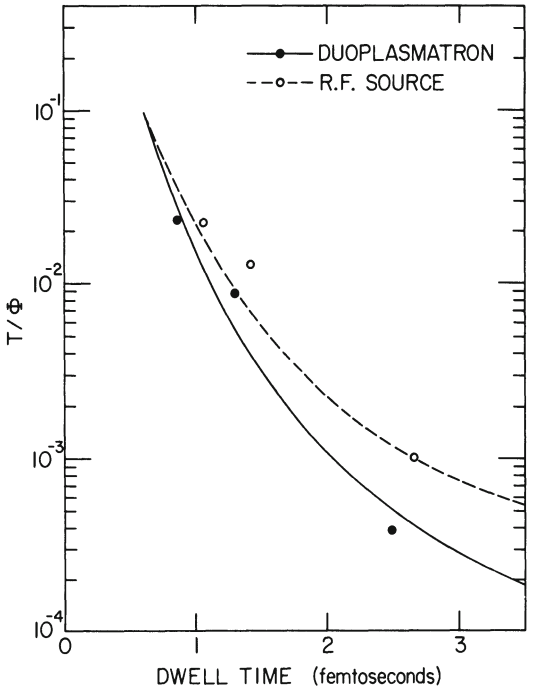

Fig. 14. Comparison of transmitted HeH^+ ion yield for 3.0-MeV ions incident on carbon targets of varying thickness when beams are prepared in duoplasmatron and rf ion sources. The lines represent the results of calculations (see Ref. 25) using the two distributions of Fig. 13 for initial radial distributions.

tions of Fig. 13, one would expect to see an enhanced yield of transmitted ions when the beam is prepared in the rf source as opposed to the yield for ions produced in the duoplasmatron. Figure 14 shows a comparison of transmission yields as a function of thickness for HeH^+ beams from each source. One sees, as expected, that the hotter rf beam is more than twice as likely to be transmitted. Calculations performed with the model of Ref. 25 reproduce the data fairly well when the radial distributions of Fig. 13 are used.

To summarize, we've seen that measurements of the angular distributions of explosion fragments from dissociations in solid targets can give quantitative information about the distribution of internuclear separations contained in the incident molecular-ion beams. These distributions, while indicating vibrational excitation, are relatively independent of ion-source tuning. The measured radial distributions are sufficiently accurate to predict other phenomena (such as transmission). With the exception of H_2^+, ions prepared

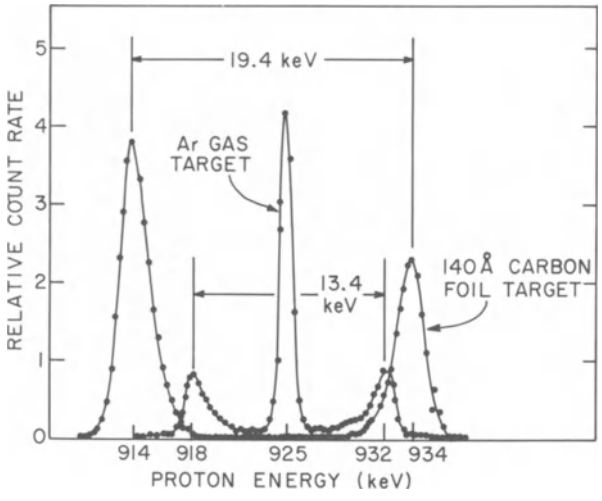

Fig. 15. Comparison of the zero-angle energy spectra for protons from 3.7-MeV $^3HeH^+$ bombarding a 140-Å carbon foil and an argon gas target at a pressure of 2×10^{-5} torr (from Ref. 17).

with a duoplasmatron ion source are vibrationally cool. Measurements on such ions as HeH^+, CH^+, OH^+, He_2^+ and other light diatomics shows these ion beams to be predominantly in the ground vibrational state [17] when prepared in the duoplasmatron. The H_2^+ beam appears to have a distribution intermediate between a Franck-Condon distribution of vibrational states and the cooler distributions observed for other ions.

b. Dissociation in Gas

When measurements similar to those above are performed with gaseous targets, the results are quite different. Figure 15 shows the zero-angle energy spectra measured for outgoing protons when a 3.7-MeV beam of $^3HeH^+$ is dissociated in a thin carbon foil and in a dilute argon gas target.

Whereas the explosion in the solid target is dominated by the bare Coulomb explosion of He^{++} and H^+, dissociations in gas are gentler and lead to less highly charged fragment ions. In this case the effects of He^+ and He° fragments are most evident and He^{++} is only seen on the tails of the spectrum. The effect of the energy loss in the solid target is also evident as a shift of $\sim$1 keV between the two spectra. To further investigate these differences, a series of measurements was undertaken to study the dissociation of H_2^+ and HeH^+ beams in a differentially pumped gas cell. Details can be found in Ref. 3.

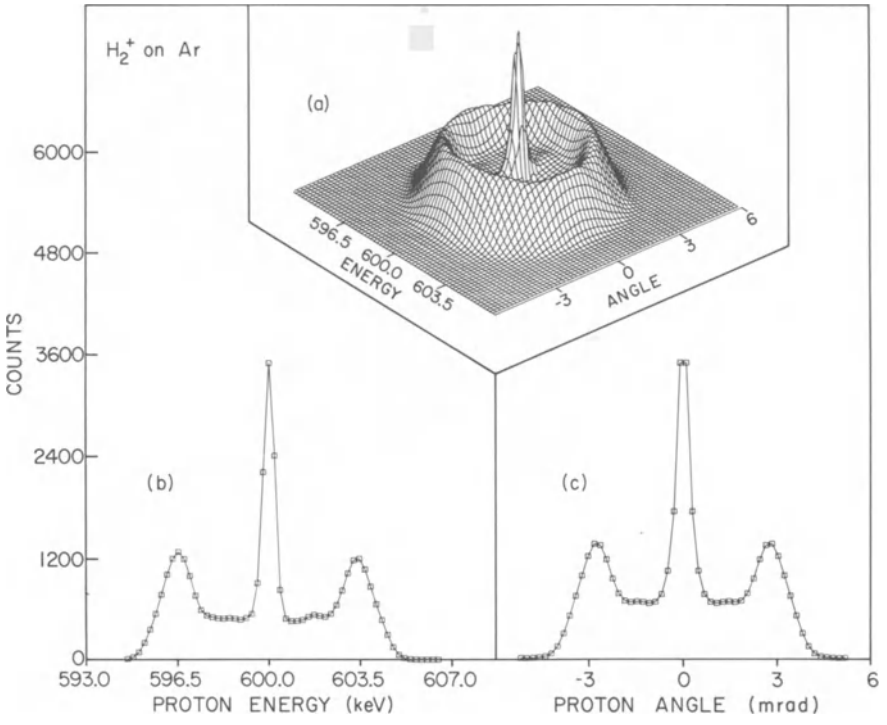

Fig. 16. (a) The "ring pattern" and (b), (c) the "cross" for protons from the dissociation of 1.2-MeV H_2^+ in Ar at 7.8 mTorr pressure.

The measured ring and cross distributions are shown in Figs. 16 and 17 for protons resulting from the dissociation in gas of 1.2-MeV H_2^+ and 3.0-MeV HeH^+ beams, respectively. For comparison the reader should refer to the solid target data for HeH^+ in Fig. 4. The most obvious difference between gas and foil data is that the gas data is dominated by a central peak and "filling" indicative of gentler, screened dissociations. This is not unexpected in view of the important role played by large impact-parameter collisions of the projectile molecule with target atoms. In the high density solid target, small impact-parameter collisions are unavoidable and all molecules in the beam are quickly ionized. In the gas target, the availability of the full range of impact parameters leads to electronic excitation of the incident molecule and subsequent dissociation through any of the repulsive final-state channels reached (see Fig. 18). These dissociative potentials are considerably flatter than 1/r at large r and produce correspondingly smaller energy releases to the separating fragments.

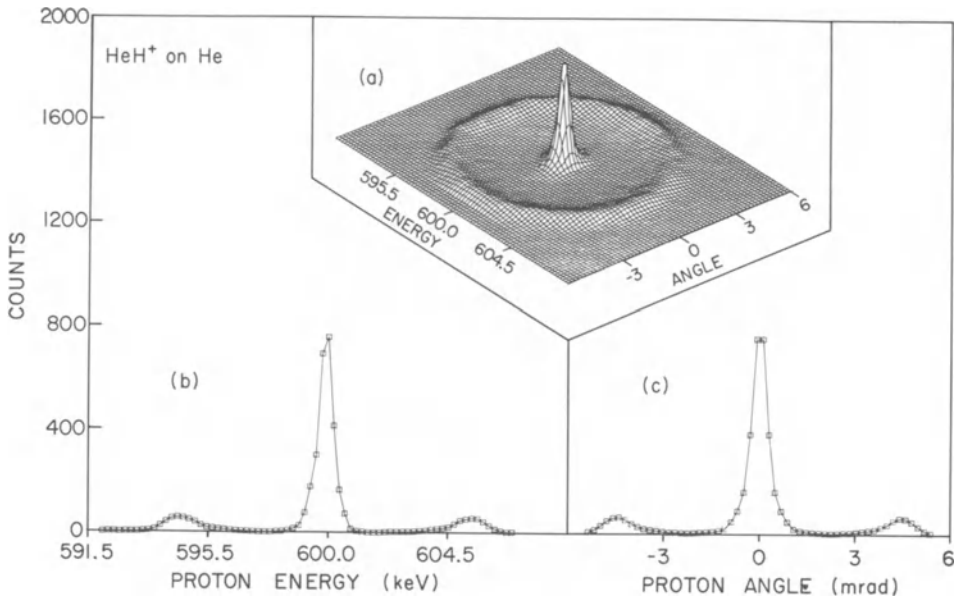

Fig. 17. (a) The "ring pattern" and (b), (c) the "cross" for protons from the dissociation of 3.0-MeV HeH^+ in He at 9.5 mTorr pressure.

Another very important difference is that the beam component which dissociates by ionization yields a symmetric ring pattern — there is no evidence of the wake realignment seen with solid targets. This is an important advantage in structural determinations; however, it is offset by the corresponding complication of multiple dissociation channels.

Using the distributions D(r) derived from the foil data, we have made similar analyses of the gas data, postulating as dissociative potentials the various U(r) shown in Fig. 18. For these data, no effects due to wake forces or multiple scattering needed to be taken into account.

It was found that no single excited electronic state is adequate to fit the observed velocity distributions. Thus, for example, states such as the $2p\pi_u$ in H_2^+ give a fair description of the low velocity part of the spectrum, but the high velocity part cannot be described without the inclusion of a Coulomb contribution. In our analysis velocity distributions were first calculated for each of the potentials shown in Fig. 18. These were then combined with weighting factors to obtain the best fits to the data. The results of this fitting procedure are shown in Figs. 19 and 20. Because of limitations of the reflection method in the tail regions of the po-

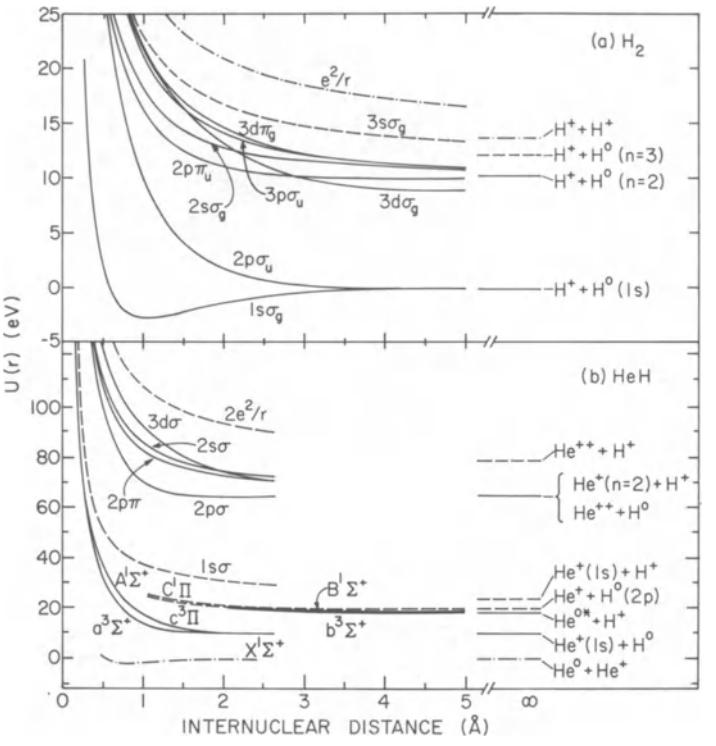

Fig. 18. Interaction potentials for various low-lying electronic states of H_2, H_2^+, HeH^+, and HeH^{++}.

tentials (discussed in Ref. 7), the fitting was performed only for $u/c > 0.5 \times 10^{-4}$. The same procedure was followed for both the longitudinal velocity spectra (0° energy scans) and the transverse velocity spectra (zero energy shift angular scans) and yielded similar results.

For H_2^+ the best fit was obtained with a combination of the $2p\pi_u$ (10%) and the Coulomb (90%) states. The $2p\sigma_u$ contribution was found, within fitting errors, to be zero for both orientations of the projectile. The potential functions used in the H_2^+ fit were taken from the tabulation of Sharp [26]. For keV bombarding energies, the $2p\sigma_u$ state plays a dominant role and it is somewhat surprising that it makes no contribution in our experiments. There is evidently a favoring of the more highly excited states (including ionization) at the higher energies involved in our work. It may also be that the $2p\sigma_u$ is artificially suppressed in our analysis because of our underlying assumptions that the excitation cross section is independent of r_o. This assumption is expected to be less valid for the $2p\sigma_u$ than for higher states. Peek [27] has shown that

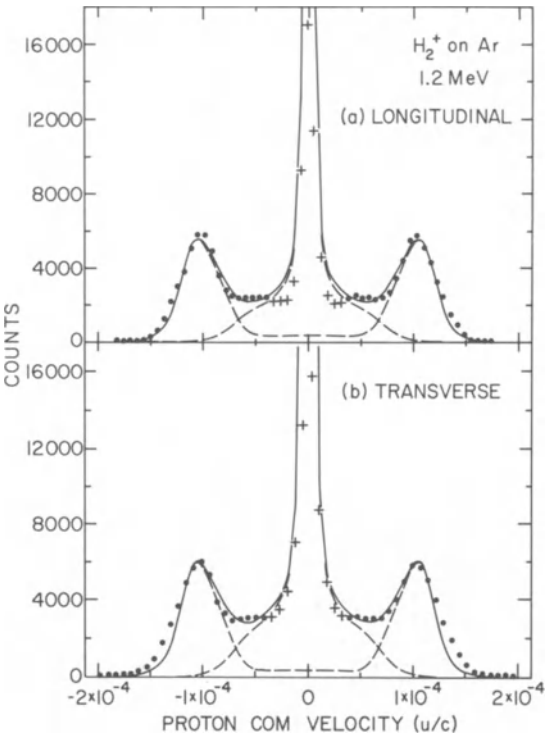

Fig. 19. Measured COM velocity distributions and least square fits for outgoing H^+ from 1.2-MeV H_2^+ incident on Ar gas at a pressure of 9.8 mTorr. Only data points shown as solid circles, corresponding to $(u/c) \geq 5 \times 10^{-4}$, were fitted.

for high projectile energies the $2p\sigma_u$ excitation probability increases with increasing r_o, thereby emphasizing the low-velocity region where our reflection method calculation is least valid. Thus our COM velocity distribution calculated for the $2p\sigma_u$ state would be rejected in the fit because of the over-emphasis of the high-velocity region.

Analysis of the HeH^+ distributions is more complicated because there are more final states to be considered for this two-electron system. The lowest-lying excited electronic states of HeH^+ that dissociate asymptotically into a proton and a neutral helium atom are the $b^3\Sigma^+$ and $B^1\Sigma^+$ states. These are therefore the most natural states to try to fit to the low velocity region of the proton spectra from HeH^+. However, the deep (several eV) minima of these curves preclude calculations with the reflection method. These potentials were rejected in the fitting procedure. The best fit to the data was obtained with only three electronic states of the HeH^{++} system (the

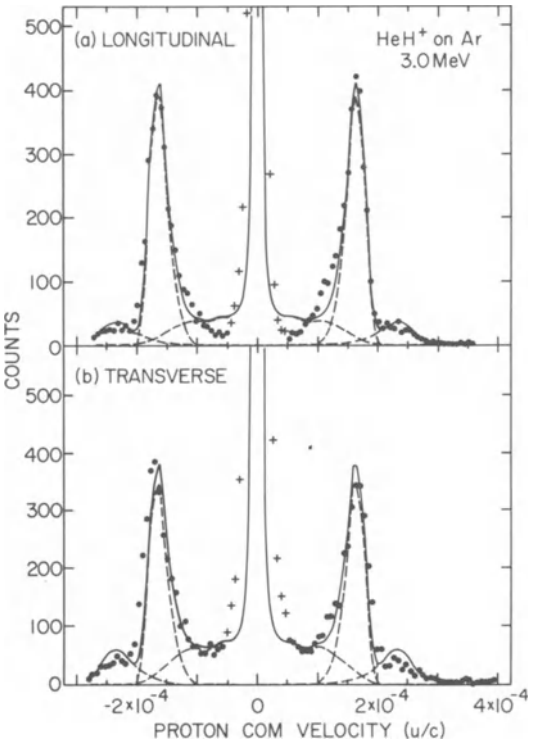

Fig. 20. Measured COM velocity distributions and least square fits for outgoing H^+ from 3.0-MeV HeH^+ incident on Ar gas at a pressure of 16.4 mTorr. Only data points shown as solid circles, corresponding to $(u/c) \geqslant 5 \times 10^{-4}$, were fitted.

1sσ, 2pσ, and 3dσ united-atom designations). The 1sσ and 3dσ states are repulsive and, at small separations, quite similar to the pure Coulomb potentials of $He^+ + H^+$ and $He^{++} + H^+$, respectively. They are, however, screened potentials and do not vary as 1/r at larger distances (see Fig. 21). The 2pσ state is partially attractive, having a slight potential minimum at ∿2 Å separation. This attraction is caused by the polarization of the H(1s) by the field of the He^{++} dissociation partner. The potential functions for HeH^+ were taken from the work of Michels [28] and Kolos and Peek [29] and for HeH^{++} from the work of Bates and Carson [30]. Similar fits were obtained for the He^+ and He^{++} spectra.

The fits in Fig. 20 were relatively unaffected by our choice of the 3dσ and 1sσ over bare Coulomb potentials since the contribution to the central peak is minimal for each. The fits show that the dissociation is dominated by the $He^+(1s) + H^+$ dissociation channel (the 1sσ electronic state of the united HeH^{++}) in agreement with

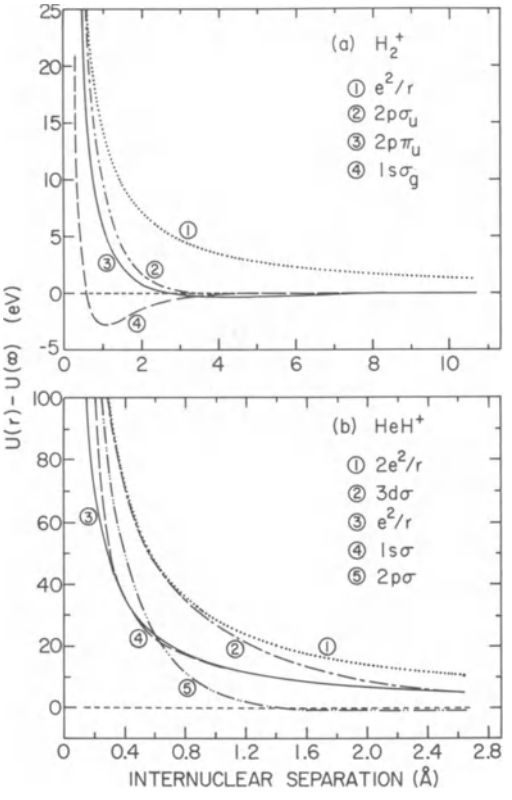

Fig. 21. Interaction potentials used in fitting the COM velocity distributions of H^+ from (a) H_2^+ and (b) HeH^+.

the observation of Stearns et al. [31]. For the longitudinal (E) orientation, we find 68%, 10%, and 23% contributions for dissociation through the $1s\sigma$, $2p\sigma$, and $3d\sigma$ channels, respectively. The transverse (θ) orientation gives 54%, 14%, and 32%, demonstrating the weak orientation dependence of the excitation cross sections.

The fits, though not as good as for the H_2^+ case, do demonstrate the qualitative features of the HeH^+ dissociation. Our neglect of the two-electron system as well as several other electronic states of HeH^{++} could account for our failure to explain the wide central peaks and detailed structures observed in the data.

The main conclusion of these experiments with gaseous targets is that whereas the solid target explosions detail the structure of the incident molecular-ion beam, dissociations in gas are a probe of the dissociative excited electronic states of the molecule.

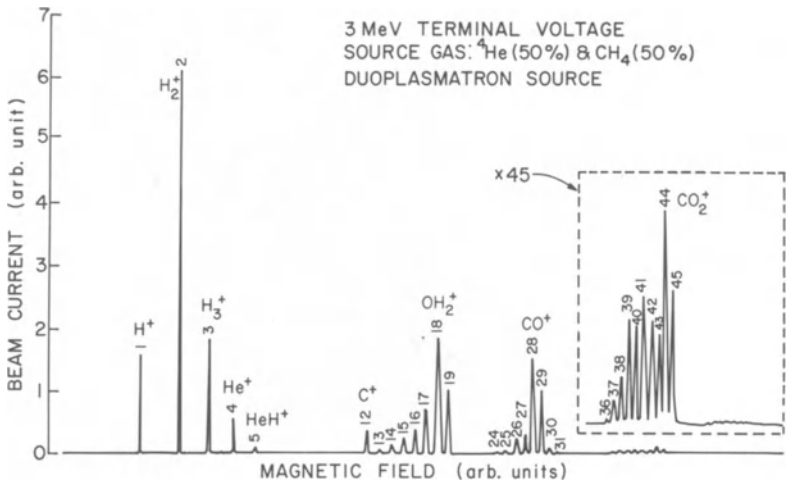

Fig. 22. A "mass-scan" of the ion beams emerging from Argonne's 4-MeV Dynamitron accelerator operating with a duoplasmatron ion source fed with a mixture of He and CH_4 gases.

VIII. Structural Studies of Polyatomic Ions

By analyzing ring patterns and crosses as described in the preceding section, bond lengths for a variety of diatomic molecular-ion projectiles can be determined with an accuracy of about 0.01 Å (see for example, Ref. 17). At Argonne, we have recently become interested in exploring the extent to which these high-energy fragmentation techniques may be extended to the problem, under discussion at this conference, of determining the geometric structures of polyatomic molecular ions [1, 4, 19, 32]. Related studies are also being conducted at Brookhaven [33] and at the Weizmann Institute [15, 34].

Although the accuracy expected from these fragmentation techniques may be poor (∿0.01 Å in bond lengths and ∿1° in bond angles for simple species) when compared with the high resolution obtainable with the photon techniques (when applicable), it nevertheless should be sufficient to resolve many conflicts between predictions of various structure calculations.

The photon emission or absorption techniques usually involve searching for extremely weak and narrow resonance lines in the presence of intense background radiation. Though the resulting structural determinations are extremely accurate, the experimental problem of obtaining sufficient column densities of molecular ions presents a severe limitation to improving signal strengths [35]. The level of accuracy obtainable through high-energy fragmentation mea-

surements should therefore be sufficient to assist practitioners of the photon techniques in zeroing in on the appropriate frequency search ranges. In contrast to the photon measurements, the fragmentation measurements usually require a reduction of incident ion-beam intensities. One further point is that as Fig. 22 illustrates, the molecular ions currently of the greatest interest in astrochemical and fusion studies are very much the same ones produced copiously by the plasma ion sources normally used in electrostatic accelerators.

A. Measurements of Single Dissociation Fragments

H_3^+. The earliest structural measurement of a polyatomic ion using these fragmentation techniques involved a joint study undertaken at the University of Lyon, the Weizmann Institute, and Argonne National Laboratory [36]. Each laboratory performed a measurement based on the Coulomb explosion of fast H_3^+ ions. Although different techniques were used at each laboratory, the three measurements produced consistent results. It was experimentally demonstrated (for the first time) that H_3^+ is equilateral triangular in shape. In the Argonne measurement this simple qualitative statement is evident from the fact that the measured ring distributions for proton dissociation fragments form a single ring similar to that of Fig. 4. A linear structure would produce an intense central peak and a non-equilateral bent structure would yield concentric rings. The observation of a single ring implies that all proton sites are equivalent and hence one deduces an equilateral triangular shape. The three measurements yielded proton-proton bond distances of 0.97 ± 0.03 Å (Argonne), 0.95 ± 0.06 Å (Lyon), and 1.1 ± 0.2 Å (Weizmann). The vibrational ground state of H_3^+ has a calculated [37] bond length of 0.91 Å. It is once again clear that our beam ions arrive at the target with some degree of vibrational excitation.

CO_2^+ and N_2O^+. Another example of the manner in which gross structures may be rapidly determined by Coulomb explosion techniques is to be found in recent studies at Argonne [38] with 3.5-MeV beams of CO_2^+ and N_2O^+. These molecular ions in their ground and low-lying states are known [39] to be linear; but while CO_2^+ has the symmetric form (O-C-O), N_2O^+ is asymmetric (N-N-O). Figure 23 shows $\theta = 0$ energy spectra for O^{4+} and C^{2+} from CO_2^+ and O^{4+} and N^{3+} from N_2O^+. Similar spectra were obtained for fragments emerging in other charge states. Each spectrum takes about 5 minutes to accumulate. The principal structural characteristics are evident from just a casual inspection of Fig. 23. The existence of only two peaks in Fig. 23a indicates that the two oxygen atoms in CO_2^+ are equivalent. The existence of just one peak in Fig. 23b shows that the carbon atom is central in a linear molecule (no net Coulomb-explosion velocity). The two peaks in Fig. 23c show that the oxygen atom in N_2O^+ lies "on the outside" and the three peaks in Fig. 23d show that one nitrogen atom is "on the outside" and that one is in the center

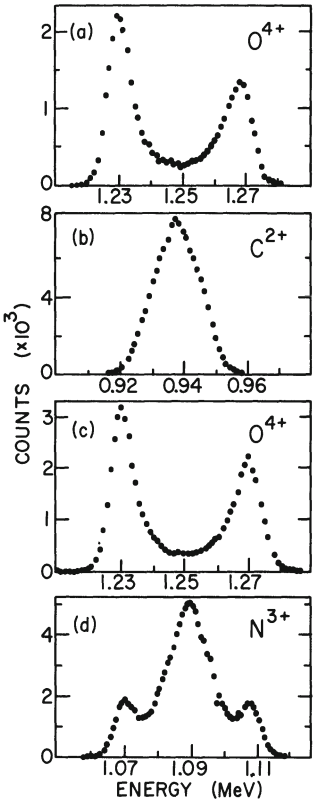

Fig. 23. Energy spectra at $\theta = 0$ for (a) O^{4+} and (b) C^{2+} resulting from 3.5-MeV CO_2^+ bombarding a 133-Å thick C foil, and for (c) O^{4+} and (d) N^{3+} resulting from 3.5-MeV N_2O^+ bombarding a 160-Å thick carbon foil [38]. The spectra are not normalized to one another.

of a linear molecule. The central peak in Fig. 23d is much more strongly populated than the two side peaks because many more incident orientations contribute to it.

From these considerations, it can be seen that by simply counting the number of peaks in each spectrum, one can infer that both CO_2^+ and N_2O^+ are linear with structures (O-C-O) and (N-N-O). To obtain precise values for the bond lengths and angles, a more detailed analysis is obviously required.

$\underline{CH_n^+ \ (n = 0\text{-}4)}$. The proton and the carbon fragments arising from the Coulomb explosion of CH^+, CH_2^+, CH_3^+, and CH_4^+ have been studied at beam velocities corresponding to 0.194 MeV/a.m.u. [40]. The singles proton spectra although reflecting vigorous Coulomb explosions are not particularly informative concerning the projectile

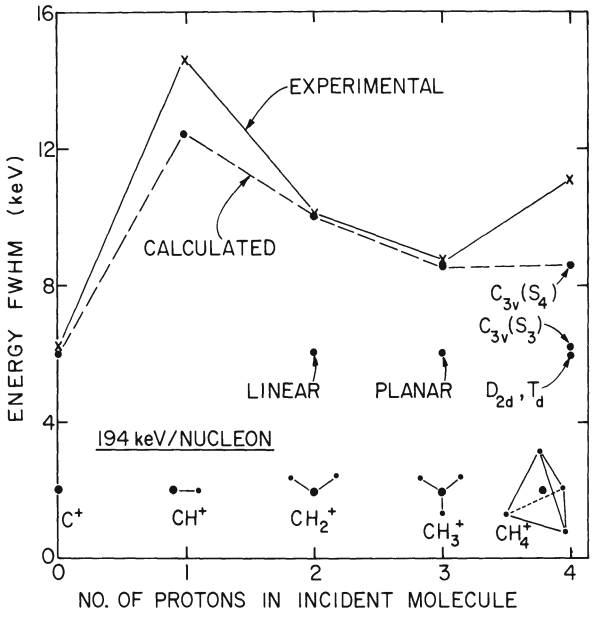

Fig. 24. Comparison of energy widths of C^{4+} spectra for $CH_n^+ \rightarrow C^{4+}$. The calculations are based on a carbon-ion effective charge of 3.5 and neglect wake forces [40].

structures. For the carbon fragments, energy straggling and multiple scattering in the target blur out the structure information in the energy and angle spectra. However, the width of the peak observed in these carbon-ion spectra is sensitive to any asymmetry in the distribution of the protons that surround the carbon atom in the projectile.

Figure 24 shows the measured energy widths (FWHM) of outgoing ($\theta = 0$) C^{4+} ions that emerge after the incident beam strikes a foil target. The value of 6.1 keV for incident C^+ represents the contribution of energy straggling convoluted with both the beam energy spread and the resolving power of the electrostatic analyzer system. The Coulomb explosion of the highly asymmetric CH^+ ions adds a large contribution which increases the measured width to 14.6 keV. For the more symmetric CH_2^+ ions, because of near cancellation of the impulses produced by each proton on the carbon ion, the Coulomb explosion is reduced and thus we measure a width of only 10.1 keV. If CH_2^+ were rigidly linear, the width would be expected to be close to the C^+ straggling value of 6.1 keV (the width would actually be somewhat greater than 6.1 keV because of charge-state fluctuation effects that modify the Coulomb explosion while the ion fragments are within the target foil). A similar effect is seen in the measurement of the carbon width for the dissociation of CH_3^+. Again,

the width is increased over the minimum that one would expect for rigid planar structure; however, it is smaller than for either of the CH^+ or CH_2^+ results. The data for CH_4^+ show a dramatic departure from this general trend. The measured width of 11.1 keV is larger than for all but the CH^+ measurement. This indicates a highly asymmetric proton distribution around the carbon nucleus and is most likely a consequence of the Jahn-Teller distortion of CH_4^+.

The dashed line in Fig. 24 shows the width calculated on the basis of a very crude model in which it is assumed that rigid structures having carbon charges of 3.5 and proton charges of 1.0 Coulomb-explode. No attempt was made to include the effects of molecular vibrations, wakes, multiple scattering, charge state distributions, etc. These calculations thus serve only as a rough guide to the possible structures of the projectiles and are not to be interpreted as determining the actual structures. The calculation for CH^+ assumes a bond length of 1.13 Å. For CH_2^+ a carbon-proton distance of 1.03 Å is assumed and the H-C-H angle is taken to be 140° (a guess based on the expectation that the bond angle will be close to the value of 131° known [39] for the isoelectronic molecule BH_2). For CH_3^+ the calculation assumes a rigid pyramidal structure with an interproton distance of 1.08 Å and with the carbon ion 0.2 Å off the proton plane. The values calculated for CH_4^+ were based on the four Jahn-Teller distorted structures derived by Dixon [41]. As noted above, taking account of vibrational excitations of the projectiles can affect the implications of these calculations. For example, CH_3^+ is commonly thought to be planar [39] and the results shown in Fig. 24 are consistent with a planar structure in which a low-frequency out-of-plane oscillation of the carbon ion exists with an amplitude of $\sim$0.2 Å.

Except for the very simplest highly symmetric polyatomic molecular ions (e.g., H_3^+), high-resolution studies on single fragments yield only gross features of the stereochemical structures. For example, our measurements on C^{2+} fragments from 3.6-MeV $C_3H_3^+$ ions dissociating in thin foils demonstrate only that the carbons sit on the corners of an approximately equilateral triangle. [That is, we have a beam of cyclopropenyl ions and not propargyl ions (which are linear in carbons).] Similarly, our measurements on single fragments from OH_2^+ show only that the protons are equivalent and that the oxygen is "in the middle." The accuracy in determining the bond length and bond angle is poor because there are wide ranges of values for these parameters that combine to give about the same Coulomb explosion velocity u for any given fragment.

A further difficulty associated with this type of measurement for polyatomic molecular ions lies in analyzing the effects of vibrational excitations of the projectiles. Excitations of some modes (e.g., symmetric breathing modes) can frequently be expected to result only in apparent changes in the bond lengths determined by the

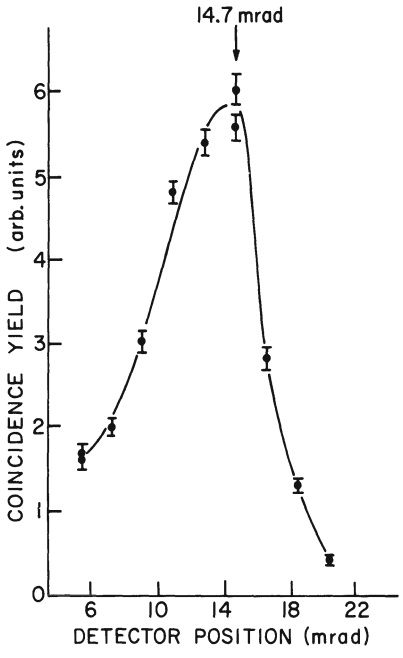

Fig. 25. Coincidence counting rate for protons from 3.6-MeV OH_2^+ dissociating in an 80-Å thick carbon foil [19]. The rate is plotted as a function of the angle between the electrostatic analyzer (set on the low energy, $\theta = 0$ proton group) and one of the movable surface-barrier detectors (Fig. 3).

Coulomb-explosion method. However, many non-symmetric modes can result in apparent structures that differ markedly from the structure of the vibrationless ground state. It is therefore important to analyze the Coulomb-explosion data in terms of the specific modes that can be excited for each projectile species considered. The analysis can be greatly simplified if the projectiles can be prepared in their ground (or at most a small range of low-lying) vibrational states — often a difficult technical task.

Measurements of single fragments, though very easy, are clearly limited to yielding only very gross structural information for most ions of interest.

B. Coincidence Measurements

The velocity spectra of singles fragments are determined primarily by the total Coulomb energy of the molecule. It is often possible to produce similar fragment velocity spectra with very

different initial structures. Polyatomic structures can be more precisely determined if spatial and temporal coincides are recorded for two or more dissociation fragments from a given projectile. By simultaneously recording energy, angle, charge state, and timing information in such coincidence measurements, it is possible to trace the simple Coulomb trajectories followed by explosion fragments back to the initial configuration of the original molecular cluster. With this large amount of data describing the final fragment trajectories, the structural ambiguities of single fragment measurements can be removed.

With this in mind, we recently revised the apparatus at Argonne to permit a wide variety of coincidence measurements. These revisions include the wide flight tube and detector chamber in Fig. 2 and the movable detector arms in Fig. 3. The system has so far been tested with various simple diatomic and triatomic projectiles (H_2^+, HeH^+, CH^+, NH^+, OH^+, H_3^+, CH_2^+, NH_2^+, OH_2^+, etc.). Preliminary results are presented below.

CH_2^+, NH_2^+, OH_2^+. Preliminary coincidence measurements have been carried out for these light dihydride ions [19]. Of the three, only OH_2^+ has previously had its structure determined experimentally. Lew and Heiber [42], using optical techniques, have found the O-H bond length to be 0.999 Å and the H-O-H bond angle to be 110.5°.

In our measurements, we've studied proton-proton coincidences from 3.6-MeV OH_2^+ dissociating in a 80-Å thick carbon foil. The dwell time in the target is $\sim$1.3 fsec. While in the solid target, the oxygen ion has an effective charge of 4.1 (from Eq. (4)). Approximately 30% of the initial Coulomb energy is liberated during the time in the target. Outside of the target, $\sim$50% of the emerging oxygen ions are O^{4+} (with roughly 20% O^{3+} and 30% O^{5+}) [43]. Because of this very narrow charge state distribution (after the fragments are already well separated), it is not necessary to measure the coincident oxygen charge state.

A typical measurement consists of defining a limited subset of the incoming projectile orientations by suitably choosing a combination of voltages to apply to the post-deflector plates and the electrostatic analyzer (ESA). A scan is then made with one or both of the detectors in the detector chamber of Fig. 3 to determine the spatial maximum of coincident fragments for that particular molecular orientation.

Figure 25 shows the results of such a spatial scan of the proton-proton double coincidence rate for the foil-induced dissociation of 3.6 MeV OH_2^+ ions. For this scan, the ESA and detectors were adjusted so that the ESA detected only protons ejected with the maximum velocity observed anti-parallel to the beam direction. We are thereby selecting only those orientations where one proton trails

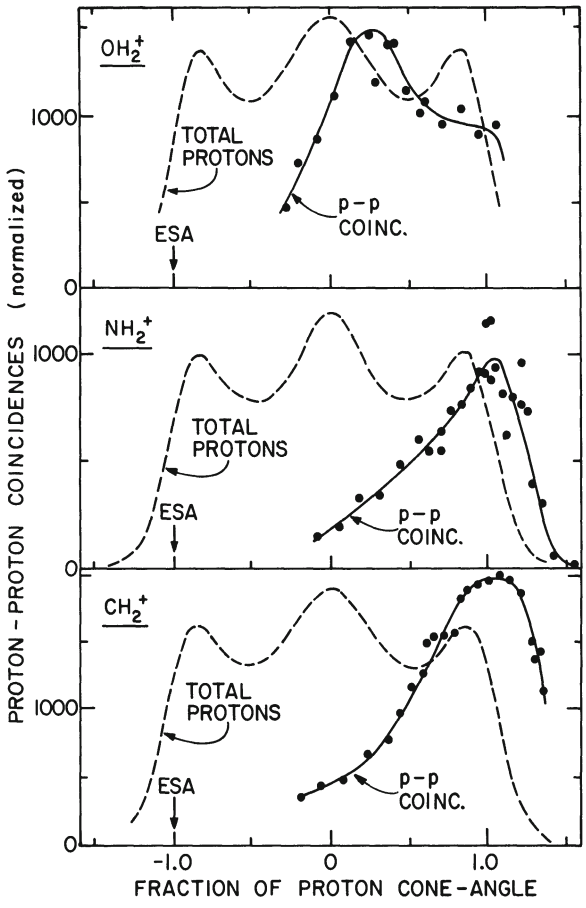

Fig. 26. The proton-proton coincidence counting rates for 3.6-MeV beams of CH_2^+, NH_2^+, and OH_2^+ dissociating in carbon foils of thicknesses 98 Å, 66 Å, and 89 Å, respectively [19]. The rates are plotted as functions of the fraction of the proton cone angle (16.25, 14.28, and 13.21 mrad for CH_2^+, NH_2^+, and OH_2^+, respectively) lying between the electrostatic analyzer (set on the protons having the maximum transverse momentum) and one of the movable surface barrier detectors (Fig. 3). Also shown are the total (energy-summed) proton-singles rates in the movable detector.

the oxygen nucleus. The remaining proton must be ejected along the cone formed by rotating the molecule around the trailing-proton-oxygen axis. From measurements of single proton fragments, the angular radius of the ring pattern was found to be 16.2 mrad. Because the coincidence rate peaks inside of this cone angle at a value of 14.7 mrad, the bent structure is immediately recognized. The bond angle should be close to $\beta = 180° - \sin^{-1}(14.7/16.2) = 115°$. Ap-

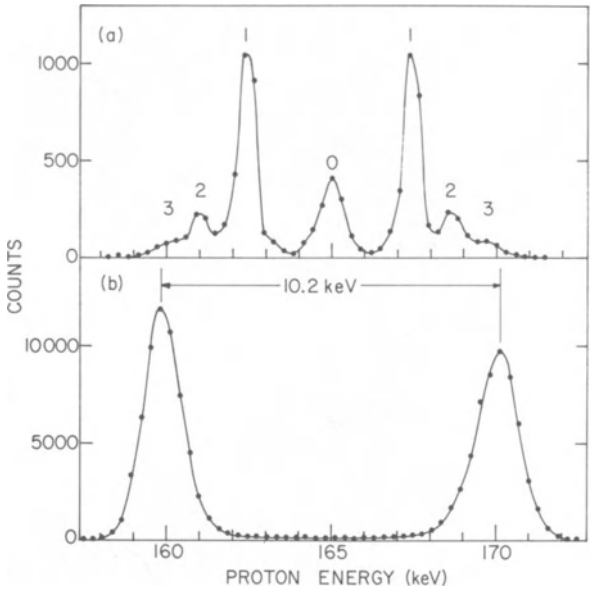

Fig. 27. Comparison of the zero-angle energy spectra for protons from 2.805-MeV OH^+ bombarding a) the residual gas (10^{-7} torr) in the scattering chamber and b) a carbon foil target 165-Å thick.

proximate corrections for the displaced centers of mass and charge and for the oxygen recoil result in values of 110 ± 2° and 1.0 ± 0.04 Å for the bond angle and bond length, respectively. These values agree with those from optical measurements [42]. Measurements with other orientations chosen in the ESA give similar results. A more detailed analysis, properly taking into account wake effects and multiple scattering, should result in a significant improvement in the level of accuracy.

Figure 26 shows a comparison of the results for foil-induced dissociation of 3.6-MeV CH_2^+, NH_2^+, and OH_2^+. For these data, the deflections are chosen so that the ESA detects only those protons with the maximum transverse momentum. The double coincidence rate for OH_2^+ peaks a little past the center of the proton cone — again consistent with a bond angle of 110°. However, for the other two projectiles, the peak occurs at the extreme angle of the proton cone — opposite the ESA. This would be consistent with a linear structure, but again vibrational effects may be playing a large role in these projectiles. In Fig. 26 the scan for CH_2^+ shows a step suggesting the admixture of beam components with a bent structure.

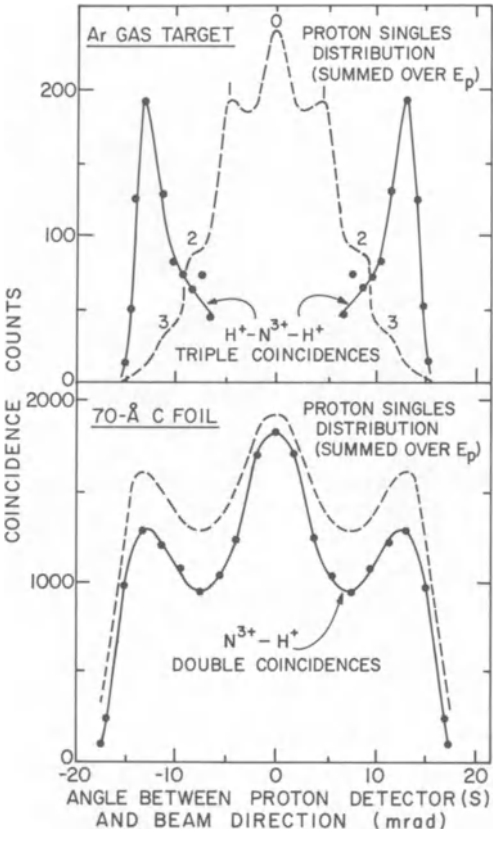

Fig. 28. Top: H^+- N^{3+}-H^+ triple coincidence counting rate for 3.6-MeV NH_2^+ ions dissociating in an Ar gas-jet target. N^{3+} ions are detected at 0° in the electrostatic analyzer. Protons are detected in the two movable detectors. The coincidence rate is plotted as a function of the angle between the (symmetrically placed) proton detectors and the beam direction.

Bottom: Same, but double coincidences (N^{3+}-H^+) obtained with a 70-Å carbon foil target. In both figures, the total (energy-summed) proton-singles rates in the movable detectors are shown as dashed curves. In the top figure, the numbers (0, 1, 2, 3) on the dashed curves refer to the corresponding nitrogen-ion charge state [19].

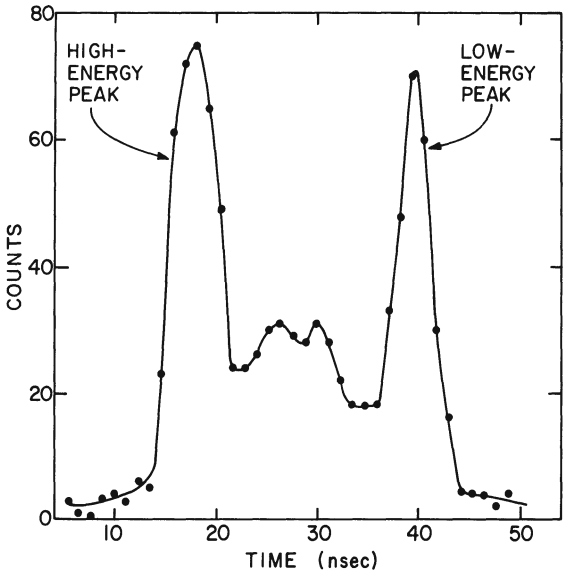

Fig. 29. Time-of-flight spectrum obtained with 3.6-MeV NH_2^+ ions dissociating in an Ar gas jet target. The time-to-amplitude converter is started by N^{3+} ions detected at 0° in the electrostatic analyzer and is stopped by the delayed signals from protons detected at 0° in one of the movable silicon surface-barrier detectors.

Although foil-induced dissociation has the virtue that essentially every incident projectile dissociates violently into individual highly-charged monoatomic ions, there are complications in the data analysis where one must take account of wake effects, target thickness, charge-state distributions, and multiple scattering. These problems do not arise if one uses a dilute gas target in which single collisions predominate. With gas targets however, there is the problem that most of the dissociations proceed through weak Coulomb explosions between ions of low charge (see Fig. 27). Also, the product fragments frequently include diatomic and polyatomic species. Thus, as in the case of singles measurements from diatomic ions, foil-induced and gas-induced dissociations of polyatomics tend to give complementary information and in studying any given projectile it is desirable to use both types of targets.

We have recently begun triple coincidence measurements, e.g., on the pairs of protons and the N^{3+} fragments arising from the dissociation of 3.6-MeV NH_2^+ ions in a dilute Ar gas jet (Fig. 28). Although the triple coincidence counting rates are low, the data are very clean and the analysis is simplified as compared with the results obtained with foil targets. These data were taken by setting

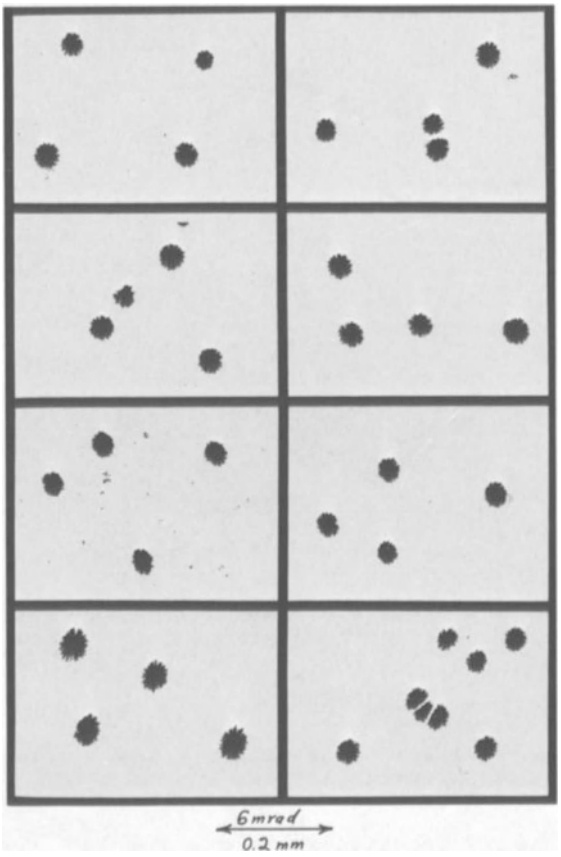

Fig. 30. Etched polycarbonate sheet after exposure to fragments from 3.5-MeV C_4^- ions dissociated in a thin carbon foil [33].

the ESA to look at all N^{3+} at 0° and scanning the other detectors symmetrically around 0° protons. The resulting timing spectrum for one of these detectors is shown in Fig. 29. As the detector moves toward the outside of the proton explosion cone, the two groups of leading and trailing protons, seen in Fig. 29, coalesce. The detailed time-of-flight information available for each point in the angular scan has not yet been taken into account in the data analysis.

To summarize, we have commenced high-resolution coincidence measurements on the fragments from foil- and gas-induced dissociation of fast polyatomic molecular ions. For OH_2^+, we are able to reproduce the bond angle and bond length found in optical experiments. The precision of the method can now be expected to improve

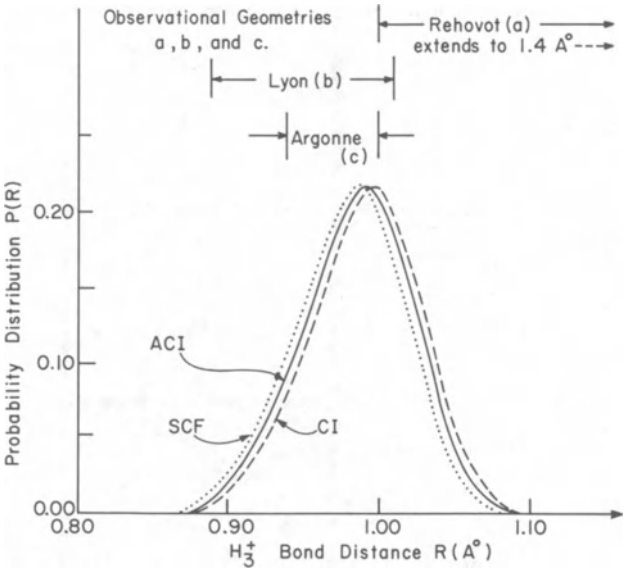

Fig. 31. Comparison between measured [36] and calculated [44] distributions in the proton-proton bond distance in H_3^+ (from Ref. 44).

considerably as more refined data-analysis procedures are developed to treat this new source of data.

IX. Other High-Energy Techniques

At the Weizmann Institute, a photographic technique was developed [36] to study H_3^+. With this technique, all of the fragments from individual projectiles were captured and rendered visible in a photographic emulsion. A similar method has recently been applied by a group at Brookhaven [33] to study the foil-induced dissociation of C_n^- beams. This group uses a polycarbonate plastic sheet as detector. Figure 30 shows such a sheet after exposure to fragments from foil-dissociated C_4^- projectiles. Inferring structure information from data such as these is difficult (except perhaps to observe that C_4^- is not linear). A higher data rate would be very desirable because a statistical analysis of the fragment patterns would then become feasible. Promising steps in this direction are now being taken both at Brookhaven and at the Weizmann Institute where electronic imaging techniques are being developed. At Brookhaven [33] a fluorescent screen used in conjunction with an image intensifier is being tested. Workers at the Weizmann Institute [34] have demonstrated that a charge-coupled semiconductor device is capable of acting as a high-resolution two-dimensional de-

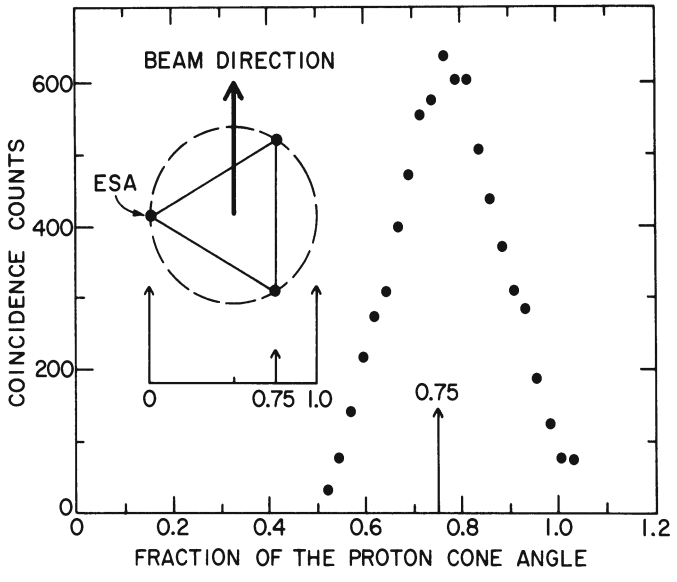

Fig. 32. Proton-proton coincidence counting rate as a function of the relative angular separation of the two detectors (the ESA and one of the movable detectors). The protons arose from 1.8-MeV H_3^+ incident on a 92-Å thick carbon foil. The ESA was set to accept only those protons with the maximum transverse velocity. The abscissa is in units of that maximum proton fragment cone diameter.

tector of charged particles. The energy resolution in each element is expected to be adequate for purposes of distinguishing masses. It is expected that this device will permit the rapid acquisition (∿50 images per second) and storage of two-dimensional projections of individual Coulomb-exploded molecular ions. The digital coordinates of the fragments in each image together with rough measures of their energies will be stored and processed by a computer.

These imaging techniques and the Argonne technique are complementary approaches to the structure problem. The one approach will produce a high rate of coincidences between all fragments for all incident projectile orientations, but little detailed information on energies, charge states, flight times, etc. The other approach selects individual charge states and projectile orientations with very precise information on parameters such as energies, flight times, direction, etc., but with low coincidence counting rates.

X. Future Directions

While the techniques described here are still in their infancy and are sure to provide valuable information about molecular-ion structures as both the technology and analysis are refined, some of the problems we have discussed appear to present formidable obstacles to immediate improvement of the measurements. In particular it now appears important to understand more fully how vibrational excitations affect the coincidence results. We have recently attempted to address this question by focussing on the simplest triatomic molecular-ion H_3^+ (and the deuterated species H_2D^+, D_2H^+, and D_3^+).

Figure 31 shows a comparison of the early singles measurements, discussed in section VIII-A, with a recent calculation by Carney [44] based on the vibrational-state population parameters of Smith and Futrell [45]. While those singles measurements yield only a single average value for the bond length, it is apparent from the calculation that vibrational excitation leads to a quite broad distribution of apparent bond distances. To further study this point, we have measured coincidence scans for the foil-induced fragmentation of H_3^+ and its deuterated species. A typical spectrum is shown in Fig. 32 for proton-proton coincidences from H_3^+. Again, as in the OH_2^+ example, one sees that the coincidence peak lies inside of the singles cone. The peak position corresponds to a bond angle of 57°; however, as expected from the calculation of Carney, the coincidence distribution is broad and asymmetric. These data (and similar spectra for H_2D^+, D_2H^+, and D_3^+) are currently being analyzed in terms of a moment analysis of the coincidence distributions to be compared with calculations by Carney [46]. The fact that the results for the deuterated species seem to show the subtle differences predicted by calculation [46] indicates that these distributions are not dominated by multiple scattering effects.

Finally, we report the results of a recent experiment at Argonne to test the feasibility of using a laser to photodissociate a fast molecular-ion beam [47]. By replacing the solid target in our apparatus with an intense laser beam, we avoid all of the previously discussed problems associated with solid targets and gain the added advantage of state selectivity by appropriate choice of laser wavelength. The disadvantages include the low count rates and ensuing experimental problems associated with background dissociations and the necessary knowledge beforehand of the initial and final states of the dissociating molecules.

Figure 33 shows the energy spectrum of a cross measured for protons produced by the laser-induced dissociation of a 2-MeV beam of H_2^+. The UV laser, crossed at 90° to the ion beam, operated at a wavelength of 1930 Å (6.42 eV). The resulting zero-angle energy spectrum shows extremely sharp peaks, the widths now being entirely determined by our energy resolution (∿700 eV). The 6-keV separation

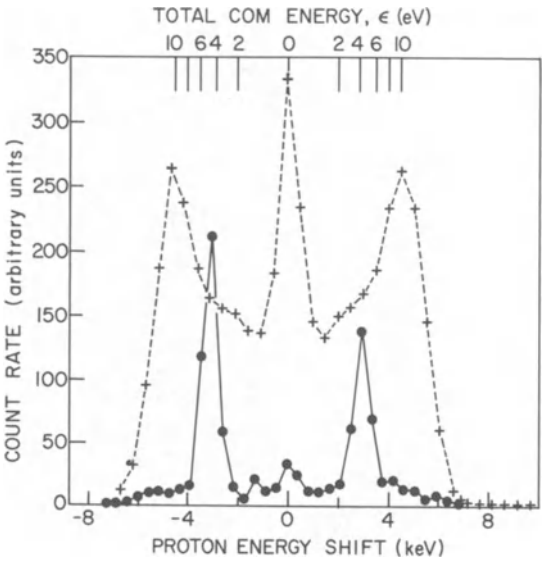

Fig. 33. Comparison of zero-angle energy spectra for the dissociation of 2-MeV H_2^+. The solid curve is for laser-induced dissociation. The dashed curve is observed for gas-induced collisional dissociation. The upper abscissa shows the correspondence between proton energy and the total energy released in the dissociation.

of the measured peaks corresponds to a total center-of-mass energy ϵ of 4.5 eV. Unfortunately, because of our energy resolution, we are observing the dissociation of a band of vibrational states (most likely v = 1-4) and thus have only limited state selectivity. Using the photoabsorption cross sections for H_2^+ calculated by Dunn [48], we have computed the expected mean-energy release to also be 4.5 eV. The calculation shows that $\sim$50% of the intensity comes from v = 2.

XI. Conclusions

We have described the main features of the Coulomb explosion of fast-moving molecular-ions and the manner in which Coulomb-explosion techniques are being applied to the problem of determining stereochemical structures of light polyatomic ions. Examples of such experiments have been presented for several ions. While these techniques are new, there is a growing effort to improve both the technology and the analysis techniques. These methods will surely make valuable contributions to the determination of molecular-ion structures in the years ahead.

Acknowledgements

I wish to acknowledge the work of Don Gemmell whose energies and talents have made possible the very active program at Argonne. In addition, I am grateful to P. J. Cooney, W. J. Pietsch, I. Plesser, Z. Vager, and B. J. Zabransky for their dedicated contributions to the expeiments described here. The work at Argonne was conducted under the auspices of the Division of Basic Energy Sciences of the U. S. Department of Energy.

References

1. D. S. Gemmell, Nucl. Instrum. Methods, 170, 41 (1980).
2. J. Remillieux, Nucl. Instrum. Methods, 170, 31 (1980).
3. E. P. Kanter, P. J. Cooney, D. S. Gemmell, K.-O. Groeneveld, W. J. Pietsch, A. J. Ratkowski, Z. Vager, and B. J. Zabransky, Phys. Rev., A20, 834 (1979).
4. D. S. Gemmell, Chemical Reviews, 80, 301 (1980).
5. R. G. Cooks (ed.), in: Collision Spectroscopy, Pleanum Press, New York (1978).
6. E. E. Salpeter, Proc. Phys. Soc., London, 63A, 1295 (1950).
7. G. W. McClure and J. M. Peek, in: Dissociation in Heavy Particle Collisions, Wiley-Interscience, New York (1972).
8. J. Los and T. R. Govers, Chapter 6 in Ref. 5 above.
9. N. Bohr, K. Dan. Vidensk. Selsk. Mat.-Fys. Medd., 18, 8 (1948).
10. D. S. Gemmell, J. Remillieux, J.-C. Poizat, M. J. Gaillard, R. E. Holland, and Z. Vager, Phys. Rev. Lett., 34, 1420 (1975).
11. Z. Vager and D. S. Gemmell, Phys. Rev. Lett., 37, 1352 (1976).
12. J. Remillieux, preceding paper, this conference.
13. See, for example, L. C. Northcliffe and R. F. Schilling, Nucl. Data Tables, A7, 233 (1970).
14. D. S. Gemmell and I. Plesser, to be published.
15. A. Breskin, A. Faibis, G. Goldring, M. Hass, R. Kaim, I. Plesser, Z. Vager, and N. Zwang, Nucl. Instrum. Methods, 170, 93 (1980); 170, 99 (1980).
16. Z. Vager, D. S. Gemmell, and B. J. Zabransky, Phys. Rev., A14, 638 (1976).
17. D. S. Gemmell, P. J. Cooney, W. J. Pietsch, A. J. Ratkowski, Z. Vager, B. J. Zabransky, A. Faibis, G. Goldring, and I. Levine, Proceedings of the 7th International Conference on Atomic Collisions in Solids, Moscow, September 19-23, 1977.
18. D. S. Gemmell, in: Radiation Research (Proc. of the Sixth Int. Congress on Radiation Research, Tokyo, Japan, May 13-19, 1979), S. Okada, M. Imamura, T. Terashima, and H. Yamaguchi (eds.) (U. of Tokyo, 1979), pp. 132-144.
19. D. S. Gemmell, P. J. Cooney, and E. P. Kanter, Nucl. Instrum. Methods, 170, 81 (1980).
20. See, for example, F. von Busch and G. H. Dunn, Phys. Rev., A5, 1726 (1972).

21. Y. Irikawa, J. Electron Spectroscopy and Related Phenomena, 2, 125 (1973).
22. J. Berkowitz and R. Spohr, J. Electron Spectroscopy and Related Phenomena, 2, 143 (1973).
23. J. Remillieux, in: Proceedings of the Fifth International Congress of Radiation Research, Academic Press, New York (1975), p. 302.
24. J. W. Butler and C. M. Davisson, Nucl. Instrum. Methods, 149, 183 (1978).
25. N. Cue, N. V. de Castro-Faria, M. J. Gaillard, J.-C. Poizat, J. Remillieux, D. S. Gemmell, and I. Plesser, Phys. Rev. Lett., 45, 613 (1980).
26. T. E. Sharp, Atomic Data, 2, 119 (1971).
27. J. M. Peek, Phys. Rev., 134, A877 (1964).
28. H. H. Michels, J. Chem. Phys., 44, 3834 (1966).
29. W. Kolos and J. M. Peek, Chem. Phys., 12, 831 (1976).
30. D. R. Bates and T. R. Carson, Proc. Roy Soc. London Ser.A, 234, 207 (1956).
31. J. W. Stearns, K. H. Berkner, R. V. Pyle, B. P. Briegleb, and M. L. Warren, Phys. Rev., A4, 1960 (1971).
32. Proceedings of the Workshop on Physics with Fast Molecular-Ion Beams, Argonne National Laboratory, Argonne, Il., August 20-21, 1979, D. S. Gemmell, ed., Physics Division Informal Report ANL/PHY-79-3 (August, 1979).
33. G. Goldring, Y. Eisen, P. Thieberger, and H. Wegner, p. 27 of Ref. 32.
34. M. Algranati, A. Faibis, R. Kaim, and Z. Vager, Nucl. Instrum. Methods, 164, 615 (1979).
35. R. C. Woods, these proceedings.
36. M. J. Gaillard, D. S. Gemmell, G. Goldring, I. Levine, W. J. Pietsch, J.-C. Poizat, A. J. Ratkowski, J. Remillieux, Z. Vager, and B. J. Zabransky, Phys. Rev., A17, 1797 (1978).
37. See, for example, L. Salmon and R. D. Poshusta, J. Chem. Phys., 59, 3497 (1973) and references contained therein.
38. D. S. Gemmell, E. P. Kanter, and W. J. Pietsch, Chem. Phys. Lett., 55, 331 (1978).
39. G. Herzberg, Electronic spectra of polyatomic molecules, Van Nostrand, Princeton (1950).
40. D. S. Gemmell, E. P. Kanter, and W. J. Pietsch, J. Chem. Phys., 72, 6818 (1980).
41. R. N. Dixon, Molec. Phys., 20, 113 (1971).
42. H. Lew and I. Heiber, J. Chem. Phys., 58, 1246 (1973); H. Lew, Can. J. Phys., 54, 2028 (1976).
43. A. B. Wittkower and H. D. Betz, Atomic Data, 5, 113 (1973).
44. G. D. Carney, Molec. Phys., 39, 923 (1980).
45. D. L. Smith and J. H. Futrell, J. Phys., B8, 803 (1975).
46. Grady D. Carney, to be published.
47. A. Edwards, R. Kutina, N. Cue, D. S. Gemmell, K. Inglis, and E. P. Kanter, to be published.
48. G. H. Dunn, Phys. Rev., 172, 1 (1968); JILA Report No. 92, (1968) unpublished.

A PROPOSED MECHANISM FOR FORMING SOME LARGER MOLECULES IN DENSE INTERSTELLAR CLOUDS

R. Claude Woods

Department of Chemistry
University of Wisconsin
Madison, Wisconsin

About 55 molecules, ranging in complexity from diatomics to the 11 atom species HC_9N, have now been firmly identified in the interstellar medium (ISM), most of them in so-called dense clouds (10^4 - $10^6/cm^3$). The general nature of the ISM and some pertinent chemical reactions have been reviewed by Watson [1]. There is now fairly wide agreement that the synthesis of many of the simpler molecules and ions, e.g., NH_3, HC_2H, HCN or HCO^+, can be relatively well understood in terms of a kinetic scheme involving ion-molecule reactions in the gas phase, along the lines proposed several years ago by Herbst and Klemperer [2]. For the larger and more complicated molecules the chemistry has not been explained in any great detail, and many astronomers are even skeptical that any satisfactory explanation in terms of ion-molecule reactions is possible. In this lecture a mechanism for forming a number of these larger molecules will be proposed, and its plausibility and consequences will be considered. Sufficient information to either firmly establish or to reject this mechanism does not appear to be available at this time, but several experiments and calculations that would clearly be pivotal in rendering such a verdict can be readily suggested. The model does indeed utilize gas phase ion molecule reactions, and it seems well connected with the subject of this conference inasmuch as structural isomerism of the ionic and neutral species plays a central role.

At first glance, when one considers the large number of molecules in the ISM and the even larger number of reactions that can couple them, the situation seems hopelessly complex, as if everything can happen and probably does. On closer consideration, however, one can see that the tremendous disparity in concentration between the simple and complex molecules and the limited magnitudes

of the rate constants for even fast ion-molecule reactions severely restrict the number of reactions that can play a significant role. Generally speaking, in any reaction of importance either the ion or the neutral reactant must be very abundant, and thus very simple. In our mechanism the most abundant ion of them all, C^+, serves as the main ionic reagent, while very simple species like methane and ammonia are the key neutral reactants. The formation of large molecules, which are orders of magnitude less abundant than small ones, generally constitutes a negligible loss mechanism for the small molecules, whose chemistry, therefore, can be and to a large extent has been explained without reference to the larger ones. In our consideration then we can consider that the concentrations of simple reagent species, e.g., H_2, H_3^+, He^+, C^+, CH_4, NH_3, HCN, e^-, are fixed parameters, decoupled from the kinetics of the larger species, and this assumption greatly simplifies the modeling problem mathematically. Among the most interesting of the large molecules are cyanoacetylene HC_3N and the cyanopolyacetylenes $H(C_2)_nCN$ (n = 2,3,4) and it was upon these that our attention was initially focused. The model we propose, however, also would explain the formation of several other important molecules (CH_3CN, CH_2CHCN, etc.) and can be readily extended to other families, especially the hydrocarbon analogs.

We begin with the two isomers HCN and HNC, which are more or less equally abundant in the ISM. This fact is attributed to their common parentage in the dissociative recombination of the ion $HCNH^+$. The latter has never been observed directly in the ISM, and we attribute this to its very low dipole moment, which we have calculated by the configuration interaction method [3]. The initial step considered is

$$HCN + C^+ \rightarrow CNC^+ + H \qquad (1)$$

and

$$HNC + C^+ \rightarrow CCN^+ + H \qquad (2)$$

The ion CCN^+ is then proposed to react according to

$$CCN^+ + CH_4 \rightarrow HC_3NH^+ + H_2 \quad , \qquad (3)$$

followed by dissociative recombination to form cyanoacetylene.

$$HC_3NH^+ + e^- \rightarrow HC_3N + H \quad . \qquad (4)$$

To summarize the kinetic analysis we can say that if (2) and (3) proceed at a typical fast ion-molecule reaction rate (no activation energy) then this sequence can readily account for the cyanoacetylene abundance that is observed in the ISM. Such calculations are necessarily of order of magnitude precision only. One

may notice that the stable isomer HC_3N, comes from the (thermodynamically) unstable isomer, HNC, while the unstable isomer, HC_2NC, would result from the analogous sequence beginning with the stable isomer, HCN. Continuing the same line of reasoning we see that HNC_3 can also be formed from the same reactants shown in (4)

$$HC_3NH^+ + e^- \quad HNC_3 + H \tag{5}$$

This then can react with C^+

$$HNC_3 + C^+ \rightarrow NC_4^+ + H \tag{6}$$

and the resultant ion can again react with methane (analogously to (3))

$$NC_4^+ + CH_4 \rightarrow HC_5NH^+ + H_2 \quad . \tag{7}$$

Of course, this ion (HC_5NH^+) can dissociatively recombine to form the stable isomer HC_5N or the carbene isomer, HNC_5, which in its turn would lead in a similar sequence to HC_7N or HNC_7.

$$HC_5NH^+ + e^- \rightarrow HC_5N + H \tag{8}$$

or

$$HC_5NH^+ + e^- \rightarrow HNC_5 + H \quad . \tag{9}$$

Again, the numerical details can be summarized by saying that if (6) and (7) proceed without activation energy the abundances of the cyanopolyacetylenes in the ISM can be explained to order of magnitude precision.

Side reactions in the sequence are inevitable and themselves lead to the synthesis of interesting molecules. Radiative association of CCN^+ with H_2 leads to CH_2CN^+

$$CCN^+ + H_2 \rightarrow CH_2CN^+ \tag{10}$$

and this in turn can react with methane to form CH_3CHCN^+

$$CH_2CN^+ + CH_4 \rightarrow CH_3CHCN^+ + H_2 \quad . \tag{11}$$

Methyl, ethyl, or vinyl cyanide have all been observed in the ISM and all their abundances can be explained semi-quantitatively by combinations of radiative associations (with H_2) and dissociative recombinations with the product ions in (10) and (11). If one begins with acetylene instead of HCN or HNC, one proceeds to diacetylene as follows:

$$HC_2H + C^+ \rightarrow HC_3^+ + H \quad (12)$$

$$HC_3^+ + CH_4 \rightarrow HC_4H_2^+ + H_2 \quad (13)$$

$$HC_4H_2^+ + e^- \rightarrow HC_4H \quad (14)$$

A side reaction in this sequence is another potential source of cyanoacetylene

$$HC_3^+ + NH_3 \rightarrow HC_3NH^+ + H_2 \quad (15)$$

(followed by (4) of course). In general, a variety of species with the same heavy atom framework but differing charges or numbers of H atoms can be formed by combinations of reactions with H_2, H_3^+, e^-, or He^+. The critical steps then in interstellar molecule synthesis are the chain building steps. We are suggesting that C^+ is the primary reagent in this chain building, an assertion made plausible by the fact that C^+ is the most abundant ion in the ISM, orders of magnitude more dense than the molecular ions. Even C^+, however, does not lead to chain building in reactions with most organic molecules. With saturated molecules the hydrogen abstraction channel or charge exchange channel are favored. For example, Adams and Smith [4] report

$$C^+ + CH_3NH_2 \rightarrow \begin{cases} CH_4N^+ + CH & (35\%) \\ CH_5N^+ + C & (65\%) \end{cases} \quad (16)$$

This explains the key role played by the highly unsaturated species like HCN, HNC, HC_2H, and HC_3N in the chemistry of the dense clouds.

In addition to the sample kinetic modeling calculations, we have been doing certain *ab initio* quantum chemical calculations to substantiate or otherwise investigate this reaction scheme. We have carried out [5] double zeta SCF calculations of the structures and CI calculations of the dipole moments of the molecules HNC_3, HCCNC, $HCCCNH^+$, NCNC, $NCCNH^+$, in hopes that their microwave spectra could be observed either in the laboratory or in the interstellar medium. Such observation in the ISM would yield very important clues to the nature of the synthetic process. The computed dipole moments determine predicted microwave absorption intensities and also enter into the calculations of several rate constants in known theories of ion-molecule reactions. We have also done DZ-SCF, DZP-SCF, and DZP-CI calculations on the crucial pair of isomers CCN^+ and CNC^+ [6]. In that work attention has been focused on the thermochemistry. A theoretical isomerization energy of 49 kcal/mole has been obtained (CNC^+ is the thermodynamically stable form) and heats of formations for both species

have been obtained from combining both experimental and theoretical information. Previously unexplained mass spectral appearance potential data [7] for C_2N^+ have been interpreted in terms of the existence of these two isomeric forms. Most importantly, reaction (2) has been demonstrated with some certainty to be exothermic, as it must be if the mechanism discussed here is to have any validity. Future work of greatest significance will be computation of a potential surface for reaction (2) to see if there is an activation barrier and a laboratory measurement of the rate constant for reaction (3), which appears to be a feasible experiment.

REFERENCES

1. W. D. Watson, Rev. Mod. Phys. 48, 513 (1976).
2. E. Herbst and W. Klemperer, Ap. J. 185, 505 (1973).
3. N. N. Haese and R. C. Woods, Chem. Phys. Lett. 61, 396 (1979).
4. N. G. Adams and D. Smith, Chem. Phys. Lett. 54, 530 (1978).
5. N. N. Haese and R. C. Woods, J. Chem. Phys. 73, 4521 (1980).
6. N. N. Haese and R. C. Woods, Ap. J. Lett. 246, 51 (1981).
7. V. H. Dibeler, R. M. Reese, and J. L. Franklin, J. Am. Chem. Soc. 83, 1813 (1961).

COMPARATIVE STUDY OF THE REACTIVITY OF GASEOUS IONS IN SELECTED INTERNAL ENERGY STATES BY USING A TANDEM AND A TRIPLE MASS SPECTROMETER

Imre Szabo

Division of Physical Chemistry 2
Chemical Center
The Lund Institute of Technology
P. O. Box 740
S-22007 Lund 7, Sweden

1. Introduction

Much of our knowledge of the structure, energetics, and other physical and chemical properties of molecular and fragment ions derives from the study of the various ways in which electromagnetic radiation and atomic particles can interact with matter. An interaction or a reaction implies that the reactants are transformed into final products, as a result of exchange of energy and particles between them. For a complete understanding of a particular interaction, we need to know the structure and energetics of the reactants, intermediate products, and final products involved.

As far as the study of the formation, reactions, and other characteristics of ionic processes occurring in the gas phase at low interaction energies are concerned, the ionization of molecules (or atoms) is usually induced by electron, photon or ion impact. Interactions of this kind may produce electrons, photons, ions, and neutrals. There are various kinds of spectroscopic methods for studying such interactions [1-7], in order to characterize ions with regard to structure and energetics.

In our laboratory continuous beams of energy selected ions are produced by ionizing neutral molecules in reactions with slow positive ions in a tandem mass spectrometer. This method of ionization is called ion impact and has been introduced by Lindholm [8]. First, it has been used only for studying the unimolecular dissociation of state selected molecular ions as a function of energy transferred to the reactant molecule in the process of its ionization. It has

been shown later by the present author [9-17] that the ion impact method is suited also for studying the subsequent reactions of state selected molecular and fragment ions with neutral molecules simply by increasing the density of molecules in the reaction chamber.

The following characteristics of consecutive ion-molecule reactions have been demonstrated experimentally by us by using a tandem mass spectrometer:

1. The reaction pathways initiated by a specific molecular or fragment ion, as well as the rate constants for the reactions involved are dependent on the amount of internal energy of those molecular ions from which the first generation of ions is formed.

2. One particular ion can be formed by two or more reactions of the same or different kinetic order depending upon the internal energy of the first generation of molecular and fragment ions.

3. The same molecular or fragment ion can be formed both in an unexcited and in an excited electronic state and can initiate consecutive ion-molecule reactions of different kinds.

The main advantage of our method is that consecutive reactions of molecular and fragment ions with molecules can be studied at known and well defined values of the internal energy of those molecular ions which form the first generation of ions.

We have recently modified our tandem instrument into a triple mass spectrometer consisting of three mass spectrometers in series. Thus, the number of subsequent ion beams is three. The second mass spectrometer of this triple instrument is used for producing a kinetic energy and state selected beam of ions by ion impact. This ion beam may consist of molecular ions, fragment ions or ions produced in consecutive ion-molecule reactions in a pure substance or in a mixture in the gas phase after ionization by ion-impact. The ion beam produced in this way is then used to ionize a "test substance" being in the gas phase in the ion source of the third mass spectrometer. Thus, a tandem or a triple mass spectrometer is suited for preparing beams of energy selected molecular and fragment ions and for studying the subsequent unimolecular and bimolecular reactions of a molecular ion in a specific electronic state. This is the first time that successful experiments with a triple mass spectrometer are reported.

The organization of this paper is as follows. Section 2 provides a brief comparison of the ionization of molecules by ion, electron, and photon impact. The purpose is to discuss the ability of these techniques for producing beams of state selected molecular and fragment ions. The principle of tandem mass spectrom-

eters and the various measurement techniques are summarized in Section 3. The various types of triple mass spectrometers and some of their possible applications in gas phase ion chemistry are discussed in Section 4. Section 5 summarizes our results obtained recently by comparing the reactivity of some gaseous ions by using a tandem and a triple mass spectrometer. The ions whose reactivity has been studied are as follows: CH_2^+ from CH_4, $C_2H_2^+$ from C_2H_2, $C_2H_2^+$ from C_2H_4 and CO^+ from CO. Some conclusions and a summary of research in progress are given in Section 6.

2. Basic Aspects for the Production of Ions in Selected Internal Energy States

2.1. The Need for Monoenergetic Ionization

The electronic state and the fragmentation behavior of a molecular ion formed upon ionization are determined by the amount of energy available in the process of initial ionization. In addition, the subsequent reactions of a given molecular or fragment ion with a given molecule can vary considerably depending upon the excitation energy of the parent molecular ion [9-17]. Consequently, the essential point in studying ionization phenomena and ionic processes is, that we need to know the identity and energy of the interacting particles and final products as well as the ways in which the available energy and particles will be transferred in the course of the reaction considered. This explains the need of experimental methods which are capable of creating monoenergetic ionization of molecules (and atoms) as well as monoenergetic excitation of molecular ions. The ionization is said to be monoenergetic, when each molecule that becomes ionized, receives the same amount of energy in the process of ionization. Molecular ions of the same kind are said to be monoenergetically excited if each of them retains the same amount of excitation energy, immediately after it has been created. When the ionization and excitation are monoenergetic, the distribution of energy deposited on to the reactant molecules as well as the distribution of excitation energy transferred on to the molecular ions created will be characterized by Dirac-delta functions. Monoenergetic ionization is essential for the understanding of experiments related to the formation, structure, energetics, and reactions of molecular and fragment ions.

Ionization of molecules in reactions with slow incident positive ions in a tandem mass spectrometer was the first method by which molecular ions and fragment ions could be prepared in selected internal energy states, and their subsequent unimolecular and bimolecular reactions investigated. The use of tandem mass spectrometers has been introduced by Lindholm [8] in order to obtain quantitative data on the dissociation of molecular ions in selected internal energy states. The technique was developed in response to the need for better understanding of the mass spectra of organic

molecules in terms of the quasi equilibrium theory, QET [18, 19]. The basic aspects of preparing molecular ions in selected internal energy states by using the ion-impact method of ionization, will be discussed in the next section.

When using electron or photon impact for producing ions, monoenergetic ionization is possible only at the ionization threshold (i.e., with electrons and photons whose energy equals the first ionization potential of the target molecule). If the energy of the ionizing electrons or photons is higher, monoenergetic ionization of the target molecules will be prevented by occurrence of autoionization and by the transfer of various amounts of kinetic energy to the electrons ejected from those molecules which become ionized. It follows from our discussion in Sections 2.3 and 2.4. The possibility of selecting molecular ions in selected internal energy states by using various coincidence techniques will be outlined in Section 2.5.

2.2 Ion Impact

In a tandem or triple mass spectrometer monoenergetic ionization of neutral molecules, M, in their ground electronic state can be accomplished by allowing a monoenergetic beam of slow reagent ions, X^+, to ionize molecules in one of four distinct types of ion-molecule reactions. These are as follows.

1. Electron or charge transfer:

$$X^+ + M \rightarrow X + M^+ \qquad (2.1)$$

2. Proton transfer:

$$X^+ + M \rightarrow (X\text{-}1) + MH^+ \qquad (2.2)$$

3. Hydride ion transfer:

$$X^+ + M \rightarrow XH + (M\text{-}1)^+ \qquad (2.3)$$

4. Ion-molecular association:

$$X^+ + M \rightarrow XM^+ \qquad (2.4)$$

The last mentioned reaction results in the formation of a collision complex. Each of the ionized fragments M^+, MH^+, $(M\text{-}1)^+$ and XM^+ may dissociate unimolecularly into a primary fragment ion in a variety of ways depending upon the internal energy content (electronic state) of the ion being considered.

In the case of electron impact, the reactant ion X^+ extracts only an electron from the reactant molecule to give a molecular ion.

If the relative kinetic energy of the interacting ion and molecule is very low (less than a few electron volts), the transfer of kinetic energy of reactants into internal energy or vice versa is negligible and the maximum energy available for the reaction equals the recombination energy, E_{re} of the reactant ion. E_{re} means the energy that is released from the reactant ion when it is neutralized ($X^+ + e \rightarrow X$) by acquiring an electron (e) of negligible kinetic energy from the reactant molecule. When transfer of kinetic energy can be avoided, the internal excitation energy, E_i, of the molecular ion formed in the electron transfer process can be expressed as:

$$E_i = E_{re} - E_{ip} \tag{2.5}$$

where E_{ip} is the ionization potential of the reactant molecule.

If the reactant ion has only one recombination energy, the distribution of energy transferred on to the reacting molecules, as well as the distribution of internal excitation energy of the molecular ions immediately after they have been created, may be characterized by a Dirac-delta function each, located at the energies E_{re} and E_i, respectively. Reactant ions having different recombination energies, will acquire electrons from different energy levels of the reactant molecule and by doing so they will produce molecular ions in different electronic states. The energy differences between the ground state of the reactant molecule and the electronic states of the molecular ion are just the ionization energies, E_{ip}, that can be observed in the photoelectron spectrum of the reactant molecule. The dissociation of molecular ions in specific internal energy states (i.e., the breakdown diagram showing the mass spectrum as a function of internal energy) can be determined by ionizing the molecule being considered with a series of incident positive ions whose recombination energy $E_{re} \geq E_{ip}$ (cf. [8]).

The advantage of using reactions with ions resulting in electron transfer rather than electron impact or photon impact to ionize the molecule is that the excitation energy E_i is known and that it is possible to form the molecular ion both in ground and in various excited ionic states with different degrees of vibrational excitation. The decomposition processes of excited molecular ions are determined by the amount of their internal excitation energy, E_i, but appears to be independent of how the ions are created and excited, i.e., whether in electron transfer reactions of slow reactant ions or by electron bombardment or by photoionization.

The relationship between the ionization and excitation process for mass spectrometry with electron transfer and photoelectron spectroscopy has been discussed by Lindholm [8] and Rabalais [20]. If there are accessible energetic states in the reactant molecule at the recombination energy of the reactant ion, then the molecule will be ionized by electron transfer and the accompanying recombination

process will be governed by the same selection rules as spectroscopic transitions. It implies also that the cross section for ionization by electron transfer will be large if there is an intense band in the photoelectron spectrum of the reactant molecule just at the same energy as the recombination energy of the reactant ion and vice versa. Thus the cross section as a function of energy (and the energy deposition function for ionization by electron transfer) should follow qualitatively the envelope of the photoelectron spectrum of the reactant molecule.

This correlation between the mass spectrum determined by using ion-impact and the photoelectron spectrum of the reactant molecule allows an assessment of which states of the molecular ion lead to the formation of fragment ions by unimolecular dissociation and what the nature of these fragment ions are. A knowledge of the identity and relative intensity of the ionized fragments formed by dissociation of molecular ions in a particular electronic state can be correlated with the bonding characteristics of the electrons ejected in forming that state. Benzene is the largest molecule for which the correlation between ion-impact mass spectra and photoelectron spectra has been discussed in detail. (Cf. [8] and p. 290 and p. 365 in [20].)

Ion-impact mass spectra may be also obtained by ionizing sample molecules in proton and hydride ion transfer reactions provided that these reactions are energetically allowed. The energy transferred to the molecule in the ionization process is relatively low which results in the formation of a quasi-molecular ion $(M + 1)^+$ and $(M-1)^+$, respectively. It will be determined by the exothermicity of the ionizing reaction whether or not the resultant ion will dissociate.

The investigation of the occurrence or non-occurrence of ion-molecule reactions resulting from proton transfer, hydride ion transfer or ion-molecule association gives information about the energetics of the ions and molecules involved. The cross section for ionization as measured in a tandem mass spectrometer of perpendicular type is usually much lower than that for ionization by electron transfer. The various modes of ionization by ion-impact are also important for the analytical use of chemical ionization in single source and tandem mass spectrometers [21].

The measurement of mass spectra induced by electron-transfer reactions allows the direct determination of breakdown graphs. One shortcoming of the method is that the dissociation of molecular ions in selected energetic states cannot be investigated as a continuous function of their internal energy. This is because the recombination energies are known only for about ca 40 positive ions [8].

Ionization by electron transfer involves an electron jump without momentum transfer at relatively large distances between the two

interacting species. This type of ionizing reaction is called resonant or near-resonant charge transfer and has generally very large cross-sections, σ, due to a long-range attractive force between the charge on the ion and the dipole induced by the reactant ion on the reactant molecule immediately prior to ionization [21]. The rate coefficient

$$k = v \cdot \sigma$$

where v is the relative velocity of the reacting species. It is generally independent of temperature, i.e., the activation energy of the reaction is zero and the reaction occurs at almost every collision. Cross section (or rate constant) and product distribution measurement [23-27] implies that direct conversion of electronic energy into kinetic energy of the products is generally inefficient. However, if there is no photoelectron band just at the energy that equals the recombination energy of the reactant ion, the interaction between the reactant ion and molecule may be strong enough to introduce additional angular momentum into the products and to allow part of the internal energy of the reactants to be converted into kinetic energy of the products. To explain why molecular and/or fragment ions may be observed in this case, distorsion of the neutral molecule prior to ionization and/or population of energy states of the molecular ion not appearing in the photoelectron spectrum have been proposed [23-26]. (Cf. [28, 29].)

The cross sections for the formation of ions acquiring some additional kinetic energy are relatively small. These ions will be scattered preferably in the direction of motion of the reactant ions and discriminated very effectively in a tandem mass spectrometer of perpendicular type [8]. When there is energy resonance (or near-resonance) for ionization, the cross section will be relatively large and the product ions will be scattered first of all in a direction perpendicularly to the beam of reactant ions and detected with high efficiency in a tandem mass spectrometer of perpendicular type.

2.3 Electron Impact

The ionization of molecules (M) by collisions with electrons (e) of about 50-100 eV kinetic energy may result in the formation of charged species in the following ways.

1. Direct ionization:

$$M + e \rightarrow M^+ + 2e$$

$$M^+ + e \rightarrow M^{n+} + (n + 1)e$$

2. Direct ionization with fragmentation:

$$M + e \rightarrow M^+ + 2e \rightarrow X^+ + Y + 2e$$

3. Autoionization, also sometimes direct ionization followed by further autoionization:

$$M + e \rightarrow M^{**} + e \rightarrow M^+ + 2e$$

$$M + e \rightarrow M^{+**} + 2e \rightarrow M^{2+} + 3e$$

4. Excitation, followed by ion pair formation:

$$M + e \rightarrow M^* + e \rightarrow X^+ + Y^- + e$$

5. Electron capture, usually followed by fragmentation:

$$M + e \rightarrow M^- \rightarrow X^- + Y$$

Each of these processes can take place simultaneously, and the electron ejected from those molecules which become ionized, may carry away various amounts of kinetic energy. Because of this, monoenergetic ionization of molecules is not possible even if the beam of ionizing electrons would be monoenergetic. Therefore, electron impact is less suited for studying the formation and energetics of molecules and fragment ions. Another disadvantage of this technique is that conventional electron beams have a large energy spread due to the Boltzmann distribution of the electrons emitted by hot filaments. Double ionization of molecules by electron impact could be investigated by measuring the two positive single charged ion fragments in coincidence [30]. Energy selected ionic states in atoms or molecules according to process one and two above, can also be studied by detecting the two outgoing electrons in coincidence after analysis of their energies and momenta [31].

2.4. Photoionization

With the advent of photoionization and, more recently, photoelectron spectroscopy methods [32-34, 20, 29] there has been less interest in the use of electron impact ionization in the study of structure and energetics of molecules and ions. Photoionization and photoelectron spectroscopy methods are capable of giving detailed information about molecular energetics with great precision in energy. However, the process of ionization induced by photon impact may also be complicated by the occurrence of autoionization and ion pair formation because a molecule may be excited by the impinging photon (like by an electron) to a superexcited electronic or vibrational state lying above the lowest ionic state. This excited state of the molecule may then undergo a radiationless decay either into an ion and an electron (of the same total energy) by

autoionization, or by ion pair formation, or eventually by predissociation into neutral fragments. Thus the simultaneous occurrence of all of these processes may cause difficulties in the differentiation of molecular and fragment ions formed by direct ionization and by other ionization processes.

The resonant photoionization technique, also called threshold or zero kinetic energy photoelectron spectroscopy [33, 34, 29] overcomes this problem by varying the photon energy and detecting only those photoelectrons with zero kinetic energy (threshold electrons). In this case the photon energy corresponds directly to the energy of the transition to an accessible ionic state, and the electrons arising from autoionization will not cause interference.

2.5. State Selection of Ions by Coincidence Techniques

When using monoenergetic electrons or photons to create ions, the electron ejected from the target molecule (or atom) may carry away a continuous amount of kinetic energy. Therefore, neither the ionization of molecules nor the excitation of molecular ions will be monoenergetic. Hence the energy deposited during the ionization process on to the target molecules as well as the excitation energy transferred on to the molecular ions, will be distributed continuously over a wide energy range. (Cf. p. 12 in Ref. [19].)

Under such circumstances, the fragmentation and characteristics of positive molecular ions can be studied only with coincidence-methods such as coincidence spectroscopy of ions [30] and electrons [31] produced by electron impact ionization of atoms or molecules, photoion-photoelectron coincidence spectroscopy (PIPECO) [33, 34], and the related threshold photoelectron spectroscopy (TPES) [34, 29]. (Threshold electrons are those which are formed with zero initial kinetic energy.)

The coincidence measurements give four types of data: (1) threshold electron spectra, (2) breakdown diagrams (i.e., mass spectra as a function of internal energy of the molecular ion), (3) time-dependent breakdown diagrams, and (4) kinetic energy release on fragmentation.

The bases of each coincidence experiment is the conservation of energy and momentum in the photoionization process. As a result, the ion internal energy E_i is given by the relationship:

$$E_i = h\nu - E_e(1 + m_e/M_i)$$

where $h\nu$ is the energy of the impinging photon, E_e is the kinetic energy of the ejected electron and m_e and M_i are the electron and ion masses, respectively. Product ions with a given internal energy E_i can be selected from the assembly of all of the ions being formed

in different energetic states, simply by detecting only those resultant ions which are in (delayed) coincidence with electrons of energy E_e.

In the varous kinds of coincidence experiments there are three measurable quantities: the ion signal, the electron signal, and the coincidence signal. Most of the coincidence studies deal with unimolecular reactions and have the ability to state select ions with energy resolution as low as about 5 meV. However, the initial preparation of energy selected ions by using electron or photon impact has very low efficiency which does not allow to prepare intense beams of energy selected ions and to study the subsequent reactions of an ion in a specific state, selected by using the coincidence technique. Consequently, the coincidence technique seems not to be suited for preparing beams of energy selected ions. Intense beams of such ions would allow to investigate the photo-dissociation of energy selected ions (cf. [35]), the photoemission of energy selected ions after excitation by electron impact (cf. [36]), and the reactions of energy selected ions with neutral molecules.

Contrary to these difficulties associated with the electron and photon impact methods of ionization, the ionization of molecules (or atoms) by ion-impact has several advantages. Ionization induced by reactions with slow positive ions in a tandem and in a triple mass spectrometer allows to prepare beams of ions in selected internal energy states and to study the subsequent unimolecular and bimolecular reactions of these ions. The same ion may be prepared in a great number of different ion-molecule reactions. In addition, a product ion may be allowed to react with an unlimited number of neutral molecules in order to get information about the energetics and reactivity of the ion considered. Differences in internal energy states of a given ion can be demonstrated by comparing the reactions of this ion with one or more neutral molecules under identical experimental conditions. As the reactivity of a gas phase ion can be studied at various amount of internal energy of this ion, the study of the reactions of this ion by using a tandem and a triple mass spectrometer constitutes a useful experimental foundation of every theoretical study of the structure energetics and reactivity of gas phase ions.

3. Tandem Mass Spectrometers: Principles and Measurement Techniques

The earliest tandem mass spectrometer was built by Lindholm [37], and since that time several of these instruments have been constructed [8, 38]. There are two basic types of fixed angle tandem mass spectrometers: perpendicular and longitudinal. In an instrument of perpendicular type the beam of product ions is analyzed at right angles to the direction of the reactant ion beam. In an instrument of longitudinal type the beam of reactant and product ions coincide.

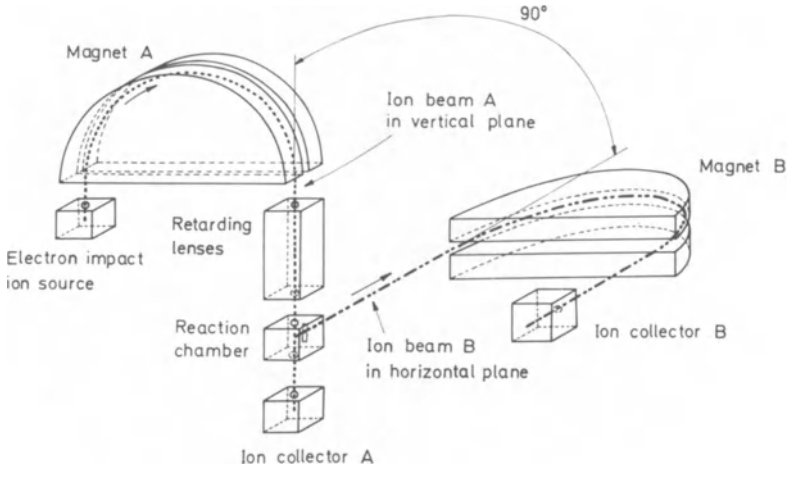

Fig. 1. Principle of tandem mass spectrometer of perpendicular type.

3.1. Tandem Mass Spectrometer of Perpendicular Type

In this instrument the second mass spectrometer is arranged to discriminate against product ions which acquire appreciable forward momentum in the interaction. Such a product ion will be carried by its momentum in a direction parallel to the reactant ion beam and it will not be collected. When the kinetic energy of the reactant ions is less than a few electron volts, the energy imparted to the target molecule may be taken to be equal to the recombination energy of the reactant ion used because the kinetic energy of the reactant ion has negligible effect on the ionization process. This is especially the case when the ionizing reaction is exothermic (resonant or near-resonant charge transfer). The mass spectrum for a given molecule is then entirely determined by the recombination energy and is independent of the composition of the reactant ion.

The breakdown diagrams obtained for a number of compounds by this technique are in fair agreement with those obtained from electron and photon impact studies [8, 12, 20].

A schematic diagram of the tandem mass spectrometer used in our laboratory is shown in Fig. 1. The reactant ions are produced in the electron impact ion source of the first mass spectrometer, accelerated to some appropriate energy between 1000 and 5000 eV, separated according to their mass-to-charge ratios in magnet A, retarded to a final energy between 900 and 2 eV in an electrostatic retarding lens system [37], and formed into a well-focused and collimated beam of reactant ions. These ions enter then the reaction (or collision) chamber and ionize molecules of the sample being

there. Incident ions which do not react within the collision chamber are detected with the help of "Ion collector A" (Faraday-cup) and a subsequent electrometer amplifier. The product ions (formed preferably by electron transfer reactions, cf. Section 2.2) are extracted out of the collision chamber by a very weak static electric field (ca. 1 V/cm) in a direction perpendicular to the beam of reactant ions, accelerated in a static electric field to a final energy between 2000 and 5000 eV, separated according to their mass-to-charge ratios in magnet B, and detected after amplification with the help of an electron multiplier and electrometer (Keithley, Model 417).

The collision chamber is filled with a gaseous sample whose pressure can be increased up to about 10^{-2} torr. The pressure is measured with an MKS Baratron capacitance manometer (Head 144H-1). For the evaluation of rate constants, the instrument is regularly recalibrated with the reaction

$$CH_4^+ + CH_4 \overset{k}{\rightarrow} CH_3 + CH_5^+ \qquad (3.1)$$

On the occasion of calibration the methane gas being at room temperature is ionized with Xe^+. The rate constant, $k = 0.9 \cdot 10^{-9}$ cm^3 $mole^{-1}$ s^{-1}, is taken from Ryan [39] and refers to 1 eV terminal kinetic energy and 18 eV ionizing electrons.

The gaseous samples used are usually distilled and repeatedly frozen and thawed under pumping.

3.2. Tandem Mass Spectrometer of Longitudinal Type

In the reaction chamber of a tandem mass spectrometer of longitudinal type the beams of reactant and product ions coincide. A schematic diagram of such an instrument is shown in Fig. 2. By employing this configuration, the product ions of mass or momentum transfer processes as well as the kinematic details of ion-molecule reactions may be observed more efficiently [38, 40-46] at relative kinetic energies from a few tenths of eV to many thousands of eV. The results summarized below in this section support the statement that first of all exothermic ion-molecule reactions occurring at low translational energies (less than a few eV) are suited for producing beams of ions in selected electronic states with various vibrational excitations.

The most interesting energy range for the production of beams of ions in selected internal energy states by ion-molecule reactions is that lying at or below the characteristic strength of a chemical bond ($\sim$5 eV). At these energies the cross section for ionization by resonant or near-resonant ion-molecule reactions (ion-dipole interactions) is very high and increases when decreasing the relative kinetic energy between the reactant ion and molecule. On the other

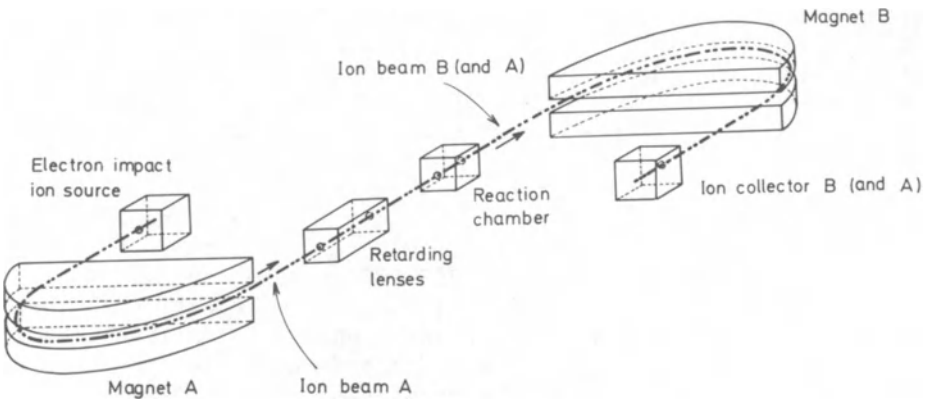

Fig. 2. Principle of tandem mass spectrometer of longitudinal type.

hand, an endothermic ion-molecule reaction exhibits an energy barrier which must be surmounted if the reaction is to occur. The energy threshold for such a reaction is the heat of the reaction (p. 272 in Ref. [46]). The cross-section is zero at kinetic energies below threshold, rises steeply at the threshold, goes through a maximum with increasing kinetic energy and then decreases. If a reaction exhibits an energy barrier and is endothermic, the threshold for subsequent dissociation of the product ion into an ion and neutral is correspondingly high.

Comparison of values and energy dependence of cross-sections for exothermic and endothermic dissociative charge transfer reactions of the same molecule has been made only for relatively few reactions (see pp. 354-374 in Ref. [22] and pp. 271-330 in Ref. [46]). The highest value of cross-section for endothermic reactions of the same molecule is throughout lower, usually by at least one order of magnitude, than those for exothermic reactions.

Crossed ion-molecule beam experiments at kinetic energies around and slightly above 1 eV reveal that most ion-molecule reactions proceed through formation of a collision complex or through an electron jump mechanism at these energies due to an attractive long range ion-dipole interaction potential ([43-46]). For exothermic reactions (such as $CH_4^+ + CH_4 \rightarrow CH_3 + CH_5^+$) occurring at low relative kinetic energies (less than a few electron volts) excellent agreement has been found between experiment [48, 49] and predictions of the classical polarization theory for ion-dipole interactions [50]. Recent modifications of this theory predict low energy rate constants and cross sections and their dependence on relative kinetic energy and temperature also for target molecules with significant permanent dipole moments in fair agreement with experiments [50]. As kinetic energy of the reactant ion increases

above ca 4-5 eV the cross section for exothermic ion molecule reactions may rise because of a change in reaction mechanism. The ion-dipole interaction model which operates at very low kinetic energies may be surmounted by the electron jump model and thereafter by the stripping model [42-45] when the kinetic energy increases.

Results of crossed ion-molecule beam experiments have brought Gentry [46] to the conclusion that it would be surprising if very low kinetic energies had much effect on reaction probability for very exothermic reactions (see pp. 247-252 in Ref. [45] and Ref. [52]). Results obtained earlier [51] with photoionization also suggest that the conversion of translational energy to internal energy to drive reactions is relatively inefficient in simple systems. Experiments on methane and some larger polyatomic molecules by using tandem mass spectrometers and pulsed single-ion source instruments have shown that at low kinetic energies (<4 eV) the translational energy has no effect on exothermic electron, proton, hydride ion transfer, and ion association reactions. However, increased decomposition of product ions at higher impacting ion velocity is clear evidence for the conversion of kinetic energy to internal energy. Similar results have also been obtained by others (see [53], pp. 354-374 in Ref. [22], and Ref. [54]).

Kinetic-to-internal energy transfer at energies above the threshold may open up some endothermic reaction channel(s) of direct collision induced dissociation of molecular and fragment ions or cause dissociation of collision complexes. Collision induced dissociation studies indicate that the energy required for such dissociations can be derived from electronic, vibronic, and/or translational energies of the collision partners [38]. The fractional yield of ions formed in such endothermic reaction channels is expected to be low if at least one resonant or near reasonant exothermic reaction channel is accessible for the same reactant ion. This consideration is confirmed by a recent study of consecutive ion molecule reactions [55] in a few gases as a function of pressure by ionizing with reactant ions whose kinetic energy was preselected subsequently at ca 2, 10, 30, 100, and 900 eV. The appearance of one or more smaller fragments may be seen at higher impacting ion velocity but this is a minor feature and seems similar to the effects of electron energy on fragmentation patterns of ions well above threshold for all dissociation processes [56]. The results show convincingly that the ion kinetic energy has very little effect on product ion distribution if the ionizing reaction is exothermic [55].

In conclusion, the above mentioned results [40-55] strongly suggest that a tandem mass spectrometer of longitudinal type may be used for producing beams of ions in selected electronic states. Furthermore, the transfer of kinetic-to-internal energy will not have significant effect on the energetic states of the product ions

as long as the ionization of molecules in the reaction chamber is accomplished by exothermic (resonant or near resonant) reactions of reactant ions of low kinetic energy.

3.3. Measurement Techniques for Gas Phase Reactions of Ions

3.3.1. Unimolecular Reactions of Ions

The following measurement techniques utilizing tandem mass spectrometers and the information derived from such studies have been reviewed earlier.

1. Crossed ion-molecule beam studies of ion-molecule reactions with fixed or variable angle tandem instruments [40, 42-45].

2. Investigation of the fragmentation of molecular ions as a function of internal energy (breakdown diagrams) by using perpendicular type tandem mass spectrometers [8, 37].

3. The use of tandem mass spectrometers of longitudinal type for studying the energy dependences and collision-induced dissociation of positive and negative ions [38, 49, 57].

One common feature of these measurement techniques is that the pressure of the reacting gas in the reaction region or collision chamber of the instrument is very low (only of the order of 10^{-6} to 10^{-5} torr) and is held constant. At these pressures, the mean free path of molecules is of the order of meters, so that the probability of collisions occurring between an ion and a molecule or an ion and another ion, is very small. Consequently, anything that happens to the molecular ion is unimolecular dissociation and/or deactivation by photon emission. The ions formed in this way are called primary ions because they represent the first generation of ions which are produced at all. The relative intensities of the various primary ions as a function of internal energy of the parent molecular ion constitute the breakdown diagram of the reactant molecule considered [8, 37, 19].

When investigating the breakdown diagram of a given molecule, the kinetic energy of the incident ion is changed stepwise between 900 and ca 2 eV and the mass spectrum is measured at 5 to 10 different kinetic energies. The velocity dependence of mass spectra gives information about whether the incident ion can cause proton and hydride ion transfer reactions or not. Metastable ions which may be present occasionally, allow the identification of ions in long-lived excited states as a function of internal energy of the parent molecular ion [58-60].

3.3.2. Ion-Molecule Reactions at Elevated Pressures

The technique for studying the kinetics and mechanisms of consecutive ion-molecule reactions in the gas phase by the use of the ion-impact method has been introduced by the present author [12-17] and accepted for use in other laboratories ([61, 38, 62] and references therein). The methods of analyzing the results have been fully described [10-12, 63, 64] and have been the object of a rigorous theoretical treatment [63, 64]. Recently [65], this theory has been modified to be valid not only for electron transfer, proton transfer, hydride ion transfer and ion association reactions of ions but also for the unimolecular dissociation and deactivation by photon emission of long-lived metastable ions [65].

When studying unimolecular reactions of ions the gas pressure of the reactant molecules in the reaction chamber is kept constant at a low value ($\leqq 10^{-5}$ torr) in order to prevent the primary ions from reacting with other molecules. However, if the gas pressure is increased the primary ions, i.e., the first generation of ions may react with molecules within the reaction chamber to form a second, third, etc., generation of ions via consecutive unimolecular and/or ion-molecule reactions. Correspondingly, these ions will be called secondary, tertiary, and so on.

Let us suppose that the initial ionization of molecules in the reaction chamber is caused by a beam of slow incident ions which have only one recombination energy. Incident ions of this kind result in monoenergetic ionization of target molecules and monoenergetic excitation of the molecular ions created as a result of exothermic electron transfer reactions. The result of this is that all of the consecutive unimolecular and ion-molecule reactions that can occur will be initiated by molecular ions in a selected internal energy state. The reactions taking place after monoenergetic ionization constitute a continuously branched chain of reactions. Evidently, the consecutive reactions of ions that can take place in a given gaseous substance after ionizing some of its molecules monoenergetically, will be determined entirely by the internal energy of the monoenergetically excited parent molecular ions.

It means that molecular ions with zero or small excitation energy will usually remain stable. Their subsequent reactions may be easily examined by increasing the gas pressure in the reaction chamber. On the other hand, molecular ions with a relatively large amount of excitation energy will usually dissociate into different primary fragment ions immediately after they have been created, i.e., before they had a chance to react with neutral molecules. Therefore, the chemical composition and relative abundances of the primary ions may be obtained from the breakdown diagram of the molecular ion at the energy that corresponds to the excitation energy of the parent molecular ion. This is valid even at elevated gas

pressures in the reaction chamber and irrespectively of whether the parent molecular ions may dissociate or not.

The subsequent unimolecular and ion-molecule reactions of one kind of monoenergetically excited molecular ion will be described by different reaction schemes depending upon the amount of excitation energy of the molecular ion considered. Reaction schemes corresponding to subsequent reactions of molecular ions in selected electronic states have been obtained earlier in our laboratory by using a tandem mass spectrometer of perpendicular type in which the initial ionization of molecules is accomplished by ion impact (see, e.g., Ref. [10-17, 66, 67]). The results reported so far by us and by others [38, 39, 61, 62] using the same measurement technique as we, support the conclusion that the ion impact method is suited for studying reactions of ions in selected electronic states. Evidence also suggests that the theory [63-65, 10, 11] agrees well with experiments.

On the contrary, ionization by electrons or photons will always result in molecular ions whose internal energies are distributed continuously over a broad energy range. The width of energy distributions of this kind may be up to 8-10 eV (cf. p. 12 in Ref. [19] and references therein). Consequently, the product ion distributions obtained by using electron or photon impact are due to unimolecular and ion-molecule reactions of molecular ions with various amounts of internal excitation energy. The reactions initiated by molecular ions in different selected energetic states will take place simultaneously and cannot be separated in space or time. Consequently, the reaction schemes corresponding to the reactions of one kind of monoenergetically excited molecular ion cannot be determined by electron or photon impact.

In the most general case, the continuously branched chain reactions initiated by one kind of monoenergetically excited molecular ions have the following characteristics.

1. The kinetic order of an ion is defined as the number of subsequent reactions that result in the formation of the ion considered. The set of those reactions which result in the production of a particular ion, X_n^+, of order n, constitute a (reaction) sequence. Each ion in such a sequence of reactions may cause a finite number of parallel reactions. Generally, parallel reactions are those in which precursor ions of the same kind and the same kinetic order react in several independent ways, leading to product ions of the same or different kinds.

2. Each reaction that occurs may signify whichever of the following alternatives:

(a) the transfer of an electron, a proton, or a hydride ion,

(b) the association of a reactant ion and a molecule, or

(c) the deactivation of the reactant ion either by unimolecular dissociation or by photon emission.

The theory [64, 66] gives the following results if we consider only bimolecular reactions of ions occurring at relatively low gas pressures and assume that:

(a) the initial ionization caused by the incident reactant ions is monoenergetic,

(b) the product ions formed in the reaction chamber are analyzed in a direction perpendicular to the beam of the incident ions, and the number of incident ions entering the collision chamber per unit time is held constant.

In this case the intensity, I_n, of an ion of order n is:

$$I_n \sim N^n \cdot E^{-(n-1)/2} \cdot l^{(n-1)/2} \cdot \Lambda_n \qquad (3.2)$$

where N is the gas pressure, E is the electric field strength and l the path length for an unreacting primary ion in the reaction chamber. Λ_n is a dimensionless constant determined by the type of ion-molecule reactions and by the masses of those ions and molecules which participate in the sequence of reactions being considered.

Formula (3.2) infers that there are three methods for determining the kinetic order (n) of ions experimentally. If two of the quantities N, E, and l are held constant, log (I_n) as a function of the logarithm of the third parameter should be a straight line, at least at low pressures, and the slope of this line equals the requested kinetic order n. The results discussed in Chapter 5 have been obtained by using this so called ion-intensity-pressure method.

For a certain reaction of an ion of order i,

$$X_i^+ + M \xrightarrow{k_i} X_{i+1}^+ + (\text{Neutral})_{i+1} \qquad (3.3)$$

the rate constant k_i is given by the expression:

$$k_i = \frac{I_{i+1}}{I_i \, N \tau_i} \times \frac{\Lambda_i}{\Lambda_{i+1}} \qquad (3.4)$$

Here, I_i and I_{i+1} are the intensities of the ions X_i^+ and X_{i+1}^+, respectively. Physically, τ_i signifies the time that an unreacting X_{i+1}^+ ion which is initially at rest at the axis determined by the beam of reactant ion, will need for a free flight to the exit slit for the product ions. (For the incident ions i = 0 and for the primary ions i = 1.)

When plotting reaction schemes, the symbols of the neutral reactant and products will be omitted in order to simplify our notations. Accordingly, reaction (3.3) will be written as:

$$X_i^+ \xrightarrow{k_i} X_{i+1}^+ \qquad (3.5)$$

3.3.3. Experimental Methods for Comparing the Reactivity of Gaseous Ions

There are four alternative means for producing one kind of (reactant) ion in different energetic states and to control the population of molecular and fragment ions in these states. These are in turn the variation of:

1. the kinetic energy of the electrons ionizing a gaseous sample in the ion source,

2. the composition and pressure of the sample in the ion source,

3. the recombination energy (and composition) of the incident ions ionizing a gaseous sample in the reaction chamber, and

4. the composition and pressure of the sample in the reaction chamber.

The first (electron energy) method is extensively used [38, 57] for studying the effects of internal energy on ion-molecule reactions and the collision induced dissociation of ions in selected internal energy states (cf. [68]).

The second method means the production of ions in the ion source through consecutive ion-molecule reactions after ionization by electron impact. Besides the gas pressure, the energy of the ionizing electrons may also be varied in order to control the population of the internal energy states. Consecutive ion molecule reactions in pure gases allow the production of beams of e.g., ion clusters such as $H^+(H_2O)_n$ with n = 1, 2, 3, ..., and protonated molecules (MH^+). Consecutive ion-molecule reactions occurring in a mixture of two or more gaseous substances may yield ions of two different origins:

1. ions produced by unimolecular and bimolecular reactions in which only molecules of one kind participate, and

2. "hybrid ions" produced in those sequences of unimolecular and bimolecular reactions in which molecules of more than one gaseous component participate. Examples for the production of ions of this kind are,

a) HF^+ from a mixture of $CClF_3$ and H_2O,

b) N_2OH^+ from a mixture of N_2O and H_2O, and

c) CHO^+, $C_2H_2O^+$, $C_2H_3O^+$, and $C_2H_4O^+$ from a mixture of CH_4 and CO (cf. [10]).

The third method means the ionization of one kind of molecule in the reaction chamber by using incident ions of different recombination energy. In these experiments, the population of internal energy states is controlled by changing the exothermicity of the ionizing reactions. As already noted, a tandem mass spectrometer is ideally suited for using this method for producing ions in selected energy states since the regions where the reactant ions are produced and where they react, are physically separated and translational and internal reactant ion excitation can be independently controlled. The composition of the primary ions as a function of internal excitation energy of the parent molecular ion is given by the breakdown diagram of the reactant molecule.

The fourth method implies the production of state selected ions by consecutive ion-molecule reactions in the reaction chamber after ionization with slow incident positive ions in known selected internal energy state(s). Since the molecules initiating consecutive ion-molecule reactions in the reaction chamber can be ionized monoenergetically, this method offers the most precise control of the population of internal energy states of ions. A beam of ions produced in this way is then used as incident ion to ionize a gaseous sample in the ion source of the third mass spectrometer in a triple instrument.

As a rule, ions of a given composition may be produced from a number of different pure substances and gaseous mixtures as a result of unimolecular reactions and/or ion-molecule reactions. The ion $C_3H_5^+$ may serve as an example. It can be produced from many hydrocarbons either as a fragment ion (i.e., as a result of unimolecular dissociation of molecular ions) or as a resultant ion of ion-molecule association reactions (e.g., in CH_4 and C_2H_4). In addition, each of the different parent ions initiating these reactions may have various amounts of excitation energy when they are formed.

The experimental methods available for comparing the reactivity of an ion of given composition differ depending on whether the ion in question is produced in the ion source or in the reaction chamber. The reactivity of ions produced in the ion source may be compared by varying the kinetic energy of the ionizing electrons and/or the gas pressure in the ion source and by examining the following characteristics of the ion to be considered.

1. The electron and ion kinetic energy dependence of cross-sections for the collision induced dissociation of the ion [38, 57] (cf. [68]).

2. The reactions caused by this ion in the reaction chamber with molecules for which we know the breakdown diagram and the mechanisms of consecutive ion-molecule reactions initiated by molecular ions in selected internal energy states.

The reaction pathways initiated by one kind of monoenergetically excited molecular ion with molecules of their parent gas as well as the rate of reaction involved may vary depending upon the amount of internal energy of those molecular ions which originate the first generation of ions. This behavior can be examined experimentally in a tandem mass spectrometer, e.g., by measuring the product ion intensities as a function of gas pressure as already noted in the foregoing section. Differences in reactivity of an ion obtained by using this or the other measuring techniques available [10, 63, 65] provide a direct proof for the existence of this particular ion in different internal energy states.

However, the absence of differences in reactivity when using incident ions with different recombination energies to ionize the parent molecules, does not prove that the ion in question will be produced in the same internal energy state even if the excitation energy of the parent molecular ion is changed. This statement is supported by the following observations.

1. The breakdown graphs of molecules usually exhibit energy ranges in which the product ion distributions are entirely independent of the excitation energy of the parent molecular ion (see, e.g., [66, 67] or the breakdown diagrams in the accompanying figures). The simplest case is when only the molecular ion is formed which does not react with its neutral counterpart except perhaps by symmetric charge transfer

$$M^+ + M \rightarrow M + M^+ \qquad (3.6)$$

2. Evidence exists that many ion-molecule reactions are insensitive to vibrational excitation of the reactant ion (cf. pp. 272-333 in Ref. [47] and pp. 374-378 in Ref. [22]).

The above mentioned methods are suited for being used in experiments with both perpendicular and longitudinal type tandem mass spectrometers. Besides these, the tandem mass spectrometer of longitudinal type offers a special technique for comparing the reactivity of gaeous ions by allowing to reduce the kinetic order of ions [69] and to examine a separate set of consecutive reactions that corresponds to a selected part of the reaction scheme.

The method of reducing kinetic orders of ions will be outlined by taking the ion chemistry of C_2H_4 as an example. Monoenergetic ionization of pure C_2H_4 at ∿15.8 eV results in the following chain of reactions at elevated pressures in the reaction chamber.

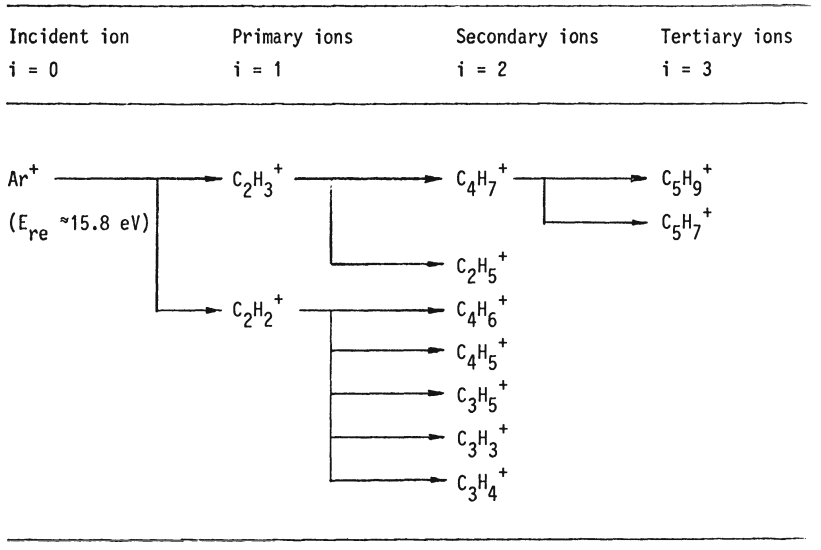

In this case the excitation energy of the parent molecular ions is $E_i \approx 5.3$ eV since $E_{re}(Ar^+) \approx 15.8$ eV, $E_{ip}(C_2H_4) \cong 10.5$ eV, and the formula $E_i = E_{re} - E_{ip}$ yields 5.3 eV. The same reaction chain is obtained also with some other incident ions such as CO_2^+ (E_{re} = 13.8 eV), CO^+ (E_{re} = 14.0 eV), and Kr^+ (E_{re} = 14.0 and 14.7 eV).

A reduction of the kinetic order of product ions may be realized by producing a beam of a selected product ion (e.g., $C_2H_3^+$ from C_2H_4) in the first mass spectrometer and by using the ions in this beam of very low (a few eV) kinetic energy to ionize molecules of their parent gas (C_2H_4) in the reaction chamber of a tandem instrument of longitudinal type. The application of the ion-intensity-pressure method yields in this case the following scheme of the resultant ion-molecule reactions.

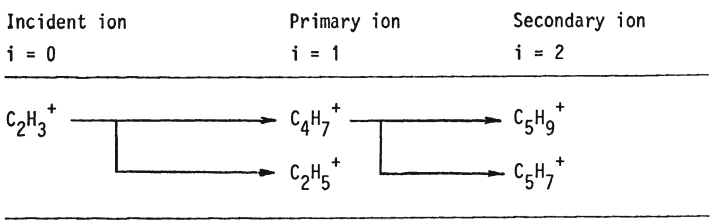

These results illustrate the following features of the method suggested for reducing the kinetic order of ions. When using one of the product ions of i-th order as incident ion for initiating sequences of reactions in the reaction chamber, the result is as follows.

(a) The kinetic order of the original product ion ($C_2H_3^+$) will be reduced from i units to zero.

(b) The kinetic orders of those ions which were originally produced by the ion chosen as incident ion, will be reduced by i units.

(c) None of the other ions originally produced by reactions of the monoenergetically excited molecular ions will be observed.

The reduction of kinetic order of ions by using this method repeatedly with different product ions, allow the examination of a separate part of the scheme of continuously branched chain reactions occurring in a pure substance or in a gaseous mixture after monoenergetic ionization. This same method will be also suited for comparing the reactivity of ions of a given composition (e.g., $C_3H_5^+$) produced from different substances in the ion source either by unimolecular dissociation of ions or by ion-molecule reactions. The reduction of kinetic orders of ions is not possible by using a tandem mass spectrometer of perpendicular type in consequence of the geometrical configuration of this instrument.

4. Triple Mass Spectrometers: Principles and Measurement Techniques

4.1. Basic Types of Fixed Angle Triple Mass Spectrometers

Instruments of this kind consist of three mass spectrometers in series with a mass and energy selected ion beam in each. They can be deduced from a tandem mass spectrometer on two ways (see Figs. 1 and 2).

(a) Firstly, by replacing the ion detector of the second mass spectrometer by a new device consisting of a decelerating electrostatic lens system, a collision (or reaction) chamber, a mass analyzer, and an ion detector following each other.

(b) Secondly, by replacing the beam of ionizing electrons in the ion source of the first mass spectrometer by a mass and energy selected beam of positive ions which are produced in a new mass spectrometer of traditional design and decelerated to a preselected terminal energy.

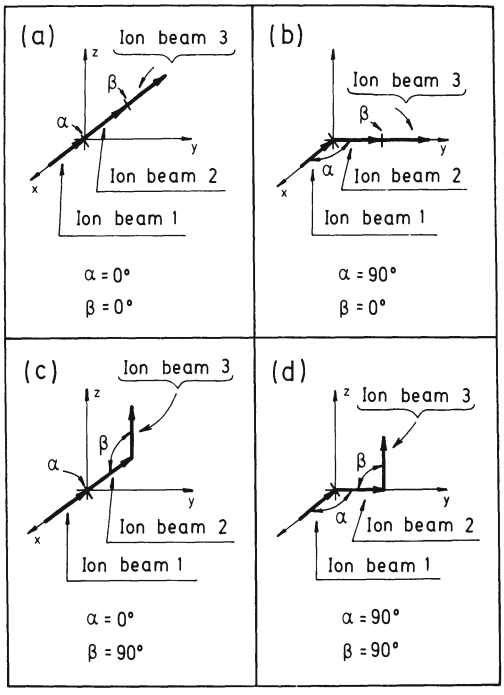

Fig. 3. Principle of fixed angle triple mass spectrometers: (a) double-in-line geometry, (b) transverse-in-line geometry, (c) in-line-transverse geometry, and (d) double-transverse geometry.

There are four basic types of fixed angle triple mass spectrometers provided that the geometric angle between the beams of incident and product ions may be zero or 90° in the ion source of the second and the third mass spectrometer, respectively. These four alternatives are illustrated in Fig. 3 in which the corresponding angles are α and β respectively. Zero degree between two subsequent ion beams corresponds to in-line geometry and 90° means transverse-geometry. Accordingly, a triple mass spectrometer may be of double-in-line type (Fig. 3a), transverse-in-line type (Fig. 3b), in-line-transverse type (Fig. 3c), or double-transverse type (Fig. 3d), respectively.

The in-line geometry exhibits the following characteristics as compared to the transverse one. First, the incident ions produced in the first of the two mass spectrometers will also run through the second instrument and will be detected together with the product ions. Second, the product ions measured are not exclusively formed by electron-, proton-, and hydride ion transfer reactions but also by the association of incident ions and molecules, eventually followed by dissociation. On the contrary, reaction sequences initiated

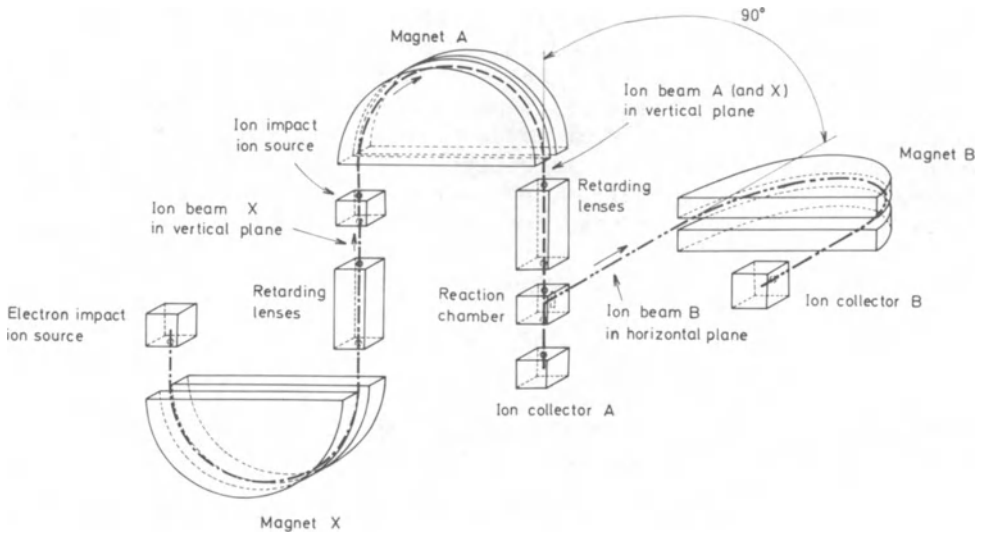

Fig. 4. A triple mass spectrometer of in-line-transverse type.

by the association of an incident ion and a neutral molecule in the reaction chamber cannot be determined if the second mass spectrometer is arranged to correspond to the transverse geometry.

The experiments reported in Chapter 5 have been carried out by using a triple mass spectrometer of in-line-transverse type. The scheme of such an instrument is shown in Fig. 4. The first ion beam was not mass selected and this prevented the use of other than noble gas ions. However, we intend to use a quadrupole mass spectrometer for this purpose in the future.

4.2. Experimental Methods for Comparing the Reactivity of Gaseous Ions

The various methods for producing ions in different internal energy states and for comparing their reactivity in a tandem mass spectrometer are described in detail in Section 3.3.3. Evidently, these methods may be used also in experiments with triple mass spectrometers. In addition, a triple instrument affords new methods of studying the reactivity of gaseous ions. Two of them will be discussed below.

A triple instrument having in-line-transverse or double-transverse geometry is especially well suited for the comparison of the reactivity of an ion in different internal energy states. The ions whose reactivity we intend to study, are produced in the ion source of the second mass spectrometer by means of ionization with slow

incident ions created in the first mass spectrometer. The ion source of the third mass spectrometer is filled with a "test sample" being in the gas phase. For each of the different test samples which come to use in these experiments we usually know the breakdown diagram and the mechanisms of consecutive ion-molecule reactions initiated by molecular ions in selected internal energy states. The population of internal energy states of the ion whose reactivity we intend to study, is controlled by ionizing the gaseous sample in the ion source of the second mass spectrometer with incident ions having various recombination energies.

The main characteristics of these experiments are as follows:

(a) The regions of reactant ion production and ion reaction are physically separated and the translational energy and the internal excitation of the reactant ion can be independently controlled.

(b) The number of different "test-samples" which can be used, is practically unlimited.

(c) In order to obtain "high sensitivity," i.e., large variations in the observed mass spectra for small deviations in the internal energy of the incident reactant ion, the breakdown diagram of the test samples chosen should show large variations in the distribution of product ions within the same energy range where the unknown internal excitation energy of the reactant ion is to be expected.

The method outlined above allows us also to compare the reactivity of gas phase ions of a given composition which may be produced from different substances with various amounts of internal excitation energy.

The method for reducing the kinetic order of ions described in Section 3.3.3 may be used also in experiments with triple mass spectrometers having in-line-transverse, transverse-in-line or double-in-line geometry. In the last-mentioned instrument the kinetic orders of ions may be reduced in two steps, i.e., both in the first and second ion source. At the same time, the ion sources of all three mass spectrometers may contain the same or different gaseous samples. This offers unique possibilities for studying consecutive ion-molecule reaction mechanisms and reactivities of ions in the gas phase.

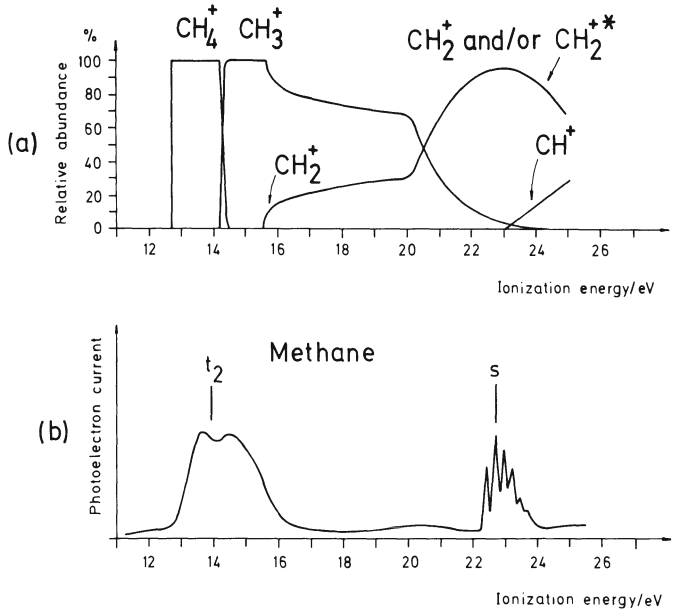

Fig. 5. (a) Breakdown diagram of CH_4 [70]. (b) Photoelectron spectrum of CH_4 [71].

5. Results

5.1. The ion CH_2^+ from CH_4

The breakdown diagram of methane determined by using the ion impact method [70] is shown in Fig. 5 together with the photoelectron spectrum [71] of the same molecule. As seen in the breakdown diagram, the fragment ion CH_2^+ is formed in small quantities in the ground state (or a state with small excitation energy) at energies between 15.5 eV and about 20 eV, but above ca 20 eV CH_2^+ is the predominating ion. An investigation of the consecutive ion-molecule reactions in methane [13] gave the following results. Above ca 20 eV the main part of the CH_2^+ ion is formed in a highly excited state and can ionize methane according to the electron transfer reaction

$$CH_2^{+*} + CH_4 \rightarrow CH_2 + CH_4^+$$

but the CH_2^+ ions formed below ca. 20 eV can not.

The reactivity of the CH_2^+ ions in these two electronic states is different because the recombination energy of the excited ion, CH_2^{+*}, is higher than the ionization potential of methane, 12.7 eV, but the recombination energy of the ground state ion, CH_2^+ is too low to allow the ionization of methane.

The spectral band in Fig. 5b covering the energy range between 12.7 eV and ca 16 eV is very broad and can be seen to contain in a double maximum. Evidently, the ionization of methane at 15.5 eV and slightly above means ionization of a bonding electron (t_2b_1). The dissociation of CH_4^+ by loss of H_2 results in the formation of CH_2^+ in the state

$$1\sigma_g^2\ 2\sigma_g^2\ 1\sigma_u^2\ 1\sigma_u^2\ ^2\Pi_u$$

The fragment CH_2^+ is expected to be linear in this state with low excitation energy (cf. [72, 73]).

Above about 20 eV the ionization of a methane molecule probably means ionization of one electron and excitation of another. The main processes for formation of CH_2^{+*} above about 20 eV are expected to result in the state

$$1\sigma_g^2\ 2\sigma_g^2\ 1\sigma_u\ 1\pi_u^2\ ^2\Sigma_u^+$$

with probably linear configuration [72].

When a linear $CH_2^+\ ^2\Pi_u$ ion is neutralized, the highest recombination energy will be obtained if the electron enters the $1\pi_u$ orbital to give

$$1\sigma_g^2\ 2\sigma_g^2\ 1\sigma_u^2\ 1\pi_u^2\ ^3\Sigma_g^-$$

Since the $1\pi_u$ electron is non-bonding, the recombination energy is expected to be equal to the ionization potential of the corresponding neutral CH_2, that is 10.4 eV. This explains the experimental observation that the methylene ions formed when ionizing methane with Ar^+ ($E_{re} \cong 15.8$ eV) cannot ionize CH_4 by electron transfer.

When the excited $CH_2^{+*}\ ^2\Sigma_u$ ion is neutralized the electron can enter the $1\sigma_u$ orbital and give a neutral methylene fragment with the structure

$$1\sigma_g^2\ 2\sigma_g^2\ 1\sigma_u^2\ 1\pi_u^2\ ^1\Sigma_g^+$$

The $1\sigma_u$ electron is bonding and its ionization potential can be expected to be equal to the ionization potential of a t_2 electron in methane. Therefore, the recombination energy must be correspondingly higher ($\gtrsim$12.7 eV) than in the preceding case, in agreement with the experimental observation reported earlier [13]. This explanation is also supported by recent quantum chemical calculations [72, 73].

The reactivity of the methylene ion in different internal energy states may be examined easily in a triple mass spectrometer by using the method outlined in Section 4.2. The results of such a comparative study are shown in Figs. 6 and 7, respectively.

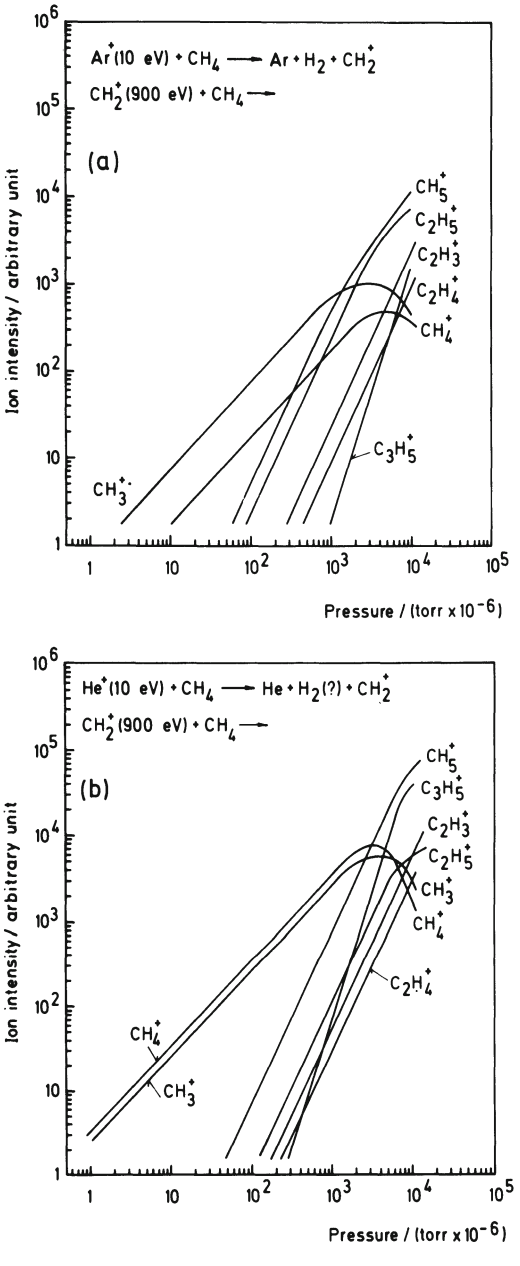

Fig. 6. Logarithmic ion-intensity pressure diagrams of CH_4 for incident CH_2^+ ions in different electronic states.

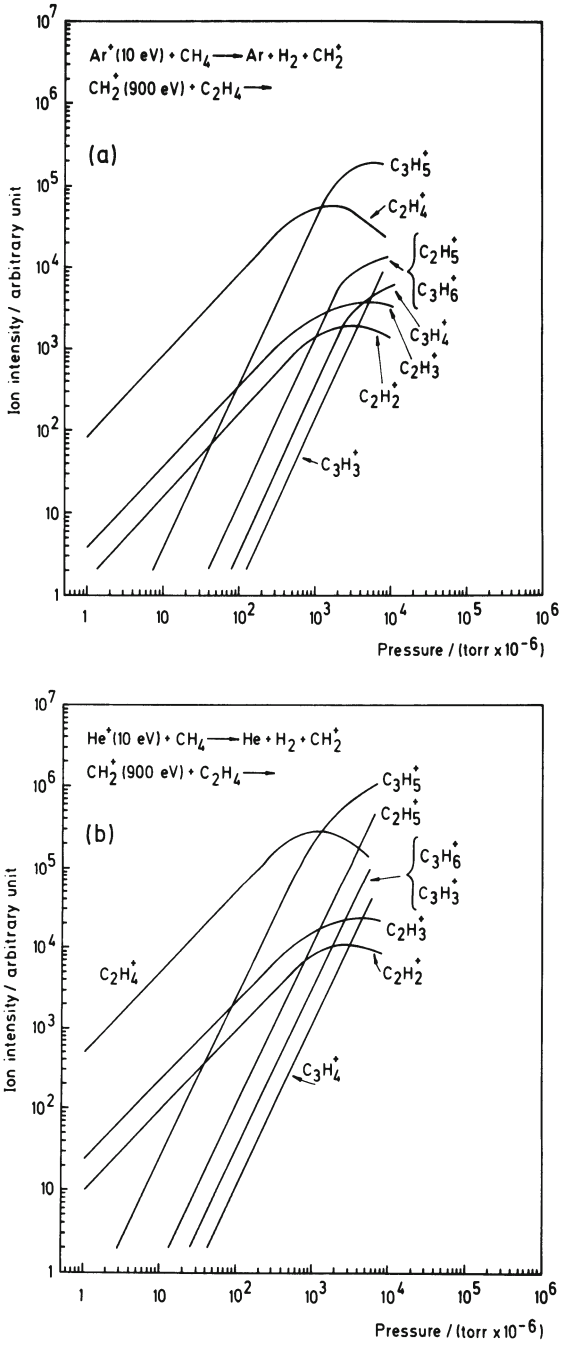

Fig. 7. Logarithmic ion-intensity pressure diagrams of C_2H_4 for incident CH_2^+ ions in different electronic states.

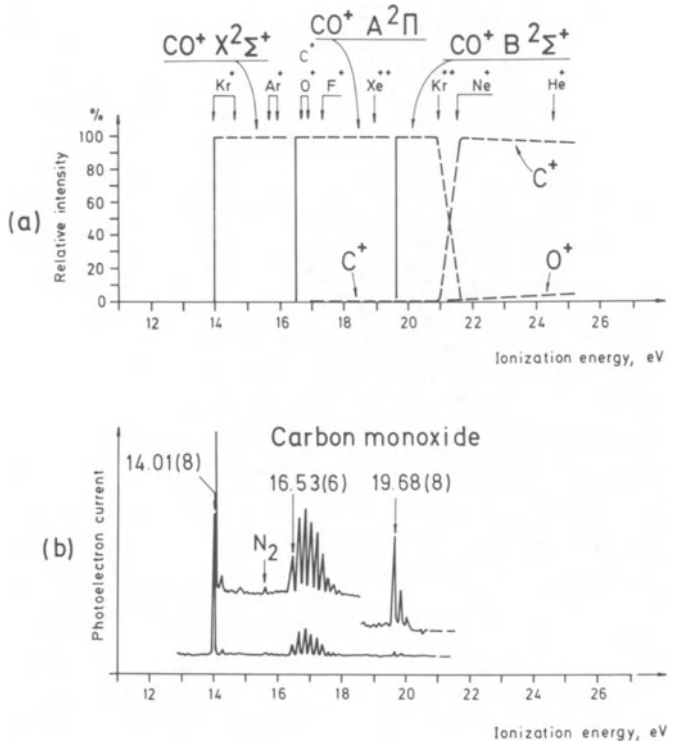

Fig. 8. (a) Breakdown diagram of CO [10]. (b) Photoelectron spectrum of CO [77].

In these experiments the population of internal energy states of the CH_2^+ ion was changed by ionizing pure methane with Ar^+ ($E_{re} \cong$ 15.8 eV and He^+ ($E_{re} \cong$ 24.5 eV), respectively. The Ar^+ and He^+ ions were produced in the first mass spectrometer and the beam of CH_2^+ in the second one. The third mass spectrometer was used for measuring the mass spectra produced from CH_4 (Fig. 6) and from C_2H_4 (Fig. 7), respectively, by the state selected CH_2^+ ions.

As seen from the comparison of Fig. 6a and 6b, the intensity of CH_4^+ produced in the third mass spectrometer is throughout larger when He^+ is used to produce the incident CH_2^+ ions instead of using Ar^+. In these two cases the CH_2^+ ions ionizing the sample gas may differ only in their internal energy states because the experimental conditions are identical in other respects.

There are differences in Fig. 6a and 6b regarding the secondary and tertiary ions too. These diferences seem to indicate that the intensity distributions for these ions are markedly influenced by

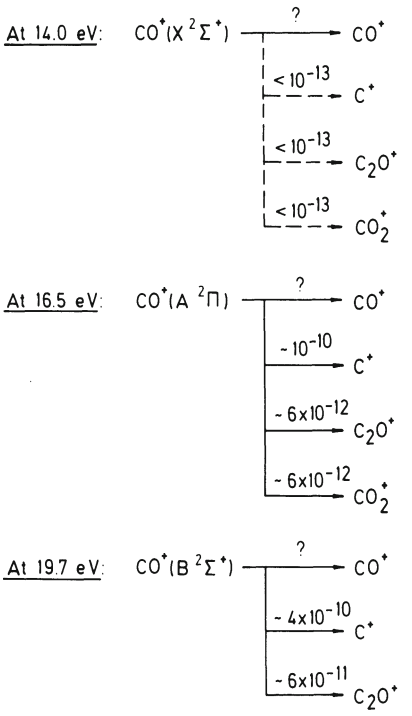

Fig. 9. Reactions of CO^+ ions in different electronic states with CO.

the internal energy state of the ion $CH_2^{\cdot+}$ that initiates the consecutive ion-molecule reactions observed.

The results in Fig. 7 were obtained by using C_2H_4 as "test substance" instead of CH_4. The differences between the ion-intensity diagrams in Fig. 7a and 7b are relatively small which can be explained as follows. As already noted, the recombination energy of CH_2^+ produced by means of Ar^+ is expected to be about 10.4 eV. This same energy should be at 12.7 eV or around this value when Ar^+ is replaced by He^+ in the first mass spectrometer. From the breakdown diagram of C_2H_4 (see Fig. 16a) it may be inferred that the molecular ion, $C_2H_4^+$, is the only primary ion at these energies. Consequently, the product ion mass spectra are insensitive to variations in incident ion recombination energy between 10.4 and about 12.7 eV. This also explains the great similarities that exist between the product ion distributions in Fig. 7a and 7b.

The results in Figs. 6 and 7 confirm our conclusions in Section 3.3.3 concerning the correlation between the breakdown diagram of a test sample and its ability to indicate small differences in reactivity of a (reactant) ion in selected internal energy states.

5.2. The CO^+ Ion from CO

The breakdown diagram [10] and the photoelectron spectrum [77] of this molecule are shown in Fig. 8a and 8b, respectively. The three bands in the photoelectron spectrum may be described in terms of the orbitals from which electrons are ejected when CO becomes ionized. The different electronic states of CO^+ as well as the various incident ions which can be used to produce CO^+ ions in these states are indicated in Fig. 8a.

The ion-molecule reactions in CO occurring when CO^+ is initially formed in different electronic states were also investigated by means of ion-impact ionization in our tandem mass spectrometer of perpendicular type [17]. The results are summarized in Fig. 9. The ground state, CO^+ X $^2\Sigma^+$, undergoes no reaction with carbon monoxide, except perhaps electron transfer. The rate constants for the formation of C^+, C_2O^+, and CO^+ must be below 10^{-13} cm^3 $mole^{-1}$ sec^{-1} because these ions cannot be detected when CO^+ is in its ground electronic state. The first excited state, CO^+ A $^2\Pi$ reacts with CO to form C^+, C_2O^+, and CO_2^+, although the rate constants for these reactions are low. The second excited state, CO^+ B $^2\Sigma^+$, reacts also with CO to from C^+ and C_2O^+ but not CO_2^+.

We have also studied the ion-molecule reactions in CO using our triple instrument, since initial ionization by electron transfer reactions of slow incident ions affords a means of forming beams of CO^+ ions in known electronic states the reactions of which can then be examined directly in the third mass spectrometer. The results of these experiments are summarized in Figs. 10 and 11. When using CH_4 as a test sample in the ion source of the third mass spectrometer (Fig. 10) the product ion distributions will be just the same with both Kr^+ (E_{re} = 14.0 and 14.7 eV) and Ar^+ ($E_{re} \simeq 15.8$ eV). This experimental observation may be explained in the same manner as the results in Fig. 7.

The recombination energy of CO^+ in its ground state equals the ionization potential of CO (14.02 eV), since the electron removed during the ionization of CO to form CO^+ in its ground state, is nonbonding as seen from the photoelectron spectrum of CO (Fig. 8a). The recombination energy of CO^+ in its first and second excited state is probably higher.

It follows from the breakdown diagram of methane (Fig. 5a) that at energies corresponding to the recombination energies of CO^+, the distributions of product ions from methane do not change significantly with ionization energy. Just the opposite is true for ethylene (Fig. 16a). This explains why the distributions of product ions from ethylene in Fig. 11 exhibit larger differences.

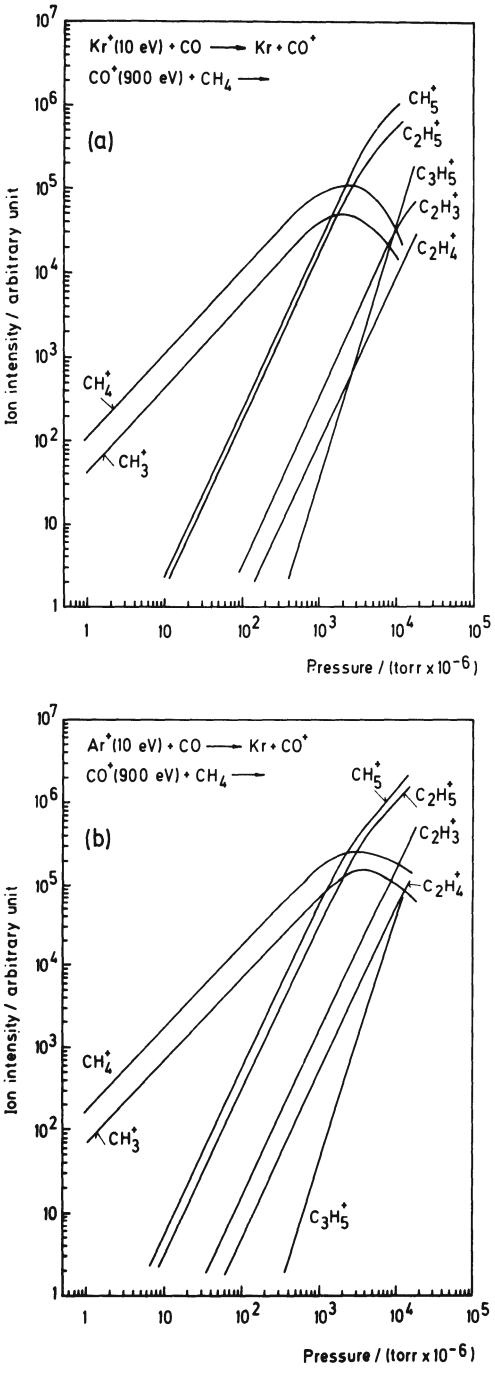

Fig. 10. Logarithmic ion-intensity pressure diagrams of CH_4 for incident CO^+ ions in different electronic states.

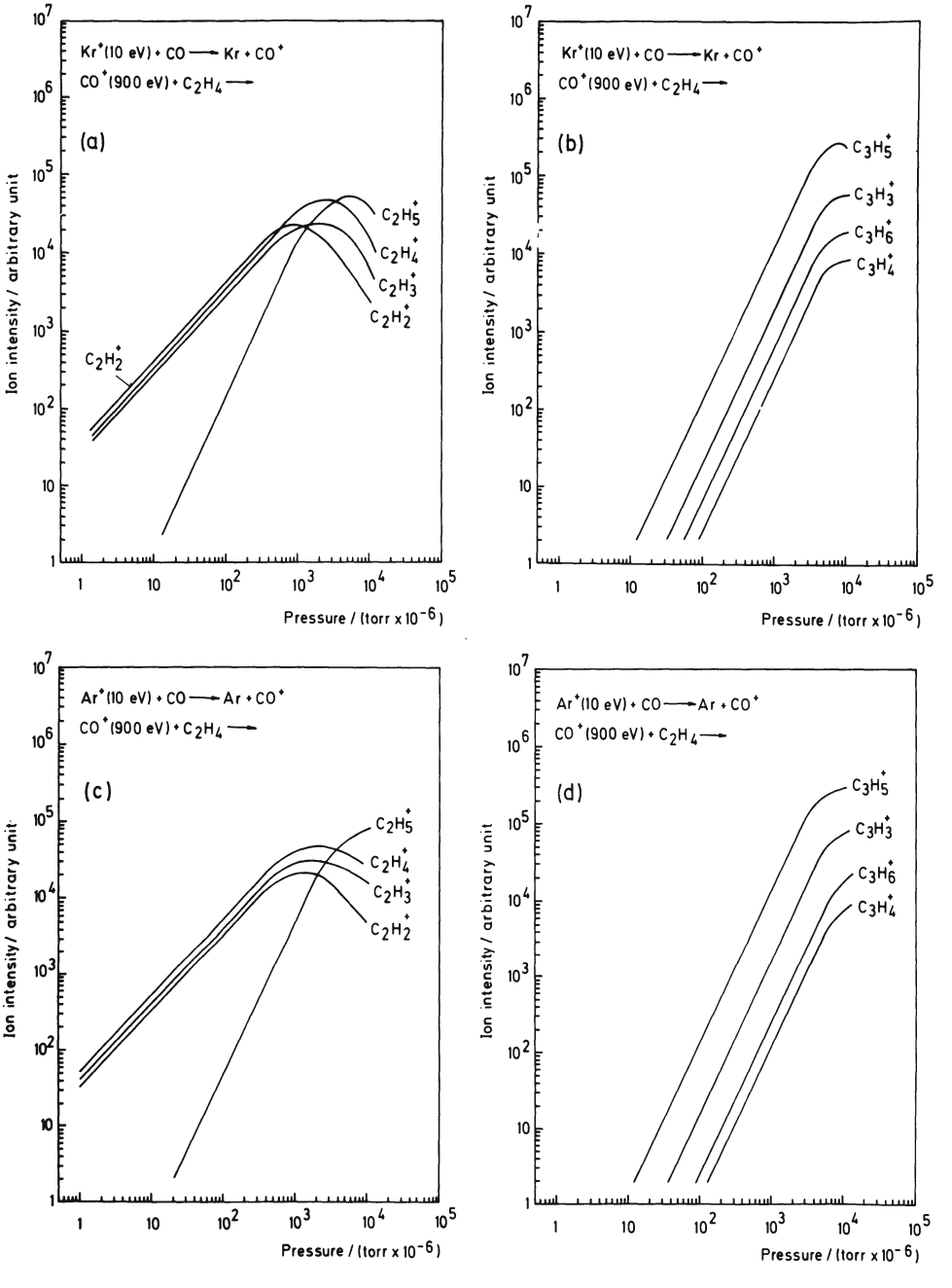

Fig. 11. Logarithmic ion-intensity pressure diagrams of C_2H_4 for incident CO^+ ions in different electronic states.

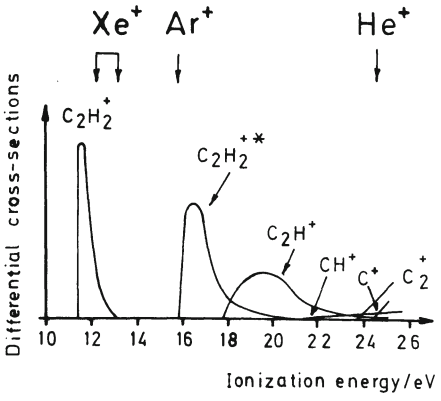

Fig. 12. Differential cross-sections for the formation of positively charged fragments from acetylene as a function of energy.

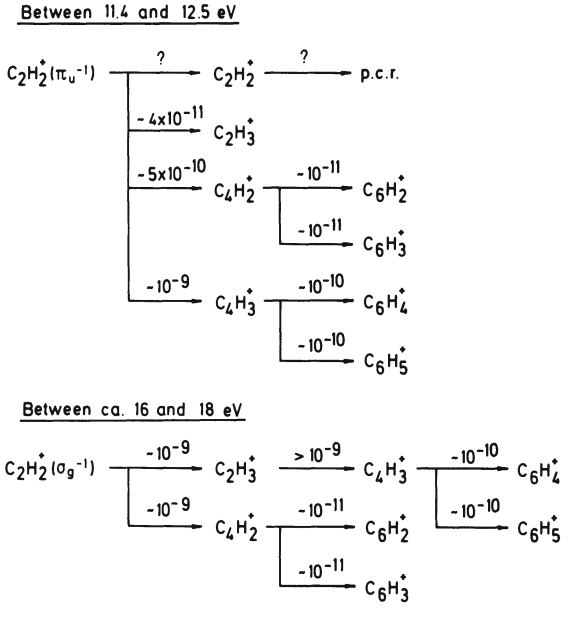

Fig. 13. Ion-molecule reactions in C_2H_2. p.c.r. = periodic chain reactions. Rate constants in $cm^3\ mole^{-1}\ sec^{-1}$. Comparison of the ion-molecule reactions initiated by acetylene ions in different electronic states in pure acetylene gas at pressures below ca 10^{-2} torr.

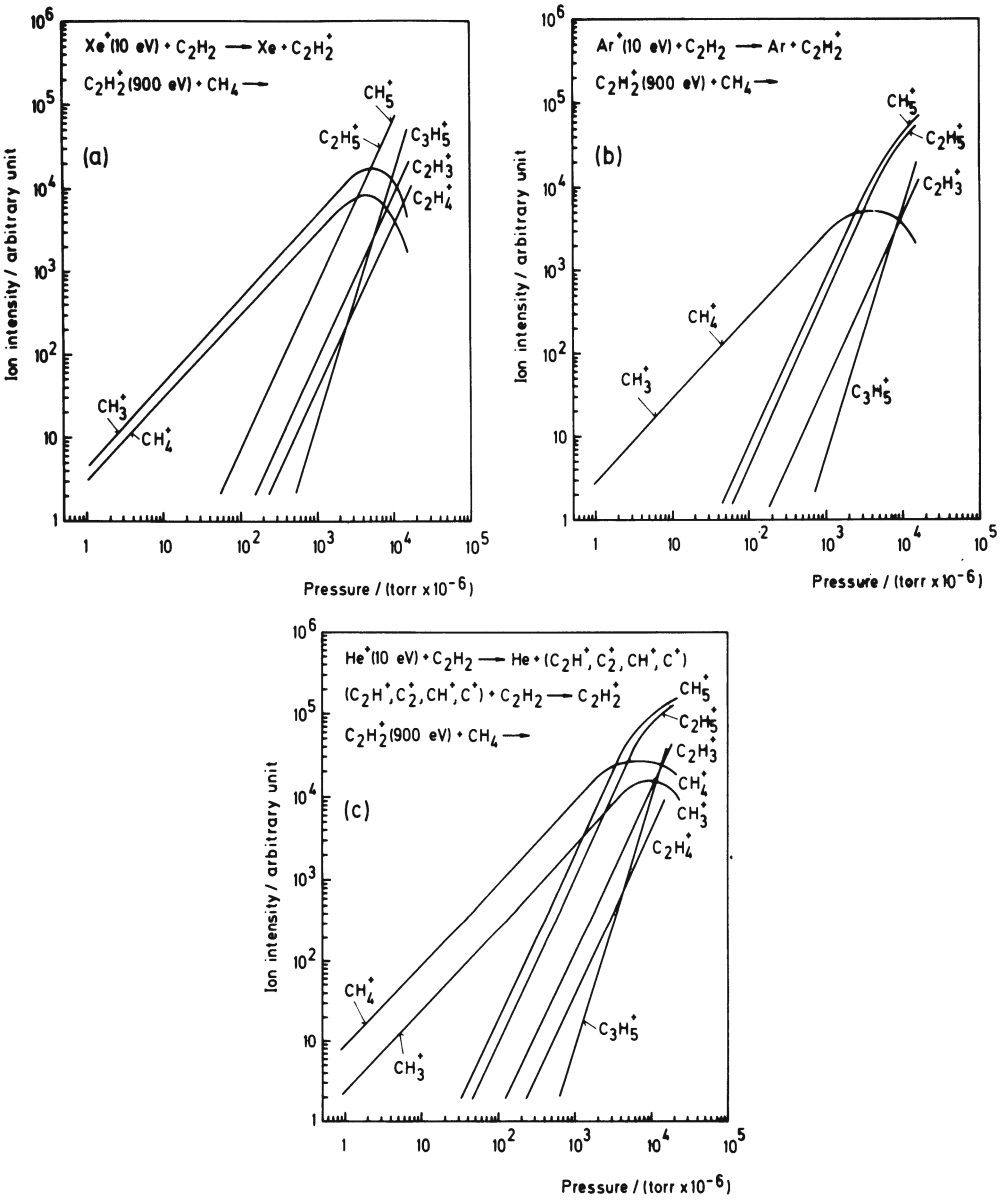

Fig. 14. Logarithmic ion-intensity pressure diagrams of CH_4 for incident $C_2H_2^+$ ions in different electronic states.

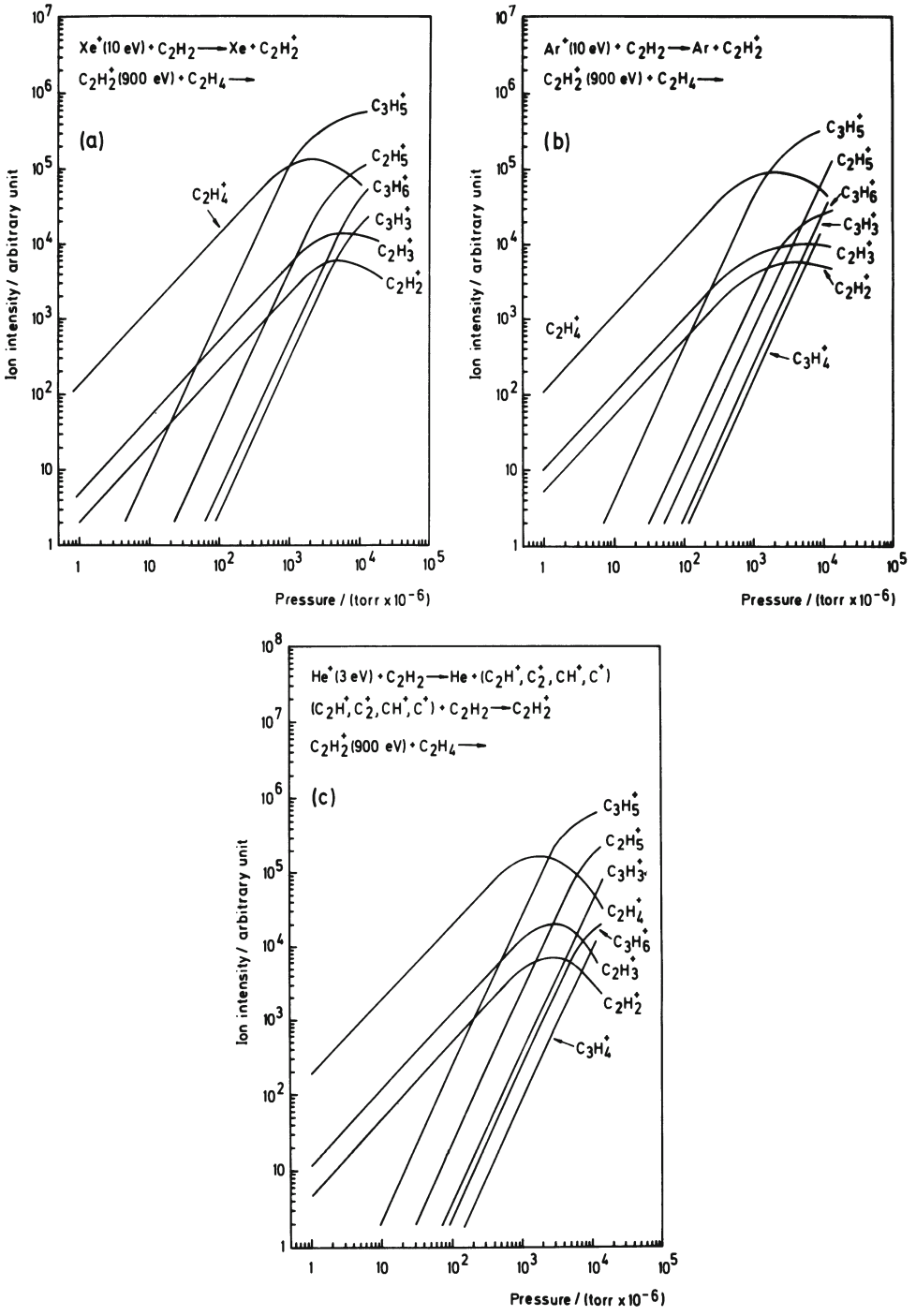

Fig. 15. Logarithmic ion-intensity pressure diagrams of C_2H_4 for incident $C_2H_2^+$ ions in different electronic states.

The lifetime of CO^+ A $^2\Pi$ (2.6×10^{-6} sec [74]) and that of CO^+ B $^2\Sigma^+$ (10^{-7} sec [75]) with respect to decay by emission of radiation to the ground state X $^2\Sigma_g^+$ are of the same order of magnitude as the time of flight for an unreacting ion in a mass spectrometer. Thus, the distribution of excited states in the CO^+ beam entering the ion source of the third mass spectrometer may be dependent on the time of flight of CO^+ ions in the second mass spectrometer.

5.3. The $C_2H_2^+$ Ion from C_2H_2

The differential cross sections for ionization of acetylene by charge transfer collisions with slow incident ions are shown in Fig. 12 [76]. At and slightly above 11.4 eV the molecular ion is formed in its ground electronic state after ionization of a C-C bonding π-electron. Removal of an electron from the $^1\pi_u$ orbital predictably excites C≡C stretching vibrations. The shape of the corresponding photoelectron band involves a short series of well resolved peaks indicating weak bonding character. This is characteristic for ionization from the highest occupied π-orbital in alkynes [77]. Above 16.36 eV the molecular ion is formed in an excited electronic state (σ_g^{-1}). This second ionization potential corresponds to ionization of a $3\sigma_g$ electron.

Using our tandem mass spectrometer of perpendicular type it was possible to distinguish the reactions of the acetylene ion in its ground electronic state with acetylene molecules from those of the acetylene ion in its excited electronic state [16]. In these experiments, the energy transferred during the initial ionization to the acetylene molecule and the excitation of the molecular ion were controlled and varied by using properly choosen incident ions. Parts of the resultant reaction schemes are reproduced in Fig. 13. According to these schemes, acetylene ions in the ground electronic state (π_u^{-1}) and in the excited electronic state (σ_g^{-1}) do not cause the same ion-molecule reactions.

Recent experiments with our triple mass spectrometer have confirmed our earlier results [16] obtained by means of a tandem instrument. The new results which we refer to are given in Figs. 14 and 15. The differences in product ion distributions shown in Fig. 14 are obviously due to the differences in internal excitation energy of the $C_2H_2^+$ ions formed after ionization with incident Xe^+, Ar^+, and He^+ ions. The result with He^+ (Fig. 14c) is interesting, because the main part of the acetylene ions used to ionize CH_4, must be formed as a result of ion-molecule reactions in pure acetylene, initiated by one or more of these primary ions, C_2H^+, C_2^+, CH^+, and probably H^+, which can be produced from acetylene at 24.5 eV (He^+).

On the contrary, the differences in product ion distributions are relatively small when using C_2H_4 as test sample (Fig. 15) in-

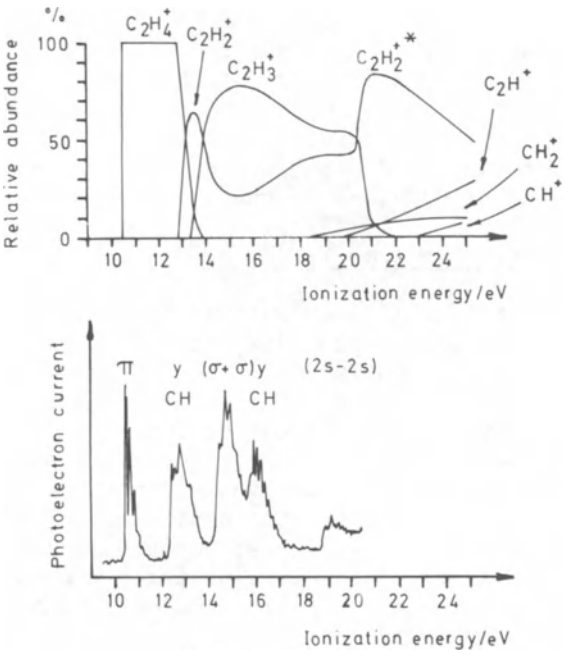

Fig. 16. (a) Breakdown diagram of C_2H_4 [9]. (b) Photoelectron spectrum of C_2H_4 [77].

stead of CH_4. The explanation of this experimental observation is that the recombination energies of the $C_2H_2^+$ ions in different electronic states are not high enough to cause dissociation of the parent $C_2H_4^+$ ions formed from ethylene (cf. Fig. 15). From the breakdown graph of ethylene (Fig. 16a) it appears, that the molecular ion, $C_2H_2^+$, is stable in the energy range between 10.48 and ca 12.8 eV. The recombination energies of the $C_2H_2^+$ ions in different electronic states are expected not to be outside of this energy range. As the electron removed from the $1\pi_u$ orbital when ionizing acetylene to form the acetylene ion in the ground electronic state (π_u^{-1}) is weakly bonding, we expect that the recombination energy will be equal to the corresponding ionization potential, 11.4 eV.

5.4. The $C_2H_2^+$ Ion from C_2H_4

It follows from the breakdown diagram of ethylene [9] shown in Fig. 16a, that the relative intensity of the acetylene fragment ion varies considerably with ionization energy. Investigation of the consecutive ion-molecule reactions in pure ethylene [12] by means of our tandem mass spectrometer has revealed that at least part of the acetylene ions formed above ca 20 eV ionization energy are in

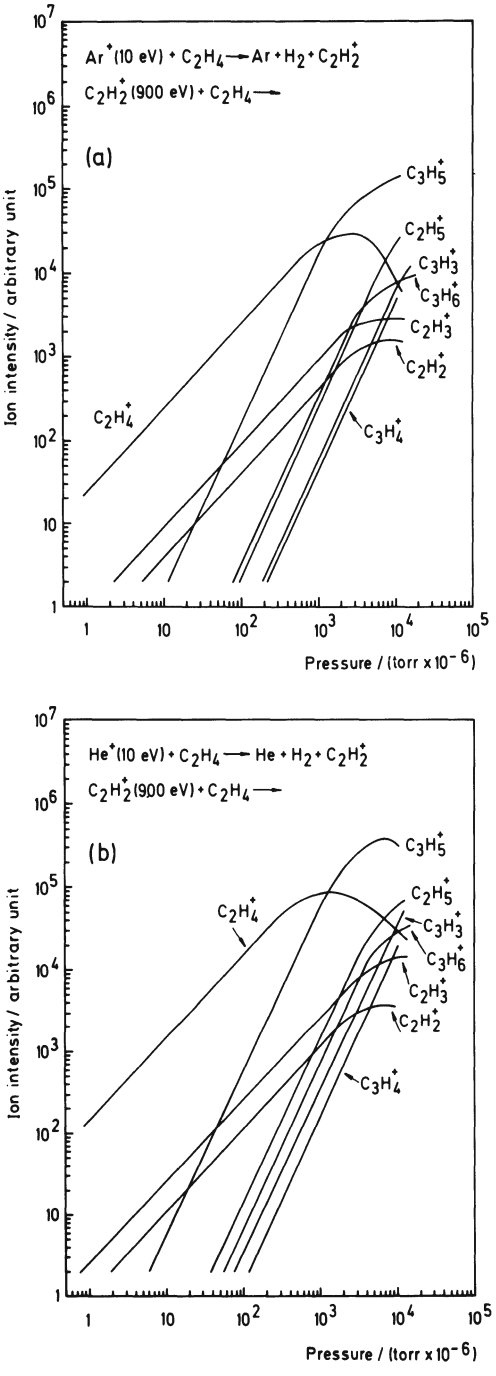

Fig. 17. Logarithmic ion-intensity pressure diagrams of C_2H_4 for incident $C_2H_2^+$ ions from ethylene in different electronic states.

an excited electronic state whose ion-molecule reactions in pure ethylene differ from those of the acetylene ions formed below ca. 20 eV.

Recent experiments with our triple mass spectrometer support this suggestion. One of the results is shown in Fig. 17. The explanation for observing small deviations only in the product ion distributions in Fig. 17a and 17b, respectively is the same as given above for Fig. 15.

Iso-butane is more suited for studying the reactivity of $C_2H_2^+$ ions in different electronic states since the distributions of ion intensities produced from this gas vary considerable in the energy range of interest. It is seen from the breakdown diagram of iso-butane which has been published earlier [58]. The results with iso-butane as test gas confirm that the acetylene ions formed above ca 20 eV ionization energy can cause ion-molecule reactions that differ from those of the acetylene ions formed below this energy from ethylene.

6. Discussion

The results available so far show convincingly the usefulness of tandem and triple mass spectrometers for studying the reactivity of gas phase ions in selected electronic states. The main advantage of this technique is that the energy transferred to the parent molecules during the initial ionization can be controlled and varied so that the dependence of the nature of the consecutive ion-molecule reactions upon the amount of this energy can be investigated.

The use of charge transfer ionization effectively resolves the complex reaction schemes resulting from other means of ionization, into simpler component schemes which correspond to monoenergetic ionization. The analysis of these schemes is both more simple and more certain. The close relationships that have been demonstrated between (consecutive) ion-molecule reactions, breakdown diagrams, photoelectron spectra as well as molecular structure and energetics, make our method suited for comparing the reactivities of gas phase ions in selected internal energy states. The results which can be obtained may constitute a solid experimental bases for quantum chemical calculations on ion-molecule reactions.

Because experiments with tandem and triple mass spectrometers have an intrinsic time delay of tens of microseconds between (reactant) ion formation and reaction, excited states of ions may undergo radiative decay to the ground state either direct or via cascade processes, before the ions reach the collision chamber where they react. Therefore, the measurement techniques described are suited for studying only relatively long-lived metastable states

of excited ions (i.e., with lifetimes $>10^{-7}$ s) present in the reactant ion beam.

Acknowledgements

This research has been supported by the Swedish Natural Science Research Council. The author wishes to express his gratitude to his fellow-workers, Messrs. Conny Hägg, Mats Lundell, Runo Stein, and Ragnar Tegner for their valuable assistance. Many thanks are also due to Mrs. Bodil Forsvik and Eva Hagen for typing.

References

1. J. B. Hasted, Physics of Atomic Collisions, Butterworths, London (1972).
2. L. G. Christophorou, Atomic and Molecular Radiation Physics, Wiley-Interscience, London (1971).
3. J. Berkowitz, Photoabsorption, Photoionization, and Photoelectron Spectroscopy, Academic Press, New York (1979).
4. A. R. West, ed., "Molecular Spectroscopy," Heyden & Son, London (1977).
5. P. Ausloos, ed., Interaction between Ions and Molecules, Plenum Press, New York (1975).
6. P. Ausloos, ed., Kinetics of Ion-Molecule Reactions, Plenum Press, New York (1979).
7. M. T. Bowers, ed., Gas Phase Ion Chemistry, Vols. 1 and 2, Academic Press, New York (1979).
8. E. Lindholm, in: "Ion-Molecule Reactions," J. L. Franklin, ed., Plenum Press, New York (1972), Vol. 2, p. 457.
9. I. Szabo, Arkiv Fysik, 31, 287 (1966).
10. I. Szabo, in: "Advances in Mass Spectrometry," Vol. 7A, N. R. Daly, ed., Heyden & Son, London (1978), p. 258.
11. I. Szabo, "Experimental determination of rate constants for consecutive ion molecule reactions," in: "Advances in Mass Spectromety," Vol. 8, A. Quayle, ed., Heyden & Son, London, (1980), p. 194.
12. I. Szabo, Arkiv Fysik, 33, 57 (1966).
13. I. Szabo, Arkiv Fysik, 35, 339 (1967).
14. I. Szabo, Int. J. Mass Spectrom. Ion Physics, 3, 103 (1969).
15. I. Szabo, Int. J. Mass Spectrom. Ion Physics, 3, 169 (1969).
16. I. Szabo and P J. Derrick, Int. J. Mass Spectrom. Ion Physics 7, 55 (1971).
17. P. J. Derrick and I. Szabo, Int. J. Mass Spectrom. Ion Physics, 7, 71 (1971).
18. W. Forst, "Theory of Unimolecular Reactions," Academic Press, New York (1973).
19. K. Levsen, "Fundamental Aspects of Organic Mass Spectrometry," Progress in Mass Spectrometry, Vol. 4, Verlag Chemie, Weinheim (1978).

20. J. W. Rabalais, "Principles of Ultraviolet Photoelectron Spectroscopy," Wiley-Interscience, New York (1977).
21. J. Sunner and I. Szabo, in: "Advances in Mass Spectrometry," Vol. 7B, N. R. Daly, ed., Heyden & Son, London (1978), p. 1383.
22. I. Koyano, "Ion-Molecule Reactions," in: "Comprehensive Chemical Kinetics, C. H. Bamford and C. F. H. Tipper, eds., Elsevier, Amsterdam (1976), p. 293.
23. J. B. Laudenslager, W. T. Huntress, Jr., M. T. Bowers, J. Chem. Phys., 61, 4600 (1974).
24. P. Ausloos, J. R. Eyler, and S. G. Lias, Chem. Phys. Lett., 30, 21 (1975).
25. M. Chau and M. T. Bowers, Chem. Phys. Lett., 44, 490 (1976).
26. V. G. Anicich, J. B. Laudenslager, W. T. Huntress, Jr., and J. H. Futrell, J. Chem. Phys., 67, 4340 (1977).
27. E. W. Kaiser, A. Crowe, and W. E. Falconer, J. Chem. Phys., 61, 2720 (1974).
28. C. E. Klots, D. M. Mintz, and T. Baer, J. Chem. Phys., 66, 5100 (1977).
29. T. Baer, "State selection by photoion-photoelectron coincidence," in: Ref. [7], Vol. 1, p. 153.
30. K. E. McCulloh, T. E. Sharp, and H. M. Rosenstock, J. Chem. Phys., 42, 3501 (1965).
31. A. Giardini-Guidoni, G. Missoni, R. Camilloni, and G. Stefani, in: "Advances in Mass Spectrometry," Vol. 7A, N. R. Daly, ed., Heyden & Son, London (1978), p. 175.
32. D. W. Turner, C. Baker, A. D. Baker, and C. R. Bundle, "Molecular Photoelectron Spectrosopy," Wiley-Interscience, New York (1970).
33. B. Brehm and E. von Puttkammer, Z. Naturforsch., Teil A, 22, 8 (1967).
34. R. Stockbauer, J. Chem. Phys., 70, 2108 (1979).
35. R. C. Dunbar, "Ion photodissociation," in: Ref. [7], Vol. 2, p. 181.
36. J. P. Maier, "Decay processes of the lowest excited electronic states of polyatomic radical cations," in: Ref. [6], p. 437.
37. E. Lindholm, in: "Ion-Molecule Reactions in the Gas Phase," Advances in Chemistry, Series, No. 58, R. F. Gould, ed., American Chemical Society, Washington, D.C. (1966), p. 1.
38. J. H. Futrell and T. O. Tiernan, in: "Ion-Molecule Reactions," J. L. Franklin, ed., Vol. 2, Plenum Press, New York (1972), p. 485.
39. S. Ikuta, K. Yoshihara, and T. Shiokawa, Bull. Chem. Soc. Japan Japan, 49, 66 (1976).
40. A. Henglein, in: "Molecular Beams and Reaction Kinetics,: Proceedings of the International School of Physics Enrico Fermi," C. Schlier, ed., Academic Press, New York (1970), p. 139.
41. G. Eisele, A. Henglein, and G. Bosse, Ber. Bunsenges. Phys. Chem., 78, 140 (1974).

42. A. Henglein, in: "Ion-Molecule Reactions in Gases," Advances in Chemistry Series, No. 58, R. F. Gould, American Chemical Society, Washington, D.C. (1966), p. 63.
43. Z. Herman and R. Wolfgang, in: "Ion-Molecule Reactions," J. L. Franklin, ed., Plenum Press, New York, Vol. 2 (1972), p. 553.
44. W. R. Gentry, "Molecular Beam Studies of Ion-Molecule Reactions," in: Ref. [6], p. 81.
45. W. R. Gentry, "Molecular Beam Techniques: Applications to the Study of Ion-Molecule Reactions," in: Ref [7], Vol. 2, p. 221.
46. W. R. Gentry, "Comments on the Gioumousis Stevenson Reaction Model," in: Ref. [6], p. 65.
47. J. L. Franklin, ed., "Ion-Molecule Reactions, Part I, Kinetics and Dynamics," Benchmark Papers in Physical Chemistry and Chemical Physics 13. Dowden, Hutchinson & Ross, Stroudsburg, Pennsylvania (1979).
48. A. Giardini-Guidoni, and L. Friedman, J. Chem. Phys., 45, 937 (1966).
49. J. H. Futrell and F. P. Abramson, in: "Ion-Molecule Reactions in the Gas Phase," Advances in Chemistry, Series No. 58, R. F. Gould, ed., American Chemical Society, Washington, D.C. (1966), p. 107.
50. T. Su and M. T. Bowers, "Classical ion-molecule collision theory," in: Ref. [7], Vol. 1, p. 83.
51. K. M. Refay and W. A. Chupka, J. Chem. Phys., 43, 2544 (1965).
52. P. M. Hierl, V. Pacak, and Z. Herman, J. Chem. Phys., 67, 2678 (1977).
53. E. Lindeman, L. C. Frees, R. W. Rozett, and W. S. Koski, J. Chem. Phys., 56, 1003 (1972).
54. D. L. Albritton, "Energy Dependences of Ion-Neutral Reactions Studied in Drift Tubes," in: Ref. [6], p. 119.
55. I. Szabo and C. Hägg, to be submitted for pulbication in the Int. J. Mass Spectrom. Ion Physics.
56. J. E. Monahan and H. E. Stanton, J. Chem. Phys., 37, 2654 (1963).
57. T. O. Tiernan, "Reactions of Negative Ions," in: Ref. [5], p. 353.
58. J. Sunner and I. Szabo, Int. J. Mass Spectrom. Ion Physics, 25, 241 (1977).
59. J. Sunner and I. Szabo, Int. J. Mass Spectrom. Ion Physics, 25, 263 (1977).
60. J. Sunner, Int. J. Mass Spectrom. Ion Physics, 32, 285 (1980).
61. T. O. Tiernan and J. H. Futrell, J. Phys. Chem., 72, 3080 (1968).
62. T. Nagatani, K. Yoshihara, and T. Shiokawa, Bull. Chem. Soc. Japan, 46, 1628 (1973).
63. I. Szabo, Int. J. Mass Spectrom. Ion Physics, 3, 103 (1969).
64. I. Szabo, Int. J. Mass Spectrom. Ion Physics, 3, 169 (1969).
65. I. Szabo, will be submitted for publication.
66. J. Sunner and I. Szabo, Int. J. Mass Spectrom. Ion Physics, 31, 193 (1979).

67. J. Sunner and I. Szabo, Int. J. Mass Spectrom. Ion Physics, 31, 213 (1979).
68. R. G. Cooks, ed., Collision Spectroscopy, Plenum Press, New York (1978).
69. I. Szabo, Physics Lett., 24A, 702 (1967).
70. H. von Koch, Arkiv Fysik, 28, 529 (1965).
71. E. Lindholm, C. Fridh, and L. Åsbrink, Faraday Discussions of the Chemical Society, 54, 127 (1972).
72. E. Lindholm, Arkiv Fysik, 37, 37 (1967).
73. C. Galloy and J. C. Lorquet, Chemical Physics, 30, 169 (1978).
74. R. G. Bennet and E. W. Dalby, J. Chem. Phys., 32, 1111 (1960).
75. R. P. Schwenker, J. Chem. Phys., 42, 1895 (1965).
76. E. Lindholm, I. Szabo, and P. Wilmenius, Arkiv Fysik, 25, 417 (1963).
77. D. W. Turner, C. Baker, A. D. Baker, and C. R. Brundle, Molecular Photoelectron Spectroscopy, Wiley Interscience, New York (1970).

LIGAND FIELD ASPECTS OF THE ELECTRONIC STRUCTURE OF MOLECULAR IONS OF METAL COORDINATION COMPOUNDS

Claudio Furlani and Giulia Mattogno

Institute of General and Inorganic Chemistry
University of Rome
Italy

The ligand field (l.f.) model describes the electronic structure of the partly filled valence shell of metal coordination compounds by means of three sets of parameters, the ligand field strength parameters, reflecting the perturbation exerted by the ligands upon the metal orbitals, the nephelauxetic ratio which is strictly connected to the covalency of coordination bonds, and the optical electronegativities representing the internal redox properties of metal complexes. The l.f. model has been so far quite successful in describing the structure and properties of chemically stable coordination compounds, and we propose to extend its use to the discussion of some aspects of the electronic structure of molecular ions produced by photoionization, and particularly of the differences from the structure and properties of the parent non-ionized molecules. Four cases will be discussed, as the removal of one electron from the parent molecule can affect (i) inner-core metal orbitals; (ii) inner core ligand orbitals; (iii) metal-centered valence orbitals or (iv) ligand-based valence orbitals.

In case (i) the equivalent core for say an octahedral complex ML_6 passes on ionization from $M(Z)^{n+}$ to $M(Z + 1)^{n+1}$, leading to slightly larger l.f. parameters (the increase in valence of M being in part counterbalanced by opposing steric effects in the adiabatically produced ML_6^{+1} species), and distinctly higher covalency implying more pronounced nephelauxetic effect, possibly seen in assigned charge-transfer shakeup satellites, and increased $X_{opt}(M)$, i.e., lower charge transfer transition energies. In some cases, the latter effect can eventually lead to redox collapse of the molecular ion, e.g., on ionization of Cu^{2+} complexes resulting in the unstable

equivalent core Zn^{3+}, against Cr^{3+} leading to redox stable Mn^{4+}. In case (ii), increase by one unit of the positive charge of one L ligand is expected to weaken substantially its donor ability, with consequent decrease of average ligand field strength, decrease in covalency, increase in $X_{opt}(L)$ and enhanced redox stability; the most evident chemical consequences are symmetry lowering and labilization, possibly leading to detachment of the ionized ligand. Valence shell metal ionization (iii) produces qualitatively the same effects as metal core ionization (however, the effective metal configuration change is $M(Z)^{n+} \rightarrow M(Z)^{n+1}$, or $d^n \rightarrow d^{n-1}$); observables can now be found in gas-phase UPS sequences of ionization energies, and several types of chemical instability can be expected as a consequence of change in d^n configuration. Thus, e.g., valence ionization of an octahedral Cr^{3+} complex leads to an effective d^2 configuration, which is Jahn-Teller unstable; a square planar Co^{2+} complex is turned into a square planar low-spin Co^{3+} species which is coordinatively unstable; octahedral high-spin Co^{2+} complexes become high-spin Co^{3+}, which is spin-state unstable. Collective ligand oxidation following ionization from ligand valence orbitals (iv) weakens slightly the ligand field (however to a different extent if bonding (σ, π) or lone pair orbitals are ionized), decreases the nephelauxetic effect, and increases $X_{opt}(L)$, eventually leading to enhanced occurrence of inverted ($M \rightarrow L$) charge transfer processes in electron-rich complexes.

SURFACE INTERACTIONS BETWEEN A WATER MOLECULE AND A FERROELECTRIC CRYSTAL OF $NaNO_2$

Caterina Ghio

Istituto di Chimica Quantistica ed Energetica
Molecolare del C.N.R.
Via Risorgimento, 35, I-56100 Pisa, Italy

The method employed in this research has been documented a few years ago [1], using as a test the same crystal considered here. Reference is made to that paper also for the description of the spatial arrangement of the atoms inside the unit cell. In the case of the isolated crystal we found that it is possible, and convenient too, to adopt a factorization (of Hartree type) of the total wavefunction, where the single factors are the wavefunctions of the Na^+ and NO_2^- ions constituting the crystal. The problem is reduced to the Hamiltonian problem of a single ion perturbed by the Coulombic interactions with the other ions L of the crystal: $H^M_{eff} = H^M + \Sigma_L V_L$, where $\Sigma_L V_L$ is the electrostatic potential generated by the remainder of the crystal. In the present case it is convenient to modify this schematization and to consider the adsorbed water molecule and a couple of ions pertaining to the crystal lattice (namely Na^+ and NO_2^-) as a unique entity. The factorization of Hartree type is maintained as far as the remainder of the crystal is concerned. The effective Hamiltonian turns out to be:

$$H^{Na^+NO_2^-\cdot H_2O}_{eff} = H^{Na^+NO_2^-\cdot H_2O} + \Sigma_L V_L$$

In this Hamiltonian, as well as in the previous one, we must perform further simplifications, concerning the explicit expression of the various V_L terms and the number of terms of the sum, in other words the dimensions of the finite portion of the crystal lattice sufficient to account for the effect of the crystal field. We have seen previously that V_L may be reduced to a potential deriving from less or more complicated sets of rigid point charges [1, 2]. The Na^+ ion is simply represented by a +1 charge, while

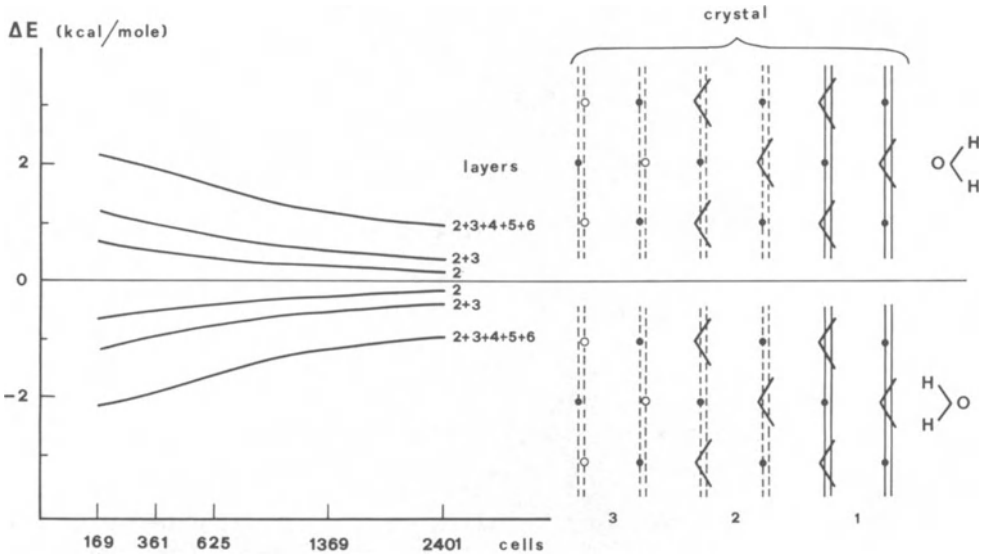

Fig. 1. Effect of the enlargment of the crystal specimen on its interaction energy with water.

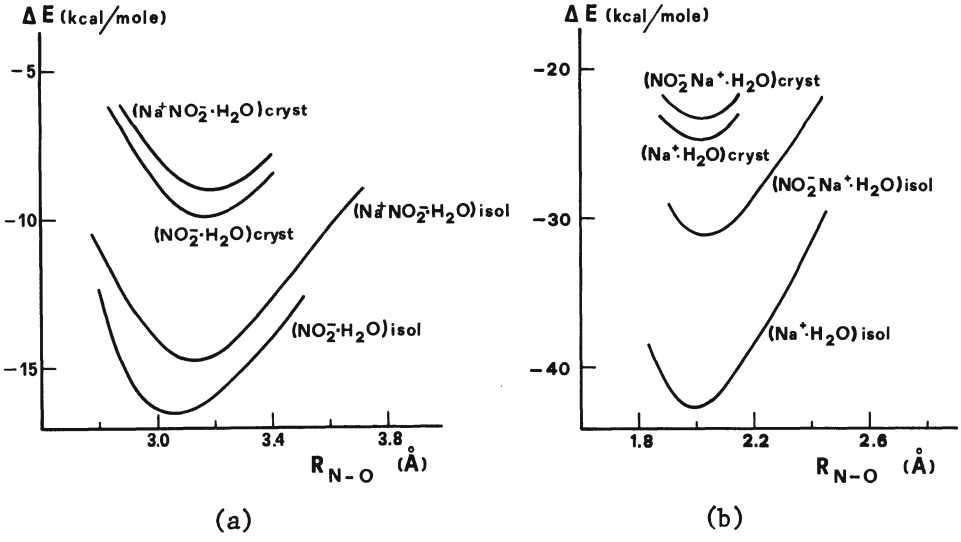

Fig. 2. Interaction energy between water and various species on the surface perpendicular to the z axis (positive part).

the NO_2^- ion is described by two models: 1P (a charge -1 in the center of charge for the ions far from z = const surface) and 9P (the same charge surrounded by other eight charges for the ions on the surface and on the underlying layer). The values and the positions of these charges selected to reproduce the SCF value of the dipole and quadrupole moments (calculated with respect to the mass center), have been scaled to minimize the difference of the description of V_L that they give with respect to the SCF description, obtained with a STO-3G basis set.

We have then determined, with purely electrostatic calculations, the dimension of the crystal sufficient to get reliable results. To do this, we have considered two positions, displayed in Fig. 1, of the water molecule on the surface of the crystal perpendicular to the z axis (in its positive part). At a fixed number of cells (fixed surface) the inclusion of additional layers produces changes in ΔE nearly equal, in absolute value, for the two H_2O molecules. At the same time an increasing of the surface gives origin to a change of ΔE of opposite sign. A rationale of the dependence of ΔE on the crystal size is easily done in terms of the field produced by the crystal specimen. A compromise between the two effects is given by the selection of crystal specimens of reduced dimensions. We have examined, with a crystal specimen corresponding to a thickness of 3 layers and to a surface extension of 169 cells, the SCF interaction between various species and water, without discarding however the possibility of performing calculations with more extended surfaces in the points that one may consider more critical.

Figure 2a shows two families of curves. The lower couple corresponds to the SCF interaction between the isolated species, that is to say, in the absence of the crystal. Between the curve of $NO_2^- \cdot H_2O$ and the one of $Na^+NO_2^- \cdot H_2O$ we can notice a displacement towards larger distances in the energy minimum and a weakening in the interaction energy. The presence of the counter-ion in fact weakens the interaction causing the equilibrium distance to lengthen.

The presence of the crystal (upper curves) weakens even more the interaction, without sensibly modifying the position of the minimum. The difference between the two curves is not marked as for the previous ones, because the counter-ion (as a charge belonging to the crystal) is present also in the lower curve. Analogous comments can be made also for Fig. 2b. The interaction energy is stronger when water is facing a Na^+ ion.

The examination of the curves pertinent to the other surface of the crystal perpendicular to z axis (negative part), not reported here, gives analogous results. We have then considered the rotations of the water around the Cartesian axes. The trend is

similar to that obtained for the isolated SCF adduct, the crystal field effect acting to reduce the interaction energy. The purely electrostatic interaction is deeper than the corresponding SCF interaction. For sake of brevity we do not report here the relative drawings, which are in agreement with chemical intuition.

We have also explored the displacement of water from an ionic site to another on both surfaces taking into account the rotations of water during the various paths.

This type of method seems to us to give a reasonably well approximated description of the interaction between molecular ions ordered in regular lattices and neutral molecules, sufficient to a first approximation treatment of the dynamics of such systems.

REFERENCES

1. C. Ghio, E. Scrocco, and J. Tomasi, in: "Environmental Effects on Molecular Structure and Properties," B. Pullman, ed., p. 329, Reidel Dordrecht (1976).
2. E. Scrocco and J. Tomasi, Adv. Quantum Chemistry, 11, 115 (1978).

Index